frontiers | Research Topics

Advanced concretes and their structural applications, volume II

Edited by
Zhigang Zhang, Cong Zhang, Dong Zhang and Jialuo He

Published in
Frontiers in Materials

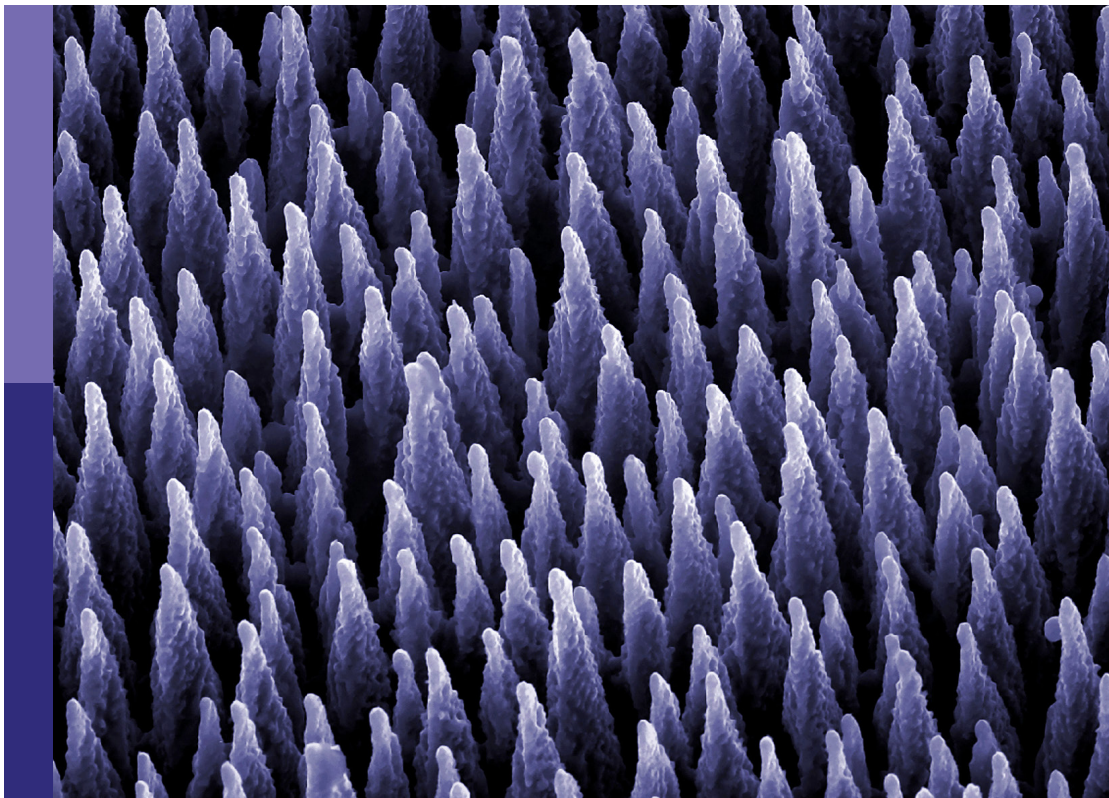

ISSN 1664-8714
ISBN 978-2-8325-2928-7
DOI 10.3389/978-2-8325-2928-7

About Frontiers

Frontiers is more than just an open access publisher of scholarly articles: it is a pioneering approach to the world of academia, radically improving the way scholarly research is managed. The grand vision of Frontiers is a world where all people have an equal opportunity to seek, share and generate knowledge. Frontiers provides immediate and permanent online open access to all its publications, but this alone is not enough to realize our grand goals.

Frontiers journal series

The Frontiers journal series is a multi-tier and interdisciplinary set of open-access, online journals, promising a paradigm shift from the current review, selection and dissemination processes in academic publishing. All Frontiers journals are driven by researchers for researchers; therefore, they constitute a service to the scholarly community. At the same time, the *Frontiers journal series* operates on a revolutionary invention, the tiered publishing system, initially addressing specific communities of scholars, and gradually climbing up to broader public understanding, thus serving the interests of the lay society, too.

Dedication to quality

Each Frontiers article is a landmark of the highest quality, thanks to genuinely collaborative interactions between authors and review editors, who include some of the world's best academicians. Research must be certified by peers before entering a stream of knowledge that may eventually reach the public - and shape society; therefore, Frontiers only applies the most rigorous and unbiased reviews. Frontiers revolutionizes research publishing by freely delivering the most outstanding research, evaluated with no bias from both the academic and social point of view. By applying the most advanced information technologies, Frontiers is catapulting scholarly publishing into a new generation.

What are Frontiers Research Topics?

Frontiers Research Topics are very popular trademarks of the *Frontiers journals series*: they are collections of at least ten articles, all centered on a particular subject. With their unique mix of varied contributions from Original Research to Review Articles, Frontiers Research Topics unify the most influential researchers, the latest key findings and historical advances in a hot research area.

Find out more on how to host your own Frontiers Research Topic or contribute to one as an author by contacting the Frontiers editorial office: frontiersin.org/about/contact

Advanced concretes and their structural applications-volume II

Topic editors

Zhigang Zhang — Chongqing University, China
Cong Zhang — Jiangnan University, China
Dong Zhang — Fuzhou University, China
Jialuo He — Washington State University, United States

Citation

Zhang, Z., Zhang, C., Zhang, D., He, J., eds. (2023). *Advanced concretes and their structural applications-volume II*. Lausanne: Frontiers Media SA.
doi: 10.3389/978-2-8325-2928-7

Table of contents

frontiers | Frontiers in Materials

TYPE Original Research
PUBLISHED 11 October 2022
DOI 10.3389/fmats.2022.1007868

OPEN ACCESS

EDITED BY
Zhigang Zhang,
Chongqing University, China

REVIEWED BY
Shan Gao,
Harbin Institute of Technology, China
Yifei Hao,
Hebei University of Technology, China
Jiangtao Yu,
Tongji University, China

*CORRESPONDENCE
Bo Wu,
bowu@scut.edu.cn

SPECIALTY SECTION
This article was submitted to Structural Materials,
a section of the journal
Frontiers in Materials

RECEIVED 31 July 2022
ACCEPTED 28 September 2022
PUBLISHED 11 October 2022

CITATION
Xiong Y, Chen Y, Wu B and Zhao G (2022), Fire resistance of composite shear walls filled with demolished concrete lumps and self-compacting concrete.
Front. Mater. 9:1007868.
doi: 10.3389/fmats.2022.1007868

Fire resistance of composite shear walls filled with demolished concrete lumps and self-compacting concrete

Yan Xiong[1], Yaxin Chen[2], Bo Wu[1]* and Guowei Zhao[3]

[1]State Key Laboratory of Subtropical Building Science, South China University of Technology, Guangzhou, China, [2]School of Civil Engineering and Transportation, South China University of Technology, Guangzhou, China, [3]Guangdong Chuangcheng Construction Supervision and Consulting Limited Liability Company, Guangzhou, China

The recycling and reuse of waste concrete is conducive to promoting the sustainable development of resources and practicing the concept of green development. Demolished concrete lumps (DCLs) and self-compacting concrete (SCC) made from waste concrete take full advantage of their recyclability. In order to fully utilize the advantages of demolished concrete lumps and self-compacting concrete in construction, applying demolished concrete lumps and self-compacting concrete to composite shear wall structures is an effective way to reduce costs and improve industrial production. In this paper, a new composite shear wall filled with demolished concrete lumps and self-compacting concrete is proposed, and its fire performance is investigated. The shear wall combines edge constraints of concrete-filled steel tubes, demolished concrete lumps and self-compacting concrete. In order to facilitate the mass pouring of demolished concrete lumps, a cavity is formed between the steel tubes at the ends and the precast walls on both sides. A double-sided fire tests was conducted on three composite shear wall specimens filled with demolished concrete lumps and self-compacting concrete at a constant axial compression ratio, where the fire-retardant coating and the wall width-to-depth ratio were considered as the main test parameters. The specimens were able to steadily withstand the predetermined axial loads during the fire resistance time of 180 min and showed good fire resistance. The concrete temperature variation trends of the three specimens in the wall section were basically the same. The fire-retardant coating on the concealed column had a significant effect on the section temperature of the steel tube, while increasing the wall width-to-depth ratio had little effect. When the axial compression ratio was 0.19, the specimens were in the expansion stage within 180 min and no compression occurred. The results show that the expansion deformation of the shear wall sprayed with fire-retardant coating on the outer surface of the concealed column is smaller than that of the shear wall without fire-retardant coating, and the axial deformation of the composite shear wall infilled with demolished concrete lumps and self-compacting concrete is not affected by increasing the wall width-to-depth ratio.

KEYWORDS

composite shear walls, fire performance, demolished concrete lumps, self-compacting concrete, experimental study

1 Introduction

Nowadays, the shear wall structure has been widely used in high-rise and super-high-rise buildings. In case of fire, it is easy to cause huge casualties and property damage. Meanwhile, shear walls are used in high-rise buildings not only as load-bearing members, but also as firewalls.

Therefore, a lot of work has been done on the fire performance of shear wall structures. Lee et al. (2013) tested the overall fire performance of 8 RC shear walls and investigated the effects of axial load level, wall thickness and other parameters on the fire performance of the walls. Ryu et al. (2020) also investigated the effects of fire time, concrete compressive strength, and heated areas on the fire resistance and mechanical properties of RC walls. Liu et al. (2010) investigated the effects of fire exposure, reinforcement ratio and the axial load under fire on the seismic behavior of RC shear walls. Bamonte et al. (2016) conducted three-sided fire tests on 3 RC walls with different load levels and boundary conditions, which showed that the applied compressive load and boundary conditions had significant effect on the magnitude of the displacements. Kang et al. (2016) conducted experiments to investigate the effects of thickness and moisture on the temperature distribution of RC walls exposed to fire.

In addition, the fire resistance of concrete shear walls with different filling materials was also investigated. Previous investigations (Go et al., 2012; Hertz, 2018) showed that reinforced lightweight aggregate concrete walls outperformed reinforced normal weight concrete walls in terms of basic mechanical properties such as ultimate load, yield load and stiffness. In other experimental studies (Ngo et al., 2013; Xiao et al., 2017; Nguyen et al., 2018) on high-strength concrete walls exposed to fire, the results showed that high-strength concrete spalled more severely when exposed to fire compared to normal-strength concrete.

Also, the fire performance of new composite shear walls has been explored. Wei et al. (2019) studied the fire performance of concrete-filled double-steel-plate composite walls with shear studs, and the results showed that fire performance of composite walls was severely affected by the axial compression ratio, the eccentricity of the axial load, and the bond strength between shear studs and concrete. Kang et al. (2019) also studied the effects of wall thickness and axial load on the capacity of fire-damaged concrete walls, and the investigation found that wall thickness had an effect on the bearing capacity of the fire-damaged walls. Du et al. (2022) conducted a one-sided fire test on four laminated composite walls with truss connectors, and found that the axial compression ratio and truss spacing to thickness ratio had a significant effect on the deformation of the walls.

The tests were also numerically analyzed and simulated. Mueller and Kurama (2019) analyzed the numerical model of RC bearing wall specimens under fire. Morita et al. (2017) performed one-sided fire tests and numerical simulations on a scaled model of reinforced concrete (RC) shear walls. It was found that the wall specimens had different deformation behaviors at different stages of the test and also gave finite element analysis results for the reduction of concrete transient strain, which were consistent with the test results. Chen et al. (2020) investigated the structural behavior and the degradation of the bearing capacity of RC walls under one-sided fire, developed a structural model, and elucidated the damage mechanism of RC walls in fire. Kumar and Kodur (2017) proposed a numerical model based on generalized three-dimensional finite elements, which could predict the thermodynamic behavior of RC walls in fire. Ni and Birely (2018) conducted numerical simulations to investigate the effect of physical seismic damage on the fire resistance of RC walls and found that cracks had a significant effect on the fire resistance of the walls.

As urbanization continues to accelerate, construction activities not only generate a large amount of construction waste, but also increase the demand for natural resources such as sand and gravel. For those waste concrete, if disposed of by open pile or simple landfill, it will not only occupy the land, but also cause serious environmental pollution. Therefore, in order to promote the sustainable development of resources and protect the environment, the recycling and reuse of waste concrete is particularly important. Recycled concrete is divided into recycled aggregate concrete (RAC) and recycled lump concrete (RLC). RAC is the most common sustainable product that uses recycled coarse aggregate (RA) produced by crushing the waste concrete to aggregate size to replace natural coarse aggregate (NA). RLC is produced by directly mixing large size demolished concrete lumps (DCLs) with natural aggregate concrete (NAC) (Limbachiya et al., 2007). DCLs are made by mixing new concrete and waste concrete blocks with characteristic sizes ranging from 60 mm to 300 mm. Compared with RAC, DCLs have the advantages of improved recycling efficiency of waste concrete, simplified the processes, and reduced recycling cost and energy consumption (Jian and Wu, 2021).

In the past 2 decades, industrialized construction has attracted more attention in many countries, including China, as a modern construction technique to replace the traditional cast-in-place concrete construction method (Wang et al., 2021). Compared with cast-in-place concrete structures, precast concrete structural systems offer better quality control, higher

construction speed, and lower construction costs (Pavese and Bournas, 2011).

Industrial fabrication of DCLs components in plants has more significant advantages (Wu et al., 2018). In this paper, a new composite shear wall filled with DCLs and self-compacting concrete (SCC) is proposed. This composite shear wall combines edge restraints of concrete-filled steel tubes, DCLs and SCC. To facilitate the mass casting of DCLs, the steel tubes at the ends and the precast walls on both sides are enclosed with a cavity formed in between. Self-compacting concrete is used for the new concrete cast inside the cavity and steel tubes, which can improve the construction efficiency of DCLs and SCC and avoid the vibration problems caused by casting concrete inside the cavity. Herringbone treatment is used for inner interface of precast walls. The transverse reinforcement in the wall extends to the end steel tube, so that the cast-in-place part and the precast part can better form a single unit and share the force.

For the study of the fire resistance of shear walls, most tests and analyses have been conducted on ordinary reinforced concrete shear walls, but few studies have been conducted on the mechanical properties of composite shear walls at high temperature. In this paper, to study the fire resistance of this new composite shear wall filled with DCLs and SCC, three composite shear wall specimens filled with DCLs and SCC were tested for fire resistance at constant axial compression ratio. The temperature field distribution of shear walls in double-sided fire with different test parameters (fire-retardant coating for steel tubes, the wall width-to-depth ratio) was investigated. In addition, the effects of different parameters on the fire resistance of shear walls were analyzed and the fire resistance limits of shear walls under double-sided fire were obtained.

2 Experimental program

2.1 Specimen design

Three composite shear wall specimens filled with DCLs and SCC were designed, bounded by the edges of concrete-filled square steel tubes. These specimens were numbered SW1 to SW3 respectively. All specimens were subjected to double-sided fire tests. The dimensions and structure of the specimens are shown in Figure 1. All specimens had rectangular cross-sections, of which SW1 and SW2 had 1,000 mm × 200 mm and SW3 had 1,200 mm × 200 mm with a wall height of 1,500 mm. The concealed columns of the specimens were thin-walled square steel tube columns filled with DCLs and SCC. The outer lengths of the steel tubes of specimens SW1 to SW3 were 200 × 200 mm with a nominal thickness of 2 mm (the measured thickness was 1.77 mm). Slots were cut in advance on the side of the steel tube in contact with the precast concrete wall. The size and number of slots were determined according to the number and diameter of the transverse reinforcement of the precast walls. The two ends of the transverse reinforcement of the two precast walls were respectively inserted into the pre-drilled slots of the two square steel tubes. The first transverse reinforcement at the upper and lower ends was threaded and tightened with nuts, while the rest of the transverse reinforcement was plain and fully extended into the square steel tubes to ensure the integrity of the precast walls and the thin-walled square steel tube concealed columns. According to the experiment, the upper and lower ends of the walls were designed with reinforced concrete rigid beams, whose stiffness was much greater than that of the walls. The upper end of the reinforced concrete rigid beam was a loading beam with a cross-section dimension of 400 mm × 400 mm, where the length of the loading beam for specimens SW1 and SW2 was 1,200 mm, and the length of the loading beam for specimen SW3 was 1,400 mm. The purpose of setting the loading beam is to ensure that the axial load can be transferred to the wall uniformly during the test, so that the specimen can bear the force uniformly. The lower reinforced concrete rigid beam was the foundation beam with the cross-section size of 500 mm × 500 mm, where the length of the foundation beam for specimens SW1 and SW2 was 1800 mm, and the length of the foundation beam for specimen SW3 was 2000 mm. The function of the foundation beam is to ensure that the specimen is fixed on the ground during the test, so as to reflect the stress and deformation of the specimen as much as possible. The main parameters explored in the design of the specimen include the fire-retardant coating of the steel tubes, and the wall width-to-depth ratio. The detailed parameters of the specimens are shown in Table 1.

2.2 Materials and properties

2.2.1 Rebar and steel

Q235B steel was used for the square steel tubes of the concealed columns of the specimens, HRB400 steel bars with a diameter of 8 mm were used for the horizontal and vertical reinforcement of the precast walls, and HRB400 steel bars with a diameter of 20 mm were used for the longitudinal reinforcement of the loading beams and the foundation beams. The yield strength and ultimate strength of the steel and reinforcement are in accordance with Metallic Materials-Tensile Testing (GB/T 228.1–2010). Details are given in Table 2.

2.2.2 Concrete

The waste concrete was obtained from a pit beam of a concrete crushing plant in Panyu District, Guangzhou, China. Before crushing, a cylindrical core sample of 75 × 75 mm (diameter × height) was obtained from the abandoned pit beam by core drilling and used to measure the compressive strength of the abandoned concrete core sample on the test day. Then, the compressive strength of the 150 mm cube was

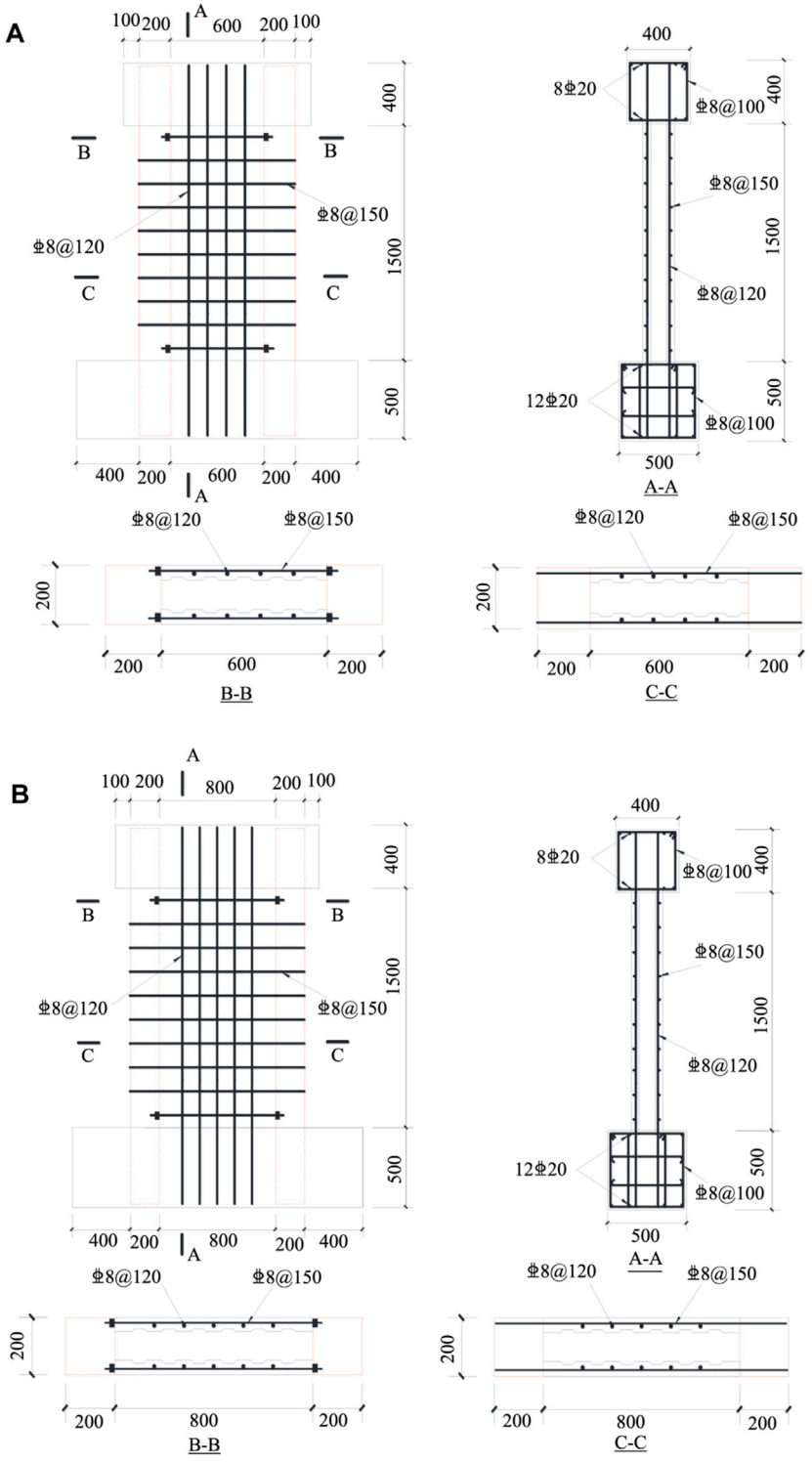

FIGURE 1
Dimensions and details of **(A)** SW1 and SW2; **(B)** SW3 (unit: mm).

TABLE 1 Detailed parameters of specimens.

Specimen	Replacement rate of waste concrete (%)	Wall width (mm)	Wall depth (mm)	Fire situation	Fire-retardant coating thickness (mm)	Axial compression ratio *n*
SW1	20	1,000	200	Double-sided fire	0	0.19
SW2	20	1,000	200	Double-sided fire	20	0.19
SW3	20	1,200	200	Double-sided fire	0	0.19

TABLE 2 Strengths of steel plate and steel bar.

Materials	Grade	Nominal thickness/diameter (mm)	Measured thickness/diameter (mm)	Yield strength (MPa)	Ultimate strength (MPa)
Steel	Q235B	2	1.77	340.7	467.6
Rebar	HRB400	8	8	430.1	594.2
	HRB400	20	20	443.6	620.2

FIGURE 2
Demolished concrete lumps (DCLs).

39.7 MPa according to Technical Specification for Testing Concrete Strength with Drilled Core. As is shown in Figure 2, the waste concrete was manually crushed into concrete blocks with characteristic dimensions of 60–80 mm.

The determination of compressive strength of 150 mm cube of the concrete was based on Standard for Test Method of Mechanical Properties on Ordinary Concrete (GB/T 50081–2002). The concrete for pouring the precast walls was commercial ordinary concrete (COC). The measured compressive strength of COC cube at 28 days was 23.5 MPa and the compressive strength at the test day was 26.7 MPa. The new concrete was commercial self-compacting concrete (CSCC). The compressive strength of CSCC cube at 28 days was 58 MPa and the compressive strength at the test day was 59 MPa. The mix proportions of COC and CSCC are shown in Table 3 and Table 4.

Before pouring CSCC, the slump extension test, as well as the T500 test and the J-ring extension test were carried out according to Technical Specification for Application of Self-compacting Concrete (JGJ/T 283–2012). The test results are shown in Table 5.

2.2.3 Fire-retardant coating

In this test, 20 mm thick fire-retardant coating was applied to the steel tube. "Outdoor non-intumescent steel structure fire-retardant coating" produced by Guangzhou Taibao Fireproof Materials Co., Ltd. was selected as the fire-retardant coating. The performance index of fire-retardant coating is shown in Table 6.

2.3 Specimen production

The specimens were poured in the following order. The first step was to pour the precast walls with plain concrete, including formwork installation and thermocouple arrangement. The second step was to assemble the precast walls and the square steel tubes. After the precast walls were cured to a certain strength, the two ends of the horizontal reinforcement of the two precast concrete walls were respectively inserted into the pre-drilled slot holes of the two rectangular steel tubes. The first horizontal reinforcement at the upper and lower ends was threaded and tightened with nuts, while the rest of the horizontal reinforcement was made of ordinary ribs that extended completely into the square steel tube. Finally, the vertical reinforcement and the square steel tube were inserted into the reinforcement cage of the foundation beam. The third

TABLE 3 Mix proportion of commercial ordinary concrete (Unit: kg/m^3).

Water	Cement	Coarse aggregate	Fine aggregate	Fly ash	Water reducing agent	Water to binder ratio
175	234	1,020	804	100	4.68	0.52

TABLE 4 Mix proportion of commercial self-compacting concrete (Unit: kg/m^3).

Water	Cement	Coarse aggregate	Fine aggregate	Microbead powder	Mineral powder	Water reducing agent	Water to binder ratio
150	413	1,020	652	104	42	8.37	0.27

TABLE 5 Test results of the workability of commercial self-compacting concrete.

T_{500} (s)	Slump extension (mm)	Grade	J-ring extension (mm)	PA (mm)	Grade	Is there any aggregate blockage near J-ring?
1.9	565	SF1	525	40	PA1	None

Notes: PA, is the difference between slump extension and J-ring extension.

TABLE 6 Index of fire-retardant coating.

Fire resistance time (h)	Drying time (h)	Bonding strength (MPa)	Compressive strength (MPa)	Dry density (kg/m$^{3)}$	Other properties
3	4	0.1	1.3	605	Qualified

step was to pour the foundation beam. The fourth step was the pouring of concrete in the cavity of the precast walls and the square steel tubes, as well as the pouring of concrete for the loading beam. One hour before pouring, the waste concrete blocks were well wetted by spraying tap water. During the formal pouring process, self-compacting fresh concrete with a thickness of about 20 mm was first poured into the cavity of the precast walls and square steel tubes, and then the waste concrete blocks and self-compacting fresh concrete were alternately placed into the cavity of the precast walls and square steel tubes with short time assisted vibration using a vibrator. Finally, the loading beam was poured with cast-in-place self-compacting concrete. The fabrication process of the specimens is shown in Figure 3A.

A variable of this test was the application of a 20 mm thick fire-retardant coating to the outer surface of the square steel tube. The fire-retardant coating was applied by the spray construction method. Before spraying the fire-retardant coating, the rust spots on the surface of steel tubes needed to be cleaned, and then the anti-rust primer was applied, and the primer was brushed after the anti-rust primer was thoroughly dried, and then the fire-retardant coating was sprayed. Fire-retardant coating and water were mixed in proportion of 1:1 for 5–10 min and sprayed on the surface of steel tube with a portable spray gun. First, the first layer of fire-retardant coating with a thickness of about 10 mm was sprayed on the surface of steel tubes, and then the second layer of fire-retardant coating with a thickness of about 10 mm was sprayed after an interval of 24 h. Finally, the total thickness of fire-retardant coating on the surface of steel tubes was 20 mm, as shown in Figure 3B.

2.4 Determination of axial compression ratio

The difference between the old and new concrete in this test is 32.3 MPa. The cube combined compressive strength of

FIGURE 3
Production process of specimens: **(A)** Concrete pouring of specimens; **(B)** Construction procedure of fire-retardant coating.

self-compacting concrete and waste concrete is defined as the average value of the calculated results of Eqs. 1,2 given by Wu et al. (2015).

$$f_{cu} = f_{cu1}(1-\eta) + f_{cu2} \times \eta \tag{1}$$

$$f_{cu} = \left(\frac{f_{cu2}}{f_{cu1}}\right)^{0.86\eta} \times f_{cu1} \times (1-\eta) + \left(\frac{f_{cu1}}{f_{cu2}}\right)^{1.1\eta} \times f_{cu2} \times \eta \tag{2}$$

In the above equations, f_{cu1} and f_{cu2} are the cube compressive strengths of self-compacting concrete and waste concrete on the test day, respectively; η is defined as the ratio of the mass of waste concrete to the mass of all concrete in the specimen.

The conversion formula between the axial compressive strength of concrete and the cube compressive strength is calculated as

$$f_c = \alpha_c f_{cu} \tag{3}$$

where for ordinary concrete of grade C50 and below, α_c is taken as 0.76; for concrete of grade C100, α_c is taken as 0.86; the values between them are taken as linear values.

For composite shear walls, the experimental axial compression ratio is given by Hou et al. (2019):

$$n = \frac{N}{f_{c1} \times A_{c1} + f_{c2} \times A_{c2} + f_y \times A_s} \tag{4}$$

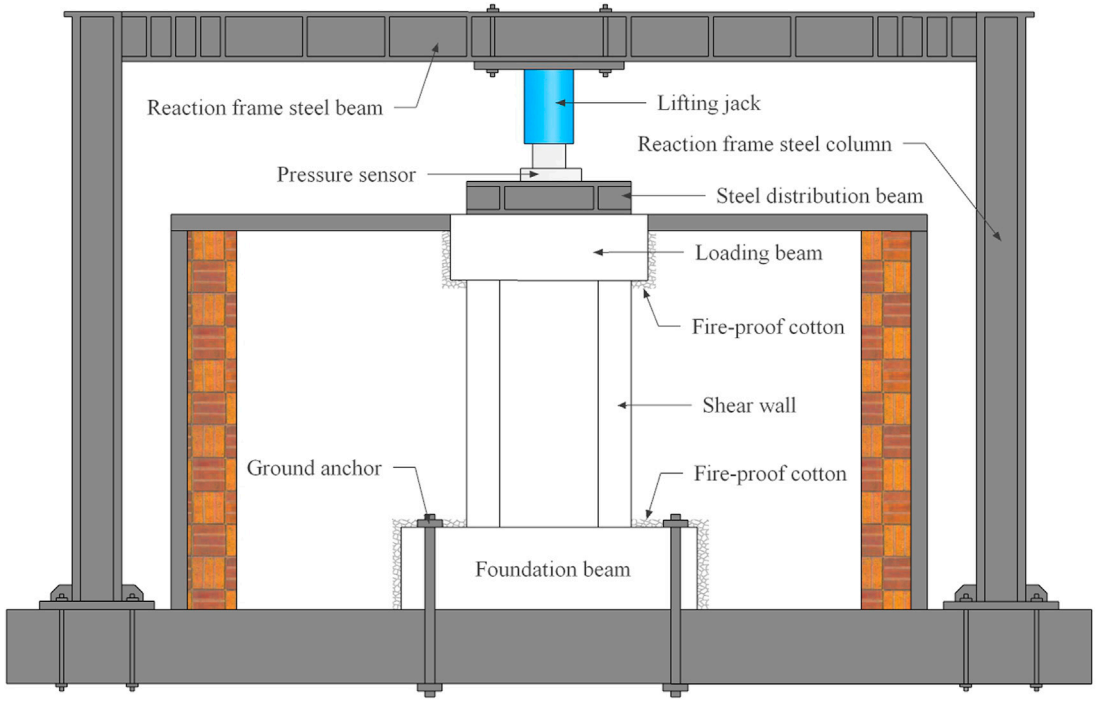

FIGURE 4
Test setup.

FIGURE 5
Fire protection treatment of specimens.

where N is the applied vertical load on the wall; A_{c1} is the cross-sectional area of the precast concrete; f_{c1} is the axial compressive strength of the precast concrete; A_{c2} is the cross-sectional area of the cast-in-place concrete; f_{c2} is the axial compressive strength of the cast-in-place concrete; A_s and f_y are the cross-sectional area and yield strength of the concealed column steel tube, respectively.

2.5 Instrumentation and measurement content

2.5.1 Instrumentation

The dimensions of the furnace chamber were 4 m × 3 m×2.2 m. The maximum load capacity of the reaction frame above the furnace was 1,800 kN, and a 200-t pressure sensor was set between the jack and the steel distribution beam for real-time monitoring of the vertical load during the test. The test setup is shown in Figure 4.

During the fire resistance test, two layers of fireproof cotton were wrapped around the concrete surfaces of the loading beam and foundation beam to ensure that the loading beam and foundation beam would not be damaged throughout the test. The left and right sides of the specimen were wrapped with two layers of fireproof cotton to ensure that both sides of the shear wall were exposed to fire. The fire protection treatment of specimens is shown in Figure 5.

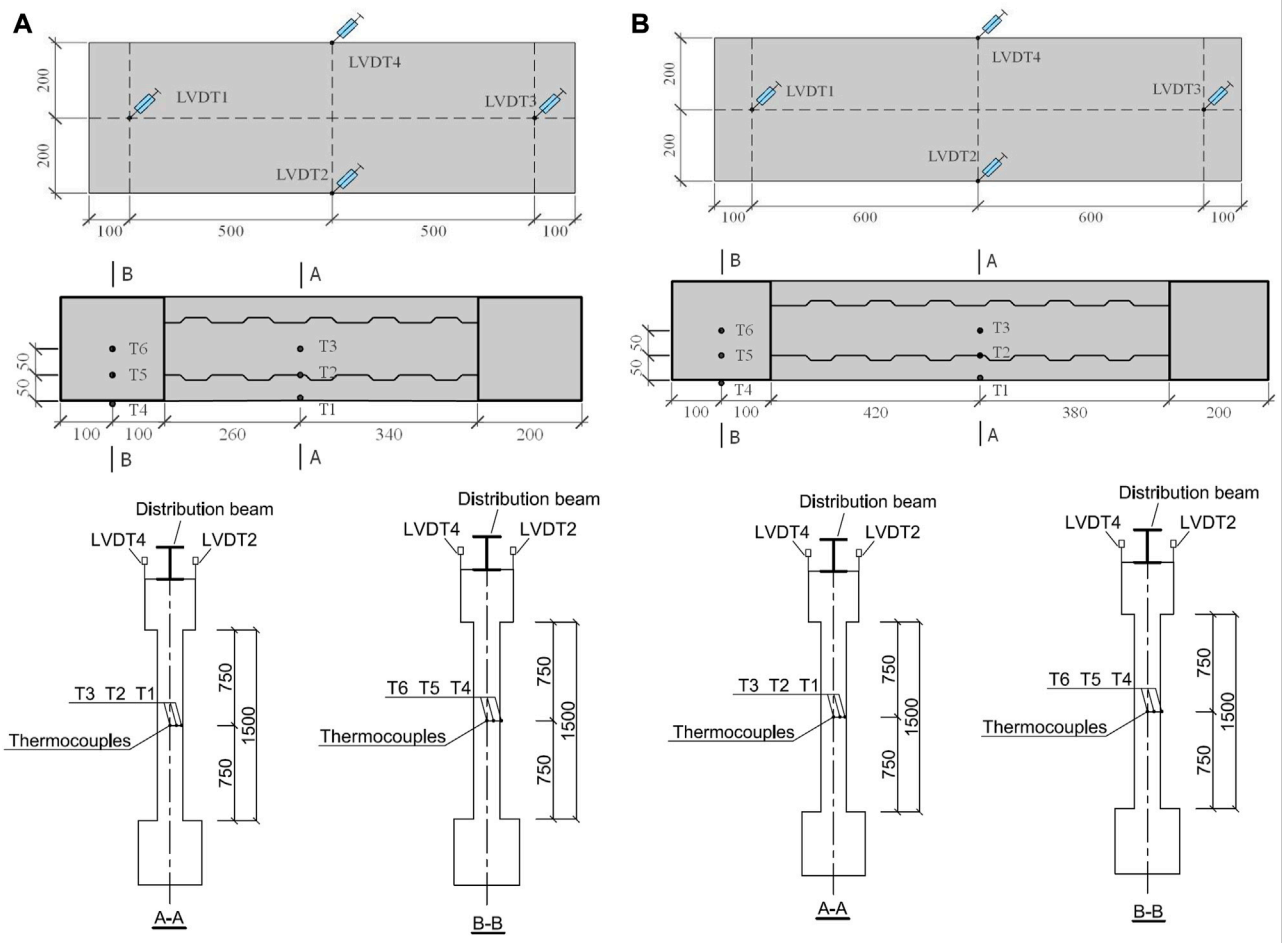

FIGURE 6
Arrangements for instrumentations of **(A)** SW1 and SW2; **(B)** SW3 (unit: mm).

After the specimen was installed, the furnace cover was closed first, then the gap between the cover and the specimen was filled with fireproof cotton to make the furnace in a closed state, and then the steel distribution beam, pressure sensor and other experimental instruments were installed. Before the test, the specimen was preloaded to 30% of the set load, and then unloaded, with the purpose of compacting the specimen and checking whether the displacement meter reading was stable and normal. Subsequently, the load was gradually applied to the set value and the load was maintained for 10 min. After the load and displacement were stabilized, the furnace was ignited. The average temperature inside the furnace was strictly controlled according to the ISO-834 standard fire temperature-time curve. A dead-load heating path was used in the test. During the test, the magnitude of the load applied by the jack was monitored in real time by the pressure sensor. If necessary, the magnitude of the load was adjusted appropriately so that the load varied within ± 5% of the set load.

2.5.2 Layout of measured points

The main components of this test include the axial deformation of the specimen, the temperature field of the specimen, and the heating curve in the test furnace. Vertical displacement meters were set around the top of the loading beam to measure the axial deformation of the shear wall during the test. The layout of the displacement meters is shown in Figure 6.

Thermocouples were embedded at 1/2 height section of the specimen to measure the internal temperature field of the specimen. Six thermocouples were embedded inside each of specimens SW1~SW3, where thermocouple T1 was located at the inner side of the precast wall and the distance from the fire surface was about 5 mm; thermocouple T2 was about 50 mm from the fire surface; thermocouple T3 was about 100 mm from the fire surface; thermocouple T4 was close to the outer wall of the square steel tube; thermocouple T5 was located at the midpoint of the line from the center of the core concrete to the outer wall of the square steel tube; thermocouple T6 was

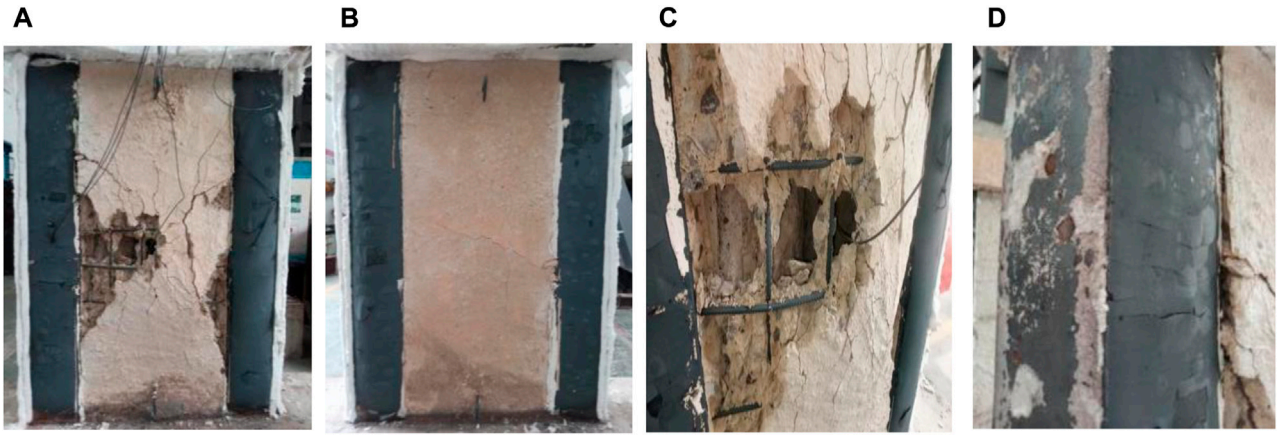

FIGURE 7
Specimen SW1 after fire test: **(A)** front; **(B)** back; **(C)** stripping of concrete in the wall and exposed reinforcing steel; **(D)** buckling of the concealed column steel tube and oxidation layer on the steel tube surface.

located at the center of the core concrete of the edge-constrained steel tube. The layout of the thermocouples is shown in Figure 6.

3 Experimental results and analysis

3.1 Test phenomenon

3.1.1 Specimen SW1

When the test of specimen SW1 began, the gauge reading of the pressure sensor rose slowly, so it was necessary to continuously adjust the hydraulic jack oil pressure to ensure that the axial pressure remained constant during the test. After the test lasted for 80 min, the pressure gauge reading stabilized. During the test, water vapor flowed out from the upper part of the loading beam. After 180 min of ignition, the specimen was in the expansion stage and was able to withstand the predetermined axial pressure stably. Considering that the specimen had reached the first-class fire resistance limit standard and the horizontal fire resistance test furnace was close to the safe burning time limit, the burning was stopped and the test was terminated.

After the test, it was found that the concrete surfaces of the specimens were all light yellow in color. The concrete spalling on one side of the specimen was serious, the horizontal and vertical reinforcement in the precast wall on the surface was exposed and bulged out, and the precast wall was separated from the cavity. On the concrete surface of the other side of the specimen, a coarse horizontal crack and several small turtle cracks without distribution pattern appeared, but there was no concrete spalling and reinforcement exposure. The outer surface of the square steel tube was dark black. Due to the long fire time, the oxidation layer on the outer surface of the steel tube was obviously flaking off and the steel tube appeared to be seriously bent. The failure mode of specimen SW1 is shown in Figure 7.

3.1.2 Specimen SW2

After the high temperature test started, the specimen SW2 was heated and expanded, and the pressure gauge reading slowly increased. During the test, the oil pressure of the hydraulic jack was continuously adjusted to keep the axial pressure from changing during the test. When the specimen was exposed to fire for 90 min, the hydraulic jack leaked oil and was reloaded after repair. Loading was completed at about 100 min, and the pressure gauge reading stabilized. During the test, water vapor flowed out of the upper part of the loading beam. After 180 min of ignition, the specimen did not fail and was still stable to the intended axial pressure. Considering that the specimen had reached the first-class fire resistance limit standard and the horizontal fire resistance test furnace was close to the safe burning time limit, the burning was stopped and the test was terminated.

At the end of the flame test, when the temperature cooled to room temperature and the furnace lid was opened, it was observed that the fire-retardant coating of the specimen had peeled off (but it can be seen from Figure 11B that the temperature field of the square steel tube cross-section did not rise rapidly throughout the open flame test. Therefore, the peeling of the fire-retardant coating occurred after the test, probably due to the vibration when the furnace lid was opened.). The concrete surface of the specimen was light yellow after the fire. The concrete on one side of the specimen near the steel tube was heavily spalled, horizontal and vertical reinforcement was exposed, and the precast walls on this side was bulging. On the other side of the specimen, several small cracks with irregular distribution appeared on the concrete surface, and

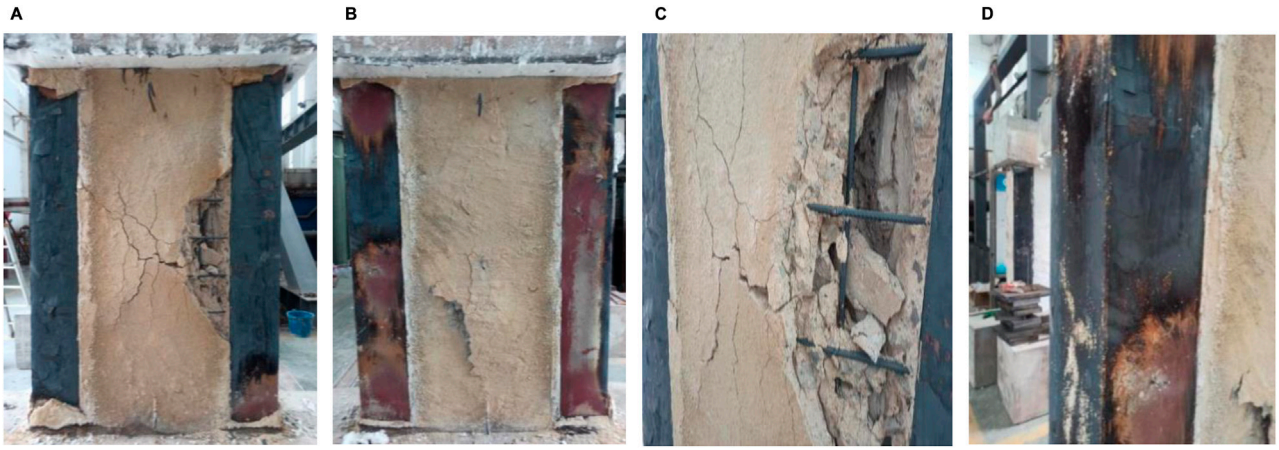

FIGURE 8
Specimen SW2 after fire test: **(A)** front; **(B)** back; **(C)** stripping of concrete in the wall and exposed reinforcing steel; **(D)** buckling of the concealed column steel tube and oxidation layer on the steel tube surface.

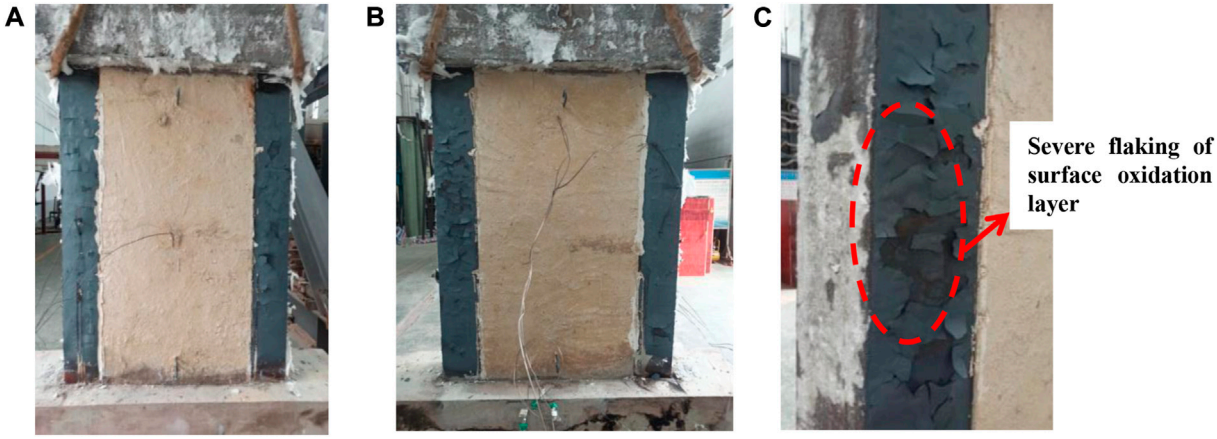

FIGURE 9
Specimen SW3 after fire test: **(A)** front; **(B)** back; **(C)** buckling of the concealed column steel tube and oxidation layer on the steel tube surface.

the concrete surface of the wall tended to spall, but no reinforcement was exposed. Since the outer surface of the steel tube was coated with fire-retardant coating, the steel tube did not bulge and the surface was relatively flat. The failure mode of specimen SW2 is shown in Figure 8.

3.1.3 Specimen SW3

After the high temperature test started, the specimen SW3 was heated and expanded, and the pressure gauge reading of the pressure sensor rose slowly. To ensure that the specimen was subjected to constant axial pressure during the test, the oil pressure of the hydraulic jack needed to be continuously adjusted. After the test lasted for 80 min, the pressure gauge reading stabilized. During the test, water vapor could be observed to spill out from above the loading beam. After 180 min of ignition, the specimen was still in the expansion stage and could also steadily withstand the predetermined axial pressure. Considering that the specimen had reached the first-class fire resistance limit standard and the horizontal fire resistance test furnace was close to the safe burning time, the burning was stopped and the test was terminated.

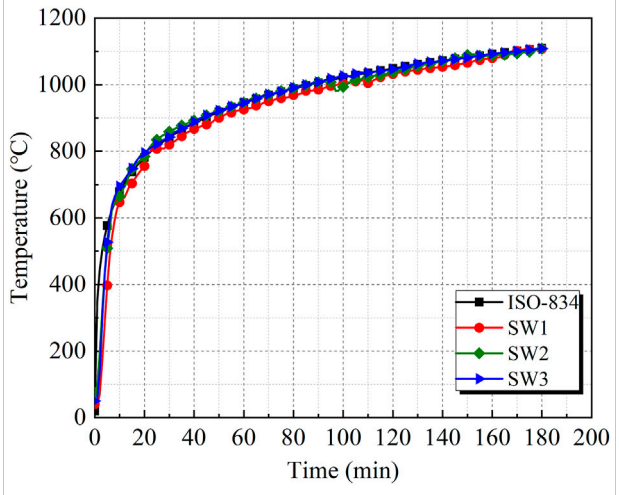

FIGURE 10
Comparison of the temperature-time curves measured in the furnace with the ISO-834 standard curve.

After the fire test, when the temperature cooled to room temperature and the furnace lid was opened, the concrete of the specimen was observed to be light yellow after the fire. There were several small cracks on the concrete surface of the precast walls on both sides of the specimen, but no spalling occurred. The horizontal and vertical reinforcement of the precast walls were not exposed. The outer surface of the steel tube of the concealed column was dark black. Due to the prolonged fire, the oxidation layer on the outer surface of the steel tube was significantly spalled off and the steel tube was severely bent. The failure mode of specimen SW3 is shown in Figure 9.

3.2 Temperature field analysis

3.2.1 Furnace temperature

Figure 10 shows the measured average air temperature-burning time curves in the furnace chamber for three specimens compared to the ISO-834 standard temperature rise curve. It can be seen from the figure that the measured heating curves of the three specimens are basically consistent with the standard fire temperature-time curve.

3.2.2 Temperature field of each measured point of the same specimen

The temperature-time curves of six measured points during the test of specimens SW1 to SW3 are shown in Figure 11. It can be seen from the figure that:

(1) The temperature of each measured point of the three specimens increased with the increase of ignition time. In the same section, the measured concrete temperature gradually decreased as the depth of the measured point increased. Most of the measured points located in the concrete had the same trend of temperature profile. When the temperature was between 100°C and 150°C, there was a significant temperature plateau, which was caused by the evaporation and heat absorption of water in the concrete. The duration of the temperature platform was longer at measured points T3 and T6 than at T2 and T5, because the farther the measured point was from the fire surface, the greater the vapor escape force and the longer it took.

(2) The temperatures of measured points T1 and T4 of specimen SW1 showed a trend of first fast and then slow, which was similar to the law of furnace temperature rise. At the beginning of the open fire test, the temperatures of measured points T5 and T6 in the concealed column were higher than the temperatures of measured points T2 and T3 at the same locations in the wall. This was because the thermal conductivity of steel was larger than that of concrete, and the temperature transfer of steel was faster than that of concrete. 120 min later, the temperature rise of measured point T2 was accelerated, which was due to the synergistic effect of fire and external load, the reinforcement in the precast wall bulged, the precast wall separated from the cavity, and the concrete surface on one side of the measured point began to produce coarse cracks and partial concrete spalling, resulting in the accelerated temperature rise of T2. 105 min later, the temperature rise rate of the measured point T3 accelerated, and finally the temperature curve of measured point T2 almost overlapped with that of measured point T3. The reason was that the measured point T3 was located in the demolished concrete lumps and self-compacting concrete, and the water vapor in C60 self-compacting concrete could not be released quickly at high temperature, and the internal vapor pressure was large, which started to burst at 380°C–458°C (Anagnostopoulos et al., 2009), leading to the gradual dislodgement of the self-compacting concrete around measured point T3. After 125 min, the measured points T2 and T3 were exposed to the same air temperature, so the measured temperatures were the same.

(3) The temperatures of measured points T1 to T3 of specimen SW2 were similar to those of specimen SW1, except that the self-compacting concrete cavity in the wall section began to burst at 150 min, resulting in an accelerated rise in temperature at measured point T3. The temperatures of measured points T4, T5 and T6 at the square steel tube section were lower than those of measured points T1, T2 and T3 at the same location of the wall. This was because the outer surface of the square steel tube of specimen SW2 was sprayed with fire-retardant coating, and the temperature rising rate of measured points of the square steel tube decreased.

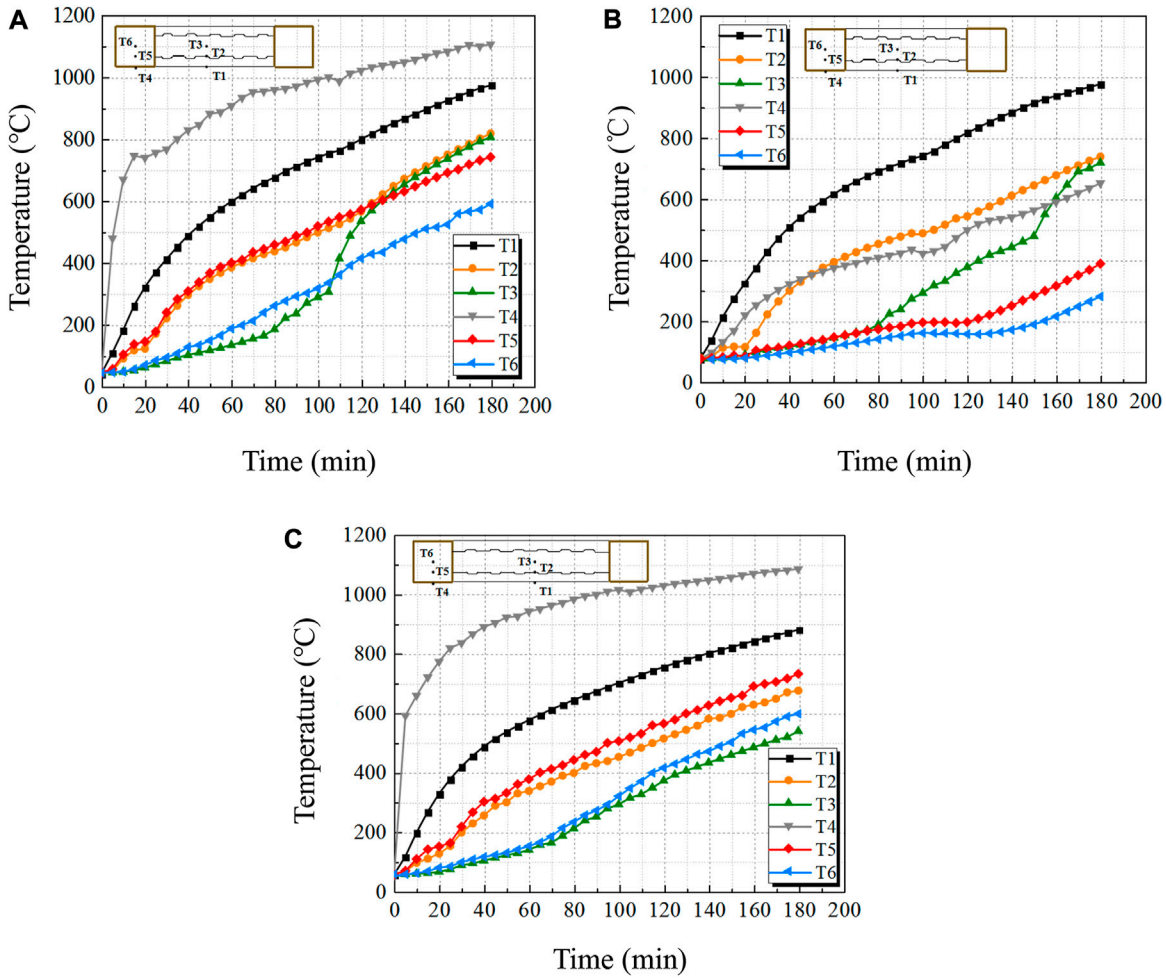

FIGURE 11
Temperature-time curves of **(A)** SW1; **(B)** SW2; **(C)** SW3.

(4) The temperature rising pattern of each measured point of specimen SW3 was basically the same as that of specimen SW1, but the temperature rise rate of measured points T2 and T3 of specimen SW3 was not faster than that of specimen SW1. This was because the specimen SW3 was more intact after the fire and there was no concrete spalling or exposed reinforcement. In the late stage of the fire, the temperature difference between the measured point T5 of the concealed column section and measured point T2 at the same location of the wall section was the same as that between measured point T6 and measured point T3, which was about 50°C.

3.2.3 Temperature fields of different specimens at the same measured point

Figure 12 shows the temperature-time comparison graphs for the same measured points of specimens SW1 to SW3. It can be seen from the figure that the temperature rise at the measured points T1 to T3 is essentially the same for all three specimens. However, specimen SW1 had the most severe concrete spalling, bursting and reinforcement bulging, followed by specimen SW2, while specimen SW3 was the most intact. Therefore, the highest temperatures were observed at the measured points T2 and T3 of specimen SW1 and the lowest temperatures were observed at specimen SW3 during the last stage of fire exposure. The temperature comparison of the three measured points T4, T5 and T6 of the concealed column section shows that increasing the wall width-to-depth ratio had little effect on the temperature of the concealed column section, and the setting of the fire-retardant coating made the temperature of measured point T4 on the outer surface of the steel tube and the temperature of measured points T5 and T6 of concrete of the specimen SW2 lower than those of specimens SW1 and SW3. At 180 min, the temperature of the measured point T4 on the outer surface of the steel tube of the specimen SW2 was about 450°C lower than

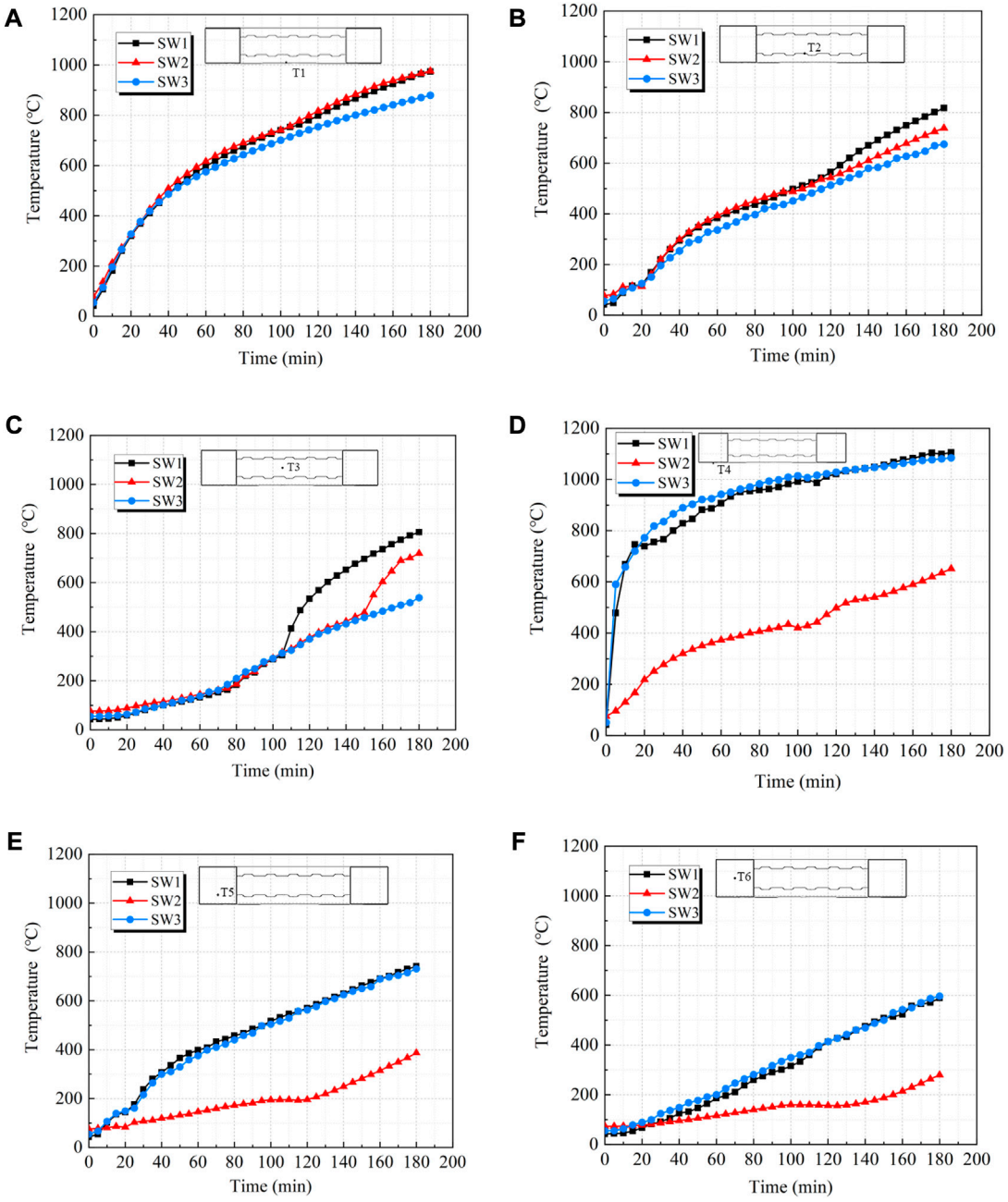

FIGURE 12
Temperature-time curves of different specimens at the same measured point: **(A)** T1; **(B)** T2; **(C)** T3; **(D)** T4; **(E)** T5; **(F)** T6.

that of specimens SW1 and SW3, and the temperature of measured point T5 and T6 in the concrete was about 350°C lower.

3.3 Analysis of axial deformation

The measured axial deformation-burning time curves of the specimens are shown in Figure 13. For the axial deformation, the expansion deformation of the specimen is positive, while the compression deformation is negative. The axial displacement of the specimen is the average of the displacement values measured by the four vertical displacement gauges. It can be seen from the test results that:

(1) In the open fire test, all three specimens were exposed to fire on both sides. The deformation of the specimens was in the

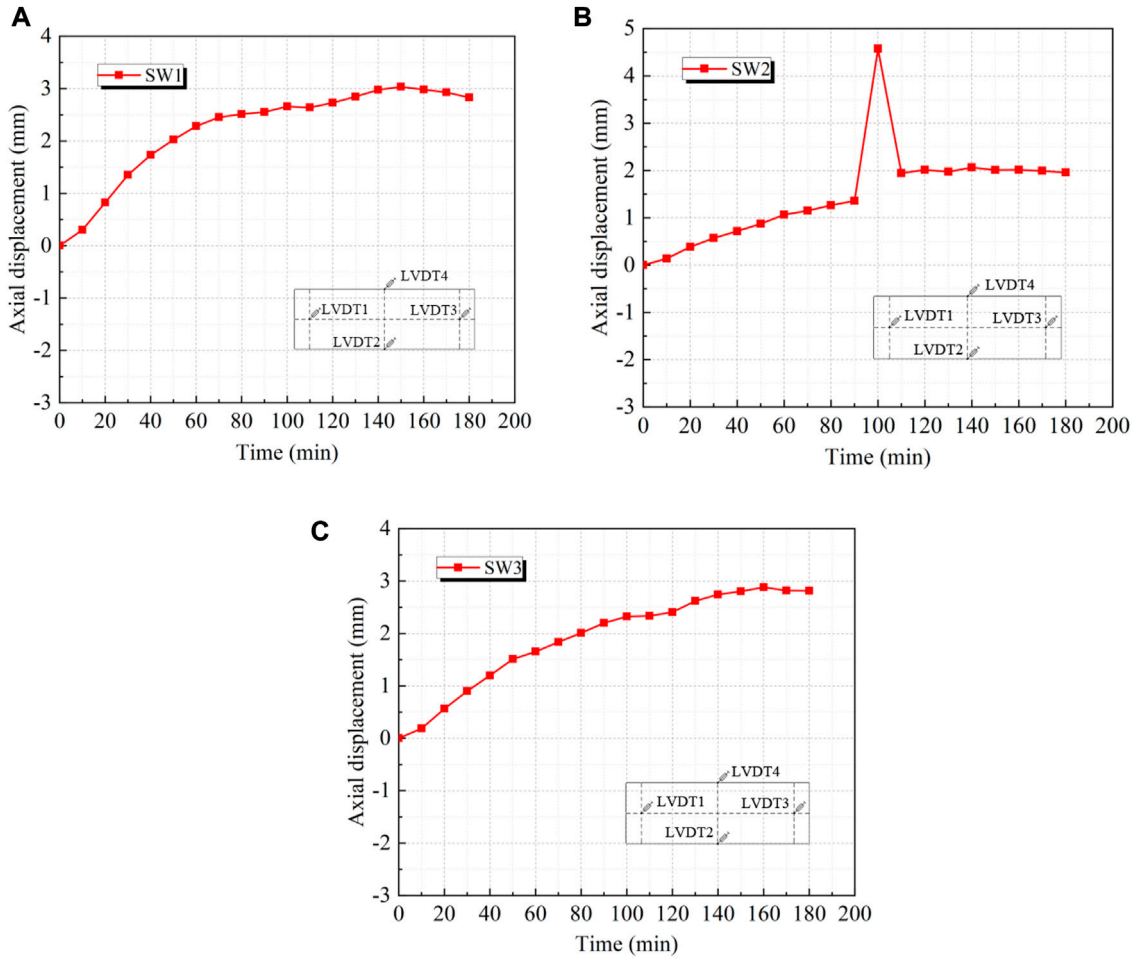

FIGURE 13
Vertical deformation-time curves of **(A)** SW1; **(B)** SW2; **(C)** SW3.

expansion stage and there was no compression. At an axial compression ratio of 0.19, the deformation values were far below the damage limit of shear wall bearing capacity, indicating that the three specimens had good fire resistance performance.

(2) The change patterns of axial displacement of specimens SW1 and SW3 were basically the same. Taking specimen SW1 as an example, the expansion deformation of specimen SW1 gradually increased within 80 min after ignition, and the axial deformation did not change much from 80 to 150 min. The expansion deformation peaked at 150 min and 160 min for both specimens, respectively, and the peak expansion deformation was comparable for both specimens, after which the expansion deformation value decreased slightly. The maximum expansion deformation of specimen SW1 was about 3.04 mm in 150 min from the beginning of ignition to the end of combustion, while the maximum expansion deformation of specimen SW3 was about 2.88 mm in 160 min. There was no significantly different in the maximum displacements of the two specimens. The main reasons were the large surplus of end-restrained column and wall bearing capacity in the case of relatively small loads, as well as the loading beam that played a role in load redistribution. It can be seen that increasing the wall width-to-depth ratio had little effect on the axial deformation of specimens.

(3) After 90 min of fire, the specimen SW2 was suspended for 10 min due to oil leakage from the hydraulic jack. At this point, the axial deformation increased by nearly 3 mm. After repair and reassembly, the specimen was still in the expansion deformation stage. During the 180 min from the start of ignition to the end of combustion (excluding the 10 min of test suspension), the maximum deformation of specimen SW2 during 140 min was about 2.07 mm, which was smaller than that of specimen SW1. This indicates that the expansion of SW2 during the test was smaller than that of

SW1. The main reason was that the fire-retardant coating was set on the outer surface of the steel tube of the concealed column, which slowed down the heat transfer to the concealed column section and reduced the expansion of the concealed column section.

4 Summary and conclusion

This paper discusses the fire performance of composite shear walls filled with DCLs and SCC restrained by the edges of concrete-filled square steel tubes. Three specimens of composite shear walls filled with DCLs and SCC were fabricated and tested for fire resistance on both sides. The effects of steel tube fire-retardant coating and the wall width-to-depth ratio on temperature field, axial deformation and fire resistance limit of composite shear walls under constant axial pressure ratio were investigated. The experimental results and analysis support the following conclusions.

(1) The phenomena of the three specimens after fire were not the same. The test results showed that concrete of the specimens without fire-retardant coating and with fire-retardant coating had different degrees of spalling and bursting, but the shear wall steel tube with fire-retardant coating was smoother than the steel tube without fire-retardant coating. With the increase of the wall width-to-depth ratio, the steel tube had bulging phenomenon, but the concrete did not spall and showed reasonable fireproof performance.
(2) The temperature change trends in the wall section of the three specimens were generally consistent. Spraying fire-retardant coating on the outer surface of the steel tube had a significant effect on the temperature of the steel tube section, while increasing the wall width-to-depth ratio of the wall had little effect on the temperature of the steel tube section.
(3) At the axial compression ratio of 0.19, all three specimens were in the expansion stage during the fire resistance test. The expansion deformation of the shear wall with fire-retardant coating on the outer surface of the steel tube was smaller than that without fire-retardant coating, while increasing the wall width-to-depth ratio had little effect on the axial deformation of the composite shear wall filled with DCLs and SCC at high temperature.

Overall, the composite shear walls filled with DCLs and SCC were able to withstand the intended axial loads stably for 180 min and had good fire resistance. This paper provides a preliminary discussion on the fire resistance of composite shear walls filled with DCLs and SCC, only the fire-retardant coating of steel tubes and the wall width-to-depth ratio on the fire resistance of composite shear walls on both sides were experimentally studied, but there are still some issues to be further investigated. And due to the limitation of the bearing capacity of the test equipment, only the fire resistance of the shear wall with an axial compression ratio of 0.19 was tested in this paper, and the fire resistance of the shear wall with larger axial compression ratio is subject to further study.

Data availability statement

The original contributions presented in the study are included in the article/supplementary material, further inquiries can be directed to the corresponding author.

Author contributions

YX contributed to the overall concept, the methodology, the funding acquisition, the supervision, the writing-review and editing. YC contributed to the data curation, the investigation, and writing original draft. BW contributed to the conceptualization, the project administration, the investigation, the writing-review and editing. GZ contributed to the conceptualization, the data curation, the investigation, and the validation.

Funding

This work was supported by National Key R&D Program of China during the 13th 5-year Plan Period (2017YFC0703303), National Natural Science Foundation of China (51878298), Natural Science Foundation of Guangdong Province (2021A1515012606), and Guangdong Provincial Key Laboratory of Modern Civil Engineering Technology (2021B1212040003).

Conflict of interest

The authors declare that the research was conducted in the absence of any commercial or financial relationships that could be construed as a potential conflict of interest.

Publisher's note

References

Anagnostopoulos, N., Sideris, K. K., and Georgiadis, A. (2009). Mechanical characteristics of self-compacting concretes with different filler materials, exposed to elevated temperatures. *Mat. Struct.* 42 (10), 1393–1405. doi:10.1617/s11527-008-9459-6

Bamonte, P., Felicetti, R., Kalaba, N., Lo Monte, F., Pinoteau, N., Miah, M. J., et al. (2016). On the structural behavior of reinforced concrete walls exposed to fire. *Key Eng. Mat.* 711, 580–587. doi:10.4028/www.scientific.net/kem.711.580

Chen, J., Hamed, E., and Gilbert, R. (2020). Structural performance of reinforced concrete walls under fire conditions. *J. Struct. Eng. (N. Y. N. Y).* 146, 04020006. doi:10.1061/(asce)st.1943-541x.0002519

Du, E., Shu, G., Qin, L., Lai, B., Zhou, X., and Zhou, G. (2022). Experimental investigation on fire resistance of sandwich composite walls with truss connectors. *J. Constr. Steel Res.* 188, 107052. doi:10.1016/j.jcsr.2021.107052

Go, C., Tang, J., Chi, J., Chen, C., and Huang, Y. (2012). Fire-resistance property of reinforced lightweight aggregate concrete wall. *Constr. Build. Mat.* 30, 725–733. doi:10.1016/j.conbuildmat.2011.12.081

Hertz, K. D. (2018). Fire resistance of concrete walls with light aggregate. *J. Struct. Fire Eng.* 9 (4), 319–341. doi:10.1108/jsfe-11-2017-0043

Hou, H., Fu, W., Qiu, C., Cheng, J., Qu, Z., Zhu, W., et al. (2019). Effect of axial compression ratio on concrete-filled steel tube composite shear wall. *Adv. Struct. Eng.* 22 (3), 656–669. doi:10.1177/1369433218796407

Jian, S., and Wu, B. (2021). Compressive behavior of compound concrete containing demolished concrete lumps and recycled aggregate concrete. *Constr. Build. Mat.* 272, 121624. doi:10.1016/j.conbuildmat.2020.121624

Kang, J., Yoon, H., Kim, W., Kodur, V., Shin, Y., and Kim, H. (2016). Effect of wall thickness on thermal behaviors of RC walls under fire conditions. *Int. J. Concr. Struct. Mat.* 10, 19–31. doi:10.1007/s40069-016-0164-5

Kang, J. Y., Yoon, H. A., Ryu, E. M., and Shin, Y. S. (2019). Analytical studies for the effect of thickness and axial load on load bearing capacity of fire damaged concrete walls with different sizes. *J. Struct. Integr. Maintenance* 4 (2), 58–64. doi:10.1080/24705314.2019.1603189

Kumar, P., and Kodur, V. K. R. (2017). Modeling the behavior of load bearing concrete walls under fire exposure. *Constr. Build. Mat.* 154, 993–1003. doi:10.1016/j.conbuildmat.2017.08.010

Lee, C., Lee, S., and Kim, H. (2013). Experimental observations on reinforced concrete bearing walls subjected to all-sided fire exposure. *Mag. Concr. Res.* 65 (2), 82–92. doi:10.1680/macr.12.00013

Limbachiya, M. C., Marrocchino, E., and Koulouris, A. (2007). Chemical–mineralogical characterisation of coarse recycled concrete aggregate. *Waste Manag.* 27 (2), 201–208. doi:10.1016/j.wasman.2006.01.005

Liu, G., Song, Y., and Qu, F. (2010). Post-fire cyclic behavior of reinforced concrete shear walls. *J. Cent. South Univ. Technol.* 17, 1103–1108. doi:10.1007/s11771-010-0603-4

Morita, T., Yamashita, H., Beppu, M., and Suzuki, M. (2017). "A study on structural behavior of reinforced concrete walls exposed to hydrocarbon fire under vertical load," in *Fire sci. Technol.* Editors K. Harada, K. Matsuyama, K. Himoto, Y. Nakamura, and K. Wakatsuki, 299–308. doi:10.1007/978-981-10-0376-9_30

Mueller, K. A., and Kurama, Y. C. (2019). Numerical modeling of three reinforced concrete bearing wall tests subject to one-sided standard fire. *ACI Struct. J.* 116 (5), 29–41. doi:10.14359/51716756

National Standards of the People's Republic of China. Metallic materials-tensile testing. *GB/T* 228, 1–2010. (in Chinese).

Ngo, T., Fragomeni, S., Mendis, P., and Ta, B. (2013). Testing of normal- and high-strength concrete walls subjected to both standard and hydrocarbon fires. *ACI Struct. J.* 110 (3), 503–510. doi:10.14359/51685607

Nguyen, K. T., Ngo, T. D., Mendis, P., and Heath, D. (2018). Performance of high-strength concrete walls exposed to fire. *Adv. Struct. Eng.* 21, 1173–1182. doi:10.1177/1369433217732500

Ni, S., and Birely, A. C. (2018). Impact of physical seismic damage on the fire resistance of reinforced concrete walls. *Constr. Build. Mat.* 182, 469–482. doi:10.1016/j.conbuildmat.2018.06.120

Pavese, A., and Bournas, D. A. (2011). Experimental assessment of the seismic performance of a prefabricated concrete structural wall system. *Eng. Struct.* 33 (6), 2049–2062. doi:10.1016/j.engstruct.2011.02.043

Ryu, E., Kim, H., Chun, Y., Yeo, I., and Shin, Y. (2020). Effect of heated areas on thermal response and structural behavior of reinforced concrete walls exposed to fire. *Eng. Struct.* 207, 110165. doi:10.1016/j.engstruct.2020.110165

Wang, T., Wang, X., Wang, L., Au-Yong, C. P., and Ali, A. S. (2021). Assessment of the development level of regional industrialized building based on cloud model: A case study in Guangzhou, China. *J. Build. Eng.* 44, 102547. doi:10.1016/j.jobe.2021.102547

Wei, F., Zheng, Z., Yu, J., and Wang, Y. (2019). Structure behavior of concrete filled double-steel-plate composite walls under fire. *Adv. Struct. Eng.* 22 (8), 1895–1908. doi:10.1177/1369433218825238

Wu, B., Peng, C., Zhao, X., and Zhou, W. (2018). Axial loading tests of thin-walled circular steel tubes infilled with cast-in-place concrete and precast segments containing DCLs. *Thin-Walled Struct.* 127, 275–289. doi:10.1016/j.tws.2018.02.008

Wu, B., Zhang, S., and Yang, Y. (2015). Compressive behaviors of cubes and cylinders made of normal-strength demolished concrete blocks and high-strength fresh concrete. *Constr. Build. Mat.* 78, 342–353. doi:10.1016/j.conbuildmat.2015.01.027

Xiao, J., Xie, Q., Li, Z., and Wang, W. (2017). Fire resistance and post-fire seismic behavior of high strength concrete shear walls. *Fire Technol.* 53 (1), 65–86. doi:10.1007/s10694-016-0582-6

frontiers | Frontiers in Materials

TYPE Original Research
PUBLISHED 13 October 2022
DOI 10.3389/fmats.2022.1023886

OPEN ACCESS

EDITED BY
Jialuo He,
Washington State University,
United States

REVIEWED BY
Xiaoqing Xu,
Tongji University, China
Fan Bai,
Beijing Jiaotong University, China

*CORRESPONDENCE
Jinlong Jiang,
jinlongjiang@mails.cqjtu.edu.cn

SPECIALTY SECTION
This article was submitted to Structural Materials,
a section of the journal
Frontiers in Materials

RECEIVED 20 August 2022
ACCEPTED 13 September 2022
PUBLISHED 13 October 2022

CITATION
Li B, Jiang J, Deng Z, Zhou H, Wang H, Jiang H and Cao Y (2022), Bending behavior of steel-UHPC composite bridge deck based on epoxy adhesive. *Front. Mater.* 9:1023886. doi: 10.3389/fmats.2022.1023886

Bending behavior of steel-UHPC composite bridge deck based on epoxy adhesive

Baojun Li[1,2], Jinlong Jiang[3]*, Zhiheng Deng[1], Heying Zhou[3], Haicui Wang[4], Haoting Jiang[3] and Yidong Cao[3]

[1]College of Civil Engineering and Architecture, Guangxi University, Nanning, China, [2]Guangxi Transportation Science and Technology Group Co., Ltd., Nanning, China, [3]School of Civil Engineering, Chongqing Jiaotong University, Chongqing, China, [4]School of River and Ocean Engineering, Chongqing Jiaotong University, Chongqing, China

Using ultra-high performance concrete (UHPC) as the pavement layer on the orthotropic steel deck (OSD) can greatly enhance the rigidity to solve the fatigue cracking of the steel deck and the resulting damage to the pavement layer. However, the thin UHPC layer limits the extensive use of the short stud connector. In this study, three types of interfaces were designed by introducing different additives into the epoxy matrix, and the shear properties of each interface and short stud connector were compared. Then, the influence of short stud connectors and optimized interface on the composite bridge deck's bending property was analyzed through the composite bridge deck's bending test. Moreover, the mechanical behavior of the interface in the composite bridge deck is discussed based on the finite element model. The results show that the ultimate load of the composite bridge deck with the optimized interface is reduced by 21.5% compared with that of the composite bridge deck with the short stud connector. However, the composite bridge deck with the optimized interface has higher bending stiffness before failure and is less affected by cyclic loading. Moreover, the composite bridge deck with the optimized interface is unsuitable for cyclic loading conditions when the defect area reaches 30%. Finally, the numerical simulation of the composite bridge deck with the optimized interface is successfully realized based on the cohesive zone model, and the applicability of the interface in the composite bridge deck is verified.

KEYWORDS

bridge engineering, UHPC, steel-UHPC composite bridge deck, epoxy adhesive, cohesive zone model

1 Introduction

Orthotropic steel bridge deck (OSD) has become the bridge deck form of large-span steel bridges because of its outstanding advantages, such as lightweight, high bearing capacity, and fast construction (Alavi et al., 2017; Freitas et al., 2017). However, insufficient stiffness of OSD can easily lead to fatigue cracking of the steel bridge deck (Fu et al., 2019) and pavement damage (Wang et al., 2020) under the coupling

effect of the reciprocating vehicle and external environmental factors. Therefore, the OSD can be paved with high- performance concrete (Zhang et al., 2020; Zou et al., 2021a; Zhang et al., 2021; Jiang et al., 2022; Zhang et al., 2022) to increase its stiffness of the OSD. Ultra-high performance concrete (UHPC), a new type of steel fiber reinforced concrete (Hung et al., 2021), has good fluidity (minimum slump is 200–250 mm (Alkaysi and El-Tawil, 2017)), high strength (compressive strength greater than 120 MPa (Zhu et al., 2020), tensile strength greater than 5 MPa (Meng and Khayat, 2017)), impact resistance (Wu et al., 2019) and excellent durability (Charron et al., 2008). Under the excellent mechanical properties of UHPC, the stiffness of OSD is significantly enhanced, and the thin pavement thickness can also ensure the crack resistance of the pavement layer, thereby realizing the light weight of the steel deck and improving the durability and service life of the steel deck (Cheng et al., 2021; Feng et al., 2021; Liu et al., 2022).

As a kind of steel-UHPC composite structure, the stiffness enhancement of UHPC pavement to OSD largely depends on the composite action at the interface. The traditional stud connectors are widely used in steel-concrete composite structures due to their simple force and convenient construction (Kruszewski et al., 2019). Still, there are the following problems when applied to OSD-UHPC composite bridge deck. Welding defects and residual stresses are inevitably introduced in a large number of stud welding operations, which is unfavorable to the fatigue resistance of steel structures (Feng et al., 2021), (Zhang et al., 2016). More adversely, the shear capacity of short studs in thin UHPC pavement is insufficient to require a large number of intensive studs installed on OSD, resulting in cumbersome welding operations (Zhang et al., 2016)- (Wang et al., 2019). Given this, the use of epoxy adhesive to realize the steel-concrete bonding interface has been applied (Bouazaoui and Li, 2008). Compared with stud connectors, the steel-concrete bonding interface can make the stress transfer at the interface between steel and concrete uniform (Larbi et al., 2009)- (Kumar et al., 2018) and avoid the stress concentration caused by the discontinuous distribution of studs (Luo et al., 2012)- (Bouazaoui et al., 2007). Meanwhile, the bonding interface can realize the rapid connection between steel structure and prefabricated concrete structure, which simplifies the construction process and improves construction efficiency (Berthet et al., 2011)- (Zhao et al., 2019). However, the brittle failure of the steel-concrete bond interface cannot be ignored (Jiang et al., 2021)- (Zhan et al., 2021), and only the use of the bond interface for precast concrete structures and steel structures has obvious application advantages. To sum up, compared with the OSD-UHPC composite bridge deck with stud connectors, a suitable interface form for fresh UHPC can be sought to realize the connection between OSD and UHPC pavement. This interface form can minimize or avoid the use of stud connectors to ensure the connection performance of OSD and UHPC pavement.

Given the hidden trouble in applying stud connectors in steel-UHPC composite structures, the composite interface formed by introducing additives based on epoxy matrix appears. Sun et al. (Sun et al., 2017) designed the interface form in which limestone is uniformly arranged on the epoxy matrix, and the test proved that the interface had high bonding properties, and the tensile and shear strength could reach about 2 MPa. Wang et al. (Wang et al., 2019) designed the composite beam LEA-6.9 with limestone interface connection uniformly arranged on the epoxy matrix and beam LHS-6.9 with stud connectors. The ultimate load of beam LEA-6.9 is 6.8% lower than that of beam LHS-6.9, indicating that the composite interface can successfully replace the stud connector. Robert et al. (Robert et al., 2007) designed the interface form of copper fiber embedded in the epoxy matrix. The pull-out behavior of copper fiber from the epoxy matrix can significantly increase the interfacial strength and fracture toughness of composites. Maloney et al. (Maloney and Fleck, 2019) studied the toughening effect of copper wire mesh in the epoxy matrix on the interface properties through double cantilever beams. They confirmed that this interface form could realize a reliable connection at the interface of composite materials. In short, introducing additives into the epoxy matrix can meet the requirements of interfacial strength and can be comparable to the stud connector.

No matter what connection mode is adopted for the composite structure, the mechanical behavior of the composite structure is largely affected by the interface performance. Therefore, the interface form with excellent mechanical properties is crucial to the mechanical properties of composite structures. This study introduced different additives into the epoxy matrix to select the interface form suitable for OSD-UHPC composite bridge deck. In order to optimize the most suitable interface, the shear behavior of various interfaces was discussed through the direct shear test. Then, the influence of optimized interface and stud connectors on the bending performance of the steel-UHPC composite bridge deck was analyzed. Finally, based on the cohesive zone model, the numerical simulation of the optimized interface and stud connectors was successfully realized, and the excellent mechanical properties of the epoxy adhesive steel-UHPC composite bridge deck were verified.

2 Interface optimization

2.1 Interface design

In order to enhance the interfacial toughness of the steel-UHPC composite bridge deck, the epoxy bonding interface (EB interface), particle embedded interface (PE interface), and fiber toughening interface (FT interface) were designed in this study. Detailed information on the designed interface and specimen is shown in Figure 1. The components of the specimen can be divided into three

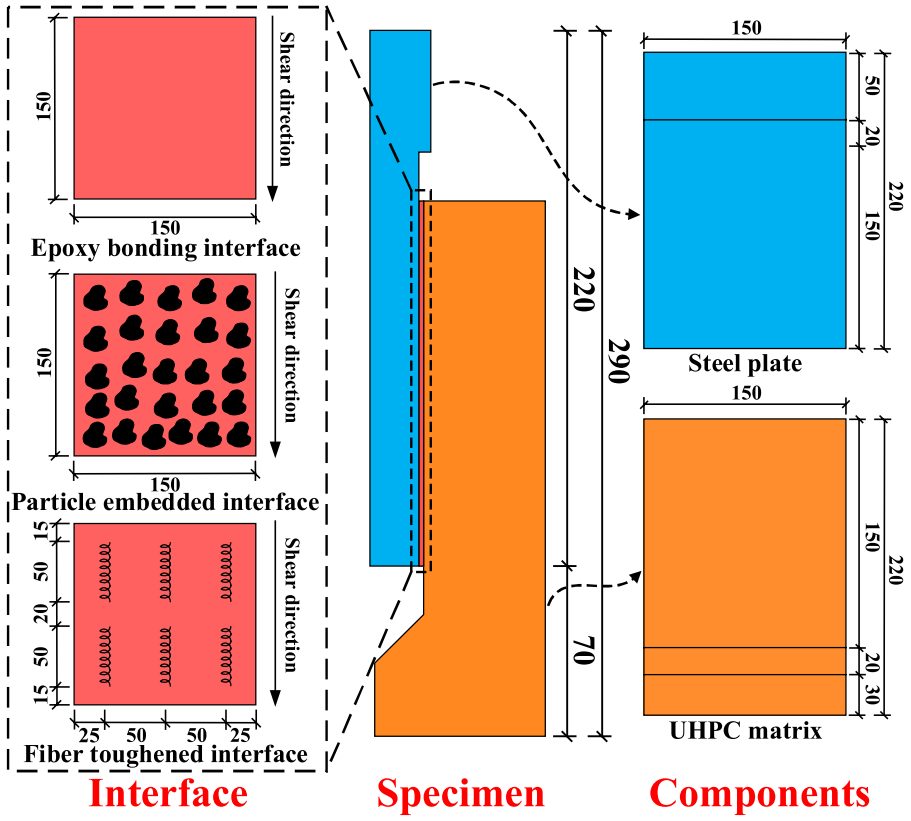

FIGURE 1
Specimen and interface design.

parts: steel plate, interface, and UHPC matrix. The thickness of the steel plate in the region 50 mm away from the top increases by 5 mm to ensure that the specimen is loaded without eccentricity. The area size of the three types of interfaces is 150 mm × 150 mm, and the thickness of the epoxy matrix is 2 mm (Berthet et al., 2011), but the composition of the interface is different. The EB interface is the epoxy matrix between the steel plate and the UHPC matrix, which can realize the connection between the steel plate and the UHPC matrix through the adhesive force. The PE interface is composed of epoxy matrix and quartz sand particles. The epoxy matrix uniformly adheres to the steel plate, and the quartz sand particles are firmly embedded on the surface of the epoxy matrix and UHPC matrix. The PE interface realizes the connection between the steel plate and UHPC matrix through the adhesive force of the epoxy matrix and the embedding effect of quartz sand particles. The particle size of quartz sand is 2–3 mm. The FT interface is composed of epoxy matrix and helical fiber. The diameter of the helical fiber is 0.5 mm, the diameter of the ring is 6mm, and the longitudinal length is 150 mm. It is arranged in two rows in the transverse direction and three columns in the longitudinal direction on the epoxy matrix. The epoxy matrix uniformly adheres to the steel plate, and the helical fibers are firmly embedded in the epoxy matrix and UHPC matrix.

TABLE 1 Design information of specimen.

Interface type	Specimen	Main material	Number
EB interface	DS-E	Epoxy adhesive	3
PE interface	DS-P	Quartz sand particle	3
FT interface	DS-F	Helical fiber	3

The FT interface realizes the connection between the steel plate and the UHPC matrix through the epoxy matrix's adhesive force and the fiber's bridging effect. The area 50 mm from the bottom of the UHPC matrix was thickened to prevent the specimen from rollover during loading. Details of all specimens are shown in Table 1.

2.2 Direct shear test scheme

The specimen was loaded by an electronic universal testing machine (MTS Exceed E45.205) with a nominal bearing capacity of 200 kN. In Figure 2, the top of the steel plate of the test piece is in flat contact with the loader, and the interface center does not deviate

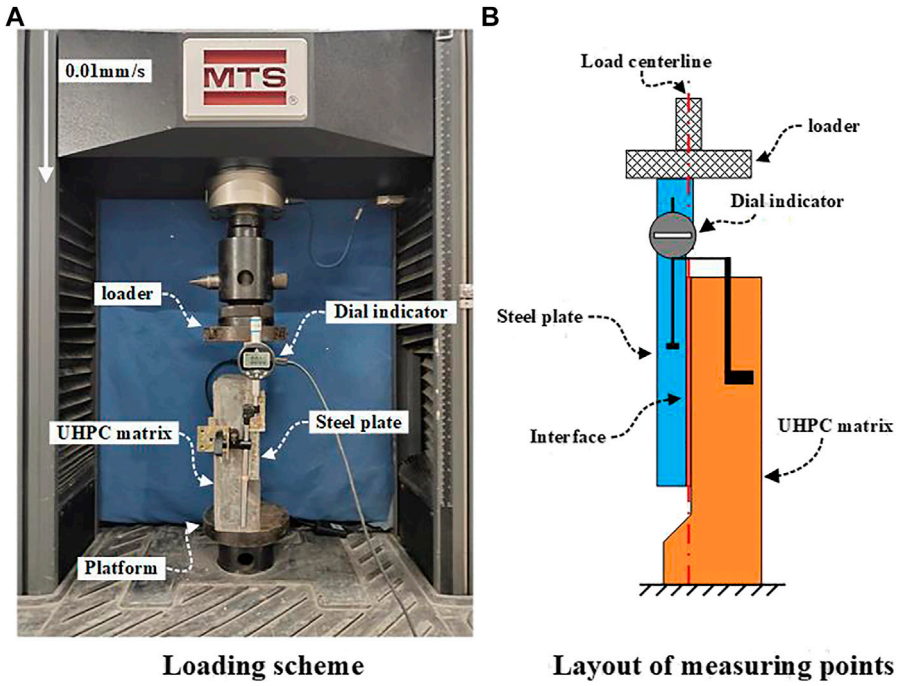

FIGURE 2
Interface test scheme. **(A)** Loading scheme. **(B)** Layout of measuring points.

from the center of the loader to avoid eccentric loading. The load on the specimen is measured by sensors in the loader. The two digital micrometers are symmetrically arranged at both ends of the interface, and the interface slip is the average value of the measured data. Before formal loading, it is necessary to move the beam slightly to make the loader fully in contact with the top of the steel plate to eliminate the gap caused by insufficient contact. The displacement loading method is adopted in the test, and the loading speed is 0.01 mm/s. During the loading process, the interface between the steel plate and UHPC matrix continuously slips until the final complete separation, leading to the failure of the specimen.

2.3 Interface comparison

According to the test results, the load-slip curves of specimen DS-E, specimen DS-P, and specimen DS-F were selected to characterize the shear behavior of the three types of interfaces. In addition, the shear performance of short studs with a diameter of 13 mm and a height of 35 mm in the thin UHPC layer was additionally considered (Cao and Shao, 2019). According to the arrangement spacing of short studs in the literature, the equivalent interface area of short studs is 200 mm × 200 mm. The shear stress of the EB interface, PE interface, FT interface, and the short stud is the ratio of specimen load to interface area, and the shear stress-slip curve is shown in Figure 3.

In Figure 3, the shear strength of the EB interface and PE interface is significantly higher than that of the FT interface and short stud connector. However, the sliding ability of the FT interface and short stud connector is much higher than that of the EB interface and PE interface. According to the shear stress-slip curve, the shear stiffness of the three types of interfaces is significantly higher than that of the short stud connector. Compared with the three types of interfaces, the shear strength of the FT interface is 1.8 MPa, much lower than the EB interface and PE interface. The shear strength of the EB interface is the largest among the three types of interfaces. Still, this interface only applies to the connection between the steel plate and the prefabricated UHPC matrix. By contrast, the shear strength of the PE interface decreases, but its stiffness exceeds that of the FT interface and the short stud connector interface, and it is suitable for connecting the steel plate with the fresh UHPC matrix. Therefore, the PE interface is applicable in the steel-UHPC composite bridge deck formed by pouring UHPC.

3 Test scheme

3.1 Specimen design

In this study, six steel-UHPC composite bridge decks of the same size were fabricated to evaluate the flexural performance of

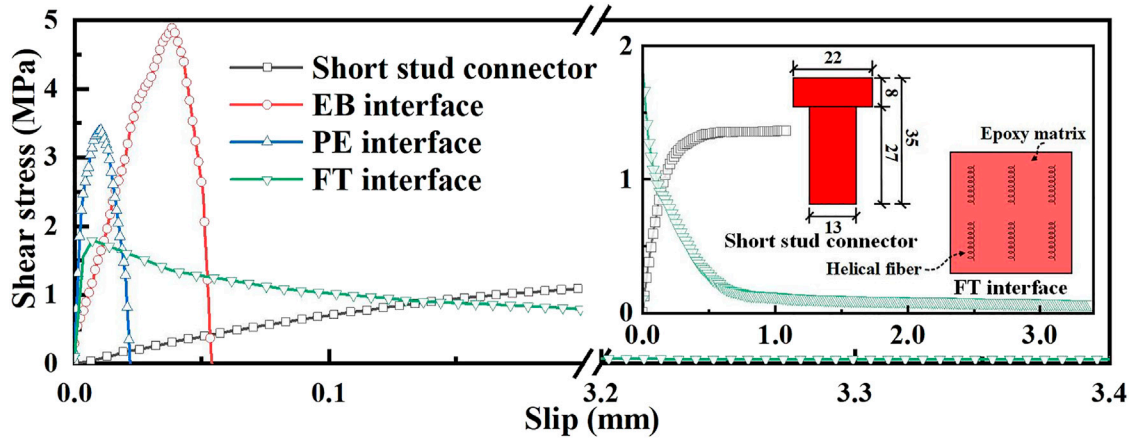

FIGURE 3
Comparison of shear stress-slip curves between short stud connector and interface.

composite bridge decks with different interfaces. As shown in Figure 4, all composite deck slabs have the same structural form and reinforcement arrangement except for the interface. The overall dimension of the steel-UHPC composite bridge deck is 1,200 × 200 × 62 mm, the size of the steel plate is 1,200 × 200 × 12 mm, and the size of the thin layer UHPC is 1,200 × 200 × 50 mm. HRB400 reinforcement with a diameter of 10 mm is arranged in the thin UHPC layer, and the arrangement spacing is 50 mm. The composite bridge deck adopts the short stud connector and the PE interface, and the defects of the PE interface are also considered. In the two types of connections, the diameter of the short stud is 13 mm, and the height is 35 mm. The PE interface comprises a 2 mm thick epoxy matrix and 2–3 mm quartz sand particles, and the quartz sand parameter is 0.23 g/cm^2. Details of all specimens are shown in Table 2. In the table, "CD" represents the steel-UHPC composite deck. "S" represents the stud. "P" represents the PE interface. "I" represents that the interface is intact without defects. "D" represents the interface defect, and the defect area accounts for 30% of the interface area. The defect position is not coated with epoxy, and its position is shown in Figure 4C. The subscripts "M" and "C" represent monotonic and cyclic loading, respectively.

3.2 Material properties

3.2.1 UHPC

In this study, UHPC is composed of cement, silica fume, quartz sand, quartz powder, water reducer, and water. The detailed raw material ratio is shown in Table 3. The volume content of polycarboxylate superplasticizer on the market is 1.5%, and the water reduction rate is greater than 35%. In order to ensure the excellent tensile properties of UHPC, the flat steel fiber with a volume content of 3% was introduced. The diameter of the steel fiber is 0.12 mm, the length is 8 mm, and the yield strength is greater than 1,200 MPa. According to Reactive powder concrete (GB/T31387-2015 (General Administration of Quality Supervision, 2015)), the compressive strength f_c, tensile strength f_t, and Young's modulus E_c respectively of UHPC were 114.6 MPa, 14.9 MPa, and 48.0 GPa, respectively.

3.2.2 Steel

Q345 grade steel and HRB400 grade reinforcement are selected for the steel-UHPC composite bridge deck. According to Metallic materials—Tensile testing—Part 1:Method of test at room temperature (GB/T 228.1-2010 (General Administration of Quality Supervision, 2010)), the yield 225 strength f_y, ultimate tensile strength f_u, and Young's modulus E_s of the steel plate and reinforcement were measured by tensile test. Table 4 summarizes the material properties of Q345 grade steel and HRB400 grade reinforcement.

3.2.3 Epoxy adhesive

The epoxy adhesive (steel adhesive CBSR-A/B) used to make the epoxy matrix is produced in Carbon Technology Group Co., Ltd. The components of CBSR-A/B were the main agent CBSR-A and curing agent CBSR-B, and the weight ratio of the two was 2:1. According to Test methods for properties of resin casting body (GB/T 2567-2021 (Zou et al., 2022)), the tensile properties of the epoxy adhesive include tensile strength f_{te} and tensile Young's modulus E_{te}, and the compressive properties include compressive strength f_{ce} and compressive Young's modulus E_{ce}. Table 5 summarizes the mechanical properties of epoxy adhesive.

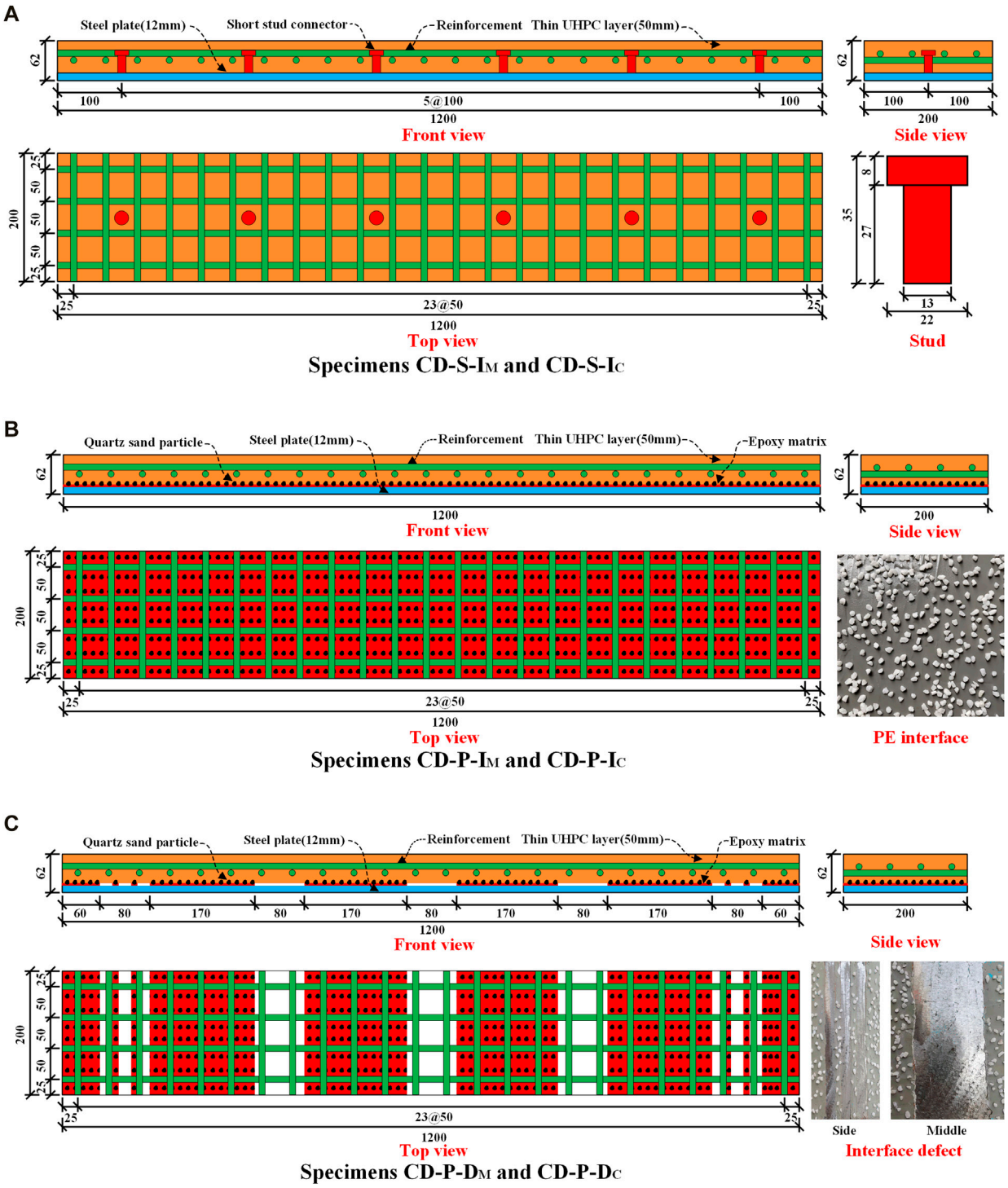

FIGURE 4
Steel-UHPC composite bridge deck. **(A)** Specimens CD-S-I_M and CD-S-I_C. **(B)** Specimens CD-P-I_M and CD-P-I_C. **(C)** Specimens CD-P-D_M and CD-P-D_C.

TABLE 2 Detailed information on the composite bridge deck.

Specimen	Interface type	Interface defect	Loading method
CD-S-I_M	Short stud connector	Intact	Monotone
CD-S-I_C	Short stud connector	Intact	Cycle
CD-P-I_M	PE interface	Intact	Monotone
CD-P-I_C	PE interface	Intact	Cycle
CD-P-D_M	PE interface	Defect (30%)	Monotone
CD-P-D_C	PE interface	Defect (30%)	Cycle

TABLE 3 Proportion of UHPC.

Component	Mass ratio	Proportion (%)
Cement	1.000	34.55
Silica fume	0.250	8.64
Quartz sand	1.100	38.01
Quartz powder	0.300	10.37
Water reducing agent	0.019	0.66
Water	0.225	7.77

TABLE 4 Material properties of steel.

Material	f_y (MPa)	f_u (MPa)	E_s (GPa)
Q345	359.5	494.0	210.0
HRB400	439.3	577.1	210.0

TABLE 5 Mechanical properties of epoxy adhesive.

Material	f_{te} (MPa)	f_{ce} (MPa)	E_{te} (MPa)	E_{ce} (MPa)
CBSR-A/B	28.4	102.4	0.8	1.1

3.3 Specimen preparation

The fabrication process of the steel-UHPC composite bridge deck is detailed in Figure 5. In Figure 5A, the surface of the steel plate is cleaned with acetone to ensure firm adhesion between the epoxy matrix and the steel plate. In Figure 5B, after the epoxy adhesive is fully mixed in the container, the epoxy adhesive is evenly applied from the center of the steel plate to the periphery to complete the production of the 2 mm thick epoxy matrix. In Figure 5C, before the epoxy matrix is cured, quartz sand particles are evenly distributed on the epoxy matrix in time. Afterward, appropriate pressure was applied to make quartz sand particles firmly embedded in the epoxy matrix. After 7 days of room temperature curing, the PE interface is completed. In contrast, the short studs are directly welded to the steel plate without additional maintenance. In Figure 5D, the steel plate and steel mesh are installed in the mold, and the spacing between the steel mesh and the top of the steel plate and UHPC layer meets the thickness requirement of the protective layer. In Figure 5E, UHPC was poured into the mold, and the mold was removed after 3 days of natural maintenance. In Figure 5F, the composite plate was cured at room temperature for 28 days, and the specimen was prepared by coating it with white paint.

3.4 Test scheme and instrument

Figure 6A shows the measuring point arrangement of the steel-UHPC composite bridge deck. All the composite bridge decks adopt a four-point loading scheme, and a hydraulic jack and distribution beam can realize the pure bending moment area of 400 mm in the middle span. The displacement sensors D-1 and D-2 are arranged at 100 mm from the edge of the composite plate to measure the deflection at the fulcrum, and the displacement sensor D-3 is arranged in the middle of the composite plate to measure the mid-span deflection. Displacement sensors S-1 to S-4 were arranged at the edge of the composite bridge deck and 300 mm away from the edge to measure the slip of the thin UHPC layer and steel plate at the interface. Strain gauges are arranged at the top, bottom, and side of the composite bridge deck at midspan to measure the strain of the thin UHPC layer and the steel plate in the pure bending area.

The bending test of the steel-UHPC composite bridge deck adopts the loading process adopted by Zou et al. (2022), as shown in Figures 6B,C. In Table 2, the same group of specimens can be divided into monotonic and cyclic loading according to the loading process. In the monotonic loading scheme (Figure 6B), three preloads with an amplitude of 30% of the predicted ultimate load (^{P}) is applied to check the potential problem during loading. Finally, continuous loading until the specimen fails. In the cyclic loading scheme (Figure 6C), the cyclic loading of 0-50% Pu and 0-70% Pu was applied ten times

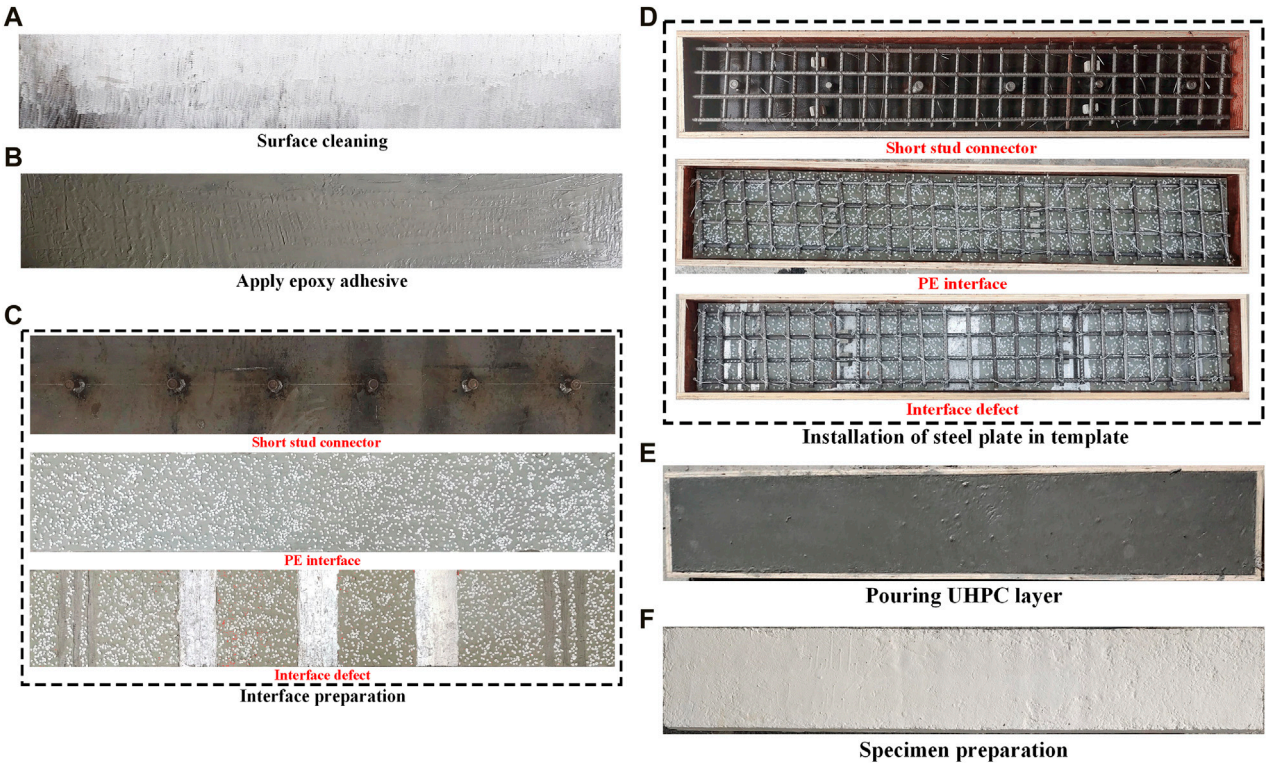

FIGURE 5
Preparation of three types of steel-UHPC composite bridge deck. **(A)** Surface cleaning. **(B)** Apply epoxy adhesive. **(C)** Interface preparation. **(D)** Installation of steel plate in template. **(E)** Pouring UHPC layer. **(F)** Specimen preparation.

after three times of pre-loading, and then the specimen was continuously loaded until failure. During the test, the development process of cracks was observed and recorded.

4 Results and analysis

4.1 Failure mode

The specimen CD-S-I_M has the following failure characteristics. At the beginning of loading, no obvious phenomenon was observed on the composite bridge deck, and the structural stiffness had not changed. After that, when loading to a certain extent, the end of the composite plate was observed to slip, and the micro-cracks at the steel-UHPC interface began to initiate. With the increasing load, the UHPC layer near the loading point produced obvious oblique cracks and cracks developed along the interface. After the steel plate yielded, the UHPC layer near the loading point was crushed locally, and the interface in the shear bending section and the end of the composite bridge deck was void, leading to the specimen's bending failure. After specimen failure, the crack distribution of specimen CD-S-I_C is more dense than that of specimen CD-S-I_M. The reason is that the cyclic loading scheme makes the stress redistribution at the steel-UHPC interface, the interface slip distribution uniform, and the damage to the UHPC layer continuously accumulates. The failure of specimens CD-S-I_M and CD-S-I_C is shown in Figures 7A,B.

The specimen CD-P-I_M has the following failure characteristics. At the beginning of loading, no cracks were observed at the interface of the composite bridge deck. With the increasing load, tiny cracks gradually appeared near the interface. Once the cracks penetrated longitudinally along the composite bridge deck, the separation occurred at the steel-UHPC interface instantaneously, and the interface slip suddenly increased. However, the flexural bearing capacity of the specimen was not lost at this time. Finally, the increasing load made the steel plate yield, and the UHPC layer near the loading point was partially crushed, resulting in the bending failure of the composite bridge deck. After the failure of the specimen, specimen CD-P-I_C appeared to have severe interface failure compared with specimen CD-P-I_M in the cyclic loading process, which reduced the combined effect of the composite bridge deck at the interface. The low sliding ability of the PE interface led to this phenomenon. The failure of specimens CD-P-I_M and CD-P-I_C is shown in Figures 7C,D.

The specimen CD-P-D_M has the following failure characteristics. At the beginning of loading, the composite bridge deck was not damaged at the interface. After that,

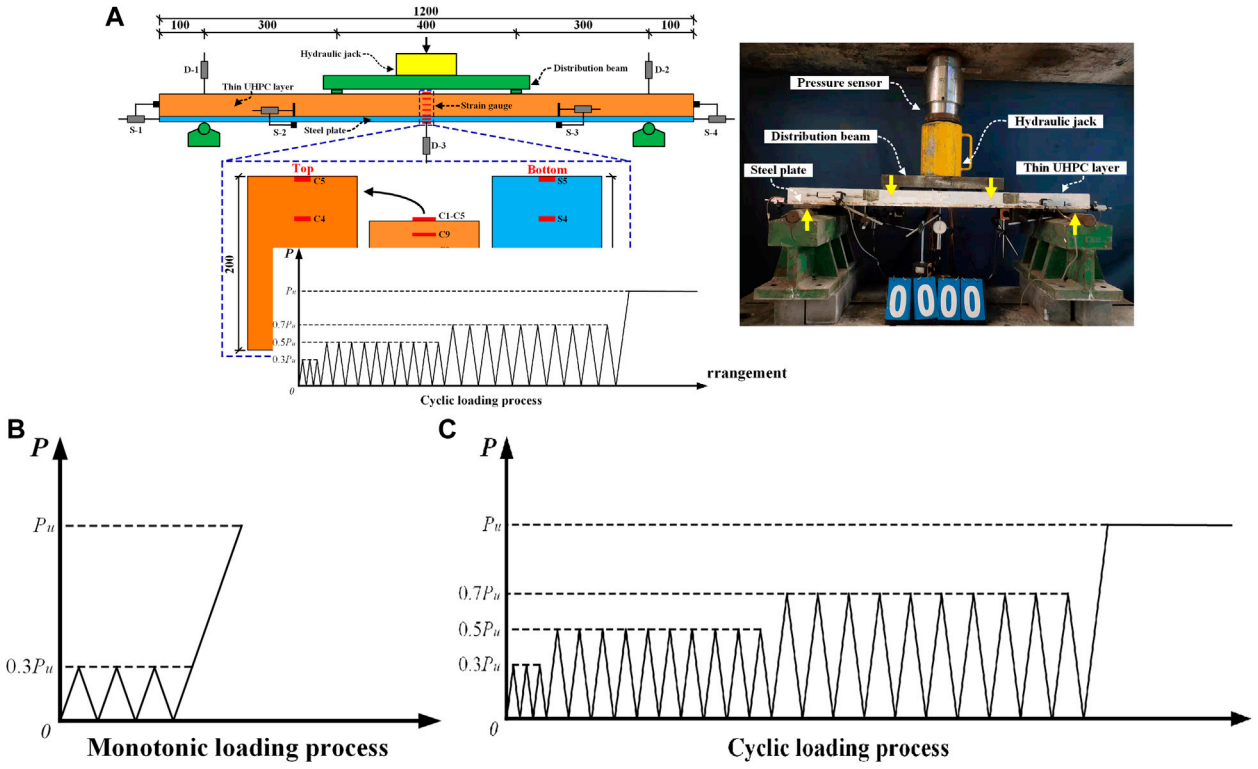

FIGURE 6
Loading scheme. **(A)** Measuring point arrangement. **(B)** Monotonic loading process. **(C)** Cyclic loading process.

when loading to a certain extent, the cracks near the interface of the composite bridge deck were penetrated, resulting in sudden separation at the interface and sudden growth of interface slip. Finally, the increasing load made the steel plate yield, and the UHPC layer near the loading point was partially crushed, resulting in the bending failure of the composite bridge deck. After the specimen is failed, the specimen CD-P-D_C has a larger interface separation than the specimen CD-P-D_M. In the case of interface defects, cyclic loading makes the connection effect of the PE interface significantly reduced, resulting in a large area of interface failure of the composite bridge deck. The failure of specimens CD-P-D_M and CD-P-D_C is shown in Figures 7E,F.

4.2 Load-deflection curve

Figure 8 shows the load-deflection curves of all composite bridge decks. In Figure 8A, specimen CD-S-I_M and specimen CD-S-I_C exhibit similar bending behavior. However, in the process of specimen failure caused by loading, the specific bending behaviors of the two types of specimens are significantly different. (a) Elastic phase. Before loading to30kN, the load and deflection of the composite bridge deck showed a linear growth relationship, and the bending stiffness of the composite bridge deck did not change. Before loading, specimen CD-S-I_C produced a significant residual deflection of 3.1 mm compared with specimen CD-S-I_M. (b) Elastic-plastic phase. With the increase of load, the end of the composite bridge deck slipped, the combined effect of the structure decreased, and the structural stiffness decreased so that the load-deflection curve increased nonlinearly. In this stage, the load-slip curves of the two types of specimens were basically coincident, and the cracks in the UHPC layer were continuously developing. (c) Yield phase. With the cracks' continuous development, the steel plate stress increased until yielding, the load no longer increased, and the mid-span deflection continued to grow. However, the damage accumulation of the UHPC layer under cyclic loading makes the mid-span deflection of specimen CD-S-I_C increase much less than that of specimen CD-S-I_M. (d) Failure phase. The load decreases rapidly with the increase of deflection, the UHPC layer near the loading point is locally crushed, and the composite bridge deck is bending failure.

In Figure 8B, specimen CD-P-I_M and specimen CD-P-I_C shows similar bending behavior, but the specimen CD-P-I_C

FIGURE 7
Failure of the steel-UHPC composite bridge deck. **(A)** Specimen CD-S-I_M. **(B)** CD-S-I_C. **(C)** CD-P-I_M. **(D)** CD-P-I_C. **(E)** CD-P-D_M. **(F)** CD-P-D_C.

suddenly shows 15.4 mm mid-span deflection under a cyclic loading scheme. The load-deflection curves of the two types of specimens are characterized as follows. (a) Elastic phase. Before loading to the ultimate load, the bending stiffness of the composite bridge deck did not change, and the load and deflection of the composite bridge deck showed a linear growth relationship. During this stage, the bending stiffness of specimen CD-P-I_C was slightly lower than that of specimen CD-P-I_M. (b) Damage phase. When loaded to the ultimate load, the PE interface on the side of the composite bridge deck appeared to have a large area failure, resulting in a sudden drop in load. The difference is that the deflection of specimen CD-P-I_C increases by 15.9% compared with specimen CD-P-I_M due to cyclic loading. (c) Failure phase. The load increases linearly with the deflection until the ultimate steel plate yields, and the UHPC layer is locally crushed near the loading point.

In Figure 8C, specimen CD-P-D_M and specimen CD-P-D_C show completely different bending behavior, indicating that when the interface defect area reaches 30%, the interface damage caused by cyclic loading cannot be ignored. In addition, the mid-span deflection of specimen CD-P-D_C suddenly increased by 15.0 mm during cyclic loading. Under the monotonic loading scheme, specimen CD-P-D_M showed similar bending behavior to specimen CD-P-I_M. The difference is that the load of specimen CD-P-D_M does not reach the ultimate load in the elastic stage, and the load-slip curve shows nonlinear growth characteristics in the failure stage. Under cyclic loading, the specimen CD-P-D_C produced a mid-span deflection of 2.4 mm before loading and then experienced elastic-plastic growth until the bending failure of the composite bridge deck.

Table 6 lists the bending properties of the three types of composite bridge decks. Compared with the composite bridge deck with short stud connectors (specimen CD-S-I_M), the ultimate load of specimen CD-S-I_C is reduced by 4.1%,and the maximum deflection is reduced by 37.8%. Compared with the

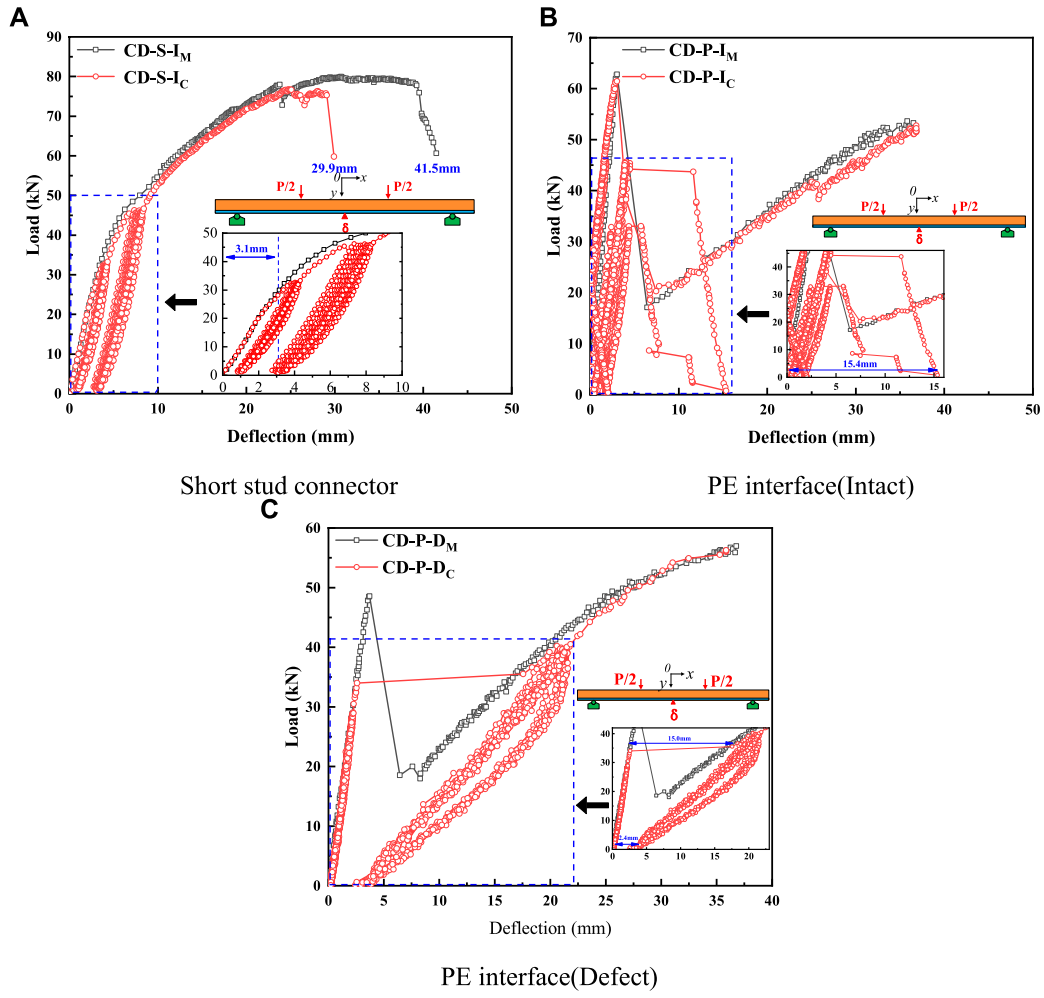

FIGURE 8
Load-deflection curve. **(A)** Short stud connector. **(B)** PE interface (Intact). **(C)** PE interface (Defact).

TABLE 6 Bending properties of steel-UHPC composite bridge deck.

Specimen	Ultimate load (kN)	Maximum deflection (mm)	Failure mode
CD-S-I_M	80.0	48.1	BF
CD-S-I_C	76.7	29.9	IF,BF
CD-P-I_M	62.8	36.5	IF,BF
CD-P-I_C	61.5	36.0	IF,BF
CD-P-D_M	57.0	36.8	IF,BF
CD-P-D_C	56.3	35.9	IF,BF

Note: BF represents the bending failure of the composite bridge deck. IF represents the interface failure of the composite bridge deck.

composite bridge deck with PE interface (specimen CD-P-I_M), the ultimate load of specimen CD-P-I_C is reduced by 2.1%, and the maximum deflection is reduced by 1.4%. Compared with the composite bridge deck with defect PE interface (specimen CD-P-D_M), the ultimate load of specimen CD-P-D_C is reduced by 1.2%, and the maximum deflection is reduced

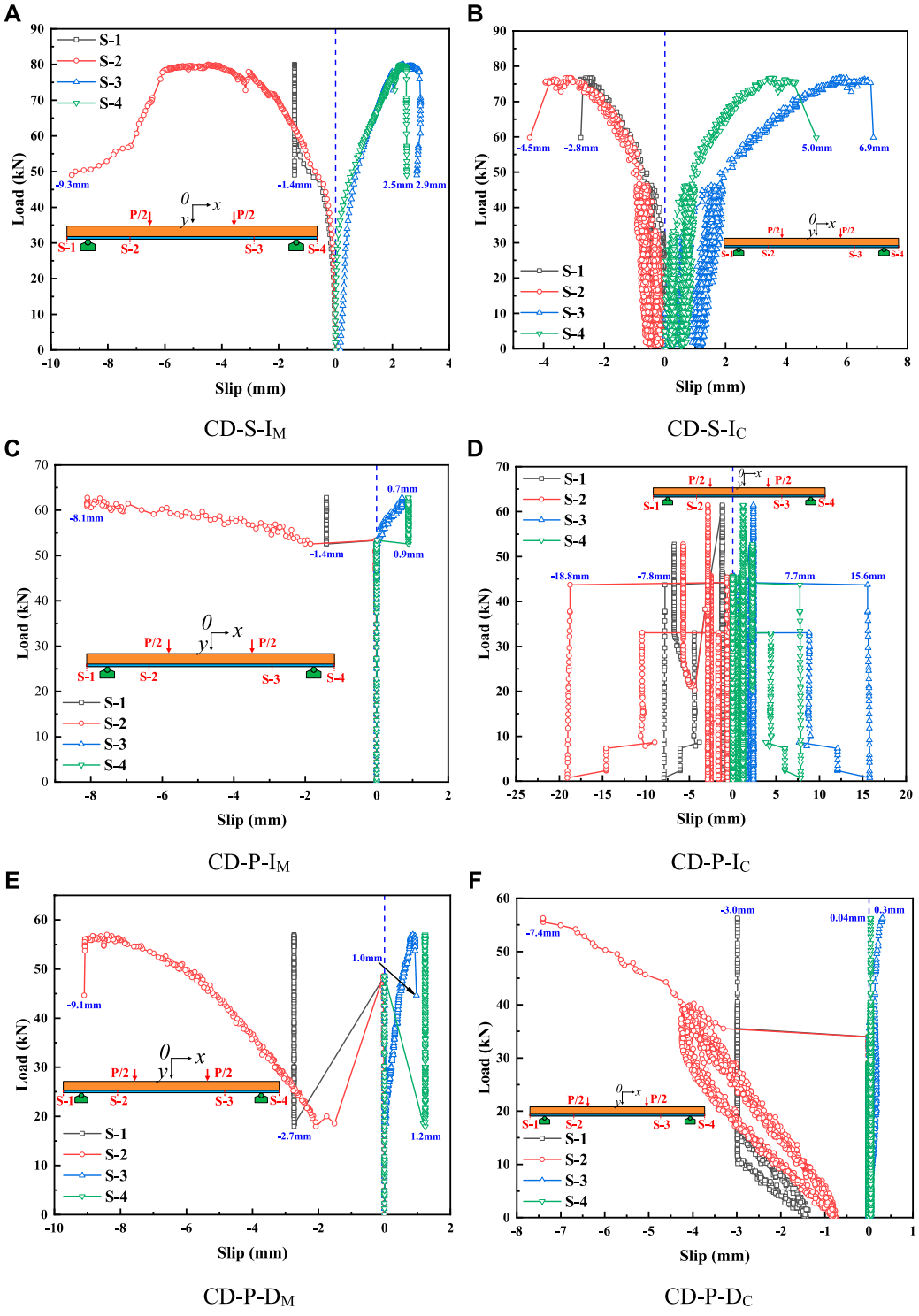

FIGURE 9
Load-slip curve. **(A)** Specimen CD-S-I$_M$. **(B)** CD-S-I$_C$. **(C)** CD-P-I$_M$. **(D)** CD-P-I$_C$. **(E)** CD-P-D$_M$. **(F)** CD-P-D$_C$.

by 2.4%. Therefore, even though the ultimate load of the specimen CD-P-I$_M$ is reduced by 21.5% compared with the specimen CD-S-I$_M$, the maximum deflection is less affected by the cyclic loading mode. In Figure 3, the main reason is that the shear stiffness of the PE interface is much larger than that of the short stud connector.

4.3 Load-slip curve

Figure 9 shows the load-slip curves of all composite bridge decks. In the figure, the maximum interface slip occurs at the interface near the loading point. The interface void in the pure bending section leads to its slip greater than that at the end of the composite bridge deck. In Figures 9A,B, the maximum interface slip of specimen CD-S-I_M is 9.3 mm, and the maximum interface slip of specimen CD-S-I_C is 6.9 mm. The maximum interface slip of composite bridge deck under cyclic loading is reduced by 25.8% compared with that under monotonic loading. In addition, the interface slip distribution of the specimen CD-S-I_C is more symmetrical along both sides of the span, indicating that the stress redistribution occurs at the interface of the composite bridge deck under cyclic loading. In Figures 9C,D, the initial crack load of specimen CD-P-I_M was 53.2kN, and the maximum interfacial slip was 8.1mm, while the initial crack load of specimen CD-P-I_C was 32.7 kN and the maximum interfacial slip was 18.8 mm. However, the maximum interfacial slip of specimen CD-P-I_C occurs during cyclic loading, not during failure. Cyclic loading causes continuous damage to the PE interface resulting in a sudden increase in interface slip. When the specimen CD-P-I_C failed, the maximum interface slip of the measuring point was 6.8 mm, 16.0% lower than that of the specimen CD-P-I_M. In addition, the interface slip distribution of the specimen CD-P-I_C is more symmetrical along both sides of the span, indicating that the PE interface can still ensure the reliable connection of the composite bridge deck at the interface under cyclic loading. The composite bridge deck produces stress redistribution at the interface.

In Figures 9E,F, the initial crack load of specimen CD-P-D_M was 19.6kN, and the maximum interfacial slip was 9.1 mm. However, due to defects in specimen CD-P-D_C, the slip occurred at the defect position when the cyclic load began, and the maximum interfacial slip was 7.4 mm. The maximum interface slip of composite bridge deck under cyclic loading is reduced by 18.7% compared with that under monotonic loading. However, the distribution of the interface slip of the specimen CD-P-D_C along both sides of the span is no longer symmetrical, indicating that the cyclic loading makes the combined action of the composite bridge deck fail at the interface. The composite bridge deck with PE interface is not suitable to bear the cyclic load when the interface defect area reaches 30%.

4.4 Strain distribution

Figure 10 shows the strain distribution of all composite bridge decks along the height direction in the midspan. In Figures 10A,B, when the load of specimen CD-S-I_M is lower than 48.5 kN, the strain at midspan is linearly distributed. As the loading continues, the strain at the midspan presents more and more obvious nonlinear distribution. The strain at the midspan of the specimen CD-S-I_C is always linearly distributed. Still, it is not continuous at the steel-UHPC interface, and the strain of the thin UHPC layer and the steel plate is linearly distributed. Under the cyclic loading scheme, the stress redistribution occurs at the interface of the composite bridge deck, resulting in a greatly reduced combination of the thin UHPC layer and steel plate at the interface. Meanwhile, when the load is higher than 46.0 kN, the strain of the thin UHPC layer near the interface increases significantly, indicating that the thin UHPC layer at the interface is gradually damaged.

In Figures 10C,D, when the load of specimen CD-P-I_M is lower than 49.0 kN, the strain at midspan is approximately linearly distributed. Before loading to the ultimate load, the PE interface can realize the reliable connection between the thin UHPC layer and steel plate. When the load is 62.8 kN, the PE interface is suddenly damaged in a large area at the end, resulting in a sudden increase in strain. The strain distribution of specimen CD-P-I_C in the loading failure process is approximately linear, indicating that the PE interface can ensure the reliable connection of the thin UHPC layer and steel plate even after cyclic damage.

In Figures 10E,F, when the load of specimen CD-P-D_M is lower than 45.3 kN, the strain at midspan is approximately linearly distributed. When the load is 57.0 kN, the PE interface is suddenly destroyed in a large area at the end, resulting in a sudden increase in strain. Compared with the specimen CD-P-I_M, the interface defect area of 30% does not significantly weaken the connection performance of the PE interface in the composite bridge deck. After cyclic loading of specimen CD-P-D_C, the thin UHPC layer near the interface has already cracked and been destroyed, so the strain is very large. Therefore, when the interface defect area is 30%, the composite bridge deck with PE interface is not suitable to bear the cyclic load.

5 Numerical simulation

5.1 Simulation procedure

In this study, the finite element model of the steel-UHPC composite bridge deck is established by ABAQUS explicit analysis method to realize the numerical simulation of the short stud connector and PE interface in the composite bridge deck. In Figure 11, based on the symmetry of the composite bridge deck, a quarter model is established to improve the calculation efficiency. The symmetry planes are plane y and plane x, respectively. The steel plate, thin UHPC layer, studs, and cube are simulated by C3D8 (three-dimensional 8-node linear solid integration element), and the reinforcement is simulated by B31 (2-node linear beam in space). The zero-

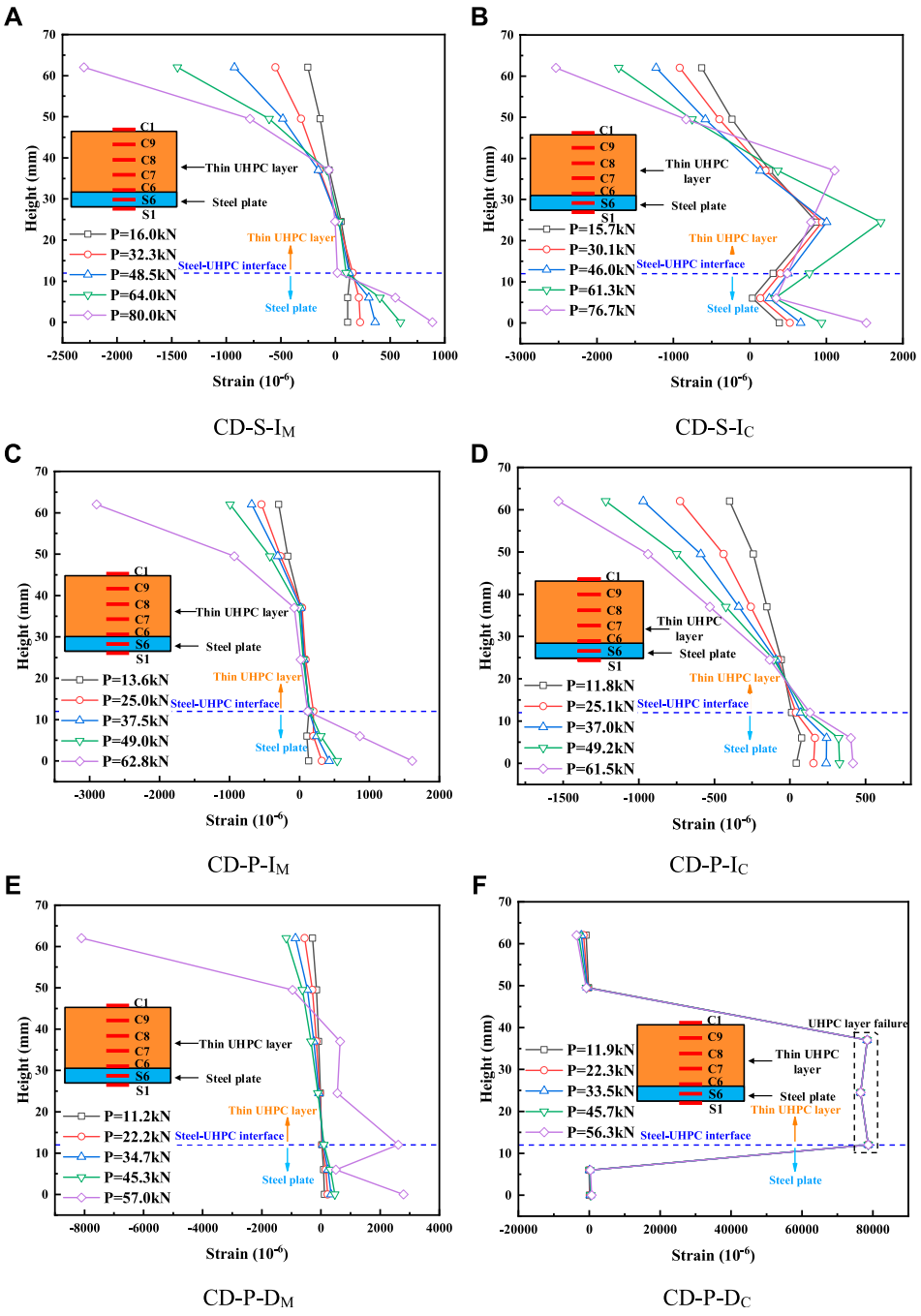

FIGURE 10
Strain distribution. **(A)** Specimen CD-S-I_M. **(B)** CD-S-I_C. **(C)** CD-P-I_M. **(D)** CD-P-I_C. **(E)** CD-P-D_M. **(F)** CD-P-D_C.

thickness cohesive element was used to simulate the mechanical behavior of the PE interface. In the model, the global cell size of the steel plate, thin UHPC layer, and reinforcement is 5 mm, and the global cell size of the cube is 10 mm.

The contact relationship between the steel plate and the thin UHPC layer, the thin UHPC layer, and the short stud connector is normal hard contact, and the tangential friction coefficient is set to 0.4 (Cao and Shao, 2019). The reinforcement is constrained inside the thin UHPC layer by the "embedded region." The PE interface and thin UHPC layer are constrained by "Tie," and the thin UHPC layer and cube are also constrained. In addition, the numerical models adopt the displacement loading method and set smooth analysis steps to avoid the fluctuation of the applied load.

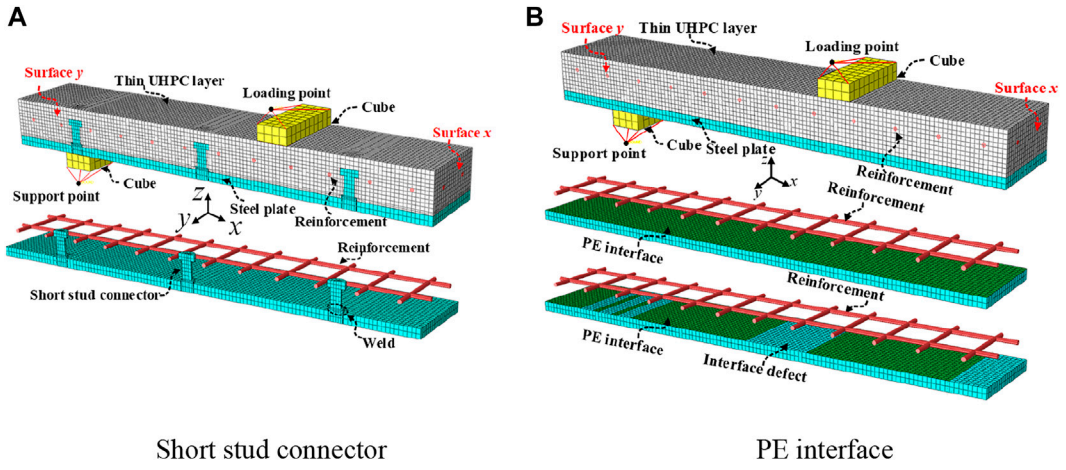

FIGURE 11
Modeling information. **(A)** Short stud connector. **(B)** PE interface.

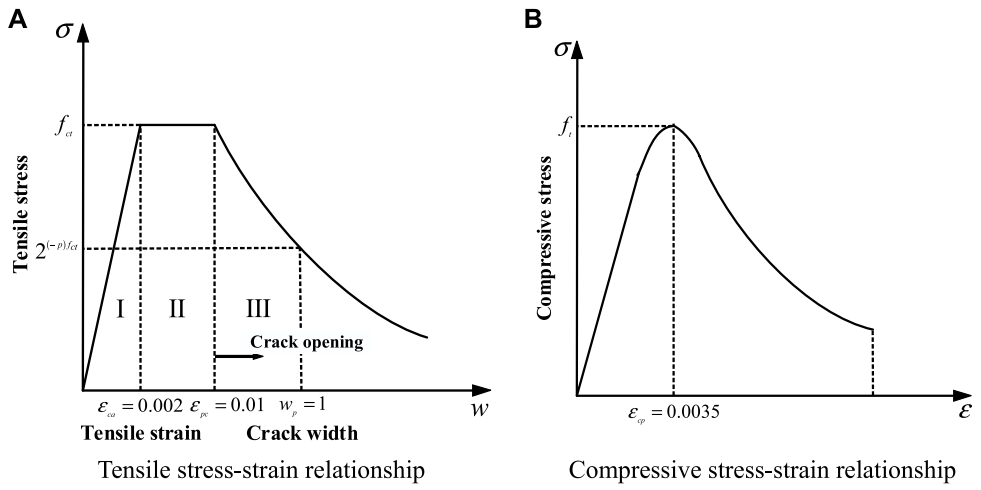

FIGURE 12
Stress-strain relationship of UHPC. **(A)** Tcnsile stress-strain relationship. **(B)** Compresssive stress-strain relationship.

5.2 Material constitutive model

5.2.1 UHPC

The concrete plastic damage (CDP) model provided by finite element software ABAQUS was used to simulate the damage and failure process of the thin UHPC layer. Therefore, the tensile and compressive behaviors of UHPC stress-strain curves need to be defined independently. Zhang et al. (2015) obtained the constitutive law under tensile load (Eq. 1) according to the tensile test of UHPC. Yang and Fang (2008) calculated the constitutive law under compression load according to the uniaxial compression test of UHPC (Eq. 2). The stress-strain relationship of UHPC is shown in Figure 12.

$$\sigma = \begin{cases} \text{I} & \dfrac{f_{ct}}{\epsilon_{ca}}\epsilon \qquad 0 < \epsilon \le \epsilon_{ca} \\ \text{II} & f_{ct} \qquad \epsilon_{ca} < \epsilon \le \epsilon_{pc} \\ \text{III} & \dfrac{f_{ct}}{\left(1 + w/w_p\right)^p} \qquad 0 < w \end{cases} \tag{1}$$

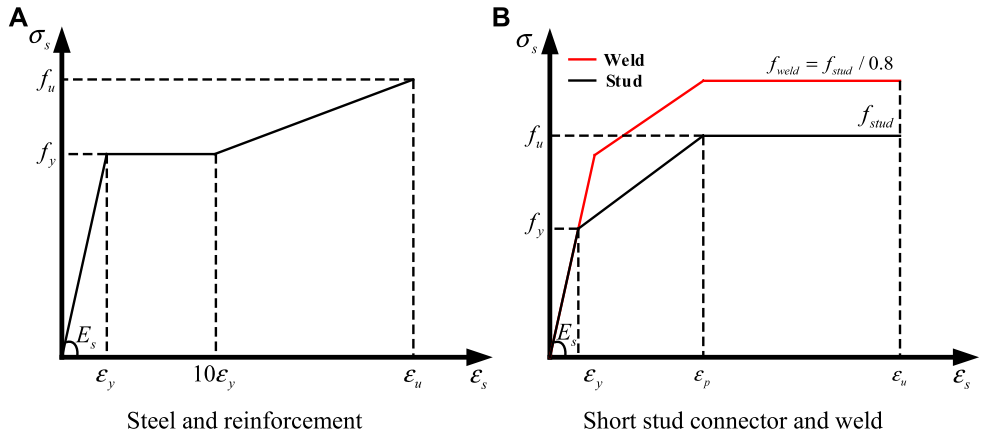

FIGURE 13
Stress-strain relationship of steel, short stud connector and weld.

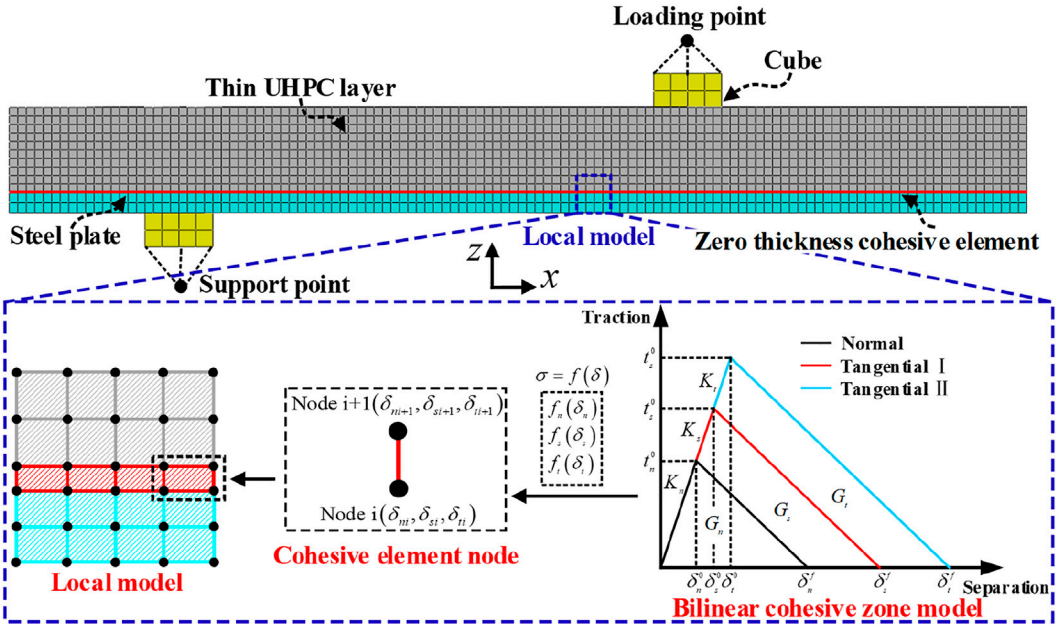

FIGURE 14
Constitutive model of cohesive element.

TABLE 7 Cohesive model parameters of PE interface.

Direction	$t^0_{n,s,t}$ (MPa)	$K_{n,s,t}$ (N/mm3)	$G_{n,s,t}$ (N/mm)
Normal	1.2	103	0.004
Tangential I	2.1	230	0.082
Tangential II	2.1	230	0.082

$$\sigma = \begin{cases} f_c \dfrac{n\xi - \xi^2}{1 + (n-2)\xi} & 0 < \epsilon \le \epsilon_{cp} \\ f_c \dfrac{\xi}{2(\xi - 1)^2 + \xi} & \epsilon > \epsilon_{cp} \end{cases} \tag{2}$$

where f_{ct} is the tensile strength of UHPC, and its value is 14.9 MPa. f_c is the cube compressive strength of UHPC, and

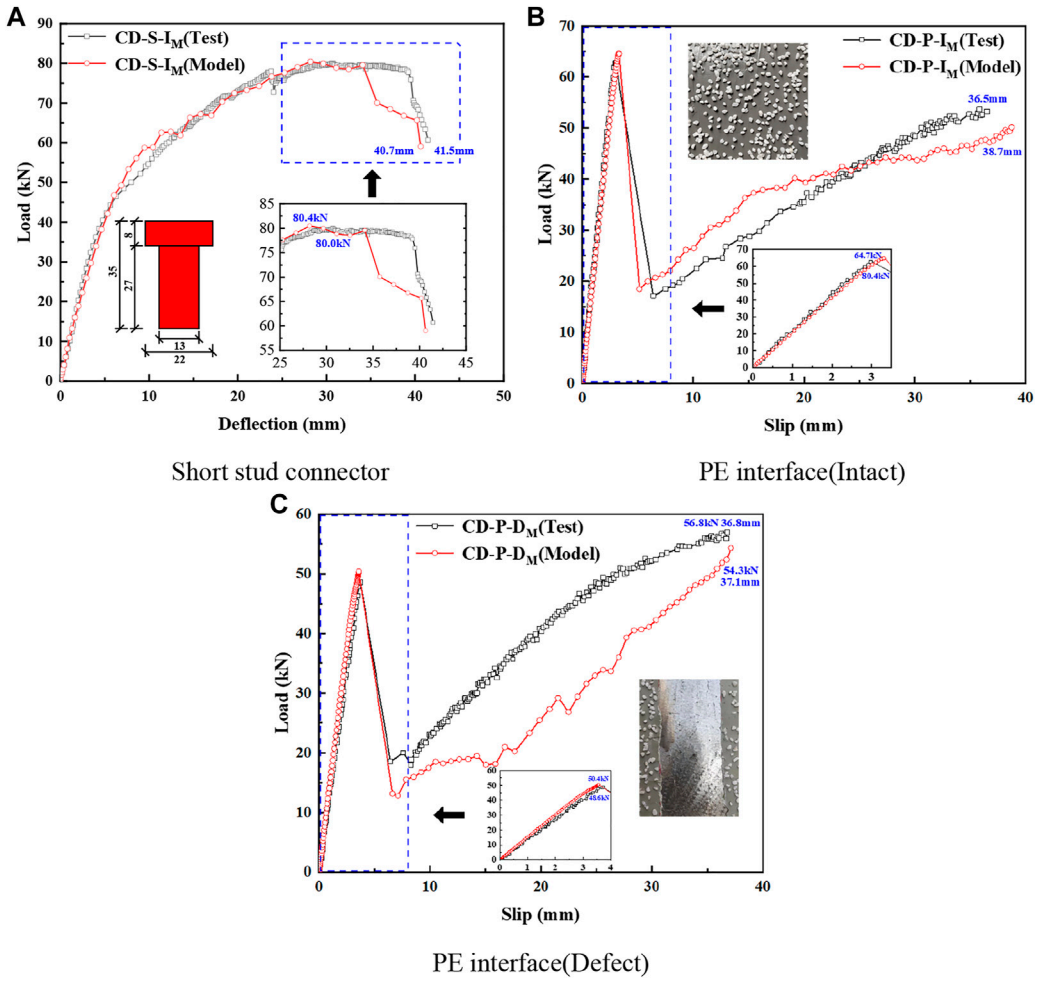

FIGURE 15
Load-deflection curves of test and model. **(A)** Short stud connector. **(B)** PE interface (Intact). **(C)** PE interface (Defact).

TABLE 8 Comparison of test and model results.

Specimen	Ultimate load (kN)			Maximum deflection (mm)		
	Test (P_u^T)	Model (P_u^M)	P_u^M/P_u^T	Test ($D_f{}^T$)	Model (D_f^M)	D_f^M/D_f^T
CD-S-I$_M$	80.0	80.4	1.01	41.5	40.7	0.98
CD-P-I$_M$	62.8	64.7	1.03	36.5	38.7	1.06
CD-P-D$_M$	56.8	54.3	0.96	36.8	37.1	1.01

its value is 114.6MPa. ξ is the strain ratio, defined as $\xi = \epsilon/\epsilon_{cp}$. n is the elastic modulus ratio, defined as $n = E_c/E_s$. ϵ_{cp} is the strain corresponding to the ultimate stress, and its value is 0.0035. E_c is the initial elastic modulus, and its value is 48.0 GPa. E_s is the secant modulus at the ultimate stress on the compressive stress-strain curve.

5.2.2 Steel and weld

The test results show that the steel plate has yielded during the bending failure of the composite bridge deck, and the reinforcement can reach the yield stress. Therefore, the constitutive relationship of steel and reinforcement is based on the trilinear stress-strain relationship (Zou et al., 2021b) in

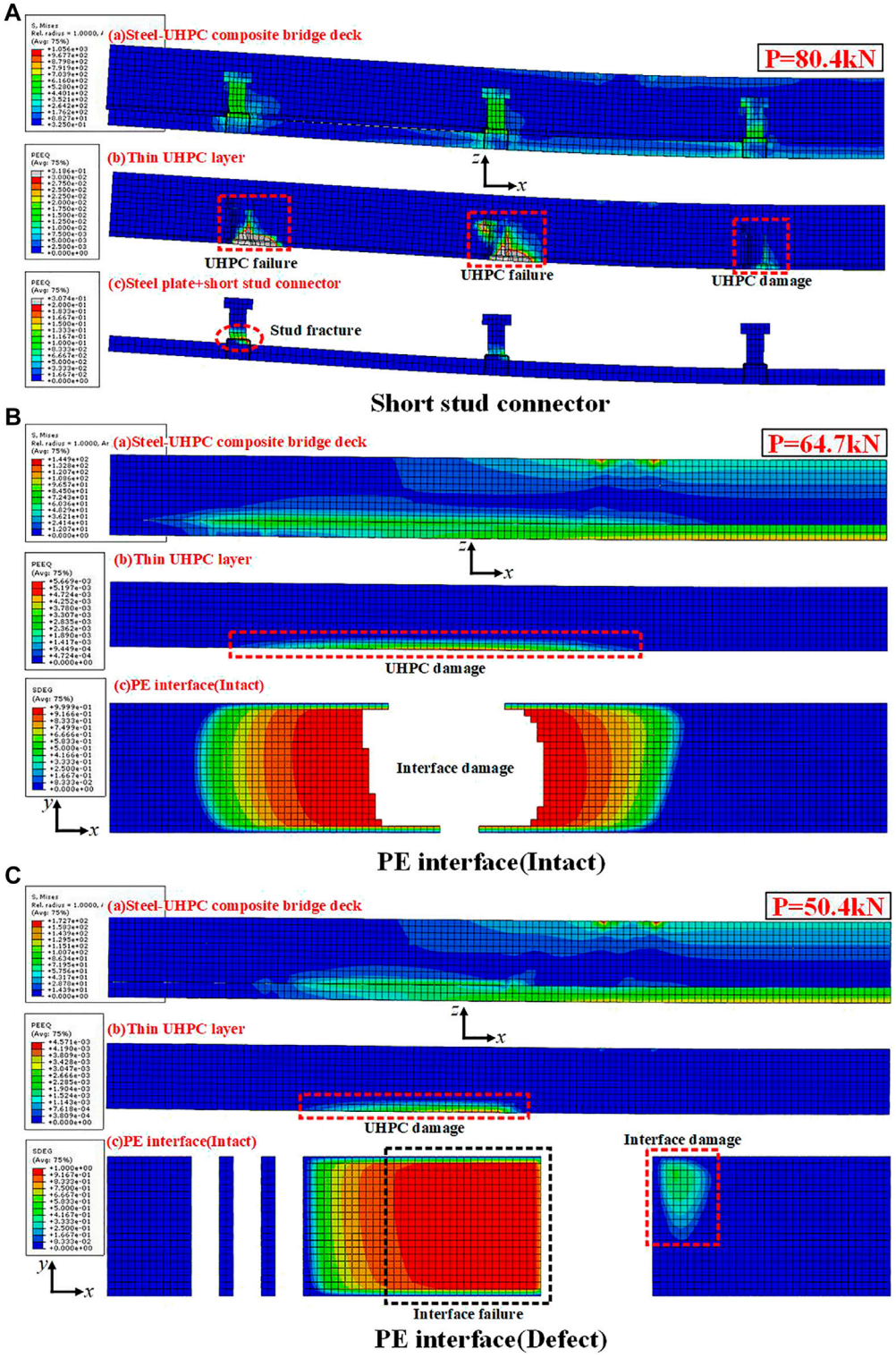

FIGURE 16
Damage of thin UHPC layer, short stud connector, and PE interface. **(A)** Short stud connector. **(B)** PE interface (Intact). **(C)** PE interface (Defact).

Figure 13A, and the mechanical properties are listed in Table 4. The first phase characterizes the elastic phase, the stress increases linearly with the strain growth, and the linear slope is the material's elastic modulus. The second phase represents the yield phase, in which the stress remains unchanged, and the strain increases to $10\epsilon_y$. After entering the third phase (strengthening phase), stress increases with strain to the ultimate strength f_u and ultimate strain ϵ_u. Meanwhile, the composite bridge deck's short stud connector and weld have experienced serious damage, and it is necessary to select the appropriate stress-strain relationship to achieve accurate numerical simulation. Therefore, the constitutive relationship of the short stud connector and the weld is based on the trilinear stress-strain relationship in Figure 13B. According to the tensile test, the yield strength f_y of the short stud connector is 420 MPa, and the ultimate strength f_u is 539 MPa. The strain ϵ_y is 0.002, ϵ_p is 0.006, and ϵ_u is 0.012. Cao et al. (Cao and Shao, 2019) have confirmed that when the weld strength f_{weld} exceeds the stud strength f_{stud} ($f_{weld} = f_{stud}/0.8$), the numerical simulation results agree well with the test results. Therefore, this stress-strain relationship ($f_{weld} = f_{stud}/0.8$) is adopted in the weld in the model.

5.2.3 Interface

The cohesive model is suitable for the numerical analysis of the steel-concrete interface. The complex interface behavior simulation can be realized by the traction- separation relationship of the nodes in the cohesive element (Ranz et al., 2020). In Figure 14, the thickness of the PE interface is much smaller than the size of the composite bridge deck. Therefore, the zero thickness cohesive element is used to simulate the PE interface. Meanwhile, the shear stress-slip curve of the PE interface in Figure 3 is bilinear. Its stress characteristics show that the cohesive model should adopt a bilinear stress-separation relationship. The constitutive law of the traction-separation relation is Eq. 3. The stress-displacement relationship of the cohesive element can be determined through the bilinear traction-separation relationship. Then the complex interface behavior simulation in the local model can be realized. The cohesive model parameters for the PE interface are detailed in Table 7.

$$t_{n,s,t} = \begin{cases} t^0_{n,s,t}\dfrac{\delta}{\delta^0_{n,s,t}} = K_{n,s,t}\delta & \delta \le \delta^0_{n,s,t} \\ t^0_{n,s,t}\dfrac{\delta^f_{n,s,t} - \delta}{\delta^f_{n,s,t} - \delta^0_{n,s,t}} & \delta^0_{n,s,t} < \delta \le \delta^f_{n,s,t} \end{cases} \tag{3}$$

where t^0_n , t^0_s , and t^0_t are the ultimate strength in the normal direction and two tangential directions of the interface, respectively. δ^0_n, δ^0_s, and δ^0_t are the separation displacements corresponding to the ultimate strength in each direction, respectively. δ^f_n, δ^f_s, and δ^f_t are the maximum displacement of interface failure in each direction. K_n, K_s, and K_t are the elastic stiffness in each direction.

5.3 Model validation

Figure 15 shows the load-deflection curves of three types of composite bridge decks (Test and model). In Figure 15A, the two types of curves show good consistency, but the difference is large in the failure phase. In Table 8, the deviation of the model calculation value P^M_u of the ultimate load of specimen CD-S-I_M from the test value P^T_u is within 1%, and the deviation of the model calculation value D^M_f of the maximum deflection from the test value D^T_f is within 2%. The results show that the contribution of stud weld in thin UHPC layer to the composite bridge deck bearing capacity can not be ignored. In Figures 15B,C, the model's calculation curve of the composite bridge deck connected by the PE interface is in good agreement with the test's curve, but the failure phase of the composite bridge deck is quite different. In Table 8, the maximum deviation of the ultimate load of specimen CD-P-I_M and specimen CD-P-D_M is within 5%, and the maximum deviation of maximum deflection is within 6%. Therefore, the composite bridge deck's bending behavior can be simulated by using the cohesive zone model (CZM) to simulate the PE interface.

5.4 Discussion

Figure 16 shows the damage of the thin UHPC layer, short stud connectors, and PE interface in various steel-UHPC composite decks. In Figure 16, the stud's equivalent plastic strain (PEEQ) is greater than 0.2, indicating that the stud fracture (Luo et al., 2016). The equivalent plastic strain (PEEQ) of UHPC is greater than 0.03, indicating the failure of UHPC (Luo et al., 2016). In addition, when the interface element's stiffness degradation (SDEG) reaches 1, the PE interface fails. SDEG is between 0 and 1, indicating PE interface damage. In Figure 16A, when the load is up to the ultimate load (p = 80.4 kN), the stress of the composite bridge deck with the short stud connector is mainly concentrated near the short stud connectors. In the composite bridge deck, UHPC outside the pure bending section is damaged, and the root of the stud at the end is fractured. In Figure 16B, the stress of the bridge deck with PE interface (Intact) is uniformly distributed along the x-axis before the interface failure (p = 64.7 kN). Meanwhile, UHPC damage occurred near the interface outside the pure bending section, and a large area of failure and damage occurred at the PE interface. In Figure 16C, the stress of the bridge deck with PE interface (Defect) is uniformly distributed along the x-axis before the interface failure (p = 50.4 kN). Although the UHPC damage in the interface defect is weaker, the failure and damage of the PE interface are more concentrated. In the steel-UHPC composite bridge deck,

the PE interface can make the stress transfer at the steel-UHPC interface more uniform than the short stud connector, and there is no failure to the thin UHPC layer before the interface failure.

6 Conclusion

This study used the PE interface to realize the reliable connection between the thin UHPC layer and the steel plate in the steel-UHPC composite bridge deck. Through the bending test of the composite bridge deck, the effects of the short stud connector and PE interface on the bending performance of the composite bridge deck were compared, and the defects of the PE interface were considered. Finally, it is verified that the cohesive zone model (CZM) can realize the finite element simulation of the PE interface in the composite bridge deck based on the test results. The following conclusions can be drawn:

(1) The shear strength of the FT interface is far lower than that of the EB interface and PE interface among the three designed interfaces. The shear strength of the PE interface is significantly lower than that of the EB interface, but it is much higher than that of the short stud connector. Among the two types of interfaces, the PE interface is more suitable for connecting steel plate and fresh UHPC matrix, which can be used as the interface of the steel-UHPC composite bridge deck.
(2) After the steel plates yield, the thin UHPC layer of the composite bridge deck with the short stud connector is locally crushed near the loading point, resulting in the bending failure of the composite deck. On the contrary, the interface on the midspan side of the composite bridge deck with PE interface failed in a large area before the steel plate yield. After the interface failure, the composite bridge deck can still withstand the load until the final bending failure.
(3) The ultimate load of specimen CD-S-I_C is decreased by 4.1% compared with specimen CD-S-I_M, and the maximum deflection is decreased by 37.8%. The ultimate load of specimen CD-P-I_C is less than 2.1% lower than that of specimen CD-P-I_M, and the maximum deflection is reduced by 2.4%. The difference in the maximum deflection reduction between specimen CD-S-I_C and specimen CD-P-I_C is attributed to the fact that the shear stiffness of the PE interface is much larger than that of the short stud connector.
(4) The slip distribution of specimen CD-P-D_C after interface defects is not symmetrical, and the thin UHPC layer at the loading point has failed. The combined action of specimen CD-P-D_C at its interface is invalidated by cyclic loading. Therefore, the composite bridge deck is unsuitable for the cyclic load when the defect area of the PE interface reaches 30%.
(5) The load-deflection curves of three types of composite bridge decks obtained from both the test and the model show good agreement. The deviation of the model calculation value P_u^M of the ultimate load of all composite decks from the test value P_u^T is within 5%, and the deviation of the model calculation value D_f^M of the maximum deflection from the test value D_f^T is within 6%. Therefore, the constitutive model of stud weld in thin UHPC layer and the cohesive zone model of PE interface can realize the numerical simulation of the bending behavior of composite bridge deck.
(6) In the steel-UHPC composite bridge deck, the PE interface can make the stress transfer at the steel-UHPC interface more uniform than the short stud connector, and there is no failure to the thin UHPC layer before the failure of the interface.

Data availability statement

The original contributions presented in the study are included in the article/supplementary material, further inquiries can be directed to the corresponding author.

Author contributions

These authors have made great contributions in the field of the steel-concrete composite structure and high-performance concrete material. All authors listed have made a substantial, direct, and intellectual contribution to the work and approved it for publication.

Acknowledgments

The authors express their sincere gratitude for the financial support provided by the Key R&D projects in Guangxi (AB19245017), the National Natural Science Foundation of China (52278147), National Natural Science Foundation of China (52208302), the Major Science and Technology Projects in Hainan (ZDKJ2021048) and the Natural Science Foundation of Chongqing City, China (cstc2020jcyj-msxmX0062).

Conflict of interest

The author BL is employed by Guangxi Communications Technology Group Co., Ltd.

The remaining authors declare that the research was conducted in the absence of any commercial or financial relationships that could be construed as a potential conflict of interest.

Publisher's note

References

Alavi, A. H., Hasni, H., Jiao, P. C., Borchani, W., and Lajnaf, N. (2017). Fatigue cracking detection in steel bridge girders through a self-powered sensing concept. *J. Constr. STEEL Res.* 128, 19–38. doi:10.1016/j.jcsr.2016.08.002

Alkaysi, M., and El-Tawil, S. (2017). Factors affecting bond development between Ultra High Performance Concrete (UHPC) and steel bar reinforcement. *Constr. Build. Mat.* 144, 412–422. doi:10.1016/j.conbuildmat.2017.03.091

Berthet, J. F., Yurtdas, I., Delmas, Y., and Li, A. (2011). Evaluation of the adhesion resistance between steel and concrete by push out test. *Int. J. Adhes. Adhes.* 31 (2), 75–83. doi:10.1016/j.ijadhadh.2010.11.004

Bouazaoui, L., and Li, A. (2008). Analysis of steel/concrete interfacial shear stress by means of pull out test. *Int. J. Adhesion Adhesives* 28 (3), 101–108. doi:10.1016/j.ijadhadh.2007.02.006

Bouazaoui, L., Perrenot, G., Delmas, Y., and Li, A. (2007). Experimental study of bonded steel concrete composite structures. *J. Constr. Steel Res.* 63 (9), 1268–1278. doi:10.1016/j.jcsr.2006.11.002

Cao, J. H., and Shao, X. D. (2019). Finite element analysis of headed studs embedded in thin UHPC. *J. Constr. Steel Res.* 161, 355–368. doi:10.1016/j.jcsr.2019.03.016

Charron, J. P., Denarie, E., and Brtihwiler, E. (2008). Transport properties of water and glycol in an ultra high performance fiber reinforced concrete (UHPFRC) under high tensile deformation. *Cem. Concr. Res.* 38, 689–698. doi:10.1016/j.cemconres.2007.12.006

Cheng, Z. Y., Zhang, Q. H., Bao, Y., Deng, P., Wei, C., and Li, M. (2021). Flexural behavior of corrugated steel-UHPC composite bridge decks. *Eng. Struct.* 246, 113066. doi:10.1016/j.engstruct.2021.113066

Feng, Z., Li, C. X., He, J., Ke, L., Lei, Z., and Vasdravellis, G. (2021). Static and fatigue test on lightweight UHPC-OSD composite bridge deck system subjected to hogging moment. *Eng. Struct.* 241, 112459. doi:10.1016/j.engstruct.2021.112459

Freitas, S. T. D., Kolstein, H., and Bijlaard, F. (2017). Fatigue assessment of full-scale retrofitted orthotropic bridge decks. *J. BRIDGE Eng.* 22 (11), 04017092. doi:10.1061/%28ASCE%29BE.1943-5592.0001115

Fu, Z. Q., Wang, Y. X., Ji, B. H., and Jiang, F. (2019). Effects of multiaxial fatigue on typical details of orthotropic steel bridge deck. *Thin-Walled Struct.* 135, 137–146. doi:10.1016/j.tws.2018.10.035

General Administration of Quality Supervision (2010). *Inspection and quarantine. Metallic materials-Tensile testing-Part 1:Method of test at room temperature*. beijing, China. (GB/T 228.1-2010) [in Chinese].

General Administration of Quality Supervision (2015). *Inspection and quarantine*. beijing, China: Reactive powder concrete. (GB/T 31387-2015)[in Chinese].

Hung, C. C., El-Tawil, S., and Chao, S. H. (2021). A review of developments and challenges for UHPC in structural engineering: Behavior, analysis, and design. *J. Struct. Eng. (N. Y. N. Y).* 147 (9), 03121001. doi:10.1061/(asce)st.1943-541x.0003073

Jiang, J. L., Zou, Y., Yang, J., Zhou, J. T., Zhang, Z. Y., and Huang, Z. L. (2021). Study on bending performance of epoxy adhesive prefabricated UHPC-steel composite bridge deck. *Adv. Civ. Eng.* 2021, 6658451. doi:10.1155/2021/6658451

Jiang, J. L., Leng, J. C., Zhang, J. T., and Guo, J. C. (2022). Interfacial behavior of the steel–UHPC composite deck with toughened epoxy bonding. *Front. Mat.* 9, 859214. doi:10.3389/fmats.2022.859214

Kruszewski, D., Zaghi, A. E., and Wille, K. (2019). Finite element study of headed shear studs embedded in ultra-high performance concrete. *Eng. Struct.* 188, 538–552. doi:10.1016/j.engstruct.2019.03.035

Kumar, P., Patnaik, A., and Chaudhary, S. (2018). Effect of bond layer thickness on behaviour of steel-concrete composite connections. *Eng. Struct.* 177, 268–282. doi:10.1016/j.engstruct.2018.07.054

Larbi, S., Ferrier, E., and Hamelin, P. (2009). Concrete to steel lap joint failure criteria under combined shear and peeling stress. *J. Constr. Steel Res.* 65 (2), 386–394. doi:10.1016/j.jcsr.2008.03.012

Liu, Y. M., Zhang, Q. H., Bu, Y. Z., and Bao, Y. (2022). Static and fatigue performance of steel bridge decks strengthened with air-cured UHPC. *STRUCTURES* 41, 203–214. doi:10.1016/j.istruc.2022.05.025

Luo, Y. B., Hoki, K., Hayashi, K., and Nakashima, M. (2016). Behavior and strength of headed stud-SFRCC shear connection. II: Strength evaluation. *J. Struct. Eng. (N. Y. N. Y).* 142 (2), 04015113. doi:10.1061/(asce)st.1943-541x.0001372

Luo, Y. J., Li, A., and Kang, Z. (2012). Parametric study of bonded steel-concrete composite beams by using finite element analysis. *Eng. Struct.* 34, 40–51. doi:10.1016/j.engstruct.2011.08.036

Maloney, K., and Fleck, N. (2019). Toughening strategies in adhesive joints. *Int. J. Solids Struct.* 158, 66–75. doi:10.1016/j.ijsolstr.2018.08.028

Meng, W. N., and Khayat, K. (2017). Effects of saturated lightweight sand content on key characteristics of ultra-high-performance concrete. *Cem. Concr. Res.* 101, 46–54. doi:10.1016/j.cemconres.2017.08.018

Ranz, D., Cuartero, J., Castejon, L., Miralbes, R., and Malon, H. (2020). A cohesive zone model approach to interlaminar behaviour of carbon/epoxy laminated curved beams. *Compos. Struct.* 238, 111983. doi:10.1016/j.compstruct.2020.111983

Robert, C. W., Mathieu, C., and Pradipta, K. D. (2007). Multiscale considerations for interface engineering to improve fracture toughness of ductile fiber/thermoset matrix composites. *Compos. Sci. Technol.* 67 (11), 2428–2437. doi:10.1016/j.compscitech.2007.01.004

Sun, Q. L., Lu, X. Y., Nie, X., Han, Z. J., and Fan, Z. S. (2017). Experimental research on tensile and shear behaviour of the interface between non-steam-cured UHPC and steel plate structure. *Eng. Mech.* 34 (9), 167–174. doi:10.6052/j.issn.1000-4750.2016.05.0361

Wang, Z., Nie, X., Fan, J. S., Lu, X. Y., and Ding, R. (2019). Experimental and numerical investigation of the interfacial properties of non-steam-cured UHPC-steel composite beams. *Constr. Build. Mater.* 195, 323–339. doi:10.1016/j.conbuildmat.2018.11.057

Wang, Q. D., Ji, B. H., Xia, J. Y., and Fu, Z. (2020). Fatigue assessment of rib-deck welds in orthotropic steel decks integrating the effect of load dispersal through asphalt surfacing. *STRUCTURES* 28, 1701–1712. doi:10.1016/j.istruc.2020.10.017

Wu, Z. M., Shi, C. J., and Khayat, K. H. (2019). Investigation of mechanical properties and shrinkage of ultra-high performance concrete: Influence of steel fiber content and shape. *Compos. Part B Eng.* 174, 107021. doi:10.1016/j.compositesb.2019.107021

Yang, J., and Fang, Z. (2008). Research on stress-strain relation of ultra high performance concrete. *Concrete* 7, 11–15. doi:10.3969/j.issn.1002-3550.2008.07.004

Zhan, Y. L., Duan, M. J., Zhang, L., Liu, C., Li, Z., and Zhao, R. (2021). Study on the shear performance of adhesive shear connectors in push-out tests. *STRUCTURES* 32, 2103–2117. doi:10.1016/j.istruc.2021.03.109

Zhang, Z., Shao, X. D., Li, W., Zhu, P., and Chen, H. (2015). Axial tensile behavior test of ultra high performance concrete. *China J. Highw. Transp.* 28 (8), 50–58.

Zhang, S. H., Shao, X. D., Cao, J. H., Cui, J., Hu, J., and Deng, L. (2016). Fatigue performance of a lightweight composite bridge deck with open ribs. *J. Bridge Eng.* 21 (7), 04016039. doi:10.1061/(asce)be.1943-5592.0000905

Zhang, Z. G., Yang, F., Liu, J. C., and Wang, S. P. (2020). Eco-friendly high strength, high ductility engineered cementitious composites (ECC) with substitution of fly ash by rice husk ash. *Cem. Concr. Res.* 137, 106200. doi:10.1016/j.cemconres.2020.106200

Zhang, Z. G., Liu, S. Y., Yang, F., Weng, Y. W., and Qian, S. Z. (2021). Sustainable high strength, high ductility engineered cementitious composites (ECC) with substitution of cement by rice husk ash. *J. Clean. Prod.* 317, 128379. doi:10.1016/j.jclepro.2021.128379

Zhang, Z. G., Liu, D., Ding, Y., and Wang, S. (2022). Mechanical performance of strain-hardening cementitious composites (SHCC) with bacterial addition. *J. Infrastruct. Preserv. Resil.* 3, 3. doi:10.1186/s43065-022-00048-3

Zhao, W., Yu, Y., and Xie, Q. S. (2019). Nonuniform interface failure of steel-concrete composite structures bonded using epoxy resin mortar. *Eng. Struct.* 184, 447–458. doi:10.1016/j.engstruct.2019.01.109

Zhu, Y. P., Zhang, Y., Hussein, H. H., and Chen, G. (2020). Numerical modeling for damaged reinforced concrete slab strengthened by ultra-high performance concrete (UHPC) layer. *Eng. Struct.* 209, 110031. doi:10.1016/j.engstruct.2019.110031

Zou, Y., Jiang, J. L., Zhou, Z. X., Wang, X. F., and Guo, J. C. (2021). Study on the static performance of prefabricated UHPC-steel epoxy bonding interface. *Adv. Civ. Eng.* 2021, 1–15. doi:10.1155/2021/6663517

Zou, Y., Qin, F. J., Zhou, J. T., Zheng, Z. C., Huang, Z. L., and Zhang, Z. Y. (2021). Shear behavior of a novel bearing-shear connector for prefabricated concrete decks. *Constr. Build. Mat.* 268, 121090. doi:10.1016/j.conbuildmat.2020.121090

Zou, Y., Guo, J. C., Zhou, Z. X., Wang, X. D., Yu, Y. J., and Zheng, K. D. (2022). Evaluation of shear behavior of PCSC shear connection for the construction of composite bridges with prefabricated decks. *Eng. Struct.* 257, 113870. doi:10.1016/j.engstruct.2022.113870

frontiers | Frontiers in Materials

TYPE Original Research
PUBLISHED 21 October 2022
DOI 10.3389/fmats.2022.1060294

OPEN ACCESS

EDITED BY
Kequan Yu,
Tongji University, China

REVIEWED BY
Mingfeng Xu,
Hebei University of Technology, China
Zhitao Chen,
Harbin Institute of Technology, China

*CORRESPONDENCE
Zhigang Zhang,
zhangzg@cqu.edu.cn

SPECIALTY SECTION
This article was submitted to Structural Materials, a section of the journal Frontiers in Materials

RECEIVED 03 October 2022
ACCEPTED 13 October 2022
PUBLISHED 21 October 2022

CITATION
Yu J, Liu D and Zhang Z (2022), Durability and life prediction analysis of recycled aggregate concrete with ceramic waste powder under freeze-thaw conditions based on impact-echo method and Grey-Markov model. *Front. Mater.* 9:1060294. doi: 10.3389/fmats.2022.1060294

Durability and life prediction analysis of recycled aggregate concrete with ceramic waste powder under freeze-thaw conditions based on impact-echo method and Grey-Markov model

Jianqiao Yu[1,2], Dawei Liu[1,2] and Zhigang Zhang[1,2]*

[1]Key Laboratory of New Technology for Construction of Cities in Mountain Area (Chongqing University), Ministry of Education, Chongqing, China, [2]School of Civil Engineering, Chongqing University, Chongqing, China

Utilizing recycled aggregate concrete (RAC) for cyclic usage in building materials is one of the most feasible methods for reducing the demand for natural aggregates in the construction sector and disposing of construction and demolition trash in landfills. Previous research has demonstrated that the weak freeze-thaw (F-T) resistance of RAC poses a significant threat to the safety of RAC structures in severe cold regions. Therefore, this paper explores the influence of ceramic waste powder (CWP) at various replacement rates on the freeze-thaw resilience of RAC. In this experiment, six groups of CWP doping ratios of 0%, 10%, 20%, 30%, 40, and 50% were designed. Before the F-T cycling test, each group of specimens' basic mechanical and physical performance data was measured throughout the regular curing age. At the conclusion of each F-T cycle, the durability performance of RAC was tested using the impact-echo method and compressive strength test. To predict the lifetime of RAC mixtures, a Grey-Markov model was created. It was found that the impact-echo method is more appropriate for assessing the durability of RAC in a freeze-thaw condition. The RAC's F-T resistance is greatest when the CWP content is 20%. The Grey-Markov model has a high degree of predictive accuracy, effectively reflecting the relationship between RAC durability and F-T cycles, and has wide practical applications.

KEYWORDS

recycled aggregate concrete (RAC), freeze-thaw, ceramic waste powder (CWP), impact-echo method, grey-markov model

1 Introduction

The construction industry is one of the primary drivers of global development in past decades. However, construction is not an environmentally friendly activity as the materials used led to the intense demand for natural resources consuming. Recycled aggregate concrete (RAC) is a kind of eco-friendly concrete manufactured by substituting natural aggregates partially or entirely with recycled aggregates which derived from waste concrete blocks in building waste after mechanical crushing, cleaning, and grading. Notably, the use of RAC not only solves the environmental issues produced by construction waste dumps, but also enables the recycling of construction waste, which has significant ecological, economic, and social relevance (Li et al., 2020; Amadi et al., 2022).

The recycled aggregates has a relatively lower apparent density, higher water absorption and crushing value as compared with natural aggregate, however, they can be blended with natural aggregates to satisfy the needed criteria for workability and strength of RAC. In pratical field, RAC has been applied in road engineering such as the Diepmannsbach Bridge in Germany and the US-41 Route in the United States (Nwakaire et al., 2020). Nevertheless, the long-term property of RAC has certain drawbacks, RAC confronts more complex durability issues in the harsh environment than that of conventional concrete, especially in severe cold regions, the micro-cracks created in recycled aggregate as a result of damage buildup during manufacture provide the preferable paths for moisture to infiltrate into the interior of RAC, and making RAC more sensitive to freeze-thaw (F-T) degradation.

In previous studies (Bennett et al., 2022; Wang et al., 2022), it has been demonstrated that mixing some supplementary cementitious materials (SCMs) can improve the F-T resistance properties of RAC. Normally, the SCMs can fill the microscopic pores within cement matrix, and thus enhance the compactness of RAC, moreover, the pozzolanic properties of SCMs can produce dense C-S-H gels, which is expected to improve the durability of RAC.

Among the various SCMs, ceramic waste powder (CWP) can absorb water and has a good filling effect (Awoyera et al., 2017) as it was used in concrete. CWP is a kind of construction waste, which is obtained from the crushing process of ceramic waste. As a residual waste, ceramic waste is often discarded at the landfill as a non-recyclable item, which is not only a waste of land resources, but also contaminates soil and water bodies. Actually, if the ceramic waste is ground to a specific fineness, under a damp/alkaline environment, the ceramic powder can chemically react with $Ca(OH)_2$ to form C-S-H gels. Therefore, CWP could be a promising SCM to be utilized in RAC. Until now, there have been no particular studies to demonstrate if CWP can improve RAC in F-T conditions, and few research on CWP as a substitute for recycled fine aggregates in RAC were investigated.

It is well known that compressive strength is often used as the main way to measure the quality of concrete. However, when concrete is eroded by the harsh environment or damaged by catastrophic factors, the compressive strength of concrete is merely an indirect assessment and does not accurately reflect the concrete's performance in the actual structures. Based on technique specifications (CECS 03-2007, 2007; GB/T 50107-2010, 2011), when there is uncertainty regarding the compressive strength test value of the RAC specimen, the non-destructive method can be utilized to evaluate the qualities of concrete under applicable requirements. In recent years, the conventional impact-echo method has attracted extensive attention. It is a quick and reasonably cost-effective method of on-site examination by using impact elastic waves. Among all the impact elastic waves, the attenuation of longitudinal wave amplitude is positively connected with the direction of propagation of normal stress, indicating that longitudinal waves create the most significant and easiest-to-receive vibrations. Hence, longitudinal wave velocity is commonly employed to measure the strength and dynamic elastic modulus of concrete. Nevertheless, when concrete is in F-T conditions, the ice creates a "false" increase in wave velocity and strength, making the durability of concrete be underestimated. Unfortunately, the current research on the correlations between wave velocity and F-T resistance of RAC is limited, especially by the impact-echo method.

Over the past decade, numerous results about durability tests on concrete indicate that environmental erosion is a gradual process for concrete. According to the previous literature findings (Zhang et al., 2020; Wang et al., 2021; Zhang et al., 2022), the relevant durability evaluation parameters of some concrete specimens still do not match the failure requirements even underwent hundreds of F-T cycles in the laboratory test condition. To ensure the durability of CWP-RAC in the F-T conditions, it is required to predict its remaining service life using mathematical models. In this regard, a Grey model can be constructed to predict the durability life of RAC (Qu et al., 2021). The Grey model has the properties of reducing sequence randomness and detecting the pattern of sample data, enabling accurate description and efficient monitoring of original data's evolving pattern. In the Grey modeling procedure, irregularly moving data are typically discarded, and the sample's overall trend is considered. This method will produce an impact on prediction accuracy because it disregards interference data. Fortunately, the most significant characteristic of the Markov chain is its capacity to examine data that fluctuates irregularly (Zhou et al., 2022). The Grey-Markov model combing Markov chain and Grey model can effectively improve the accuracy of predictions.

In this paper, it investigated the influence of various CWP contents on the impact echo propagation properties of RAC under F-T conditions, and produced performance degradation curves for compressive strength and relative dynamic elastic

TABLE 1 Raw materials used for RAC mixes.

Raw material	Property type	Contents							
Cement	Chemical compositions	SiO_2	Fe_2O_3	Al_2O_3	CaO	MgO	SO_3	K2O	LOI
		26.7%	4.9%	11.5%	48.9%	3.0%	2.1%	1.6%	1.3%
	Mineralogical phase compositions	C_3S	C_2S	C_3A	C_4AF	Gypsum	$Ca(OH)_2$		
		56.7%	21.1%	3.6%	12.0%	3.1%	3.5%		
Ceramic waste powder	Chemical compositions	SiO_2	Fe_2O_3	Al_2O_3	CaO	MgO	SO_3	K2O	LOI
		67.8%	0.8%	24.4%	1.6%	2.5%	0.2%	0.9%	1.8%
	Physical properties	Mean particle size		Void fraction		Water content		Apparent density	
		5.7 μm		30.3%		0.4%		2950 kg m^{-3}	
Natural coarse aggregate	Physical properties	Void fraction		Water content		Water absorption		Apparent density	Bulk density
		45.3%		0.3%		0.6%		2710 kg m^{-3}	1610 kg m^{-3}
Natural fine aggregate	Physical properties	Void fraction		Water content		Water absorption		Apparent density	Bulk density
		36.1%		3.8%		2.6%		2640 kg m^{-3}	1630 kg m^{-3}
Recycled coarse aggregate	Physical properties	Void fraction		Water content		Water absorption		Apparent density	Bulk density
		48.8%		0.5%		5.7%		2560 kg m^{-3}	1428 kg m^{-3}
Recycled fine aggregate	Physical properties	Void fraction		Water content		Water absorption		Apparent density	Bulk density
		38.6%		0.9%		6.5%		2450 kg m^{-3}	1507 kg m^{-3}

TABLE 2 Mixed proportions of RAC (kg/m^3).

Mixture	Cement	CWP	Water	NCA	NFA	RCA	RFA
CWP-0	400	0	200	1017	583	257	382
CWP-10	400	38	200	1017	583	257	344
CWP-20	400	77	200	1017	583	257	305
CWP-30	400	115	200	1017	583	257	267
CWP-40	400	153	200	1017	583	257	229
CWP-50	400	191	200	1017	583	257	191

modulus (derived from the data collected using the impact-echo method). On this basis, a Grey-Markov model is used to predict the life of RAC. The results is expected to provide theoretical support for engineering applications.

2 Experimental programs

2.1 Materials and methods

In this study, the ingredients in the production of RAC include ordinary Portland cement of P.O 42.5 grade, pulverized ceramic waste powder (CWP), water, natural coarse aggregate (NCA), natural fine aggregate (NFA), recycled coarse aggregate (RCA), and recycled fine aggregate (RFA). The chemical compositions and physical properties of these raw materials are listed in Table 1. The particle size of CWP was below 45 microns. Even though recycled aggregates have high water absorption and low bulk density, the overall difference in physical properties between recycled aggregates and natural aggregates is not evident. Table 2 lists the six RAC mix proportions used in this study. Six RAC mixtures were made in accordance with the technical standard for recycled concrete structures (JGJ/T 443-2018, 2018) by substituting RFA at equal volume weight with varying volume contents of CWP. The CWP-0 was used as the control group, and the corresponding

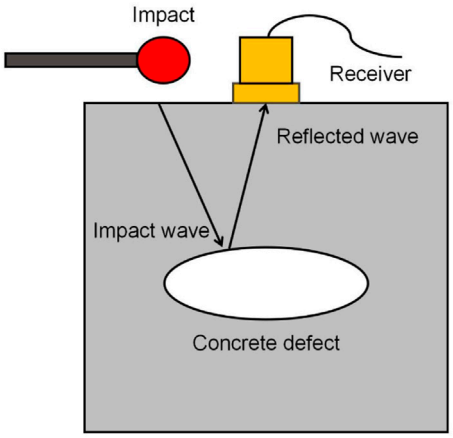

FIGURE 1
Principle of impact-echo method.

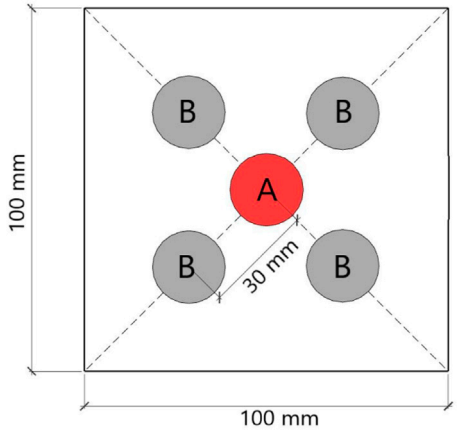

FIGURE 2
The arrangement of excitation sources. Point **(A)** is the receiver. Point **(B)** is the excitation source.

formulated strength grade was C30. The numbers in the mixture represent the replacement-ratio of RFA to CWP.

The RAC mixtures were made using with a cube-shaped plastic trial mold with a size of 100 mm × 100 mm × 100 mm. During mixing process, all dry solid ingredients were initially mixed for 60 s. Then the water were added and mixed for another 120 s until the paste reached a homogeneous status. In final, the RAC paste was poured into the molds and stored at ambient temperature (around 25°C) with plastic films. After 24 h, the RAC specimens were demolded and cured under temperature of 20 ± 2°C and relative humidity of 95% until test.

2.2 Experimental procedures

2.2.1 Impact-echo method

Figure 1 depicts the principle of the impact-echo method. The basic premise is to deliver a temporary impact to excitation source on concrete surface, and the resulting impact elastic wave propagates along the interior of concrete and produces reflected waves when it contacts internal defects such as pores, honeycomb, delamination, etc. Then, the reflected waves are sent back to the surface of concrete and received by a receiver situated close to excitation source. Meanwhile, it is possible to convert the fluctuating signals received by receiver into amplitude spectrum. The primary peak in the amplitude spectrum is caused by the interface where the wave impedance changes. Finally, according to the peak frequency (f), the impact elastic wave velocity can be determined using Eq. 1:

$$V = 2hf/\gamma \tag{1}$$

where V is the impact elastic wave velocity (m/s), h is the height of the specimen (m), and f is the peak frequency (Hz). A form factor γ is added because the specimen's form influences the measurement of wave velocity. According to experiments conducted by Krzemień et al. (Krzemień and Hager, 2015), γ can be 0.9 for the same cubic specimen size, and the impact elastic wave velocity is then rectified to a one-dimensional wave velocity.

In this paper, the testing apparatus utilizes the impact echo tester, which comprises a 12.5 mm diameter impact hammer, receiving sensor, and signals acquisition system. When the excitation source is subjected to a impact, the longitudinal, shear, and Rayleigh waves will propagate in all directions. The primary detection basis of the impact-echo method is the longitudinal wave in impact elastic wave, as the vibration direction of the excitation source and the longitudinal wave propagation direction are identical, resulting in the quickest longitudinal wave propagation speed. During on-site test, the test surface should be smoothed using an abrasive wheel to ensure that the excitation source and measurement point surface are well linked. Four excitation sources are positioned diagonally along the end face at a distance of 30 mm from the receiver, as depicted in Figure 2. Each excitation source is impacted twice at least to ensure that the receiver receives two correct data. For the specimens that have reached the relevant curing age (7 days, 28 days), three specimens of each group will be tested, 24 wave velocities will be obtained for each group, and the average value will be used as the group's final wave velocity.

2.2.2 Compressive strength test

According to the specifications of China codes (GB/T 50081-2019, 2019), the compressive strength test was conducted. During the test, the load was continually applied at a loading

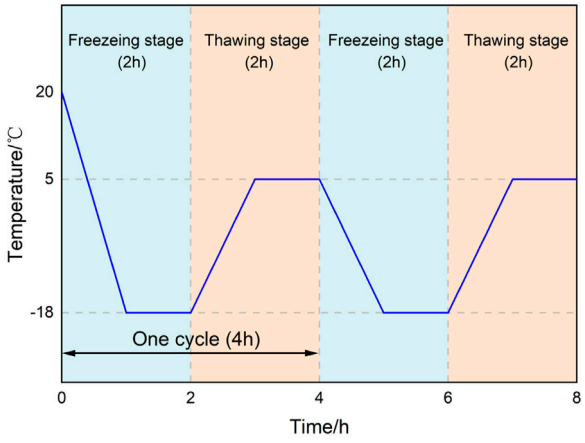

FIGURE 3
Freeze-thaw scheme.

rate of 0.8 MPa/s without impact until the sample was damaged to the point of failure. When the specimens of each mix proportion are cured for 7 days and 28 days, the group's compressive strength is determined by averaging the values of three specimens. During data processing, the compressive strength findings were calculated using Eq. 2, and translated to standard specimen strength using a conversion factor of 0.95.

$$f_c = \frac{F_{\max}}{A} \tag{2}$$

Where, f_c is the cubic compressive strength (MPa), $F_{\max}$ is the maximal force required to destroy the specimen (N), A is the compressive area (mm^2).

2.2.3 Freeze-thaw cycling test

Figure 3 depicts the F-T cycle regime for this test, which consisted of 300 cycles. Prior to freez-thaw test, the RAC specimens were cured until 28 days. Each F-T cycle lasts 4 h, consisting of 2 h of freezing and 2 h of thawing. During F-T conditions, the central of the specimen underwent a minimum temperature of −18 ± 2°C and a maximum temperature of 5 ± 2°C. As durability-related data, the impact elastic wave velocity and compressive strength of each RAC mixture were tested every 25 cycles.

The so-called durability of concrete refers to the ability of concrete to sustain its work performance under predictable working conditions. Since the wave velocity of the impact elastic wave has a positive correlation with the physical and mechanical properties of concrete materials, such as density, Poisson's ratio, and dynamic elastic modulus, thus the wave velocity can be a non-destructive test method to determine the durability evaluation parameters for the F-T test. According to the relevant specification for durability test design (GB/T 50082-2009, 2009), the relative dynamic modulus of elasticity (RDME) E_r can be used as an assessment parameter for F-T test. Wichtmann et al. (Wichtmann and Triantafyllidis, 2010) concluded that the relationship between wave velocity and dynamic elastic modulus, as shown in Eq. 3:

$$V = \sqrt{\frac{E_d}{\rho}} \tag{3}$$

where E_d is the dynamic elastic modulus (MPa), ρ is the density of concrete (kg/m^3).

The formula for calculating the RDME can be calculated from Eq. 4:

$$E_r = \frac{E_{dn}}{E_{d0}} = \frac{v_n^2}{v_0^2} \times 100\% \tag{4}$$

where E_{dn}, E_{d0} denote the dynamic elastic modulus after n test cycles and the initial stage, respectively. V_n, v_0 denote the impact elastic wave velocity measured after n test cycles and the initial stage, respectively. When $E_r \leq 60\%$, it indicates that the specimen meets the threshold for durability failure.

In addition, the relevant specification also provides for the compressive strength damage factor can be used as a supplementary criterion to determine whether concrete durability is compromised. The calculation formula for the compressive strength damage factor is presented in Eq. 5:

$$K_f = \frac{f_{cn}}{f_{c0}} \times 100\% \tag{5}$$

where K_f is the compressive strength damage factor, f_{cn}、f_{c0} denote the compressive strength after n test cycles and the initial stage, respectively. When $K_f \leq 75\%$, it indicates that the specimen meets the threshold for durability failure.

From Eq. 4 and (Eq. 5), the two durability damage deterioration indices can be obtained, which can be used to evaluate the F-T durability of concrete from both non-destructive and destructive perspectives, respectively. For the current test design, it is crucial to normalize the aforementioned two durability parameters so that the disparities between the two degradation indicators may be compared more objectively throughout the same test cycle. Hence, based on the durability failure thresholds of E_r and K_f, the RDME evaluation parameter ξ_1 and compressive strength evaluation parameter ξ_2 were established (Eq. 6 and Eq. 7).

$$\xi_1 = \frac{E_r - 0.60}{0.40} \times 100\% \tag{6}$$

$$\xi_2 = \frac{K_f - 0.75}{0.25} \times 100\% \tag{7}$$

When either ξ_1 or ξ_2 reaches 0, it is evident that the specimen has met the durability failure criterion, and the test of the group must be terminated.

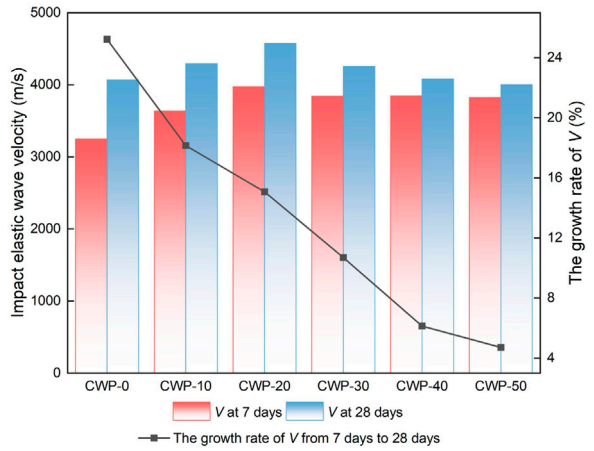

FIGURE 4
Impact elastic wave velocity of RAC mixtures.

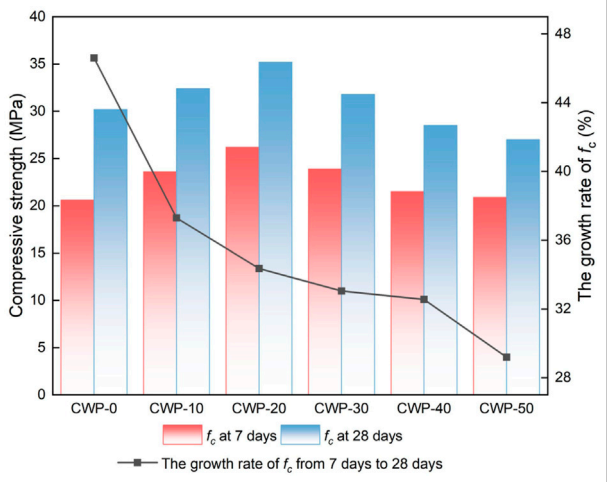

FIGURE 5
Compressive strength of RAC mixtures.

3 Results and discussion

3.1 Impact elastic wave velocity of RAC mixtures

Figure 4 plots the impact elastic wave velocity of RAC mixtures. As is evident from Figure 4, the wave velocity of all RAC specimen groups combined with CWP was greater than that of CWP-0 after 7 days of curing. Since the velocity of the impact elastic wave is directly proportional to the degree of concrete compactness, the wave velocity can be utilized to determine the degree of concrete curing. Shokouhi et al. (2017) reported that the propagation path of elastic waves at the concrete defect interface will increase and the measured wave velocity must inevitably drop as the wave impedance rate of air is significantly lower than that of concrete. The increase in early wave velocity of CWP-RAC mixtures is mostly attributable to the pozzolanic activity and the physical filling effect of CWP.

At 28 days curing age, the final wave velocity of CWP-RACs exhibits an increasing and then declining trend with increasing CWP contents. The CWP-20 had the highest wave velocity of 4573 m/s, which was 12.44% greater than that of control group (CWP-0). However, when the CWP doping was increased to 50%, the wave velocity was only 4002 m/s, which was slower than that of control group. This implies that a specific amount of CWP can effectively compensate for the high porosity of recycled aggregates when added to the mixture. When the CWP doping level reaches 20%, the tiny pores within the RAC are well-filled and the larger pores will not expand significantly. However, when CWP doping exceeds 20%, due to the excessive substitution of RFA, the larger pores will enlarge, resulting in a reduction in RAC compactness, even though the tiny pores are well filled. In addition, the growth rate curve of wave velocity from 7 days to 28 days of curing age reveals that the capability to enhance RAC wave velocity declines gradually as the CWP doping rises. The CWP-40 and CWP-50 only raised the wave velocity by 6.14% and 4.71%, respectively, which was much less than that of control group (increased by 25.22% for CWP-0). The results indicate that an excess amount of CWP is not conducive to maintaining the pozzolanic reaction with cement hydration product, and enhancing the compactness of the RAC in the later stage of curing.

3.2 Compressive strength of RAC mixtures

Figure 5 illustrates the compressive strength of RAC mixtures at 7 days–28 days curing age. It shows that the compressive strength of CWP-RAC mixtures is basically consistent with the performance of impact elastic wave velocity: the higher the wave velocity, the greater the strength. Compared to the control group, the compressive strength of the specimens at 7 days in each of the CWP-doped groups was enhanced to varying degrees, which is consistent with the conclusions reached in the study by Chen et al. (2022). This is mainly because that CWP has a higher water absorption rate and a rougher particle surface than that of RFA. The moisture content in the pores is high during the early stages of RAC formation, and the cement hydration hardening process has not yet been completed, while the water absorption of CWP is greater than that of RFA, which reduces the actual water-cement ratio around cement-based material involved in the hydration reaction and aids in the development of RAC strength. On the other hand, CWP, which is obtained by artificial crushing, has a rougher and

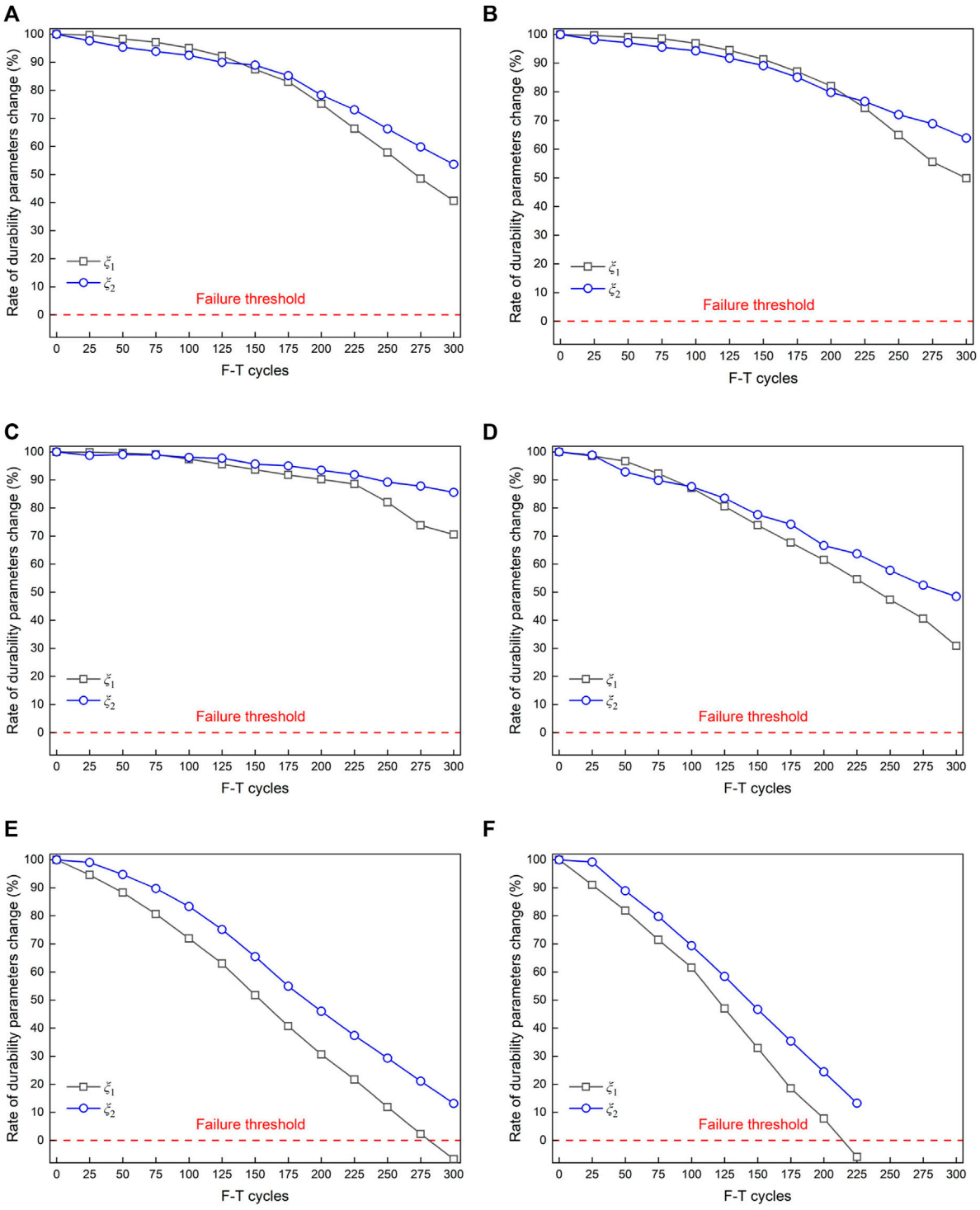

FIGURE 6
The rate of durability evaluation parameters change of RAC mixtures. **(A)** CWP-0. **(B)** CWP-10. **(C)** CWP-20. **(D)** CWP-30. **(E)** CWP-40. **(F)** CWP-50.

more angular surface than RFA, which likewise enhances the adhesion between aggregate and cement paste.

According to the 28 days compressive strength data, the compressive strength of each set of specimens increases and subsequently drops as CWP doping increases. Specifically, the compressive strength of CWP-20 at 28 days is 35.2 MPa, which is the greatest value among all specimens. This result is 16.56% more than that of CWP-0's. Peng et al. (2020) reported that because CWP has a smaller void fraction than recycled aggregates, it has a higher pressure-bearing capability than recycled aggregates. Therefore, the compressive strength of RAC was greatly enhanced by substituting CWP for a portion of RFA. It should be noted that, the compressive strength of CWP-40 and CWP-50 at 28 days were lower than that of control group. This implies that there is a residual unhydrated component of excess CWP following the secondary hydration reaction with $Ca(OH)_2$, which leads to bonding issues at the interface of the aggregate and cement. As a result, the specimen is easily damaged during the compression process, and the compressive strength of RAC decreases gradually when CWP content is greater than 20%. Similarly, as demonstrated by the growth curve of compressive strength from 7 days to 28 days of curing age, in the late curing stage, the compressive strength increases of RAC mixed with CWP is not as great as that of the control group. This is because that CWP reacts rapidly with the hydration products in RAC during the early stage of curing, hence realizing early strength. As the curing age increases, the effect of CWP on the augmentation of compressive strength of RAC decreases due to the gradual reduction of the active substance on the surface of the cement particles (Zhang et al., 2021).

3.3 F-T durability of RAC mixtures

Figures 6A–F presents the time-changing curves of the durability evaluation parameters of RAC mixtures, which was calculated from the impact elastic wave velocity and compressive strength after the samples underwent the increasing numbers of F-T cycles. As shown in Figure 6, all ξ_1 values of RAC mixtures dropped as the number of F-T cycles increased, indicating that the degree of RDME degradation of specimens increased as the number of F-T cycles grew. This is due to the fact that temperature fluctuations produce non-uniform thermal displacement between the cement paste and aggregate, and the freezing and expansion of water in the pore structure causes increased hydrostatic and osmotic pressures. The aforementioned conditions can contribute to a rise in cracks, porosity, and other defects in RAC, reducing the compactness of the specimen and thus leading to a decrease in RDME. The comparison reveals that CWP-0 has a ξ_1 value of 40.63% after 300 F-T cycles. The CWP-20 has the best F-T resistance with a ξ_1 value of 70.58% after 300 F-T cycles, which is significantly greater than that of control group. The reason is that CWP has lower water content and void fraction than RFA, which caused the relatively lower volume expansion rate of RAC specimens during F-T cycling to that of control group specimens, and effectively limiting the propagation of cracks and lateral deformation in the micro-structure of RAC due to F-T cycling, thereby reducing the degradation of RDME in a F-T environment. As CWP content increased, the ξ_1 curve degradation trend of CWP-30, CWP-40, and CWP-50 grew progressively. In particular, CWP-40 and CWP-50 approach durability failure after 300 and 225 cycles, respectively. This implies that the addition of an excessive amount of CWP is not conducive to the hydration of the RAC, and will result in the creation of additional pores. Under F-T conditions, the water in these pores condenses into solid ice, and the volume increases, resulting in expansion stress that reduces the durability performance of RAC.

According to the viewpoint of Silva et al. (2016), there is an intrinsic connection between the RDME of RAC and its compressive strength. Comparing the deterioration trends of ξ_1 and ξ_2 curves in Figures 6A–F, it reveals that the compressive strength diminishes progressively with the deterioration of RDME under the F-T conditions. Furthermore, the specimens that was used to measure wave velocity and compressive strength were chosen at random, so the cause of durability damage to RAC strength from F-T cycles can be considered the same as that of RDME. However, from the results of the F-T cycle, it is evident that the change in ξ_2 is later than the change in ξ_1 during the overall cycle period. For instance, when the ξ_1 curves of CWP-40 and CWP-50 are close to the failure threshold, the ξ_2 curves are still a considerable distance away from durability failure. This indicates that RDME is more sensitive to condition factors when used as a durability evaluation parameter compared to the compressive strength damage factor. The primary cause of the discrepancy between the ξ_1 and ξ_2 curves is the variation in test methods, physical quantity definitions, etc. The compressive strength test is obtained by the recovery force of the instantaneous elastic deformation produced by the pressure tester's continuous application of load at a fixed loading rate, i.e., it reflects the change in the surface strength of the material, and such results are subject to some error. Nevertheless, the impact-echo test is a thorough reflection of the specimen's physical qualities, such as dynamic elastic modulus, density, and internal micro-crack development, which has a definite physical significance. The deterioration of RAC by an F-T condition occurs from the outside to the inside, and RDME is an exhaustive reflection of the specimen's overall structural and microscopic features. Consequently, ξ_1 is more susceptible to RAC internal flaws than ξ_2, and if there is a fault in the compressive strength test, but the wave velocity can be established precisely, then RDME more effectively reflects the degree of RAC deterioration, hence reducing the impact

of test errors. In view of this, considering the three aspects of test impact elastic wave velocity, compressive strength and F-T durability, it is suggested that the amount of CWP in RAC should not exceed 30%, with a recommended value of 20%.

4 Durability life prediction based on Grey-Markov model

4.1 The process of establishing the grey model

The majority of the Grey models consist of GM(1,1) and GM(1,n), with the former used for univariate analysis and the latter for multivariate analysis. The experimental design of this investigation was based on a single variable, CWP contents, and hence the GM(1,1) model was selected to predict the durability life of RAC. The modeling steps are as follows:

Step 1: Write the differential equation based on the GM(1,1) model's definition:

$$\frac{dx^{(1)}}{dt} + ax^{(1)} = b \tag{8}$$

where, a is the development coefficient and b is the grey effect coefficient (Yu et al., 2021).

Step 2: From the GM(1,1) model's definition, derive the difference equation:

$$x^{(0)}(t) + az^{(1)}(t) = b \quad \Rightarrow \quad x^{(0)}(t) = b - az^{(1)}(t) \tag{9}$$

where, $x^{(0)}(t)$ denotes the original data series, $x^{(0)}(t) = \{x^{(0)}(1), x^{(0)}(2), \ldots x^{(0)}(n)\}, n > 0$. $z^{(1)}(t)$ is a sequence of means about $x^{(0)}(t)$, $z^{(1)} = \{z^{(1)}(2), z^{(1)}(3), \ldots, z^{(1)}(n)\}, n > 0$.

Step 3: Accumulate $x^{(0)}(t)$ to generate a calculation:

$$x^{(1)}(t) = \left\{ \sum_{i=1}^{1} x^{(0)}(i), \sum_{i=1}^{2} x^{(0)}(i), \ldots, \sum_{i=1}^{n} x^{(0)}(i) \right\}, i > 0 \tag{10}$$

Step 4: Solve for $z^{(1)}(t)$:

$$z^{(1)}(t) = 0.5 \times \left(x^{(1)}(t) + x^{(1)}(t+1) \right) \tag{11}$$

Step 5: Simplify Eq. 11 and use the matrix form to represent.

$$\begin{bmatrix} a \\ b \end{bmatrix} = \left(B^T B\right)^{-1} B^T Y_n \tag{12}$$

where, $B = \begin{bmatrix} -z^{(1)}(1) & -z^{(1)}(2) & \ldots & -z^{(1)}(n) \\ 1 & 1 & \ldots & 1 \end{bmatrix}^{\mathrm{T}}$, $Y_n = \left[X^{(0)}(2) \;\; X^{(0)}(3) \;\; \cdots \;\; X^{(0)}(n) \right]^{\mathrm{T}}$.

TABLE 3 Refer to the accuracy test level.

Level	Δ	γ	C	ω
I	0.01	0.90	0.35	0.95
II	0.05	0.80	0.50	0.80
III	0.10	0.70	0.65	0.70
IV	0.20	0.60	0.80	0.60

Step 6: Solve the matrix to derive the values of a and b:

$$a = \frac{\sum_{t=2}^{n} z^{(1)}(t) \sum_{t=2}^{n} x^{(1)}(t) - (n-1) \sum_{t=2}^{n} z^{(1)}(t) x^{(1)}(t)}{(n-1) \sum_{t=2}^{n} \left[z^{(1)}(t)\right]^2 - \left[\sum_{t=2}^{n} z^{(1)}(t)\right]^2} \tag{13}$$

$$b = \frac{\sum_{t=2}^{n} \left[z^{(1)}(t)\right]^2 \sum_{t=2}^{n} x^{(0)}(t) - \sum_{t=2}^{n} z^{(1)}(t) \sum_{t=2}^{n} z^{(1)}(t) x^{(0)}(t)}{(n-1) \sum_{t=2}^{n} \left[z^{(1)}(t)\right]^2 - \left[\sum_{t=2}^{n} z^{(1)}(t)\right]^2} \tag{14}$$

Step 7: The discrete-time response equation of the GM(1,1) model is obtained by bringing the derived a and b into Eq. 8:

$$\hat{x}^{(1)}(t) = \left(x^{(0)}(1) - \frac{b}{a} \right) e^{-a(t-1)} + \frac{b}{a} \tag{15}$$

Step 8: The resultant response equation is subjected to a single cumulative subtraction, from which the predicted values of the GM(1,1) model can be calculated as follows:

$$\hat{x}^{(0)}(t) = \hat{x}^{(1)}(t) - \hat{x}^{(1)}(t-1) \tag{16}$$

There are usually four methods for testing the accuracy of Grey model (Qin et al., 2022), which are: the average relative error method Δ, the correlation degree test γ, the posterior error ratio test C, and the small error probability test ω. Among them, for the calculation of Δ, it is also necessary to establish the relative error $\varepsilon^{(0)}(t)$ as follows:

$$\varepsilon^{(0)}(t) = \frac{x^{(0)}(t) - \hat{x}^{(0)}(t)}{x^{(0)}(t)} \tag{17}$$

$$\Delta = \frac{1}{n} \sum_{t=1}^{n} \left| \varepsilon^{(0)}(t) \right| \tag{18}$$

In addition, other accuracy test formulae are not essential to the building of the model presented in this research; therefore, the relevant formula derivation analysis will not be developed. Those interested can find the details in the literature (Yang and Liu, 2008; Jiang et al., 2017; Mao et al., 2020). Table 3 displays the regularly used accuracy test level standard.

TABLE 4 Model accuracy test results.

Test method	Δ	γ	C	ω
Test result	0.011	0.602	0.349	1.000
Accuracy level	II	IV	I	I

4.2 Markov state transition probability matrix

Referring to the author's previous research (Yu et al., 2022), the Markov chain based on the division of $\varepsilon^{(0)}(t)$ into k states can be expressed as Eq. 19:

$$\otimes_i = [\otimes_{1i}, \otimes_{2i}] \tag{19}$$

The state transfer probability of Markov chain is calculated as follows:

$$P_{ij}(k) = P\left(X_{k+1} = j \middle| X_k = i\right) \tag{20}$$

Therefore, the k-step transfer probability can be calculated as in Eq. 21:

$$P_{ij}(k) = M_{ij}(k) \Big/ M_i \tag{21}$$

where, $P_{ij}(k)$ is the probability of transferring from state i to state j after k steps. $M_{ij}(k)$ denotes the number of transfers from state i to state j after k steps. M_i denotes the number of original data in state i.

Meanwhile, the k-step state transfer probability matrix is as follows:

$$P(k) = \begin{bmatrix} p_{11}^{(k)} & p_{12}^{(k)} & \cdots & p_{1k}^{(k)} \\ p_{21}^{(k)} & p_{22}^{(k)} & \cdots & p_{2k}^{(k)} \\ \vdots & \vdots & \vdots & \vdots \\ p_{k1}^{(k)} & p_{k2}^{(k)} & \cdots & p_{kk}^{(k)} \end{bmatrix} \tag{22}$$

If there are m states and the present state is, the future state and the corresponding probability $P_{ij}(k)$ can be known based on the i-th row of the k-step state transfer matrix. The final calculation of Grey-Markov model can be obtained as follows:

$$\hat{x}(t) = \sum_{j=1}^{m} \frac{1}{2}\left(\frac{1}{1-\otimes_{1j}} + \frac{1}{1-\otimes_{2j}}\right)\hat{x}_0(t)P_{ij}(k) \tag{23}$$

4.3 Analysis of prediction results

Based on theF-T durability test results, the CWP-20 with the best test performance will be chosen to describe the derivation process of the Grey-Markov model in detail. Since the Grey model requires the data to be positive in the calculation process, the ξ_1 value is no longer utilized and has been replaced with the E_r value (the failure threshold of E_r is 60%).

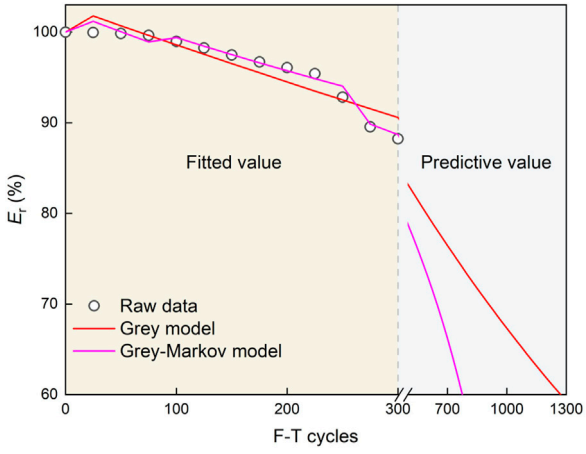

FIGURE 7
Model prediction results of Grey and Grey-Markov.

Following step 1 to step 8, the results of the Grey model for CWP-20 are as follows:

$$\begin{cases} \hat{x}^{(1)}(t) = -9655.9225e^{-0.0106t} + 9755.9224 \\ \hat{x}^{(0)}(t) = \hat{x}^{(1)}(t) - \hat{x}^{(1)}(t-1) \end{cases} \tag{24}$$

Correspondingly, the results of the model accuracy test are shown in Table 4.

From the test results in Table 4, it can be seen that the average relative error, correlation degree, posterior error ratio, and the small error probability of the Grey model have accuracy levels of II, IV, I, and I, respectively. Hence, the Grey prediction accuracy level is finally determined as IV, which cannot be used directly to predict the durability life of CWP-20 in the future time and has the necessity of applying the Markov chain.

During the initial phase of the Markov chain, the results of the $\varepsilon^{(0)}(t)$ operation are combined to classify the relative error into three states:

State 1: overestimated state, $\varepsilon^{(0)}(t)$ between [−0.05,−0.01].
State 2: exact state, $\varepsilon^{(0)}(t)$ between [−0.01,0.01].
State 3: Underestimated state, $\varepsilon^{(0)}(t)$ between [0.01,0.05].

Following Eqs. (19)–(22), the one-step state transfer matrix of CWP-20 can be obtained as follows:

$$\begin{bmatrix} 0.50 & 0.50 & 0.00 \\ 0.29 & 0.57 & 0.14 \\ 0.00 & 0.33 & 0.67 \end{bmatrix} \tag{25}$$

Referring to the Markov chain prediction principle (Bradley, 1999), the state transfer matrix of each step can be obtained next. The predicted values of the Grey model are then rectified following

TABLE 5 E_r value fitting results for CWP-20 during 300 F-T cycles.

F-T cycles	Raw data (%)	Grey model		Grey-markov model	
		Fitted value (%)	Error value (%)	Fitted value (%)	Error value (%)
0	100.00	100.00	0.00	100.00	0.00
25	99.96	101.77	1.82	101.19	1.23
50	99.85	100.70	0.85	100.05	0.20
75	99.63	99.64	0.01	98.92	0.71
100	98.97	98.59	0.38	99.39	0.43
125	98.24	97.55	0.70	98.44	0.21
150	97.47	96.52	0.97	97.51	0.05
175	96.71	95.51	1.25	96.61	0.11
200	96.08	94.50	1.65	95.73	0.37
225	95.42	93.50	2.01	94.87	0.58
250	92.82	92.52	0.33	94.03	1.31
275	89.54	91.54	2.24	89.86	0.35
300	88.23	90.58	2.66	88.70	0.54
		Average error (%)	1.14	Average error (%)	0.47

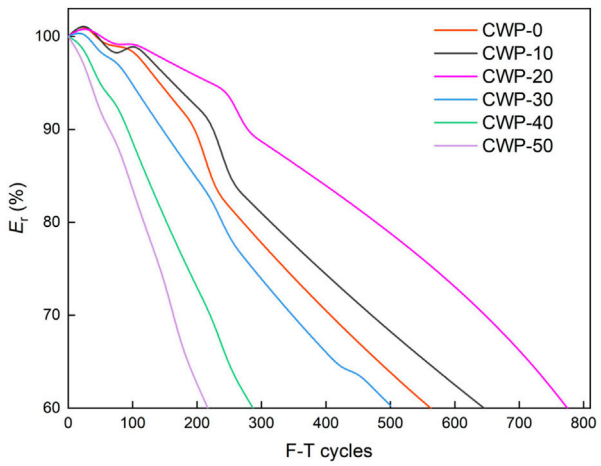

FIGURE 8
Durability life prediction curve of RAC mixtures based on Grey-Markov model.

Eq. 23, and the final prediction results of the two models are depicted in Figure 7. The fitting findings of E_r values for CWP-20 for 0–300 F-T cycles are provided in Table 5 to compare the prediction accuracy of the two models more logically.

As can be seen from Table 5, the maximum error of the E_r fitted value of CWP-20 for the Grey model is 2.66% and the average error is 1.14%, as well as its overall performance, which is inferior to that of the Grey-Markov model. For the prediction results of the Grey-Markov model, the maximum error of the E_r fitted value of CWP-20 is 1.31% and the average error is 0.47%. It is evident that the upgraded model can fully utilize the information provided by the original data to create accurate predictions for data with significant stochastic volatility. As evidenced in Figure 7, the Grey model predicts an overall smooth curve because it is a method for fitting the raw data to an exponential curve. According to the Grey model's prediction, the CWP-20's durability will fail after 1275 F-T cycles, which is a dubious outcome (Ray et al., 2021; Magbool, 2022). The results of the Grey-Markov model fit can fluctuate synchronously with the actual values, and the $\varepsilon^{(0)}(t)$ derived from the Markov chain in the later F-T cycles are deemed to be overestimated, so the actual occurrence values may be lower than the predicted results of the Grey model. From this, This indicates that the Grey-Markov model's prediction that CWP-20 will approach durability failure after 775 F-T cycles is accurate.

With the confirmation that the Grey-Markov model has high prediction accuracy, to further comprehend the durability damage trend of CWP-RACs in the F-T environment, the life prediction of E_r values of all specimens was performed by this model, and the results are shown in Figure 8. As shown in Figure 8, the durability life prediction for the control group is 575 cycles, and only CWP-10 and CWP-20 are anticipated to have a longer life. After 500 cycles, CWP-30 is predicted to be below CWP-0 and will fail in durability. CWP-40 and CWP-50 will fail after 300 and 225 cycles, respectively, which is consistent with the experimental measurement data and again verifies the Grey-Markov model's high fitting accuracy. Overall, a massive amount of CWP harms the F-T resistance of RAC, whereas a little amount of CWP can greatly increase the F-T resistance of RAC.

5 Conclusion

In this paper, the influence of ceramic waste powder (CWP) addings on the freeze-thaw (F-T) resistance of recycled aggregate concrete (RAC) was investigated. The main conclusions can be drawn as follows.

1) CWP can significantly increase the early mechanical characteristics and compactness of RAC, and the compressive strength and impact elastic wave velocity of RAC doped with CWP were greater than those of conventional RAC specimens after 7 days. However, when the age of curing increased, the performance-enhancing capacity of CWP on RAC declined gradually.
2) During the F-T test of RAC, the RDME obtained by the impact-echo method can be employed as a durability evaluation parameter that is more susceptible to environmental conditions than the compressive strength evaluation parameter. The data from RDME indicate that a little amount of CWP can greatly improve the durability of RAC, however, an excess of CWP can have the opposite effect.
3) The Grey-Markov model can more accurately depict the deterioration trend of CWP-RAC durability damage in a F-T condition. With the impact-echo test data, the predicted data closely resembles the test situation. In engineering practice, it is more practical to test and maintain CWP-RAC in severe cold regions.

Data availability statement

The raw data supporting the conclusions of this article will be made available by the authors, without undue reservation.

Author contributions

JY: Conceptualization, Methodology, Validation, Data curation, Writing–original draft. DL: Validation, Data curation. ZZ: Conceptualization, Methodology, supervisor, funding acquisition, Writing–review and editing.

Funding

The authors would like to thank the National Natural Science Foundation of China (Grant No. 52078083), and Natural Science Foundation Project of Chongqing (cstc2020jcyj-msxmX0901), and 111 Project of China (Grant No. B18062), and the Fundamental Research Funds for the Central Universities (Grant No. 2021CDJQY-008) for partial support of this work.

Conflict of interest

The authors declare that the research was conducted in the absence of any commercial or financial relationships that could be construed as a potential conflict of interest.

Publisher's note

All claims expressed in this article are solely those of the authors and do not necessarily represent those of their affiliated organizations, or those of the publisher, the editors and the reviewers. Any product that may be evaluated in this article, or claim that may be made by its manufacturer, is not guaranteed or endorsed by the publisher.

References

Amadi, I. G., Beushausen, H., and Alexander, M. G. (2022). Multi-technique approach to enhance the properties of fine recycled aggregate concrete. *Front. Mat.* 9, 893852. doi:10.3389/fmats.2022.893852

Awoyera, P. O., Akinmusuru, J. O., and Moncea, A. (2017). Hydration mechanism and strength properties of recycled aggregate concrete made using ceramic blended cement. *Cogent Eng.* 4 (1), 1282667. doi:10.1080/23311916.2017.1282667

Bennett, B., Visintin, P., and Xie, T. (2022). Global warming potential of recycled aggregate concrete with supplementary cementitious materials. *J. Build. Eng.* 52, 104394. doi:10.1016/j.jobe.2022.104394

Bradley, R. C. (1999). Equivalent mixing conditions for Markov chains. *Statistics Probab. Lett.* 41 (1), 97–99. doi:10.1016/S0167-7152(98)00143-6

CECS 03-2007 (2007). *Technical specification for testing concrete strength with drilled core*. Beijing, China: China Standard Press.

Chen, X., Zhang, D., Cheng, S., Xu, X., Zhao, C., Wang, X., et al. (2022). Sustainable reuse of ceramic waste powder as a supplementary cementitious material in recycled aggregate concrete: Mechanical properties, durability and microstructure assessment. *J. Build. Eng.* 52, 104418. doi:10.1016/j.jobe.2022.104418

GB/T 50081-2019 (2019). *Standard for test methods of concrete physical and mechanical properties*. Beijing, China: China Architecture& Building Press.

GB/T 50082-2009 (2009). *Standard for test methods of long-term performance and durability of ordinary concrete*. Beijing, China: China Architecture& Building Press.

GB/T 50107-2010 (2011). *Standard for evaluation of concrete compressive strength*. Beijing, China: China Standard Press.

JGJ/T 443-2018 (2018). *Technical standard for recycled concrete structures*. Beijing, China: China Architecture& Building Press.

Jiang, S., Liu, S., Fang, Z., and Liu, Z. (2017). "Distance measuring and sorting method of general grey number based on kernel and grey degree," in 2017 International Conference on Grey Systems and Intelligent Services, 43–45. doi:10.1109/GSIS.2017.8077667

Krzemień, K., and Hager, I. (2015). Post-fire assessment of mechanical properties of concrete with the use of the impact-echo method. *Constr. Build. Mater.* 96, 155–163. doi:10.1016/j.conbuildmat.2015.08.007

Li, P., Zhao, Y., Long, X., Zhou, Y., and Chen, Z. (2020). Ductility evaluation of damaged recycled aggregate concrete columns repaired with carbon fiber-reinforced polymer and large rupture strain FRP. *Front. Mat.* 7, 568036. doi:10.3389/fmats.2020.568036

Magbool, H. M. (2022). Utilisation of ceramic waste aggregate and its effect on eco-friendly concrete: A review. *J. Build. Eng.* 47, 103815. doi:10.1016/j.jobe.2021.103815

Mao, S., Kang, Y., Zhang, Y., Xiao, X., and Zhu, H. (2020). Fractional grey model based on non-singular exponential kernel and its application in the prediction of electronic waste precious metal content. *ISA Trans.* 107, 12–26. doi:10.1016/j.isatra.2020.07.023

Nwakaire, C. M., Yap, S. P., Onn, C. C., Yuen, C. W., and Ibrahim, H. A. (2020). Utilisation of recycled concrete aggregates for sustainable highway pavement applications: A review. *Constr. Build. Mater.* 235, 117444. doi:10.1016/j.conbuildmat.2019.117444

Peng, K., Qiao, H., and Chen, K. (2020). Field exposure test of ceramic-recycled gradient concrete based on Wiener process. *Aust. J. Civ. Eng.* 18 (2), 286–293. doi:10.1080/14488353.2020.1786295

Qin, Y., Guan, K., Kou, J., Ma, Y., Zhou, H., and Zhang, X. (2022). Durability evaluation and life prediction of fiber concrete with fly ash based on entropy weight method and grey theory. *Constr. Build. Mater.* 327, 126918. doi:10.1016/j.conbuildmat.2022.126918

Qu, Z., Li, M., Zhang, Z., Cui, M., and Zhou, Y. (2021). Dynamic optimization method of transmission line parameters based on grey support vector regression. *Front. Energy Res.* 9, 634207. doi:10.3389/fenrg.2021.634207

Ray, S., Haque, M., Sakib, M. N., Mita, A. F., Rahman, M. D. M., and Tanmoy, B. B. (2021). Use of ceramic wastes as aggregates in concrete production: A review. *J. Build. Eng.* 43, 102567–107102. doi:10.1016/j.jobe.2021.102567

Shokouhi, P., Rivière, J., Lake, C. R., Bas, P. Y. L., and Ulrich, T. J. (2017). Dynamic acousto-elastic testing of concrete with a coda-wave probe: Comparison with standard linear and nonlinear ultrasonic techniques. *Ultrasonics* 81, 59–65. doi:10.1016/j.ultras.2017.05.010

Silva, R. V., Brito, J., and Dhir, R. K. (2016). Establishing a relationship between modulus of elasticity and compressive strength of recycled aggregate concrete. *J. Clean. Prod.* 112 (4), 2171–2186. doi:10.1016/j.jclepro.2015.10.064

Wang, P., Qiao, H., Li, Y., Chen, K., Feng, Q., and Nian, T. (2021). Durability of organic coated reinforced magnesium oxychloride cement concrete. *Struct. Concr.* 22 (5), 2595–2610. doi:10.1002/suco.202000094

Wang, Y., Liu, Z., Wang, Y., Wang, D., Yuan, C., and Liu, R. (2022). Effect of recycled aggregate and supplementary cementitious material on the chloride threshold for steel bar corrosion in concrete. *Constr. Build. Mater.* 346, 128418. doi:10.1016/j.conbuildmat.2022.128418

Wichtmann, T., and Triantafyllidis, T. (2010). On the influence of the grain size distribution curve on P-wave velocity, constrained elastic modulus Mmax and Poisson's ratio of quartz sands. *Soil Dyn. Earthq. Eng.* 30 (8), 757–766. doi:10.1016/j.soildyn.2010.03.006

Yang, Y., and Liu, S. (2008). "Kernels of grey numbers and their operations," in 2008 IEEE International Conference on Fuzzy Systems, 826–831. doi:10.1109/FUZZY.2008.4630466

Yu, J., Qiao, H., Hakuzweyezu, T., and Zhu, F. (2022). Damage and deterioration model of basalt fiber/magnesium oxychloride composites based on GM(1, 1)-markov in the salt spray corrosion environment. *J. Renew. Mat.* 10 (11), 2973–2987. doi:10.32604/JRM.2022.019620

Yu, J., Qiao, H., Zhu, F., and Wang, X. (2021). Research on damage and deterioration of fiber concrete under acid rain environment based on GM(1, 1)-markov. *Materials* 14, 6326. doi:10.3390/ma14216326

Zhang, Z., Liu, D., Ding, Y., and Wang, S. (2022). Mechanical performance of strain-hardening cementitious composites (SHCC) with bacterial addition. *J. Infrastruct. Preserv. Resil.* 3, 3. doi:10.1186/s43065-022-00048-3

Zhang, Z., Liu, S., Yang, F., Weng, Y., and Qian, S. (2021). Sustainable high strength, high ductility engineered cementitious composites (ECC) with substitution of cement by rice husk ash. *J. Clean. Prod.* 317, 128379. doi:10.1016/j.jclepro.2021.128379

Zhang, Z., Yang, F., Liu, J., and Wang, S. (2020). Eco-friendly high strength, high ductility engineered cementitious composites (ECC) with substitution of fly ash by rice husk ash. *Cem. Concr. Res.* 137, 106200. doi:10.1016/j.cemconres.2020.106200

Zhou, L., Zhou, X., Liang, H., Huang, M., and Li, Y. (2022). Hybrid short-term wind power prediction based on Markov chain. *Front. Energy Res.* 10, 899692. doi:10.3389/fenrg.2022.899692

frontiers | Frontiers in Materials

TYPE Original Research
PUBLISHED 17 November 2022
DOI 10.3389/fmats.2022.1057128

OPEN ACCESS

EDITED BY
Ramadhansyah Putra Jaya,
Universiti Malaysia Pahang, Malaysia

REVIEWED BY
Piotr Smarzewski,
Military University of Technology, Poland
Abdullah Zeyad,
Jazan University, Saudi Arabia

*CORRESPONDENCE
Yasin Onuralp Özkılıç,
yozkilic@erbakan.edu.tr

SPECIALTY SECTION
This article was submitted to Structural Materials, a section of the journal Frontiers in Materials

RECEIVED 29 September 2022
ACCEPTED 02 November 2022
PUBLISHED 17 November 2022

CITATION
Zeybek Ö, Özkılıç YO, Çelik Aİ, Deifalla AF, Ahmad M and Sabri Sabri MM (2022), Performance evaluation of fiber-reinforced concrete produced with steel fibers extracted from waste tire. *Front. Mater.* 9:1057128. doi: 10.3389/fmats.2022.1057128

Performance evaluation of fiber-reinforced concrete produced with steel fibers extracted from waste tire

Özer Zeybek[1], Yasin Onuralp Özkılıç[2]*, Ali İhsan Çelik[3], Ahmed Farouk Deifalla[4], Mahmood Ahmad[5] and Mohanad Muayad Sabri Sabri[6]

[1]Department of Civil Engineering, Faculty of Engineering, Mugla Sitki Kocman University, Mugla, Turkey, [2]Department of Civil Engineering, Faculty of Engineering, Necmettin Erbakan University, Konya, Turkey, [3]Department of Construction, Tomarza Mustafa Akincioglu Vocational School, Kayseri University, Kayseri, Turkey, [4]Structural Engineering and Construction Department, Future University in Egypt, New Cairo, Egypt, [5]Department of Civil Engineering, University of Engineering and Technology Peshawar (Bannu Campus), Bannu, Pakistan, [6]Peter the Great St. Petersburg Polytechnic University, St. Petersburg, Russia

With the increasing number of vehicles in the world, the amount of waste tires is increasing day by day. In this case, the disposal of expired tires will cause serious environmental problems. In recent years, instead of disposing of tire wastes, most of them have been started to be recycled to produce fiber-reinforced concrete. Thus, steel fibers recovered from waste tires have been preferred as an alternative to industrial steel fibers due to their environmentally friendly and low-cost advantages. In this study, an experimental study was carried out to explore the effect of fiber content on the fresh and hardened state of the concrete. To achieve this goal, compression, splitting tensile, and flexure tests were carried out to observe the performance of the concrete with tire-recycled steel fibers with the ratios of 1%, 2% and 3%. There is an improvement in the mechanical properties of the concrete with the increase of the volume fraction of the steel fiber. However, a significant reduction in workability was observed after the addition of 2% steel fibers. Therefore, it is recommended to utilize 2% tire-recycled steel fibers in practical applications. Furthermore, experimental results of concrete with tire-recycled steel fibers were collected from the literature and empirical equations based on these results were developed in order to predict the compressive and splitting tensile strengths.

KEYWORDS

waste tire, recycled steel fiber, fiber-reinforced concrete, compressive, splitting tensile, flexural, mechanical behavior

1 Introduction

Concrete consists of various ingredients, including cement, aggregates (fine and coarse), water, and some additives and it is widely used as a building material in the civil engineering applications such as dams, bridges, and roads (Shukla, 2013; Vieira et al., 2016; Seetharam et al., 2017; Alabi, 2020; Prabu et al., 2020; Zeyad, 2020; Alwesabi et al., 2021; Magbool and Zeyad, 2021; Ming et al., 2021; Abdullah et al., 2022; Adil et al., 2022; Zeyad et al., 2022). However, it has many shortcomings such as brittleness and low tensile strength. One way to eliminate these drawbacks is to use classical/conventional reinforcements, i.e., transverse, and longitudinal reinforcement. Longitudinal reinforcement resists tensile or compressive stresses. They are in the form of steel bars and placed at a specific interval in the element cross-section. Transverse reinforcement such as stirrups and ties are used to withstand shear. To mitigate shear failures, the number of transverse reinforcements is increased in the critical zones. However, this can lead to increase costs and labor demands (Yuan et al., 2020; Zamanzadeh et al., 2015; Meda et al., 2005; Failla et al., 2002). In this case, the common and efficient way is to use a certain number of fibers. Different types of fibers such as steel, glass, natural and synthetic have been widely used as reinforcement in the concrete mixture. Steel fibers are the most used fiber type to amplify the mechanical properties of concrete (Anil, 2018; Jabir et al., 2020) and they are employed in the form of short discrete lengths and different ratios of length to diameter varying between 20 and 100 in the mixture (Behbahani et al., 2011). According to some experimental studies on beams (Zamanzadeh et al., 2015; Failla et al., 2002; Jabir et al., 2020), steel fibers provide a similar -post-cracking performance when compared to beams reinforced with steel stirrups. Furthermore, steel fibers assist to enhance shear capacity, which leads to reduced crack width. In this way, the failure pattern changes from brittle shear to ductile flexural failure (Zamanzadeh et al., 2015; El-Sayed, 2019). Thus, to obtain the desired quality in concrete, it is also widely preferred to replace the stirrups in the concrete mixture completely or partially with steel fibers (Rashid and Balouch, 2017). Either industrial steel fibers or recycled steel fibers or hybrid fibers (industrial and recycled) are utilized as a reinforcement (Aghaee et al., 2015; Leone et al., 2016; Caggiano et al., 2017; Domski et al., 2017; Hu et al., 2018; Carrillo et al., 2020; Simalti and Singh, 2020). After observing the good performance of industrial steel fibers on concrete, it was concentrated on steel fibers obtained from wastes. Furthermore, research on obtaining fiber from waste materials other than natural resources or raw materials has increased since production of the industrial steel fibers has disadvantages such as greenhouse gas emissions and high cost (Groli et al., 2014; Sengul, 2016; Mastali et al., 2018; Zheng et al., 2018; Isa et al., 2020; Liew and Akbar, 2020; Gul et al., 2021; Qin and Kaewunruen, 2022).

The mostly used recycled steel fibers are obtained from expired vehicle tires (Qin and Kaewunruen, 2022). A typical tire generally consists of carbon, rubbers, steel wire, and additives (Ahmed et al., 2021). Although the service life of vehicle tires vary depending on the road type, usage, and material quality in the tires, it can reach approximately 5 years or up to 40000 km (Sengul, 2016; Barišić et al., 2021). The increase in the number of vehicles in recent years will lead to an increase in the number of wastes after the life span of tires. Then, waste and disposal stage may lead to a huge threat to the environment and high cost. Thus, instead of disposal of waste, recycling, and reuse of them in many industries are viable solutions (Karalar et al., 2022a; Alani et al., 2022; de Azevedo et al., 2022; Martínez-García et al., 2022; Qaidi et al., 2022; Zeybek et al., 2022). In addition to being environmentally friendly, steel fibers extracted from waste are more economical when compared to industrial steel fiber (Ghorpade and Rao, 2010; Mastali et al., 2018; Liew and Akbar, 2020). Many research studies were conducted to investigate the effect of tire-recycled steel fibers on the mechanical properties of concrete. Wu et al. (2016) investigated the impact of tire-recycled fibers on the behavior of concrete materials and it was shown that steel fiber lessens crack width in the concrete. Pilakoutas et al. (2004) studied the reuse of tire steel fibers as a reinforcement in concrete. They mentioned that recovered steel fibers may be replaced by conventional reinforcements, and they can help shorten construction time. Neocleous et al. (2006) evaluated the suitability of existing design guidelines for the concretes with fibers recovered from used and tried to propose a more appropriate approach for flexural design. They also developed a stress-strain curve to obtain the flexural strength of concrete with recycled fibers. Aiello et al. (2009) conducted pull-out tests on concrete with tire-recycled steel fibers obtained by the mechanical process to investigate adhesion between the concrete and the fiber matrix. According to the study, there should be an allowable volume ratio of fibers for the workability of concrete. For a traditional concrete mixer, this ratio should be less than 0.26%. However, it can be used up to 0.46% for a planetary mixer. A study conducted by Aghaee and Yazdi, (2014) stated that the usage of waste wires in concrete provides a positive effect on the mechanical properties of lightweight concrete specimens. Especially, waste wire provides high tensile and flexural strength to the concrete. Rashid and Balouch, (2017) studied the effect of steel fibers recovered from waste tires on the shear resistance of reinforced concrete beams considering four-point bending test. In addition to shear resistance, failure modes, crack propagation and width were also investigated. Workability of concrete with tire-recycled steel fiber is decreased when the amount of fibers increases. Köroğlu, (2018) searched the usage of recycled steel fibers from waste tires in functionally graded self-compacting concrete. Mechanical properties of the concrete were investigated for fresh and hardened conditions. It has been shown that the workability of fresh concrete reduces with increasing fiber content. The effect of steel fiber extracted from waste tires on the mechanical performance of concrete was examined by Zhang and Gao, (2020). Compressive strength, tensile strength, and

TABLE 1 Chemical properties of PC.

(%)	SiO2	AAl2O3	Fe2O3	CaO	MgO	SO3
PC	20.40	5.41	2.82	63.04	1.74	2.50

toughness properties were compared with those of industrial fiber reinforced concrete (IFRC), taking into account different dosages. Gul et al. (2021) carried out a study to investigate the performance of concrete with recycled steel fiber extracted from waste tires. Fiber length and dosages were selected prime variables in their study. They tried to obtain the optimum dosage and length of the steel fibers used in the concrete mixture. Revuelta et al. (2021) compared mechanical behaviors of tire-cycled steel fiber reinforced concrete with those of industrial steel fibers. It has been shown that tire-recycled steel fibers and industrial steel fibers provide similar performance when the same amount of fiber is used. Senesavath et al. (2022) investigated the influence of purified and non-purified recycled tire steel fiber on fresh and hardened concrete performance. Their study showed that purified recycled tire steel fiber provides better tensile strength when compared to non-purified recycled tire steel fiber. Singh and Kaushik, (2001) and (Frančić Smrkić et al., 2017), studied concrete with steel fibers under fatigue loading. Frančić Smrkić et al. (2017) mentioned that current design models underestimate fatigue resistance of the fiber reinforced concrete and they proposed more rational model for this type of concrete.

The above-mentioned studies showed the usability of recycled steel fiber recovered from waste tires in civil engineering applications. However, there is a research need for the optimum amount of fiber in concrete. To pursue this goal, the performance of the concrete with steel fibers generated from tire wastes was investigated and compared by considering different volume fractions of steel fiber. An experimental study was conducted on some test specimens consisting of recycled steel fibers. For each test specimen, the effect of recycled steel fibers on the physical and mechanical properties of concrete was studied for fresh and hardened cases. Optimum fiber dosages were identified for concrete with tire-recycled steel fibers based on the fresh and hardened properties. More importantly is that very few empirical equations to predict the capacities of the concrete with recycled steel fibers from tires are available in the literature. To achieve this aim, the studies were collected from the literature and empirical equations were developed to predict the compression and splitting tensile capacities.

2 Experimental program

2.1 Materials and mixture proportions

CEM I 32.5 Portland Cement was utilized in this study and its chemical properties are depicted in Table 1. Maximum fine aggregate sizes of 4 mm and coarse aggregate sizes of 12 mm were utilized. The ratio of water to cement was selected as 0.60 while the ratio of cement to aggregate was selected as 0.22. The ratio of fine aggregate (0–4 mm) was around 48% while the ratio of coarse aggregate (4–12 mm) was around 52%. In mix design, 360 kg/m^3 cement, 180 kg/m^3 water, 790 kg/m^3 fine aggregate and 850 kg/m^3 coarse aggregate were added.

The steel wires obtained from tires were utilized to investigate the influence of fiber amount on the mechanical properties in terms of compressive strength, split tensile strength, and bending performance of concrete. The utilized steel wires are shown in Figure 1A. The shape of recycled steel wires obtained from tires was linear. The length of the recycled steel wires was divided into small portions before being used it. Yoo et al. (2017) revealed in their study that the medium-length of fibers exhibited higher flexural strengths compared to the longer fiber. Therefore, it was tried to obtain the same length proportion not larger than 5 cm in length to get optimum results. Figure 1B demonstrates the proportion of the lengths utilized in the steel wires. In this study, a reference mixture including no fiber and six mixtures were designed. Three different fiber volume ratios including 1%, 2%, and 3% were studied.

2.2 Mix procedure, workability, and slump test

For the mixing procedure, all aggregates, cement, and water were initially mixed in the mixer. Then, the required recycled steel wires were mixed into small pieces to prevent aggregation and to accomplish the uniform distribution of steel wires in the concrete mixture. Although the steel wires were slowly added to the mixture, aggregation was observed to initiate in the mixture with 3%. Workability was significantly decreased after a 2% fiber content ratio. Slump tests were also performed. The results of the slump test were indicated in Figure 2. It is seen that slump values with steel wires are lower than that of the reference specimen. Moreover, the slump value decreases as the fiber ratio increases.

After mixing, the mixture was poured into molds and vibrated for 30 s. The samples were kept a room temperature for 24 h after casting. Then the samples were tested after 28 days of curing.

2.3 Test procedure

Three different tests were conducted to evaluate the influence of recycled steel wire types and fiber ratio. These tests including compressive, splitting tensile, and bending strength tests are depicted in Figure 3. For each mixture, three repetitions were tested and an average of them was reported. Compression tests were conducted based on ASTM C39/C39M (C39&C39M A, 2003). ASTM C496-96 was utilized for splitting tensile test while ASTM C78/C78M-22 was used for flexural tests.

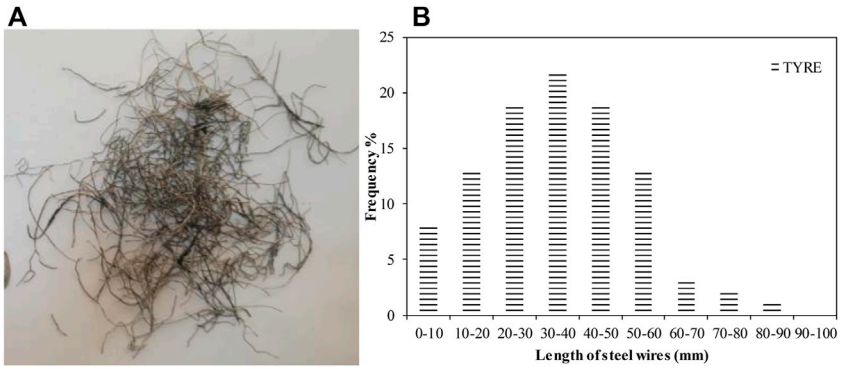

FIGURE 1
Recycled **(A)** steel wires **(B)** obtained from tires.

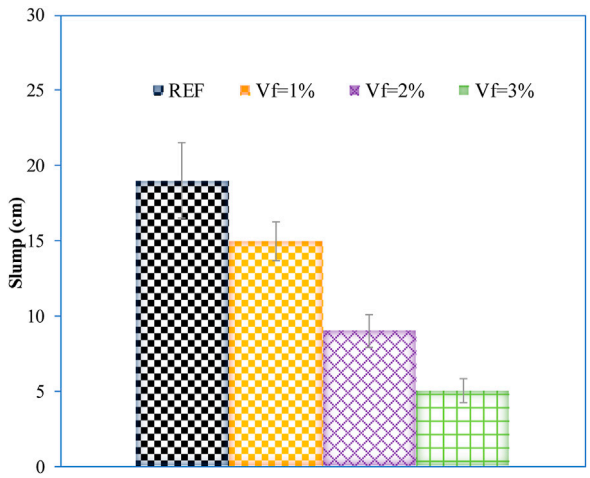

FIGURE 2
Slump test.

Two different compressive strength tests were carried out using cube samples with 150 × 150 × 150 mm and cylindrical samples with a diameter of 100 mm and a height of 200 mm. The speed of loading was 6 kN/s and the tests were conducted up to failure. Using cylindrical samples, compressive strength and compressive strength curves were obtained. On the other hand, cube samples were used to obtain only compressive strength. The splitting tensile tests were also utilized using cylindrical samples with a diameter of 100 mm and a height of 200 mm. The speed of loading was 5 kN/min and the tests were conducted up to a drop 50% in strength. Three-point bending test was performed to compare the flexural strength of the samples with different mixtures. The samples had dimensions of 100 × 100 × 400 mm, and a span length was 300 mm. The speed of loading was 0.5 mm/sec. The flexural behavior of the mixtures was determined by the load-displacement curves.

3 Experimental results and discussions

3.1 Compressive strength of cubic samples

Figure 4 shows the compressive test results of 150 × 150 × 150 mm cubic samples. The graph in Figure 4B shows, from left to right, the compressive strength results of samples of reference and recycled steel wires additive concrete. It is pleasing that the samples with waste material have superior compressive strength compared to the reference samples. In Figure 4B, it is evident that the rising graphite increases the compressive strength as the ratio of waste tire wire in the concrete increases.

To predict the compressive strength of the concrete with recycled steel wires, an equation was derived considering fiber volume ratio and plain concrete strength. Compressive strength with recycled steel wires can be computed using the following proposed equation:

$$f_{TYRE,c} = f_c^{'}\left(1 + 0.15V_f\right) \quad (1)$$

where $f_c^{'}$ is the compressive strength of plain concrete, $f_{\mathrm{TYRE},c}$ is the compressive strength of concrete with bead wires, V_f is fiber volume ratio.

The compression strength values, and their differences obtained as a result of the cubic compression test are presented in Table 2. The compression strength values results obtained by the experimental and proposed equations are very close to each other. A maximum of 2% difference was detected between the experimental and proposed equation. While the compression strengths value of the reference samples was 29.5 MPa, it

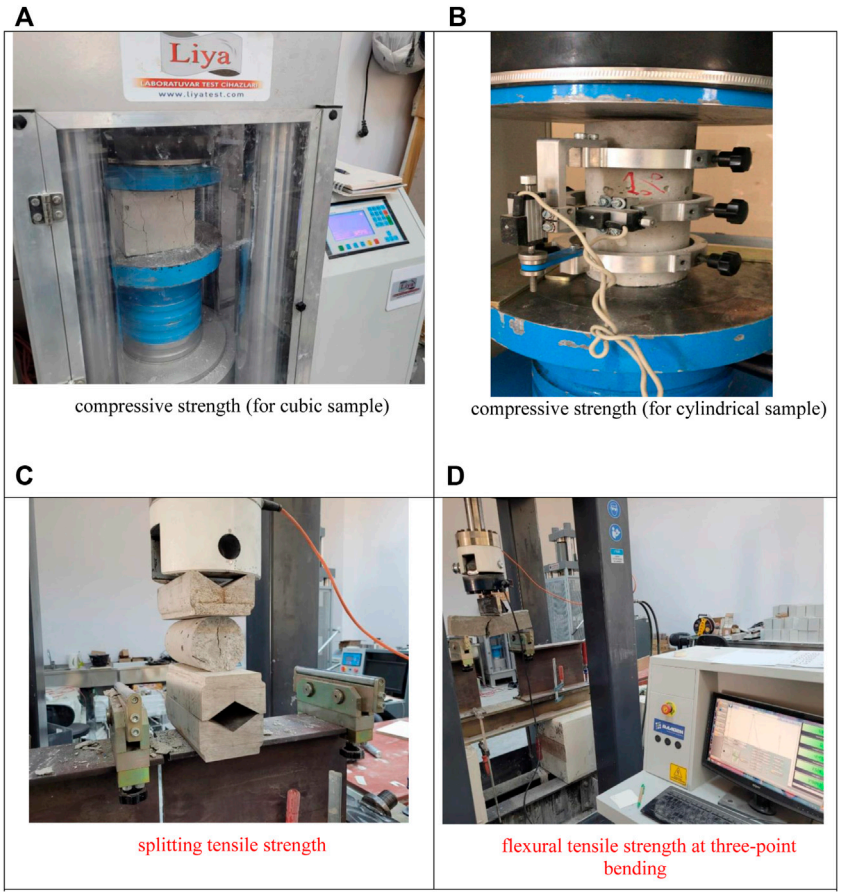

FIGURE 3
Mechanical test setups **(A)** compressive strength (for cubic sample) **(B)** compressive strength (for cylindrical sample) **(C)** splitting tensile strength **(D)** flexural tensile strength at three-point bending.

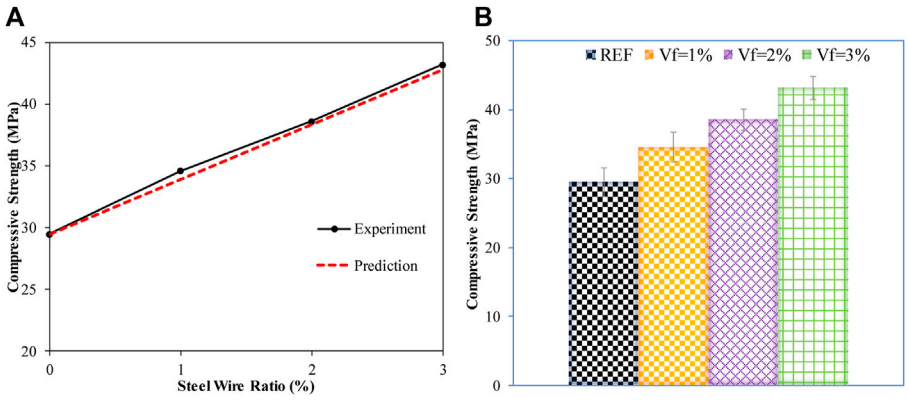

FIGURE 4
Results **(A)** of compressive **(B)** strength.

TABLE 2 Experimental and predicted compressive strength.

Vf	Tire	
%	Experiment	Prediction
0	29.5	29.5
1	34.6	33.9
2	38.6	38.4
3	43.2	42.8

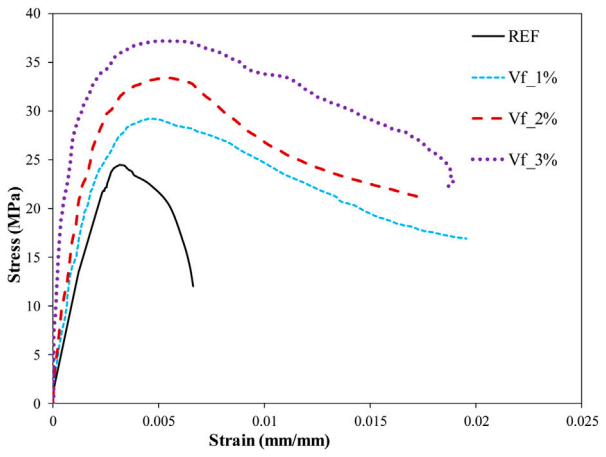

FIGURE 5
Results of compressive cylindrical samples.

increased to 34.6 MPa with a 1% tire additive. In the 2% contribution, a compressive strength raised to 38.6 MPa. Finally, compression strength with 3% additive strength was 43.2 MPa. Gao et al. (2017) found that the compressive strength increased by 1.03% in the test of 1% wire reinforced cubic concrete. The compressive strength of the tire doped specimen confirms the results of (Gao et al., 2017). Yazıcı et al. (2007) in their study added three different fiber volumes of 0.5%, 1.0%, and 1.5. They found that the strength of concrete increased between 4% and 19%. In this study, it is seen that the compressive strength of concrete increases between 17% and 42% with the tire additive. It should be noted that with the addition of waste fibers, the compressive strength of fiber-reinforced concrete increases, but after a certain value of waste fiber content, there is a decrease in workability (Yazıcı et al., 2007).

3.2 Compressive strength of cylindrical samples

Figure 5 depicts the compressive strength result of cylindrical samples. The results have not only increased the maximum strength of the concrete but also increased the toughness capacity thanks to recycled steel wire additive. As the steel wire additive ratio increased, the strength increased proportionally. Table 3 shows the compressive strength results of the cylindrical concrete samples. While the maximum strength was 29 MPa with 1% steel wire additive, the strength was 32 MPa with 2% steel wire additive. This strength increased to 37 MPa if 3% steel wire was utilized. The test results reveal that concrete with 29.5 MPa strength can be increased to 37 MPa which is a 25% increase in the capacity. Neves and Fernandes de Almeida, (2005) stated in their study that up to 1.5% of fiber additives increase the compressive strength of concrete, but decrease Young's modulus slightly. However, in this study, it is understood from the graph that the rate of increase in waste fiber slightly increased in Young's modulus. The obtained results support the statement that (Shah Surendra and Rangan, 1970) stated in their study that fibers significantly improved the ductility of concrete, as evidenced by increased final compressive concrete strains and toughness. Lee, (2017), in his study with 0.25%, 0.375%, and 0.50% fiber volume ratios, determined that the energy absorption capacity increased as the fibre volume ratio in the concrete increased. It is also understood from the curves in Figure 5 that the energy absorption capacity continues at higher rates depending on the increasing fibre volume ratio.

3.3 Splitting tensile strength

A splitting tensile strength test is performed to investigate the effects of steel wires on the tensile strength of concrete. Figure 6 shows the splitting tensile strength result of samples with reference and volume fracture (V_f) of 1%–3% steel wire. Table 4 demonstrates the splitting tensile strength of the samples. Splitting tensile strength increased from 2.83 to 3.24 MPa with 1% V_f steel wire. This strength increased to 3.87 when V_f of 3% steel wire was utilized.

To predict the splitting tensile strength of concrete with recycled steel wire, an equation was derived based on the fiber ratio and compressive strength of plain concrete. Splitting tensile strength with recycled steel wires can be computed using the following proposed equation:

$$f_{TYRE,t} = \sqrt{f_c'}\left(0.52 + 0.06V_f\right) \quad (2)$$

where f_c', $f_{\mathrm{TYRE},t}$ is splitting tensile strength of concrete with bead wires. The obtained results were confirmed with experimental results. Figure 6A compares experimental method results with proposed equation estimates. The fact that the graphic lines overlap proves the accuracy of the proposed equation based on the experimental work. Table 3 gives the experimental and predicted splitting tensile strength results. The experimental result of the reference sample was 2.83,

TABLE 3 Experimental and predicted splitting tensile strength.

Vf	Tire(MPa)	
%	Experiment	Prediction
0	2.83	2.82
1	3.24	3.15
2	3.54	3.48
3	3.87	3.80

while the analytical solution result was 2.82 MPa. A maximum of 3% difference was detected between the predicted capacity and experimental results.

3.4 Flexural performance

The flexural performance of concrete according to volume ratio is shown in Figure 7. While 1% tire provided the flexural performance of around 3.8 kN. It was increased to 5 kN when 2% steel wire was utilized. The addition of 3% fiber provided flexural strength of 6.3 kN. With the 2% tire additive, more than 100% flexural strength was obtained. Since longer waste fiber was utilized in this study, the result was better than the results of (Yoo et al., 2017).

One of the most important results obtained from this study is the toughness of concrete. Figure 8 shows the toughness values. In general, ductile materials have high toughness and brittle materials have low toughness. According to the results obtained, it is seen that the waste fiber additive provides very high toughness. Soulioti et al. (2011) in their experimental study with steel fibers with different geometries, revealed that hook-tipped fibers provide better toughness in concrete than fibers with wavy geometry. Yoo et al. (2017) have argued on the contrary that spun fibers provide the highest flexural strength, but exhibit similar strength and weaker toughness than straight fibers at a V_f equal to or greater than 1.5%. They stated that at a V_f equal to or higher than 1.0%, lower flexural strength and toughness were observed in samples with hooked fibers compared to straight ones.

3.5 Damage analysis

Beams are mechanically accepted structural elements that transfer loads of the usage area to the vertical carriers. Therefore, it is an important issue to perform damage analysis according to the additives added. It has been observed that microcracks occur

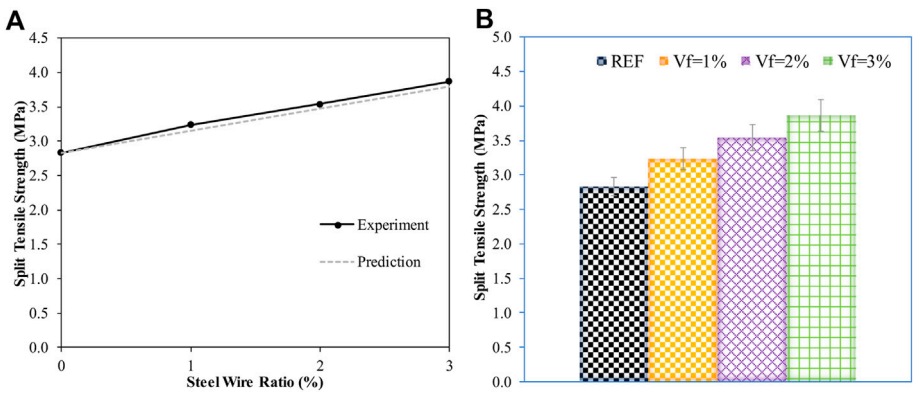

FIGURE 6
Results **(A)** of splitting **(B)** tensile strength.

TABLE 4 | Statistical measures for compression and splitting tensile strength.

	Compression strength	Splitting tensile strength
Average	1.10	1.30
Standard Deviation	0.13	0.21
Maximum	1.56	1.79
Minimum	0.86	0.85

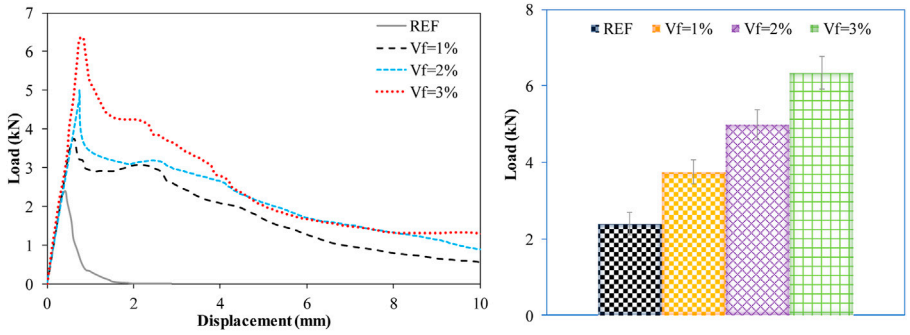

FIGURE 7
Effects of fiber volume fraction on flexural strength.

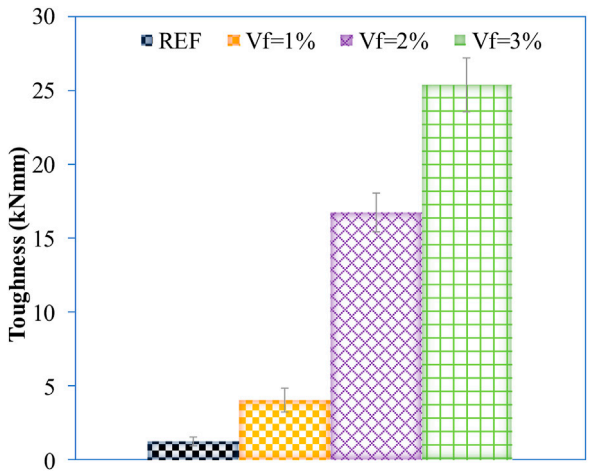

FIGURE 8
Effects of fiber volume fraction on toughness.

in the tensile region of the beam when the fracture strength is reached, especially in fiber-reinforced samples. The addition of steel waste tires stabilized the crack development until the maximum load was reached. When the initial tensile failure was developed in the reference samples, there was a sudden decrease in load capacity, whereas a slower decrease occurred in the fiber-doped samples. As seen in Figure 9, the crack formation has moved towards the compression zone. Therefore, the stability of the beam section under the natural axis was effectively maintained by the fiber bridging region being resistant to fiber rupture. Finally, the fibers that caused the beam sample to fail were completely withdrawn. In all beam specimens, the fracture was observed at the moment constant region of the beam. The fibers drawn on the cracked surface and the tensile fractures on the concrete matrix are visible in Figure 9.

Microstructural analysis (SEM) was performed from the sample pieces taken from recycled steel wire added samples. The SEM images in Figure 10 were obtained by magnifying 500 times. The image on the right is generally projected as an enlargement of the pattern on the left. Important findings are marked on the figures. Images showing the key findings are shown in Figure 10. Figures 10A–F show detailed the interaction between waste steel fibers and concrete. Figure 10A shows hydrated cement, aggregate, and fibers. Figure 10B shows the concrete distribution of the ettringite and the spacing between them. Ettringite develops due to a high content of the mineral sulphate calcium sulfoaluminate. Ettringite is formed in mortar and concrete by the effect of sulphate. Ettringite generally increases the compressive strength of concrete thanks to its Figure 10B also shows pores associated with ettringite. Figure 10C shows the distribution of aggregates in concrete, surface quality, and voids. Cement hydration may be poor at points where voids are high. Figure 10D shows the fine aggregate and cement combination with good hydration. The interface between the steel fiber and the concrete is shown in Figure 10E. There may be a gap on one side of the fiber. Figure 10F shows the steel fiber interface up close. It is seen that it exhibits good adhesion with cementitious concrete.

4 Comparison with the existing SFRC studies

When considering existing research findings, tire-recycled fiber is feasible to enhance some properties of the concrete. By conducting experimental studies, compressive strength, flexural strength, and split tensile strength were obtained for tire-reinforced concrete with different amounts of steel fiber. In the studies, amount of fiber, type (industrial or recycled), length, and diameter of the fiber were the main variables. In this part of the study, compressive strength and split tensile strength values for plain concrete (normal concrete without fibers) and reinforced concrete with steel fibers (either industrial, recycled, or hybrid) were collected from the

FIGURE 9
Damaged view of the beam with 3% waste fibers.

literature. Experimental results obtained from these existing studies conducted by many researchers (Leone et al., 2016; Aghaee et al., 2015; Gul et al., 2021; Mastali et al., 2018; Groli et al., 2014; Köroğlu, 2018; Saatçi and Batarlar, 2017; Samarakoon et al., 2019; Zhang and Gao, 2020; Centonze et al., 2012; Dehghanpour and Yılmaz, 2018; Al-Tikrite and Hadi, 2017; Vistos et al., 2018; Nataraja et al., 1999; Dorr et al., 2019; Sengul, 2018; Ł and Suchorzewski, 2018; Awal et al., 2013; Chern and Young, 1989; Najim et al., 2018; Shi et al., 2020; Rossli and Ibrahim, 2012) were presented in Figures 11, 12. Industrial fiber reinforced concrete (IFRC), recycled fiber reinforced concrete (RFRC) and hybrid fiber reinforced concrete (HFRC) cases were shown in these figures. Relative compressive strength of steel fiber reinforced concrete to the reference or plain concrete without fibers were plotted against fiber content (%) used in the mixture as shown in Figure 11. The compressive strength value of the fiber reinforced concrete is generally higher than that of plain concrete. This indicates that steel fibers play a positive role in increasing strength. Since steel fibers have high tensile toughness, they can limit degradation and crack width under different loading conditions. In other words, steel fibers provide a confinement effect on the mixture by arresting cracks when the number of fibers increases (Shah et al., 2022). This effect delays the rupture in the test specimens. However, in some experimental studies, as shown in Figure 11, it was observed that the compression strength of the reinforced concrete with steel fiber was smaller than plain concrete when fiber content increases since a high amount of fiber lead to a reduction in the workability in the concrete mixture. On the other hand, in some studies, although there was an increase in the compression strength up to a certain threshold value of the fiber dosage, further increasing the steel fiber addition led to a decrease in the compression value. The maximum increase in strength was observed study conducted by Mastali et al. (2018). The use of 1.5% industrial steel fiber resulted in a 56% increase in compression strength of the plain concrete specimens. On the other hand, the maximum decrease in compression strength occurred in the experimental study performed by Vistos et al. (2018). The utilization of 0.5% hybrid steel fiber led to a 14% reduction in the concrete strength. Fiber length also plays an important role in the compressive strength and splitting tensile strength of the fiber-reinforced concrete. Long fibers provide higher splitting tensile strength, while short fibers provide high compressive strength (Gul et al., 2021).

In the same manner, the splitting tensile strength of fiber reinforced concrete was normalized by that of plain concrete as shown in Figure 12. There is a similar observation in the findings of the split tensile strength of the test specimens. The maximum increase in the split tensile strength was observed in the study carried out by (Köroğlu, 2018). The employing of 5.0% industrial steel fiber caused a 79% increase in the split tensile strength of functionally graded self-compacting concrete. On the other hand, the largest decrease in tensile strength was observed in the study (Gul et al., 2021). When 10.16 cm lengths of recycled steel fiber with 1% volume fracture were added, a 15% reduction occurred in the splitting tensile strength of concrete test specimens. It should be noted finding obtained from the current study showed that values for both compression strength and splitting tensile strength increase with increasing fiber content and the proposed empirical equations are shown in Figures 11, 12.

As depicted in Figures 11, 12, most normalized strength values are above 1.0; this means that steel fibers have a generally positive effect in increasing both compressive and splitting tensile strength. Considering all data collected from the literature, the average, standard deviation, maximum and

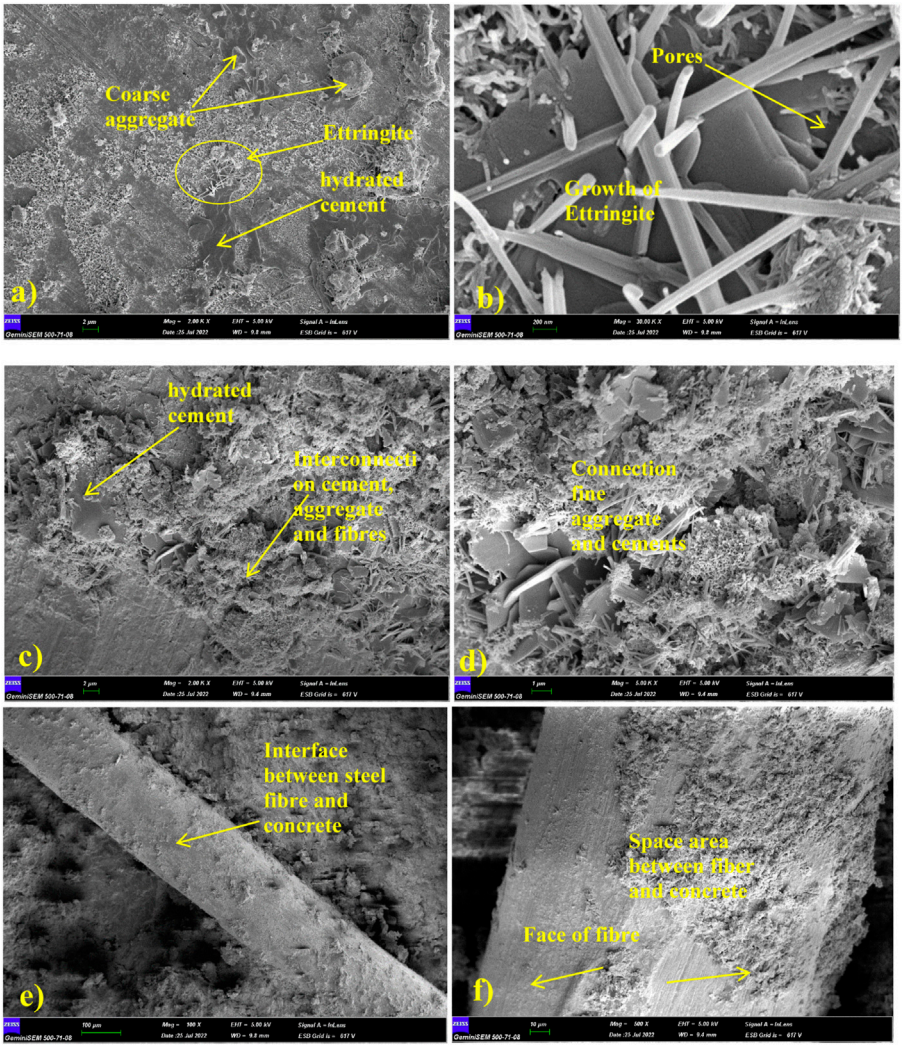

FIGURE 10
Microstructure view of samples.

minimum values of the normalized strength ratios were shown in Table 4.

As shown in the experimental part of the study, there is a linear increase in the compression strength and splitting tensile strength. Thus, by applying curve-fitting to the data obtained from the experimental study conducted in this study empirical equations were derived for practical purposes. Using these proposed equations, both compression strength and splitting tensile strength of the steel fiber reinforced concretes may be estimated considering different steel fiber amount. According to the test results, 2% is proposed as the optimum fiber amount to prevent workability issues in the concrete mixture. According to the studies conducted by Köroglu and Ashour, (2019), (Yazıcı et al., 2007; Revuelta et al., 2021; Hu et al., 2018), it was stated that volume fraction of steel fiber significantly affects the workability of concrete. Test results of Köroglu and Ashour, (2019) showed that excess fiber added in concrete reduced the workability of concrete and reduced flow diameter in flow table test. Furthermore, the optimum fiber content values for concrete mixes are recommended between 0.5% and 2.5% (Pierre et al., 1999) and (Song and Hwang, 2004). Adding a low amount of fibers prevents fiber balling and produces the concrete with homogeneous material consistency and good workability (Song and Hwang, 2004). Thus, considering our experimental test results, a 2% volume of fiber is recommended as the optimum fiber dosage for practical applications. Recommendation of 2% was also utilized in many studies (Özkılıç et al., 2021; Aksoylu et al., 2022; Karalar et al., 2022b; Çelik et al., 2022). As already mentioned, there is a decrease in the strength values after a certain fiber content. Thus, new generalized strength equations

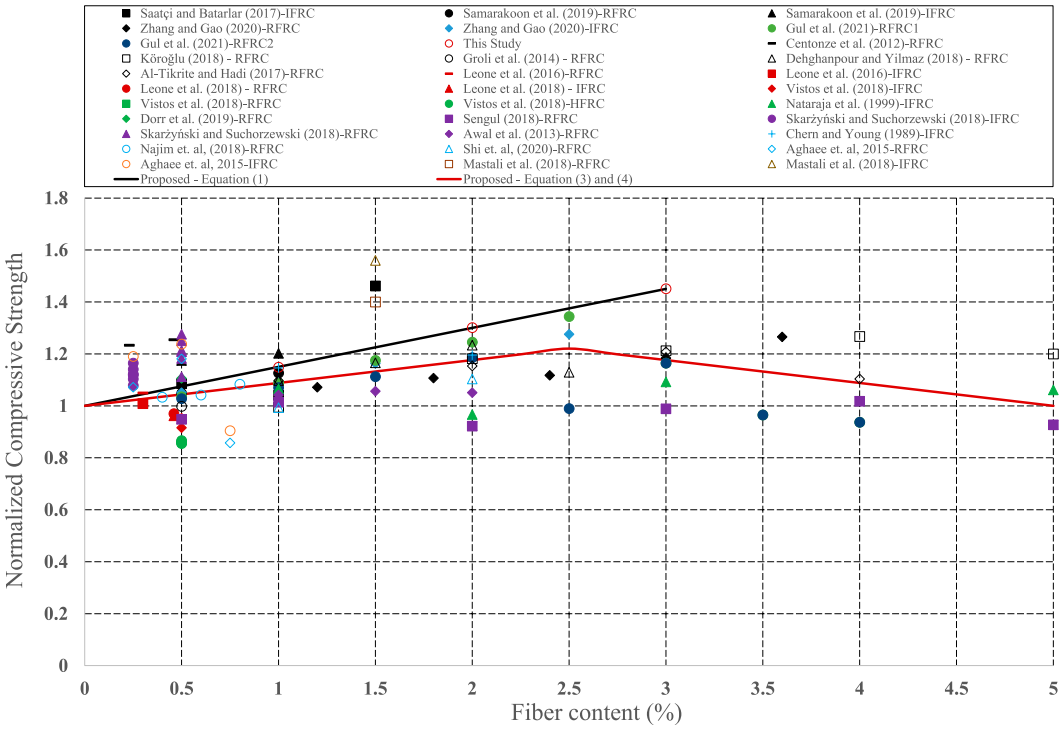

FIGURE 11
Variation of the normalized compressive strength of the steel fiber reinforced concrete with the fiber content.

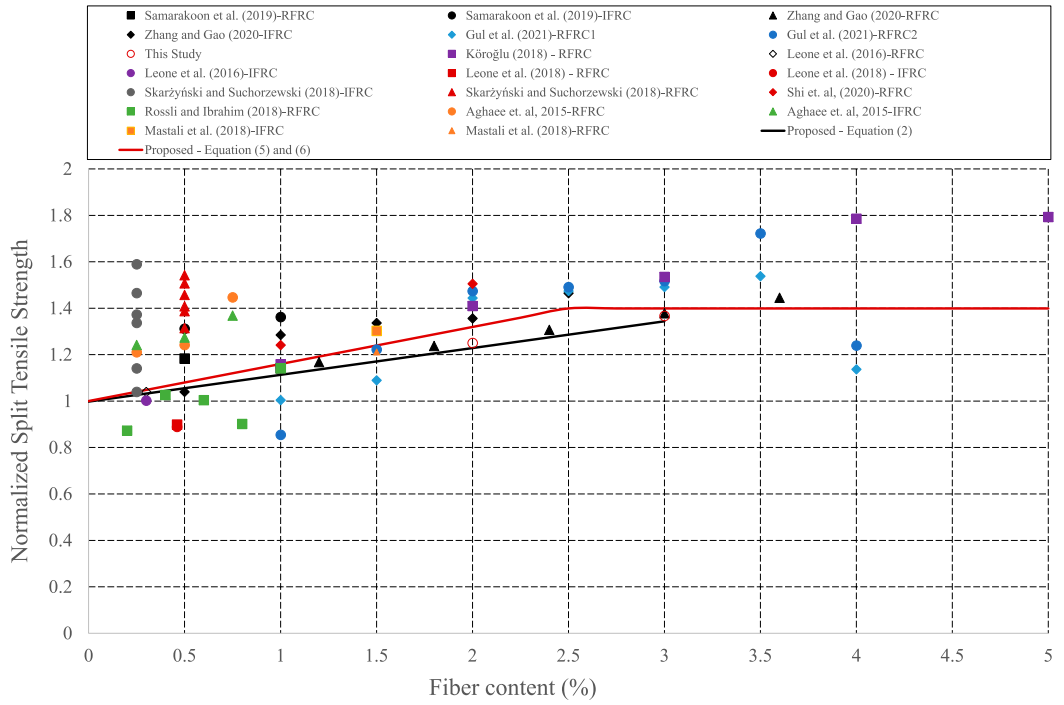

FIGURE 12
Variation of the splitting tensile strength of the steel fiber reinforced concrete with the fiber content.

taking into account the reduction in the strengths have been developed as follows:

$$f_{TYRE,c} = f_c^{'} + 2.6V_f \quad \text{if } V_f \le 2.5 \tag{3}$$

$$f_{TYRE,c} = 1.22f_c^{'} - 2.6\left(V_f - 2.5\right) \quad \text{if } 5 > V_f \le 2.5 \tag{4}$$

$$f_{TYRE,t} = 0.521\sqrt{f_c^{'}} + 0.452V_f \quad \text{if } V_f \le 2.5 \tag{5}$$

$$f_{TYRE,t} = 0.729\sqrt{f_c^{'}} \quad \text{if } 5 > V_f \le 2.5 \tag{6}$$

5 Conclusion and summary

This paper investigates the effect of steel fiber generated from expired vehicle tires on concrete performance. For this purpose, an experimental study was conducted by considering three different steel fiber contents of 1%, 2% and 3%. The engineering properties of concrete produced with waste tire in terms of the fresh and hardened cases were examined. Furthermore, empirical equations are also derived as a function of the fiber ratio to easily calculate the compressive strength and splitting tensile strength. The following can be drawn from this study:

1) The slump test results show that the slump value decreases as the fiber ratio increases. Workability of concrete with tire-recycled steel fiber is also decreased when the amount of fibers increases.
2) The compressive test results showed that compression strength of concrete in cubic samples increased with the addition of the wire steel fibers. Compared to the reference sample, the compressive strength value increased by 17% with 1% wire steel fibers additive, 30% with 2% wire steel fibers and 46% with 3% wire steel fibers. In cylindrical samples, the compressive strength of concrete also increased according to the amount of waste wire. Compared to the reference sample, the compressive strength of the concrete increased by 18% with 1% wire steel fibers additive, 45% with 2% wire steel fibers and 58% with 3% wire steel fibers.
3) The tensile test results on cylindrical samples showed there is a proportional increase with the steel fiber addition. The addition of 1%, 2%, and 3% wire steel fibers increased splitting tensile strength of concrete by 15%, 25%, and 36%, respectively, compared to plain concrete.
4) The flexural strength values show that the flexural strength increases proportionally with the addition of high wire fiber. It was observed that the addition of wire fiber gives positive results in flexural strength compared to the reference sample. The addition of 1%, 2%, and 3% wire steel fibers increased flexural strength of concrete by 77%, 272%, and 795%, respectively,
5) The toughness test results showed that there is a proportional increase between the ductility and the toughness. Respectively, 4, 16, and 26 times more toughness occurred compared to the reference sample.
6) The developed expressions for the compressive strength and splitting tensile strength can successfully estimate the capacity; therefore, these equations have the potential to be implemented into design guidelines of the concretes with fibers recovered from used tires.
7) Based on the fresh and hardened properties of concrete, 2% is recommended as the optimum of amount for tire-recycled steel fiber. It should be also noted that this ratio can be changed using very low or high water cement ratio or using superplasticizer.

Data availability statement

The raw data supporting the conclusion of this article will be made available by the authors, without undue reservation.

Author contributions

ÖZ: investigation, writing—original draft preparation, writing—review and editing YOÖ: Conceptualization, methodology, formal analysis, investigation, resources, data curation, writing—original draft preparation AD: writing—original draft preparation, writing—review and editing AÇ: formal analysis, writing—original draft preparation, writing—review and editing MA: writing—original draft preparation, writing—review and editing MMSS: resources, writing—original draft preparation, writing—review and editing, funding.

Funding

The research is partially funded by the Ministry of Science and Higher Education of the Russian Federation under the strategic academic leadership program “Priority 2030” (Agreement 075-15-2021-1333 dated 30.09.2021).

Conflict of interest

The authors declare that the research was conducted in the absence of any commercial or financial relationships that could be construed as a potential conflict of interest.

Publisher’s note

All claims expressed in this article are solely those of the authors and do not necessarily represent those of their affiliated

organizations, or those of the publisher, the editors and the reviewers. Any product that may be evaluated in this article, or claim that may be made by its manufacturer, is not guaranteed or endorsed by the publisher.

References

Abdullah, G. M. S., Alshaikh, I. M. H., Zeyad A, M., Magbool, H. M., and Bakar, B. H. A. (2022). The effect of openings on the performance of self-compacting concrete with volcanic pumice powder and different steel fibers. *Case Stud. Constr. Mater.* 17, e01148. doi:10.1016/j.cscm.2022.e01148

Adil, W., Ur Rahman, F., S Abdullah, M. G., Tayeh, B. A., and Zeyad, A. M. (2022). Effective utilization of textile industry waste-derived and heat-treated pumice powder in cement mortar. *Constr. Build. Mater.* 351, 128966. doi:10.1016/j.conbuildmat.2022.128966

Aghaee, K., Yazdi, M. A., and Tsavdaridis, K. D. (2015). Investigation into the mechanical properties of structural lightweight concrete reinforced with waste steel wires. *Mag. Concr. Res.* 67, 197–205. doi:10.1680/macr.14.00232

Aghaee, K., and Yazdi, M. A. (2014). Waste steel wires modified structural lightweight concrete. *Mat. Res.* 17, 958–966. doi:10.1590/1516-1439.257413

Ahmed, H. U., Faraj, R. H., Hilal, N., Mohammed, A. A., and Sherwani, A. F. H. (2021). Use of recycled fibers in concrete composites: A systematic comprehensive review. *Compos. Part B Eng.* 215, 108769. doi:10.1016/j.compositesb.2021.108769

Aiello, M. A., Leuzzi, F., Centonze, G., and Maffezzoli, A. (2009). Use of steel fibres recovered from waste tyres as reinforcement in concrete: Pull-out behaviour, compressive and flexural strength. *Waste Manag.* 29, 1960–1970. doi:10.1016/j.wasman.2008.12.002

Aksoylu, C., Özkılıç, Y. O., Hadzima-Nyarko, M., Işık, E., and Arslan, M. H. J. S. (2022). Investigation on improvement in shear performance of reinforced-concrete beams produced with recycled steel wires from waste tires. *Sustainability* 14, 13360. doi:10.3390/su142013360

Al-Tikrite, A., and Hadi, M. N. S. (2017). Mechanical properties of reactive powder concrete containing industrial and waste steel fibres at different ratios under compression. *Constr. Build. Mater.* 154, 1024–1034. doi:10.1016/j.conbuildmat.2017.08.024

Alabi, S. A. (2020). Predictive models for evaluation of compressive and split tensile strengths of recycled aggregate concrete containing lathe waste steel fiber. *Jordan J. Civ. Eng.*, 14.

Alani, A. A., Lesovik, R., Lesovik, V., Fediuk, R., Klyuev, S., Amran, M., et al. (2022). Demolition waste potential for completely cement-free binders. *Materials* 15, 6018. doi:10.3390/ma15176018

Alwesabi, E. A. H., Bakar, B. H. A., Alshaikh, I. M. H., Zeyad, A. M., Altheeb, A., and Alghamdi, H. (2021). Experimental investigation on fracture characteristics of plain and rubberized concrete containing hybrid steel-polypropylene fiber. *Structures* 33, 4421–4432. doi:10.1016/j.istruc.2021.07.011

Anil, N. (2018). Mechanical properties of steel fiber reinforced self-compacting concrete. *Int. J. Eng. Technol. IJET* 4, 33–40. doi:10.19072/ijet.340259

Awal, A. S. M. A. A. A. S. M. A., Yee, L. L., and Hossain, M. Z. (2013). Fresh and hardened properties of concrete containing steel fibre from recycled tire. *Malays. J. Civ. Eng.* 25.

Barišić, I., Zvonarić, M., Grubeša, I. N., and Šurdonja, S. (2021). Recycling waste rubber tyres in road construction. *Archives Civ. Eng.* 67, 499–512.

Behbahani, H. P., Nematollahi, B., and Farasatpour, M. (2011). *Steel fiber reinforced concrete: A review*.

Caggiano, A., Folino, P., Lima, C., Martinelli, E., and Pepe, M. (2017). On the mechanical response of hybrid fiber reinforced concrete with recycled and industrial steel fibers. *Constr. Build. Mater.* 147, 286–295. doi:10.1016/j.conbuildmat.2017.04.160

Carrillo, J., Lizarazo-Marriaga, J., and Lamus, F. (2020). Properties of steel fiber reinforced concrete using either industrial or recycled fibers from waste tires. *Fibers Polym.* 21, 2055–2067. doi:10.1007/s12221-020-1076-1

Çelik, A. İ., Özkılıç, Y. O., Zeybek, Ö., Özdöner, N., and Tayeh, B. A. (2022). Performance assessment of fiber-reinforced concrete produced with waste lathe fibers. *Sustainability* 14, 11817. doi:10.3390/su141911817

Centonze, G., Leone, M., and Aiello, M. A. (2012). Steel fibers from waste tires as reinforcement in concrete: A mechanical characterization. *Constr. Build. Mater.* 36, 46–57. doi:10.1016/j.conbuildmat.2012.04.088

Chern, J-C., and Young, C-H. (1989). Compressive creep and shrinkage of steel fibre reinforced concrete. *Int. J. Cem. Compos. Lightweight Concr.* 11, 205–214. doi:10.1016/0262-5075(89)90100-0

de Azevedo, A. R. G., Marvila, M. T., de Oliveira, M. A. B., Umbuzeiro, C. E. M., Huaman, N. R. C., and Monteiro, S. N. (2022). Perspectives for the application of bauxite wastes in the development of alternative building materials. *J. Mater. Res. Technol.* 20, 3114–3125. doi:10.1016/j.jmrt.2022.08.092

Dehghanpour, H., and Yılmaz, K. (2018). Mechanical and impact behavior on recycled steel fiber reinforced cementitious mortars. *Sci. Her. Voronezh State Univ. Archit. Civ. Eng.* 39.

Domski, J., Katzer, J., Zakrzewski, M., and Ponikiewski, T. (2017). Comparison of the mechanical characteristics of engineered and waste steel fiber used as reinforcement for concrete. *J. Clean. Prod.* 158, 18–28. doi:10.1016/j.jclepro.2017.04.165

Dorr, B. J., Kanali, C. L., and Onchiri, R. O. (2019). Shear performance of recycled tyres steel fibres reinforced lightweight concrete beam using palm kernel shear as partial replacement of coarse aggregate. *Int. J. Eng. Res. Technol.* 12, 1818–1823.

El-Sayed, T. A. (2019). Flexural behavior of RC beams containing recycled industrial wastes as steel fibers. *Constr. Build. Mater.* 212, 27–38. doi:10.1016/j.conbuildmat.2019.03.311

Failla, C., Toniolo, G., and Ferrara, L. (2002). *Structural design of prestressed precast roof elements made with steel fibre reinforced concrete*. BIBM 2002 International Conference, Istanbul.

Frančić Smrkić, M., Damjanović, D., and Baričević, A. (2017). Application of recycled steel fibres in concrete elements subjected to fatigue loading. *Građevinar* 69, 893–905.

Gao, D., Zhang, L., and Nokken, M. (2017). Compressive behavior of steel fiber reinforced recycled coarse aggregate concrete designed with equivalent cubic compressive strength. *Constr. Build. Mater.* 141, 235–244. doi:10.1016/j.conbuildmat.2017.02.136

Ghorpade, V. G., and Rao, H. S. (2010). Strength and permeability characteristics of Fibre reinforced recycled aggregate concrete with different fibres. *Nat. Environ. Pollut. Technol.* 9, 179–188.

Groli, G., Pérez Caldentey, A., and Soto, A. G. (2014). Cracking performance of SCC reinforced with recycled fibres–an experimental study. *Struct. Concr.* 15, 136–153. doi:10.1002/suco.201300008

Gul, A., Alam, B., Iqbal, M. J., Ahmed, W., Shahzada, K., Javed, M. H., et al. (2021). Impact of length and percent dosage of recycled steel fibers on the mechanical properties of concrete. *Civ. Eng. J.* 7, 1650–1666. doi:10.28991/cej-2021-03091750

Hu, H., Papastergiou, P., Angelakopoulos, H., Guadagnini, M., and Pilakoutas, K. (2018). Mechanical properties of SFRC using blended manufactured and recycled tyre steel fibres. *Constr. Build. Mater.* 163, 376–389. doi:10.1016/j.conbuildmat.2017.12.116

Isa, M. N., Pilakoutas, K., Guadagnini, M., and Angelakopoulos, H. (2020). Mechanical performance of affordable and eco-efficient ultra-high performance concrete (UHPC) containing recycled tyre steel fibres. *Constr. Build. Mater.* 255, 119272. doi:10.1016/j.conbuildmat.2020.119272

Jabir, H. A., Abid, S. R., Murali, G., Ali, S. H., Klyuev, S., Fediuk, R., et al. (2020). Experimental tests and reliability analysis of the cracking impact resistance of UHPFRC. *Fibers* 8, 74. doi:10.3390/fib8120074

Karalar, M., Bilir, T., Çavuşlu, M., Özkılıç, Y. O., and Sabri, M. M. S. Use of recycled coal bottom ash in reinforced concrete beams as replacement for aggregate. 2022, 1064604.

Karalar, M., Özkılıç, Y. O., Deifalla, A. F., Aksoylu, C., Arslan, M. H., Ahmad, M., et al. (2022). Improvement in bending performance of reinforced concrete beams

produced with waste lathe scraps. *Sustainability* 14, 12660. doi:10.3390/su141912660

Köroglu, M. A., and Ashour, A. (2019). Mechanical properties of self-compacting concrete with recycled bead wires. *rdlc* 18, 501–512. doi:10.7764/rdlc.18.3.501

Köroğlu, M. A. (2018). Behavior of composite self-compacting concrete (SCC) reinforced with steel wires from waste tires. *Revista de Construcción J. Constr.* 17, 484–498.

Ł, Skarżyński, and Suchorzewski, J. (2018). Mechanical and fracture properties of concrete reinforced with recycled and industrial steel fibers using Digital Image Correlation technique and X-ray micro computed tomography. *Constr. Build. Mater.* 183, 283–299. doi:10.1016/j.conbuildmat.2018.06.182

Lee, J-H. (2017). Influence of concrete strength combined with fiber content in the residual flexural strengths of fiber reinforced concrete. *Compos. Struct.* 168, 216–225. doi:10.1016/j.compstruct.2017.01.052

Leone, M., Centonze, G., Colonna, D., Micelli, F., and Aiello, M. A. (2016). Experimental study on bond behavior in fiber-reinforced concrete with low content of recycled steel fiber. *J. Mat. Civ. Eng.* 28, 04016068. doi:10.1061/(asce)mt.1943-5533.0001534

Liew, K. M., and Akbar, A. (2020). The recent progress of recycled steel fiber reinforced concrete. *Constr. Build. Mater.* 232, 117232. doi:10.1016/j.conbuildmat.2019.117232

Magbool, H. M., and Zeyad, A. M. (2021). The effect of various steel fibers and volcanic pumice powder on fracture characteristics of Self-Compacting concrete. *Constr. Build. Mater.* 312, 125444. doi:10.1016/j.conbuildmat.2021.125444

Martínez-García, R., Jagadesh, P., Zaid, O., Şerbănoiu, A. A., Fraile-Fernández, F. J., de Prado-Gil, J., et al. (2022). The present state of the use of waste wood ash as an eco-efficient construction material: A review. *Materials* 15, 5349. doi:10.3390/ma15155349

Mastali, M., Dalvand, A., Sattarifard, A. R., and Illikainen, M. (2018). Development of eco-efficient and cost-effective reinforced self-consolidation concretes with hybrid industrial/recycled steel fibers. *Constr. Build. Mater.* 166, 214–226. doi:10.1016/j.conbuildmat.2018.01.147

Meda, A., Minelli, F., Plizzari, G. A., and Riva, P. (2005). Shear behaviour of steel fibre reinforced concrete beams. *Mat. Struct.* 38, 343–351. doi:10.1617/14112

Ming, Y., Chen, P., Li, L., Gan, G., and Pan, G. (2021). A comprehensive review on the utilization of recycled waste fibers in cement-based composites. *Materials* 14, 3643. doi:10.3390/ma14133643

Najim, K. B., Saeb, A., and Al-Azzawi, Z. (2018). Structural behaviour and fracture energy of recycled steel fibre self-compacting reinforced concrete beams. *J. Build. Eng.* 17, 174–182. doi:10.1016/j.jobe.2018.02.014

Nataraja, M. C., Dhang, N., and Gupta, A. P. (1999). Stress–strain curves for steel-fiber reinforced concrete under compression. *Cem. Concr. Compos.* 21, 383–390. doi:10.1016/s0958-9465(99)00021-9

Neocleous, K., Tlemat, H., and Pilakoutas, K. (2006). Design issues for concrete reinforced with steel fibers, including fibers recovered from used tires. *J. Mat. Civ. Eng.* 18, 677–685. doi:10.1061/(asce)0899-1561(2006)18:5(677)

Neves, R. D., and Fernandes de Almeida, J. C. O. (2005). Compressive behaviour of steel fibre reinforced concrete. *Struct. Concr.* 6, 1–8. doi:10.1680/stco.2005.6.1.1

Özkılıç, Y. O., Aksoylu, C., and Arslan, M. H. (2021). Experimental and numerical investigations of steel fiber reinforced concrete dapped-end purlins. *J. Build. Eng.* 36, 102119. doi:10.1016/j.jobe.2020.102119

Pierre, P., Pleau, R., and Pigeon, M. (1999). Mechanical properties of steel microfiber reinforced cement pastes and mortars. *J. Mat. Civ. Eng.* 11, 317–324. doi:10.1061/(asce)0899-1561(1999)11:4(317)

Pilakoutas, K., Neocleous, K., and Tlemat, H. (2004). "Reuse of tyre steel fibres as concrete reinforcement," in Proceedings of the Institution of Civil Engineers-Engineering Sustainability. (Thomas Telford Ltd), Vol. 157 (3), 131–138.

Prabu, M., Vignesh, K., Saii Prasanna, N., Praveen, C., and Mohammed Nafeez, A. (2020). Experimental study on concrete in partial replacement of fine aggregate with lathe waste. *Int. J. Sci. Eng. Res.* 11, 68–72.

Qaidi, S., Najm, H. M., Abed, S. M., Özkılıç, Y. O., Al Dughaishi, H., Alosta, M., et al. (2022). Concrete containing waste glass as an environmentally friendly aggregate: A review on fresh and mechanical characteristics. *Materials* 15, 6222. doi:10.3390/ma15186222

Qin, X., and Kaewunruen, S. (2022). Environment-friendly recycled steel fibre reinforced concrete. *Constr. Build. Mater.* 327, 126967. doi:10.1016/j.conbuildmat.2022.126967

Rashid, K., and Balouch, N. (2017). Influence of steel fibers extracted from waste tires on shear behavior of reinforced concrete beams. *Struct. Concr.* 18, 589–596. doi:10.1002/suco.201600194

Revuelta, D., Carballosa, P., García Calvo, J. L., and Pedrosa, F. (2021). Residual strength and drying behavior of concrete reinforced with recycled steel fiber from tires. *Materials* 14, 6111. doi:10.3390/ma14206111

Rossli, S., and Ibrahim, I. (2012). *Mechanical properties of recycled steel tire fibres in concrete*. Malaysia: Fac Civil Eng, University of Technology.

Saatçi, S., and Batarlar, B. (2017). Çelik fiber katkılı etriyesiz betonarme kirişlerin davranışı. *Gazi Univ. Muhendislik-Mimarlik Fak. Derg.* 32, 1143–1154. doi:10.17341/gazimmfd.369512

Samarakoon, S. M. S. M. K., Ruben, P., Wie Pedersen, J., and Evangelista, L. (2019). Mechanical performance of concrete made of steel fibers from tire waste. *Case Stud. Constr. Mater.* 11, e00259. doi:10.1016/j.cscm.2019.e00259

Seetharam, P. G., Bhuvaneswari, C., Vidhya, S., and Vishnu Priya, M. (2017). Studies on properties of concrete replacing lathe scrap. *Int. J. Eng. Res. Technol.* 6, 382–386.

Senesavath, S., Salem, A., Kashkash, S., Zehra, B., and Orban, Z. (2022). The effect of recycled tyre steel fibers on the properties of concrete. *Pollack* 17, 43–49. doi:10.1556/606.2021.00388

Sengul, O. (2016). Mechanical behavior of concretes containing waste steel fibers recovered from scrap tires. *Constr. Build. Mater.* 122, 649–658. doi:10.1016/j.conbuildmat.2016.06.113

Sengul, O. (2018). Mechanical properties of slurry infiltrated fiber concrete produced with waste steel fibers. *Constr. Build. Mater.* 186, 1082–1091. doi:10.1016/j.conbuildmat.2018.08.042

Shah, S. H. A., Ali, B., Ahmed, G. H., Tirmazi, S. M. T., El Ouni, M. H., and Hussain, I. (2022). Effect of recycled steel fibers on the mechanical strength and impact toughness of precast paving blocks. *Case Stud. Constr. Mater.* 16, e01025. doi:10.1016/j.cscm.2022.e01025

Shah Surendra, P., and Rangan, B. V. (1970). Effects of reinforcements on ductility of concrete. *J. Struct. Div.* 96, 1167–1184. doi:10.1061/jsdeag.0002601

Shi, X., Brescia-Norambuena, L., Grasley, Z., and Hogancamp, J. (2020). Fracture properties and restrained shrinkage cracking resistance of cement mortar reinforced by recycled steel fiber from scrap tires. *Transp. Res. Rec.* 2674, 581–590. doi:10.1177/0361198120924407

Shukla, A. K. (2013). Application of CNC waste with recycled aggregate in concrete mix. *Int. J. Eng. Res. Appl.* 3, 1026–1031.

Simalti, A., and Singh, A. P. (2020). Comparative study on direct shear behavior of manufactured and recycled shredded tyre steel fiber reinforced self-consolidating concrete. *J. Build. Eng.* 29, 101169. doi:10.1016/j.jobe.2020.101169

Singh, S. P., and Kaushik, S. K. (2001). Flexural fatigue analysis of steel fiber-reinforced concrete. *Mater. J.* 98, 306–312.

Song, P. S., and Hwang, S. (2004). Mechanical properties of high-strength steel fiber-reinforced concrete. *Constr. Build. Mater.* 18, 669–673. doi:10.1016/j.conbuildmat.2004.04.027

Soulioti, D. V., Barkoula, N. M., Paipetis, A., and Matikas, T. E. (2011). Effects of fibre geometry and volume fraction on the flexural behaviour of steel-fibre reinforced concrete. *Strain* 47, e535–e541. doi:10.1111/j.1475-1305.2009.00652.x

Vieira, D. R., Calmon, J. L., and Coelho, F. Z. (2016). Life cycle assessment (lca) applied to the manufacturing of common and ecological concrete: A review. *Constr. Build. Mater.* 124, 656–666. doi:10.1016/j.conbuildmat.2016.07.125

Vistos, L., Galladini, D., Xargay, H., Caggiano, A., Folino, P., and Martinelli, E. (2018). "Hybrid industrial/recycled SFRC: Experimental analysis and design," in Proceedings of Italian Concrete Days 2016. ICD 2016. Lecture Notes in Civil Engineering. Editors M. di Prisco and M. Menegotto (Springer), Vol. 10.

Wu, Z., Shi, C., He, W., and Wu, L. (2016). Effects of steel fiber content and shape on mechanical properties of ultra high performance concrete. *Constr. Build. Mater.* 103, 8–14. doi:10.1016/j.conbuildmat.2015.11.028

Yazıcı, Ş., İnan, G., and Tabak, V. (2007). Effect of aspect ratio and volume fraction of steel fiber on the mechanical properties of SFRC. *Constr. Build. Mater.* 21, 1250–1253. doi:10.1016/j.conbuildmat.2006.05.025

Yoo, D-Y., Kim, S., Park, G-J., Park, J-J., and Kim, S-W. (2017). Effects of fiber shape, aspect ratio, and volume fraction on flexural behavior of ultra-high-performance fiber-reinforced cement composites. *Compos. Struct.* 174, 375–388. doi:10.1016/j.compstruct.2017.04.069

Yuan, F., Chen, M., and Pan, J. (2020). Flexural strengthening of reinforced concrete beams with high-strength steel wire and engineered cementitious composites. *Constr. Build. Mater.* 254, 119284. doi:10.1016/j.conbuildmat.2020.119284

Zamanzadeh, Z., Lourenço, L., and Barros, J. (2015). Recycled steel fibre reinforced concrete failing in bending and in shear. *Constr. Build. Mater.* 85, 195–207. doi:10.1016/j.conbuildmat.2015.03.070

Zeyad, A. M. (2020). Effect of fibers types on fresh properties and flexural toughness of self-compacting concrete. *J. Mater. Res. Technol.* 9, 4147–4158. doi:10.1016/j.jmrt.2020.02.042

Zeyad, A. M., Hakeem, I. Y., Amin, M., Tayeh, B. A., and Agwa, I. S. (2022). Effect of aggregate and fibre types on ultra-high-performance concrete designed for radiation shielding. *J. Build. Eng.* 58, 104960. doi:10.1016/j.jobe.2022.104960

Zeybek, Ö., Özkılıç, Y. O., Karalar, M., Çelik, A. İ., Qaidi, S., Ahmad, J., et al. (2022). Influence of replacing cement with waste glass on mechanical properties of concrete. *Materials* 15, 7513. doi:10.3390/ma15217513

Zhang, Y., and Gao, L. (2020). Influence of tire-recycled steel fibers on strength and flexural behavior of reinforced concrete. *Adv. Mater. Sci. Eng.* 2020, 1–7. doi:10.1155/2020/6363105

Zheng, Y., Wu, X., He, G., Shang, Q., Xu, J., and Sun, Y. (2018). Mechanical properties of steel fiber-reinforced concrete by vibratory mixing technology. *Adv. Civ. Eng.* 2018, 1–11. doi:10.1155/2018/9025715

frontiers | Frontiers in Materials

TYPE Original Research
PUBLISHED 09 December 2022
DOI 10.3389/fmats.2022.1071316

OPEN ACCESS

EDITED BY
Dong Zhang,
Fuzhou University, China

REVIEWED BY
Meng Guo,
Beijing University of Technology, China
Peiwen Hao,
Chang'an University, China
Yiwei Weng,
Hong Kong Polytechnic University,
Hong Kong SAR, China

*CORRESPONDENCE
Zuo-Cai Wang,
wangzuocai@hfut.edu.cn

SPECIALTY SECTION
This article was submitted to Structural Materials, a section of the journal Frontiers in Materials

RECEIVED 16 October 2022
ACCEPTED 28 November 2022
PUBLISHED 09 December 2022

CITATION
Niu S-L, Wang J-Y, Wang Z-C, Wang D-H, Sun X-T and Zhao X (2022), Overall feasibility assessment of polyester polyurethane concrete used as steel bridge deck pavement. *Front. Mater.* 9:1071316. doi: 10.3389/fmats.2022.1071316

Overall feasibility assessment of polyester polyurethane concrete used as steel bridge deck pavement

Shi-Lei Niu[1], Jun-Yi Wang[2], Zuo-Cai Wang[1,3]*, Dong-Hui Wang[4], Xiao-Tong Sun[1] and Xi Zhao[1]

[1]Department of Civil Engineering, Hefei University of Technology, Hefei, China, [2]Ningbo Road Technology Industrial Group Co., Ltd., Ningbo, China, [3]Anhui Province Infrastructure Safety Inspection and Monitoring Engineering Laboratory, Hefei, China, [4]China Railway Major Bridge Reconnaissance & Design Institute Co., Ltd., Wuhan, China

Traditional pavement materials used in the orthotropic steel bridge deck suffer from various pavement distresses and thus reduce the service life of the steel bridge. Therefore, this study proposed a novel engineered material named polyester polyurethane concrete (PPUC) for the steel bridge deck pavement. Indoor laboratory experiments and numerical comparison analysis were conducted to comprehensively assess the feasibility of PPUC as the steel bridge deck pavement and ordinary Portland cement (OPC), guss asphalt concrete (GAC), asphalt mastic concrete (SMAC) and epoxy asphalt concrete (EAC) were used as references compared with PPUC. After the specimens of PPUC were prepared by mixing polyester polyurethane binder (PPUB) and aggregate with the binder-aggregate ratio of 15%, the specimens were subjected to compressive test, splitting tensile test, flexural tensile strength test, wheel tracking test, low-temperature cracking test, freeze-thaw splitting test, shear test and pull-out test. The mechanical performance comparison of different pavement structures with different materials was also analyzed using finite element analysis method. Results show that PPUC presents higher mechanical properties (compressive, tensile and flexural strength) compared to OPC, and it has good durability properties compared to SMAC, GAC, and EAC, such as high temperature stability, low temperature cracking resistance and water stability. In addition, PPUC has strong adhesive property with steel deck and does not change significantly with temperature changes. The finite element simulation results show that the maximum tensile strength and maximum compressive strength of PPUC in the single-layer structure are 0.51 MPa and 3.52 MPa respectively, which are much smaller than the experimental values and those of other materials. The maximum tensile strength and maximum shear strength of PPUC in the PPUC + SMAC composite structure are 0.232 MPa and 0.148 MPa respectively, which are also much smaller than the experimental values and those of other structures. The mechanical performance comparison results indicate that PPUC pavement structure can improve the overall stiffness of the steel bridge deck and protect the wear layer. These results support that the PPUC has a promising application for the steel bridge deck pavement.

KEYWORDS

polyester polyurethane concrete, steel bridge deck pavement, mechanical properties, durability properties, adhesive property, mechanical performance comparison

1 Introduction

The orthotropic steel bridge deck is widely used in the large-span steel bridge all over the world due to its light weight, large span capacity and comfortable driving performance (He et al., 2021; Huang et al., 2022; Liu G et al., 2022). However, the existence of transverse and longitudinal ribs has a significant impact on the force conditions of steel deck pavement. When the steel deck pavement is subjected to vehicle load, some harmful load effects such as negative bending moment, stress concentration and interface slip will be found at the corresponding position on the pavement (Kainuma et al., 2016; Ma et al., 2018). Besides, a greater deformation of pavement occurs on the orthotropic steel deck compared with the ordinary pavement built on solid subgrade (Luo et al., 2017). Therefore, the requirements for the steel bridge deck pavement material are more stringent than those of the ordinary road pavement with following properties: high strength, good deformation ability, good bonding ability, high temperature stability, low temperature crack resistance and durability (Shao et al., 2013; Zeng et al., 2022; Zhu et al., 2022).

At present, the asphalt mixtures are widely used as the pavement materials for the steel bridge deck comprising guss asphalt concrete (GAC), stone mastic asphalt concrete (SMAC) and epoxy asphalt concrete (EAC). However, they are highly sensitive to ambient temperature, displaying viscoelasticity and brittleness at high and low temperature respectively, leading to a variety of surface damages such as cracking, rutting, pushing, and potholes etc. (Ma et al., 2018; Fan and Luo, 2021; He et al., 2021). For instance, GAC presents poor high temperature stability and is prone to rutting in spite of its excellent waterproof, anti-cracking and anti-aging properties. SMAC with good flexibility, anti-cracking and permanent deformation resistance presents an insufficient bond strength between the pavement and the steel bridge deck (Jiang et al., 2020; Liu Y et al., 2022). EAC shows high strength, relatively strong high-temperature stability, low-temperature crack resistance and permanent deformation ability. Moreover, it also has certain ability to resist fatigue and chemical erosion. However, the preparation process is complicated due to the strict controls of time and temperature in construction and the material cost of EAC is high (Chen C et al., 2018; Jiang et al., 2020; Liu Z et al., 2022). Therefore, there is an unmet need to develop a novel material formulation and a pavement structure, prolonging the service life of steel deck pavement (Alrefaei and Dai, 2022).

Polyurethane, produced by the reaction of multiorganic isocyanate and various hydrogen donors, contains various carbamate groups (-NHCOO-) on the main chain of the macromolecular structure, presenting superior properties of wear resistance, high temperature resistance, good mechanical properties and excellent adhesive ability (Jiang et al., 2020; Xu et al., 2020; Alrefaei and Dai, 2022). Moreover, it is highly flexible and elastic, which can be subjected to a greater deformation. Therefore, it is highly relevant to use as a paving material to increase the service life of steel bridge deck (Jiang et al., 2020; Meng et al., 2021). In recent years, polyurethane concrete has been gradually applied to bridge pavement engineering. Ningbo Lubao Company has developed polyester polyurethane concrete (PPUC), which has good durability, strong adhesion with steel, early strength, low temperature workability, etc. At present, PPUC has been applied to many bridge projects in China. In addition, PPUC is easily prepared at the room temperature and contributes to the carbon emissions reduction, thus protecting the environment (Xu et al., 2020).

In recent years, the polymer concrete has received increasing attention, designating to the term of cement concrete materials mixed with polymer materials. J.P. Romualdi et al. mixed steel fiber and concrete to form a steel fiber polymer concrete with good bending resistance for enhancing durability of steel structure. But its flexibility is too poor to ensure the coordinated deformation of steel bridge surface and pavement (Han et al., 2014; Kim et al., 2014; Romualdi and Mandel, 2021). Song et al. produced a polymer alloy material by mixing different kinds of polymers with concrete to produce polymer alloy material in a laboratory scale. Results showed that the developed composite exhibited properties of light and high-strength, good bonding performance and high-temperature performance Song et al. (2012). Yang et al. (2020) developed polyurethane void elastic pavement with the good rutting resistance. Hong et al. introduced polyurethane-based friction courses and polyurethane concrete suitable for tunnel pavement. Results indicated that they had excellent mechanical and functional properties Hong et al. (2020). Lu et al. produced polyurethane concrete with great waterproofing property by comparatively adjusting the aggregate gradation and discovered that it had good on-road performance and durability Lu et al. (2019). Chen J et al. (2018) studied the frost resistance of polyurethane concrete and discovered that polyurethane concrete could significantly postpone the ice generation procedure. Li et al. (2019) studied the difference between high performance polyurethane pervious mixture and porous asphalt mixture from aspects of mechanical properties, functional properties and void microscopic characteristics through indoor tests and found that the former had excellent mechanical and functional properties. Wang et al. (2014) investigated the characteristics of strength and road performance of porous polyurethane macadam mixture, and analyzed the temperature impacts on its strength and

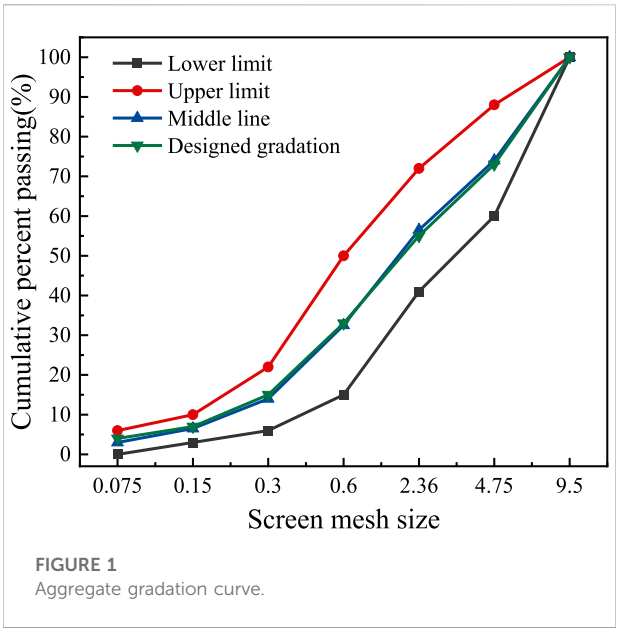

FIGURE 1
Aggregate gradation curve.

deformation resistance. Wang et al. (2017) developed a porous elastic pavement using polyurethane, which exhibited good noise reduction properties, superior low temperature tensile properties, anti-abrasion resistance and rutting resistance. Cong et al. (2018) conducted experimental studies on the basic properties of polyurethane binders and polyurethane permeable mixtures and analyzed the effect of immersion damage on the mixtures. These studies indicate that polyurethane mixtures, with good mechanical properties and high temperature characteristics, are promising candidate materials for the pavement applications.

In this study, PPUC was used as the pavement material for the steel bridge deck. The characteristics of PPUC were comprehensively investigated and compared with the traditional asphalt mixture (GAC, SMAC and EAC) and ordinary Portland cement (OPC). The structure of this paper is as follows. Firstly, the PPUC specimens were prepared. Then, the mechanical property test, wheel tracking test, low-temperature bending test and freeze-thaw splitting test were carried out to evaluate the characteristics of the material, followed by the evaluation of shear test and pull-out test (Munoz et al., 2014). Finally, the numerical simulation was implemented to compare mechanical performance of different pavement structures with different materials.

2 Material performance test

2.1 Raw materials and specimen preparation

PPUC, a thermosetting mixture, was prepared by mixing polyester polyurethane binder (PPUB) and a certain gradation of aggregate at room temperature. The compressive test was used for the optimum binder-aggregate ratio design. According to the test results, the optimum proportion of binder and aggregate was obtained as 15%–17%. In this study, 15% was determined as the optimum binder-aggregate ratio. Aggregate, as an important component of concrete, was used to enhance the mechanical properties of concrete. In this study, natural sand and natural gravel were used as aggregates, with the nominal particle of 0.075–4.75 mm and 4.75–9.5 mm respectively. The gradation of the aggregate is presented in Figure 1. The technical properties of the PPUB and the aggregate are shown in Table 1.

PPUC standard specimens of different sizes were prepared following the Standard for Test Methods of Physical and Mechanical Properties of Concrete (GB/T50081-2019, 2019) and the Test Procedure for Asphalt and Asphalt Mixture for Highway Engineering (JTG E20-2011, 2011). The preparation of PPUC specimens was clearly specified as follows: after mixing the aggregates uniformly according to the design gradation, they were added to the concrete experimental mixer and mixed in a dry state at room temperature for 3 min. Then PPUB was evenly mixed with the aggregate for 3 min. And then, the fresh PPUC mixture was cast into the mold to prepare PPUC specimens with different dimensions and all specimens were cured at room temperature for 24 h. Finally, all specimens were demolded and then maintained at a temperature of 20 ± 2°C before the tests. The relevant test items and specimen dimensions are shown in Table 2.

GAC, EAC, and SMAC are commonly used as bridge deck materials which consist of asphalt, aggregate and mineral powder. In this study, composite modified asphalt (80% SBS modified asphalt + 20% TLA lake asphalt), epoxy asphalt and SBS modified asphalt were used to prepare the asphalt mixture (GAC, EAC and SMAC, respectively). The basalt with a good angular performance was chosen as the coarse and fine aggregate. Limestone mineral powder was used as a filler to stabilize the internal concrete structure. The performance indicators of the raw materials all meet the requirements of the JTG E20-2011 and the Technical Specification for Design and Construction of Highway Steel Bridge Deck Pavement (JTG/T3364-02-2019, 2019). GAC, EAC were prepared using AC-10 gradation and SMAC were prepared using AC-13 gradation.

2.2 Mechanical properties test

The mechanical properties of PPUC were mainly assessed by compressive strength, tensile strength and flexural tensile strength and compared with those of ordinary Portland cement (OPC) (Zhang et al., 2020a). A cube specimen of 150 mm × 150 mm × 150 mm was subjected to a universal testing machine with the loading rate of 0.5 MPa/s for the compressive test as shown in Figure 2A. The tensile strength of PPUC was indirectly measured by splitting tensile test. Typically, the splitting strength is higher than the direct tensile strength. The specimen with dimension of

TABLE 1 Technical properties of the PPUB and the aggregate.

Test items	Technical properties	Test results	Technical requirements	Test method
PPUB	Tensile strength (MPa)	15.7	≥10	GB/T1040
	Fracture elongation (%)	34	≥25	GB/T1040
	Thermosetting property (300°C)	No melting	No melting	GB/T30598
	Water absorption (%)	0.1	≤0.3	GB/T1034
Aggregate	Density (g/cm^2)	2.62	≥2.4	T0304
	Water absorption (%)	1.3	≤2.0	T0304
	Moisture content (%)	0.25	≤0.3	T0305
	Firmness (%)	8	≤12	T0340

TABLE 2 Specimen dimensions in different test items.

Experimental items	Test method	Dimension/mm	References specification
Compressive strength	Cube compressive strength test	150 × 150 × 150	GBT 50081
Tensile strength	Splitting tensile test	150 × 150 × 150	GBT 50081
Flexural tensile strength	Four-point bending test	150 × 150 × 550	GBT 50081
High-temperature stability	Wheel tracking test	300 × 300 × 50	JTG E20-2011
Low-temperature crack resistance	Three-point bending test	250 × 30 × 35	JTG E20-2011
Water stability	Freeze-thaw splitting test	ϕ101.6 × 63.5	JTG E20-2011

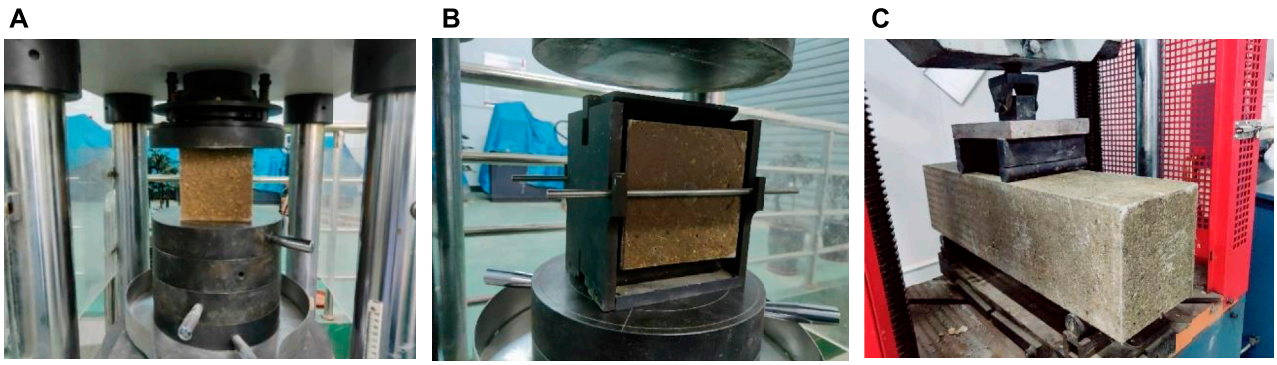

FIGURE 2
Mechanical properties test procedure. **(A)** Compressive test, **(B)** Splitting tensile test, **(C)** Flexural tensile test.

150 mm × 150 mm × 150 mm was placed on a special clamp and applied with a loading rate of 0.08 MPa/s (Figure 2B). The specimen of 150 mm × 150 mm × 550 mm was performed by the flexural tensile strength test with the bottom supported and restrained. The distance between the two supports was 450 mm, and the length of the pure bending section was 150 mm. The loading rate in the test was determined as 0.5 MPa/s. The test process is shown in Figure 2C.

As shown in Table 3, the mechanical properties of PPUC with compressive strength of 75.3 MPa, splitting tensile strength of 8.4 MPa and flexural tensile strength of 22.4 MPa are significantly higher than those of OPC and allocated in C70 strength grade, suggesting promising basic mechanical properties for the steel bridge deck pavement. The damage of the concrete sample is mainly attributed to the growth of microcracks in the matrix, which may lead to the failure of the concrete. Similar to

TABLE 3 Mechanical properties.

Material	Compressive strength (MPa)	Splitting tensile strength (MPa)	Flexural tensile strength (MPa)
PPUC	75.3	8.4	22.4
OPC	32.1	1.8	4.2

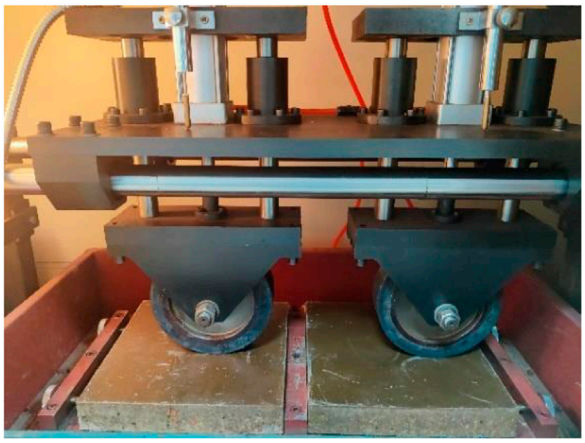

FIGURE 3
The schematic diagram of the gradient concrete test block.

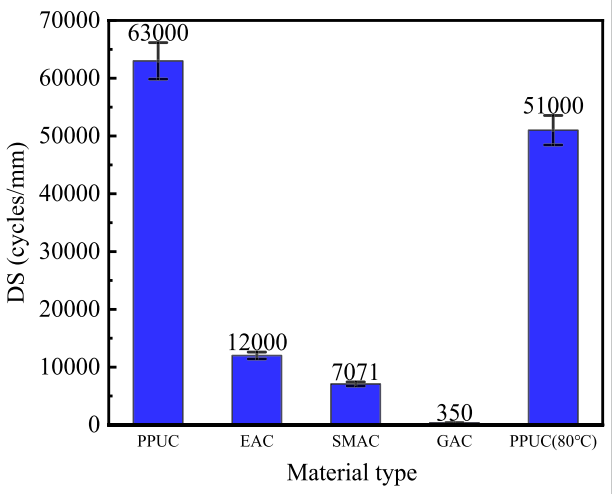

FIGURE 4
Wheel tracking test result.

the rubber concrete, PPUC is stiffened by the well-dispersed fine elastomeric resins. When the structure is deformed by the external forces, the elastomeric resin helps to resist cracking (Cai et al., 2012; Ho et al., 2012; Wang et al., 2019).

2.3 Wheel tracking test

The temperature of steel bridge decks can reach up to 70°C in summer, which has a significant influence on the service life of paving material (Luo et al., 2017; W. and L., 2012). In this sense, wheel tracking test was performed to evaluate the ability of PPUC resisting the repeated loading temperature of 60°C (Figure 3). The dynamic stability (DS) was used as the evaluation index. Briefly, the concrete specimens with dimensions of 300 mm × 300 mm × 50 mm were subjected to wheel tracking tests by following T0719-2011 (JTG E20-2011, 2011). The test wheel tires were made of solid rubber with an outer diameter of 200 mm and a wheel width of 50 mm. The rubber tires pressure was designed as 0.7 ± 0.05 MPa, and the speed of rolling back and forth was 42 times/min. The rutting specimens were fixed on the operating platform in the test box and the internal temperature was maintained at 60°C throughout the test.

The larger DS indicates the greater ability of concrete material to resist the rutting deformation and the DS of pavement material is required to be larger than 3500 cycles/mm. In this study, the DS of EAC, SMAC, and GAC were also measured for the comparison. It can be observed in Figure 4 that the DS values of both PPUC and EAC are larger than 10000 cycles/mm while the DS of PPUC is about six times higher than that of EAC and significantly higher than that of SMAC and GAC respectively. Moreover, the decrease of DS for PPUC (19%) is smaller than that of EAC, SMAC and GAC respectively in case of high temperature at 80°C. The rutting depth of the PPUC under the wheel-track loading is neglectable indicating the little rutting deformation occurred. It is mainly due to the higher rigidity and elastic resilience of the polyurethane binder that helps the PPUC specimens to resist the rutting deformation (Jiang et al., 2020).

2.4 Low-temperature bending test

The shrinkage deformation in the road surface and tensile stress generated in the inner pavement layer at a low temperature may allow the pavement layer susceptible to temperature shrinkage cracks (Liu G et al., 2022). Due to the high elastic modulus of PPUC, a large temperature stress will be generated as the temperature drops, which will easily cause crack-ing. Following the T0715-2011 (JTG E20), the bending beam test was performed at −20°C and -10°C

FIGURE 5
Low-temperature bending test procedure.

respectively to evaluate the low temperature crack resistance of PPUC as shown in Figure 5. Maximum bending and tensile strain (MBTS), bending and tensile strength modulus (BTSM) and bending and tensile strength (BTS) were used as evaluation indexes. Specimens with dimensions of 250 mm × 30 mm × 35 mm were assessed with the loading rate of 50 mm/min.

As presented in Figure 6, results show that the MBTS of PPUC (3545 με) is larger than those of EAC and SMAC (2706 and 2893με, respectively), indicating PPUC presents a better low-temperature resilience. Moreover, there is no significant difference between the MBTS values of PPUC at -10°C and -20°C (3545 and 3048με, respectively) suggesting that PPUC is less sensitive to a low temperature. The BTSM of PPUC is much close to that of EAC and dramatically larger than that of SMAC indicating that the two types of concrete with higher elastic modulus are prone to higher temperature stresses with the decrease of temperature. As for the BTS value, it can be seen that PPUC shows a higher value than EAC and about 2 times higher than SMAC, implying that PPUC exhibits better low-temperature strength. These results show that PPUC can reduce the probability of crack generation and deformation extension under the low temperature condition, and improve the durability of paving materials.

2.5 Freeze-thaw splitting test

The moisture in the pavement reduces the adhesion of PPUC binder and aggregate. Therefore, after being subjected to the repeated tests of traffic loads and temperature changes, the pavement will suffer from diseases such as extrusion deformation and pits. Referring to the test procedure of T0729-2011 (JTG E20), the freeze-thaw splitting test was implemented to evaluate the water damage resistance of PPUC. In this test, a cylindrical specimen with a diameter of 101.6 ± 0.25 mm and a height of 63.5 ± 1.3 mm was formed by the Marshall compaction method and performed the freeze-thaw cycling by the freeze-thaw testing machine. After that, the specimens were placed on the splitting tester with a loading rate of 50 mm/min, as presented in Figure 7. The freeze-thaw splitting tensile strength ratio (STSR) of the specimens before and after the water damage was measured to evaluate the water stability of PPUC.

As shown in Table 4, it can be observed that the splitting strength of PPUC before and after the freeze-thaw cycling are significantly higher than those of EAC and SMAC (7.85 and 7.30 MPa respectively), indicating PPUC has a greater indirect tensile strength compared to SMAC and particularly EAC which is usually considered to be a thermosetting paving material with good water stability. It can be also found that the STSR of PPUC (93%) is larger than that of EAC (83%). The STSR of SMAC (95%) is greater than that of PPUC due to the addition of modifier, which improves the resistance of SMAC to water damage. These results show that PPUC has a good stability performance as the steel bridge deck pavement material under the coupling effect of water vapor and temperature.

3 Pavement structure performance test

3.1 Shear test

The failure of interface shear between the pavement and the steel deck is one of the main reasons for the deterioration of steel deck pavement quality (Zhang et al., 2020b; Lu et al., 2021; Majumder and Saha, 2021; Guan et al., 2022). Therefore, the shear strength between PPUC and steel plate was measured by the 45° oblique shear test, as illustrated in Figure 8. The specimen with the size of 100 mm × 100 mm × 40 mm was assessed by the oblique shear test using the loading rate of 10 mm/min. Moreover, in order to investigate the effect of temperature on the bonding layer, the shear test was conducted using two temperature configurations: room temperature (25°C) and high temperature (70°C) respectively. SMAC and EAC were used as control groups. The shear strength was calculated by Eq. 1:

$$\tau = \frac{F \times \sin\alpha}{S} \quad (1)$$

Where τ is the shear strength, F is the ultimate load when the specimen is damaged, S is the shear area of the specimen, and α is the shear angle at 45°.

Results show that the shear failure occurs at the interface between the PPUC and the steel plate at both the room

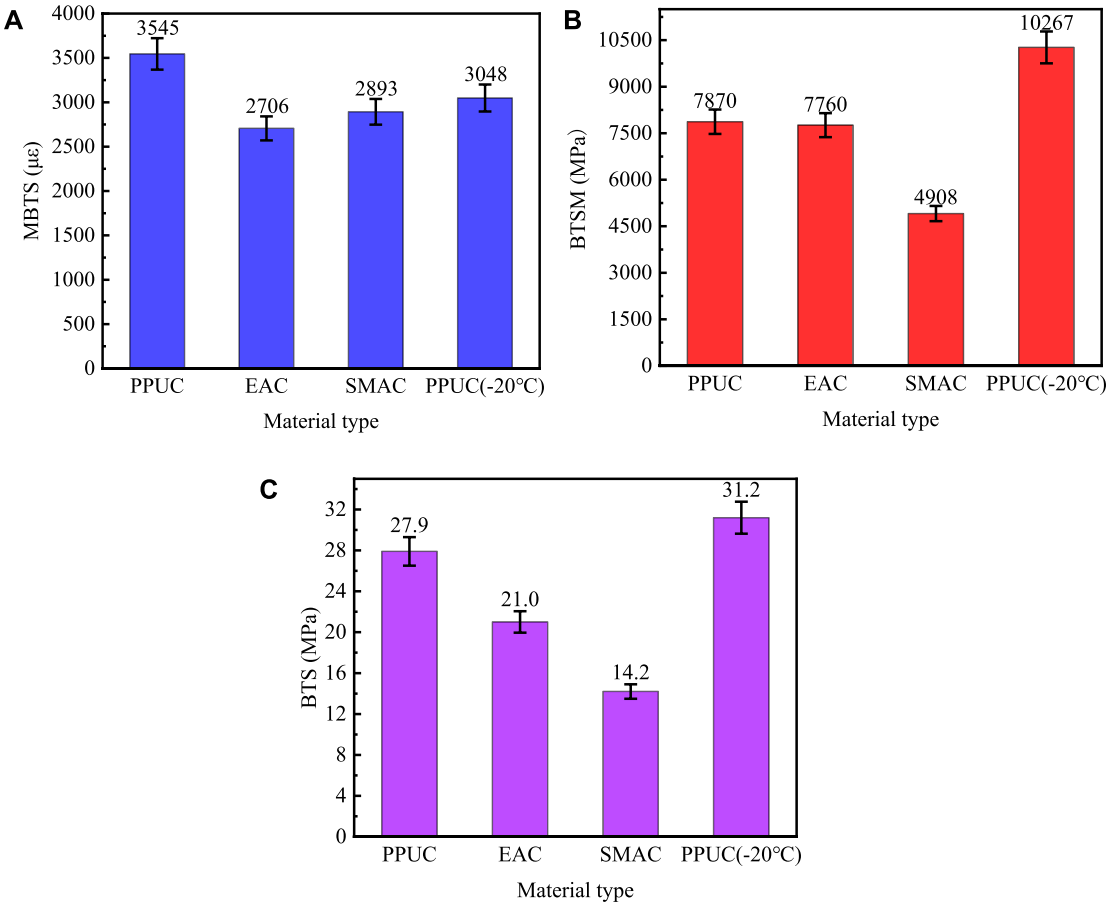

FIGURE 6
Low-temperature bending test results. **(A)** MBTS, **(B)** BTSM, **(C)** BTS.

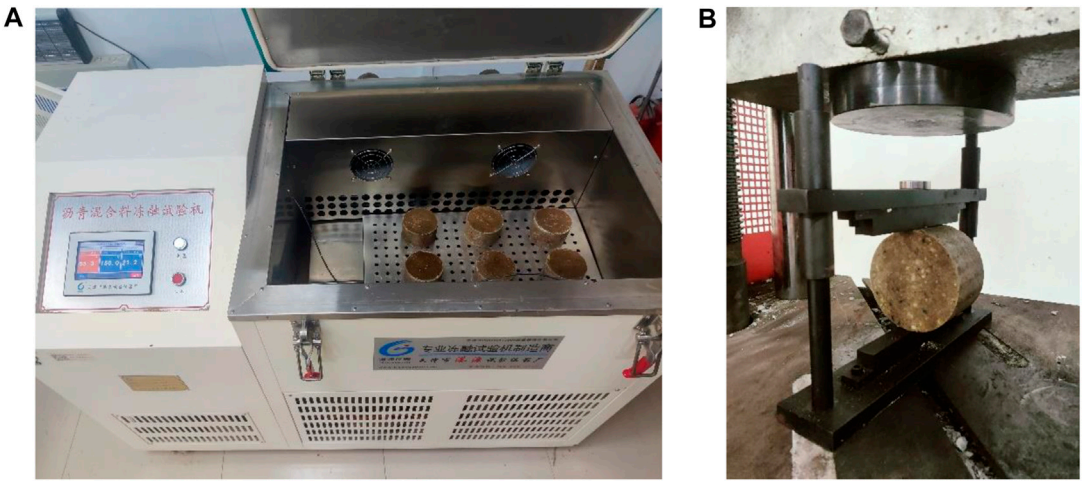

FIGURE 7
Freeze-thaw splitting test procedure. **(A)** Freeze-thaw cycle procedure; **(B)** Splitting test.

TABLE 4 The results of the freeze-thaw splitting test.

Material type	Strength before freeze-thaw (MPa)	Strength after freeze-thaw (MPa)	STSR (%)
PPUC	7.85	7.30	93
EAC	5.24	4.37	83
SMAC	1.57	1.49	95

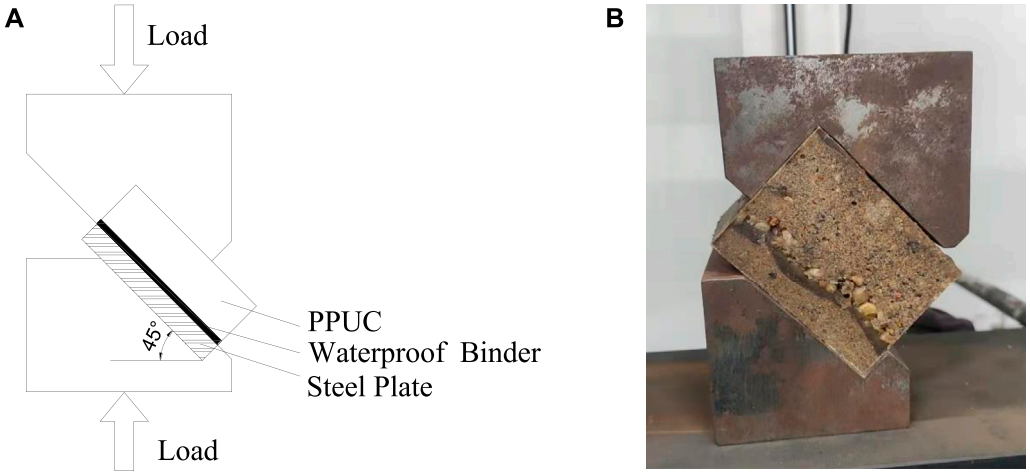

FIGURE 8
Shear test procedure. **(A)** Schematic of the shear test; **(B)** Test photo of the shear test.

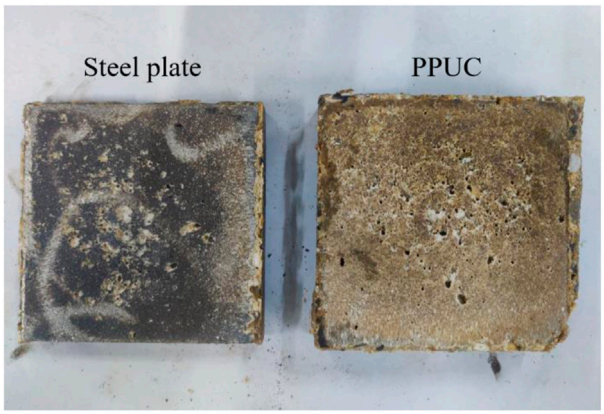

FIGURE 9
Failure mode of shear test.

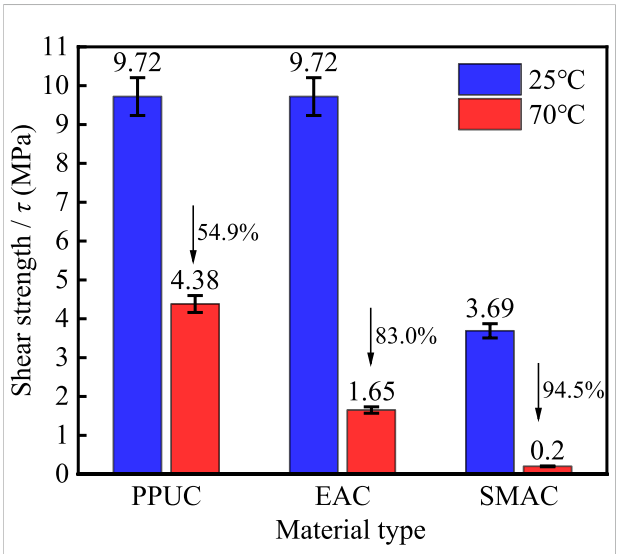

FIGURE 10
Shear test results.

temperature and high temperature condition, indicating the measured damage stress is the bond layer shear strength. The failure mode of the specimen is shown in Figure 9. Results in Figure 10 also show that the shear strength of PPUC (9.72 MPa) is same as that of EAC and much greater than that of SMA (3.69 MPa). With the temperature increase up to 70°C, all specimens exhibit a decreasing trend in terms of shear strength. However, PPUC shows the minimum variation of

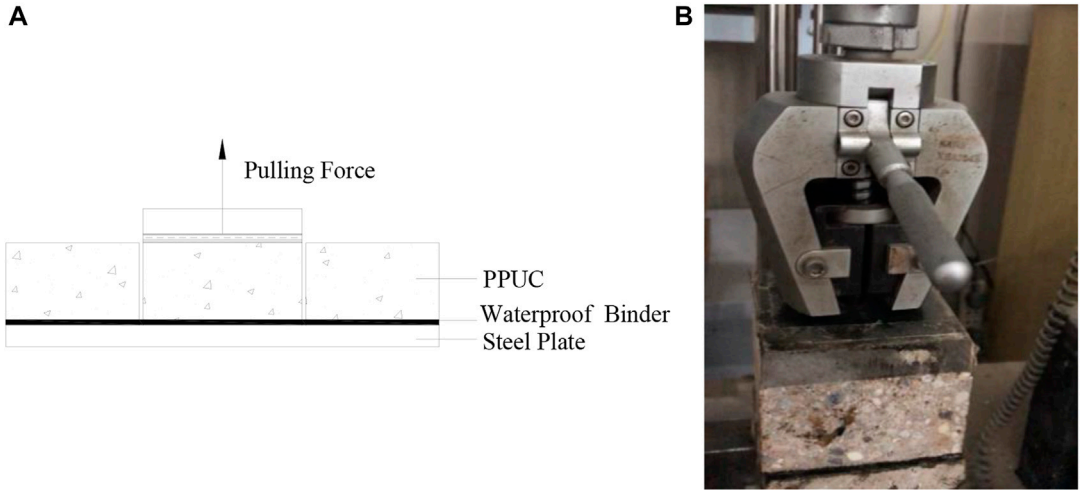

FIGURE 11
Pull-out test procedure. **(A)** Schematic diagram of the pull-out test; **(B)** Test set up of the pull-out test.

shear strength decreasing rate (54.9%) comparing with EAC and SMAC (83.0% and 94.5%, respectively). This might be attributed to the thermosetting property of PU allowing PPUC more stable at the high temperature than asphalt materials.

3.2 Pull-out test

The pull-out test was performed to investigate the adhesive characteristic between specimens and steel plate. The specimen dimension and test method were same as those of the oblique shear test. The specimens were bonded with a special jig using epoxy resin and performed the pull-out tests after the epoxy resin was completely cured for 24 h at 25°C and 70°C respectively. The schematic and experimental set-up is shown in Figure 11. The samples were applied with the vertical tensile force with a uniform rate of 10 mm/min until they braked and the maximum load was read. The condition of the fracture surface was observed and the failure location was also recorded. The pull-out strength was calculated by Eq. 2:

$$P = \frac{F}{S} \tag{2}$$

Where P is the pull-out strength, F is the ultimate load when the specimen is damaged, and S is the bottom surface area of the pull-out jig.

In this test, the failure surface is also located at the interface between the steel plate and PPUC pavement, suggesting the damage stress is the interlayer bond strength. Its failure mode is shown in Figure 12. Figure 13 also shows that the pull-out strength between PPUC and the steel plate (6.23 MPa) is 1.3 times higher than that of EAC (4.83 MPa), and significantly higher than that of SMA

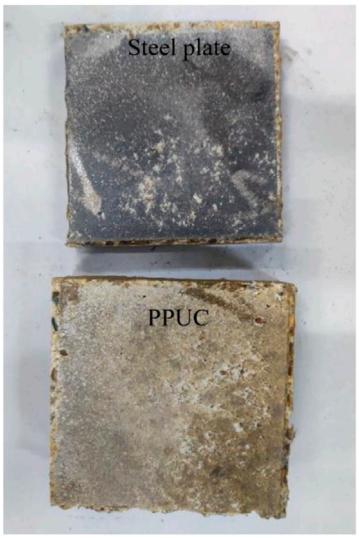

FIGURE 12
Failure mode of pull-out test.

(1.92 MPa) at room temperature of 25°C, indicating that PPUC has strong bond strength with the steel plate. In addition, as the temperature increases to 70°C, the pull-out strength of PPUC, EAC and SMA decreases by 29.2%, 72.5% and 80.7%, respectively. Similar to the shear strength, it can be attributed to the fact that the thermosetting property of PPUC makes its pull-out strength (4.41 MPa) higher at high temperature of 70°C. These results show the minimum difference of PPUC pull-out strength switching from room temperature to high temperature and higher bond strength of PPUC maintained at high temperature compared with other paving materials.

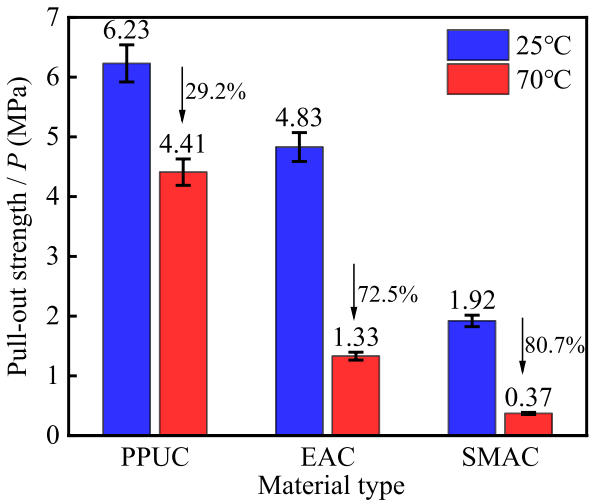

FIGURE 13
Pull-out test results.

4 Mechanical performance comparison of different pavement structures

4.1 Finite element model of the pavement structure

In this study, the model of the pavement structure was established based on three basic assumptions (Ma et al., 2018). 1) the pavement material is an isotropic material. 2) the interface of pavement layer is continuous. 3) the weight of steel deck and pavement is ignored.

The model was consisted of eight U-shaped stiffeners and four transverse diaphragms, as shown in Figure 14. The eight-node hexahedral linear reduction integral solid element (C3D8R) was used for steel deck and pavement. The mesh size was chosen to be 50 mm and the whole model was discretized into a total of 95020 elements. The interfaces of pavement layer were all defined as continuous, which means that a perfect bond was assumed at the interfaces in the finite element analyses. So, the binder layer was not specifically treated in the calculation and was considered in the bridge deck pavement. In addition, since the thickness of the waterproof bonding layer was negligible compared with that of the pavement layer, the waterproof bonding layer was not set in this model. The interlayer contact state was set to "Tie connection" for constraining the relative deformation and movement between two adjacent surfaces. The relevant geometric and material parameters of the pavement structure model are shown in Table 5 (Ma et al., 2018) and Table 6 (Li et al., 2013; Xue et al., 2020; Lv et al., 2021; Wang et al., 2021). The beam was simply supported at both ends and the bottom of the transverse diaphragm was completely consolidated. Considering the local stress characteristics of orthotropic steel deck under loading, the influence of these constraints on the finite element analysis can be ignored.

According to the Technical Standard for Highway Engineering (JTG B01-2014, 2015), the steam-overload 20 level was used as the calculated load. The simulated test load was designated as 0.758 MPa after considering 30% impact effect. The contact area between wheel and pavement was a rectangular plane of 600 mm × 200 mm. The position of wheel load has a great impact on the mechanical properties of steel deck pavement. Therefore, in order to determine the most unfavorable load position, different load conditions were tested along with the transverse and longitudinal directions shown in Figure 15. Three

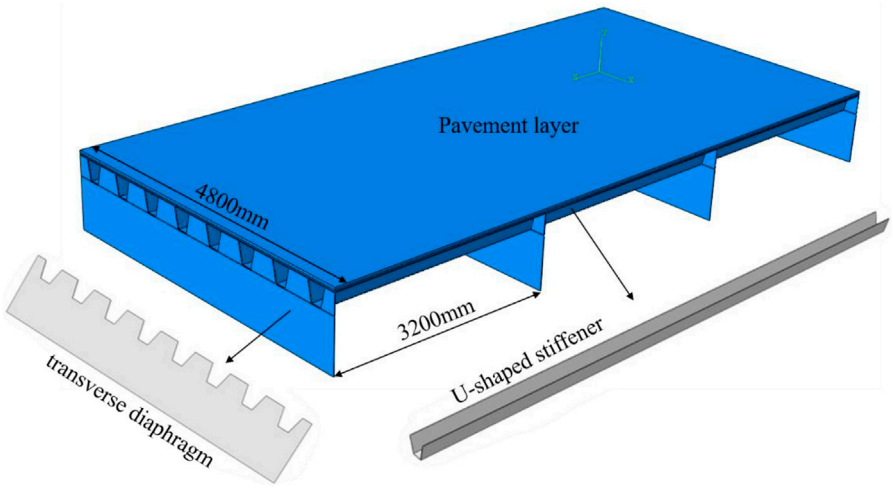

FIGURE 14
Finite element model of the pavement structure.

TABLE 5 Geometric parameters of the pavement structure model.

Geometric parameters	Value (mm)
Steel deck thickness	14
Diaphragm plate thickness	10
Diaphragm plate height	1000
Diaphragm plate spacing	3200
Stiffener thickness	8
Top width of stiffener	300
Bottom width of stiffener	170
Stiffener height	280
Stiffener spacing	600
PPUC overlay thickness (Composite pavement)	20
SMAC overlay thickness (Composite pavement)	30
PPUC overlay thickness (Single-layer pavement)	40

TABLE 6 Material parameters of the pavement structure model.

Material type	Elastic modulus (MPa)	Poisson ratio
PPUC	16000	0.3
SMAC	2020	0.3
EAC	4500	0.3
GAC	5000	0.3
Steel	210000	0.25

transverse load positions were considered in Figure 15A: Load I, the wheel pressure center acts on the midpoint of a stiffener; Load II, the wheel pressure center acts on the midpoint of two adjacent stiffeners; Load III, the wheel pressure center acts on the midpoint of one side of the stiffener. Figure 15B shows these three transverse loads move longitudinally from the midspan to the transverse diaphragm with intervals of 200 mm. There are totally nine longitudinal load positions labeled as Load 1 to 9.

4.2 Analysis of the most unfavorable load position

A single-layer PPUC pavement structure was selected to determine the most unfavorable load position of the steel bridge deck pavement. The maximum transverse tensile stress and the maximum vertical displacement of the paving layer were chosen as the verification indexes and their variation pattern is shown in the Figure 16. It can be observed that the longitudinal load position variation has a significant effect on the mechanical response of the pavement structure. With the decrease of distance between the load position and the transverse diaphragm, the maximum transverse tensile stress and the maximum vertical displacement of the paving layer are significantly decreased. Both the two verification indexes reach to the maximum value when the load is applied on the midspan of the steel bridge panel (Load 1). In the direction of the transverse bridge, two maximum values are reached when the load is applied on the midpoint of two adjacent stiffeners (Load II). Therefore, Load 1 and Load II are the most unfavorable load positions of the steel deck pavement structure.

4.3 Comparison of single-layer pavement structure

PPUC, SMAC, GAC and EAC were selected as the pavement materials for the single-layer pavement structure comparison. The midspan crossbridge direction distance was selected as the comparison route and the comparison results are shown in Figure 17 when the wheel load is applied to the most unfavorable load position.

Figures 17A, B show the vertical displacement of the pavement and steel bridge deck at the comparison route. It can be seen that the vertical displacement of pavement is minimal when the PPUC is used as the steel deck pavement material with the maximum displacement value of 0.583 mm. Similarly, the vertical displacement of the steel bridge deck (0.58 mm) is also minimal. Results also show that the vertical displacement of the pavement and steel bridge deck presents a decreasing trend with the increase of the pavement material elastic modulus.

Figure 17C presents the variation of transverse stress in the pavement over the comparison route. The larger elastic modulus of PPUC enables it to bear a greater stress. The maximum transverse compressive stress occurs at the most unfavorable load position, and the maximum transverse tensile stress occurs at the spot of 800 mm far from the middle of transverse span. The value of the maximum transverse tensile stress (0.51 MPa) of PPUC is less than the tensile strength obtained from the test (8.4 MPa). Similarly, the value of the maximum transverse compressive stress of PPUC (3.52 MPa) is less than the test value (75.3 MPa). The Mises stress distribution of steel bridge deck is shown in Figure 17D. Two stress concentration phenomena are observed in the steel bridge deck with SMAC, GAC and EAC pavement layers with the maximum Mises stress values over 8 MPa in these two locations. However, the use of PPUC pavement structure improves the stress on the steel bridge deck and reduces the number of stress concentration locations and the maximum stress amplitude. The maximum Mises stress occurred at the most unfavorable load position of the steel bridge deck for PPUC (7.89 MPa) is significantly smaller than those of the steel bridge deck with other three pavement structures. These

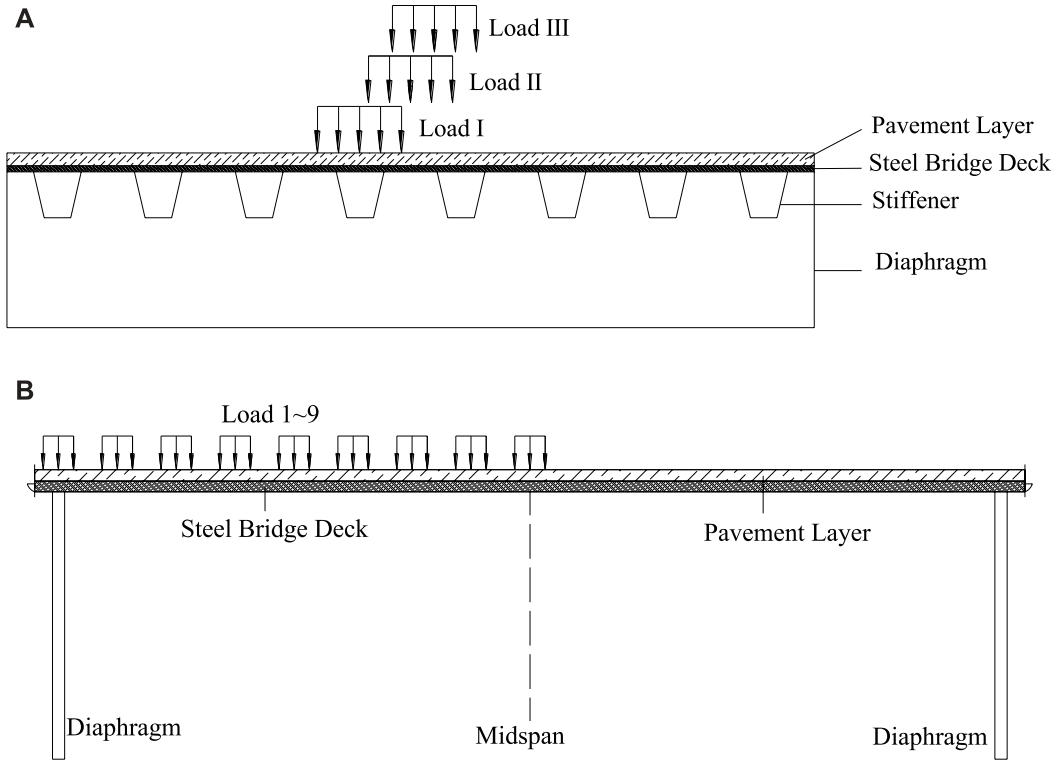

FIGURE 15
Load distribution on the pavement structure. **(A)** Transverse load distribution; **(B)** Longitudinal load distribution.

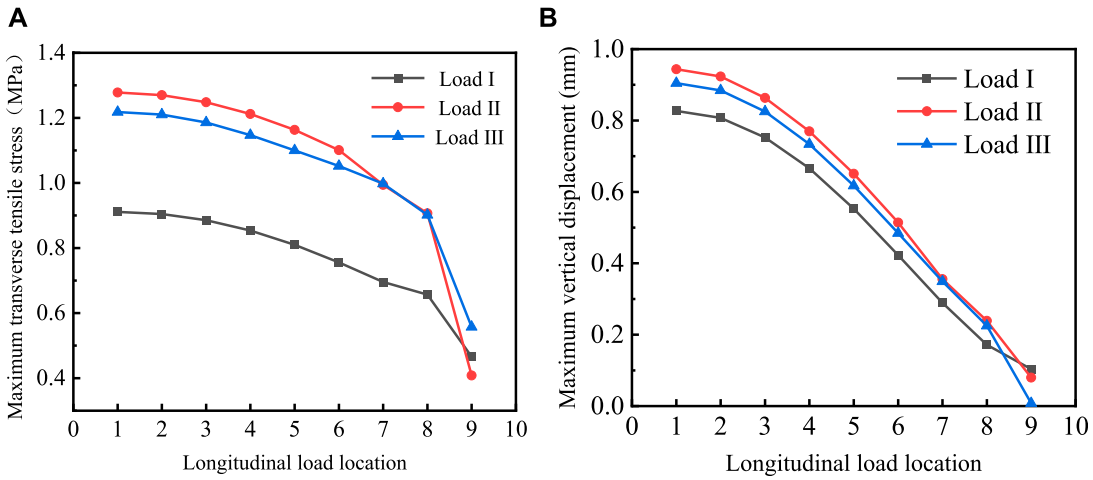

FIGURE 16
Analysis of the most unfavorable load position. **(A)** Maximum transverse tensile stress of the pavement; **(B)** Maximum vertical displacement of the pavement.

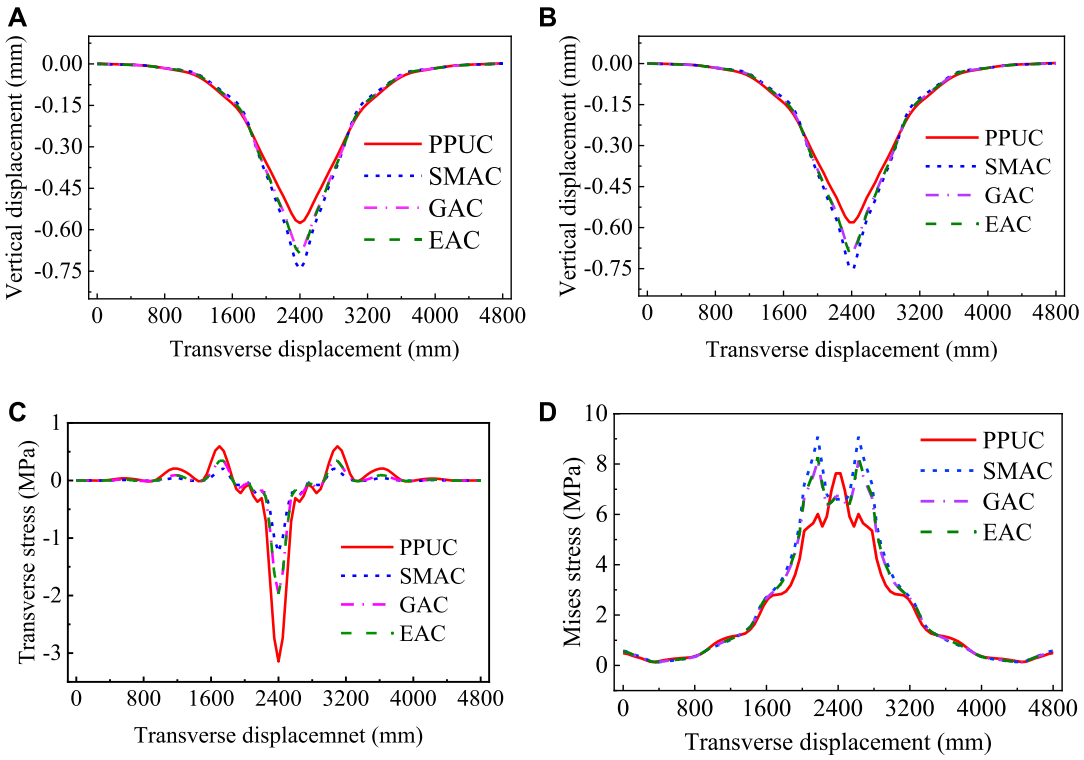

FIGURE 17
Comparison results of single-layer pavement structure using different materials. **(A)** Vertical displacement of the pavement; **(B)** Vertical displacement of the steel deck; **(C)** Transverse tensile stress of the pavement; **(D)** Mises stress of the steel bridge deck.

results indicate that the PPUC pavement layer contributes to distributing the stress on the steel bridge deck and improving the overall stiffness of the steel bridge deck.

4.4 Comparison of composite pavement structure

As for the composite pavement structure, the SMAC was used as the upper layer material and the PPUC, GAC and EAC were used as the lower layer materials. Therefore, there are three kinds of composite pavement structures: PPUC + SMAC, GAC + SMAC, EAC + SMAC. The comparison results are shown in Figure 18.

Figure 18A shows the maximum transverse tensile stress of the pavement. Results show that the PPUC pavement structure presents the smallest value of the maximum transverse tensile stress in terms of the upper layer (0.2316 MPa) while that of the lower layer is the largest (0.649 MPa) compared to other two composites. It can be concluded that the maximum transverse tensile stress in the lower layer decreases while that in the upper layer increases with the elastic modulus of lower layer material decreasing. The longitudinal cracking in the wear layer is one of the most common pavement distresses for the steel bridge deck pavement. Excessive transverse tensile stresses can easily contribute to the generation of longitudinal cracks, and subsequently damaging the steel bridge deck. The use of PPUC makes the maximum transverse tensile stress in the upper layer smaller, which reduces the generation and development of longitudinal cracks. The larger shear stress that occurs inside the pavement layer can cause shear damage, which produces the pavement distresses of slippage and swell. It can be seen from Figure 18B that the maximum longitudinal shear stress variation pattern of the upper and lower layers in the composite pavement structure is similar to that of the tensile stress and the PPUC pavement layer bears more tensile and shear stresses, contributing to the protection of the upper layer and minimizing the pavement diseases occurred in the upper layer. This result indicates that the use of PPUC reduces the yield stress of steel bridge deck.

Figure 18C demonstrates the maximum Mises stress variation pattern for the lower layer and steel bridge deck. With decreasing the elastic modulus of the lower layer pavement material, the maximum Mises stress in the lower layer gradually decreases while that in the steel bridge deck increases. Figure 18D presents the maximum vertical

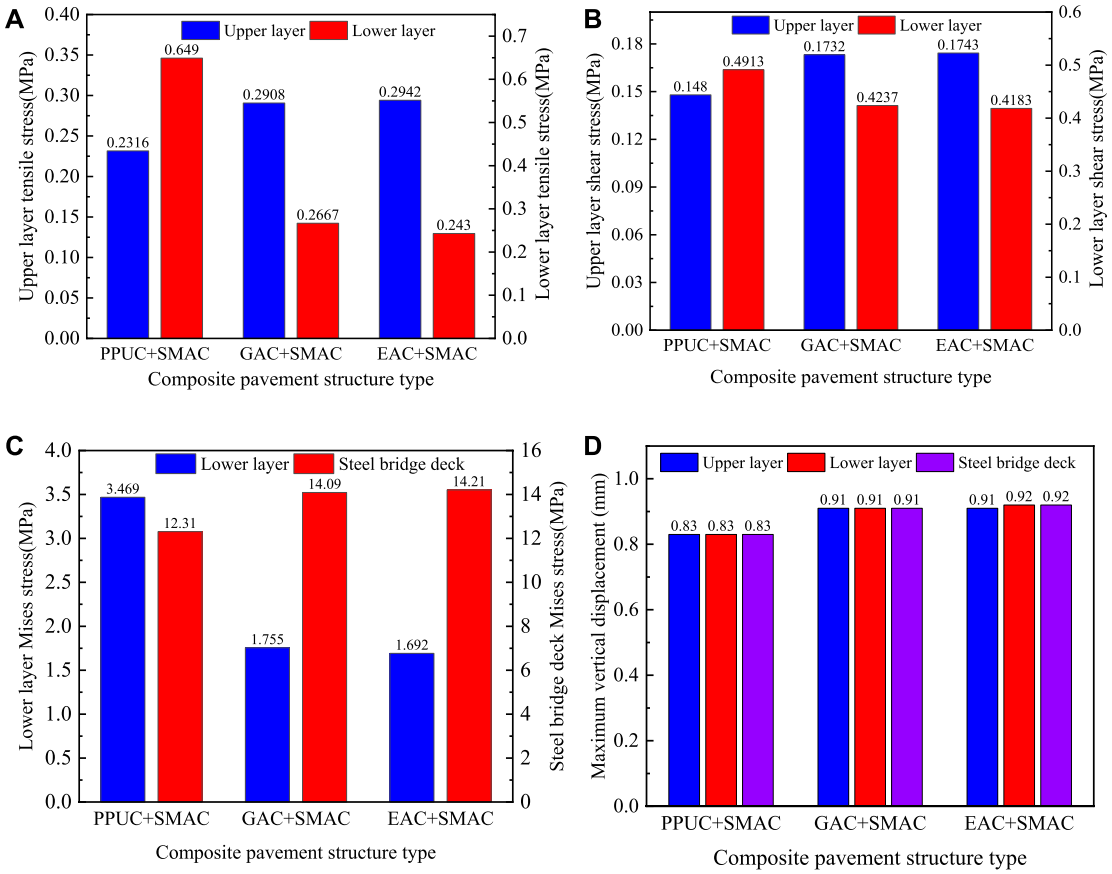

FIGURE 18
Comparison results of different composite pavement structures. **(A)** Maximum transverse tensile stress of the pavement; **(B)** Maximum shear stress of the pavement; **(C)** Mises stress of the lower layer and steel bridge deck; **(D)** Maximum vertical displacement of the pavement and steel bridge deck.

displacement of the upper layer, lower layer and steel bridge deck respectively. Results show that the maximum vertical displacement of PPUC + SMAC pavement structure is the smallest among the three composite pavement structures. This indicates that the PPUC + SMAC pavement structure has better riding comfort under the same traffic load. The above results show that the PPUC pavement layer is beneficial to improve the overall stiffness of the steel bridge deck, reduce the maximum force on the steel bridge deck, protect the wear layer and extend the service life of the steel deck pavement structure.

5 Conclusion

In this paper, PPUC was proposed as the steel bridge deck pavement material. Its mechanical properties, durability and shear bond properties were comprehensively investigated by both the experiments and finite element analysis. In comparison, the commonly used steel bridge deck pavement materials including EAC, SMAC and GAC were also investigated as references. Based on the study results, the conclusions can be summarized as follows.

(1) PPUC presents large compressive, tensile and flexural tensile strength of 75.3, 8.4, and 22.4 MPa, respectively, which meet the strength demands of the steel bridge for the opening traffic and the subsequent service.
(2) The results of wheel tracking test, low-temperature bending test and freeze-thaw splitting test show that PPUC presents the better high temperature deformation resistance, low temperature cracking resistance and water stability performance compared to EAC, SMAC and GAC materials. Moreover, these properties are not significantly changed in the extreme severe environments, such as at high temperatures of 70°C, low temperatures of −20°C and cyclic freeze-thawing circumstances.
(3) According to the results of the shear test and the pull-out test, the oblique shear strength (9.72 MPa) and pull-out strength

(6.23 MPa) between PPUC and steel deck are greater than those of EAC and SMAC at 25°C. Moreover, the decrease of these strengths for PPUC at high temperature of 70°C is much smaller than that of the other two materials. These results indicate that the PPUC pavement structure has stronger bonding properties and resistance to the perpetual deformation.

(4) The finite element analysis results show that the most unfavorable load position of the steel deck pavement structure is Load II (the wheel pressure center acts on the midpoint of two adjacent stiffeners) and Load 1 (the wheel pressure center acts in the middle of the span). The PPUC single-layer pavement structure and the PPUC + SMAC composite pavement structure have better mechanical properties. Therefore, PPUC is a feasible material for the future steel bridge deck pavement.

Data availability statement

The raw data supporting the conclusion of this article will be made available by the authors, without undue reservation.

Author contributions

S-LN: Methodology, validation, data curation, writing—original draft; J-YW: Methodology, validation; Z-CW: Conceptualization, formal analysis, investigation, writing—review and editing; D-HW: Validation, data curation; X-TS: Vali-dation, data curation; XZ: Validation, data curation.

Funding

Financial support of this study was provided in part by the National Natural Science Foundation of China under grand Nos. 51922036 and 52278301, by the Fundamental Research Funds for the Central Universities under grand No. JZ2020HGPB0117, and by the Science Technology Research and Development Program Project of China Railway Group Co., Ltd. (2020-major-01). The results and opinions expressed in this paper are those of the authors only, and they don't necessarily represent those of the sponsors.

Conflict of interest

J-YW was employed by Ningbo Road Technology Industrial Group Co., Ltd.

D-HW was employed by China Railway Major Bridge Reconnaissance & Design Institute Co., Ltd.

The remaining authors declare that the research was conducted in the absence of any commercial or financial relationships that could be construed as a potential conflict of interest.

Publisher's note

All claims expressed in this article are solely those of the authors and do not necessarily represent those of their affiliated organizations, or those of the publisher, the editors and the reviewers. Any product that may be evaluated in this article, or claim that may be made by its manufacturer, is not guaranteed or endorsed by the publisher.

References

Alrefaei, Y., and Dai, J. G. (2022). Effects of delayed addition of polycarboxylate ether on one-part alkali-activated fly ash/slag pastes: Adsorption, reaction kinetics, and rheology. *Constr. Build. Mat.* 323, 126611. doi:10.1016/j.conbuildmat.2022.126611

Cai, D., Jin, J., Yusoh, K., Rafiq, R., and Song, M. (2012). High performance polyurethane/functionalized graphene nanocomposites with improved mechanical and thermal properties. *Compos. Sci. Technol.* 72, 702–707. doi:10.1016/j.compscitech.2012.01.020

Chen C, C., Eisenhut, W. O., Lau, K., Buss, A., and Bors, J. (2018). Performance characteristics of epoxy asphalt paving material for thin orthotropic steel plate decks. *Int. J. Pavement Eng.* 21, 397–407. doi:10.1080/10298436.2018.1481961

Chen J, J., Xie, M., Hao, W., Xie, P., and Wei, H. (2018). Experimental study on antiicing and deicing performance of polyurethane concrete as road surface layer. *Constr. Build. Mat.* 161, 598–605. doi:10.1016/j.conbuildmat.2017.11.170

Cong, L., Wang, T. J., Tan, L., Yuan, J. J., and Shi, J. C. (2018). Laboratory evaluation on performance of porous polyurethane mixtures and OGFC. *Constr. Build. Mat.* 169, 436–442. doi:10.1016/j.conbuildmat.2018.02.145

Fan, X., and Luo, R. (2021). Experimental study on crack resistance of typical steel-bridge deck paving materials. *Constr. Build. Mat.* 277, 122315. doi:10.1016/j.conbuildmat.2021.122315

GB/T50081-2019 (2019). *Standard for test methods of concrete physical and mechanical properties*. Beijing: Ministry of housing and urban rural development of the people's Republic of China.

Guan, Y., Wu, J., Sun, R., Ge, Z., Bi, Y., and Zhu, D. (2022). Shear behavior of short headed studs in Steel-ECC composite structure. *Eng. Struct.* 250, 113423. doi:10.1016/j.engstruct.2021.113423

Han, B. J., Yoon, S. I., Choi, B. J., Choi, J. W., and Park, S. K. (2014). Analysis study on fatigue stress on the orthotropic steel deck applied polymer concrete pavement. *J. Korea Inst. Struct. maintenance Insp.* 18, 68–77. doi:10.11112/jksmi.2014.18.5.068

He, Q., Zhang, H., Li, J., and Duan, H. (2021). Performance evaluation of polyurethane/epoxy resin modified asphalt as adhesive layer material for steel-UHPC composite bridge deck pavements. *Constr. Build. Mat.* 291, 123364. doi:10.1016/j.conbuildmat.2021.123364

Ho, A. C., Turatsinze, A., Hameed, R., and Vu, D. C. (2012). Effects of rubber aggregates from grinded used tyres on the concrete resistance to cracking. *J. Clean. Prod.* 23, 209–215. doi:10.1016/j.jclepro.2011.09.016

Hong, B., Lu, G., Gao, J., Dong, S., and Wang, D. (2020). Green tunnel pavement: Polyurethane ultra-thin friction course and its perfor-mance characterization. *J. Clean. Prod.* 289, 125131. doi:10.1016/j.jclepro.2020.125131

Hong-Chang, W., and Guo-Fen, L. (2015). Study on high-temperature stability of composite gussasphalt concrete. *Mater. Res. Innovations* 19, S5-494–S5-499. doi:10.1179/1432891714z.0000000001139

Huang, Y., Chen, S., and Gu, P. (2022). Interface stress analysis and fatigue design method of steel-ultra high performance concrete composite bridge deck. *Structures* 38, 1453–1464. doi:10.1016/j.istruc.2022.03.005

Jiang, Z., Tang, C., Yang, J., You, Y., and Lv, Z. (2020). A lab study to develop polyurethane concrete for bridge deck pavement. *Int. J. Pavement Eng.* 23, 1404–1412. doi:10.1080/10298436.2020.1804063

JTG B01-2014 (2015). *Technical standard of highway engineering*. Beijing: Ministry of transport of the people's Republic of China.

JTG E20-2011 (2011). *Standard test methods of bitumen and bituminous mixtures for highway engineering*. Beijing: Ministry of transport of the people's Republic of China.

JTG/T3364-02-2019 (2019). *Technical specification for design and construction of highway steel bridge deck pavement*. Beijing: Ministry of transport of the people's Republic of China.

Kainuma, S., Yang, M., Jeong, Y.-s., Inokuchi, S., Kawabata, A., and Uchida, D. (2016). Experiment on fatigue behavior of rib-to-deck weld root in orthotropic steel decks. *J. Constr. Steel Res.* 119, 113–122. doi:10.1016/j.jcsr.2015.11.014

Kim, T., Baek, J., Lee, H. J., and Lee, S. Y. (2014). Effect of pavement design parameters on the behaviour of orthotropic steel bridge deck pavements under traffic loading. *Int. J. Pavement Eng.* 15, 471–482. doi:10.1080/10298436.2013.839790

Li, G., Cao, M., Wang, H., and Zhu, H. (2013). Stress analysis of deck pavement of continuous steel box girder. *Strategic Study CAE* 15, 79–83. doi:10.3969/j.issn.1009-1742.2013.08.014

Li, T. S., Lu, G. Y., Wang, D. W., and Hong, B. (2019). Key properties of high-performance polyurethane bounded pervious mixture. *China J. Highw. Transp.* 32, 158–169. doi:10.19721/j.cnki.1001-7372.2019.04.013

Liu G, G., Qian, Z., and Xue, Y. (2022). Comprehensive feasibility evaluation of a high-performance mixture used as the protective course of steel bridge deck pavement. *Constr. Build. Mat.* 322, 126419. doi:10.1016/j.conbuildmat.2022.126419

Liu Y, Y., Qian, Z., Gong, M., Huang, Q., and Ren, H. (2022). Interlayer residual stress analysis of steel bridge deck pavement during gussasphalt pavement paving. *Constr. Build. Mat.* 324, 126624. doi:10.1016/j.conbuildmat.2022.126624

Liu Z, Z., Zang, C., Zhang, Y., Jiang, J., Yuan, Z., Liu, G., et al. (2022). Mechanical properties and antifreeze performance of ce-ment-based composites with liquid paraffin/diatomite capsule low-temperature phase change. *Constr. Build. Mat.* 341, 127773. doi:10.1016/j.conbuildmat.2022.127773

Lu, G., Renken, L., Li, T., Wang, D., Li, H., and Oeser, M. (2019). Experimental study on the polyurethane bound pervious mixtures in the application of permeable pavements. *Constr. Build. Mat.* 202, 838–850. doi:10.1016/j.conbuildmat.2019.01.051

Lu, Z., Feng, Z.-g., Yao, D., Li, X., Jiao, X., and Zheng, K. (2021). Bonding performance between ultra-high performance concrete and asphalt pavement layer. *Constr. Build. Mat.* 312, 125375. doi:10.1016/j.conbuildmat.2021.125375

Luo, S., Lu, Q., Qian, Z., Wang, H., and Huang, Y. (2017). Laboratory investigation and numerical simulation of the rutting performance of double-layer surfacing structure for steel bridge decks. *Constr. Build. Mat.* 144, 178–187. doi:10.1016/j.conbuildmat.2017.03.172

Lv, S., Shang, T., Wang, H., and Song, Q. (2021). Research on repair Technology of existing steel-UHPC composite bridge deck. *China Concr. Cem. Prod.* 7, 88–92. doi:10.19761/j.1000-4637.2021.07.088.05

Ma, H., Zhang, Z., Ding, B., and Tu, X. (2018). Investigation on the adhesive characteristics of Engineered Cementitious Composites (ECC) to steel bridge deck. *Constr. Build. Mat.* 191, 679–691. doi:10.1016/j.conbuildmat.2018.10.056

Majumder, S., and Saha, S. (2021). Shear behaviour of RC beams strengthened using geosynthetic materials by external and internal confinement. *Structures* 32, 1665–1678. doi:10.1016/j.istruc.2021.03.107

Meng, L., Wang, Y., and Zhai, X. (2021). Experimental and numerical studies on steel-polyurethane foam-steel–concrete-steel panel un-der impact loading by a hemispherical head. *Eng. Struct.* 247, 113201. doi:10.1016/j.engstruct.2021.113201

Munoz, M. A. C., Harris, D. K., Ahlborn, T. M., and Froster, D. C. (2014). Bond performance between ultrahigh-performance concrete and normal-strength concrete. *J. Mat. Civ. Eng.* 26, 839–844. doi:10.1061/(ASCE)MT.1943-5533.0000890

Romualdi, J. P., and Mandel, J. A. (1964). Tensile strength of concrete affected by uniformly distributed and closely spaced short lengths of wire reinforcement. *J. Mat. Sci.* 61 (6), 657–672.

Shao, X. D., Huang, Z., Zhao, H., Chen, B., and Liu, M. (2013). Basic performance of the composite deck system composed of ortho-tropic steel deck and ultrathin RPC layer. *J. Bridge Eng.* 18, 417–428. doi:10.1061/(asce)be.1943-5592.0000348

Song, Y. X., Yang, J., and Wang, J. Q. (2012). Research on basic mechanical properties of polymer concrete strengthened with basalt fiber. *J. North China Inst. Water Conservancy Hydroelectr. Power* 33, 18–20. doi:10.19760/j.ncwu.zk.2012.06.005

Wang, D., Liu, P., Leng, Z., Lu, G., and Buch, M., (2017). Suitability of PoroElastic Road Surface (PERS) for urban roads in cold regions: Mechanical and functional performance assessment. *J. Clean. Prod.* 165, 1340–1350. doi:10.1016/j.jclepro.2017.07.228

Wang, H. M., Li, R. K., and Wang, X. (2014). Strength and road performance for porous polyurethane mixture. *China J. Highw. Transp.* 27, 24–31. doi:10.19721/j.cnki.1001-7372.2014.10.004

Wang, J., Dai, Q., Si, R., and Guo, S. (2019). Mechanical, durability, and microstructural properties of macro synthetic Polypropylene (PP) fiber-reinforced rubber concrete. *J. Clean. Prod.* 234, 1351–1364. doi:10.1016/j.jclepro.2019.06.272

Wang, M., Shang, F., Xiao, L., and Bao, G. (2021). Composite beam fatigue damage law of steel bridge deck gussasphalt pavement. *J. Chongqing Jiaot. Univ. Nat. Sci. Ed.* 40, 84–88+102. doi:10.3969/j.issn.1674-0696.2021.03.13

Xu, S., Xu, M., Zhang, Y., Guo, Y., Peng, G., and Xu, Y. (2020). An indoor laboratory simulation and evaluation on the aging resistance of polyether polyurethane concrete for bridge deck pavement. *Front. Mat.* 7, 237. doi:10.3389/fmats.2020.00237

Xue, Z., Wang, Y., and Wang, H. (2020). Mechanics property analysis for A new steel bridge deck pavement with UTAC-UHPC. *For. Eng.* 36, 76–84. doi:10.16270/j.cnki.slgc.2020.04.011

Yang, B., He, Z. Y., Liu, P., Li, K., Sheng, X. Y., and Li, L. (2020). Preparation and performance evaluation of polymer alloy for steel deck pavement. *Appl. Chem. Indus* 49, 3095–3102. doi:10.16581/j.cnki.issn1671-3206.20201022.003

Zeng, Z., Li, C., Wang, S., Liu, Y., Chen, Z., and Lv, Y. (2022). Study on shear performance of short bolt interface in ECC–steel bridge deck composite structure. *Appl. Sci. (Basel).* 12, 2685. doi:10.3390/app12052685

Zhang, Y., Zhang, C., Zhu, Y., Cao, J., and Shao, X. (2020b). An experimental study: Various influence factors affecting interfacial shear performance of UHPC-NSC. *Constr. Build. Mat.* 236, 117480. doi:10.1016/j.conbuildmat.2019.117480

Zhang, Y., Zhu, Y., Qu, S., Kumar, A., and Shao, X. (2020a). Improvement of flexural and tensile strength of layered-casting UHPC with aligned steel fibers. *Constr. Build. Mat.* 251, 118893. doi:10.1016/j.conbuildmat.2020.118893

Zhu, J. X., Xu, L. Y., Huang, B. T., Weng, K. F., and Dai, J. G. (2022). Recent developments in Engineered/Strain-Hardening Cementitious Composites (ECC/SHCC) with high and ultra-high strength. *Constr. Build. Mat.* 342, 127956. doi:10.1016/j.conbuildmat.2022.127956

frontiers | Frontiers in Materials

TYPE Original Research
PUBLISHED 16 December 2022
DOI 10.3389/fmats.2022.1056620

OPEN ACCESS

EDITED BY
Cong Zhang,
Jiangnan University, China

REVIEWED BY
Jun He,
Changsha University of Science and Technology, China
Zhao-Dong Xu,
Southeast University, China

*CORRESPONDENCE
Zongping Chen,
zpchen@gxu.edu.cn

SPECIALTY SECTION
This article was submitted to Structural Materials,a section of the journal Frontiers in Materials

RECEIVED 29 September 2022
ACCEPTED 02 December 2022
PUBLISHED 16 December 2022

CITATION
Wang X, Li J, Huang L, Xie W and Chen Z (2022), Mechanical behavior of spiral reinforcement recycled aggregate concrete round columns under axial compression after spraying water at high temperatures.
Front. Mater. 9:1056620.
doi: 10.3389/fmats.2022.1056620

Mechanical behavior of spiral reinforcement recycled aggregate concrete round columns under axial compression after spraying water at high temperatures

Xin Wang[1], Junya Li[2,3], Leiqun Huang[4], Wangjun Xie[1] and Zongping Chen[2,3,5]*

[1]Guangxi Transport Vocational and Technical College, Nanning, China, [2]College of Architecture and Civil Engineering, Nanning University, Nanning, China, [3]College of Civil Engineering and Architecture, Guangxi University, Nanning, China, [4]Guangxi Road and Bridge Group Construction Engineering Co., Ltd., Nanning, China, [5]Key Laboratory of Disaster Prevention and Structure Safety of the Ministry of Education, Guangxi University, Nanning, China

Spiral hoops can effectively enhance the load-bearing capacity of recycled aggregate concrete columns, and the mechanical performance of such a member after experiencing fire and a fire sprinkler is very important for its application and promotion. Aiming at this problem, the mechanical behavior of spiral reinforcement recycled aggregate concrete round columns under axial compression after spraying water at high temperatures cooling was investigated. Three parameters including recycled coarse aggregate replacement ratio, temperature, and pitch of screw stirrups were taken into consideration. 26 specimens were designed for static loading test. The failure modes of regenerated concrete columns with spiral reinforcement were observed after cooling by high-temperature water spraying. The mechanical properties of specimens under different cooling modes after high temperatures were obtained and analyzed. The results indicate that the effect of the recycled aggregate replacement ratio on the performance of the specimens was mainly in terms of peak displacement. And the reduction in the spiral stirrup spacing increases the peak load and ductility coefficient of the specimens. The high temperature above 600°C has a obvious effect on the mechanical properties of the specimens. Water spray cooling can reduce the appearance of small cracks on the surface of the specimens and their peak displacement. The calculation method of bearing capacity of regenerated spiral reinforced concrete columns cooled by high-temperature water spraying was discussed.

KEYWORDS

spiral reinforcement recycled aggregate concrete, round columns, axial compression, spraying water at high temperature, mechanical behavior

1 Introduction

Recycled concrete refers to the new concrete prepared by mixing discarded concrete blocks with gradation in a certain proportion after processing, partially or fully replacing natural aggregates such as sand and gravel. The use of recycled aggregates, especially those from demolition waste or prefabricated concrete residues is an effective means of building green projects and maintaining sustainable development. (Behera et al., 2014). As an important part of recycled concrete application, reinforcement recycled concrete structure has the structural performance characteristics of reinforced concrete and the advantages of recycled coarse aggregate recycling. It has prominent application prospects in engineering practice. Researchers have not only conducted in-depth research on materials (Limbachiya et al., 2012.; Chen et al., 2014; Cao et al., 2016; Zheng et al., 2021)and components (Ajdukiewicz et al., 2007; Wang et al., 2011; Chen et al., 2013), but also carried out experimental research and theoretical analysis on the seismic performance of related specimens in terms of joints and structural systems. (Xiao et al., 2006; Cao et al., 2011; Liu et al., 2011; Lu et al., 2021; Xu et al., 2021).

In recent years, with the frequent occurrence of building fires, to provide the necessary basis for post-disaster safety assessment of structural components, it is particularly important to promote research on the residual bearing capacity of structural components after a fire disaster or high temperature. Researchers have also continued to advance their research on materials, computational methods and computational models. (Wu, 2003; Lu and Su, 2010; Ni and Gernay, 2020; Dai et al., 2021; Li et al., 2022; Yu et al., 2022; Shahraki et al., 2022; De Silva et al., 2022; Ge et al., 2022).

Currently, studies on the high-temperature resistance of recycled concrete structures are gradually gaining attention. Studies on the strength evolution, failure mechanism and residual strength of recycled concrete materials under the influence of high temperatures have shown that recycled aggregate concrete produced from recycled concrete, bricks and other construction wastes has a better quality performance at high temperatures (Garcia-Troncoso et al., 2013). The residual properties of them are similar to those of ordinary concrete (Laneyrie et al., 2016), but the strength degradation after high temperatures is greater than that of the ordinary one. With the growth of recycled aggregates' substitution rate, the rate of increase in the internal temperature of concrete and the fire resistance limit gradually decreases (Dong et al., 2013; Algourdin et al., 2022). The relative residual compressive strength of recycled concrete after high temperature will be greater than that of ordinary concrete under the same conditions when the substitution rate is greater than a certain threshold and is positively correlated with the substitution rate. (Xiao and Huang, 2006; Mohammad et al., 2021). Scholars have also studied the performance of steel-reinforced recycled concrete short columns, steel reinforced concrete T-shaped column,recycled concrete-filled steel tubes and cylinders after high temperatures, and explored the various factors affecting their performance (Chen et al., 2015; Wang et al., 2022; Chen et al., 2022).

The process of high temperature and rapid cooling would affect the development of micro-cracks and weaken the interface area, thus changing the physical and mechanical properties of concrete. (Ercolani et al., 2017). Different cooling methods can lead to differences in the mechanical properties of components that have experienced high temperatures. In practical engineering, most fires in buildings are extinguished by fire sprinklers. Studies have shown that spray cooling has a positive effect on the strength recovery of high-strength concrete after high temperatures (Chen et al., 2018).

With the characteristics of quick and convenient construction and molding of internally reinforced frames and good mechanical performance, spiral-reinforced restrained concrete columns have been widely used in practical engineering. The mechanical properties of recycled concrete reinforced with spiral reinforcement have been studied in depth in various aspects. (Woo et al., 2018; Muhammad J.M et al., 2019; Muhammad et al., 2020; Huang et al., 2021; Raza et al., 2021; Kumar et al., 2022). Spiral hoops can also play a positive role in improving the fire resistance of components (Zhou et al., 2022).

In the actual fire environment, buildings are often subjected to high temperatures along with the cooling effect caused by fire sprinkler cooling measures, which may have an impact on the mechanical property degradation pattern of recycled concrete. However, there is a lack of research on the performance of recycled concrete cylindrical members with spiral reinforcement after water spraying at high temperatures. Such a lack and ambiguity of assessment criteria threaten people's lives and can bring difficulties to post-disaster reconstruction and accountability, thus greatly limiting the further application of such structures.

To study the performance degradation law of spiral reinforcement recycled aggregate concrete round columns after high temperatures and spraying water cooling, three parameters including recycled coarse aggregate replacement ratio, temperature, and pitch of screw stirrups were taken into consideration as the variate. In this paper, each specimen's physical and mechanical properties are analyzed in depth through the comparison of axial compression tests. The formulae for calculating the residual bearing capacity are given to provide a reference for further research and post-disaster evaluation of spiral-reinforced recycled concrete cylindrical structures.

2 Experimental program

2.1 Preparation of specimens

A total of 26 recycled aggregate concrete cylindrical specimens with spiral stirrups were designed, and the section

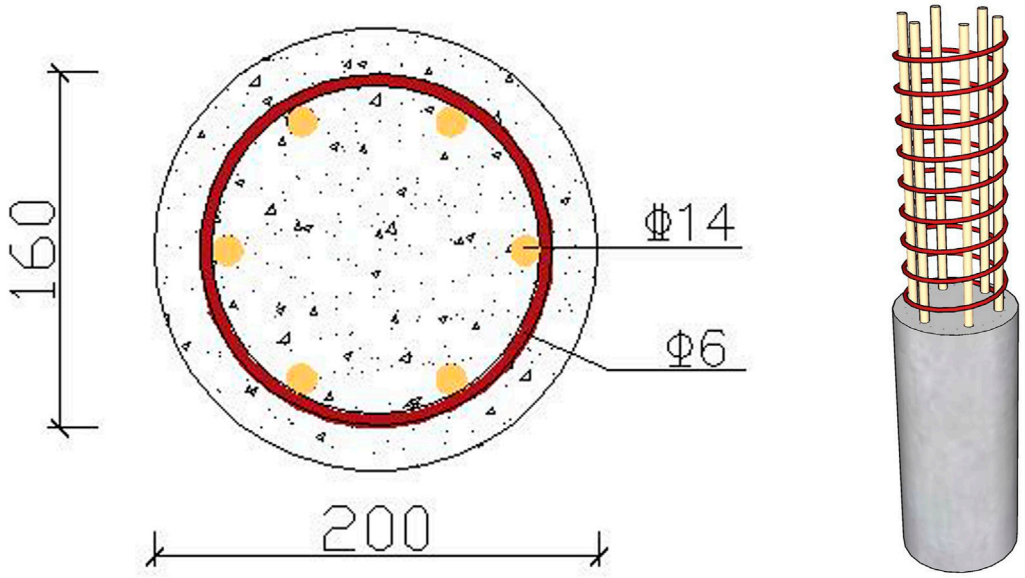

FIGURE 1
Cross-sectional dimensions and reinforcement.

size was uniform to a circular section of 200 mm in diameter. The height of the specimens was 910 mm, and the longitudinal reinforcement ratio was 2.94%. The Cross-sectional dimensions and reinforcement are shown in Figure 1.

Parameters such as the replacement rate of recycled coarse aggregate γ, temperature T, spiral stirrup spacing S, and cooling method after high temperature (natural cooling and spraying water cooling) were included in the design of the specimen considering. The specific design parameters are shown in Table.1.

2.2 Mechanical property of the material

The recycled coarse aggregate used in the specimens was obtained from the waste concrete test block with the original design strength of C30 in the laboratory, which was mechanically crushed and sieved. The size of recycled coarse aggregate is between 5 mm and 26.5 mm with continuous gradation. The natural coarse aggregates were also sieved under the same conditions. The physical property indexes of the coarse aggregates are shown in Table 2.

The specimens were made of ordinary river sand, ordinary Portland cement and urban tap water. and the mix proportion was designed according to the C30 strength standard. Recycled concrete is based on a replacement rate of 0%. Different replacement rates only change the proportion of recycled coarse aggregate and natural coarse aggregate. The specific mix ratio is shown in Table.3.

The HPB400 screw-thread steel bars with a diameter of 14 mm were used as the longitudinal reinforcement, and the HPB300 round bars with a diameter of 6 mm were used as the stirrup. According to the ***Metallic materials-Tensile testing-Part 1: Method of test at room temperature*** (GB/T 228.1-2010), the yield strength of the two kinds of two reinforcement are 442.32MPa and 439.77 MPa respectively, and the tensile ultimate strength is 570.44MPa and 618.24 MPa respectively. The international standard cylinder block with a size of 150 mm × 300 mm is reserved when the specimens were poured. The measured compressive strength fc is shown in Table.3.

2.3 Experimental equipment and cooling method

2.3.1 Heating equipment

The box-type industrial resistance furnace was used to raise the temperature of the test piece, The resistance furnace is 1200 mm × 600 mm × 400 mm in size, 45 kW in power and 950°C in rated temperature, and the heating equipment is shown in Figure 2A. The specimen was kept constant for 60 min in the furnace after reaching the target temperature, and the measured heating curve in the furnace is shown in Figure 2B. Due to the limitation of resistance furnace equipment, the temperature in the furnace will drop for a period during the heating process to 600°C and 800°C, then rise to the target temperature.

TABLE 1 Design parameters and burning loss rate.

Numbering	γ/%	T/°C	S/mm	Cooling method	Burning loss rate l/%
CRACC-1	0	20	30	—	—
CRACC-2	0	200	30	WC	.19
CRACC-3	0	400	30	WC	1.38
CRACC-4	0	600	30	WC	2.84
CRACC-5	0	800	30	WC	5.13
CRACC-6	30	600	30	WC	2.99
CRACC-7	30	800	30	WC	6.38
CRACC-8	50	600	30	WC	2.77
CRACC-9	50	800	30	WC	5.83
CRACC-10	70	600	30	WC	3.24
CRACC-11	70	800	30	WC	6.29
CRACC-12	100	20	30	—	—
CRACC-13	100	200	30	WC	0
CRACC-14	100	400	30	WC	.53
CRACC-15	100	600	30	WC	3.37
CRACC-16	100	600	50	WC	3.78
CRACC-17	100	600	70	WC	3.69
CRACC-18	100	800	30	WC	9.40
CRACC-19	100	800	50	WC	6.63
CRACC-20	100	800	70	WC	6.81
CRACC-21	100	600	30	NC	6.74
CRACC-22	100	600	50	NC	6.24
CRACC-23	100	600	70	NC	6.54
CRACC-24	100	800	30	NC	9.18
CRACC-25	100	800	50	NC	8.59
CRACC-26	100	800	70	NC	8.92

Note: γ is the replacement rate of recycled coarse aggregate; T is the maximum temperature experienced; S is the spacing of spiral stirrups; WC means water spraying cooling; and NC means natural cooling.

TABLE 2 Parameters of coarse aggregate.

The type of coarse aggregate	ρ_1/(kg/m^3)	ρ_0/(kg/m^3)	w/%	G_e/%
Natural coarse aggregate	1577	2701	0.70	12.4
Recycled coarse aggregate	1432	2639	3.79	14.0

Note: ρ1 is stacking mass density; ρ0 is the apparent mass density; w is water absorption and the Ge is the crushing index.

2.3.2 Cooling method

Based on the current actual firefighting situation, two cooling methods, natural cooling and spraying water cooling, were decided as the research arguments for the experiment. The specimens were first brought up to the target temperature and kept constant in the furnace for 60 min. Then the specimens were immediately removed and subjected to simulated fire sprinkler cooling. The specimen

TABLE 3 Concrete proportion.

γ/%	W/C	ρ	Material usage/(kg/m3)					Strength grade	f_c/MPa
			m_c	m_w	m_s	m_{NAC}	mRAC		
0	.43	.32	488.4	210	536	1139	0	C30	24.66
30	.43	.32	488.4	210	536	797.3	341.7		25.35
50	.43	.32	488.4	210	536	569.5	569.5		29.13
70	.43	.32	488.4	210	536	341.7	797.3		23.66
100	.43	.32	488.4	210	536	0	1139		25.42

Note: W/C is water-cement ratio; ρ is sand ratio; mc, mw, ms, mNAC, and mRAC are the dosages of cement, water, sand, natural coarse aggregate and recycled coarse aggregate, respectively.

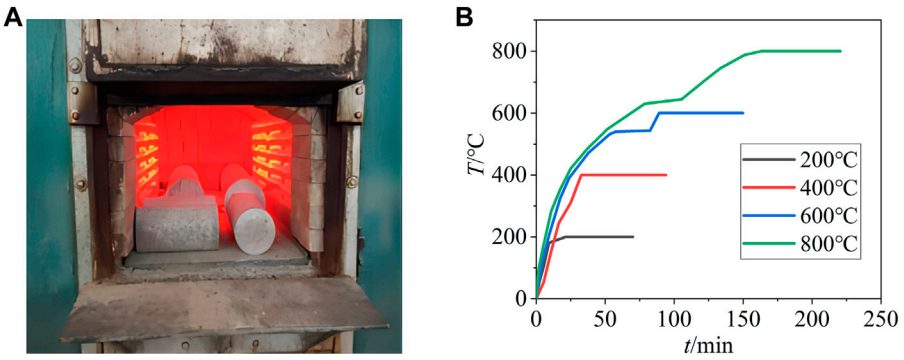

FIGURE 2
(A) Heating equipment **(B)** Furnace heating curves.

was continuously sprayed for 25 min, and the water flow shall be kept as consistent as possible. The specimens naturally cooled were kept in the resistance furnace until they were cooled to room temperature. The spray cooling in the test is shown in Figure 3.

2.3.3 Loading setup

The YAW-10000J microcomputer-controlled electro-hydraulic servo compression-shear test machine in the structural hall of Guangxi University was used to carry out the axial compression loading test of the specimens after high temperatures and spraying water cooling. Leveling should be done with a horizontal ruler before loading, and the uneven place was paved with fine sand. Both ends of the test piece were wrapped with FRP carbon fiber cloth and sleeved with specially processed hoops with a height of 5 mm to prevent the end from being damaged in advance. The displacement-controlled loading method was adopted in the test, and the loading rate was 1 mm/min. Stop loading when the load decreased by more than 85% or displacement deformation was over large. The loading setup is shown in Figure 4.

FIGURE 3
Water cooling.

FIGURE 4
Loading setup.

3 Experimental results and analysis

3.1 Change in the appearance

When the high temperature was completed, there was no obvious change in the surface of the specimens at 200°C and 400°C. There were a large number of irregular cracks on the surface of the specimens at 600°C and 800°C. At 800°C, the cracks were and the width was slightly larger than that at 600°C.

After spraying water cooling, there was no obvious phenomenon in the specimen at 200°C, weak white smoke was generated in the specimen at 400°C, and there was no obvious change in the appearance of the specimen after spraying water at 200°C and 400°C. At 600°C, the specimen produced white smoke under the action of water spraying. After water spraying, the fine cracks on the surface of the specimen were weakened and reduced, and there was a small amount of loss on the surface. At 800°C, the specimen produced a large amount of white smoke under the action of water spraying. After it, there is still few white smokes produced. The fine cracks on the surface were also weakened and reduced, water stains appeared at the cracks, and the surface loss was relatively serious.

After spray cooling, at 200°C, the specimen had no obvious change compared with normal temperature. At 400°C, the color of the specimen slightly deepened, showing light gray and yellowish. When the temperature reached 600°C, the surface color of the specimen became deeper and yellowish, and many irregular cracks appear. At 800°C, the specimen surface turned grayish-white, and there were more irregular cracks on the surface. Apparent changes in specimens before and after spraying is shown in Figure 5.

3.2 High temperature burning loss rate of specimens

The specimens under different cooling methods before and after high temperatures were weighed to obtain the mass loss rate after high temperatures. Figure 6A shows the relationship between the temperature and burning loss rate of each specimen after high-temperature water spraying under different recycled coarse aggregate replacement rates. Among the picture, WC means water spraying cooling, and NC means natural cooling.

It can be seen from the figure that with the increase in temperature, the burning loss rate of the specimen increases gradually. The mass of the specimen is almost not lost at 200°C. At 400°C, the burning loss rate of the specimen increases slightly, but it is not obvious for the whole. At 600°C, there is little difference in the loss on ignition rate of each substitution rate. At 800°C, the specimen concrete becomes crisp, the surface appears peeling phenomenon, and the burning loss rate is relatively large.

Figure 6B shows the relationship between the burning loss rate and temperature of specimens with different spacing spiral stirrups under different cooling methods. It can be seen from the figure that the overall burning loss rate under natural cooling is higher than that under spray cooling, and the effect of spiral stirrup spacing on the burning loss rate is not obvious. This is because the quality loss of the naturally cooled specimens is mainly due to the evaporation of water

FIGURE 5
Apparent changes of specimens after spraying.

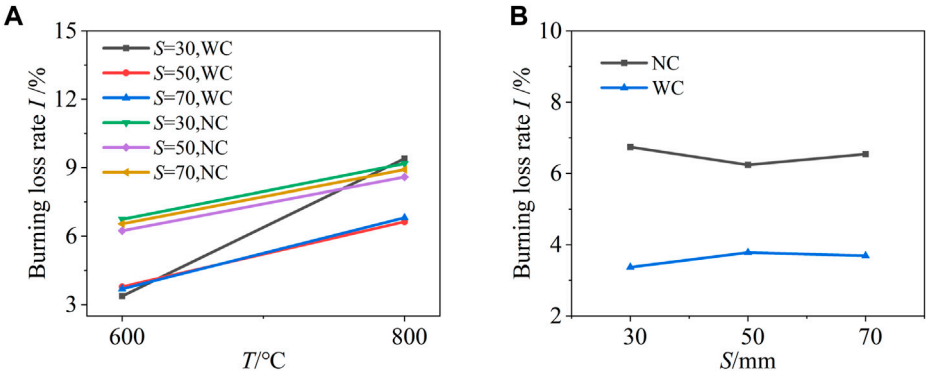

FIGURE 6
Influence of different factors on burning loss rate. **(A)** Coarse aggregate replacement ratio; **(B)** Cooling method and stirrup spacing.

and the peeling and flaking of the concrete; while the specimens cooled by water spraying, although a large amount of water evaporated during the process of exposure to high temperature, in the process of simulated fire spraying, some of the water re-infiltrated into the interior of the specimens and a series of chemical reactions occurred with the aggregates, and the quality of the specimens increased during this process compared to the effect of high temperature.

3.3 Failure process and shape of the specimen under stress

The overall failure process of spiral-reinforced concrete specimens was roughly the same. After the vertical cracks appeared, the outer concrete peeled off, the inner core concrete continued to maintain the bearing capacity for a while, and the final specimens were damaged due to excessive deformation or stirrups crushed by longitudinal reinforcement.

At room temperature and 200°C, the first vertical crack appeared at about 0.8 N_u (N_u is the peak load). With the increase in load, the inclined crack zone was formed on the surface of the specimen, and the concrete protective layer was massively exfoliated. Due to the confinement effect of stirrups, the specimen continued to be subjected to force for a while, and then the longitudinal reinforcement of the specimen was deformed too large to squeeze out the spiral reinforcement, and the specimen was destroyed. At 400°C, the first vertical crack appeared around 0.7 N_u, and with the increase of load, multiple parallel vertical cracks were formed in the outer concrete. At 600°C, vertical

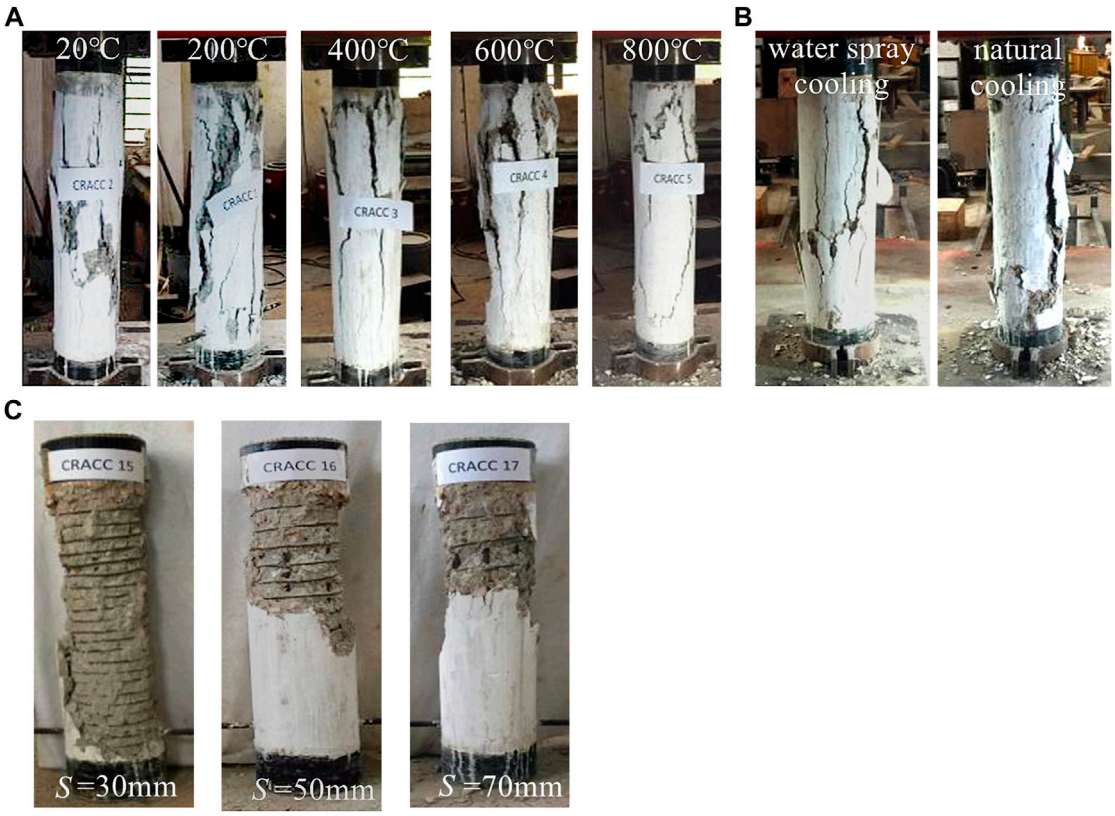

FIGURE 7
Final failure modes. **(A)** Failure modes of specimens at different temperatures; **(B)** Failure modes of specimens under different cooling methods; **(C)** Failure modes of specimens with different spiral reinforcement space.

cracks appeared in the specimen at about 0.5–0.6 N_u. The cracks developed irregularly with the increase in load, and then the concrete peeled off. At 800°C, vertical cracks appeared in the specimen about 0.3–0.4 N_u, the load increased gradually, and the spalling volume of concrete was also larger. The failure process under different temperatures is shown in Figure 7A.

Figure 7B shows the failure modes under different cooling methods. Compared with the specimens cooled by spraying, the cracks appeared relatively later and the stripped volume of concrete was smaller in the specimens under natural cooling.Figure 7C shows the failure modes under different spiral reinforcement spacing. The concrete spalling volume tends to be positively correlated with the spiral reinforcement spacing.

3.4 Main parameters of feature points

The main parameters of specimens under different cooling methods after high temperature, including peak load N_u, peak displacement Δp, initial stiffness EA and displacement ductility coefficient μ are given in Table. 4. The initial stiffness EA takes the secant stiffness of .4 times the peak load point at the rising section of the load-displacement curve. In displacement ductility coefficient $\mu = \Delta u/\Delta y$, Δu takes the corresponding displacement when the load drops to 85% peak load, and Δy is the yield displacement value, which is determined by referring to the general yield bending moment method.

3.5 Load-displacement curves

The axial load-displacement curve of the specimen during the whole failure process was obtained, as shown in Figure 8. Among them, γ is the recycled coarse aggregate replacement ratio, S is the spacing of spiral stirrups; WC means spraying water cooling, and NC means natural cooling. The figure shows that the peak load of the specimen will decrease with the increase in temperature. Peak displacement fluctuates within a certain range at 600°C and lower temperatures, but the difference is not significant.

However, at 800°C, the peak displacement of the specimen will increase significantly. The higher the temperature is, the

TABLE 4 Main parameters of feature points.

Numbering	γ/%	T/°C	Cooling method	N_u/kN	Δ_p/mm	EA/MN	Δ_y/mm	Δ_u/mm	μ
CRACC-1	0	20	—	1376.0	13.846	253.859	6.415	25.047	3.90
CRACC-2	0	200	WC	1295.0	11.579	256.033	5.697	26.700	4.69
CRACC-3	0	400	WC	1256.5	10.937	199.248	7.699	22.195	2.88
CRACC-4	0	600	WC	1265.0	11.807	183.962	8.847	24.959	2.82
CRACC-5	0	800	WC	1168.5	18.034	134.225	10.050	24.020	2.39
CRACC-6	30	600	WC	1311.0	12.656	167.012	9.489	26.327	2.77
CRACC-7	30	800	WC	1133.0	20.185	112.861	11.795	30.447	2.58
CRACC-8	50	600	WC	1443.5	8.843	241.113	6.972	13.328	1.91
CRACC-9	50	800	WC	942.0	17.320	159.602	7.242	>21.749	>3.00
CRACC-10	70	600	WC	1373.0	11.916	270.391	8.116	23.663	2.92
CRACC-11	70	800	WC	1184.0	17.224	148.589	10.343	26.283	2.54
CRACC-12	100	20	—	1326.5	12.863	261.308	5.809	>28.128	>4.84
CRACC-13	100	200	WC	999.5	8.710	214.630	5.577	22.195	3.98
CRACC-14	100	400	WC	1226.0	19.707	187.596	8.987	>27.671	>3.08
CRACC-15	100	600	WC	1319.0	13.801	186.704	9.043	22.496	2.49
CRACC-16	100	600	WC	1137.0	7.751	224.777	5.725	11.266	1.97
CRACC-17	100	600	WC	1040.0	8.112	189.404	5.801	10.223	1.76
CRACC-18	100	800	WC	674.0	22.784	88.787	9.757	>34.074	>3.49
CRACC-19	100	800	WC	929.0	13.003	121.049	9.360	19.763	2.11
CRACC-20	100	800	WC	841.5	10.776	128.670	7.695	15.514	2.02
CRACC-21	100	600	NC	1017.5	12.851	177.652	6.909	29.115	4.21
CRACC-22	100	600	NC	1160.5	8.903	229.683	5.822	11.430	1.96
CRACC-23	100	600	NC	1045.5	6.792	243.448	4.802	9.344	1.95
CRACC-24	100	800	NC	793.5	20.301	120.960	8.818	31.226	3.54
CRACC-25	100	800	NC	713.0	10.087	104.853	7.735	18.688	2.42
CRACC-26	100	800	NC	564.0	9.472	400.624	6.191	14.255	2.30

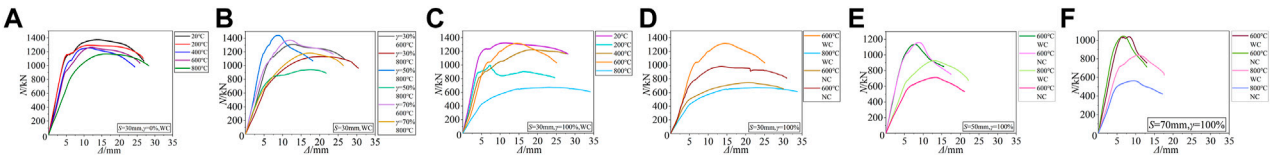

FIGURE 8
Load-displacement curves. **(A)** S = 30 mm, γ = 0%, WC; **(B)** S = 30 mm, WC; **(C)** S = 30 mm, γ = 100%, WC; **(D)** S = 30 mm, γ = 100%; **(E)** S = 50 mm, γ = 100%; **(F)** S = 70 mm, γ = 100%.

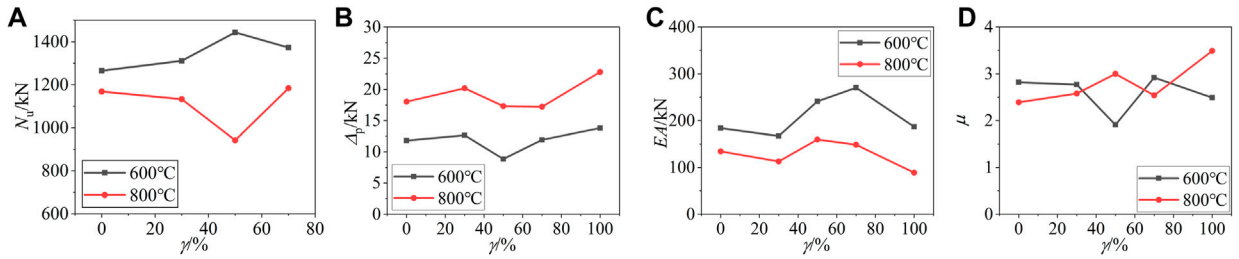

FIGURE 9
Influence of replacement ratio on mechanical properties. **(A)** peak load; **(B)** peak displacement **(C)** initial stiffness **(D)** displacement ductility coefficient.

smaller the initial secant slope of the curve is, and it decreases significantly after 600°C, the initial secant slope after high temperatures and spraying water cooling is higher than that after natural cooling, which is more obvious at 800°C.

4 Analysis of influencing factors

4.1 Replacement ratio of recycled coarse aggregate

According to Table.4, when the maximum temperature is less than 400°C, the peak load of the specimen decreases slightly with the increase of the replacement ratio. Compared with the 0% replacement ratio specimen, the 100% replacement rate specimen decreases by 3.6% and 2.4% respectively at room temperature and 400°C. Figure 9A shows the curve of peak load *versus* replacement ratio at high temperatures. When the maximum temperature is 600°C, the peak load of specimens increases slightly with the increase in replacement ratio, and the peak load of specimens with 30%–70% replacement rates increases by 3.6%,1.4%, and 8.5%, respectively. When the maximum temperature reaches 800°C, the peak load of the specimen fluctuates with the increase of the substitution rate, but the overall trend is still slightly upward. Overall, the replacement rate of recycled aggregate has little effect on the peak load of the specimen.

The peak displacement of fully recycled concrete specimens is lower than that of ordinary concrete specimens at room temperature and 200°C, 15.6%, and 33.0% respectively. Figure 9B shows the graph curves of the peak displacement of the specimen with the replacement rate at high temperatures. The peak displacement of specimens with the highest temperature of 600°C or 800°C increases with the increase in replacement rate. And the rise in peak displacement is greater for specimens experiencing a temperature of 800°C.The peak displacement of specimens with 30%–100% replacement ratio increase by 3.0%, −20.4%, 3.2%, and 17.8% respectively at 600°C. At 800°C, it increases by 21.8%, 7.4%, 8.5%, and 36.2% respectively.

Figure 9C shows the curves of the initial stiffness of the specimen with the change of replacement ratio at different temperatures. It can be seen from the figure that when the maximum temperature is 600°C or 800°C, the initial stiffness decreases firstly and then recovers, and finally decreases again with the increase of the replacement ratio. On the one hand, compared with natural coarse aggregates, recycled coarse aggregates have higher water absorption, and the water content of recycled concrete is larger under the same environmental conditions. Under high-temperature conditions, the recycled concrete has more evaporable water, and to a certain extent, the evaporation of water can slow down the increase of internal temperature of concrete, thus reducing the damage of high temperature on the elastic modulus of concrete; on the other hand, due to the existence of physical defects such as micro-cracks at the interface between cement and recycled coarse aggregate, the recycled concrete itself has mechanical property defects, and the larger the replacement rate of recycled coarse aggregate. On the other hand, because of the physical defects such as micro-cracks at the interface between cement and recycled coarse aggregate, the recycled concrete itself has mechanical defects, and the larger the substitution rate of recycled coarse aggregate, the more serious the mechanical defects will be. When $\gamma < 30\%$ or $\gamma > 70\%$, the latter plays a dominant role, so with the increase of replacement rate, the modulus of elasticity of recycled concrete gradually decreases, and the axial compression stiffness of steel pipe recycled concrete specimens also gradually decreases; when $30\% < \gamma < 70\%$, the former plays a dominant role, the result is the opposite.

On the whole, the average ductility of specimens with a 100% substitution rate is 6.7% higher than that of specimens with a 0% substitution rate. Figure 9D shows the variation curve of the displacement ductility coefficient with replacement ratio. When the maximum temperature is 600°C or 800°C, the ductility of the specimen changes

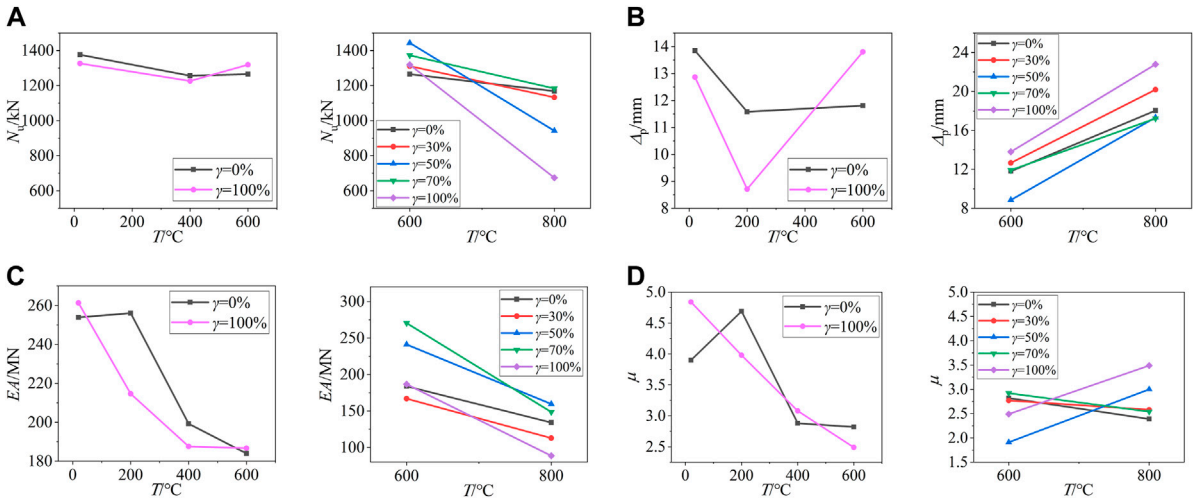

FIGURE 10
Influence of temperature on mechanical properties. **(A)** peak load; **(B)** peak displacement **(C)** initial stiffness **(D)** displacement ductility coefficient.

relatively small with the change of replacement ratio. At 800°C, with the increase of the replacement ratio, the ductility of the specimen will increase slightly.

4.2 Temperature

Figure 10A shows the variation curves of the peak load with temperature under different replacement rates. It can be seen from the figure that when the temperature is 400°C, the bearing capacity of the specimen will decrease slightly with the increase in temperature. This is because the free water inside the concrete is lost after the specimen experiences a high temperature of 400°C, and the concrete absorbs a large amount of free water when spraying water. The change of temperature difference in this process will cause the internal deformation of the concrete to be uncoordinated to a certain extent, resulting in micro-cracks, which will reduce the bearing capacity of the concrete; At 400°C–600°C, because of the uneven temperature field inside and outside the concrete during the heating process, the temperature rise process of the internal concrete will be relatively slow, and the existence of spiral stirrup will make this process slower. Therefore, the performance damage of internal core concrete can be alleviated to a certain extent by spraying water cooling immediately after high temperature. Consequently, the bearing capacity of specimens after high-temperature water spraying cooling is relatively flat. When the maximum temperature is between 600°C and 800°C, the core concrete is subjected to high temperatures. The loss of free water and bound water causes severe damage to its internal structure, which leads to a continued decrease in the bearing capacity of the specimen.

Figure 10B shows the curves of peak displacement *versus* temperature under different replacement ratios. It can be seen from the figure that the peak displacement of the specimen fluctuates in the range of 10 mm–14 mm when the temperature is less than 600°C. Among them, the peak displacement was slightly lower at 200°C. At 800°C, the peak displacement of the specimen was significantly increased. Compared with the specimen experiencing the highest temperature of 600°C, the peak displacement of the specimen experiencing the highest temperature of 800°C with different substitution rates increased by 38% on average. This may be caused by the evaporation of water inside the specimen after high temperature and becoming loose, and the concrete being continuously compacted before the peak load.

Figure 10C shows the variation curves of the initial stiffness of the specimen with temperature under different substitution rates. It can be seen from the figure that with the increase in temperature, the initial stiffness of the specimen generally shows a continuous downward trend. When the maximum temperature is below 600°C, the decrease in the initial stiffness of the specimen is relatively small. When the maximum temperature is 600°C, the initial stiffness of 0% and 100% specimens decreases by 27.53% and 28.6% respectively compared with the specimens at room temperature. When the temperature is between 600°C and 800°C, the initial stiffness decreases slightly, and the initial stiffness of the specimens with 0%–100% replacement ratio decreased by 27%, 32.4%, 33.8%, 45%, and 52.4%, respectively.

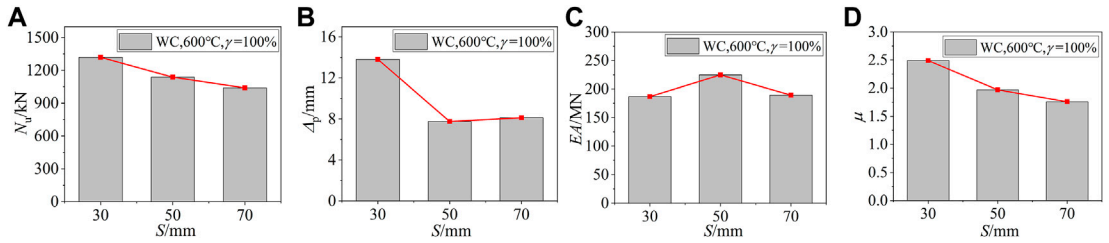

FIGURE 11
Influence of spacing on mechanical properties. **(A)** peak load; **(B)** peak displacement **(C)** initial stiffness **(D)** displacement ductility coefficient.

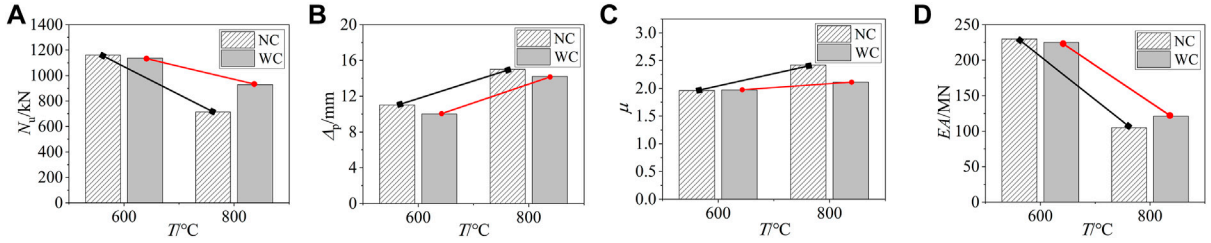

FIGURE 12
Influence of different cooling methods on mechanical properties. **(A)** peak load; **(B)** peak displacement **(C)** initial stiffness **(D)** displacement ductility coefficient.

Figure 10D shows the curves of displacement ductility *versus* temperature under different replacement ratios. It can be seen from the figure that the ductility of specimens with a 0% replacement rate and a 100% replacement rate decreases with the increase in temperature. When the maximum temperature was 600°C, the ductility of specimens with 0% and 100% replacement rates decreased by 27.7% and 48.6%, respectively. However, when the maximum temperature is between 600°C and 800°C, the ductility coefficient of the specimen is relatively stable, and the ductility of the specimens with different replacement rates is not much different at the same temperature.

4.3 Spiral stirrup spacing

The specimens with the highest temperature of 600°C, cooling by spraying and substitution rate of 100% were taken to study the influence of stirrup spacing on each performance. Figure 11 shows the variation curves of mechanical properties of specimens with the increase of stirrup spacing S. The peak load of specimens with 30mm, 50mm, and 70 mm spacing decreases nearly linearly. The peak load of specimens with 50mm and 70 mm spacing is 13.8% and 21.2% lower than that of specimens with 30 mm spacing. The peak displacement of specimens with 50 mm spacing is 37.9% lower than that of specimens with 30 mm spacing, while the peak displacement of specimens with 70 mm spacing is similar to that of specimens with 50 mm spacing, which is 36.5% lower than that of specimens with 30 mm spacing. The initial stiffness of the specimen with 50 mm spacing is the largest among the three specimens, which increases by 20.4% compared with the specimen with 30 mm spacing, while the initial stiffness of the specimen with 70 mm spacing is similar to that of the specimen with 30 mm spacing, which increases by 1.4%. The ductility coefficient decreases with the increase of stirrup spacing. Compared with 30 mm spacing specimens, 50mm and 70 mm spacing specimens decrease by 20.9% and 29.3% respectively. This is because the spiral reinforcement produces a larger restraint on the specimen, the smaller the hoop spacing, the more obvious the restraint effect, so the better the ductility of the specimen and the more fully the reinforcement plays its role.

4.4 Cooling method

Figure 12 shows the difference in mechanical properties of the recycled concrete cylinder with spiral reinforcement under different cooling methods. It can be seen from the figure that

there is little difference in the peak load between the two cooling methods at 600°C. At 800°C, the peak load of the natural cooling specimen decreases more than that of the spraying water cooling specimen, and the peak load decreases by 23.3% compared with the specimens cooled by spraying water. This may be because when the specimen experiences a temperature of 800°C, its internal water evaporates a lot, and in the process of water spraying cooling, the water penetrates the interior of the specimen under the action of water pressure and a series of physical or chemical reactions occur with the aggregate, thus strengthening the bearing capacity of the specimen.

The peak displacement of specimens under natural cooling is always larger than that under spray cooling, which is 10% and 5% higher at 600°C and 800°C, respectively. Different cooling methods have no significant effect on the initial stiffness of the specimen. At 600°C, the ductility coefficient of the specimen after water spraying cooling and natural cooling has little difference. At 800°C, the ductility coefficient after natural cooling is greatly improved than that after water spraying cooling. This is since compared to natural cooling, at the same temperature, spraying water cooling causes a drastic temperature change, which produces more serious damage to the concrete in a short period, making the cracks at the interface between cement and recycled coarse aggregate larger, and therefore the greater the defect in the mechanical properties of concrete.

5 Bearing capacity analysis

5.1 Damage analysis

Recycled concrete with spiral reinforcement is subject to considerable damage after the action of high temperatures, resulting in a reduction of the structural load-bearing capacity. According to the damage theory, the high temperature leads to defects in the specimen, reducing the effective section. Therefore, the parameter D is introduced to describe the damage degree of the specimen.

$$D = 1 - \frac{S^*}{S}. \tag{1}$$

In Eq. 1, S and S^* denote respectively the sum of the cross-sectional area under non-destructive conditions and the effective area after damage.

Since the resultant force of specimens before and after the damage is equal, Eq. 2 can be obtained:

$$\sigma \cdot S = \sigma^* \cdot S^*. \tag{2}$$

According to the hypothesis of equivalent strain, Eq. 3 is obtained as follows. σ and σ^* are the effective stress before and after damage, respectively. E and E^* indicate the modulus of elasticity when the material is undamaged and the modulus of elasticity after damage, respectively. ε is the stress caused by the effective stress acting on the damaged material or the stress caused by it under non-destructive conditions.

$$\varepsilon = \frac{\sigma^*}{E} = \frac{\sigma}{E^*}. \tag{3}$$

According to the above formula, Eq. 4 can be derived as follow:

$$\sigma = E\varepsilon(1 - D). \tag{4}$$

Considering the initial defects caused by high-temperature damage on the specimen, to define the damage degree of high-temperature specimens (200°C, 400°C, 600°C, and , 800°C), the elastic modulus E of the specimen at room temperature (20°C) is used to determine the elastic modulus E_0 at non-destructive (Su, Z. and Chen, Z., 2021; Sun, B., et al., 2022), and Eq. 5 can be obtained:

$$D = 1 - \frac{E_T}{E_0}. \tag{5}$$

In Eq. 5, E_T is the elastic modulus of the specimen cooled by spraying after high temperature: E_0 is the elastic modulus of specimens at room temperature. The larger the D value, the greater the damage to the specimen.

Figure 13A shows the variation trend of the damage degree with temperature under different substitution rates. It can be seen that the higher the temperature of the specimen is, the greater the damage degree is. When the temperature is less than 600°C, the damage degree of the specimen rises little with the increase in temperature, but when the temperature reaches 800°C, the damage degree of the specimen increases sharply. The addition of recycled coarse aggregate will increase the damage to the concrete after high temperatures and spraying water cooling. Compared with ordinary spiral-reinforced concrete, the damage degree of spiral-reinforced recycled concrete block is more severely affected by temperature.

The specimens with the maximum temperature of 600°C and the replacement rate of the recycled coarse aggregate of 800°C were taken to study the influence of spiral reinforcement spacing and cooling method on the damage degree. As shown in Figure 13B, when the spray cooling method is adopted, the D decreases first and then increases with the increase of spacing. The damage is minimized when the spacing is 50 mm. When natural cooling is adopted, the D decreases with the increase of spacing. When the spacing of spiral reinforcement is 30 mm, the damage of the specimen can be reduced by spray cooling, but when the spacing is 50 mm and 70 mm, the damage of the specimen increases.

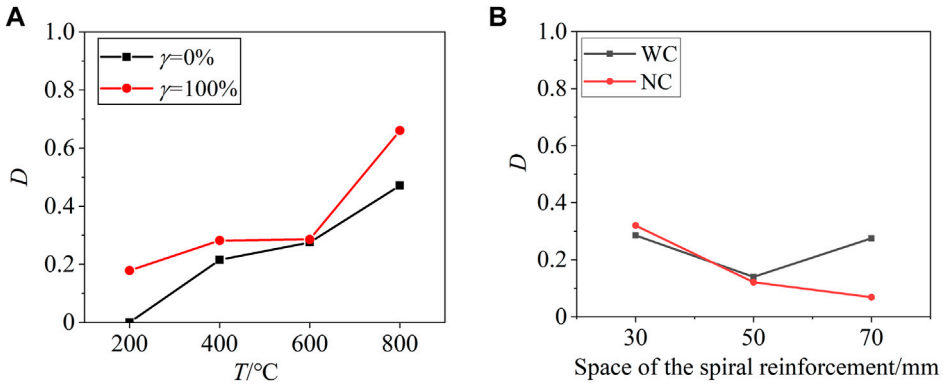

FIGURE 13
(A) The change of damage degree of specimens with temperature under different substitution rates. **(B)** Effect of spiral rib spacing on damage degree under different cooling methods.

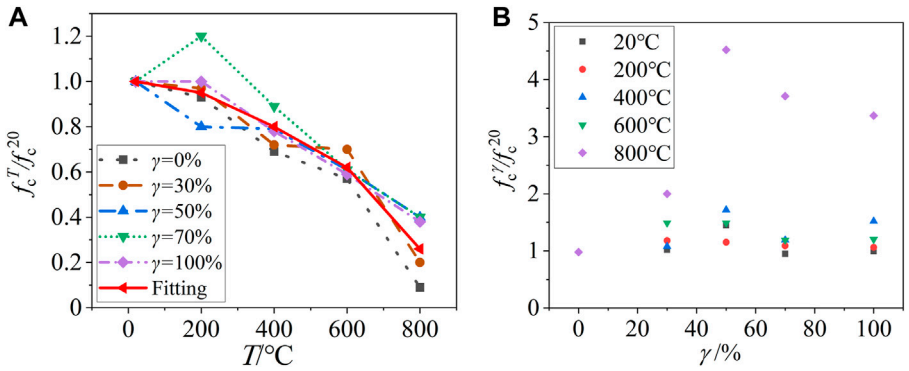

FIGURE 14
(A) Effect of temperature on strength of specimen; **(B)** Effect of replacement ratio on strength of specimens.

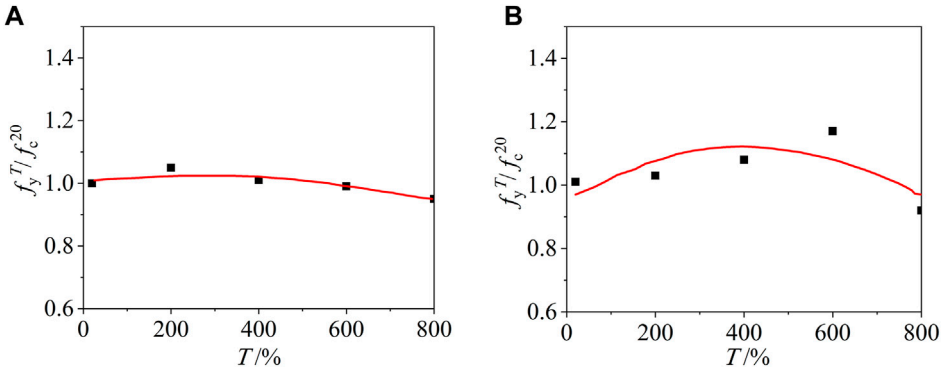

FIGURE 15
Effect of temperature on tensile strength of reinforcement. **(A)** longitudinal reinforcement; **(B)** stirrup.

TABLE 5 Comparison between calculated and measured values of bearing capacity of specimens.

Numbering	γ/%	T/°C	Cooling method	Bearing capacity/kN		Calculated value/Test value
				Calculated value	Test value	
CRACC-1	0	20	WC	1128.6	1376	.82
CRACC-2	0	200	WC	1173.4	1295	.91
CRACC-3	0	400	WC	1137	1256.5	.90
CRACC-4	0	600	WC	1057.4	1265	.84
CRACC-5	0	800	WC	860.4	1168.5	.74
CRACC-6	30	600	WC	1061	1311	.81
CRACC-7	30	800	WC	1030.1	1133	.91
CRACC-8	50	600	WC	1063.4	1443.5	.74
CRACC-9	50	800	WC	1093.3	942	1.16
CRACC-10	70	600	WC	1065.9	1373	.78
CRACC-11	70	800	WC	1116.5	1184	.94
CRACC-12	100	20	WC	1129.6	1326.5	.85
CRACC-13	100	200	WC	1192.3	999.5	1.19
CRACC-14	100	400	WC	1152.5	1226	.94
CRACC-15	100	600	WC	1069.5	1319	.81
CRACC-16	100	600	WC	890.1	1137	.78
CRACC-17	100	600	WC	813.2	1040	.78
CRACC-18	100	800	WC	1076.4	674	1.60
CRACC-19	100	800	WC	917.1	929	.99
CRACC-20	100	800	WC	848.8	841.5	1.01
CRACC-21	100	600	NC	1069.5	1017.5	1.05
CRACC-22	100	600	NC	890.1	1160.5	.77
CRACC-23	100	600	NC	813.2	1045.5	.78
CRACC-24	100	800	NC	1076.4	793.5	1.36
CRACC-25	100	800	NC	917.1	713	1.29
CRACC-26	100	800	NC	848.8	564	1.50

5.2 Bearing capacity analysis

The performances of recycled concrete and steel bars are quite different after spraying water at high temperatures. The bearing capacity of reinforced recycled concrete members composed of the two is also quite different from that of members without spraying water at high temperatures. Therefore, the use of the conventional formula for calculating the residual bearing capacity of spiral-reinforced recycled concrete will lead to a significant difference between the calculated value and the actual situation. It is necessary to modify the coefficient of the existing bearing capacity formula of spiral stirrup members in the specification.

According to the influence of temperature and recycled coarse aggregate replacement rate on the strength of recycled concrete cylinder blocks, the data were normalized and fitted to obtain the influence law of temperature and replacement rate on the strength of recycled concrete. Depending on the significant difference in the rate of decrease in strength of specimens at different temperature stages, the curves were divided into three different temperature segments: $20^{\circ}C \leq T < 200^{\circ}C$, $200^{\circ}C \leq T \leq 600^{\circ}C$, $600^{\circ}C < T \leq 800^{\circ}C$ for regression fitting.

The effect of temperature on the strength of recycled concrete block is obtained by the above method as shown in Figure 14A. (f_c^T represents the strength of the material after experiencing different temperatures, f_c^{20} represents the strength of the material at room temperature, and f_c^{γ} represents the compressive strength at different substitution rates)

$$N = \alpha_1 \beta f_c A_{cor} + \alpha_2 f_y A_s + 2\alpha_3 f_{yt} \frac{\pi d_{cor} A_{st}}{s}, \quad (6)$$

$$\alpha_1 = \begin{cases} -0.27 \times \dfrac{T}{800} + 1.007, & 0°\text{C} \le T \le 200°\text{C} \\ -0.68 \times \dfrac{T}{800} + 1.11, & 200°\text{C} \le T \le 600°\text{C} \\ -1.32 \times \dfrac{T}{800} + 1.59, & 600°\text{C} \le T \le 800°\text{C} \end{cases} \quad (7)$$

$$\alpha_2 = -3 \times 10^{-7} T^2 + 0.0002T + 1.0065 \; 20°\text{C} \le T \le 800°\text{C}, \quad (8)$$

$$\alpha_3 = -1 \times 10^{-6} T^2 + 0.0008T + 0.9522 \; 20°\text{C} \le T \le 800°\text{C}, \quad (9)$$

$$\beta = \begin{cases} 0.0031\gamma + 1.0384, & 0°\text{C} \le T \le 200°\text{C}, \\ 0.067\gamma + 1.0748, & 200°\text{C} \le T \le 600°\text{C}, \\ -6.175\gamma^2 + 8.8457\gamma + 0.7932, & 600°\text{C} \le T \le 800°\text{C}, \end{cases} \quad (10)$$

The influence coefficient α_1 (Eq. 7) of temperature on the residual strength of recycled concrete is obtained by fitting.

The influence of recycled coarse aggregate replacement rate on the strength of recycled concrete test block is shown in Figure 14B. The influence coefficient β (Eq. 10) of replacement rate on the residual strength of recycled concrete is obtained by fitting.

After spray cooling at different temperatures, the strength changes of the plain hoop and thread longitudinal reinforcement were also different. The influence of temperature on the tensile strength of longitudinal reinforcement after spraying water at high temperatures is shown in Figure 15A. The influence coefficient α_2 (Eq. 8) of temperature on longitudinal reinforcement after spraying water at high temperature is fitted.

The influence of temperature on the tensile strength of the stirrup after spraying water at high temperature is shown in Figure 15B and the influence coefficient α_3 (Eq. 9) of temperature on the stirrup is obtained by fitting.

Based on the existing formula for calculating the bearing capacity of spiral stirrup members, the influence of temperature and substitution rate on a recycled concrete and the influence of temperature on reinforcement is considered. According to the data obtained from this test, the bearing capacity formula of the spiral stirrup member is corrected by the coefficient, and the corrected bearing capacity formula of the spiral stirrup member is obtained.

The comparison between the calculated and experimental values of the axial compression bearing capacity of the spiral reinforcement recycled concrete column after spraying water at high temperature is shown in Table.5. Among them, the calculated value of bearing capacity is obtained from the modified formula.

The average value of the ratio of calculated value to measured value was .89, and the variance was .017. The bearing capacity calculated by the fitting formula is relatively safe. Therefore, the formula can be used to calculate the bearing capacity of axial compression members experiencing water spraying at high temperatures in practice.

As seen in Table 5, for axial compression members with natural cooling after high temperature, when the temperature exceeds 600°C, the bearing capacity calculated by the formula is significantly higher than the measured value, so the formulas do not apply to this situation.

In summary, Eqs 6–10 applies to the calculation of the axial compression bearing capacity of the spiral-reinforced recycled concrete cylinder after water spraying cooling, which has experienced a maximum temperature of 0°C–800°C and a spiral reinforcement spacing of 30 mm–70 mm, or it can be used for similar axial compression members with natural cooling, which has experienced a maximum temperature not exceeding 600°C.

6 Conclusion

- After high temperatures and spraying water cooling, the concrete protective layer on the exterior of the spiral-reinforced recycled concrete column peeled off firstly, and then the core concrete part continues to play its bearing capacity for some time. Finally, the internal longitudinal reinforcement deformation is too large to squeeze the spiral stirrup, resulting in the loss of bearing capacity. The higher the temperature is, the earlier the first vertical crack occurs.
- The effect of the recycled aggregate replacement ratio on the performance of the specimens was mainly in terms of peak displacement. The peak displacement increases with the growth of the replacement ratio when the temperature exceeds 600°C, but has the opposite trend at temperatures below 200°C.The smaller the spiral stirrup spacing is, the larger the spalling area of the outer concrete is when the specimen is finally destroyed, and the higher the peak load and ductility coefficient are. The specimens with 50 mm and 70 mm spiral bar spacing had better displacement deformation capacity when water spray cooling was used. Comparing the test results at each temperature, it can be seen that a high temperature above 600°C will have a very obvious effect on the mechanical properties of the specimens.
- Compared with natural cooling, cooling by water spraying can reduce the appearance of small cracks on the surface of the specimen, and reduce the peak displacement of the specimen. When the specimen experienced a temperature

of 800°C, water spray cooling can better preserve the remaining load capacity of the specimen, but will reduce the ductility of the specimen.

- Based on the test results, considering the influence of recycled coarse aggregate replacement rate and temperature, the bearing capacity formula of spiral reinforcement members in the specification was modified. The calculated values are in good agreement with the experimental values.

Data availability statement

The raw data supporting the conclusion of this article will be made available by the authors, without undue reservation.

Author contributions

Data curation, XW; investigation, JL; writing original draft, LH and WX; writing-review and editing, ZC.

Funding

This research report was financially supported by the National Natural Science Foundation of China (No. 51578163), Guangxi Science and Technology Base and Talent Special Project (AD21075031), Guangxi Key R&D Project (AB21220012), Central Funding Project for Local Science and Technology Development (ZY21195010), Special fund project for Bagui scholars [(2019) No. 79], Nanning Key R&D Project (20223024).

Acknowledgments

The authors are very grateful for the support of the above project funds.

Conflict of interest

Author LH was employed by the company Guangxi Road and Bridge Group Construction Engineering Co., Ltd.

The remaining authors declare that the research was conducted in the absence of any commercial or financial relationships that could be construed as a potential conflict of interest.

Publisher's note

References

Ajdukiewicz, A. B., and Kliszczewicz, A. T. (2007). Comparative tests of beams and columns made of recycled aggregate concrete and natural aggregate concrete. *J. Adv. Concr. Technol.* 5 (2), 259–273. doi:10.3151/jact.5.259

Algourdin, N., Pliya, P., Beaucour, A. L., Noumowé, A., and di Coste, D. (2022). Effect of fine and coarse recycled aggregates on high-temperature behaviour and residual properties of concrete. *Constr. Build. Mater.* 341, 127847. doi:10.1016/j.conbuildmat.2022.127847

Behera, M., Bhattacharyya, S. K., Minocha, A. K., Deoliya, R., and Maiti, S. (2014). Recycled aggregate from C&D waste & its use in concrete a breakthrough towards sustainability in construction sector: A review. *Constr. Build. Mater.* 68, 501–516. doi:10.1016/j.conbuil

Cao, W., Liu, Q., Zhang, J., Zhang, Y., and Yin, H. (2011). Research on seismic performance of lowrise recycled concrete shear walls. *J. Beijing Univ. Technol.* 37 (03), 409–417.

Cao, W., Zhu, K., Jiang, W., Chen, G., Lin, D., and Peng, S. (2016). Experimental study on stress-strain constitutive relationship of high strength recycled concrete. *J. Nat. Disasters* 25 (02), 167–172. doi:10.13577/j.jnd.2016.0220

Chen, J. (2018). Study on the interfacial bonding property of high strength concrete pipe after simulated fire water cooling. Master's thesis. Nanning (China). Guangxi University.

Chen, Z., Chen, Y., and Yao, K. (2014). Experimental research on mechanical behavior and influence factor of recycled coarse aggregate concretes under triaxial compression. *J. Build. Struct.* 35, 72–81. doi:10.14006/j.jzjgxb.2014.12.010

Chen, Z., Fan, J., Ye, P., and Zhen, W. (2013). Experimental study on mechanical behavior of reinforced recycled aggregate concrete beams. *Build. Struct.* 43 (09), 92–99. doi:10.19701/j.jzjg.2013.09.017

Chen, Z., Jia, H., and Li, S. (2022). Bond behavior of recycled aggregate concrete-filled steel tube after elevated temperatures. *Constr. Build. Mater.* 325, 126683. doi:10.1016/j.conbuildmat.2022.126683

Chen, Z., Ye, P., Xv, J., and Liang, Y. (2015). Mechanical behavior of reinforced recycled aggregate concrete short columns under axial compression after high temperature. *J. Build. Struct.* 36 (06), 117–127. doi:10.14006/j.jzjgxb.2015.06.015

Dai, J., Xu, Z. D., Gai, P. P., and Hu, Z. W. (2021). Optimal design of tuned mass damper inerter with a Maxwell element for mitigating the vortex-induced vibration in bridges. *Mech. Syst. Signal Process.* 148, 107180. doi:10.1016/j.ymssp.2020.107180

De Silva, D., Andreini, M., Bilotta, A., De Rosa, G., La Mendola, S., Nigro, E., et al. (2022). Structural safety assessment of concrete tunnel lining subjected to fire. *Fire Saf. J.* 134, 103697. doi:10.1016/j.firesaf.2022.103697

Dong, H., Wang, P., Cao, W., Zhang, J., and Bian, J. (2013). Experimental study and theoretical analysis on fire resistant performance of recycled concrete tubular structures. *J. Build. Struct.* 34 (08), 65–71. doi:10.14006/j.jzjgxb.2013.08.001

Ercolani, G., Ortega, N. F., Priano, C., and Senas, L. (2017). Physical–mechanical behavior of concretes exposed to high temperatures and different cooling systems. *Struct. Concr.* 18 (3), 487–495. doi:10.1002/suco.201500202

Garcia-Troncoso, N., Li, L., Cheng, Q., Mo, K. H., and Ling, T.-C. (2021). Comparative study on the properties and high temperature resistance of self-compacting concrete with various types of recycled aggregates. *Case Stud. Constr. Mater.* 15, 00678. doi:10.1016/j.cscm.2021.e00678

Ge, T., Xu, Z. D., and Yuan, F. G. (2022). Predictive model of dynamic mechanical properties of VE damper based on acrylic rubber–graphene oxide composites considering aging damage. *J. Aerosp. Eng.* 35 (2), 04021132. doi:10.1061/(asce)as.1943-5525.0001385

Huang, L., Liang, J., Gao, C., and Yan, L. (2021). Flax FRP tube and steel spiral dual-confined recycled aggregate concrete: Experimental and analytical studies. *Constr. Build. Mater.* 300, 124023. doi:10.1016/j.conbuildmat.2021.124023

Kumar, M. V., Siddaramaiah, Y. M., and Raj, S. J. (2022). Shear behaviour of GFRP retrofitted spiral transverse reinforced concrete beams with partially replaced recycled aggregates. *Mater. Today Proc.* 65, 1642–1650. doi:10.1016/j.matpr.2022.04.700

Laneyrie, C., Beaucour, A.-L., Green, M. F., Hebert, R. L., Ledesert, B., and Noumowe, A. (2016). Influence of recycled coarse aggregates on normal and high performance concrete subjected to elevated temperatures. *Constr. Build. Mater.* 111, 368–378. doi:10.1016/j.conbuildmat.2016.02.056

Li, H., Xu, Z., Gomez, D., Gai, P., Wang, F., and Dyke, S. J. (2022). A modified fractional-order derivative zener model for rubber-like devices for structural control. *J. Eng. Mech.* 148 (1), 04021119. doi:10.1061/(asce)em.1943-7889.0002027

Limbachiya, M., Meddah, M. S., and Ouchagour, Y. (2012). Use of recycled concrete aggregate in fly-ash concrete. *Constr. Build. Mater.* 27 (1), 439–449. doi:10.1016/j.conbuildmat.2011.07.023

Liu, B., Chen, L., Zhou, A., Zhen, Y., and Fu, L. (2011). Experimental study on seismic behavior of recycled aggregate concrete beam-column interior-joints. *J. Build. Struct.* 32, 109–115.

Lu, H., Xu, Z. D., Iseley, T., and Matthews, J. C. (2021). Novel data-driven framework for predicting residual strength of corroded pipelines. *J. Pipeline Syst. Eng. Pract.* 12 (4), 04021045. doi:10.1061/(asce)ps.1949-1204.0000587

Lu, Z., and Su, L. (2010). The Chinese research progress on damage mechanism and evaluation on method of concrete structure after fire in China. *J. Build. Struct.* 31 (2), 202–209.

Mohammad, A., Abdulsamee, H., and Amin, A. (2021). Experimental study on compressive strength of recycled aggregate concrete under high temperature. *Struct. Durab. Health Monit.* 15, 335–348. doi:10.32604/sdhm.2021.015988

Muhammad, J. M., Kazmi, S. M. S., Wu, Y. F., Patnaikuni, I., Zhou, Y., and Xing, F. (2020). Stress strain performance of steel spiral confined recycled aggregate concrete. *Cem. Concr. Compos.* 108, 103535. doi:10.1016/j.cemconcomp.2020.103535

Muhammad, J. M., Wu, Y. F., Kazmi, S. M. S., Patnaikuni, I., Zhou, Y., and Xing, F. (2019). Stress-strain behavior of spirally confined recycled aggregate concrete: An approach towards sustainable design. *Resour. Conserv. Recycl.* 146, 127–139. doi:10.1016/j.resconrec.2019.03.043

Ni, S., and Gernay, T. (2020). Predicting residual deformations in a reinforced concrete building structure after a fire event. *Eng. Struct.* 202, 109853. doi:10.1016/j.engstruct.2019.109853

Raza, A., Manalo, A. C., Rafique, U., AlAjarmeh, S., and Khan, Q. Z. (2021). Concentrically loaded recycled aggregate geopolymer concrete columns reinforced with GFRP bars and spirals. *Compos. Struct.* 268, 113968. doi:10.1016/j.compstruct.2021.113968

Shahraki, M., Hua, N., Elhami-Khorasani, N., Tessari, A., and Garlock, M. (2022). Residual compressive strength of concrete after exposure to high temperatures: A review and probabilistic models. *Fire Saf. J.* 2022, 103698. doi:10.1016/j.firesaf.2022.103698

Su, Z., and Chen, Z. (2021). Study on axial compression properties and damage of concrete filled square or circular steel tube columns after being subjected to elevated-temperatures spray cooling. *Fire Sci. Technol.* 40 (12), 1762–1769.

Sun, B., Liu, X., and Xu, Z. D. (2022). A multiscale bridging material parameter and damage inversion algorithm from macroscale to mesoscale based on ant colony optimization. *J. Eng. Mech.* 148 (2), 04021150. doi:10.1061/(asce)em.1943-7889.0002067

Wang, Y., Gong, J., Qu, S., Zhang, B., and Chen, Y. (2022). Mechanical properties of steel reinforced concrete T-shaped column after high temperature. *Structures* 46, 852–867. doi:10.1016/j.istruc.2022.10.117

Wang, Y., Chen, J., Zong, B., and Geng, R. (2011). Mechanical behavior of axially loaded recycled aggregate concrete filled steel tubular stubs and reinforced recycled aggregate concrete stub. *J. Build. Struct.* 32, 170–177. doi:10.14006/j.jzjgxb.2011.12.002

Woo, K. S., Lee, B. S., Kim, Y. S., Lee, S. H., and Kim, K. H. (2018). Structural performance of recycled aggregate concrete confined by spiral reinforcement. *J. Asian Archit. Build. Eng.* 17 (3), 541–548. doi:10.3130/jaabe.17.541

Wu, B. (2003). *The mechanical properties of reinforced concrete structures after fire*. Beijing, China: Science Press, 135–140.

Xiao, J., and Huang, Y. (2006). Residual compressive strength of recycled concrete after high temperature. *J. Build. Mater.* 9 (03), 255–259. doi:10.1016/j.conbuildmat.2016.02.056

Xiao, J., Sun, Y., and Falkner, H. (2006). Seismic performance of frame structures with recycled aggregate concrete. *Eng. Struct.* 28 (1), 1–8. doi:10.1016/j.engstruct.2005.06.019

Xu, Z. D., Yang, Y., and Miao, A. N. (2021). Dynamic analysis and parameter optimization of pipelines with multidimensional vibration isolation and mitigation device. *J. Pipeline Syst. Eng. Pract.* 12 (1), 04020058. doi:10.1061/(asce)ps.1949-1204.0000504

Yu, M., Hu, X., Xu, L., and Cheng, S. (2022). A general unified method for calculating fire resistance of CFST columns considering various types of steel and concrete. *J. Build. Eng.* 59, 105125. doi:10.1016/j.jobe.2022.105125

Zheng, Y., Zhang, Y., and Zhang, P. (2021). Methods for improving the durability of recycled aggregate concrete: A review. *J. Mater. Res. Technol.* 15, 6367–6386. doi:10.1016/j.jmrt.2021.11.085

Zhou, J., Chen, Z. P., Zhou, C. H., and Jin, C. G. (2022). Eccentric compression behavior and bearing capacity calculation of steel-concrete composite square columns confined with spiral bars. *Eng. Mech.* 39. doi:10.6052/j.issn.1000-4750.2021.08.0613

frontiers | Frontiers in Materials

TYPE Original Research
PUBLISHED 19 December 2022
DOI 10.3389/fmats.2022.1094696

OPEN ACCESS

EDITED BY
Zhigang Zhang,
Chongqing University, China

REVIEWED BY
Tengfei Xu,
Southwest Jiaotong University, China
Haijun Wu,
Chongqing Jiaotong University, China

*CORRESPONDENCE
Yin Shen,
shenyin@tongji.edu.cn

SPECIALTY SECTION
This article was submitted to Structural Materials, a section of the journal Frontiers in Materials

RECEIVED 10 November 2022
ACCEPTED 06 December 2022
PUBLISHED 19 December 2022

CITATION
Huang G, Wu B, Shen Y, Wang L and Li G (2022), Comparative experiment of steel bar corrosion at concrete construction joints.
Front. Mater. 9:1094696.
doi: 10.3389/fmats.2022.1094696

Comparative experiment of steel bar corrosion at concrete construction joints

Guohua Huang[1], Binzhong Wu[1], Yin Shen[2]*, Li Wang[1] and Guoping Li[2]

[1]Powerchina Roadbridge Group Co., LTD, Beijing, China, [2]College of Civil Engineering, Tongji University, Shanghai, China

Introduction: Construction joint is common and even inevitable in most of the reinforcement concrete structures. This study was to assess the effect of construction joints on chloride-induced corrosion of reinforcing steel in concrete.

Methods: Test parameters included two environmental conditions (salt solution immersion condition and cyclic wet-dry condition), two forms of construction joint (direct wet joint and roughened wet joint) and four types of steel bar (mild steel bar, ferritic stainless-steel bar, austenitic-ferritic stainless-steel bar and epoxy-coated steel bar). The corrosion test of 90 specimens was carried out by electrochemical accelerated corrosion method. The weight loss of each steel bar and steel bar section in specimens was measured. An influence coefficient (k_j) of construction joint on local weigh loss of steel bars was defined.

Results: Except for epoxy-coated steel bars, the most severe corrosion of experimental steel bars in concrete specimens all occurred at the joints, while the corrosion in non-joint sections of steel bars was relatively uniform and less. The weight loss rate of specimens has the range of 1.18% to 15.73% with an average value of 6.22%. The average k_j of mild steel bars, S11203 stainless steel bars, and S23043 stainless steel bars are 1.38, 1.92, and 1.97, respectively. The average k_j of specimens in immersion condition and cyclic wet-dry condition are 1.44 and 2.07. The corrosion of epoxy-coated steel bars mainly occurred at the damage locations of epoxy coating, not mainly at the joints.

Conclusion: Chloride-induced corrosion of steel bars at construction joints was always more severe than at non-joints, especially in cyclic wet-dry environments, even for stainless-steel bar, but epoxy-coated steel bars were excluded.

KEYWORDS

construction joint, steel bar corrosion, electrochemical acceleration corrosion, immersion, wet–dry cycle

1 Introduction

Reinforced concrete structures are widely used in coastal engineering. Many studies have shown that the durability failure of reinforced concrete structures in the marine environment is mainly due to the corrosion of reinforcement in concrete (Goyal et al., 2018; Choe et al., 2020). In the literature, many researches have been performed on reinforcement corrosion in continuously casted concrete members (Guoping et al., 2011; Andrade 2019). However, due to the concrete construction methods and capacity of mixing plan and manpower, it is very common for concrete to be poured in segments or batches in reinforced concrete structures (Sung-Won and Seung-Jun 2016). Construction joints are concrete-to-concrete interfaces formed by placing fresh or hardened concrete parts against a hardened concrete substrate.

From the literature, construction joint is also a kind of cold joint (Yoon et al., 2020). Kara (2021) conducted strength and durability tests on concrete with cold joints and found that after dry-wet cycles, the weight loss of concrete with cold joints was greater than that of the monolithic concrete sample, and the tensile strength loss rate was 42.07%. Zega et al. (2021) experimented and found that the cold joint in normal concrete had a decrease in flexural and compressive strength, so did with the concrete with superplasticizer. Vanlalruata and Marthong (2021) conducted flexural strength tests of 40 beams and showed that the loss in flexural strength due to the present of cold joint in a reinforced concrete beam ranges from 2% to 20% for different mix and age of the joints. Those indicated that the concrete with cold joint is more prone to cracking under working conditions because of the loss of tensile strength, which accelerates the degradation of concrete (Yang et al., 2018).

Moreover, Li et al. (2017) conducted a series of accelerated carbonation tests and proved that the carbonation depth of concrete at a construction joint was higher than that of monolithic concrete even in the absence of tensile stress. Several salt solution immersion tests showed that the chloride penetration at a construction joint was faster. Mun and Kwon (2016) presented an evaluation of cold joint and loading conditions on chloride diffusion behavior, and the study showed that chloride diffusion coefficient under 30% level of compressive stress significantly increases by 1.7 times compared with normal condition. Li et al. (2016) conducted a salt solution immersion test on six specimens with direct wet joints, roughened wet joints and epoxied joints and conclude that monolithic concrete had optimal resistance to chloride ions, better than the direct wet joints and roughened wet joints. Shen et al. (2019) conducted a freeze–thaw cycle test in the laboratory and found that construction joints increased the mass loss of specimens. Many studies have pointed out that construction joint may become the weakness of concrete durability. Therefore, the steel bars at the construction joints are relatively easier to contact with chloride ions, water vapor, oxygen and other substances that accelerate the corrosion of steel bars (Koh et al., 2019). Once the harmful substances reach the critical concentration, the steel bars will begin to rust at the construction joints, reducing the effective section areas of the steel bars and endangering the durability and safety of the structure.

For the study of steel corrosion, most of them use electrochemical technology. In the 1950s, electrochemical techniques were applied to study the corrosion of steel in cement-based materials (Stern and Geaby 1957). In the study of durability of reinforced concrete structures, electrochemical technology is basically used to accelerate the corrosion of steel bars in concrete. Although it must be noted that there are obvious differences between electrochemical accelerated corrosion and natural corrosion in terms of electrochemical mechanism, corrosion products and corrosion morphology (Song et al., 2008), electrochemical accelerated corrosion can qualitatively characterize the degradation of structural performance. With the development of durability research, electrochemical technology has been applied to the study of mechanical properties of corroded steel bars, bond-slip performance of corroded reinforced concrete (Zhou et al., 2015; Zhou et al., 2017), structural performance degradation of reinforced concrete beams (Ou and Nguyen 2016) and piers (Yuan et al., 2018; Zhou et al., 2020). At present, many specifications are based on the data of electric accelerated corrosion method for the deformation calculation, mechanical performance evaluation and life prediction theory of corroded reinforced concrete members.

Many tests have pointed out that the construction joints have a negative effect on the durability of concrete, and the conclusions are based on indicators such as carbonation coefficient and chloride diffusivity. However, the corrosion propagation test of steel bars at the joints that can accurately represent the performance degradation of concrete structures has not been reported. Therefore, this paper explored the corrosion morphology of steel bars at joints, compared the difference of steel bar rust amount at joints and non-joints, and investigated the corrosion characteristics of different steel bars at joints. The comparative test in this paper was to provide basic test data and reference for further research and helped engineers to further understand the impact of construction in harsh marine environment on the long-term corrosion resistance of important infrastructure such as bridges.

The present study mainly focuses on the comparison of steel corrosion test phenomena at construction joints and the analysis and interpretation of measured data under different steel bar types, joint types and different environments. The material transportation at construction joints will be examined in a future study by means of meso-scale numerical simulation.

2 Materials and methods

2.1 Materials

The concrete material and mix proportions are listed in Table 1. Crushed stone with maximum aggregate size distributed from 5 to 25 mm was used as the coarse aggregate. River sand with a fineness

TABLE 1 Concrete material and mix proportions.

Concrete strength[a] (MPa)	Water/cement ratio	Cement (kg)	Fine aggregate (kg)	Coarse aggregate (kg)	Water (kg)	Water reducer (%)
49.99	0.36	482	598	1147	173	0.8

[a]Concrete strength is the average cubic compressive strength of three 150 mm test cubes.

TABLE 2 Chemical composition of rebars.

Steel type	Chemical composition (%)									
	C	Si	Mn	P	S	Ni	Cr	Mo	Cu	N
MS/EP	0.25	0.8	1.6	0.045	0.045	—	—	—	—	—
S11203	0.03	1.0	1.0	0.04	0.03	0.6	11.0	—	—	—
S23043	0.03	1.0	2.5	0.035	0.03	3.00	21.5	0.05	0.05	0.05

Note: MS, mild steel rebar; EP, epoxy-coated steel rebar; S11203, ferritic stainless steel rebar (named S11203 in GB/T 20878-2007, China); S23043, austenitic-ferritic (duplex) stainless steel rebar (named S23043 in GB/T 20878-2007, China).

TABLE 3 Details of parameters and quantities.

Condition	Joint type	Steel bar type	Id	Quantity
Immersion	Roughened wet joint	Mild steel	IC-RJ-MS	6
		Epoxy-coated steel	IC-RJ-EP	5
		Stainless steel S11203	IC-RJ-S11203	5
		Stainless steel S23043	IC-RJ-S23043	5
	Direct wet joint	Mild steel	IC-DJ-MS	6
		Epoxy-coated steel	IC-DJ-EP	5
		Stainless steel S11203	IC-DJ-S11203	5
		Stainless steel S23043	IC-DJ-S23043	5
Wet–dry cycle	Roughened wet joint	Mild steel	WD-RJ-MS	6
		Epoxy-coated steel	WD-RJ-EP	6
		Stainless steel S11203	WD-RJ-S11203	6
		Stainless steel S23043	WD-RJ-S23043	6
	Direct wet joint	Mild steel	WD-DJ-MS	6
		Epoxy-coated steel	WD-DJ-EP	6
		Stainless steel S11203	WD-DJ-S11203	6
		Stainless steel S23043	WD-DJ-S23043	6

Note: IC, immersion condition; WD, wet–dry cycle condition; RJ, roughened wet joint; DJ, direct wet joint.

modulus of 2.71 was chosen as the fine aggregate in the mixes. The water/cement ratio for the mixtures was 0.36.

All test rebars were ribbed with a diameter of 16 mm and yield design strength of 400 MPa. The chemical composition of rebars are listed in Table 2.

2.2 Test parameters

A total of 16 categories were considered, including 90 specimens. A construction joint was made in the middle of each specimen, and the specimens were long enough, so that both

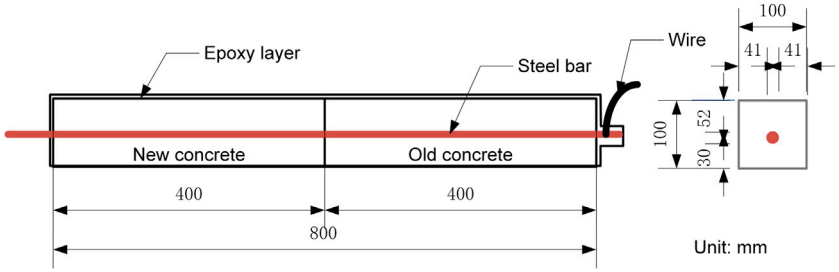

FIGURE 1
Specimen dimensions.

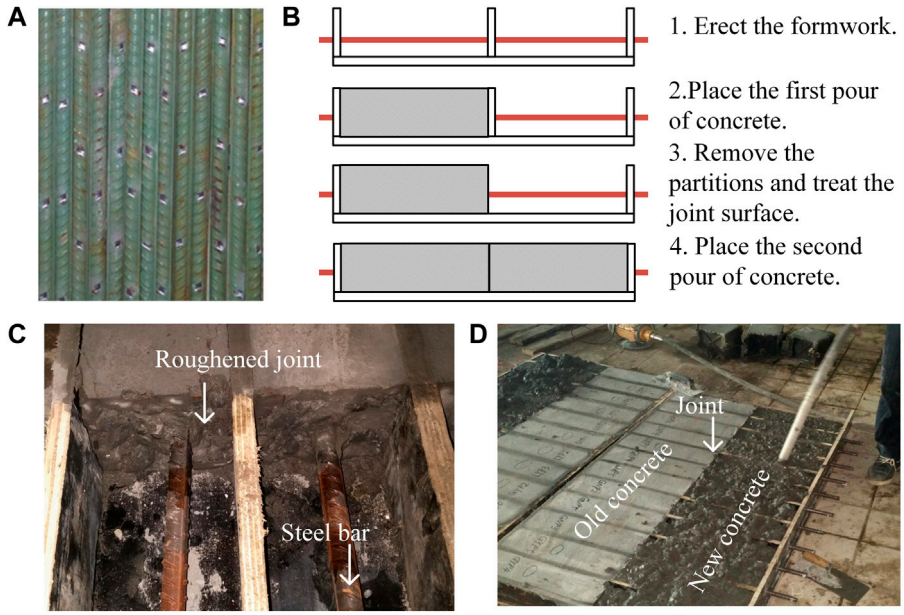

FIGURE 2
Specimen preparation. **(A)** Epoxy-coated rebars. **(B)** Fabrication process. **(C)** Roughened interface at joint. **(D)** Specimen casting.

side parts of specimens that didn't contain joints could be as control parts, and the test conditions were exactly the same, so this experiment didn't design separate control specimens. The experimental parameters are described as follows:

1) Two marine environmental conditions (James et al., 2019) were selected, namely a chlorine salt solution immersion condition and a cyclic wet–dry condition. The former was used to simulate a seawater immersion environment, and the latter was used to simulate the tidal environment.
2) Two forms of construction joint were studied, the direct wet joint and roughened wet joint (Júlio et al., 2004). Direct wet joint refers to a joint formed by pouring fresh concrete directly without special treatment on the substrate surface, while roughened wet joint refers to a joint with a substrate surface roughened by jack hammers.
3) Four types of rebar were tested: mild steel bar, ferritic stainless-steel bar (named S11203 in GB/T 20878-2007, China), austenitic-ferritic (duplex) stainless-steel bar (named S23043 in GB/T 20878-2007, China), and epoxy-coated rebar. These are the main types of rebar commonly used in concrete structures in marine and coastal harsh environments (Lollini et al., 2019).

The experimental categories and specimen quantities are listed in Table 3.

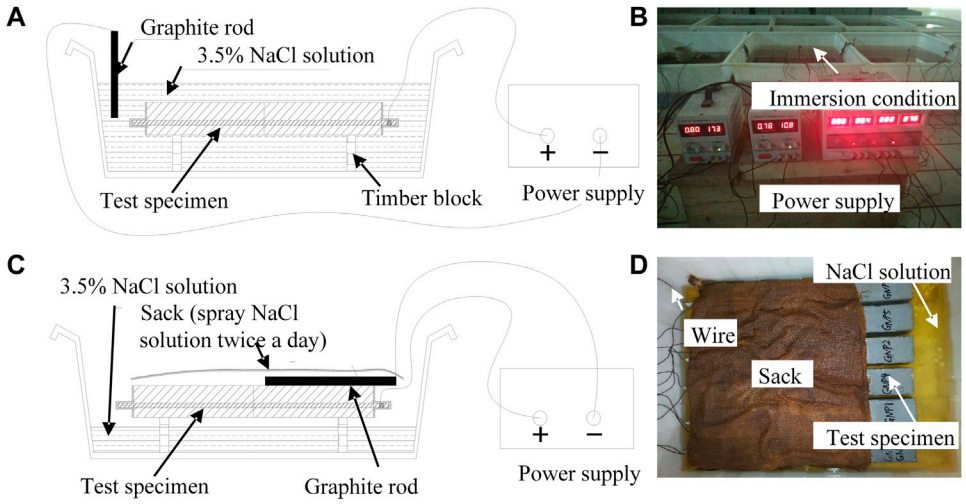

FIGURE 3
Electrochemically accelerated corrosion. **(A,B)** Immersion condition. **(C,D)** Wet–dry cycle condition.

2.3 Specimen fabrication

The design of specimens referred to the Standard for Testing the Long-Term Performance and Durability of Ordinary Concrete (GB/T 50082-2009, China). Thus, the dimensions 100 × 100 × 800 mm were selected for concrete prism specimens. A construction joint was located in the middle of each specimen as shown in Figure 1. The concrete cover thickness of the steel bar at the bottom was designed as 30 mm. The bottom surface of the specimen was set as the exposed face to experimental conditions, and the side and top surface were sealed with epoxy resin to avoid the intrusion of chloride ions.

The length of each rebar was 900 mm. First, all mild steel and stainless-steel bars were polished to remove the rust spots. For epoxy-coated rebars (Figure 2A), man-made scratches were added to the epoxy coating to simulate irregular damage in the transportation of epoxy rebars and concrete construction. The epoxy coating at scratches was completely damaged and the substrate was exposed. The size of a scratch was about equal to the rib spacing of rebar and the scratches was evenly distributed. The ratio of coating damage was about 5%. Then, all rebars were labeled and the length and weight were accurately measured.

Each specimen was molded in two parts and the fabrication process is shown in Figure 2B. The part of old concrete was first casted. After 3 days, all partitions at joints were removed. In 2 days, the joint interface on old concrete of each specimen with roughened joint was artificially scabbled as shown in Figure 2C, and kept in a saturated surface dry state according to current construction practice in China. Then the part of new concrete was placed as shown in Figure 2D. After three more days, all formworks were removed, and all specimens were placed in a standard maintenance room with a temperature of 20°C ± 2°C and a relative humidity of 95% for 28 days.

2.4 Test method

The comparative experiments were carried out by the electrochemical acceleration corrosion method. Direct current in a parallel manner was used to accelerate corrosion, as shown in Figure 3.

For Group IC in the immersion condition, all specimens directly and completely immersed in chlorine salt solution (Figures 3A, B). Given that the salinity of seawater is of 3.5% NaCl, a 3.5 wt% NaCl solution was used for corrosion experiments. As the water in the basin evaporated, the solution level in the basin was checked every 3 days and the water was supplemented in time. The steel bar was connected with the positive electrode of the steady voltage DC power supply as the anode of the electrochemical reaction; the graphite rod was directly placed in the solution as a cathode.

For Group WD in the dry-wet cycle condition, all specimens were supported by bolsters above the chloride solution (Figures 3C, D), and the same solution was sprayed periodically onto the specimens twice a day. Graphite rod as cathode, directly flat on the top of the specimen. In order to prevent the solution from evaporating too quickly and length of exposure to the humid environment being too short after spraying, a layer of gauze was spread on specimens, and a thick cotton sack covered the gauze for moisture storage.

Before the experiments were conducted, all specimens were placed in the experimental conditions for 1 week to ensure that

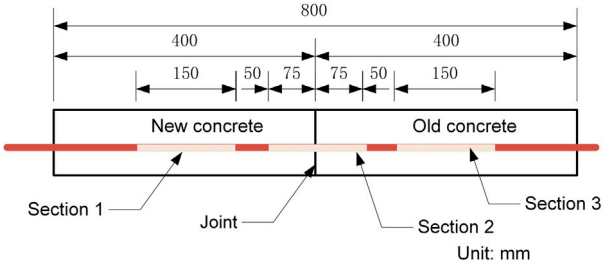

FIGURE 4
Sections of rebar.

the subsequent electrochemical reaction could formed an electrical circuit.

The initial current density was controlled at about 100 μA/cm^2, which was checked periodically to ensure its stability. In the dry stage of dry-wet cycles, the current density was significantly reduced. In order to reflect the influence of dry-wet cycle conditions, only the current density in the wet stage was stably controlled during the test. The corrosion time was set at 60 days.

After corrosion experiments, the specimens were broken, and the steel bars were taken out. The concrete adhering to the steel bars was scraped off. Then, the steel bars were pickled with 12% hydrochloric acid solution, rinsed, and dried for weighing.

After each full steel bar was accurately weighed, the mild steel bars and two types of stainless-steel bars were cut into multiple sections and three of them were taken. The length and position of the cut sections are shown in Figure 4. The length and weight of each section were accurately measured.

The weight loss rates of full rebars were calculated as follows:

$$L_\omega = \frac{\omega_0 - \omega}{\omega_0} \times 100\%$$

In the equation above L_ω is weight loss rate of the steel bar; ω_0 is the weight of the steel bar before corrosion (g); and ω is the mass of the corroded steel bar after pickling (g).

Assuming that the initial mass of steel bar was uniformly distributed along the length, the initial mass of each section was determined proportionally, and then the rust amount of each section was calculated. An influence coefficient of construction joint on local weight loss of a rebar was defined and calculated as follows:

$$k_j = \frac{2m_2}{m_1 + m_3}$$

In the equation above m_2 is the rust amount of the rebar in joint section 2 (g); m_1 is the rust amount of the rebar in non-joint section 1 (g); and m_3 is the rust amount of the rebar in non-joint section 3 (g).

3 Test results and discussion

3.1 Rust morphologies

Most of the specimens developed rust expansion cracks on the side of the concrete cover exposed to test conditions, as shown in Figure 5. All the cracks appeared along the direction of steel bars, and there were no cracks in the vertical direction of steel bars. No interface cracks developed at the joint, and the joint interface maintained good continuity before and after the test. Because the width of rust expansion cracks is affected by many factors such as the shape of bar and the presence of stirrups (Okazaki et al., 2020), the width of cracks in the experiments was not measured. However, by observing the cracks of all specimens, it was found that the crack widths of WD specimens (Figure 5A) were relatively larger than those of IC specimens (Figure 5B). In addition, the type of steel bar had a significant impact on the widths of the rust expansion cracks. The widths of cracks on mild steel specimens were obviously the largest, while those on stainless steel specimens were relatively small, and there were almost no visible cracks on specimens with epoxy-coated rebars.

The rust morphologies of rebars at different positions are shown in Figure 6.

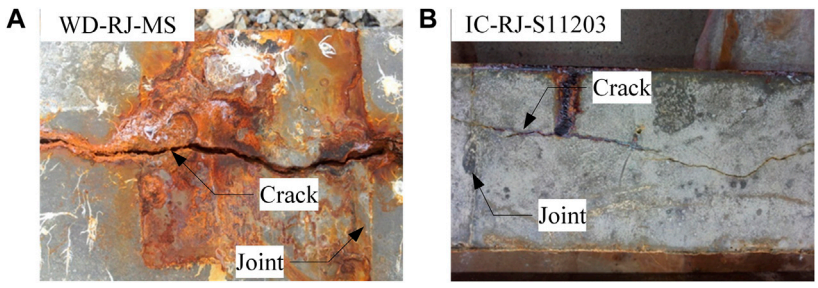

FIGURE 5
Rust expansion cracks on specimens. **(A)** WD-RJ-MS. **(B)** IC-RJ-S11203.

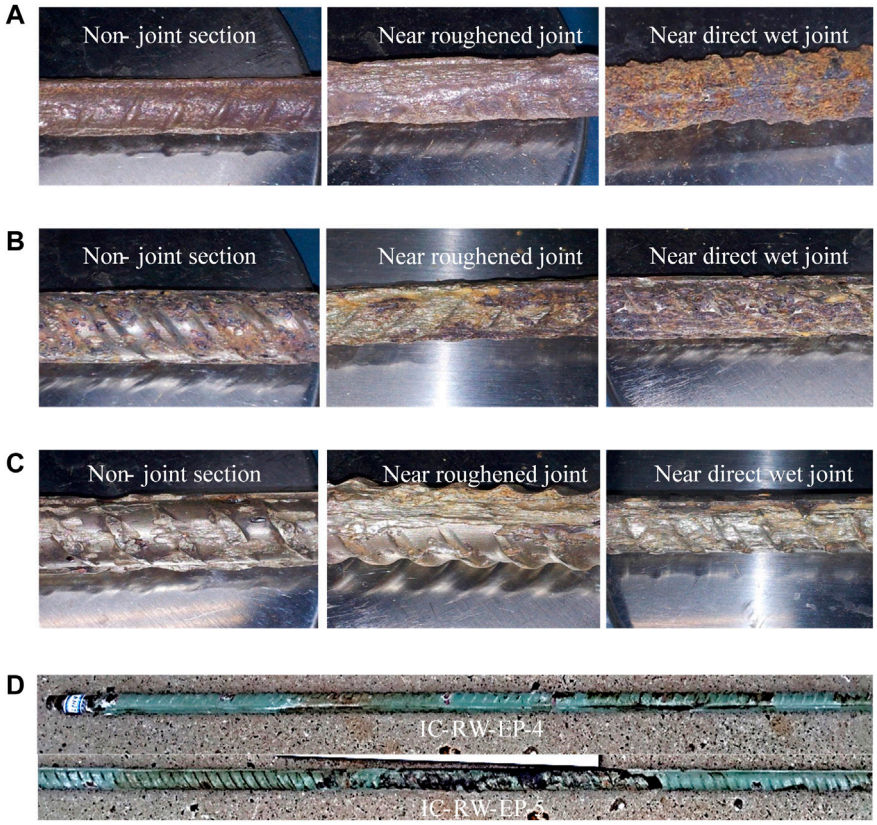

FIGURE 6
Rust morphologies of rebars. **(A)** Mild steel rebars. **(B)** S11203 rebars. **(C)** S23043 rebars. **(D)** Epoxy-coated steel rebars.

For mild steel bars (Figure 6A), the most severe corrosion of steel bars occurred at the joints. The corrosion developed from the joints to both sides. Most of mild steel bar surface was relatively smooth, some mild steel bars had longitudinal gullies, which was different from natural corrosion under pitting (Alonso et al., 2019). The corrosion of the non-joint section was more uniform along the surface of mild steel bar, and there was no obvious pitting corrosion. However, the concrete cover side of mild steel bar was more severely corroded than the backside, and the cross section of mild steel bar was elliptical after corrosion.

For S11203 stainless steel bars (Figure 6B), corrosion was mainly concentrated at the joints. The corrosion of the concrete cover side of S11203 bar was more severe, and no obvious corrosion was found on the side away from the cover. Moreover, the corrosion of S11203 bar at the joint was transversely fine and wavy, with less pit corrosion, which was quite different from that of mild steel bar. There were many corrosion pits and some corrosion spots on the surface of S11203 steel bar away from the joint.

The corrosion of S23043 stainless steel bar (Figure 6C) was similar to that of S11203. At the joints, the corrosion surface of S23043 bar was relatively smooth and the pitting corrosion was relatively less. However, far away from the joint, the corrosion pit of S23043 steel bar was larger and less intensive than that of S11203, which was probably because the composition of the two stainless steel bars was different. S23043 was a duplex stainless-steel bar, which was mainly composed of austenite and ferrite (Alonso et al., 2019), while S11203 was mainly composed of ferrite, and the chloride pitting resistance of ferrite was better than austenite (Chen 2020), so S23043 bar corrosion pit was generally larger.

The corrosion of epoxy-coated steel bars (Figure 6D) mainly occurred at the damage locations of epoxy coating (Sohail et al., 2019), not mainly at the joints. There were large corrosion pits at the damage locations, and brown rust adhered to the epoxy coating of the steel bars and the coating tended to peel off. When the epoxy coating at the joint was damaged and the damage was on the side of the concrete cover, the corrosion of the epoxy steel bar was the most severe, but there was no obvious corrosion on the backside.

Compared with mild steel bars, the rust of stainless-steel bars decreased from the joint to both sides more significantly and obviously. This phenomenon was due to the different

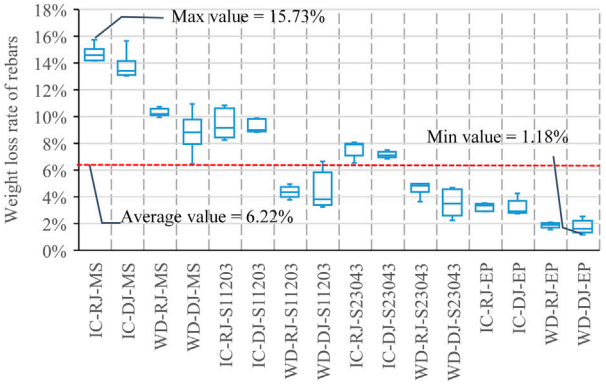

FIGURE 7
Weight loss rates of rebars.

content and form of iron in the two types of rebars. For mild steel bars with a high iron content, the electrolytic cells formed on the surface of rebars were more uniform, so the rust was more uniform. For stainless steel bars, because the iron was in the form of ferrite, austenite and other complexes, the large potential difference on the surface of rebars led to uneven distribution of the electrolytic cells. Therefore, the rust of the stainless-steel bars at the joints was relatively significant.

In general, except for epoxy-coated steel bars, the most severe corrosion of other steel bars all occurred at the joints, and the corrosion decreased from the joints to both sides, while the corrosion in non-joint sections was relatively uniform and less.

3.2 Weight loss rate of full bar

The box chart of the weight loss rate of all groups of full rebars is shown in Figure 7. There are no abnormal outliers in the figure. The average value of the weight loss rate of each group of specimens is shown in Table 4. The loss rate of specimens has the range of 1.18%–15.73% with an average value of 6.22%, which shows that there are big differences between different series.

3.3 Comparison of weight loss rate of full bar

In Figure 8, the box chart of the weight loss rate of rebars is shown by category. The figure shows that the average relationship of the weight loss rate of full rebars is mild steel bars > S11203 rebars > S23043 bars > epoxy-coated rebars. This means that the corrosion resistance of mild steel bars is the worst, and that of stainless-steel bars is better. Among them, the corrosion resistance of S23043 rebars is slightly better than that of S11203 rebars. The corrosion of

TABLE 4 Weight loss and percentage.

Id	$\overline{\omega_0}$ (g)	$\overline{\omega_0 - \omega}$ (g)	$\overline{L_\omega}$	$\overline{m_2}$ (g)	$\overline{0.5(m_1 + m_3)}$ (g)	$\overline{k_j}$
IC-RJ-MS	1222.77	179.53	14.68%	43.69	33.16	1.32
IC-DJ-MS	1219.92	167.34	13.71%	37.92	32.33	1.17
WD-RJ-MS	1215.06	125.11	10.29%	30.56	21.69	1.41
WD-DJ-MS	1212.00	106.77	8.81%	27.24	17.02	1.63
IC-RJ-S11203	1292.70	121.97	9.46%	36.28	20.97	1.73
IC-DJ-S11203	1308.09	121.36	9.28%	29.26	20.10	1.46
WD-RJ-S11203	1319.66	57.73	4.37%	19.14	9.74	1.97
WD-DJ-S11203	1302.69	58.20	4.46%	17.51	7.03	2.54
IC-RJ-S23043	1293.68	98.37	7.61%	28.51	18.19	1.57
IC-DJ-S23043	1258.18	89.91	7.14%	25.53	18.25	1.40
WD-RJ-S23043	1249.78	58.16	4.65%	18.42	7.99	2.33
WD-DJ-S23043	1251.76	44.12	3.53%	17.27	7.15	2.58
IC-RJ-EP	1288.80	41.61	3.23%	—	—	—
IC-DJ-EP	1288.36	41.11	3.19%	—	—	—
WD-RJ-EP	1286.85	24.19	1.88%	—	—	—
WD-DJ-EP	1283.91	22.39	1.74%	—	—	—

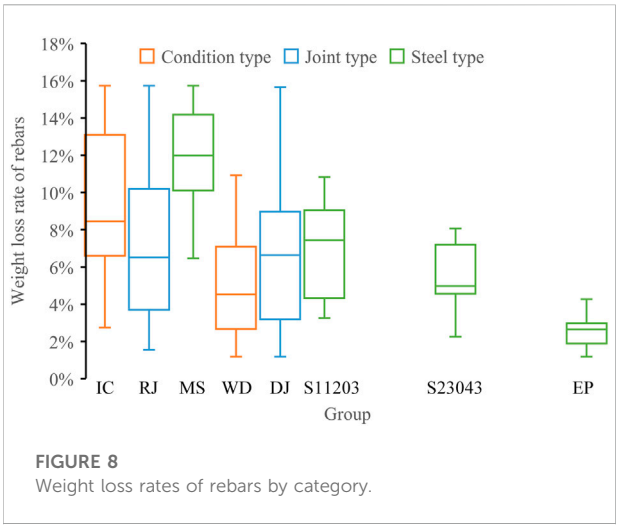

FIGURE 8
Weight loss rates of rebars by category.

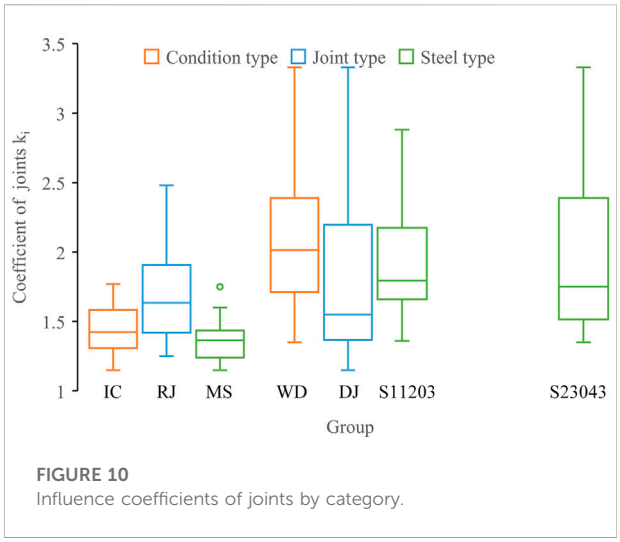

FIGURE 10
Influence coefficients of joints by category.

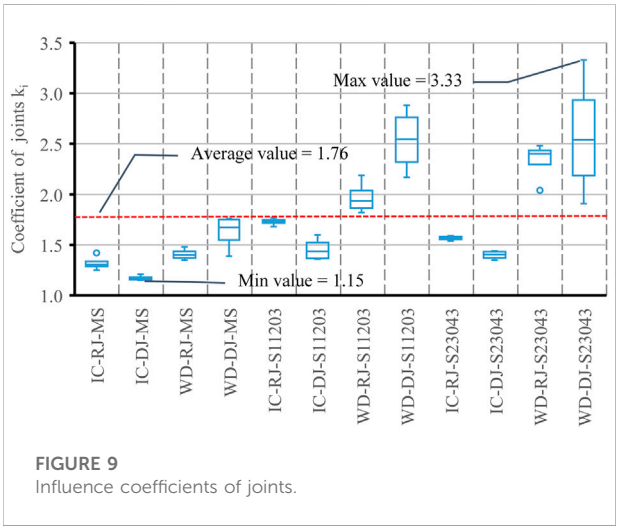

FIGURE 9
Influence coefficients of joints.

epoxy-coated rebars is the smallest, and the fluctuation is also the smallest.

From the perspective of joint type, the average rust amount of roughened wet joint (RJ) specimens is slightly greater than that of direct wet joint (DJ) specimens, and the fluctuations of the two categories are not much different. The ratio of the weight loss rate of RJ specimens to DJ specimens has an average value of 1.09. It is generally believed that the roughening is beneficial to the joint interface, which can make it better connect into a whole and conducive to load transfer (Santos and Julio 2011; Santos et al., 2012). However, experiments have shown that the interfacial scabbling deteriorates the compactness of the interface to a certain extent. The main reason may be that scabbling by a mechanism or high-pressure water flow causes certain damage to the concrete surface. This damage leads to micro-cracks on the surface of the concrete and makes it easier for chloride ions to pass through the concrete cover to the surface of the steel bars.

From the perspective of condition type, the rust amounts of rebars in the immersion environment are greater than that in the wet–dry cycle environment. The average ratio of weight loss rate is 1.71, but this does not mean that the immersion environment is more unfavorable than the wet–dry cycle environment. From the point of view of the test conditions, the energization time under the immersion environment was significantly longer, and the current in the dry environment stage under the wet–dry cycle environment was relatively small, which led to a slower electrochemical corrosion reaction.

3.4 Effect of joint on local weight loss

Considering that the corrosion resistance of epoxy steel bars was mainly determined by the quality of epoxy coating during the test time, the effect of concrete cover was less evident. Therefore, when the steel bars were cut off to compare the corrosion of joints and non-joints, the epoxy coated steel bars were excluded, and only the mild steel bars and two types of stainless steel bars were cut and weighed and analyzed.

The box diagram of the influence coefficient of construction joint on local weight loss (k_j) in 48 specimens is shown in Figure 9. The average rust amounts of rebars in the interception section and the average influence coefficient of construction joint on local weight loss are shown in Table 4. It can be seen that the rust amounts of steel sections at the joints of all concrete specimens are significantly greater than those of the non-joint sections. The influence coefficient of construction joint is in the range of 1.15–3.33, with an average value of 1.76. According to the experimental phenomena, the corrosion of each steel bar at the non-joint sections was relatively uniform, so the corrosion rate could be deduced by local weight loss in non-joint sections.

But the corrosion of steel bars at the joint sections are significantly higher than those of non-joint sections, the corrosion rate of steel bars may not effectively reflect this uneven phenomenon. So the influence coefficient of construction joint on local weight loss (k_j) can negatively reflected the influence of joints on the rust uniformity of rebars in concrete specimens with joints to some extent, and the construction joints are indeed a weakness of concrete durability.

In Figure 10, the box chart of the influence coefficient of construction joint on local weight loss is shown by category. The average influence coefficients of construction joint of mild steel bars, S11203 stainless steel bars, and S23043 stainless steel bars are 1.38, 1.92, and 1.97, respectively. The influence coefficients of construction joint of mild steel bars have relatively small fluctuation. The amount of rust in mild steel sections at construction joints is higher than that of stainless-steel sections as shown in Table 4, which is consistent with the aforementioned rust distribution of mild steel and stainless-steel bars. However, it can be concluded that the rust uniformity of mild steel bars affected by construction joints is relatively better, and the two types of stainless-steel bars have worse uniformity. Therefore, in coastal concrete structures using stainless steel reinforcement, it is recommended to consider the concentrated corrosion of steel bars that may occur at the joints.

The average influence coefficients of RJ specimens and DJ specimens are 1.72 and 1.80, respectively, and DJ specimens have more fluctuation as shown in Figure 10. From the perspective of the relationship of joint section and non-joint section, the interfacial roughening has no significant effect on the corrosion uniformity of rebars. However, the rust amounts of joint sections in RJ specimens are significantly greater than in DJ specimens as shown in Table 4. The ratio of the two ranges from 1.07 to 1.24, with an average value of 1.13, which is slightly larger than the ratio of the overall weight loss rate (1.09). This shows that roughening does cause certain defects to the faces on old concrete and affects the density of the joints. That is, roughening is to a certain extent unfavorable to the resistance to the penetration of chloride ions at construction joints.

The average influence coefficients of IC specimens and WD specimens are 1.44 and 2.07, respectively, and WD specimens have more fluctuation as shown in Figure 10. This indicates that the rust uniformity of rebars in the immersion environment is significantly lower than in the wet–dry cycle environment. The ratio of the two ranges from 0.54 to 0.97, with an average value of 0.72. This shows that the corrosion of rebars at the joints is more severe in the wet–dry cycle environment; that is, to say, the rust amounts of rebars in the immersion environment may be higher than in the wet–dry cycle conditions, but the wet–dry cycle conditions are relatively more unfavorable for the joints.

The test results showed that the construction joint had become the weakness of durability in concrete. According to the analysis of joint details and concrete characteristics, there were three main reasons. First, because of the difference of concrete pouring sequence, the construction joint is different from the general continuous casting concrete, and there is no coarse aggregate crossing distribution on the construction joint interface. Without the block of coarse aggregate, the transmission capacity of harmful substances in cement mortar is stronger. Secondly, in the early stage of hydration heat, the water in the newly casted concrete will migrate to the concrete substrate, resulting in an increase in the water-cement ratio of the fresh concrete near the interface, thereby reducing the durability of the interface. Finally, there are shrinkage differences in different casting ages of concrete. The restrained shrinkage will produce tensile strain in fresh concrete, which further deteriorates the durability of the interface.

4 Conclusion

In most of the reinforcement concrete structures, construction joint is common and even inevitable. This study deals with the effect of construction joint on corrosion of reinforcement in concrete. Based on experimental studies conducted, the following conclusions have been drawn:

1) Corrosion morphologies of four kinds of experimental steel bars in concrete were different. Except for epoxy-coated steel bars, the most severe corrosion of experimental steel bars all occurred at the joints, while the corrosion in non-joint sections was relatively uniform and less. The rust amounts of rebars at the joint sections were significantly greater than those of the non-joint sections, and the influence coefficient of construction joint on local weight loss is 1.15–3.33, with an average value of 1.76. And meanwhile, the corrosion of epoxy-coated steel bars mainly occurred at the damage locations of epoxy coating, not mainly at the joints.
2) Under the same environmental conditions and joint types, the corrosion resistance of stainless-steel bars and epoxy-coated steel bars at the joint is significantly better than that of mild steel bars. The corrosion uniformity of mild steel bars affected by joints is better, and that of stainless-steel bars is poor. Therefore, it is still necessary to pay attention to the concentrated corrosion of stainless-steel bars that may occur at joints in coastal concrete structures. The corrosion resistance of epoxy coated steel bars at the joint depended on the coating state.
3) The influence coefficients of construction joint on local weight loss in the immersion environment are significantly lower than that of the wet–dry cycle environment. This

indicated that the corrosion of rebars at the joints under the wet–dry cycle environment is more severe, and it is relatively unfavorable to the durability of the joints.

4) The interfacial roughening had no significant effect on the corrosion uniformity of rebars. However, roughening caused certain defects to the concrete at the joints, which was unfavorable for the resistance of the joints to the penetration of chloride ions.

Data availability statement

The original contributions presented in the study are included in the article/Supplementary Material, further inquiries can be directed to the corresponding author.

Author contributions

GH, BW, YS, and GL contributed to the design of this research and analyzed and discussed the results of this research. YS and GL contributed to the methodology and performance of the experiments, including specimen fabrication, the electrochemical acceleration corrosion testing, and preparing the initial draft. BW and LW reviewed, edited, and prepared the final draft of this manuscript.

Funding

This research was funded by National Key Research and Development Program of China (Grant number 2013CB036303) and Scientific Research Project of Powerchina Roadbridge Group Co., Ltd. (Grant number HHZ-JGY-FW-07).

Acknowledgments

The authors are also highly grateful to Jinxin LI for his important support in material preparation and measurements during the testing phase of this research.

Conflict of interest

Authors GH, BW, and LW were employed by the company Powerchina Roadbridge Group Co., LTD.

The authors declare that this study received funding from Scientific Research Project of Powerchina Roadbridge Group Co., Ltd. The funder had the following involvement in the study: study design, decision to publish, and preparation of the manuscript.

The remaining authors declare that the research was conducted in the absence of any commercial or financial relationships that could be construed as a potential conflict of interest.

Publisher's note

Supplementary Material

The Supplementary Material for this article can be found online at: https://www.frontiersin.org/articles/10.3389/fmats.2022.1094696/full#supplementary-material

References

Alonso, M. C., Luna, F. J., and Criado, M. (2019). Corrosion behavior of duplex stainless steel reinforcement in ternary binder concrete exposed to natural chloride penetration. *Constr. Build. Mater.* 199, 385–395. doi:10.1016/j.conbuildmat.2018.12.036

Andrade, C. (2019). Correction to: Propagation of reinforcement corrosion: Principles, testing and modelling. *Mat. Struct.* 53 (1), 1. doi:10.1617/s11527-019-1420-3

Chen, C. (2020). An electrochemical investigation of corrosion behavior of 316l austenitic stainless steel reinforcement in concrete exposed to acidic environment. *Int. J. Electrochem. Sci.* 15 (2), 1634–1642. doi:10.20964/2020.02.48

Choe, G., Shinohara, Y., Kim, G., Lee, S., Lee, E., and Nam, J. (2020). Concrete corrosion cracking and transverse bar strain behavior in a reinforced concrete column under simulated marine conditions. *Appl. Sci.* 10 (5), 1794. doi:10.3390/app10051794

Goyal, A., Pouya, H. S., Ganjian, E., and Claisse, P. (2018). A review of corrosion and protection of steel in concrete. *Arab. J. Sci. Eng.* 43 (10), 5035–5055. doi:10.1007/s13369-018-3303-2

Guoping, L., Fangjian, H., and Yongxian, W. (2011). Chloride ion penetration in stressed concrete. *J. Mat. Civ. Eng.* 23 (8), 1145–1153. doi:10.1061/(asce)mt.1943-5533.0000281

James, A., Bazarchi, E., Chiniforush, A. A., Aghdam, P. P., Hosseini, M. R., Akbarnezhad, A., et al. (2019). Rebar corrosion detection, protection, and rehabilitation of reinforced concrete structures in coastal environments: A review. *Constr. Build. Mater.* 224, 1026–1039. doi:10.1016/j.conbuildmat.2019.07.250

Júlio, E. N. B. S., Branco, F. A. B., and Silva, V. t. D. (2004). Concrete-to-concrete bond strength. Influence of the roughness of the substrate surface. *Constr. Build. Mater.* 18 (9), 675–681. doi:10.1016/j.conbuildmat.2004.04.023

Kara, I. B. (2021). Experimental investigation of the effect of cold joint on strength and durability of concrete. *Arab. J. Sci. Eng.* 46 (11), 10397–10408. doi:10.1007/s13369-021-05400-5

Koh, T. H., Kim, M. K., Yang, K. H., Yoon, Y. S., and Kwon, S. J. (2019). Service life evaluation of rc t-girder under carbonation considering cold joint and loading effects. *Constr. Build. Mater.* 226, 106–116. doi:10.1016/j.conbuildmat.2019.07.106

Li, G. P., Hu, H., and Ren, C. (2017). Resistance of segmental joints to carbonation. *ACI Mat. J.* 114 (1), 137–148. doi:10.14359/51689487

Li, G. P., Hu, H., and Ren, C. (2016). Resistance of segmental joints to chloride ions. *ACI Mat. J.* 113 (4), 471–481. doi:10.14359/51688931

Lollini, F., Carsana, M., Gastaldi, M., and Redaelli, E. (2019). Corrosion behaviour of stainless steel reinforcement in concrete. *Corros. Rev.* 37 (1), 3–19. doi:10.1515/corrrev-2017-0088

Mun, J.-M., and Kwon, S.-J. (2016). Evaluation of chloride diffusion coefficients in cold joint concrete considering tensile and compressive regions. *J. Korea Concr. Inst.* 28 (4), 481–488. doi:10.4334/jkci.2016.28.4.481

Okazaki, S., Okuma, C., Kurumatani, M., Yoshida, H., and Matsushima, M. (2020). Predicting the width of corrosion-induced cracks in reinforced concrete using a damage model based on fracture mechanics. *Appl. Sci.* 10 (15), 5272. doi:10.3390/app10155272

Ou, Y. C., and Nguyen, N. D. (2016). Influences of location of reinforcement corrosion on seismic performance of corroded reinforced concrete beams. *Eng. Struct.* 126, 210–223. doi:10.1016/j.engstruct.2016.07.048

Santos, D. S., Santos, P. M. D., and Dias-da-Costa, D. (2012). Effect of surface preparation and bonding agent on the concrete-to-concrete interface strength. *Constr. Build. Mater.* 37, 102–110. doi:10.1016/j.conbuildmat.2012.07.028

Santos, P. M. D., and Julio, E. N. B. S. (2011). Factors affecting bond between new and old concrete. *ACI Mat. J.* 108 (4), 449–456. doi:10.14359/51683118

Shen, Y., Liu, J., Zhou, S. Y., and Li, G. P. (2019). Experimental investigation on the freeze-thaw durability of concrete under compressive load and with joints. *Constr. Build. Mater.* 229, 116893. doi:10.1016/j.conbuildmat.2019.116893

Sohail, M. G., Salih, M., Al Nuaimi, N., and Kahraman, R. (2019). Corrosion performance of mild steel and epoxy coated rebar in concrete under simulated harsh environment. *Int. J. Build. Pathol. Adapt.* 37 (5), 657–678. doi:10.1108/Ijbpa-12-2018-0099

Song, H., Niu, D. T., and Li, S. H. (2008). "Comparison of electrochemical accelerated corrosion and corrosion in natural environment," in *Advances in concrete structural durability* (Hangzhou China: ICDCS 2008), 1130–1135.

Stern, M., and Geaby, A. L. (1957). Electrochemical polarization. *J. Electrochem. Soc.* 104 (1), 56. doi:10.1149/1.2428496

Sung-Won, Y., and Seung-Jun, K. (2016). Effects of cold joint and loading conditions on chloride diffusion in concrete containing ggbfs. *Constr. Build. Mater.* 115, 247–255. doi:10.1016/j.conbuildmat.2016.04.010

Vanlalruata, J., and Marthong, C. (2021). Effect of cold joint on the flexural strength of rc beam. *J. Struct. Integr. Maintenance* 6 (1), 28–36. doi:10.1080/24705314.2020.1823556

Yang, H.-M., Lee, H.-S., Yang, K.-H., Ismail, M. A., and Kwon, S.-J. (2018). Time and cold joint effect on chloride diffusion in concrete containing ggbfs under various loading conditions. *Constr. Build. Mater.* 167, 739–748. doi:10.1016/j.conbuildmat.2018.02.093

Yoon, Y.-S., Yang, K.-H., and Kwon, S.-J. (2020). Service life of ggbfs concrete under carbonation through probabilistic method considering cold joint and tensile stress. *J. Build. Eng.* 32, 101826. doi:10.1016/j.jobe.2020.101826

Yuan, W., Guo, A. X., Yuan, W. T., and Li, H. (2018). Shaking table tests of coastal bridge piers with different levels of corrosion damage caused by chloride penetration. *Constr. Build. Mater.* 173, 160–171. doi:10.1016/j.conbuildmat.2018.04.048

Zega, B. C., Prayuda, H., Monika, F., Saleh, F., and Wibowo, D. E. (2021). Effects of cold joint and its direction on the compressive and flexural strength of concrete. *Int. J. GEOMATE.* 20 (82), 86–92. doi:10.21660/2021.82.j2086

Zhou, H. J., Liang, X. B., Wang, Z. Q., Zhang, X. L., and Xing, F. (2017). Bond deterioration of corroded steel in two different concrete mixes. *Struct. Eng. Mech.* 63 (6), 725–734. doi:10.12989/sem.2017.63.6.725

Zhou, H. J., Lu, J. L., Xv, X., Zhou, Y. W., and Xing, F. (2015). Experimental study of bond-slip performance of corroded reinforced concrete under cyclic loading. *Adv. Mech. Eng.* 7 (3), 168781401557378. doi:10.1177/1687814015573787

Zhou, H. J., Xu, Y. N., Peng, Y. R., Liang, X. B., Li, D. W., and Xing, F. (2020). Partially corroded reinforced concrete piers under axial compression and cyclic loading: An experimental study. *Eng. Struct.* 203, 109880. doi:10.1016/j.engstruct.2019.109880

frontiers | Frontiers in Materials

TYPE Review
PUBLISHED 19 December 2022
DOI 10.3389/fmats.2022.1066796

OPEN ACCESS

EDITED BY
Zhigang Zhang,
Chongqing University, China

REVIEWED BY
Lili Kan,
University of Shanghai for Science and Technology, China
Yan Xiong,
South China University of Technology, China
Lijun Ouyang,
University of Shanghai for Science and Technology, China

*CORRESPONDENCE
Likang Tian,
616000363@qq.com

SPECIALTY SECTION
This article was submitted to Structural Materials, a section of the journal Frontiers in Materials

RECEIVED 11 October 2022
ACCEPTED 06 December 2022
PUBLISHED 19 December 2022

CITATION
Jiang F, Long X, Tian L, Tan Y and Yu J (2022), Tensile strain-hardening cementitious composites and its practical exploration without reinforcement: A review. *Front. Mater.* 9:1066796. doi: 10.3389/fmats.2022.1066796

Tensile strain-hardening cementitious composites and its practical exploration without reinforcement: A review

Fangming Jiang[1], Xiong Long[2], Likang Tian[1,2]*, Yan Tan[2] and Jiangtao Yu[1,2]

[1]College of Civil Engineering, Tongji University, Shanghai, China, [2]School of Civil Engineering, Architecture and Environment, Hubei University of Technology, Wuhan, China

Steel is widely used as reinforcement for brittle structural materials such as concrete structure and unreinforced masonry structure (URM). However, the job wasted in steel reinforcement installation and the following corrosion hinder the development of construction industry. The emergence of strain-hardening cement composites (SHCC) provides an opportunity for steel-free construction. This paper provides a comprehensive review of the properties of SHCC and the corresponding practical exploration without reinforcement. The authors herein begin with a discussion on the superior properties of SHCC and its structural applications on the RC structure. Following this, the application of SHCC to retrofit URM is reviewed. Finally, we presents the advances of SHCC used in 3D concrete printing (3DCP) technology, and discuss the feasibility of SHCC structures without reinforcements in the future. When these explorations are coupled with appropriate theoretical models, true values for auto-construction without steel reinforcement will emerge.

KEYWORDS

strain-hardening cementitious composites, strengthening masonry building, 3D concrete print, without reinforcement, automatic construction

Introduction

Mechanical behavior of structures depends on the mechanical properties of structural materials. In the past, unreinforced masonry (URM) buildings were widely used around the world, while it processed poor strength and low ductility. With the emergency of steel and concrete, reinforced concrete (RC) structures became the most popular forms for civil engineering constructions. Meantime, steel reinforcements were also used in retrofitting URM. However, due to some inherent defects of concrete, such as brittleness, concrete is prone to cracking under tensile and bending loads, which may lead to serious steel corrosion in service life. Various damages in infrastructures, i.e., roads, bridges and water conservancy, are closely related to the brittleness of concrete and steel corrosion (Herrmann, 2013). Moreover, insufficient ductility of concrete is also one of the major causes to the structural damages under natural disasters. Take earthquake for

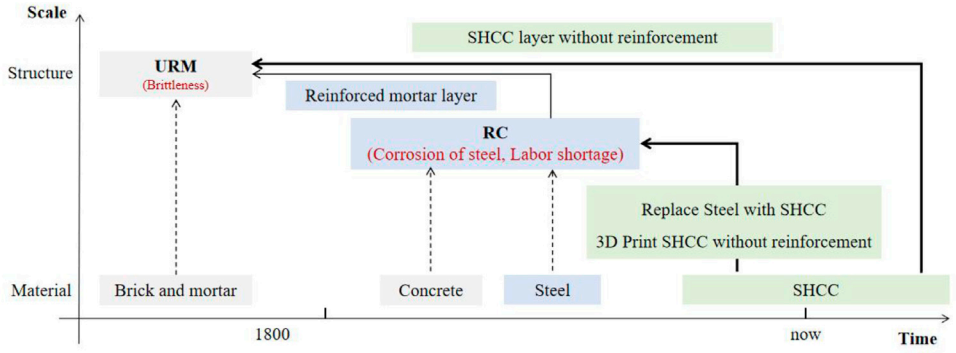

FIGURE 1
Structural application of SHCC without reinforcements.

example, the previous earthquake disaster statistics indicated that RC structures widely suffered concrete crushing and steel bar buckling under major earthquakes.

More importantly, due to population aging nowadays, labor shortage hinders the development of construction construction industry. The main challenges of civil engineering are the high demand for labor, the high cost of form-work, and the poor environmental sustainability. In recent years, 3D concrete printing (3DCP) technology was widely studied. However, the requirement for steel reinforcement, whose location is incompatible with the 3DCP process, is a significant obstacle to 3DCP.

A lot of work has gone into enhancing the characteristics of concrete in order to address the aforementioned issues. Numerous studies on fiber reinforced concrete (FRC) have shown that the mechanical properties of concrete are significantly enhanced by discontinuous short fibers used in cementitious matrix. In particular, strain-hardening cement composites (SHCC) process excellent tensile properties (Jun and Mechtcherine, 2010). In accordance with the principle of micro-mechanics in design, SHCC has a tensile capacity of more than 3% while maintaining a fiber volume fraction of no more than 2%. About two orders of magnitude more ductility (tensile strain capacity) exists in SHCC than in conventional cement. Multiple cracking with the widths smaller than 100 μm provide SHCC remarkably resistant to a variety of environmental exposure conditions (Li, 2012).

Considering the special features and excellent properties, it is not surprising that SHCC is gaining interest as a material for existing building retrofitting and innovative concrete manufacturing methods. This paper provides a comprehensive review of the structural application of SHCC without reinforcement, as shown in Figure 1. The authors herein begin with a discussion on the superior properties of SHCC and its structural applications on the RC structure. Particularly, a type of SHCC reinforced by polyethylene (PE) fibers is introduced, which processes similar deformability level with steel used in engineering. Following this, the application of SHCC to retrofit URM is reviewed. Finally, we presents the advances in 3DCP SHCC, and discuss the feasibility of SHCC structures without reinforcements in the future. Based on these discussions, more explorations in the SHCC materials and 3DCP technology would be identified in the future.

Development of SHCC

Design theory

SHCC is developed using fracture mechanics and micro-mechanics principles. The fiber, matrix and the interface between them might be tailored to gain the desired tensile strain-hardening properties, as shown in Figure 2A. First, particular types of fiber and the matrix's compressive strength should be optimized. Following this, fiber-pullout test is designed to measure the fiber bridging strength (σ_0) and the crack opening (δ), as illustrated in Figure 2B. The maximum complementary energy of fiber bridging (J_b') could also be determined. Strength and energy criteria should be met simultaneously to achieve excellent tensile properties (Li VC and Leung, 1992). The tensile stress at first crack (σ_{ss}) must be less than σ_0, according to the strength criterion (Eq. 1). This could guarantee the steady state of cracking. Additionally, the crack tip toughness (J_{tip}) should be less than J_b'. It is the critical condition for multi-cracking feature of SHCC. Both of the aforementioned criteria must be met by adjusting the characteristics of the fiber, cementitious matrix, and their interface.

$$\sigma_{ss} < \sigma_0 \tag{1}$$

$$J_{tip} < J_b' \tag{2}$$

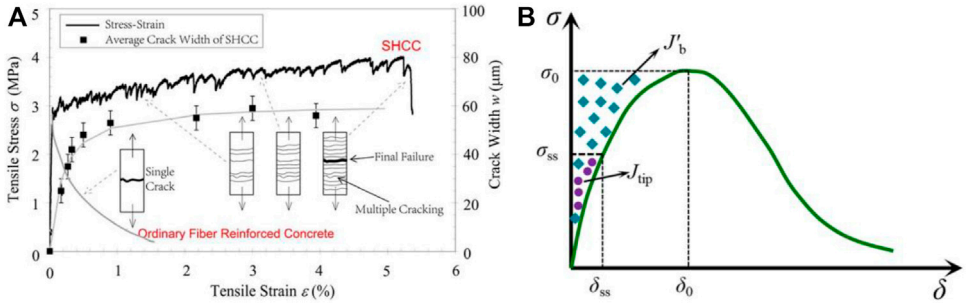

FIGURE 2
(A) Excellent tensile features of SHCC designed by micro-mechanics (Yu et al., 2018a). **(B)** Fiber bridging stress (σ) and the crack opening (δ) curve obtained from fiber-pullout test (Ding et al., 2022).

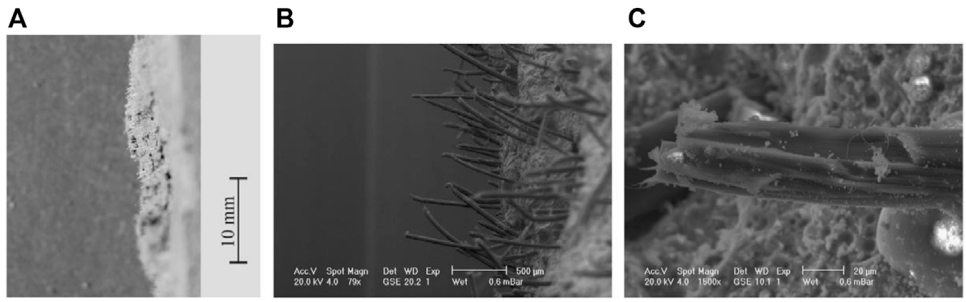

FIGURE 3
Pullout lengths of PVA fibers **(A,B)** and typical shape of fibre fracture **(C)** (Mechtcherine et al., 2011).

Mechanical property

Due to the high modulus and ease of diffusion, PVA fiber has been the most often utilized material in the production of conventional SHCC. The chemical link between the fiber and the cementitious matrix is very powerful as a result of the hydrophilic quality of PVA fiber, which is not desirable and causes premature fiber rupture (Figure 3) before maximizing the fiber reinforcement capability (Yu et al., 2018b). And thus lowers the possibility for pseudo-strain-hardening behavior. As a result, various common treatments have been applied to weaken the strength of fiber/matrix interface and raise the tensile strain capacity of PVA-SHCC, including oil coating for PVA fiber and the supplement of an air-entraining agent. However, the normal-strength matrix can handle the PVA fiber's comparatively modest tensile strength (i.e., 1,600 MPa). As a result, the compressive strength of PVA-SHCC is typically lower than 60 MPa. Additionally, the lower elastic modulus of PVA-SHCC is lower elastic modulus compared to regular concrete would result in greater deformation, particularly under compression stresses (Ding et al., 2020a).

Additionally, PE fibers with a higher molecular weight are employed to create SHCC. Due to its hydrophobic nature, PE fiber has lower chemical bonding strength but better tensile strength and elastic modulus as compared to the PVA fiber. PE fibers typically pull out rather than burst during the onset and spread of cracks (Figure 4) (Wang et al., 2020a). Based on these features of PE fiber, ultra-high ductile cementitious composites (UHDCC) was developed, which showed mean tensile strains of over 8%, with certain mixtures even exceeding 12% (Yu et al., 2017). It is demonstrated that the ultra-high fracture bridging capability is the reason for high ductility of PE-SHCC (Zhang et al., 2020; Zhang et al., 2021). As a result, PE-SHCC could exhibit excellent tensile behavior with the high fracture toughness matrix (Yu et al., 2018c). Other mechanical properties of PE-SHCC were also investigated, ranging from normal strength to high strength (Ding et al., 2018a; Wang et al., 2019).

In order to increase the practical application of SHCC, a comprehensive examination of the tensile qualities of all-grade strength SHCC was carried out (Yu et al., 2021a). Through experimental research, the size effect (Yu et al., 2020a) and the rate-dependent tensile properties (Yu et al.,

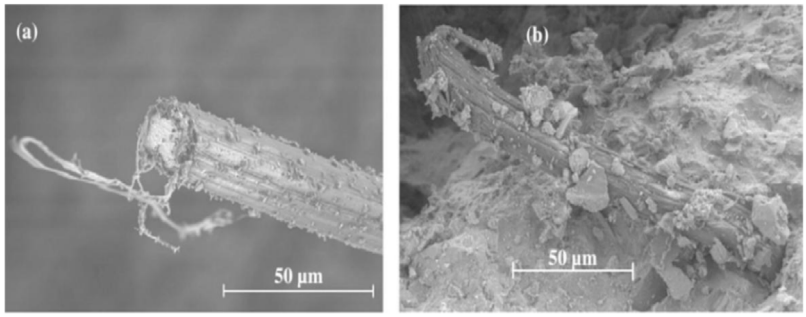

FIGURE 4
PE fiber pulled out from high strength matrix in **(A)** quasi-static and **(B)** dynamic regimes (Curosu et al., 2016).

FIGURE 5
(A) Crushing of concrete in RC specimen **(B)** Crack patterns in SHCC enhanced specimen.

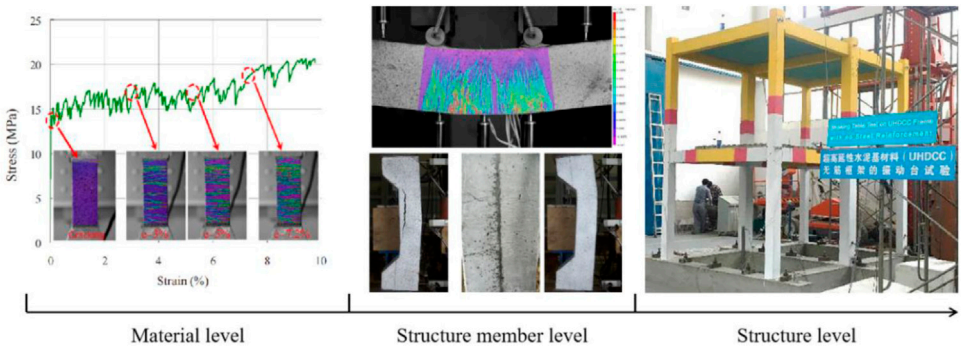

FIGURE 6
Muti-scale tests on the feasibility of PE-SHCC for construction without steel reinforcement.

2018d) of SHCC were explored. Furthermore, a performance-based design concept for SHCC was given out based on the necessary mechanical and crack pattern qualities (Li et al., 2019).

Structural application on RC structures

Due to the exceptional mechanical properties of SHCC, it has already been applied into major places, including beam-column

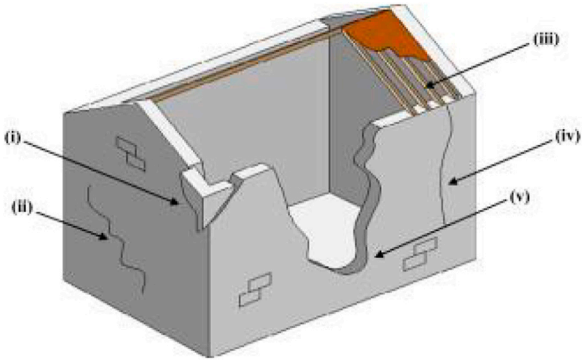

FIGURE 7
Common failure modes of URM structures, extracted from CENAPRED.

FIGURE 8
Out-of-plane collapse of walls caused by junction failure.

connection (Figure 5) and infill masonry in RC structures (Qudah and Maalej, 2014; Liao et al., 2022a). Test results have proven that SHCC can reduce the use of reinforcement and even eliminate it under certain conditions (Liao et al., 2022b). As a result, fewer steel reinforcements are needed for reinforced SHCC beams, which provides practical value in civil engineering (Ding et al., 2018b).

As illustrated in Figure 6, the mechanical properties of PE-SHCC were experimentally investigated at the various levels to confirm the viability of PE-SHCC structures without steel reinforcement (Yu et al., 2018e). The plain PE-SHCC beams exhibited mechanical properties that are comparable to those of RC beams with a steel reinforcement ratio of 0.5%–1.5%. The loading capacity of the plain PE-SHCC column was comparable to that of an RC column with a 0.8% steel ratio. Comparison between RC frame and PE-SHCC frame was conducted through shaking table tests (Yu et al., 2019). Under seismic action, PE-SHCC frame exhibited remarkable cracking control and complied with several seismic codes.

Application of SHCC to retrofit URM

Failure modes of URM buildings under seismic action

URM structures have limited shear strength and ductility resulting in sudden calamitous failures in the process of earthquake. The failure modes of masonry wall mainly include two categories: in-plane cracking failure of walls and out-of-plane collapse of walls and roofing Figure 7. Depicts typical failure modes of URM structures.

Above all, the out-of-plane collapse of walls caused by junction failure is the prime way of failure as shown in Figure 8 (Papanicolaou et al., 2007). Well constructed connection between walls can effectively avoid this type of failure. However, the falling of floor slab caused by collapse of walls is a severe failure mechanism resulting in a high mount of the fatalities. It is therefore vitally important to improve connection between walls and floor slab. This can save hundreds of thousands of buildings and lives.

Only when the walls and floor slab are well connected, the shear capacity of the walls can be mobilized through the development of shear cracks. Figure 9 shows four typical in-plane failure modes of masonry walls in plane, mainly including shear failure, sliding failure, overturning failure and corner crushing (Macabuag et al., 2012). The shear-compression ratio and the connection between mortar and bricks are the vital factors to determine the in-plane failure mode of masonry walls. Therefore, high shear strength and better interconnects between masonry walls are remarkably significant for masonry buildings to resist seismic load and other serious secondary disasters.

Conventional strengthening and SHCC strengthening

Engineers keep learning a lesson from the tragic disasters happened on URM buildings. After the Tangshan earthquake happened in 1976, a great mount of researches were carried out on retrofitting URM with reinforced mortar layer. Through a great quantity experimental study, the anti-seismic reinforcement of masonry with reinforced mortar layer has been adopted in JGJ 116-98, which is the industry standard technical code for seismic reinforcement of buildings in China. Figure 10 shows the practice of strengthening brick wall with double-sided steel reinforced mortar layer in practice.

However, this traditional strengthening method has many shortcomings. For example, the reinforced layer is made of steel

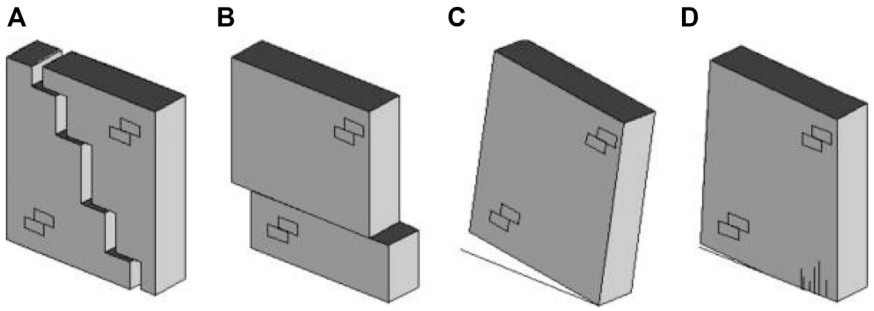

FIGURE 9
The various in-plane failure modes of masonry walls: **(A)** shear failure **(B)** sliding failure **(C)** overturning failure **(D)** corner crushing.

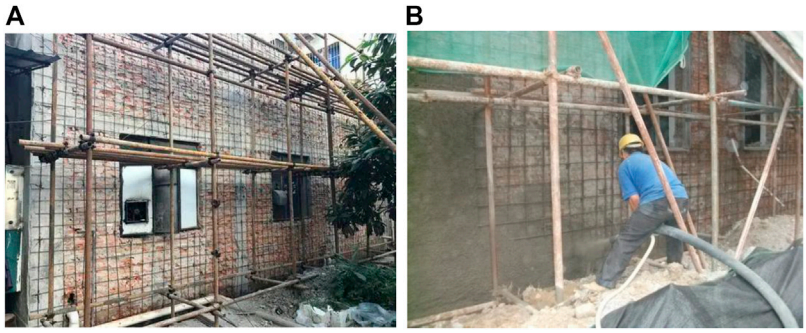

FIGURE 10
Strengthening brick wall with double-sided reinforced mortar layer: **(A)** installing steel mesh and **(B)** mortar spraying.

reinforcement and mortar, which is much stiffer than the original masonry wall. Under extremely seismic impact, the composites system is incompatibility with the masonry substrate, and the material utilization rate of reinforcement is low. The reinforced mortar layer is generally in the range of 30–50 mm, too thick as used for indoor strengthening. Therefore, an increasing number of explorations were conducted on how to apply high-performance material to strengthening URM structures with higher efficiency, lower cost and better seismic enhancement.

As early as 1994, Victor Li found that the shear performance of SHCC is better than that of traditional concrete. Moreover, after the shear cracking, the stress of traditional concrete decrease sharply with the strain, while SHCC shows the unique characteristics of strain-hardening. It is considered that SHCC can be used in structures requiring both strength and ductility (Li, 2012). In recent years, the seismic performance of masonry structures strengthened with SHCC has been systematically studied, mainly including in-plane shear capacity, out-of-plane bending capacity, energy dissipation capacity, and structural integrity (Maalej et al., 2010; Mosallam and Banerjee, 2011).

Most studies on the in-plane shear capacity of masonry walls were carried out through diagonal compression tests (Brignola et al., 2008). It is found that the shear strength of masonry structure strengthened by SHCC was increased by 1.8–5.7 times, and its energy dissipation capacity was increased by at least 35 times (Dong et al., 2022a). The brittle failure of masonry structure can be significantly improved by multiple cracks in SHCC surface layer, as shown in Figure 11 (Dehghani et al., 2013). The strength and ductility of masonry walls were improved more significantly by double-sided strengthening than that single-sided strengthened. In addition, the masonry structure without any interface treatment does not suffer from interface stripping failure prior to structural failure. This demonstrated that SHCC and masonry can work well together, which is the key to making full use of SHCC materials. It is due to the comparatively low elastic modulus and thickness (20–30 mm) of the SHCC used in strengthening.

It is found that SHCC can greatly improve the out-of-plane strength and ductility of masonry structure through bending test, local-loading test, uniform-loading test and low-speed impact

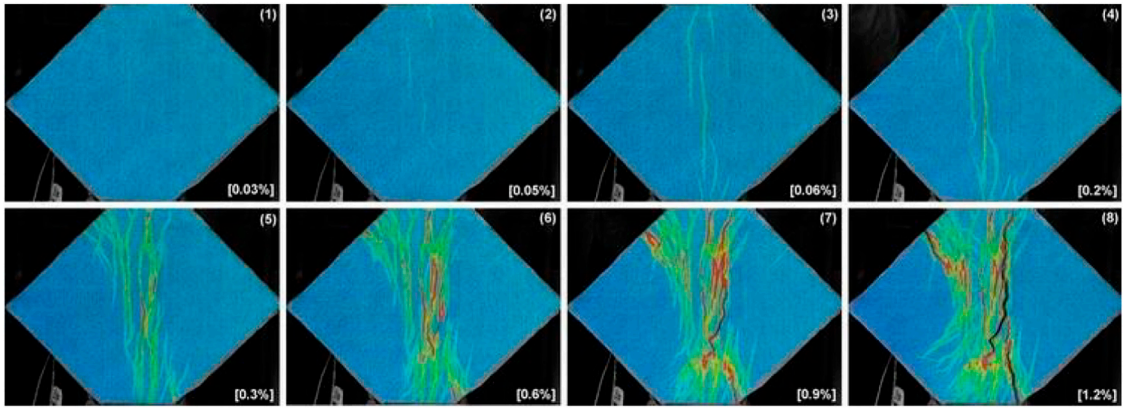

FIGURE 11
Widening of surface cracks in the SHCC layer for specimen.

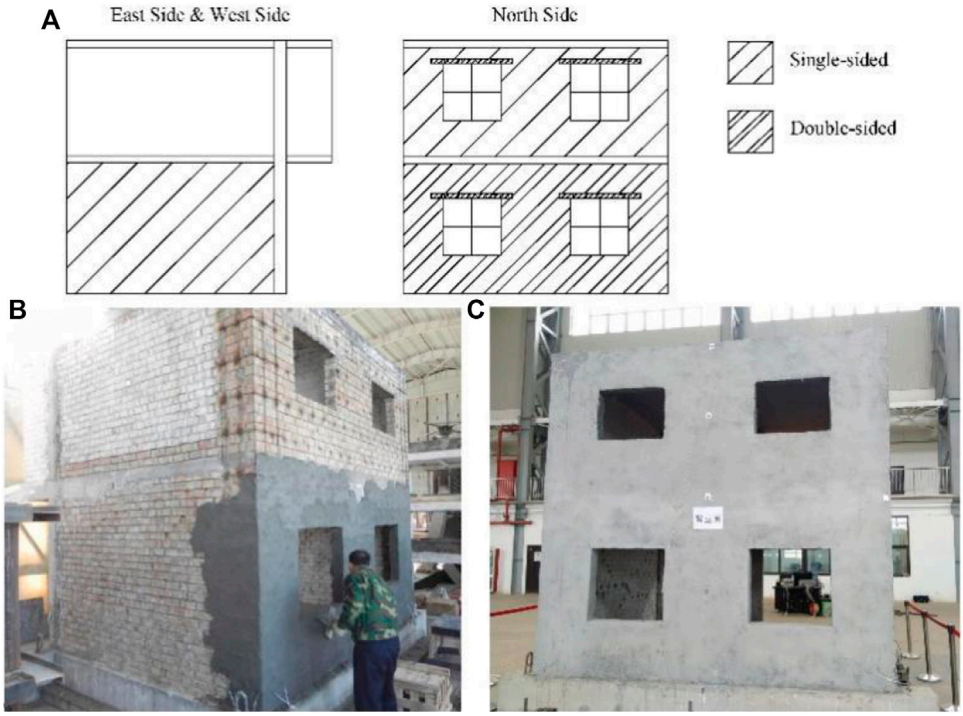

FIGURE 12
Shaking table test of SHCC strengthened masonry building **(A–C)**.

test (Singh and Munjal, 2020). This can effectively prevent masonry structure from collapse and destruction in earthquake and other sudden disasters. Moreover, parameter analysis was carried out in combination with ABAQUS simulation. Some better reinforcement details such as width to thickness ratio of SHCC surface layer is proposed.

Compared with the diagonal compression test, the stress state of the quasi-static test is closer to the engineering. The test results show that the strength, stiffness, ductility and energy dissipation capacity of masonry structure reinforced by SHCC can be improved by 56%–111% (Deng et al., 2020). In addition, SHCC can effectively restrain the

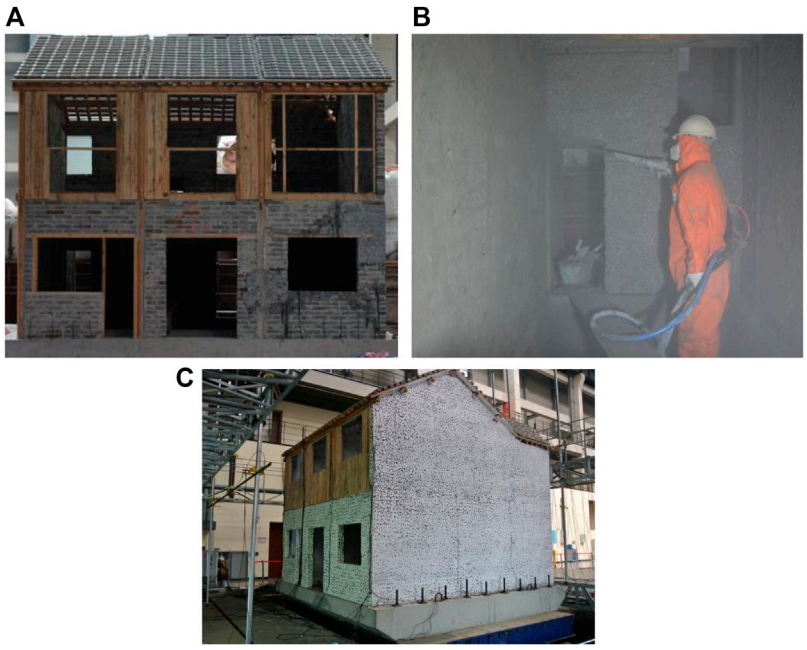

FIGURE 13
Chuan-dou timber-framed masonry building: **(A)** Earthquake damaged building, **(B)** Process of spraying UHDC layer and **(C)** Shaking table test of the strengthened masonry building.

cracking of masonry and improve its brittle failure (Lin et al., 2014; Choi et al., 2016). The in-plane shear strength of the reinforced masonry structure has been improved, while the bottom of the wall has become a relatively weak part. Therefore, the structure is prone to slip failure when the height to width ratio is small. If the connection between the wall and the beam or the floor is specially strengthened, the properties of the SHCC surface layer will be more fully utilized, thus further improving the seismic performance of the overall masonry structure (Esmaeeli et al., 2013; Dehghani et al., 2015). In addition, many scholars tried to spray SHCC surface layer for masonry strengthening, which further simplified the construction process without reducing the reinforcement quality (Kyriakides and Billington, 2014; Li et al., 2018).

Experimental studies were conducted on whole masonry buildings strengthened with SHCC material. As illustrated in Figure 12, the seismic performance of the masonry building before and after retrofitting were comparably observed by shaking table test. It is found that SHCC layer can significantly improves damage pattern, deformability and overall stiffness of structure, delays the degradation of structure stiffness. Meanwhile, the masonry building strengthened by SHCC outperformed the similar one strengthened with steel-grid-reinforced mortar layer (Deng et al., 2019).

As plotted in Figure 13, an earthquake damaged Chuan-dou timber-framed masonry building was retrofitted by using UHDC (Dong et al., 2022b). Shaking table tests were carried out on the original and the retrofitted masonry building. Experimental results demonstrated that the seismic behavior and ductility of Chuan-dou timber-framed masonry building were improved obviously. The structural integrity of the strengthened building for earthquake resistance was also much better than that of the unreinforced building. The features of SHCC, such as high ductility, high toughness and ease of constructions, promote wide use in structural retrofitting (Zhu et al., 2021).

TABLE 1 Comparison of different reinforcement materials.

Materials	HPFL	SHCC
Weight of reinforcement layer	High	Moderate
Stiffness of reinforcement layer	High	Moderate
Thickness of reinforcement layer	30–40 mm	10–20 mm
Utilization rate of materials	Low	Max
Cooperative ability with masonry	Low	Max
Construction process	Complex	Simple
Durability	Good	Good
Single-side reinforcement	No	Yes
Material cost	Low	High

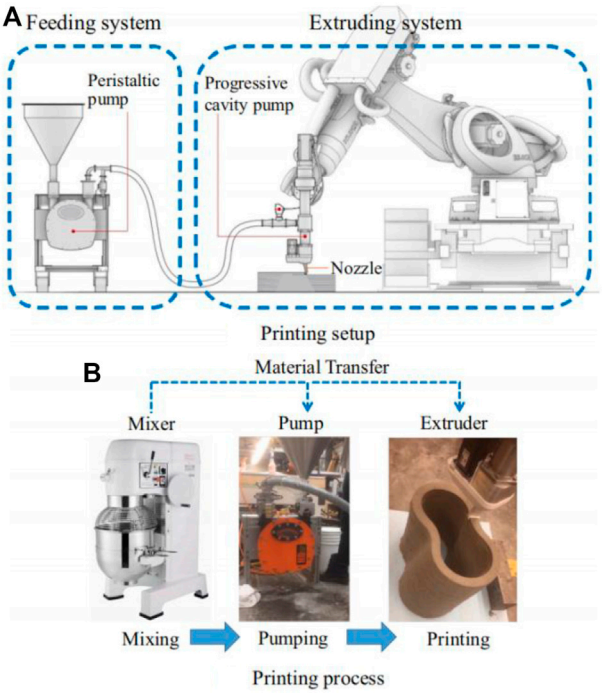

FIGURE 14
Printing equipment **(A)** and process **(B)**.

Comparison between SHCC and reinforced mortar

Compared with the reinforced mortar, SHCC with the characteristics of multi-cracking and strain-hardening has its special advantage in strengthening masonry building. Meanwhile, the proper stiffness and good bond with the block make it work well with the original structure. Moreover, the SHCC material is easy to construction by either spraying or artificial plastering. Furthermore, by increasing the connection between walls and floors/roofing, SHCC layer can improve the integrity of masonry buildings and consequently avoid collapse of buildings under earthquake action. In addition, the original architectural features of ancient buildings can be preserved by single-sided strengthening. Table 1 compares the characteristics of several different reinforcement materials.

3D concrete print of SHCC

Extrusion-based 3DCP

Powder-based 3D printing technique (Yu et al., 2020b) and extrusion-based nozzle-printing technique (Buswell et al., 2018) are the two primary varieties of 3DCP. Extrusion-based concrete printing is currently the most widely utilized technique owing to its simplicity of use, speed of construction, and suitability with the creation of light weight structures (Wang et al., 2020b). As shown in Figure 14, the extrusion-based 3DCP process is popular and has a multi—stage process (Yu et al., 2021b). This method doesn't need a framework or particles and might be utilized for printing with the proper cementitious material. For continuous construction, the fresh combinations must first be easily pumped from the mixer to the printing nozzle, i.e., pumpability. After that, the mixtures must have the ability to be continually extruded through the printing nozzle, i.e., extrudability. The extruded filaments must also be able to support the weight of upper layers, maintain their original shape without deforming, and firmly stack up layer after layer without showing any visible distortion, i.e., buildability (Ma et al., 2018; Panda et al., 2018).

Fresh property of SHCC

Specific qualities of concrete materials, both in fresh and hardened state, are needed by 3DCP (Ma et al., 2018; Lu et al., 2019). Fresh property, such as pumpability, extrudability, and buildability, becomes more important (Wangler et al., 2019). Sometimes these properties are conflicting in nature, and achieving their coordination is an important challenge.

The mechanical behavior of 3DCP-SHCC as well as the fresh behavior were widely analyzed. The ideal open time range for continuous printing was established by various flowability studies, as depicted in Figure 15. Pumpability and buildability were tested using a 1.5 m high 3DP-SHCC twisted column with 150 printed layers that were each 10 mm thick (Li et al., 2020). It was discovered that fibers and nanoparticles will improve the rheological characteristics for form retention (Chu et al., 2021). The results demonstrate that SHCC exhibit respectable work-ability in 3D printing (Ye et al., 2021a).

Mechanical property of printed SHCC

The mechanical behavior of 3DCP-FRC with various types of fibers, including basalt, steel, and polypropylene, have all been studied on various scales. No strain hardening tendency has been observed, with the exception of mortars explicitly created as SHCC (Chu et al., 2021).

The in-plane properties of extruded SHCC tend to be better that of the cast SHCC, as seen in Figure 16 (Soltan and Li, 2018).

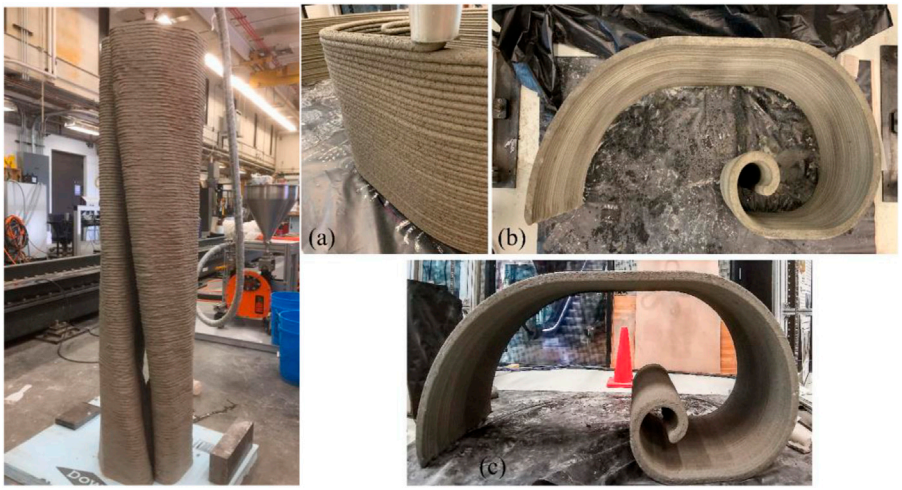

FIGURE 15
Rheological properties of fresh SHCC: **(A)** printing process and **(B, C)** printed specimens.

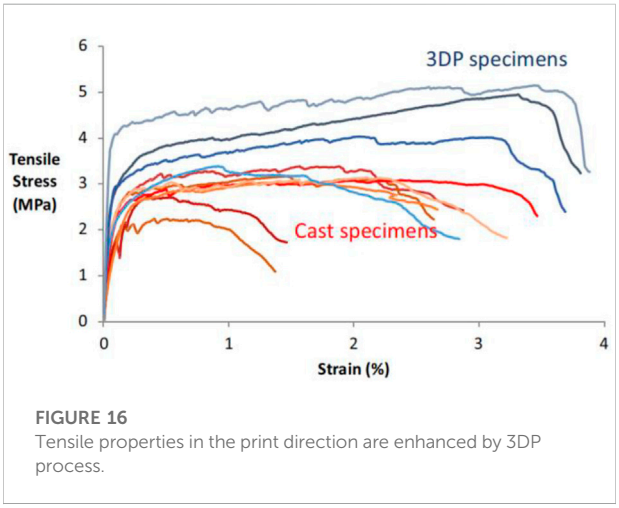

FIGURE 16
Tensile properties in the print direction are enhanced by 3DP process.

The robotically printed specimens showed the typical numerous micro-cracking and strain-hardening characteristic (Ogura et al., 2018). The fiber alignment parallel to the printing direction was greatly improved by the reduced nozzle size and larger fiber volume percentage. As a result, the printed specimens surpassed the mold-cast specimens mechanically (Arunothayan et al., 2021). Due to the strong compressive and flexural strengths and deflection-hardening behavior of SHCC, it is possible to make thinner 3D-printed structures with a significant reduction in or elimination of conventional steel bars (Arunothayan et al., 2020). Additionally, the printed PE-SHCC has superior deformability and energy dissipation than mold-cast specimens in some loading directions (Ye et al., 2021b).

Special mechanical properties in printed SHCC

Model cast concrete is regarded as isotropic. However, the multi-layer structure might introduce anisotropy in terms of durability and strength. The issue is more complicated for SHCC. The fiber orientation in the manufactured filament itself is not random. As a result, it is reasonable to anticipate that ductility and strength will vary in different directions. Some primary explorations on 3D-SHCC anisotropy have been carried out. Differences in the mechanical properties of interlayer separation and compression have been identified (Ding et al., 2020b).

Moreover, some advantages were also found in this hierarchical structures (Ye et al., 2021c). Inspired by natural nacre, a type of novel 3DCP-PE-SHCC member was developed. It exhibited better mechanical behavior than model cast members, especially in ductility and toughness as shown in Figure 17. It was demonstrated that the interface between layers could release the stress concentration and induce the crack-deflection, which is similar to nacre toughing motifs. The results further verified the significant potential of the 3DCP-SHCC structures without reinforcements.

Summary and outlook

This review paper discusses the superior properties of the SHCC and its applications in a variety of types of structures. The high ductility and toughness of SHCC make it possible to release the concrete from the steel reinforcements. As a result, a serious

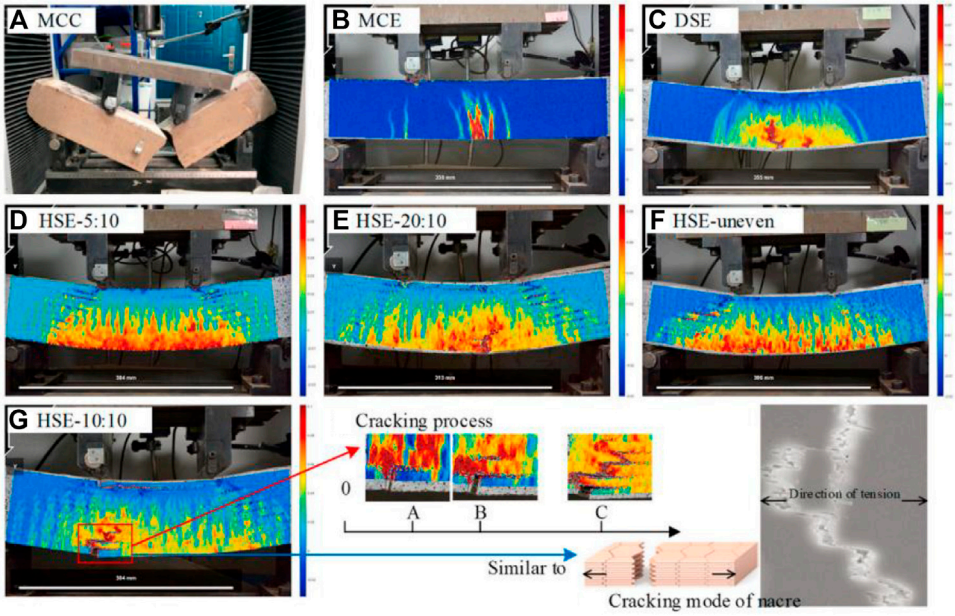

FIGURE 17
Mechanical behavior of nacre-inspired 3DCP-SHCC beams: **(A–F)** normal design beams and **(G)** nacre-inspired beam.

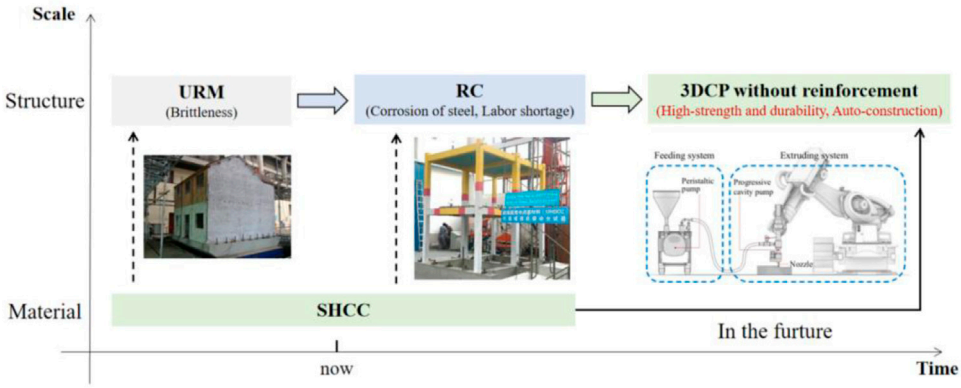

FIGURE 18
Structural applications of SHCC in different types of structures.

of structural applications of SHCC have been developed, as shown in Figure 18.

For the URM structures, brittleness and poor shear performance should be reinforced to meet current structural requirements. Compared with steel reinforced method, SHCC layer has been proved to be a better method. For the concrete structures, the feasibility of using SHCC without steel reinforcement has been verified at material, structural member and structure levels.

In the future, 3DCP would become a reasonable technology to solve the labor shortage problem of construction industry. In this context, 3DCP-SHCC structures have been widely investigated. The printed SHCC exhibits a serious of features, such as high ductility, high toughness, and anisotropic properties. Additionally, a nacre-inspired 3DCP-SHCC with enhanced mechanical properties is developed. This is further demonstrating the potential of the 3DCP-SHCC structures without reinforcements.

There remain a number of areas of needed research in 3DCP-SHCC structures without reinforcement. These include for example the interface between layers, the full-scale structural behaviors, and response to seismic action. Moreover, the workability and shrinkage of 3DCP-SHCC should be noticed in the future, which provide necessary conditions for engineering applications. When these explorations are coupled with theoretical models, true values for 3DCP-SHCC without reinforcement will emerge.

Author contributions

FJ: Conceptualization, Writing—original draft. XL: Investigation. LT: Investigation, Supervision. YT: Investigation. JY: Conceptualization, Funding acquisition, Supervision.

Conflict of interest

The authors declare that the research was conducted in the absence of any commercial or financial relationships that could be construed as a potential conflict of interest.

Publisher's note

All claims expressed in this article are solely those of the authors and do not necessarily represent those of their affiliated organizations, or those of the publisher, the editors and the reviewers. Any product that may be evaluated in this article, or claim that may be made by its manufacturer, is not guaranteed or endorsed by the publisher.

References

Arunothayan, A. R., Nematollahi, B., Ranade, R., Bong, S. H., and Sanjayan, J. (2020). Development of 3D-printable ultra-high performance fiber-reinforced concrete for digital construction. *Constr. Build. Mater.* 257, 119546. doi:10.1016/j.conbuildmat.2020.119546

Arunothayan, A. R., Nematollahi, B., Ranade, R., Bong, S. H., Sanjayan, J. G., and Khayat, K. H. (2021). Fiber orientation effects on ultra-high performance concrete formed by 3D printing. *Cem. Concr. Res.* 143, 106384. doi:10.1016/j.cemconres.2021.106384

Brignola, A., Frumento, S., Lagomarsino, S., and Podestà, S. (2008). Identification of shear parameters of masonry panels through the *in-situ* diagonal compression test. *Int. J. Archit. Herit.* 3 (1), 52–73. doi:10.1080/15583050802138634

Buswell, R. A., Leal de Silva, W. R., Jones, S. Z., and Dirrenberger, J. (2018). 3D printing using concrete extrusion: A roadmap for research. *Cem. Concr. Res.* 112, 37–49. doi:10.1016/j.cemconres.2018.05.006

Choi, H.-K., Bae, B.-I., and Choi, C.-S. (2016). Lateral resistance of unreinforced masonry walls strengthened with engineered cementitious composite. *Int. J. Civ. Eng.* 14 (6), 411–424. doi:10.1007/s40999-016-0026-1

Chu, S. H., Li, L. G., and Kwan, A. K. H. (2021). Development of extrudable high strength fiber reinforced concrete incorporating nano calcium carbonate. *Addit. Manuf.* 37, 101617. doi:10.1016/j.addma.2020.101617

Curosu, I., Mechtcherine, V., and Millon, O. (2016). Effect of fiber properties and matrix composition on the tensile behavior of strain-hardening cement-based composites (SHCCs) subject to impact loading. *Cem. Concr. Res.* 82, 23–35. doi:10.1016/j.cemconres.2015.12.008

Dehghani, A., Fischer, G., and Nateghi Alahi, F. (2013). Strengthening masonry infill panels using engineered cementitious composites. *Mat. Struct.* 48 (1-2), 185–204. doi:10.1617/s11527-013-0176-4

Dehghani, A., Nateghi-Alahi, F., and Fischer, G. (2015). Engineered cementitious composites for strengthening masonry infilled reinforced concrete frames. *Eng. Struct.* 105, 197–208. doi:10.1016/j.engstruct.2015.10.013

Deng, M., Dong, Z., Wang, X., Zhang, Y., and Zhou, T. (2019). Shaking table tests of a half-scale 2-storey URM building retrofitted with a high ductility fibre reinforced concrete overlay system. *Eng. Struct.* 197, 109424. doi:10.1016/j.engstruct.2019.109424

Deng, M., Zhang, W., and Li, N. (2020). In-plane cyclic loading tests of concrete hollow block masonry walls retrofitted with high ductile fiber-reinforced concrete. *Constr. Build. Mater.* 238, 117758. doi:10.1016/j.conbuildmat.2019.117758

Ding, T., Xiao, J., Zou, S., and Zhou, X. (2020). Anisotropic behavior in bending of 3D printed concrete reinforced with fibers. *Compos. Struct.* 254, 112808. doi:10.1016/j.compstruct.2020.112808

Ding, Y., Yu, J.-t., Yu, K.-Q., and Xu, S.-l. (2018). Basic mechanical properties of ultra-high ductility cementitious composites: From 40 MPa to 120 MPa. *Compos. Struct.* 185, 634–645. doi:10.1016/j.compstruct.2017.11.034

Ding, Y., Yu, K.-Q., Yu, J.-t., and Xu, S.-l. (2018). Structural behaviors of ultra-high performance engineered cementitious composites (UHP-ECC) beams subjected to bending-experimental study. *Constr. Build. Mater.* 177, 102–115. doi:10.1016/j.conbuildmat.2018.05.122

Ding, Y., Yu, K., and Li, M. (2022). A review on high-strength engineered cementitious composites (HS-ECC): Design, mechanical property and structural application. *Structures* 35, 903–921. doi:10.1016/j.istruc.2021.10.036

Ding, Y., Yu, K., and Mao, W. (2020). Compressive performance of all-grade engineered cementitious composites: Experiment and theoretical model. *Constr. Build. Mater.* 244, 118357. doi:10.1016/j.conbuildmat.2020.118357

Dong, F., Li, Z., Yu, J., Jiang, F., and Wang, H. (2022). Shaking-table test on a two-story timber-framed masonry structure retrofitted with ultra-high ductile concrete. *J. Struct. Eng. (N. Y. N. Y).* 148 (1). doi:10.1061/(asce)st.1943-541x.0003164

Dong, F., Wang, H., Jiang, F., Xing, Q., and Yu, J. (2022). In-plane shear behavior of masonry panels strengthened with ultra-high ductile concrete (UHDC). *Eng. Struct.* 252, 113609. doi:10.1016/j.engstruct.2021.113609

Esmaeeli, E., Manning, E., and Barros, J. A. O. (2013). Strain hardening fibre reinforced cement composites for the flexural strengthening of masonry elements of ancient structures. *Constr. Build. Mater.* 38, 1010–1021. doi:10.1016/j.conbuildmat.2012.09.065

Herrmann, A. W. (2013). ASCE. *2013 report card for America's infrastructure*. http://www.infrastructurereportcard.org/road-infrastructure.

Jun, P., and Mechtcherine, V. (2010). Behaviour of Strain-hardening Cement-based Composites (SHCC) under monotonic and cyclic tensile loading. *Cem. Concr. Compos.* 32 (10), 801–809. doi:10.1016/j.cemconcomp.2010.07.019

Kyriakides, M. A., and Billington, S. L. (2014). Cyclic response of nonductile reinforced concrete frames with unreinforced masonry infills retrofitted with engineered cementitious composites. *J. Struct. Eng. (N. Y. N. Y).* 140 (2). doi:10.1061/(asce)st.1943-541x.0000833

Li, L., Cai, Z., Yu, K., Zhang, Y. X., and Ding, Y. (2019). Performance-based design of all-grade strain hardening cementitious composites with compressive strengths from 40 MPa to 120 MPa. *Cem. Concr. Compos.* 97, 202–217. doi:10.1016/j.cemconcomp.2019.01.001

Li Vc, L. C., and Leung, C. K. Y. (1992). Steady-state and multiple cracking of short random fiber composites. *J. Eng. Mech.* 118 (11), 2246–2264. doi:10.1061/(asce)0733-9399(1992)118:11(2246)

Li, V. C., Bos, F. P., Yu, K., McGee, W., Ng, T. Y., Figueiredo, S. C., et al. (2020). On the emergence of 3D printable engineered, strain hardening cementitious composites (ECC/SHCC). *Cem. Concr. Res.* 132, 106038. doi:10.1016/j.cemconres.2020.106038

Li, V. C. (2012). Tailoring ecc for special attributes: A review. *Int. J. Concr. Struct. Mat.* 6 (3), 135–144. doi:10.1007/s40069-012-0018-8

Li, Y., Zhu, J., and Wang, Z. (2018). Investigation on mechanical properties of masonry infill wall strengthened with ECC. *KSCE J. Civ. Eng.* 23 (1), 295–306. doi:10.1007/s12205-018-5424-2

Liao, Q., Su, Y., Yu, J., and Yu, K. (2022a). Compression-shear performance and failure criteria of seawater sea-sand engineered

cementitious composites with polyethylene fibers. *Constr. Build. Mater.* 345, 128386.

Liao, Q., Su, Y., Yu, J., and Yu, K. (2022b). Torsional behavior of BFRP bars reinforced engineered cementitious composites beams without stirrup. *Eng. Struct.* 268, 114748.

Lin, Y.-W., Wotherspoon, L., Scott, A., and Ingham, J. M. (2014). In-plane strengthening of clay brick unreinforced masonry wallettes using ECC shotcrete. *Eng. Struct.* 66, 57–65. doi:10.1016/j.engstruct.2014.01.043

Lu, B., Weng, Y., Li, M., Qian, Y., Leong, K. F., Tan, M. J., et al. (2019). A systematical review of 3D printable cementitious materials. *Constr. Build. Mater.* 207, 477–490. doi:10.1016/j.conbuildmat.2019.02.144

Ma, G., Li, Z., and Wang, L. (2018). Printable properties of cementitious material containing copper tailings for extrusion based 3D printing. *Constr. Build. Mater.* 162, 613–627. doi:10.1016/j.conbuildmat.2017.12.051

Maalej, M., Lin, V. W. J., Nguyen, M. P., and Quek, S. T. (2010). Engineered cementitious composites for effective strengthening of unreinforced masonry walls. *Eng. Struct.* 32 (8), 2432–2439. doi:10.1016/j.engstruct.2010.04.017

Macabuag, J., Guragain, R., and Bhattacharya, S. (2012). Seismic retrofitting of non-engineered masonry in rural Nepal. *Proc. Institution Civ. Eng. - Struct. Build.* 165 (6), 273–286. doi:10.1680/stbu.10.00015

Mechtcherine, V., Millon, O., Butler, M., and Thoma, K. (2011). Mechanical behaviour of strain hardening cement-based composites under impact loading. *Cem. Concr. Compos.* 33 (1), 1–11. doi:10.1016/j.cemconcomp.2010.09.018

Mosallam, A., and Banerjee, S. (2011). Enhancement in in-plane shear capacity of unreinforced masonry (URM) walls strengthened with fiber reinforced polymer composites. *Compos. Part B Eng.* 42 (6), 1657–1670. doi:10.1016/j.compositesb.2011.03.015

Ogura, H., Nerella, V. N., and Mechtcherine, V. (2018). Developing and testing of strain-hardening cement-based composites (SHCC) in the context of 3D-printing. *Mater. (Basel)* 11 (8), 1375. doi:10.3390/ma11081375

Panda, B., Unluer, C., and Tan, M. J. (2018). Investigation of the rheology and strength of geopolymer mixtures for extrusion-based 3D printing. *Cem. Concr. Compos.* 94, 307–314. doi:10.1016/j.cemconcomp.2018.10.002

Papanicolaou, C. G., Triantafillou, T. C., Papathanasiou, M., and Karlos, K. (2007). Textile reinforced mortar (TRM) versus FRP as strengthening material of URM walls: Out-of-plane cyclic loading. *Mat. Struct.* 41 (1), 143–157. doi:10.1617/s11527-007-9226-0

Qudah, S., and Maalej, M. (2014). Application of Engineered Cementitious Composites (ECC) in interior beam–column connections for enhanced seismic resistance. *Eng. Struct.* 69, 235–245. doi:10.1016/j.engstruct.2014.03.026

Singh, S. B., and Munjal, P. (2020). Out-of-Plane response of ECC strengthened masonry wallets with openings. *KSCE J. Civ. Eng.* 24 (7), 2078–2087. doi:10.1007/s12205-020-1346-x

Soltan, D. G., and Li, V. C. (2018). A self-reinforced cementitious composite for building-scale 3D printing. *Cem. Concr. Compos.* 90, 1–13. doi:10.1016/j.cemconcomp.2018.03.017

Wang, L., Jiang, H., Li, Z., and Ma, G. (2020). Mechanical behaviors of 3D printed lightweight concrete structure with hollow section. *Arch. Civ. Mech. Eng.* 20 (1), 16. doi:10.1007/s43452-020-00017-1

Wang, Y., Liu, F., Yu, J., Dong, F., and Ye, J. (2020). Effect of polyethylene fiber content on physical and mechanical properties of engineered cementitious composites. *Constr. Build. Mater.* 251, 118917. doi:10.1016/j.conbuildmat.2020.118917

Wang, Y., Wei, L., Yu, J., and Yu, K. (2019). Mechanical properties of high ductile magnesium oxychloride cement-based composites after water soaking. *Cem. Concr. Compos.* 97, 248–258. doi:10.1016/j.cemconcomp.2018.12.028

Wangler, T., Roussel, N., Bos, F. P., Salet, T. A. M., and Flatt, R. J. (2019). Digital concrete: A review. *Cem. Concr. Res.* 123, 105780. doi:10.1016/j.cemconres.2019.105780

Xu, S., Hou, L.-J., and Zhang, X.-F. (2012). Shear behavior of reinforced ultrahigh toughness cementitious composite beams without transverse reinforcement. *J. Mat. Civ. Eng.* 24 (10), 1283–1294. doi:10.1061/(asce)mt.1943-5533.0000505

Ye, J., Cui, C., Yu, J., Yu, K., and Dong, F. (2021). Effect of polyethylene fiber content on workability and mechanical-anisotropic properties of 3D printed ultra-high ductile concrete. *Constr. Build. Mater.* 281, 122586. doi:10.1016/j.conbuildmat.2021.122586

Ye, J., Cui, C., Yu, J., Yu, K., and Xiao, J. (2021). Fresh and anisotropic-mechanical properties of 3D printable ultra-high ductile concrete with crumb rubber. *Compos. Part B Eng.* 211, 108639. doi:10.1016/j.compositesb.2021.108639

Ye, J., Yu, K., Yu, J., Zhang, Q., and Li, L. (2021). Designing ductile, tough, nacre-inspired concrete member in metric scale. *Cem. Concr. Compos.* 118, 103987. doi:10.1016/j.cemconcomp.2021.103987

Yu, J., Yao, J., Lin, X., Li, H., Lam, J. Y., Leung, C. K., et al. (2018). Tensile performance of sustainable Strain-Hardening Cementitious Composites with hybrid PVA and recycled PET fibers. *Cem. Concr. Res.* 107, 110–123. doi:10.1016/j.cemconres.2018.02.013

Yu, J., Ye, J., Zhao, B., Xu, S., Wang, B., and Yu, K. (2019). Dynamic response of concrete frames including plain ductile cementitious composites. *J. Struct. Eng. (N. Y. N. Y).* 145 (6). doi:10.1061/(asce)st.1943-541x.0002292

Yu, K.-Q., Yu, J.-T., Dai, J.-G., Lu, Z.-D., and Shah, S. P. (2018). Development of ultra-high performance engineered cementitious composites using polyethylene (PE) fibers. *Constr. Build. Mater.* 158, 217–227. doi:10.1016/j.conbuildmat.2017.10.040

Yu, K., Ding, Y., and Zhang, Y. X. (2020). Size effects on tensile properties and compressive strength of engineered cementitious composites. *Cem. Concr. Compos.* 113, 103691. doi:10.1016/j.cemconcomp.2020.103691

Yu, K., Li, L., Yu, J., Wang, Y., Ye, J., and Xu, Q. (2018). Direct tensile properties of engineered cementitious composites: A review. *Constr. Build. Mater.* 165, 346–362. doi:10.1016/j.conbuildmat.2017.12.124

Yu, K., Li, L., Yu, J., Xiao, J., Ye, J., and Wang, Y. (2018). Feasibility of using ultra-high ductility cementitious composites for concrete structures without steel rebar. *Eng. Struct.* 170, 11–20. doi:10.1016/j.engstruct.2018.05.037

Yu, K., McGee, W., Ng, T. Y., Zhu, H., and Li, V. C. (2021). 3D-printable engineered cementitious composites (3DP-ECC): Fresh and hardened properties. *Cem. Concr. Res.* 143, 106388. doi:10.1016/j.cemconres.2021.106388

Yu, K. Q., Dai, J.-G., Lu, Z.-D., and Poon, C.-S. (2018). Rate-dependent tensile properties of ultra-high performance engineered cementitious composites (UHP-ECC). *Cem. Concr. Compos.* 93, 218–234. doi:10.1016/j.cemconcomp.2018.07.016

Yu, K., Wang, Y., Yu, J., and Xu, S. (2017). A strain-hardening cementitious composites with the tensile capacity up to 8%. *Constr. Build. Mater.* 137, 410–419. doi:10.1016/j.conbuildmat.2017.01.060

Yu, K., Zhu, H., Hou, M., and Li, V. C. (2021). Self-healing of PE-fiber reinforced lightweight high-strength engineered cementitious composite. *Cem. Concr. Compos.* 123, 104209. doi:10.1016/j.cemconcomp.2021.104209

Yu, S., Du, H., and Sanjayan, J. (2020). Aggregate-bed 3D concrete printing with cement paste binder. *Cem. Concr. Res.* 136, 106169. doi:10.1016/j.cemconres.2020.106169

Zhang, Z., Liu, S., Yang, F., Weng, Y., and Qian, S. (2021). Sustainable high strength, high ductility engineered cementitious composites (ECC) with substitution of cement by rice husk ash. *J. Clean. Prod.* 317, 128379. doi:10.1016/j.jclepro.2021.128379

Zhang, Z., Yang, F., Liu, J.-C., and Wang, S. (2020). Eco-friendly high strength, high ductility engineered cementitious composites (ECC) with substitution of fly ash by rice husk ash. *Cem. Concr. Res.* 137, 106200. doi:10.1016/j.cemconres.2020.106200

Zhu, H., Yu, K., and Li, V. C. (2021). Sprayable engineered cementitious composites (ECC) using calcined clay limestone cement (LC3) and PP fiber. *Cem. Concr. Compos.* 115, 103868. doi:10.1016/j.cemconcomp.2020.103868

frontiers | Frontiers in Materials

TYPE Original Research
PUBLISHED 21 December 2022
DOI 10.3389/fmats.2022.1058407

OPEN ACCESS

EDITED BY
Zhigang Zhang,
Chongqing University, China

REVIEWED BY
Tao Ma,
Southeast University, China
Sadegh Karimpouli,
University of Zanjan, Iran

*CORRESPONDENCE
Zheng Han,
zheng_han@csu.edu.cn

SPECIALTY SECTION
This article was submitted to Structural Materials, a section of the journal Frontiers in Materials

RECEIVED 30 September 2022
ACCEPTED 06 December 2022
PUBLISHED 21 December 2022

CITATION
Mohammed MA, Han Z, Li Y, Al-Huda Z, Li C and Wang W (2022), End-to-end semi-supervised deep learning model for surface crack detection of infrastructures. *Front. Mater.* 9:1058407.
doi: 10.3389/fmats.2022.1058407

End-to-end semi-supervised deep learning model for surface crack detection of infrastructures

Mohammed Ameen Mohammed[1], Zheng Han[1,2]*, Yange Li[1,3], Zaid Al-Huda[4], Changli Li[1] and Weidong Wang[1,3]

[1]School of Civil Engineering, Central South University, Changsha, Hunan, China, [2]Hunan Provincial Key Laboratory for Disaster Prevention and Mitigation of Rail Transit Engineering Structures, Changsha, Hunan, China, [3]The Key Laboratory of Engineering Structures of Heavy Haul Railway, Ministry of Education, Changsha, Hunan, China, [4]School of Computing and Artificial Intelligence, Southwest Jiaotong University, Chengdu, Sichuan, China

Surface crack detection is essential for evaluating the safety and performance of civil infrastructures, and automated inspections are beneficial in providing objective results. Deep neural network-based segmentation methods have demonstrated promising potential in this purpose. However, the majority of these methods are fully supervised, requiring extensive manual labeling at pixel level, which is a vital but time-consuming and expensive task. In this paper, we propose a novel semi-supervised learning model for crack detection. The proposed model employs a modified U-Net, which has half the parameters of the original U-Net network to detect surface cracks. Comparison using 20 epochs shows that the modified U-Net network requires only 15% training time of the traditional U-net, but improves the accuracy by 20% upwards. On this basis, the proposed model (modified U-Net) is trained based on an updated strategy. At each stage, the trained model predicts and segments the unlabeled data images. The new strategy for updating the training datasets allows the model to be trained with limited labeled image data. To evaluate the performance of the proposed method, comprehensive image datasets consisting of the DeepCrack, Crack500 datasets those open to public, and an expanded dataset containing 2068 images of concrete bridge surface crack with our independent manual labels, are used to train and test the proposed method. Results show that the proposed semi-supervised learning method achieved quite approaching accuracies to the established fully supervised models using multiple accuracy indexes, however, the requirement for the labeled data reduces to 40%.

KEYWORDS

deep learning, crack detection, semi-supervisded, image segementation, infrastructure

1 Introduction

Existence of surface cracks has a significant impact on the safety and endurance of infrastructure such as roads and bridges Biondini and Frangopol. (2016) Rafiei and Adeli (2017). Cracking is an inevitable phenomenon indicating the degradation of infrastructure performance. It is getting common when infrastructure approaches their life expectancy. With an aging population and rising labor costs, the ability to inspect the structure continuously and automatically with a reduced workforce has become a critical research path Maeda et al. (2018) and Liu et al. (2019b). Manual visual inspection is a well-known technique for inspecting and evaluating the health of the civil infrastructure. This kind of solution is low efficiency, highly reliant on experts and time-consuming Nguyen et al. (2021). The accuracy of damage diagnosis is largely dependent on the inspectors' skill level and experience. As a result, automatic crack detection is critical for achieving the objectivity and efficiency required for damage assessment Adhikari et al. (2014).

Numerous automatic or semi-automatic systems have been proposed, using advanced sensors for assessment, such as line scanning cameras Gavilán et al. (2011), accelerometers Radopoulou and Brilakis (2017), RGB-D sensors Tsang and Lo (2006), black-box cameras Kim and Ryu (2014), and 3D laser scanners Bursanescu et al. (2001) and Zhang et al. (2018b). The equipment with these sensors, as well as the relevant systems are usually costly. For instance, between the year of 2012 and 2013, the Ohio Department of Transportation (ODOT) was offered five choices for pavement inspections at the cost of $1.12 million, including a collection system, web hosting, workstations, and training. In general, the average cost for pavement inspections and monitoring is estimated as $48.75/km in Netherlands Seraj et al. (2017). It is comparable in United Kingdom, that the average cost is reported ranging from $27.89/km to $55.77/km in the previous studies Radopoulou and Brilakis (2017), Hadjidemetriou and Christodoulou (2019). Due to the high cost of vehicles equipped with sensors for road inspections, the relevant agencies and government departments cannot afford to spend a high price to inspect the entire road as much as possible Woo and Yeo (2016).

With the advances of computing power and the advent of artificial intelligence, image processing, and computer vision-based approaches became increasingly effective at analyzing and detecting surface cracks of infrastructures Cao et al. (2020). Many automated or semiautomated computer-aided crack detection methods have been proposed, including threshold segmentation Zhu et al. (2007) and Li et al. (2022), histogram transforms Patricio et al. (2005), region growing Zhou et al. (2016) and Li et al. (2011), edge detection Ayenu-Prah and Attoh-Okine (2008). Although these algorithms laid a solid foundation and inspired the automated crack detection, they require extensive manual feature engineering, while the detection results are likely to influenced by noise because of the crack images complexity. These limitations are debated up to date.

Recently, deep learning (DL)-based computer vision methods have achieved state-of-the-art performance in various computer vision-based tasks Krizhevsky et al. (2012), Ren et al. (2015), Long et al. (2015), Peng et al. (2020), and Han et al. (2021b). Various methods those based on convolutional neural network (CNN) have been applied to identify the crack detection of structures, including image classification Gopalakrishnan et al. (2017) and Mohammed et al. (2021), object detection Cheng and Wang (2018) and Xu et al. (2019), and semantic segmentation Tong et al. (2019), Zhou et al. (2019), and Al-Huda et al. (2021). Generally, these previous DL-based methods can be categorized into three major kinds, i.e., the binary classifier that distinguishes between crack and non-crack images for the input images Nhat-Duc et al. (2018), anchor boxes used to highlight cracks in images by the object detector Huyan et al. (2019), and pixel-level semantic segmentation that able to specific segment pixels of the crack from background pixels in images Huyan et al. (2020). Among these methods, pixel-level crack segmentation delineates the geometric features of the cracks, therefore, should be considered as a more effective solution in engineering practice, where the geometric features of the cracks are required to determine the type, length, width, and severity of the crack Dong et al. (2020).

However, comparing to the binary classifier and anchor boxes methods, the pixel-level semantic segmentation of CNNs often suffers from loss of information and an imbalance in the quantity of cracked and non-cracked pixels in their early versions. Downsampling methods (e.g., max-pooling) lose information from the feature map and obstruct the pursuit of pixel-perfect accuracy. Zhang et al. (2017) developed a method for segmenting cracks at the pixel level based on CNN called CrackNet. CrackNet does not contain pooling layers, and the feature map size is constant in all layers to prevent information loss. They also made progressive strengthening that the improved versions of CrackNet II and CrackNet V Zhang et al. (2018a) and Fei et al. (2018) were released, which are more accurate and faster. Cheng et al. (2018) and Jenkins et al. (2018) demonstrated high-precision segmentation of cracks at the pixel level using U-Net. A skip connection between the encoder and decoder can recover the information loss in the U-Net upsampling method for pixel-level image segmentation Ronneberger et al. (2015), Tang et al. (2021), and Karimpouli and Kadyrov (2022) proposed a Double-Unet to overcome inability to reconstruct HR features in the decoder part of the U-net. Results show that SRDUN performs more realistic than conventional networks. Liu et al. (2020) proposed a detection and segmentation method for road cracks, and the YOLOv3 model was used to determine the kind and crack position of the input image, which was then

used as an input to the U-Net segmentation. Zhu et al. (2022) used an unmanned aerial vehicle (UAV) to collect pavement images and then used deep learning to detect six types of distress, including four crack types (e.g., fatigue crack). Han et al. (2021a) proposed a sampling block with a convolutional neural network implementation called CrackW-Net, thereby developing a novel pixel-level semantic segmentation network for pavement crack segmentation.

As can be seen from the abovementioned studies, the semantic segmentation methods have been extensively used in crack detection and can be used as the basis for crack morphological feature measurement. However, the majority of the current crack detection semantic segmentation methods are fully supervised learning-based Liu et al. (2019b) and Xu et al. (2019), which require supervising the model's training process using amount of the labeled image data. In these labeled image data, the cracks of the infrastructure surface are commonly manual delineated and separated from the non-crack area. The quality of these manual labeled image data significantly influences the detection accuracy of the model. In this sense, the application of DL-based semantic segmentation methods to crack detection is limited owing to that the labeling work is time-consuming. For instance, pixel-wise labeling spends about 15 times longer to complete than bounding anchor box labeling, and even 60 times longer than image-level classification Dong et al. (2020). To this end, different kinds of weak annotations were used in many methods, such as bounding box Dai et al. (2015), and scribble Lin et al. (2016) to annotation at pixel-wise. Despite the fact that there is no difficulty because a massive dataset is not required, but the cracks can have complex topological structures and can span the entire image. As a result, scribble or bounding box annotation is an ineffective technique for crack detection Al-Huda and Li (2022). With image-wise label, annotation time and workload can be significantly reduced, allowing this task to be applied more effectively to pavement crack segmentation task.

To overcome the issue of insufficient data, the semi-supervised learning method is an alternative solution, which fully utilize unlabeled data, reducing labeling workload while maintaining accuracy. Some current studies, Li et al. (2020) and Shim et al. (2020) have begun to use this kind of method, and proposed an adversarial learning-based semi-supervised crack segmentation method. The model consists of a segmentation network and a discrimination network. Given an input crack image, the segmentation network generates a prediction map, and the discriminator network separates the prediction map from the ground truth label map. Wang and Su (2021) proposed a semi-supervised semantic segmentation network for crack detection. The proposed method consists of a student model and a teacher model. The two models use the EfficientUNet to extract multi-scale crack feature information, which reduces image information loss. However, most of the previous semi-supervised learning-based studies for crack segmentation majorly use adversarial learning or similar networks, therefore, it is difficult to achieve good training results unless the training process ensures synchronization and balance between the two adversarial networks Wang et al. (2017) and Goodfellow et al. (2016).

In order to address these issues, in this paper we propose a novel semi-supervised method for crack image segmentation. The modified U-Net is applied in the proposed method. Then, to minimize the requirement for the labeled image data, a novel dataset update strategy that updates the given training dataset are proposed. The modified U-Net-based convolutional neural network was used to avoid the difficulties associated with manually extracting features. A open-source, however, unlabeled GitHub dataset for bridge crack images Li et al. (2019) is used. The images in this dataset are independently labeled. To evaluate the performance of the proposed method, the labeled bridge crack dataset, and two other open-source dataset, i.e., DeepCrack and Crack500, are used to train and test the proposed method. The proposed method was compared to the fully supervised methods by conducting experiments on two public datasets. The following are main contributions:

- A novel semi-supervised learning-based semantic segmentation framework for crack images, which significantly reduces the workload associated with data annotation, is proposed.
- The improved U-Net-based convolutional neural network was used to avoid the difficulties associated with manually extracting features.
- The new bridge crack image dataset was carefully labeled and used to train and test the model based on unlabeled GitHub bridge crack open-source dataset Li et al. (2019). This manual labeled dataset will be available and released to public along with this paper.
- The proposed method was compared to the fully supervised methods by conducting experiments on two public datasets. The results demonstrate that the proposed method achieves comparable results to fully supervised methods while reducing human labeling efforts.

The remaining of this paper is organized as follows. **Section 2** presents the research methodology; **Section 3** presents the datasets and evaluation metrics; **Section 4** presents the experimental results; **Section 5** presents discussions and comparative study to verify the segmentation performance; finally, the study's conclusions are presented in **Section 6**.

2 Methodologies

2.1 Overview of the proposed method

The fully supervised deep learning methods depends on the quality and amount of the labeled crack images dataset, which is commonly manual labeled, time-consuming, and costly. The main goal of this method is to use a limited number of labeled crack images to achieve satisfactory results. For this purpose, a new method for crack image segmentation based on semi-supervised learning is proposed to address this issue.

This section details our semi-supervised framework for crack segmentation using image-level labels as semi supervision annotations. It aims to bridge the gap between the fully and the weakly supervised semantic segmentation methods for pavement crack segmentation, while reducing human labeling efforts. The proposed framework has four main steps: 1) Contrast Limited Adaptive Histogram Equalization (CLAHE) Reza (2004) is adapted to mitigate the detrimental effects of uneven illumination on input images *via* contrast limited adaptation; 2) the Supervised model is trained on labeled data images; 3) an initial pixel-level annotation is obtained by using the trained model (supervised) to predict and segment unlabeled data images; 3) the semi-supervised model is trained on labeled data and high-confidence predictions; 4) update the training dataset by combining labeled data and high confident predictions to train the semi-supervised model. 5) steps 3,4 are repeated until all images in the data set required to train the model are used, and 6) use the final model to predict the label of the test set and evaluate.

As shown in **Figure 1**, the input image is enhanced by CLAHE, as a preprocessing step. Then, trained the modified U-Net deep neural network on a small amount of labeled crack data and then predict and segment the unlabeled data image. Next, the previously used dataset is updated and combined with the highly confident predictions to train the semi-supervised model. The specifics of the proposed methodology are discussed in more detail in the following **Section 2.3**.

2.2 The modified U-Net model

In order to implement an automated crack image analysis system, it is necessary first to segment the cracks. Complex feature engineering and selecting the most suitable classifier are essential to achieve satisfactory segmentation results, and this task is time-consuming and labor-intensive. A modified U-Net-based Convolutional Neural Network is used to avoid difficulties with manually extracting features.

U-Net Ronneberger et al. (2015) is a fully convolutional neural network-based model for solving the issue of biomedical image semantic segmentation. The model consists of a contraction path and an expansion path, and the input image is compressed into a multichannel feature map passing through the feature extraction path. The encoder uses max-pooling (strides = 2) and convolutional layers with an increasing number of filters to continuously reduce image size, followed by activation (ReLU). The number of filters in the convolutional layers decreases during decoding, followed by gradual upsampling in the subsequent layers to the top. The contracting and expansive paths in a traditional UNet network are nearly symmetrical. However, due to downsampling methods (e.g., maximum pooling), information from the feature map is lost, and the pursuit of pixel-perfect accuracy is hampered. In addition, traditional UNet networks contain many parameters that hinder network speed.

In this paper, in order to address the above issues, a modified U-Net-based crack segmentation method is proposed in this study. **Figure 2** shows the modified UNet network. The basic of the U-Net method has been illustrated in detail in previous studies Ronneberger et al. (2015) and Tang et al. (2021). The modified U-Net focuses on the following aspects.

To reduce the number of network parameters and increase the speed of network training, the modified U-Net network has half the parameters of the original UNet network, which is capable of accurately and automatically detecting cracks with a high level of spatial precision. Additionally, Same padding was added in the modified UNet network to achieve the size of the output feature map is similar to the input feature map size. **Table 1** shows the comparison of network architecture performance results, the DeepCrack dataset was used for the experiment, and it seems clear that Modified U-Net has the best performance across all metrics and requires the least amount of training time.

The *i*th input crack image is represented by x (i). The standard binary cross-entropy loss is the loss function used to train the U-Net. The formula is as in Eq. **1**.

$$L(\theta) = -\frac{1}{N}\sum_{i=1}^{n}\left(y_i log\hat{y}_{\theta xi}\right) + \left(1-y_i\right) log\left(1-\hat{y}_{\theta xi}\right) \tag{1}$$

where y_i represents the ground-truth and $\hat{y}_{\theta xi}$ represents the predicted label for the *i*th input image. The parameters θ of the U-Net model optimization issue can be estimated as shown in Eq. **2**.

$$\theta^{*} = \left(arg_{\theta}^{minL(\theta)}\right) \tag{2}$$

This optimization problem was solved using the Adaptive Moment Estimation (Adam) algorithm Kingma and Ba (2014).

2.3 Dataset updating method

The proposed semi-supervised method aims to obtain satisfactory crack segmentation with a limited amount of labeled data. In practice, obtaining a large number of unlabeled crack

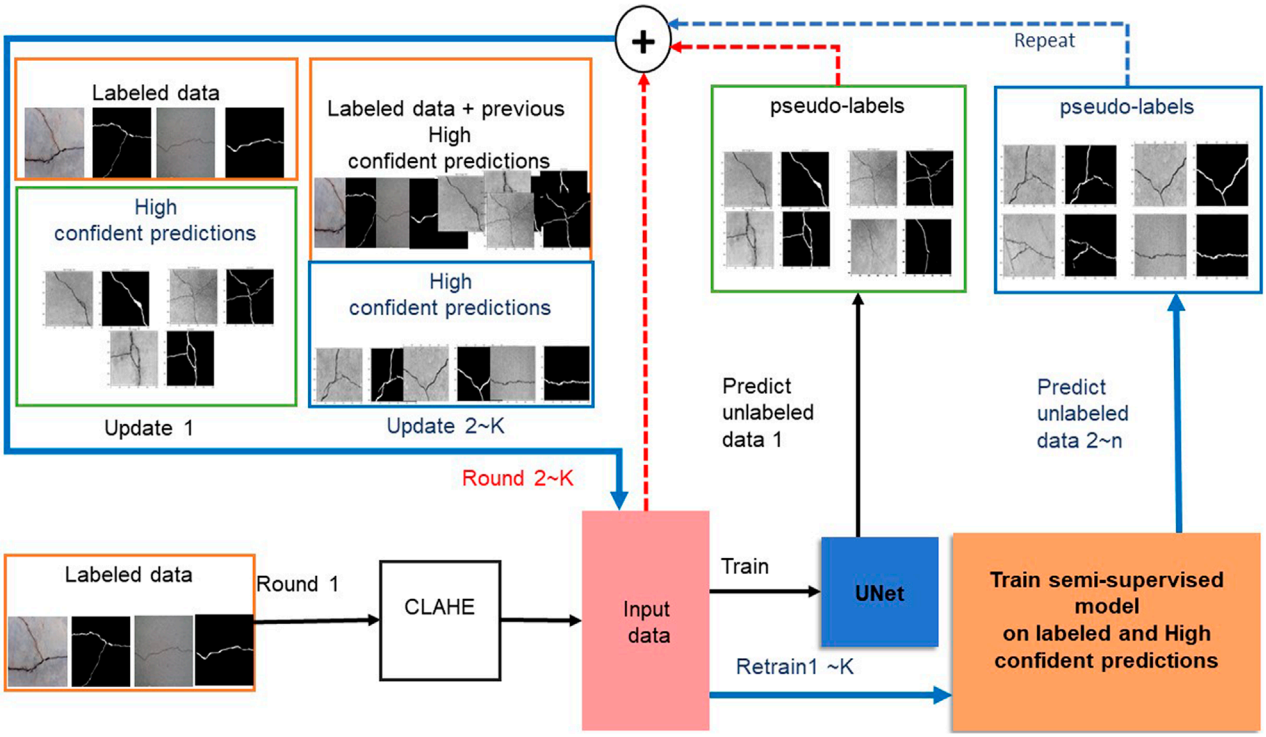

FIGURE 1
The schematic representation of the proposed semi-supervised method. 1) The Supervised model is trained on labeled data images, then 2) uses the trained model (supervised) to predict and segment unlabeled data images. Then 3) the semi-supervised model is trained on labeled data and high-confidence predictions. 4) This semi-supervised trained model re-labeling unlabeled images. The above steps (3, 4) are repeated until all images in the data set required to train the model are used.

images is relatively easy. The dataset updating strategy used to utilize these images, as shown in Figure 3. The goal of the dataset update strategy is to label unlabeled images automatically, therefore, increasing the total amount of the labeled images data, which helps to estimate the network parameters. The following is a detailed description of the implementation procedure.

Assume that the training dataset is $S = \{x_n, y_n, x_{non_m}\}$, where $n = n_i: N$, $1: M$ and $S_1 \cup S_2$. The subset $S_1 = x_n, y_n; n = n_i: N$ represents the labeled dataset, while the subset $S_2 = x_{non_m}; m = m_i: M$ represents the unlabeled dataset. The x_n denotes the $n-th$ crack image and the y_n represents the $n-th$ ground-truth label. The x_{non_m} represents the $m-th$ crack image without ground truth. The output of the U-Net model is denoted by the symbol $\hat{y}_\theta$ and Eq. 2 is used to estimate the parameter θ. Let y_{pred_m} denote the predicted label of x_{non_m}. After that, we can get y_{pred_m} by Eq. 3.

$$y_{pred_m} = \hat{y}_\theta\left(x_{non_m}\right). \tag{3}$$

The training dataset S_n can then be updated as follows:

$$S^* = \left\{x_n, y_n, x_{non_m}, y_{pred_m}\right\}, where, n = n_i: N, m_i: M \tag{4}$$

The parameters θ of the U-Net model will be recalculated with the updated dataset S^* as input, during training and validation of the semi-supervised model, the loss is primarily used to assess the discrepancy between the predicted and actual values, the dice coefficient is selected as monitoring criteria to guide hyper-parameter learning. The whole process of the proposed semi-supervised learning method for the crack image segmentation is shown in Algorithm 1.

3 Evaluation

3.1 Datasets

The performance evaluation was done by performing experiments using two publicly available crack datasets, i.e., DeepCrack and Crack500 dataset, with the embedded ground truth labels.

1) DeepCrack dataset Liu et al. (2019a). There are 537 images with a resolution of 544 × 384 pixels. Ground truth images at the pixel level are available. This dataset was used to evaluate the proposed method. Figure 4 shows some images of the DeepCrack dataset.

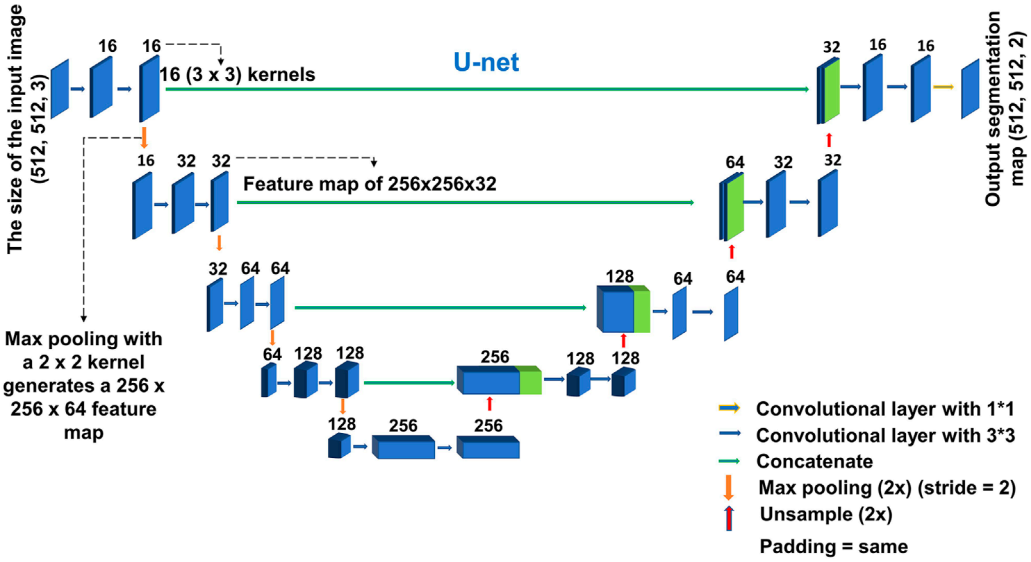

FIGURE 2
The architecture of the modified U-Net model.

TABLE 1 Comparison of network architecture performance results on DeepCrack dataset for 20 epochs.

Network architectures	Training time (s)	Accuracy	Precision	Recall	F1-score
Traditional UNet	1,471	0.9824	0.8621	0.6505	0.6821
Modified U-Net	223	0.9896	0.8864	0.7683	0.8229

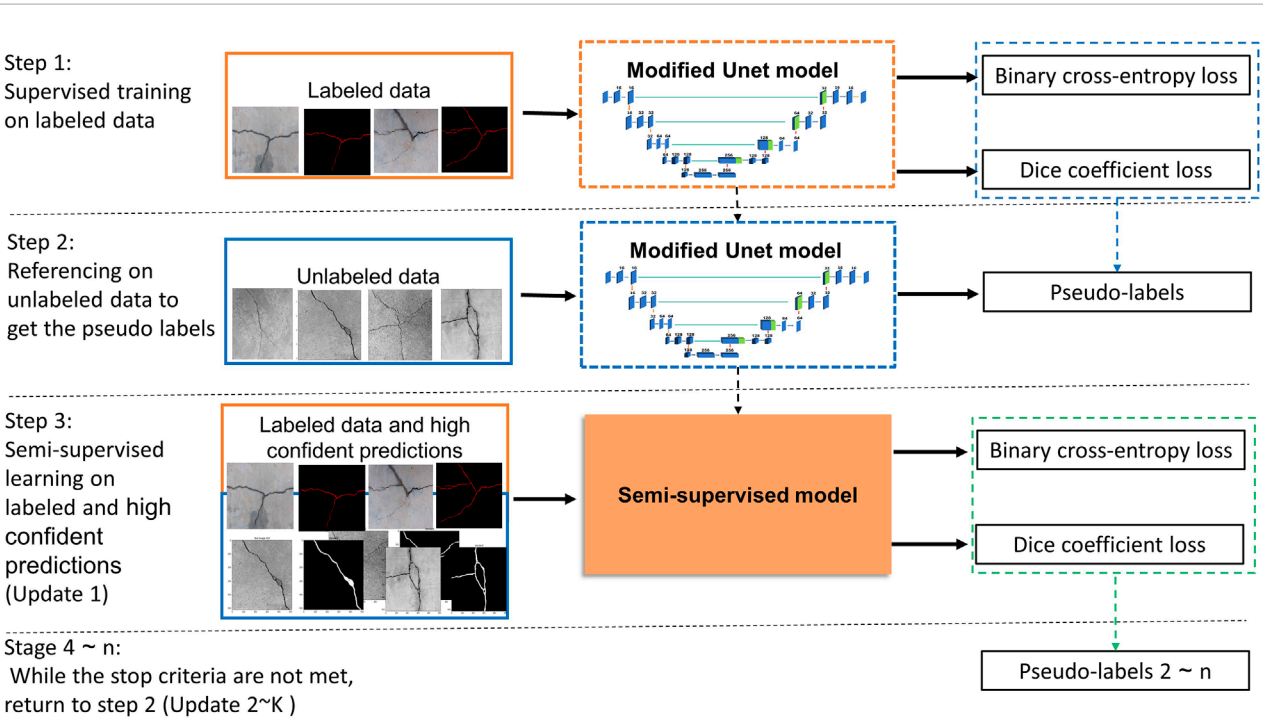

FIGURE 3
The main framework of the proposed dataset updating strategy.

Input: Training dataset $S = \{x_n, y_n, x_{non_m}\}$
Output: Label predicted y_{pred_m} for unlabeled data x_{non_m}
STEP 1: Initialization
- Learning method: learning rate, batch size, epoch
- Choose labeled data S for training the modified U-Net model

STEP 2:
- Update the modified U-Net model parameters θ by solving Eq. 2
- Calculate Binary cross-entropy loss for the labeled data S
- Calculate Dice coefficient loss for the labeled data S

STEP 3:
- Predict the pseudo-label y_{pred_m} using Eq. 3

STEP 4:
- Using pseudo-label probability that have greater than a threshold value
- Update the training dataset S^* by combining labeled data and pseudo-labels using Eq. 4
- Training the modified U-Net model on the updated training dataset S^*
- Calculate Binary cross-entropy loss for the labeled data S^*
- Calculate Dice coefficient loss for the labeled data S^*

STEP 5:
- while the stop criteria are not met, do
- Return to STEP 3
- end while

STEP 6: Use the final model to predict the label of the test set and evaluate

Algorithm 1. Semi-supervised learning method for the crack images segmentation.

2) Crack500 dataset Yang et al. (2019). There are 3,792 training images, 696 validation images, and 2,246 test images, all with a fixed size of 640 × 360 pixels and a variety of crack types. This dataset presents a challenge due to the complex inference factors such as uneven lighting conditions and shadows. Some samples are shown in **Figure 5**.

To guarantee the robustness of the proposed method, we also expand the dataset upon on DeepCrack and Crack500 dataset. Li et al. (2019) released a bridge crack image data in 2019. However, this dataset does not contain ground truth labels, therefore, cannot be directly used for training. We independently made manual pixel-level labels for the contained bridge crack images, generating a new expanded dataset for crack semantic segmentation.

3) Bridge cracks dataset with independent manual labels. The images are from a realistic crack dataset available to the public. This dataset includes 2068 crack images with a resolution of 1,024 × 1,042. These images were taken on a real bridge using the CMOS camera built into the DJI Phantom4 Pro drone. Pixel-level ground truth for this dataset was carefully manually created using the Labelme tool to train and test the proposed model. Some samples are shown in **Figure 6**. This manual labeled dataset will be available and released to public along with this paper.

3.2 Evaluation metrics

This study used six metrics to evaluate fully supervised and semi-supervised models. The relationship between the ground truth and the predicted result for each pixel can be divided into True Positive (TP), False Positive (FP), False Negative (FN), and True Negative (TN) for the binary pixel-level classification task. For crack detection, TP denotes the number of pixels correctly predicted as cracks which the ground truth is also a crack; FP denotes the number of pixels illogically predicted as cracks but are non-cracks in the ground truth; FN denotes the number of pixels predicted as non-cracks, but are the ground truth is a crack, and TN denotes the number of pixels predicted as non-cracks for which the ground truth is also a non-crack. To evaluate the performance of a model, many indexes describing the result accuracy have been proposed, including precision, recall, F1-score, and IoU. Precision represents the fraction of relevant instances among the retrieved ones. Recall is the fraction of all relevant instances that are actually retrieved, the F-score, which can balance precision and recall effects and provide a more comprehensive assessment of the performance of a classifier and Intersection of union (IoU) is the overlap area of the predicted segmentation and the ground truth divided by the union area of the predicted segmentation and the ground truth. Equations **5–8** presents precision, recall, F1-score, and Intersection of union (IoU). The precision, recall, and F-score metrics did not consider TN. In contrast, the area under the ROC curve (AUC) metric considers the TN and provides a more comprehensive evaluation of the method performance. In addition, the ROC curves can be plotted by thresholding the anomaly scores, and the Area Under the ROC Curve (AUC) can be calculated to quantify anomaly detection performance. AUC is also used to evaluate performance compared to unsupervised anomaly detection methods. Furthermore, pixel accuracy is the most basic metric for indicating the proportion of correctly predicted pixels.

$$Precision = \frac{TP}{(TP + FP)}. \tag{5}$$

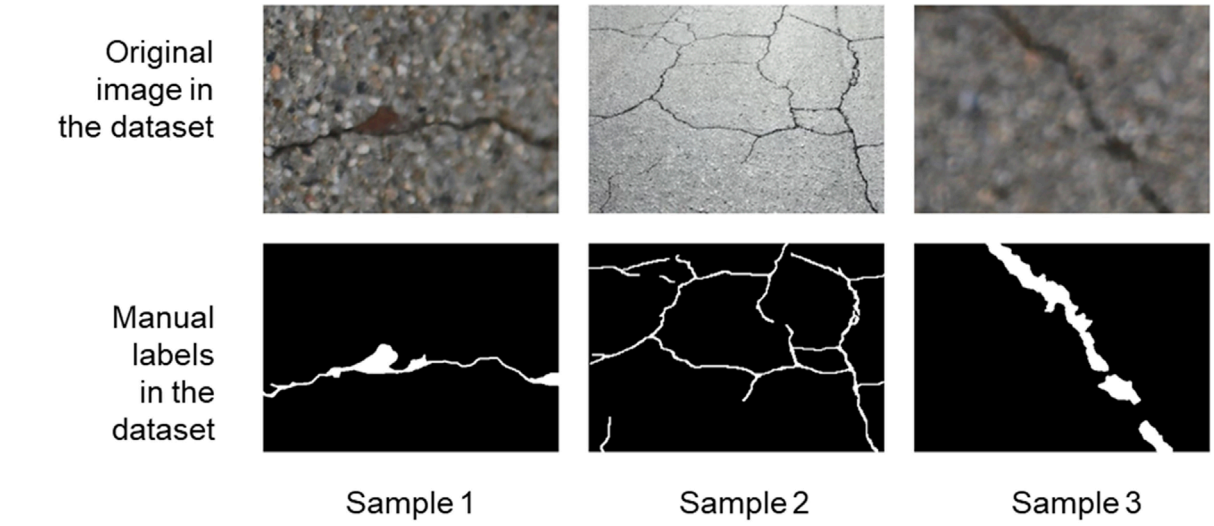

FIGURE 4
Samples of source images and crack labels in DeepCrack dataset Liu et al. (2019a).

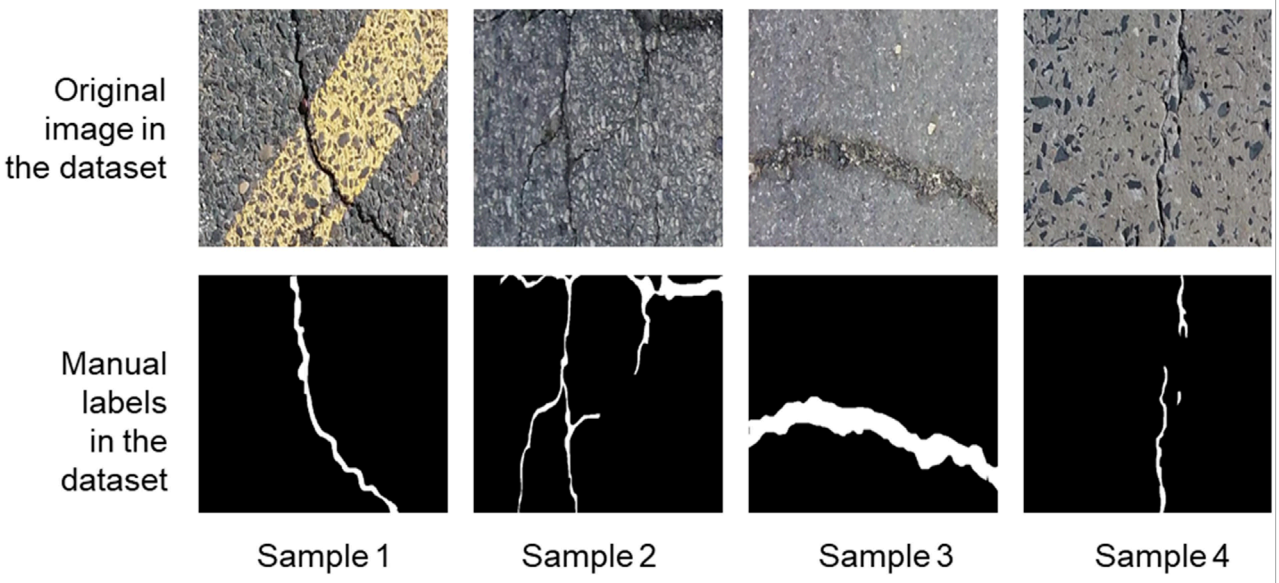

FIGURE 5
Samples of source images and crack labels in Crack500 dataset Yang et al. (2019).

$$Recall = \frac{TP}{(TP + FN)} \tag{6}$$

$$F_{1-score} = 2\frac{(Precision \star Recall)}{(Precision + Recall)} \tag{7}$$

$$IOU = 2\frac{(Precision \star Recall)}{(Precision + Recall - Precision \star Recall)} \tag{8}$$

4 Results

4.1 Training implementation

The models were trained with a fixed learning rate of 0.001 for 100 epochs. The loss and optimization functions were binary cross-entropy and Adam, respectively. Batch sizes of 24 were used to train the models. When the validation loss function is

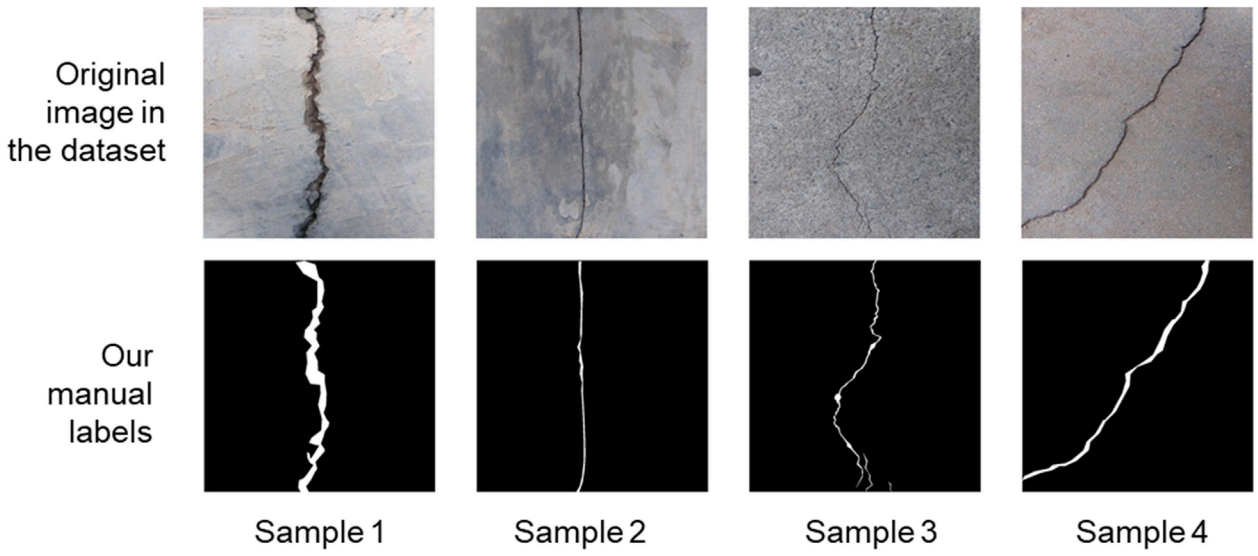

FIGURE 6
Samples of source images in Li et al. (2019), and our manual crack labels in Bridge cracks dataset.

reduced, the models' weights are preserved to reduce overfitting. The models were trained using the Keras, Tensorflow and Python libraries on the Google Colaboratory virtual environment. During training and validation, the loss is primarily used to assess the discrepancy between the predicted and actual values, the dice coefficient is selected as monitoring criteria to guide hyper-parameter learning. Figure 7 shows the loss curve and the dice curve during validation. It observes that network performance differs across datasets, which is not surprising given the fact that different datasets have cracks of varying shapes and sizes, complex backgrounds, and varied surface conditions. In DeepCrack images, background intensity and crack intensity are with high contrast. Therefore, most cracks can be accurately extracted from pavement images. While Crack500 makes crack segmentation challenging due to its diverse widths and shapes. The background textures of most crack images are complex. The same problem exists in the Bridge cracks dataset. It also observes that the loss value of the 80% Crack500 dataset is higher than that of the other dataset because the proposed method added pseudo labels to the previous dataset to update it and train the proposed model (80% pseudo labels added to 80% labeled data). The more pseudo labels there are, the greater the loss because the accuracy of those labels is insufficient due to the variety of widths and shapes and the fact that the background textures of most crack images in the Ckack500 dataset are complex.

4.2 Experiment configuration

The proposed semi-supervised method was trained on the bridge crack dataset (Our labeled dataset). 20%, 40%, 60%, and 80% of the labeled data were used to train and test the semi-supervised crack segmentation method. When trained with 20% of the labeled data, the semi-supervised model automatically generates labels for 80% of unlabeled data by dataset updating strategy. When trained with 40%, 60%, and 80% of the labeled data, the semi-supervised model automatically generates labels twice or three times as much as the number of the training labeled data. Data augmentation was used to generate sufficient training data to ensure the generalization ability of the semi-supervised model. The quantitative results of the semi-supervised method on the bridge crack dataset are shown in Table 2. The results of the semi-supervised method were better in terms of recall, F1-Score, AUC, and IOU when only 60% of the labeled data was used. In addition, the model automatically generated labels for the unlabeled data that were twice as large as the labeled quantity. It is demonstrated that the semi-supervised method achieved good crack segmentation results. The results of the semi-supervised method on the test sets for bridge crack segmentation are shown in Figure 8. Dashed red dashed rectangle denote FP error. The DeepCrack and Crack500 datasets were used to train and test the proposed model in order to comprehensively evaluate its performance.

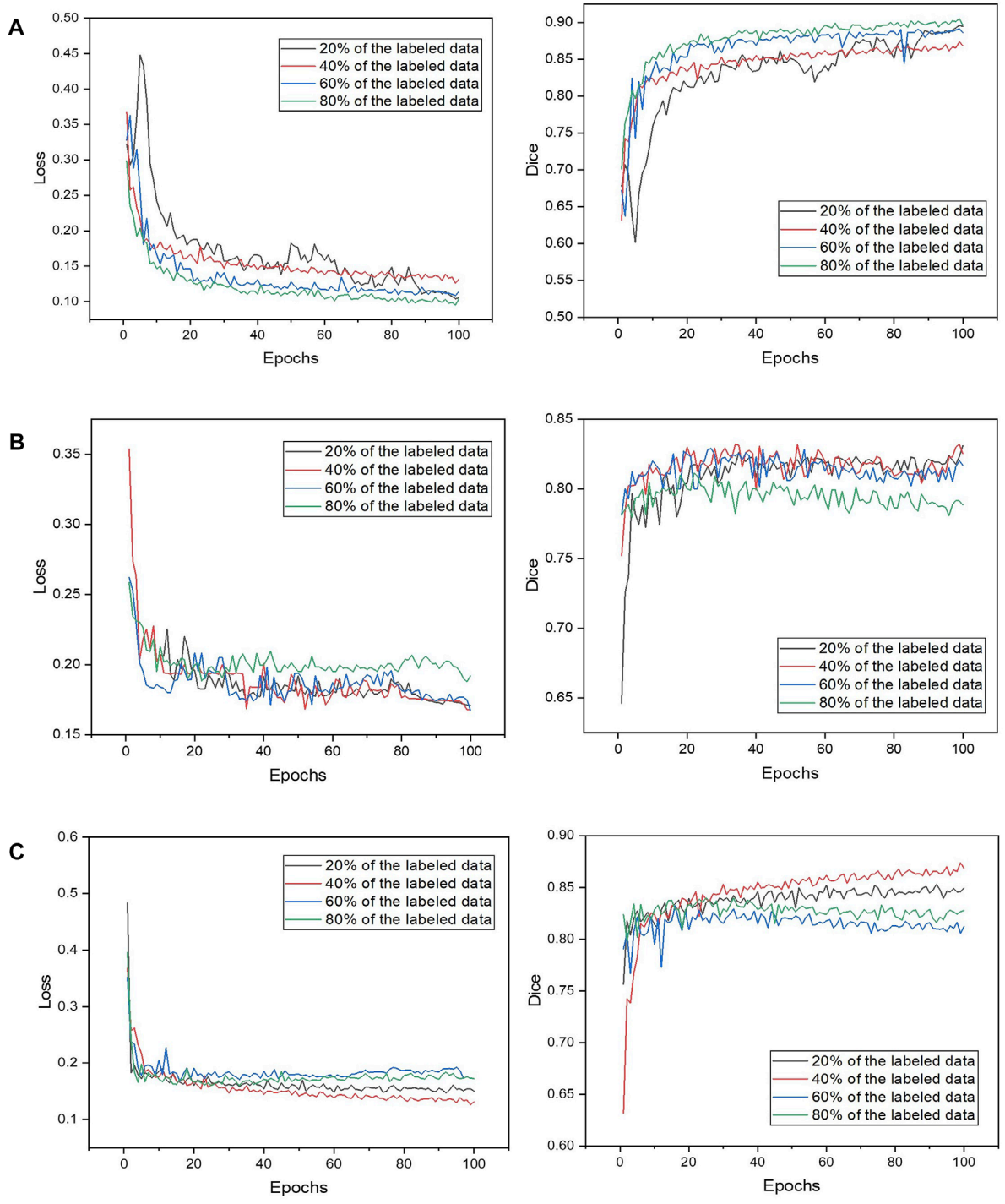

FIGURE 7
The loss curve and the dice curve during validation. **(A)** DeepCrack dataset; **(B)** Crack500 dataset; **(C)** The bridge crack dataset.

As in previous experiments, the training was performed on 20%, 40%, 60%, and 80% of the labeled data, respectively. The experimental results of the two datasets show that semi-supervised learning-based crack segmentation is effective. The quantitative results of the semi-supervised method are shown in Tables 3, 4. When only 60% of DeepCrack's labeled data is used, the semi-supervised model outperforms the others in terms of F1-Score, AUC, and IOU. Additionally, the model

TABLE 2 The bridge crack dataset: Comparison of crack segmentation performance between fully supervised learning (FSL) and semi-supervised learning (SSL).

	Labeled data use (%)	Accuracy	Precision	Recall	F1-score	AUC	IOU
FSL	20	0.9530	0.8797	0.3509	0.5010	0.6737	0.3346
	40	0.9561	0.7074	0.5941	0.6458	0.7882	0.4769
	60	0.9581	0.6888	0.6925	0.6902	0.8349	0.5270
	80	0.9589	0.6934	0.6976	0.6955	0.8376	0.5331
SSL	20	0.95465	0.8789	0.3787	0.5293	0.6875	0.35995
	40	0.9576	0.7193	0.6083	0.6591	0.7956	0.4916
	60	0.9589	0.6898	0.7079	0.6987	0.8425	0.5370
	80	0.9602	0.7153	0.6790	0.6967	0.8297	0.5345

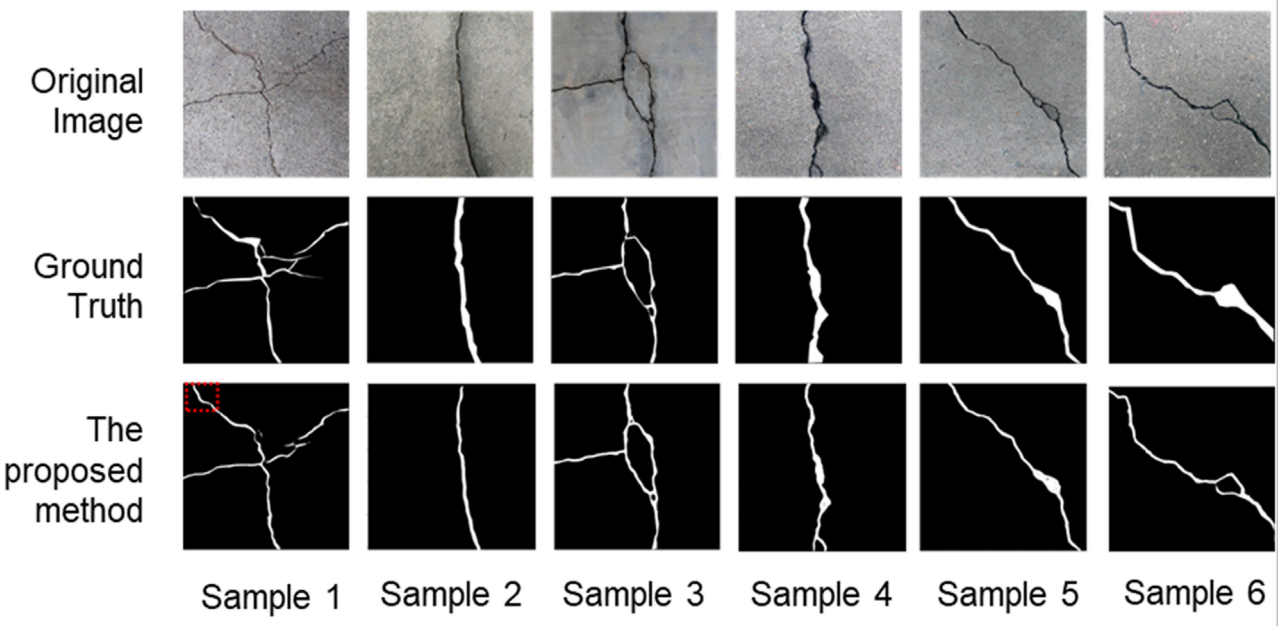

FIGURE 8
The bridge crack: Semi-supervised pixel-level segmentation results on the test set. Areas denoted by dashed red rectangles indicate FP errors.

TABLE 3 The DeepCrack dataset: Comparison of crack segmentation performance between supervised learning (FSL) and semi-supervised learning (SSL).

	Labeled data use (%)	Accuracy	Precision	Recall	F1-score	AUC	IOU
FSL	20	0.9823	0.8468	0.7578	0.7799	0.8755	0.66432
	40	0.9852	0.8400	0.8389	0.8395	0.9156	0.7233
	60	0.9856	0.8568	0.8265	0.8413	0.9099	0.7261
	80	0.9861	0.8574	0.8383	0.8478	0.9158	0.7358
SSL	20	0.9811	0.8184	0.7777	0.7932	0.8843	0.65782
	40	0.9849	0.8320	0.8445	0.8382	0.9181	0.7215
	60	0.9861	0.8519	0.8434	0.8482	0.9182	0.73645
	80	0.9862	0.8630	0.8333	0.8479	0.9134	0.7360

TABLE 4 The Crack500 dataset: Comparison of crack segmentation performance between fully supervised learning (FSL) and semi-supervised learning (SSL).

	Labeled data use (%)	Accuracy	Precision	Recall	F1-score	AUC	IOU
FSL	20	0.9559	0.6234	0.6057	0.6144	0.7916	0.4434
	40	0.9571	0.6238	0.6547	0.6389	0.8152	0.4694
	60	0.9601	0.6542	0.6625	0.6583	0.8205	0.4907
	80	0.9610	0.6581	0.6793	0.6685	0.8288	0.5021
SSL	20	0.9567	0.6333	0.6016	0.6171	0.7901	0.4462
	40	0.9616	0.6884	0.6151	0.6497	0.7990	0.4811
	60	0.9607	0.6681	0.6416	0.6546	0.8110	0.4865
	80	0.9619	0.6724	0.6685	0.6705	0.8242	0.5043

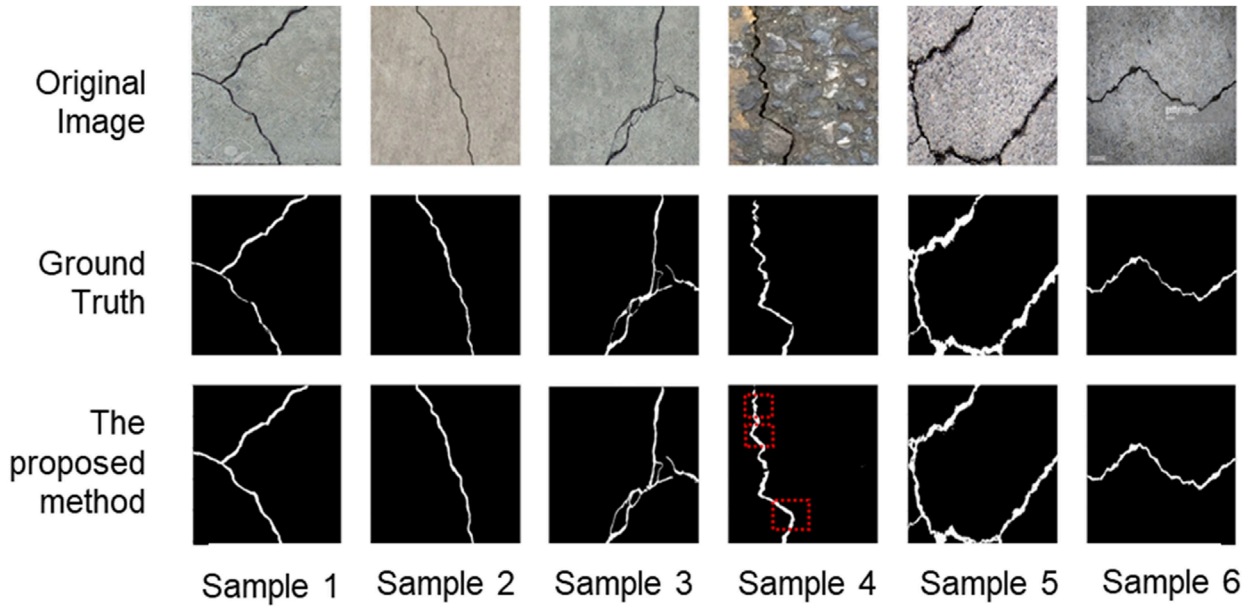

FIGURE 9
The DeepCrack: Semi-supervised pixel-level segmentation results on the test set. Areas denoted by dashed red rectangles indicate FP errors.

automatically generated labels twice as large as the labeled quantity for the unlabeled data. While outperformed the others in terms of recall, AUC, and IOU when trained on the Crack500 dataset with 80% labeled data. The semi-supervised learning strategy employs both unlabeled and labeled data to obtain rich data and optimize the segmentation model's performance. Figures 9, 10 show samples of segmentation results of the semi-supervised model on the test set of the DeepCrack and Crack500 datasets, respectively. Although the semi-supervised method achieves good crack segmentation results, some FN and FP errors cannot be completely avoided. Dashed red rectangles indicate FP errors. The experimental results of the two datasets show that semi-supervised learning-based crack segmentation is effective.

5 Discussion

5.1 Comparison with fully supervised learning

The proposed semi-supervised segmentation method and the fully supervised segmentation method are trained with the same training parameters to achieve convergence.

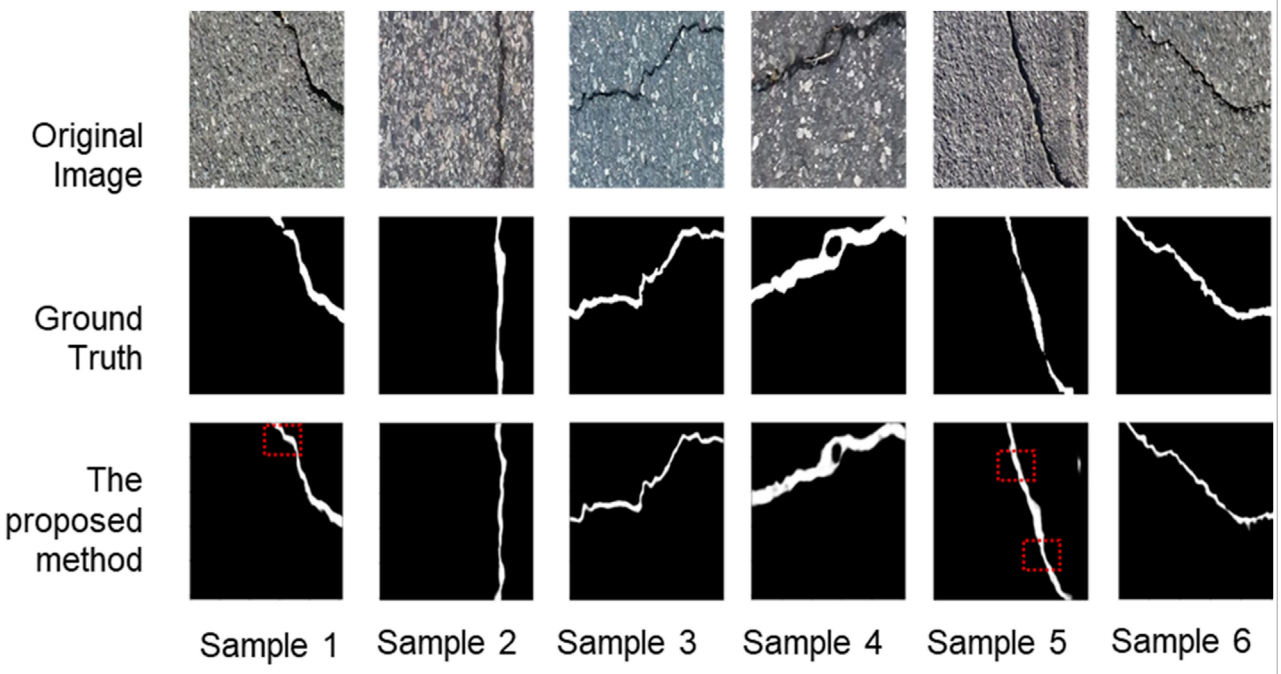

FIGURE 10
The Crack500: Semi-supervised pixel-level segmentation results on the test set. Areas denoted by dashed red rectangles indicate FP errors.

First, the performance of the fully supervised method and semi-supervised method were compared on the bridge crack dataset (Our labeled dataset). 20%, 40%, 60%, and 80% of the labeled data were used to train and test the semi-supervised crack segmentation method. The quantitative comparison results between the fully supervised and semi-supervised methods are shown in **Table 2**. Comparing the semi and fully supervised methods and training on a bridge crack dataset with 20% labeled data, the proposed semi-supervised produced the same or improved performance metrics of accuracy, recall, F1 score, AUC, and IOU results. A similar trend of improvement of accuracy, precision, recall, F1-score, AUC, and IOU was observed when training on bridge crack dataset with 40%, 60%, and 80% labeled data. When 20% and 80% of the labeled data were used for training, the results were still acceptable compared to the fully supervised approach. Although there was a 0.08% difference in precision and a 0.79% difference in AUC, it significantly reduced the workload of data labeling.

Furthermore, the semi-supervised segmentation approach produces better results than the fully supervised approach in most metrics, proving the proposed model's efficacy.

Secondly, compared the performance of the fully supervised method and semi-supervised method was on the DeepCrack and Crack500 datasets in order to comprehensively evaluate its performance. As in previous experiments, the training was performed on 20%, 40%, 60%, and 80% of the labeled data, respectively. From the results shown in **Tables 3**, **4**. It is obvious that the proposed model has clear advantages. The semi-supervised approach provided better results than the fully supervised approach in most metrics. As shown in the tables, the segmentation results of the fully supervised and semi-supervised methods also improve as the number of labeled data increases; this is in line with the fact that increasing the number of labeled images in a deep neural network model improves parameter estimation accuracy.

The semi-supervised method is superior to the fully supervised method for crack segmentation because the workload associated with labeled data is significantly reduced while ensuring accuracy. The experimental results of the two datasets show that semi-supervised learning-based crack segmentation is effective.

5.2 Comparison with Pix2Pix cGAN method

The Pix2Pix method Isola et al. (2017) and Kyslytsyna et al. (2021) is a well-known strategy for image-to-image translation. It is based on a conditional generative adversarial network, in which a target image is generated and conditioned on an input image. The generator of the Pix2Pix model uses a U-Net based architecture Ronneberger et al. (2015) and the discriminator of the model uses a convolutional "PatchGAN" classifier that only penalizes the structure at the scale of image

TABLE 5 The bridge crack dataset: Comparison of crack segmentation performance between Pix2Pix cGAN method and ours method.

Method	Labeled data use	Precision	Recall	F1-score
Pix2Pix cGAN	20% of the labeled data	0.6172	0.5351	0.5619
	40% of the labeled data	0.7036	0.582	0.6259
	60% of the labeled data	0.7145	0.5895	0.6352
	80% of the labeled data	0.7457	0.6093	0.6604
Ours	20% of the labeled data	0.8789	0.3787	0.5293
	40% of the labeled data	0.7193	0.6083	0.6591
	60% of the labeled data	0.6898	0.7079	0.6987
	80% of the labeled data	0.7153	0.6790	0.6967

TABLE 6 The DeepCrack dataset: Comparison of crack segmentation performance between Pix2Pix cGAN method and ours method.

Method	Labeled data use	Precision	Recall	F1-score
Pix2Pix cGAN	20% of the labeled data	0.7396	0.6489	0.6865
	40% of the labeled data	0.749	0.656	0.6948
	60% of the labeled data	0.7582	0.6629	0.7027
	80% of the labeled data	0.7761	0.6726	0.7159
Ours	20% of the labeled data	0.8184	0.7777	0.7932
	40% of the labeled data	0.8320	0.8445	0.8382
	60% of the labeled data	0.8519	0.8434	0.8482
	80% of the labeled data	0.8630	0.8333	0.8479

TABLE 7 The Crack500 dataset: Comparison of crack segmentation performance between Pix2Pix cGAN method and ours method.

Method	Labeled data use	Precision	Recall	F1-score
Pix2Pix cGAN	20% of the labeled data	0.6755	0.5803	0.6164
	40% of the labeled data	0.6815	0.5877	0.6238
	60% of the labeled data	0.702	0.6042	0.642
	80% of the labeled data	0.7063	0.6117	0.6494
Ours	20% of the labeled data	0.6333	0.6016	0.6171
	40% of the labeled data	0.6884	0.6151	0.6497
	60% of the labeled data	0.6681	0.6416	0.6546
	80% of the labeled data	0.6724	0.6685	0.6705

patches. In order to verify the effectiveness of the proposed method, the results were compared with Pix2Pix method on the bridge crack, DeepCrack and Crack500 datasets. Three metrics were considered for performance comparison which include precision, recall, and F1-Score. The quantitative comparison results between Pix2Pix cGAN and semi-supervised methods are shown in **Tables 5**–**Tables 7**. The proposed method outperforms Pix2Pix cGAN in all metrics when 40% of the labeled data is used on a bridge crack dataset, but for Pix2Pix cGAN using 20%, 40%, and 60% of the labeled data. The proposed method outperforms Pix2Pix cGAN in all metrics when 20% of the labeled data is used on a DeepCrack dataset, but for Pix2Pix cGAN using 20%, 40%, and 60% of the labeled data. The proposed method outperforms Pix2Pix cGAN in terms of recall and F1-Score when 40% of labeled data is used on the Crack500 dataset, but for the Pix2Pix cGAN method 20%, 40% and 60% of labeled data are used.

TABLE 8 Comparison of crack segmentation performance results on DeepCrack.

Method		Accuracy	Precision	Recall	F1-score
HED Xie and Tu (2015)		0.983	0.797	0.799	0.798
SegNet Badrinarayanan et al. (2017)		0.982	0.800	0.768	0.784
RCE Liu et al. (2017)		0.985	0.832	0.799	0.815
DeepCrack Liu et al. (2019a)		0.980	0.779	0.735	0.756
DeepCrack Zou et al. (2018)		0.988	0.874	0.837	0.855
Crackseg Song et al. (2020)		0.984	0.815	0.804	0.812
Deeply supervised network Qu et al. (2021)		0.988	0.867	0.850	0.858
Ours method	20% of the labeled data	0.981	0.818	0.778	0.793
	40% of the labeled data	0.985	0.832	0.845	0.838
	60% of the labeled data	0.986	0.852	0.843	0.848
	80% of the labeled data	0.986	0.863	0.833	0.848

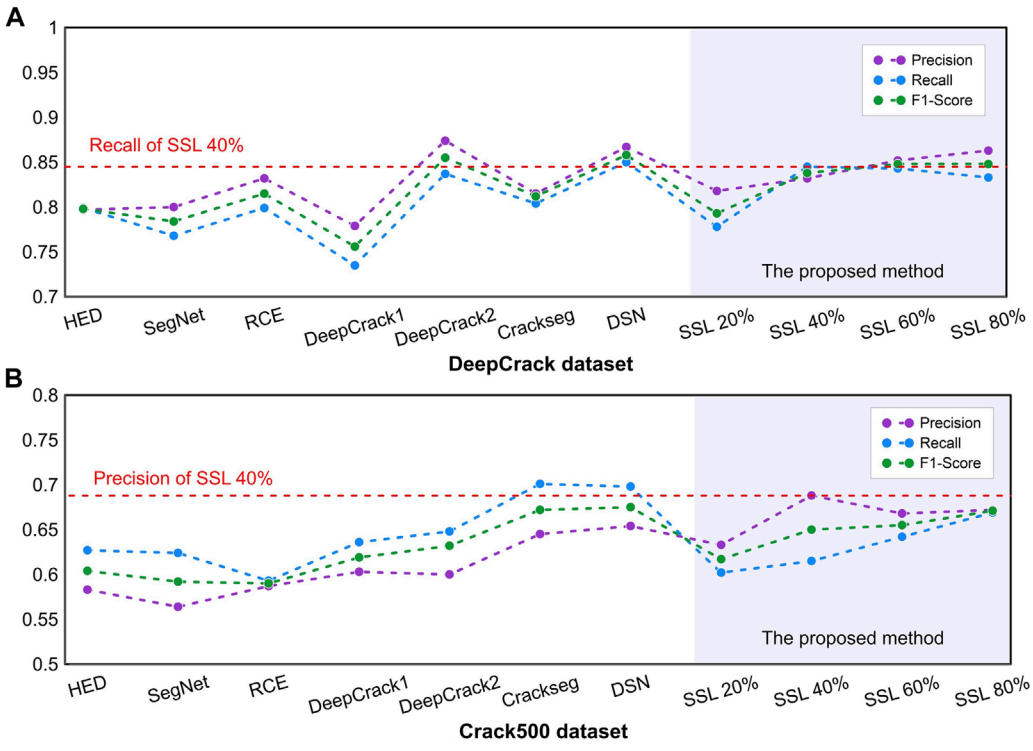

FIGURE 11
Comparison between precision, recall and F1-Score of all fully supervised and the proposed semi-supervised methods on DeepCrack and Crack500 datasets.

5.3 Comparison with the existing fully supervised methods

In order to verify the effectiveness of the proposed method, the results were compared with current state-of-the-art methods on DeepCrack and Crack500 datasets. Four metrics were considered for performance comparison which include accuracy, precision, recall, and F1-Score.

5.3.1 Comparison on DeepCrack dataset

Table 8 shows the comparison of crack segmentation performance results on DeepCrack dataset. The deeply

TABLE 9 Comparison of crack segmentation performance results on DeepCrack.

Method		Accuracy	Precision	Recall	F1-score
HED Xie and Tu (2015)		0.954	0.583	0.627	0.604
SegNet Badrinarayanan et al. (2017)		0.952	0.564	0.624	0.592
RCE Liu et al. (2017)		0.952	0.587	0.593	0.590
DeepCrack Liu et al. (2019a)		0.956	0.603	0.636	0.619
DeepCrack Zou et al. (2018)		0.956	0.600	0.648	0.632
Crackseg Song et al. (2020)		0.962	0.645	0.701	0.672
Deeply supervised network Qu et al. (2021)		0.963	0.654	0.698	0.675
Ours method	20% of the labeled data	0.957	0.633	0.602	0.617
	40% of the labeled data	0.962	0.688	0.615	0.650
	60% of the labeled data	0.961	0.668	0.642	0.655
	80% of the labeled data	0.962	0.672	0.669	0.671

supervised network outperforms the others in terms of accuracy, recall, and F1-Score. When the semi-supervised method was compared to the deeply supervised network, the proposed method results were still acceptable despite 0.2%, 0.4%, 1.7%, and 1% gaps in accuracy, precision, recall, and F1-Score respectively. In addition, method significantly reduced the workload associated with data labeling. Furthermore, when 40% of the labeled data was only used, the proposed method was second best by outperforming HED, SegNet, RCE, DeepCrack Liu et al. (2019a), and Crackseg in all metrics. **Figure 11A** shows a comparison between precision, recall and F1-Score of all fully supervised and the proposed semi-supervised methods on DeepCrack dataset.

5.3.2 Comparison on Crack500 dataset

As shown in **Table 9**, the proposed method outperformed competitive methods in terms of precision, and the deeply supervised network outperformed the others in terms of accuracy and F1-Score. At the same time, the Crackseg outperformed the other methods in terms of recall. When 20% of the labeled data was only used, the proposed method outperformed HED, SegNet, and RCE in all metrics. Furthermore, when 80% of the labeled data was used, the proposed method outperformed HED, SegNet, RCE, DeepCrack Liu et al. (2019a), and DeepCrack in all metrics. **Figure 11B** shows a comparison between precision, recall and F1-Score of all fully supervised and the proposed semi-supervised methods on Crack500 dataset.

The experimental results of the Deepcrack and Crack500 datasets demonstrate that the proposed method is effective. Compared to the fully supervised segmentation method, the semi-supervised method significantly reduced the workload associated with the data labeling while ensuring accuracy. In addition, recent studies have shown that the semi-supervised method for crack detection is effective Wang and Su (2021) Li et al. (2020) and Shim et al. (2020).

5.4 Limitations

Although the semi-supervised approach outperforms the fully supervised methods, and the results show that the proposed method is capable of avoiding the issue of insufficient manual labeling while ensuring accuracy, the proposed method has some limitations worth discussing. A major limitation is with the network type used. The network type is critical in achieving a satisfactory result for image segmentation. We used a modified U-Net deep learning network in this paper; we will experiment with another network using the same semi-supervised approach in the future. In addition, no research has been conducted on quantifying geometric features such as crack depth, width, and length to assess civil structures' health.

6 Conclusion

This paper proposes a novel semi-supervised learning method for crack segmentation based on deep learning. The proposed approach combines deep neural networks and a semi-supervised learning strategy to address the issue of labeling cracked images, which is expensive in terms of both finance and human resources. The semi-supervised learning approach combines labeled and unlabeled data to obtain and optimize the performance of the segmentation model. The experimental results of the DeepCrack and Crack500 datasets demonstrate that the proposed method is effective. Compared to the fully supervised segmentation method, the semi-supervised method significantly reduced the workload associated with

the data labeling while ensuring accuracy. Moreover, results show that the proposed semi-supervised learning method achieved quite approaching accuracies to the established fully supervised models using multiple accuracy indexes, however, the requirement for the labeled data reduces to 40%.In future research, the results of crack image segmentation will be used to calculate the quantification of geometric features such as crack depth, width, and length to assess civil structures' health. Crack segmentation research will also be applied in engineering.

Data availability statement

The original contributions presented in the study are included in the article/Supplementary Material, further inquiries can be directed to the corresponding author.

Author contributions

MM, YL, and ZA-H designed the algorithm. MM, CL, and wrote the manuscript. ZA-H and WW collected the data and edited the manuscript.

Funding

This study was financially supported by the National Key Research and Development Program of China (Grant No. 2018YFD1100401); the National Natural Science Foundation of China (Grant No. 52078493); the Natural Science Foundation for Excellent Young Scholars of Hunan (Grant No. 2021JJ20057); the Natural Science Foundation of Hunan Province (Grant No. 2022JJ30700); the Innovation Provincial Program of Hunan Province (Grant No. 2020RC3002), and the Science and Technology Plan Project of Changsha (No. kq2206014). These financial supports are gratefully acknowledged.

Acknowledgments

The authors also extend gratitude to editor-in-chief and two reviewers for their insightful comments.

Conflict of interest

The authors declare that the research was conducted in the absence of any commercial or financial relationships that could be construed as a potential conflict of interest.

Publisher's note

All claims expressed in this article are solely those of the authors and do not necessarily represent those of their affiliated organizations, or those of the publisher, the editors and the reviewers. Any product that may be evaluated in this article, or claim that may be made by its manufacturer, is not guaranteed or endorsed by the publisher.

References

Adhikari, R., Moselhi, O., and Bagchi, A. (2014). Image-based retrieval of concrete crack properties for bridge inspection. *Automation Constr.* 39, 180–194. doi:10.1016/j.autcon.2013.06.011

Al-Huda, Z., Peng, B., Li, T., and Alfasly, S. (2022). Weakly supervised pavement crack semantic segmentation based on multi-scale object localization and incremental annotation refinement. *Appl. Intell. (Dordr).* 52. doi:10.1007/s10489-022-04212-w

Al-Huda, Z., Peng, B., Yang, Y., Algburi, R. N. A., Ahmad, M., Khurshid, F., et al. (2021). Weakly supervised semantic segmentation by iteratively refining optimal segmentation with deep cues guidance. *Neural comput. Appl.* 33, 9035–9060. doi:10.1007/s00521-020-05669-x

Ayenu-Prah, A., and Attoh-Okine, N. (2008). Evaluating pavement cracks with bidimensional empirical mode decomposition. *EURASIP J. Adv. Signal Process.* 2008, 861701–861707. doi:10.1155/2008/861701

Badrinarayanan, V., Kendall, A., and Cipolla, R. (2017). Segnet: A deep convolutional encoder-decoder architecture for image segmentation. *IEEE Trans. Pattern Anal. Mach. Intell.* 39, 2481–2495. doi:10.1109/tpami.2016.2644615

Biondini, F., Frangopol, D. M., et al. (2016). Life-cycle performance of deteriorating structural systems under uncertainty: Review. *J. Struct. Eng. (N. Y. N. Y).* 142, F4016001. doi:10.1061/(asce)st.1943-541x.0001544

Bursanescu, L., Bursanescu, M., Hamdi, M., Lardigue, A., and Paiement, D. (2001). "Three-dimensional infrared laser vision system for road surface features analysis," in *Romopto 2000: Sixth conference on optics (SPIE)*, 4430, 801–808.

Cao, W., Liu, Q., and He, Z. (2020). Review of pavement defect detection methods. *Ieee Access* 8, 14531–14544. doi:10.1109/access.2020.2966881

Cheng, J. C., and Wang, M. (2018). Automated detection of sewer pipe defects in closed-circuit television images using deep learning techniques. *Automation Constr.* 95, 155–171. doi:10.1016/j.autcon.2018.08.006

Cheng, J., Xiong, W., Chen, W., Gu, Y., and Li, Y. (2018). "Pixel-level crack detection using u-net," in *TENCON 2018-2018 IEEE region 10 conference* (IEEE), 0462–0466.

Dai, J., He, K., and Sun, J. (2015). "Boxsup: Exploiting bounding boxes to supervise convolutional networks for semantic segmentation," in *Proceedings of the IEEE international conference on computer vision*, 1635–1643.

Dong, Z., Wang, J., Cui, B., Wang, D., and Wang, X. (2020). Patch-based weakly supervised semantic segmentation network for crack detection. *Constr. Build. Mater.* 258, 120291. doi:10.1016/j.conbuildmat.2020.120291

Fei, X., Branke, J., and Gülpınar, N. (2018). New sampling strategies when searching for robust solutions. *IEEE Trans. Evol. Comput.* 23, 273–287. doi:10.1109/tevc.2018.2849331

Gavilán, M., Balcones, D., Marcos, O., Llorca, D. F., Sotelo, M. A., Parra, I., et al. (2011). Adaptive road crack detection system by pavement classification. *Sensors* 11, 9628–9657. doi:10.3390/s111009628

Goodfellow, I., Pouget-abadie, J., Mirza, M., Xu, B., and Warde-farley, D. (2016). Generative modeling generative modeling. *Annu. Plant Rev.*

Gopalakrishnan, K., Khaitan, S. K., Choudhary, A., and Agrawal, A. (2017). Deep convolutional neural networks with transfer learning for computer vision-based data-driven pavement distress detection. *Constr. Build. Mater.* 157, 322–330. doi:10.1016/j.conbuildmat.2017.09.110

Hadjidemetriou, G. M., and Christodoulou, S. E. (2019). Vision-and entropy-based detection of distressed areas for integrated pavement condition assessment. *J. Comput. Civ. Eng.* 33, 04019020. doi:10.1061/(asce)cp.1943-5487.0000836

Han, C., Ma, T., Huyan, J., Huang, X., and Zhang, Y. (2021a). Crackw-net: A novel pavement crack image segmentation convolutional neural network. *IEEE Trans. Intell. Transp. Syst.* 23, 22135–22144. doi:10.1109/tits.2021.3095507

Han, Z., Chen, H., Liu, Y., Li, Y., Du, Y., and Zhang, H. (2021b). Vision-based crack detection of asphalt pavement using deep convolutional neural network. *Iran. J. Sci. Technol. Trans. Civ. Eng.* 45, 2047–2055. doi:10.1007/s40996-021-00668-x

Huyan, J., Li, W., Tighe, S., Xu, Z., and Zhai, J. (2020). Cracku-net: A novel deep convolutional neural network for pixelwise pavement crack detection. *Struct. Control Health Monit.* 27, e2551. doi:10.1002/stc.2551

Huyan, J., Li, W., Tighe, S., Zhai, J., Xu, Z., and Chen, Y. (2019). Detection of sealed and unsealed cracks with complex backgrounds using deep convolutional neural network. *Automation Constr.* 107, 102946. doi:10.1016/j.autcon.2019.102946

Isola, P., Zhu, J.-Y., Zhou, T., and Efros, A. A. (2017). "Image-to-image translation with conditional adversarial networks," in *Proceedings of the IEEE conference on computer vision and pattern recognition*, 1125–1134.

Jenkins, M. D., Carr, T. A., Iglesias, M. I., Buggy, T., and Morison, G. (2018). "A deep convolutional neural network for semantic pixel-wise segmentation of road and pavement surface cracks," in *2018 26th European signal processing conference (EUSIPCO)* (IEEE), 2120–2124.

Karimpouli, S., and Kadyrov, R. (2022). Multistep super resolution double-u-net (srdun) for enhancing the resolution of berea sandstone images. *J. Petroleum Sci. Eng.* 216, 110833. doi:10.1016/j.petrol.2022.110833

Kim, T., and Ryu, S. (2014). Pothole db based on 2d images and video data. *J. Emerg. Trends Comput. Inf. Sci.* 5, 527–531.

Kingma, D. P., and Ba, J. (2014). *Adam: A method for stochastic optimization. arXiv preprint arXiv:1412.6980*.

Krizhevsky, A., Sutskever, I., and Hinton, G. E. (2012). Imagenet classification with deep convolutional neural networks. *Adv. neural Inf. Process. Syst.* 25.

Kyslytsyna, A., Xia, K., Kislitsyn, A., Abd El Kader, I., and Wu, Y. (2021). Road surface crack detection method based on conditional generative adversarial networks. *Sensors* 21, 7405. doi:10.3390/s21217405

Li, C., Li, Y., Han, Z., Du, Y., Mohammed, M. A., Wang, W., et al. (2022). A novel multiphase segmentation method for interpreting the 3d mesoscopic structure of asphalt mixture using ct images. *Constr. Build. Mater.* 327, 127010. doi:10.1016/j.conbuildmat.2022.127010

Li, G., Wan, J., He, S., Liu, Q., and Ma, B. (2020). Semi-supervised semantic segmentation using adversarial learning for pavement crack detection. *IEEE Access* 8, 51446–51459. doi:10.1109/access.2020.2980086

Li, L.-F., Ma, W.-F., Li, L., and Lu, C. (2019). Research on detection algorithm for bridge cracks based on deep learning. *Acta Autom. Sin.* 45, 1727–1742.

Li, Q., Zou, Q., Zhang, D., and Mao, Q. (2011). Fosa: F* seed-growing approach for crack-line detection from pavement images. *Image Vis. Comput.* 29, 861–872. doi:10.1016/j.imavis.2011.10.003

Lin, D., Dai, J., Jia, J., He, K., and Sun, J. (2016). "Scribblesup: Scribble-supervised convolutional networks for semantic segmentation," in *Proceedings of the IEEE conference on computer vision and pattern recognition*, 3159–3167.

Liu, J., Yang, X., Lau, S., Wang, X., Luo, S., Lee, V. C.-S., et al. (2020). Automated pavement crack detection and segmentation based on two-step convolutional neural network. *Computer-Aided. Civ. Infrastructure Eng.* 35, 1291–1305. doi:10.1111/mice.12622

Liu, Y., Cheng, M.-M., Hu, X., Wang, K., and Bai, X. (2017). "Richer convolutional features for edge detection," in *Proceedings of the IEEE conference on computer vision and pattern recognition*, 3000–3009.

Liu, Y., Yao, J., Lu, X., Xie, R., and Li, L. (2019a). Deepcrack: A deep hierarchical feature learning architecture for crack segmentation. *Neurocomputing* 338, 139–153. doi:10.1016/j.neucom.2019.01.036

Liu, Z., Cao, Y., Wang, Y., and Wang, W. (2019b). Computer vision-based concrete crack detection using u-net fully convolutional networks. *Automation Constr.* 104, 129–139. doi:10.1016/j.autcon.2019.04.005

Long, J., Shelhamer, E., and Darrell, T. (2015). "Fully convolutional networks for semantic segmentation," in *Proceedings of the IEEE conference on computer vision and pattern recognition*, 3431–3440.

Maeda, H., Sekimoto, Y., Seto, T., Kashiyama, T., and Omata, H. (2018). Road damage detection and classification using deep neural networks with smartphone images. *Computer-Aided Civ. Infrastructure Eng.* 33, 1127–1141. doi:10.1111/mice.12387

Mohammed, M. A., Han, Z., and Li, Y. (2021). Exploring the detection accuracy of concrete cracks using various cnn models. *Adv. Mater. Sci. Eng.* 2021, 1–11. doi:10.1155/2021/9923704

Nguyen, N. H. T., Perry, S., Bone, D., Le, H. T., and Nguyen, T. T. (2021). Two-stage convolutional neural network for road crack detection and segmentation. *Expert Syst. Appl.* 186, 115718. doi:10.1016/j.eswa.2021.115718

Nhat-Duc, H., Nguyen, Q.-L., and Tran, V.-D. (2018). Automatic recognition of asphalt pavement cracks using metaheuristic optimized edge detection algorithms and convolution neural network. *Automation Constr.* 94, 203–213. doi:10.1016/j.autcon.2018.07.008

Patricio, M., Maravall, D., Usero, L., and Rejón, J. (2005). "Crack detection in wooden pallets using the wavelet transform of the histogram of connected elements," in *International work-conference on artificial neural networks* (Springer), 1206–1213.

Peng, B., Al-Huda, Z., Xie, Z., and Wu, X. (2020). Multi-scale region composition of hierarchical image segmentation. *Multimed. Tools Appl.* 79, 32833–32855. doi:10.1007/s11042-020-09346-y

Qu, Z., Cao, C., Liu, L., and Zhou, D.-Y. (2021). A deeply supervised convolutional neural network for pavement crack detection with multiscale feature fusion. *IEEE Trans. Neural Netw. Learn. Syst.* 33, 4890–4899. doi:10.1109/tnnls.2021.3062070

Radopoulou, S. C., and Brilakis, I. (2017). *Automated detection of multiple pavement defects*.

Rafiei, M. H., and Adeli, H. (2017). A novel machine learning-based algorithm to detect damage in high-rise building structures. *Struct. Des. Tall Spec. Build.* 26, e1400. doi:10.1002/tal.1400

Ren, S., He, K., Girshick, R., and Sun, J. (2015). Faster r-cnn: Towards real-time object detection with region proposal networks. *Adv. neural Inf. Process. Syst.* 28.

Reza, A. M. (2004). Realization of the contrast limited adaptive histogram equalization (clahe) for real-time image enhancement. *J. VLSI Signal Processing-Systems Signal Image Video Technol.* 38, 35–44. doi:10.1023/b:vlsi.0000028532.53893.82

Ronneberger, O., Fischer, P., and Brox, T. (2015). "U-net: Convolutional networks for biomedical image segmentation," in *International Conference on Medical image computing and computer-assisted intervention* (Springer), 234–241.

Seraj, F., Meratnia, N., and Havinga, P. J. (2017). "Rovi: Continuous transport infrastructure monitoring framework for preventive maintenance," in *2017 IEEE international conference on pervasive computing and communications* (PerComIEEE), 217–226.

Shim, S., Kim, J., Cho, G.-C., and Lee, S.-W. (2020). Multiscale and adversarial learning-based semi-supervised semantic segmentation approach for crack detection in concrete structures. *IEEE Access* 8, 170939–170950. doi:10.1109/access.2020.3022786

Song, W., Jia, G., Zhu, H., Jia, D., and Gao, L. (2020). Automated pavement crack damage detection using deep multiscale convolutional features. *J. Adv. Transp.* 2020, 1–11. doi:10.1155/2020/6412562

Tang, Y., Zhang, A. A., Luo, L., Wang, G., and Yang, E. (2021). Pixel-level pavement crack segmentation with encoder-decoder network. *Measurement* 184, 109914. doi:10.1016/j.measurement.2021.109914

Tong, Z., Gao, J., Wang, Z., Wei, Y., and Dou, H. (2019). A new method for cf morphology distribution evaluation and cfrc property prediction using cascade deep learning. *Constr. Build. Mater.* 222, 829–838. doi:10.1016/j.conbuildmat.2019.06.160

Tsang, D. C., and Lo, I. M. (2006). Influence of pore-water velocity on transport behavior of cadmium: Equilibrium versus nonequilibrium. *Pract. Period. Hazard. Toxic. Radioact. Waste Manage.* 10, 162–170. doi:10.1061/(asce)1090-025x(2006)10:3(162)

Wang, K., Gou, C., Duan, Y., Lin, Y., Zheng, X., and Wang, F.-Y. (2017). Generative adversarial networks: Introduction and outlook. *IEEE/CAA J. Autom. Sin.* 4, 588–598. doi:10.1109/jas.2017.7510583

Wang, W., and Su, C. (2021). Semi-supervised semantic segmentation network for surface crack detection. *Automation Constr.* 128, 103786. doi:10.1016/j.autcon.2021.103786

Woo, S., and Yeo, H. (2016). Optimization of pavement inspection schedule with traffic demand prediction. *Procedia - Soc. Behav. Sci.* 218, 95–103. doi:10.1016/j.sbspro.2016.04.013

Xie, S., and Tu, Z. (2015). "Holistically-nested edge detection," in *Proceedings of the IEEE international conference on computer vision*, 1395–1403.

Xu, Y., Wei, S., Bao, Y., and Li, H. (2019). Automatic seismic damage identification of reinforced concrete columns from images by a region-based deep convolutional neural network. *Struct. Control Health Monit.* 26, e2313. doi:10.1002/stc.2313

Yang, F., Zhang, L., Yu, S., Prokhorov, D., Mei, X., and Ling, H. (2019). Feature pyramid and hierarchical boosting network for pavement crack detection. *IEEE Trans. Intell. Transp. Syst.* 21, 1525–1535. doi:10.1109/tits.2019.2910595

Zhang, A., Wang, K. C., Fei, Y., Liu, Y., Tao, S., Chen, C., et al. (2018a). Deep learning–based fully automated pavement crack detection on 3d asphalt surfaces with an improved cracknet. *J. Comput. Civ. Eng.* 32, 04018041. doi:10.1061/(asce)cp.1943-5487.0000775

Zhang, A., Wang, K. C., Li, B., Yang, E., Dai, X., Peng, Y., et al. (2017). Automated pixel-level pavement crack detection on 3d asphalt surfaces using a deep-learning network. *Computer-Aided Civ. Infrastructure Eng.* 32, 805–819. doi:10.1111/mice.12297

Zhang, D., Zou, Q., Lin, H., Xu, X., He, L., Gui, R., et al. (2018b). Automatic pavement defect detection using 3d laser profiling technology. *Automation Constr.* 96, 350–365. doi:10.1016/j.autcon.2018.09.019

Zhou, S., Sheng, W., Wang, Z., Yao, W., Huang, H., Wei, Y., et al. (2019). Quick image analysis of concrete pore structure based on deep learning. *Constr. Build. Mater.* 208, 144–157. doi:10.1016/j.conbuildmat.2019.03.006

Zhou, Y., Wang, F., Meghanathan, N., and Huang, Y. (2016). Seed-based approach for automated crack detection from pavement images. *Transp. Res. Rec.* 2589, 162–171. doi:10.3141/2589-18

Zhu, J., Zhong, J., Ma, T., Huang, X., Zhang, W., and Zhou, Y. (2022). Pavement distress detection using convolutional neural networks with images captured via uav. *Automation Constr.* 133, 103991. doi:10.1016/j.autcon.2021.103991

Zhu, S., Xia, X., Zhang, Q., and Belloulata, K. (2007). "An image segmentation algorithm in image processing based on threshold segmentation," in *2007 third international IEEE conference on signal-image technologies and internet-based system* (IEEE), 673–678.

Zou, Q., Zhang, Z., Li, Q., Qi, X., Wang, Q., and Wang, S. (2018). Deepcrack: Learning hierarchical convolutional features for crack detection. *IEEE Trans. Image Process.* 28, 1498–1512. doi:10.1109/tip.2018.2878966

frontiers | Frontiers in Materials

TYPE Original Research
PUBLISHED 06 January 2023
DOI 10.3389/fmats.2022.1084999

OPEN ACCESS

EDITED BY
Cong Zhang,
Jiangnan University, China

REVIEWED BY
Amir R. Masoodi,
Ferdowsi University of Mashhad, Iran
Shao-Bo Kang,
Chongqing University, China

*CORRESPONDENCE
Yingbin Li,
281650659@qq.com

SPECIALTY SECTION
This article was submitted to Structural Materials, a section of the journal Frontiers in Materials

RECEIVED 31 October 2022
ACCEPTED 15 December 2022
PUBLISHED 06 January 2023

CITATION
Wang S, Li Y, Liu Z and Cheng T (2023), Calculation model of concrete-filled steel tube arch bridges based on the "arch effect".
Front. Mater. 9:1084999.
doi: 10.3389/fmats.2022.1084999

Calculation model of concrete-filled steel tube arch bridges based on the "arch effect"

Shaorui Wang, Yingbin Li*, Zengwu Liu and Tianlei Cheng

School of Civil Engineering, Chongqing Jiaotong University, Chongqing, China

In view of the limitations of the current code based on the equivalent beam-column method with the "rod mode" instead of the "arch mode" for the calculation of concrete-filled steel tube arch bridges, this paper takes the real bearing mechanism of the arch as the starting point and analyzes the different bearing mechanisms of the arch and eccentric pressurized column. The concrete-filled steel tube arch model test was carried out to analyze the deformation state and damage mode, and the geometric non-linear bending moment of the measured arch was compared with the bending moment value calculated by the eccentricity increase coefficient of the "rod mode." The results showed that the transfer of internal force is from the axial force to the arch axis, causing the vertical reaction force and horizontal thrust. However, the eccentric compression column only produced the vertical force at the bottom and combines with the lateral deformation indirectly generated by the eccentric distance. In addition, the deformation stage of the arch is basically the same as that of the eccentric compression column. The final failure mode of the arch is 4-hinge damage, and the final failure mode of the eccentric compression column is single-hinge damage. The preliminary geometric non-linear bending moment value obtained by the two modes accords well. Therefore, the main factors for the difference in the bearing mechanism between the two modes are different force structures, force transmission routes, and sources of deformation. Due to the difference in the bearing mechanism, the final failure mode is different, and the deformation ability of the arch is weakened by using the "rod mode" instead of the "arch mode." The geometric non-linear bending moment of the control section calculated by the eccentricity increase coefficient is conservative, but the influence of the geometric non-linearity of other sections is not considered enough.

KEYWORDS

concrete-filled steel tube arch, arch mode, geometric non-linearity, coefficient of eccentricity increase, equivalent beam and column method, eccentric compression column

1 Introduction

The concrete-filled steel tube (CFST) arch bridge having good span performance, superior bearing capacity, and graceful shape has been widely used. The CFST arch is restrained by the steel tube which significantly improves the compression resistance and spanning ability of the arch ribs, and the current braceless construction method of the arch bridge has matured, so the strong spanning ability, convenient construction method, and the ultra-high requirements for the foundation make the CFST arch bridge especially suitable for mountain and river canyons with treacherous terrain. However, large-span arch bridges are often affected by geometric non-linearity, and the damage rules are similar to those of eccentrically stressed columns (beam columns) due to the presence of both bending moments and axial forces in the arch cross-section. Therefore, the current specification (Ministry of Transport of the People's Republic of

China, 2015) usually equates the arch to a straight beam and column under eccentric compression for relevant calculation and takes the second-order effect of the arch into account by introducing the coefficient of the eccentricity increase coefficient to simplify the calculation. Although the eccentric compression column can basically reflect the failure law of the arch, the transverse deformation of the eccentric straight beam and column is produced by bending moment or transverse force. In contrast, the deformation of the arch is directly produced by the vertical load on the arch. The two deformation sources are different. In addition, the arch axis will generate additional internal forces including additional bending moments after compression. Also, the real internal forces of the arch are difficult to calculate, which is also different from the eccentrically compressed straight rod beam column (Chen, 2016). Therefore, several scholars have conducted the following relevant studies for the CFST arch structure with a special combination of forces:

Liu and Sun (2021) carried out six uniform load tests on CFST arches and studied the ultimate bearing capacity and deformation and failure characteristics of CFST round arch specimens. The results showed that the circular arch yields first at the inside of the arch foot, and the curvature at different positions of the specimen is no longer consistent. The steel tube at the arch foot will uplift obviously and the hoop action of the steel pipe on the concrete will fail when the CFST arches reach the ultimate bearing capacity. Li and Lei (2022) studied the influencing factors of the bearing capacity of CFST arches by numerical simulation and found that the arch had a great limitation on displacement in the elastic stage, and the ultimate bearing capacity was relatively high. The bearing capacity decreases obviously after reaching the peak value, but it showed good elongation performance. Zhao et al. (2021) used the fiber model technology to define the element bearing ratio by homogeneous generalized yield function and proposed the elastic modulus reduction method to evaluate the stable bearing capacity of the dumbbell-type CFST arch by strategically reducing the elastic modulus of the high-stress element. The results showed that stability had a significant impact on the CFST arch. The elastic modulus adjustment method has higher accuracy and efficiency than the incremental non-linear finite element method. Zhang et al. (2022) designed some concrete-filled steel tubular CFST columns and studied the influence of constraint effect coefficient and eccentricity on their mechanical properties. The results showed that the ultimate bearing capacity increases approximately linearly, and the ultimate deflection slightly decreases with the increase in the CFRP constraint effect coefficient. The ultimate bearing capacity of the specimen with large eccentricity decreases obviously, and the deflection corresponding to the ultimate bearing capacity is lower. Huo and Han (2014) compiled a program to analyze the non-linear behavior rules of five special-shaped arch bridges with their characteristics and revealed that the beam-column effect was the most critical factor affecting the essence of the arch and beam composite butterfly arch bridge. The non-linear method was used to calculate the tensile force of the cable by considering the vertical effect of the cable. Zou et al. (2023a) and Zou et al. (2023b) investigated composite and lattice web-concrete combination structures with hollow steel pipes and UHPC combinations and carried out load bearing tests on both combinations, and the results showed good load bearing performance, which can be used in pre-buried sections of CFST arch bridges to improve the load bearing capacity. Bradford and Pi (2014) investigated the effects of geometric non-linearity on the long-term in-plane performance of crown-pin CFST arches under the sustained central concentrated loading, and the analytical solutions for their non-linear response and buckling loads were derived, and the results showed that the long-term deformation predicted by the non-linear analysis resulted in a significant reduction in the serviceability limit state reserve of crown-pin CFST arches. Guo et al. (2022) deduced the calculation formula of the eccentricity increase coefficient based on the basic principle of the variational method and the interaction characteristics of the tie arch structure after deformation. The calculation results were compared with the finite element and the standard, and the results showed that the standard calculation results were large. The finite element calculation results were small, and the method calculation results adopted were moderate. Wang (2009) used the theory of the Updated Lagrangian (U.L.) finite element formulation, and the incremental equation of the virtual work of a three-dimensional (3D) beam for a geometric non-linear analysis of the space structure is established. The eccentric bearing capacity of CFST members is studied, and the results show that the larger the eccentric distance is, the lower the ultimate bearing capacity is, but with better ductility. Liu et al. (2011) and Wang and Guo (2020) studied the load carrying capacity and stability of a CFST arch bridge with fly-bird-type, calculated linear and non-linear stability coefficients, and analyzed the damage modes and load–displacement curves, and the results showed that the linear elastic buckling method does not reflect the true damage mode of this structure, and the effects of both geometric and material non-linearity cannot be ignored. Yang et al. (2020) proposed an adaptive strategy of the elastic modulus adjustment for the ultimate bearing capacity of the CFST arch, and the effectiveness of the method was proven by a large number of tests. Ye (2013) and Wu et al. (2015) studied the effects of length-to-slenderness ratio and sagittal-to-span ratio on the bearing capacity and suggested the essential difference between the arch and column. Wei et al. (2010), Wei et al. (2009), and Chen et al. (2004) used the equivalent beam-column method to calculate the ultimate bearing capacity of the CFST parabolic arch, and the comparison results with finite elements showed that this method is more accurate. Yuan et al. (2020), Jiang et al. (2018), and Zhang and Yu (2013) studied the out-of-plane stability of CFST arches, explored the effect of non-linearity on the stability coefficients, and proposed a method for calculating the correlation coefficients for stability calculations. Bradford and Pi (2014) investigated the effects of geometric non-linearity on the long-term in-plane behavior of crown-pinned circular CFST arches under a continuous central concentrated load and showed that geometric non-linearity has a significant effect on the long-term behavior of crown-pinned CFST arches.

The research on the ultimate bearing capacity and the eccentricity increase coefficient of the CFST arch is abundant, but the research foundation is still built based on the ideas of the "rod mode." The research on the calculation pattern of the CFST arch based on the "arch effect" is deficient. In view of this, this paper discussed the differences between the bearing mechanism of the "arch mode" and the "rod mode" and proposed a new calculation model for the real geometric non-linear internal forces of the arch after force deformation. In this paper, we carried out model tests on the single-pipe arch of steel pipe concrete; analyzed the load–displacement curves, strains, and damage modes of the whole process damage of two single-point loading conditions; and verified the difference between the "arch mode" and "rod mode" damage modes. The comparison of model test and regulation was based on the equivalent beam-column method for non-linear bending moments in arch geometry, and

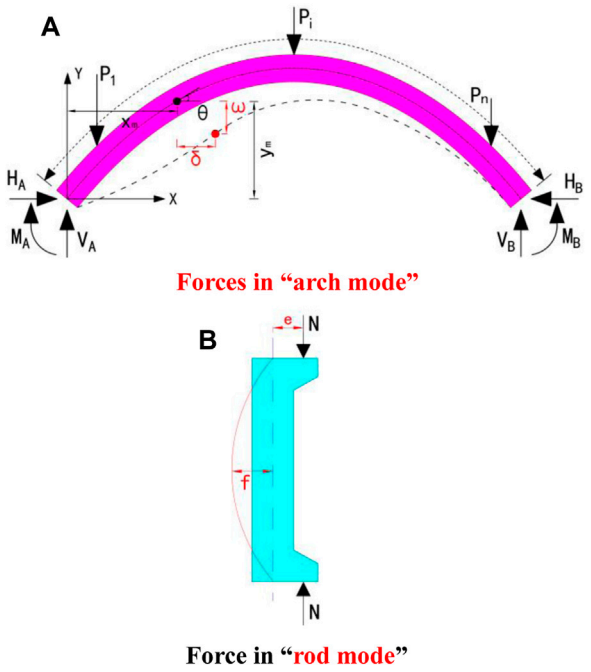

FIGURE 1
Stress characteristics of the "arch mode" and "rod mode": **(A)** Forces in "arch mode"; **(B)** Force in "rod mode".

the analysis of the differences between the two calculation results and the advantages of the calculation mode was carried out based on the arch effect. The regulation of using the "rod mode" instead of the "arch mode" in the calculation of CFST arch bridges is discussed. Based on the differences of the two modes in the bearing mechanism, this paper proposes the real internal force calculation mode of each section after the deformation of the arch. The mode provided new ideas for the future calculation mode of the bearing capacity and stability of large-span arch bridges. Also, it can help optimize the arch axis, arch rib section form, and structure.

2 The bearing mechanism of the "arch mode"

If the branch buckling mode of the unhinged arch is anti-symmetric, as shown in Figure 1A, the horizontal thrust will be generated at the support, and the axial pressure will be generated in the section under the vertical load of the arch. Therefore, the actual internal force of any section can be calculated as Formula 1, after the arch deformation reaches a new equilibrium state.

$$M_g = M_A + V_A(x_m + \delta) - H_A(y_m - \omega) - \sum P(x_m - x_{pi}). \quad (1)$$

According to the theory of deflection, the calculation of the axial force in the arch section can be expressed approximately as

$$N_g = \frac{H_A}{\cos\theta} = \frac{V_A - \sum P_i}{\sin\theta}. \quad (2)$$

Type: M_g—real bending moment of any section of the arch; N_g—arch section axial force; θ—angle between the tangent line and horizontal direction at any position of the arch axis; M_A—arch foot bending moment; V_A—vertical reaction of the arch foot; H_A—horizontal reaction of the arch foot; x_m—x coordinate of section; y_m—y coordinate of the section; δ—horizontal displacement of the section; ω—vertical displacement of the section; P_i—acting external load on the arch; x_{pi}—x coordinate of the external load P_i.

It is not difficult to see that the presence of the horizontal thrust reduces the bending moment in the arch, and the arch axis will produce additional internal forces including the additional bending moment after compression under the action of pressure, which is $\Delta M_g = N_g \omega \cos\theta$.Therefore, the bearing mechanism of the unhinged arch can be summarized as follows: under the action of external load, the axial force in the arch is transferred to the arch foot through the arch axis, generating horizontal thrust and vertical reaction force at the arch foot, and the external load directly produces deformation. In the new equilibrium state after deformation, the section bending moment is mainly composed of the linear bending moment, which is $M_r = M_A + V_A x_m - H_A y_m - \sum P_i(x_m - x_{pi})$ and the non-linear bending moment, which is $\Delta M_r = V_A \delta + H_A \omega$. The axial force is not affected by non-linearity. Therefore, the failure of the bearing capacity of the arch mainly comes from the linear bending moment generated by the internal force of the arch foot and the external load and the non-linear bending moment directly generated by the external load.

However, based on the principle of the equivalent beam-column method, the current domestic standard equates the arch ring to a simply supported eccentric compression column with a length of .36 S (S is the arc length of the arch axis), as shown in Figure 1B (Lin and Chen, 2016). The internal force of the section is as follows:

$$M_c = N(e + f), \quad (3)$$

$$N_c = N. \quad (4)$$

Type: M_c—real bending moment of the eccentric compression column section; N_c—eccentric compression column axial force N—eccentric force; e—Eccentricity, and f—transverse deformation of the cross section.

It can be found from the analysis of the real internal force of the eccentric compression column that the eccentric force transfer to the fixed end along the axis directly forms the vertical reaction force. The axial force is equal to the eccentric force. The cross-section bending moment is produced by the eccentricity, and thus it indirectly leads to lateral deformation. So, the bearing capacity of eccentric compression column destruction mainly comes from the vertical force produced by the linear bending moment and transverse deformation and eccentricity of the additional bending moment.

In view of the differences in the bearing mechanisms of the "arch mode" and "rod mode," the load-bearing capacity model test of the CFST single-pipe arch was carried out from the real force mode of the arch. By analyzing the load–displacement state, the damage mode and the real internal force in the arch in the geometrically non-linear stage, the difference between the "arch mode" and "rod mode" is verified, and a new calculation model of the CFST arch bridge based on the arch effect is proposed.

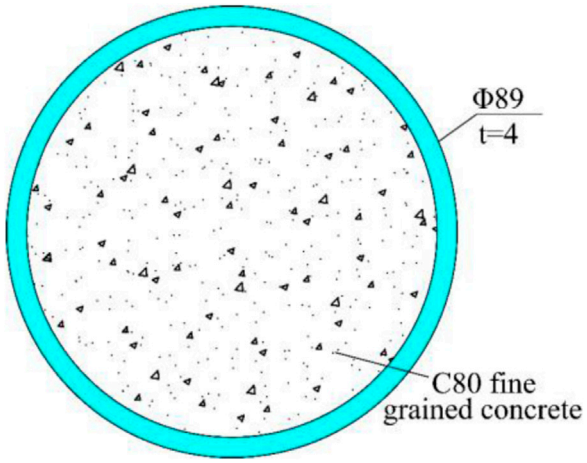

FIGURE 2
Cross-section of the arch rib.

3 Single-tube model test of the "arch mode"

3.1 Model design and production

A catenary steel tube single-tube arch bridge with a calculated span of 95 m was used as the prototype. The ratio of the sagittal span was 1/3.5, the calculated sagittal height was 27.143 m, the arch axis coefficient was 1.5, the diameter of the steel tube was 1.55 m, the wall thickness of the arch foot was 26 mm, and the rest was 22 mm, and C60 concrete was poured into the tube.

The test arch was scaled down at 1:16, with a reduced span of 5.938 m and a calculated height of 1.696 m. Due to the limitation of market steel pipe specifications, the pipe wall was too thin according to the actual scale ratio, so the full-span diameter and wall thickness of the steel pipe were set at 89 mm and 4 mm, respectively, according to the existing market specifications, as shown in Figure 2. Scale parameters and scale deviation values are shown in Tables 1, 2.

The steel pipe material was Q345, and the arch was perfused with C80 fine-grain concrete. After curing for 28 days, the compressive strength of six concrete blocks was tested. The compressive strength of the cube was 51.85 MPa, the compressive strength of the prismatic core was 32.4 MPa, and the elastic modulus was 3.4834×10^4 MPa. Steel tube yield strength was 361 MPa, tensile strength was 540 MPa, and the elastic modulus was 2.1×10^5 MPa.

The vault and L/4 loading conditions were designed to test the in-plane deformation state, strain distribution, and failure mode of the whole process of the arch. The overall design is shown in Figure 3.

3.2 Designs of the test device and measuring point

A 50-t hydraulic jack was adopted. The top of the jack was a pressure sensor, and the bottom design disk was in contact with the arch rib loading block to ensure uniform force. The skewback reaction device was a triangular steel structure. The test was mainly conducted to study the load bearing capacity of the arch under vertical load in-plane deformation. In order to avoid out-of-plane deformation causing out-of-plane instability damage to the structure, the whole arch set five transverse limits to ensure that the arch was only in-plane free deformation during the loading process. The contact surface between the limit and the arch was coated with a tetrafluoro plate to reduce friction. The main device configuration is shown in Figure 3 and Figure 4A. Percentage gauges and strain gauges were used to test the displacement and strain in the whole process. Two percentage gauges were set at each L/8 to measure the horizontal and vertical displacement, and four percentage gauges were set at each skewback to monitor whether deflection occurred, as shown in Figure 4B. Strain gauges are set at the L/8 and the section of the two arch feet. The upper and lower edges of the section are arranged in annular and longitudinal directions, respectively, while only longitudinal directions are arranged on the side. Fifty-four strain gauges are arranged in the whole arch, as shown in Figure 5.

TABLE 1 Parameters of the scaled section.

Project	Span (m)	Rise (m)	String pipe diameter (m)	Wall thickness (m)	Inner diameter of chords (m)
Original bridge	95	27.143	1.55	.026	1.498
Ideal scale value	5.938	1.696	.0969	.00163	.09364
Actual scale value	5.938	1.696	.089	.004	.081

TABLE 2 Scale size deviation.

Project	Ideal scale value	Actual scale value	Percentage deviation (%)
Area (m^2)	.00048786	.00106814	118.95
In-plane moment of inertia (m^4)	5.5366E-07	9.67E-07	74.62
Compressive stiffness (N/m)	100498797	220037149	118.95
Bending stiffness ($N{\cdot}m^2$)	114053.946	199161.125	74.62

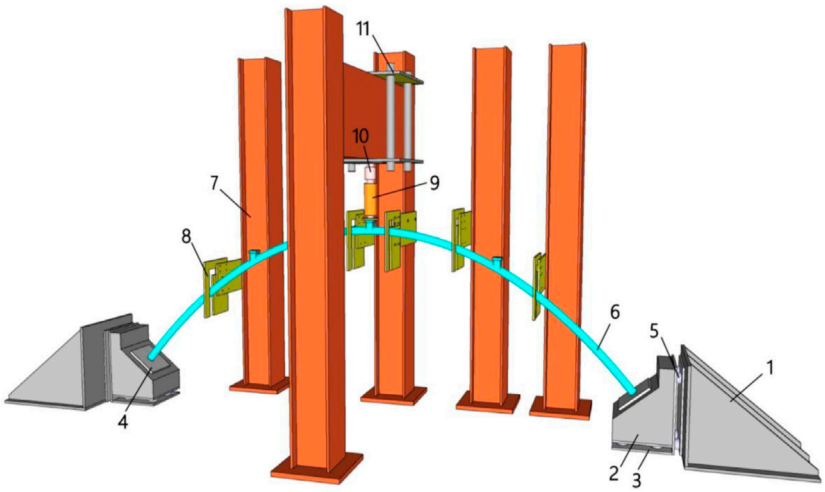

1—Skewback reaction tower; 2—Skewback; 3—Skewback bearing plate; 4—Skewback embedded parts; 5—Skewback pressure sensor; 6—Arch; 7—Pillar; 8—Lateral limit; 9—Jack; 10—Jack pressure sensor; 11—Jack reaction frame;

FIGURE 3
Overall diagram of the model.

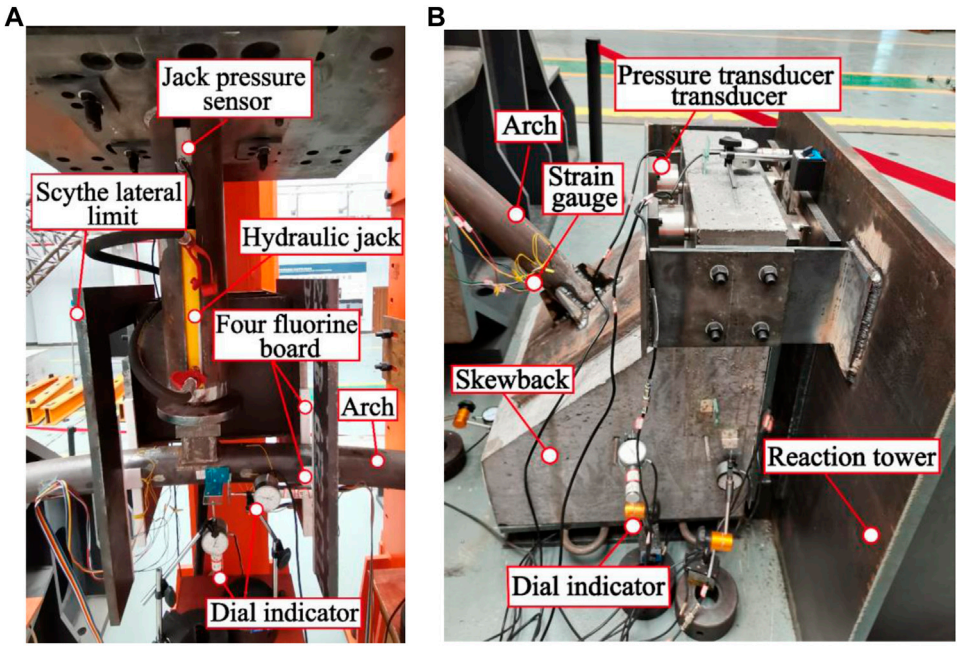

Main test equipment Structural diagram of the skewback

FIGURE 4
Real diagram of local construction: **(A)** Main test equipment; **(B)** Structural diagram of the skewback.

3.3 Measurement method for internal force

According to Eq. 1, the real internal forces of any section can be calculated if the internal forces of the arch foot, section displacement, and external load are known, based on the calculation principle of the real internal forces in the arch. The section displacement and external load can be directly measured by the test, while the actual measurement of the internal forces of the arch foot is difficult to measure. In this paper, the separation skewback method in Li (2012) was used to measure the internal force of the arch foot. Four sensors were installed on the back and bottom of the skewback to measure the horizontal thrust and

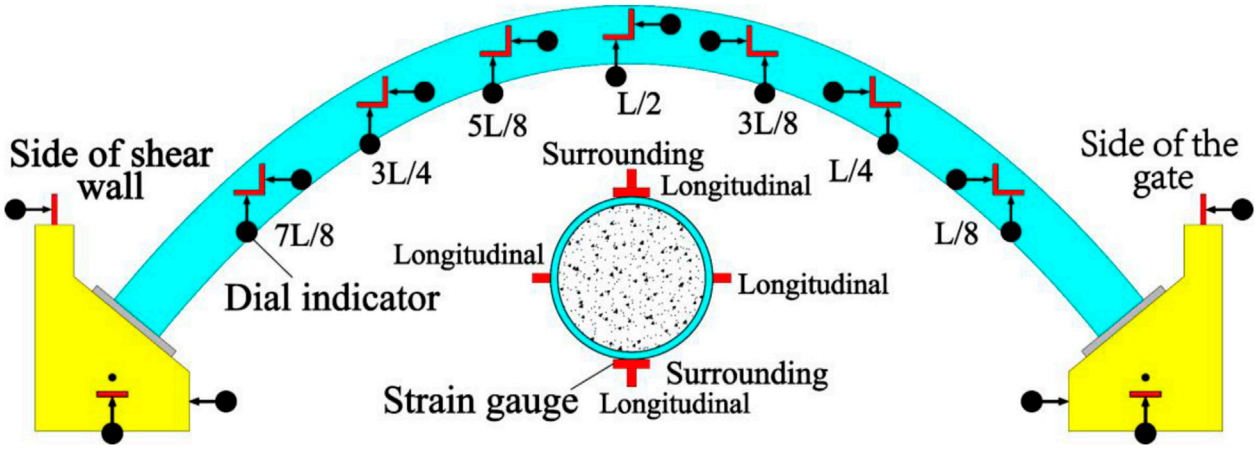

FIGURE 5
Placement of displacement and strain measurement points.

FIGURE 6
Four-point loading skewback.

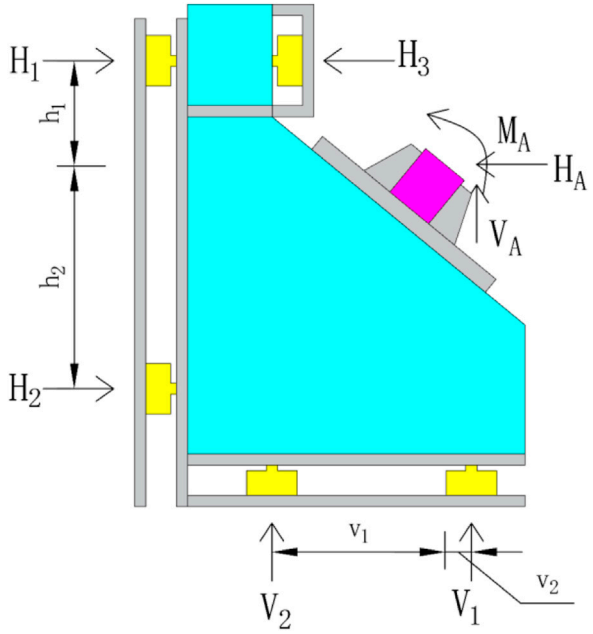

FIGURE 7
Schematic diagram of calculation of the internal force of the arch foot.

vertical reaction force, as shown in Figure 8. Due to the effect of the arch foot bending moment, the skewback will have a trend of in-plane rotation. It was found in finite element analysis that the arch foot at both ends of the vault loading has a negative bending moment, and the skewback rotates clockwise. In four-point loading, there is a negative bending moment at the arch foot close to the loading point, and the skewback rotates clockwise, while there is a positive bending moment at the arch foot far away from the loading point, and the skewback rotates counterclockwise. To accurately measure the horizontal thrust of the arch foot and limit the rotation of the skewback, two sensors are set at the front of the top of the vault loading base (Figure 4B). Two sensors are set at the front of the top and the front of the bottom of the skewback near and far from the loading point of the four-point loading (Figure 6; Figure 4B). Then, the bending moment, horizontal reaction force, and vertical reaction force of the arch foot are calculated according to the static equivalence principle. The calculation principle is shown in Figure 7.

Through force analysis, the actual calculation formula of the arch foot bending moment, horizontal reaction force, and vertical reaction force can be obtained as follows:

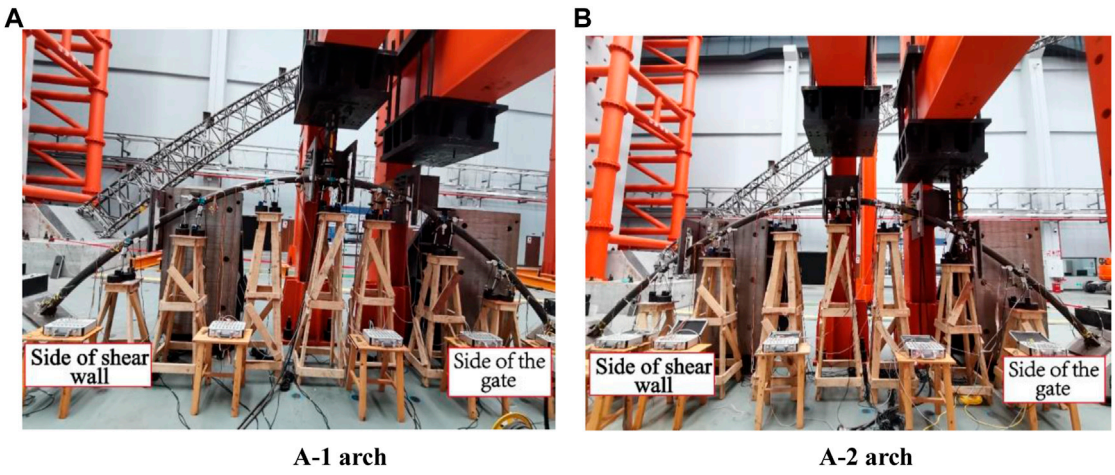

FIGURE 8
Initial state: **(A)** A-1 arch; **(B)** A-2 arch.

TABLE 3 Hierarchical loading value (Unit: kN).

Vault loading condition				Quarter section loading condition			
Classification	Load value	Classification	Load value	Classification	Load value	Classification	Load value
1	.500	11	30.891	1	.400	11	24.713
2	1.000	12	35.891	2	.800	12	28.713
3	1.750	13	40.891	3	1.400	13	32.713
4	2.875	14	45.891	4	2.300	14	36.713
5	4.563	15	50.891	5	3.650	15	40.713
6	7.094	16	55.891	6	5.675	16	44.713
7	10.891	17	60.891	7	8.713	17	48.713
8	15.891	18	63.391	8	12.713	18	50.713
9	20.891	19	64.641	9	16.713	19	50.838
10	25.891	20	65.266	10	20.713	—	—

$$\begin{cases} H_A = H_1 + H_2 - H_3 \\ V_A = V_1 + V_2 \\ M_A = H_1 h_1 - H_2 h_2 - H_3 h_3 - \\ \qquad V_1 v_1 + V_2 v_2 \end{cases} \cdot \tag{5}$$

Type: H_A—horizontal reaction force; H_1, H_2, H_3—net force value of each drainage smooth reaction force sensor; h_1, h_2, h_3—vertical distance from each drainage reaction sensor to the center of the arch foot; V_1, V_2—net force value of each row of the vertical reaction sensor; v_1, v_2—horizontal distance from each row of vertical reaction sensors to the center of the arch foot.

3.4 Test steps

First, the reaction tower and skewback should be precisely positioned. It was necessary to pre-push it to eliminate the anchor hole clearance after the reaction tower was installed. Then, the arch ribs were erected and the hanging hammer was used to ensure that the arch was in a vertical state without initial transverse deviation. Finally, the loading device and test device are installed. The initial state after the preparation is shown in Figure 8. Formal loading needs to be graded according to the results of finite element ultimate bearing capacity analysis, that is, the ultimate force of 0%–3% or so average .5 kN/level, 3%–5% or so average 1 kN/level, 5%–10% or so average 2 kN/level, and 10% after the average 5 kN/level until failure, with each

TABLE 4 Description of working conditions.

Model number	Loading condition
A-1	Vault loading condition
A-2	Quarter section loading condition

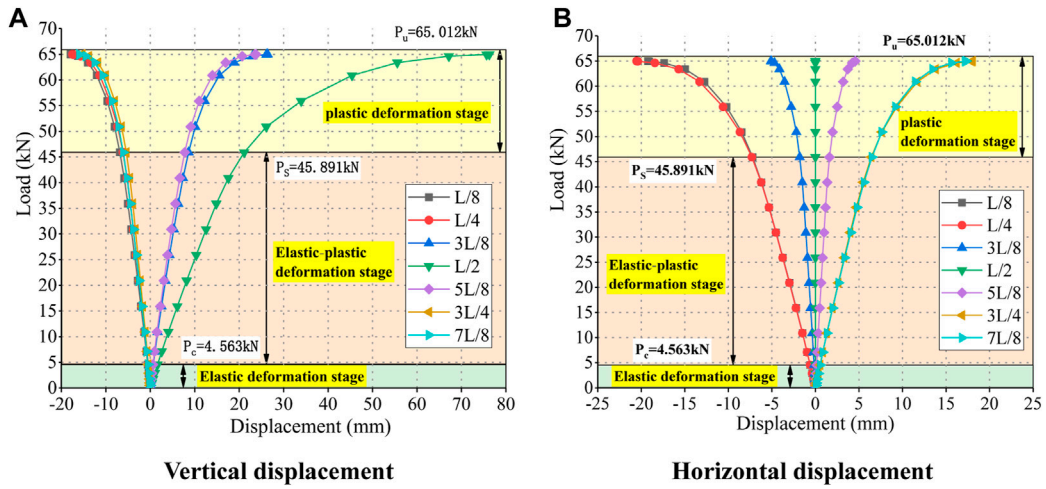

FIGURE 9
A-1 arch of the load–displacement curve: **(A)** Vertical displacement; **(B)** Horizontal displacement.

static loading level of 2 min after the stability of the reading. Full-arch graded loading values are shown in Table 3. The test designed two loading conditions. The arch top loading arch rib was named A-1 and 4-point loading condition arch rib was named A-2. The description of the conditions is given in Table 4 and the actual loading figure is shown in Figure 8.

3.5 Analysis of test results

3.5.1 Load–displacement curve

According to Table 3, the load–displacement curves of each section of the A-1 arch and A-2 arch are shown in Figures 9, 10 (vertical displacement is "+" downward and horizontal displacement direction of shear wall side arch is "+"). The whole deformation process of the arch can be roughly divided into three stages:

(1) Elastic deformation stage. When the A-1 arch was loaded to 4.563 kN (.07 P_u) and the A-2 arch was loaded to 3.65 kN (.073 P_u), the load–displacement curves of each section basically changed linearly, and the arch was in the stage of linear elastic change, almost unaffected by non-linear influence.
(2) Elastic–plastic deformation stage. With the increase in the load, the slope of the curve gradually decreases, and the arch enters the stage of elastic–plastic deformation. The sections, especially the sections at loading points, are gradually affected by geometric non-linearity. At this stage, the upper critical load limit for arch A-1 was about 45.891 kN (.71 P_u), and the upper critical load limit for arch A-2 was about 40.713 kN (.81 P_u).
(3) Plastic deformation stage. With the increase in the load, the deflection of the loading point increases continuously, the slope of the curve increases faster, and the curve gradually tends to be horizontal. Under the double non-linear action, the arch has a slight change in load, a sharp increase in displacement, and a reduction in load value. The load could not be increased continuously when the A-1 and A-2 arches were added to 65.012 kN and 50.275 kN, respectively.

The results of failure load–displacement curves under two working conditions showed that the ultimate bearing capacity of the A-1 arch was P_u = 65.012 kN, the maximum vertical displacement of the loading point was 76.31 mm, and the maximum horizontal displacement of the L/4 section was 20.53 mm. The ultimate bearing capacity of the A-2 arch was P_u = 50.275 kN, and the maximum vertical displacement and horizontal displacement of the loading point are 108.96 mm and 84.96 mm, respectively. The comparison between the test results under the ultimate load and the preliminary FEM calculation is shown in Table 5. The comparison results showed that the difference between the test ultimate bearing capacity value and the preliminary calculation was less than 2%, and the displacement difference was about 10%. It indicated that the ultimate bearing capacity test values of the two working conditions are accurate. The real CFST arch shows superior deformation capacity compared with the theoretical calculation.

3.5.2 The strain state under ultimate load

All steel tube surfaces in L/8 and two arch feet were decorated with a strain gauge, as shown in Figure 5. As the deformation of the test arch was mainly in-plane deformation, only the edge of the steel tube on the longitudinal strain under the ultimate load was analyzed. It is given in Section 3.1 that the measured yield strength of the steel pipe was 361 MPa, the modulus of elasticity was 2.1 × 10^5 MPa, and the steel pipe yield strain was $\varepsilon_y = \sigma_y/E = 1719$. The whole arch strain and tube concrete crack distribution are shown in Figure 11. The positive direction of the transverse coordinate axis indicates gate side arch seat to shear wall side arch seat. The specific analysis of concrete cracks will be shown in the next section. The strain distribution results showed that the steel pipe at the location

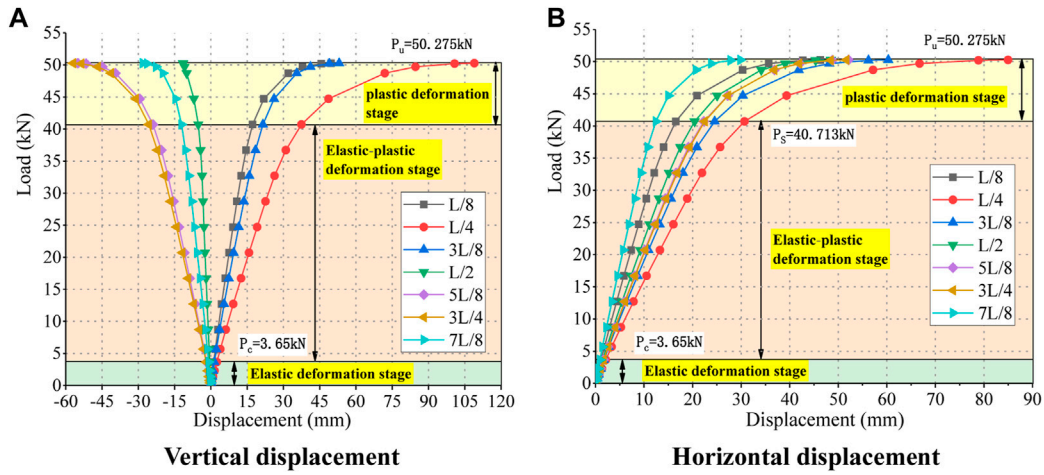

FIGURE 10
A-2 arch of the load–displacement curve: **(A)** Vertical displacement; **(B)** Horizontal displacement.

TABLE 5 Comparison between the test value and preliminary calculated value of the ultimate load.

Category	A-1 arch			A-2 arch		
	Test result	Preliminary calculated value	Percentage of difference	Test result	Preliminary calculated value	Percentage of difference
Ultimate bearing capacity (kN)	65.012	65.266	−.39%	50.275	50.838	−1.11%
Maximum vertical displacement (mm)	76.31	69.53	9.75%	108.96	96.31	13.13%
Maximum horizontal displacement (mm)	20.53	19.02	7.94%	−84.96	−75.73	12.19%

where the concrete cracks appear had yielded. The tensile and compressive strain values of the upper and lower edges of the steel pipe were basically symmetric, and the strain at the upper and lower edges of the loading site reached the peak. The strain distribution and the location of cracks corresponded with each other.

3.5.3 Damage state

The initial state of two loading conditions and the overall deformation state under the ultimate load are shown in Figure 12. The concrete in the tube after destruction is shown in Figure 13.

It can be seen that the vault has obvious vertical sag in the ultimate state of the bearing capacity of the A-1 arch. There are several small vertical micro-cracks perpendicular to the arch axis extending upward to the lower edge of the concrete in a certain area at both ends of the loading point. There was an obvious bulge near the L/4 section, and a macroscopic crack on the upper edge of the concrete extends downward perpendicular to the axis of the arch. There was a slight depression near the cross-section of the two arch feet, and a macroscopic crack on the lower edge of the concrete extends upward perpendicular to the axis of the arch.

In the ultimate state of the bearing capacity of the A-2 arch, the L/4 section was inclined to sag, and there was a macroscopic crack at the lower edge of the concrete perpendicular to the arch axis extending upward. The arch foot section of the gate side was slightly raised, and there was a macroscopic crack on the upper edge of the concrete that was perpendicular to the arch axis extending downward. There was an obvious bulge near the 3L/4 section, and a macroscopic crack on the upper edge of the concrete extends downward perpendicular to the axis of the arch. There was a slight depression near the section of the arch foot on the shear wall side, and a macroscopic crack at the lower edge of the concrete extends upward perpendicular to the arch axis.

Combined with Figure 10 and the aforementioned failure states, it can be seen that the four crack positions of the concrete in the tube after failure under the two working conditions all appear near the extreme point of the tensile strain of the steel tube, which was a tensile failure. At this time, the concrete at the crack stops working, indicating that plastic hinges are formed at the four positions in the arch and that the structure cannot continue to bear. Therefore, the failure mode of the arch was the 4-hinge failure, and the structure forms a geometrically variable system and loses the bearing capacity.

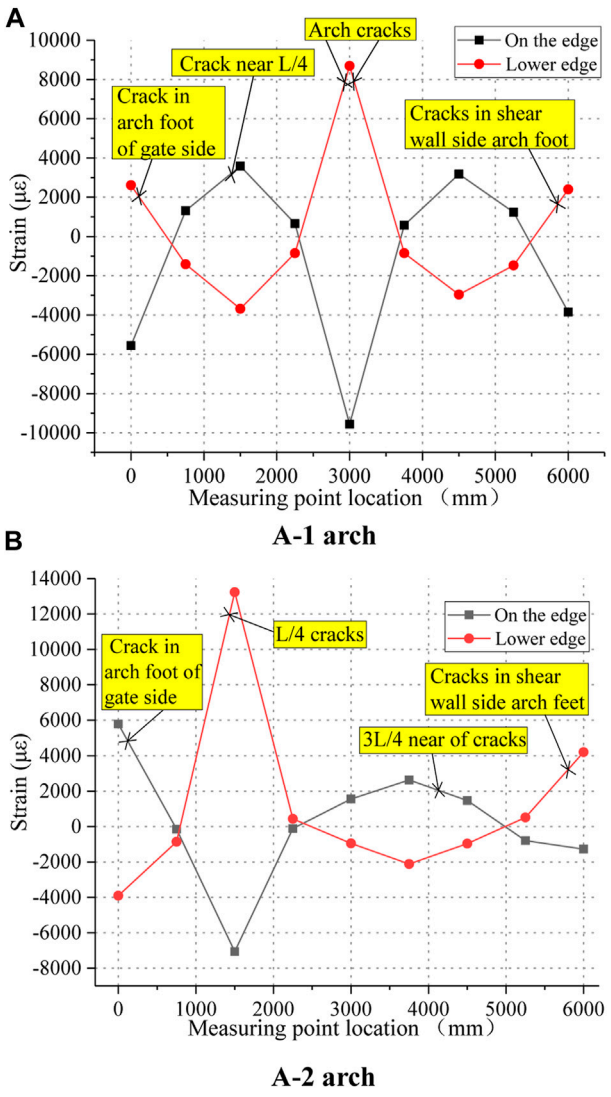

FIGURE 11
Strain and crack distribution of concrete in the tube under ultimate load: **(A)** A-1 arch; **(B)** A-2 arch.

4 Comparative analysis of the "arch mode" and "rod mode"

In Section 3.5.1, the loading interval of the A-1 arch with obvious geometric non-linearity is given as 4.563 kN–45.891 kN, and that of the A-2 arch is 3.65 kN–40.713 kN. The calculation section of the A-1 and A-2 arches and the selection of loads outside the geometric non-linear loading interval are listed in Table 6. The geometric non-linear bending moment values of the two calculation modes are compared under the corresponding external load.

4.1 Calculated geometric non-linear bending moment values for the regulation

In the current JTG/TD65-06-2015 code (concrete-filled steel tube arch bridge design code) (Ministry of Transport of the People's Republic of China, 2015), the eccentricity increasing coefficient η is introduced into the calculation formula of the ultimate bearing capacity of the CFST arch to consider the geometric non-linearity of the arch. The main parameters of the formula are the Euler critical force formula and first-order linear axial force, as shown in Eq. 6. It can be seen that the arch is equivalent to an eccentric compression column for calculation based on the equivalent beam-column method in the arch bridge specification. Its essence is that the first-order bending moment obtained by elastic calculation is enlarged by the eccentricity increasing coefficient, which is equal to the moment existing in the control section of the actual component. Then, the geometric non-linear bending moment is calculated, as shown in Eq. 7.

$$\eta = \frac{1}{1 - 0.4N/N_E}, \tag{6}$$

$$M' = \eta M. \tag{7}$$

Type: η—eccentricity increase coefficient; Euler critical force $N_E = \frac{\pi^2 E_{sc} A_{sc}}{\lambda^2}$, of which, E_{sc}—combined the elastic modulus of CFST, A_{sc}—combined the cross-sectional area of CFST; N—first-order linear axial force, M'—geometric non-linear bending moment, and M—linear bending moment.

According to the section-related parameters of the test arch provided in Section 3.1, the Eulerian critical force N_E = 304.3 kN can be calculated. The first-order linear axial force and bending moment can be calculated by finite elements as recommended in the regulation. So, the first-order linear axial force and bending moment of the test arch were calculated by Midas/civil, as shown in Table 7.

The Eulerian critical force and the first-order axial force and bending moment values corresponding to the external loads P_1~P_4 in Table 7 are substituted into Eqs 6, 7, obtaining the eccentricity increasing coefficient η and geometric non-linear bending moment values M' of the corresponding sections, as shown in Table 8.

4.2 Measured geometric non-linear bending moment values based on the arch effect calculation model

According to the geometric non-linear internal force calculation model based on the arch effect proposed in this paper according to Eq. (1), the real geometric non-linear bending moment in the arch can be calculated by substituting the measured load–displacement results and the coordinate position of the cross-section. The cross-section positions and the measured external loads P_1~P_4 correspond to the horizontal displacement δ and vertical displacement ω (arch foot displacement is 0), as shown in Tables 9, 10.

The measured values of horizontal thrust H_A, vertical reaction V_A, bending moment M_A, and other cross-section geometric non-linear bending moment values M_g in the arch foot of the gate side are shown in Table 11.

4.3 Comparative analysis

The geometric non-linear moment values calculated by the regulation in Table 8 are compared with the real geometric non-linear moment values of the CFST arch measured in Table 11, as shown in Table 12 and Figure 14.

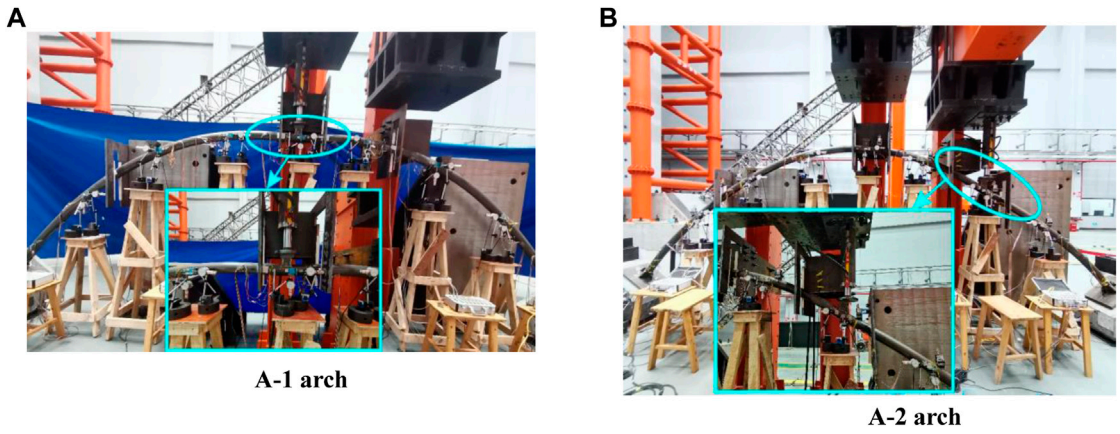

FIGURE 12
State after destruction: **(A)** A-1 arch; **(B)** A-2 arch.

TABLE 6 Selection of calculation parameters.

Condition	Calculate the cross section			Loading (kN)			
				P_1	P_2	P_3	P_4
A-1	Arch foot	L/4	Vault	15.891	25.891	35.891	45.891
A-2	Arch foot	L/4	3L/4	16.713	24.713	32.713	40.713

TABLE 7 First-order linear axial forces (N) and bending moments (M) calculated by finite elements.

Condition	P_1		P_2		P_3		P_4	
	N (kN)	M (kN·m)	N (kN)	M (kN·m)	N (kN)	M (kN·m)	N (kN)	M (kN·m)
A-1	14.246	2.825	23.211	4.602	32.177	6.38	41.142	8.157
	14.969	−1.849	24.389	−3.012	33.809	−4.176	43.229	−5.339
	12.879	4.845	20.984	7.893	29.089	10.942	37.193	13.991
A-2	15.789	−4.41	23.346	−6.521	30.904	−8.632	38.462	−10.742
	5.615	6.024	8.302	8.908	10.99	11.792	13.677	14.675
	8.28	−2.185	12.243	−3.231	16.206	−4.276	20.17	−5.322

TABLE 8 Geometric non-linear bending moment values calculated by the regulation (unit: kN).

Condition	Cross-section position	P_1		P_2		P_3		P_4	
		η	M'	η	M'	η	M'	η	M'
A-1	Gate-side arch foot	1.019	2.879	1.031	4.747	1.044	6.662	1.057	8.623
	L/4	1.020	−1.886	1.033	−3.112	1.047	−4.370	1.060	−5.661
	Vault	1.017	4.928	1.028	8.117	1.040	11.377	1.051	14.710
A-2	Gate-side arch foot	1.021	−4.503	1.032	−6.727	1.042	−8.997	1.053	−11.314
	L/4	1.007	6.069	1.011	9.006	1.015	11.965	1.018	14.944
	3L/4	1.011	−2.209	1.016	−3.284	1.022	−4.369	1.027	−5.467

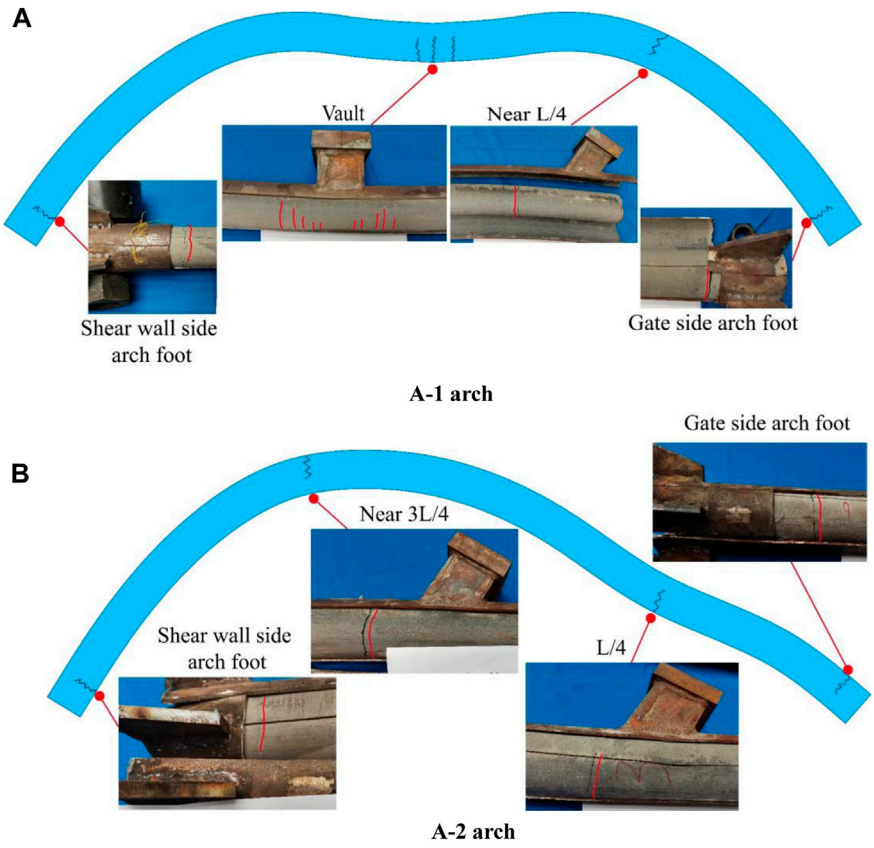

FIGURE 13
Failure state of concrete in the pipe after failure: **(A)** A-1 arch; **(B)** A-2 arch.

TABLE 9 A-1 arch P_1~P_4 measured displacement (unit: mm).

Loading	L/4		Vault	
	δ	ω	δ	ω
P_1	−2.23	−1.89	.00	6.08
P_2	−3.76	−3.16	.00	10.35
P_3	−5.34	−4.47	.00	14.86
P_4	−7.30	−6.13	.00	21.14

TABLE 10 A-2 arch P_1~P_4 measured displacement (unit: mm).

Loading	L/4		3L/4	
	δ	ω	δ	ω
P_1	10.53	12.50	8.14	−9.38
P_2	16.05	19.16	12.39	−14.22
P_3	21.94	26.37	16.82	−19.23
P_4	30.70	37.47	22.50	−25.64

The comparison results show that the results of the two modes at the beginning of the geometric non-linearity of the A-1 and A-2 arches are in good agreement. As the load was increased, the geometric non-linearity has the greatest effect under the critical external load P4 at the end of the elasto-plastic phase. At this time, the measured value of the arch foot section of the A-1 arch is 2.04% larger than the regulation calculation value, the measured value of the L/4 section is about 6.81% larger than the regulation calculation value, and the measured value of the arch top section is about 3.38% smaller than the regulation calculation value. The measured value of the arch foot section of the A-2 arch is about 5.31% larger than the regulation calculated value, the measured value of the L/4 section is about .73% smaller than the regulation calculated value, and the measured value of the 3L/4 section is about 15.73% larger than the regulation calculated value. It shows that the geometric non-linear moment value of the control section of the CFST arch calculated by the eccentricity increase coefficient in the regulation is conservative, but the influence of geometric non-linearity of other sections is not considered enough, and the local damage of other sections may occur before the control section under the action of the large vertical load, which also shows that the calculation mode of the regulation, considering the whole arch affected by geometric non-linearity due to the eccentricity increase coefficient, is not reasonable.

TABLE 11 Measured values of geometric non-linear internal forces (unit: kN m).

Condition	Cross-section position	Internal force	P_1	P_2	P_3	P_4
A-1	Gate-side arch foot	H_A	12.764	20.823	28.917	37.431
		V_A	7.947	12.947	17.948	22.947
		M_A	2.872	4.721	6.615	8.799
	L/4	M_g (L/4)	−1.915	−3.161	−4.444	−6.046
	Vault	M_g (L/2)	4.889	8.048	11.272	14.213
A-2	Cross-section position	H_A	7.976	11.794	15.638	19.796
		V_A	13.946	20.623	27.309	34.1
		M_A	−4.514	−6.774	−.134	-11.915
	L/4	M_g (L/4)	6.098	9.109	12.149	14.835
	3L/4	M_g (3L/4)	−2.321	−3.501	−4.745	−6.327

TABLE 12 Comparison of regulation values and measured values (unit: kN m).

Condition	Cross-section position	Loading	Regulation value	Measured value	Difference ratio (%)
A-1	Gate-side arch foot	P_1	2.88	2.87	−.24
		P_2	4.75	4.72	−.54
		P_3	6.66	6.62	−.70
		P_4	8.62	8.80	2.04
	L/4	P_1	−1.89	−1.92	1.53
		P_2	−3.11	−3.16	1.58
		P_3	−4.37	−4.44	1.69
		P_4	−5.66	−6.05	6.81
	Vault	P_1	4.93	4.89	−.80
		P_2	8.12	8.05	−.85
		P_3	11.38	11.27	−.92
		P_4	14.71	14.21	−3.38
A-2	Gate-side arch foot	P_1	−4.50	−4.51	.23
		P_2	−6.73	−6.77	.69
		P_3	−9.00	−9.13	1.52
		P_4	−11.31	−11.92	5.31
	L/4	P_1	6.07	6.10	.48
		P_2	9.01	9.11	1.14
		P_3	11.96	12.15	1.54
		P_4	14.94	14.84	−.73
	3L/4	P_1	−2.21	−2.32	5.07
		P_2	−3.28	−3.50	6.61
		P_3	−4.37	−4.75	8.60
		P_4	−5.47	−6.33	15.73

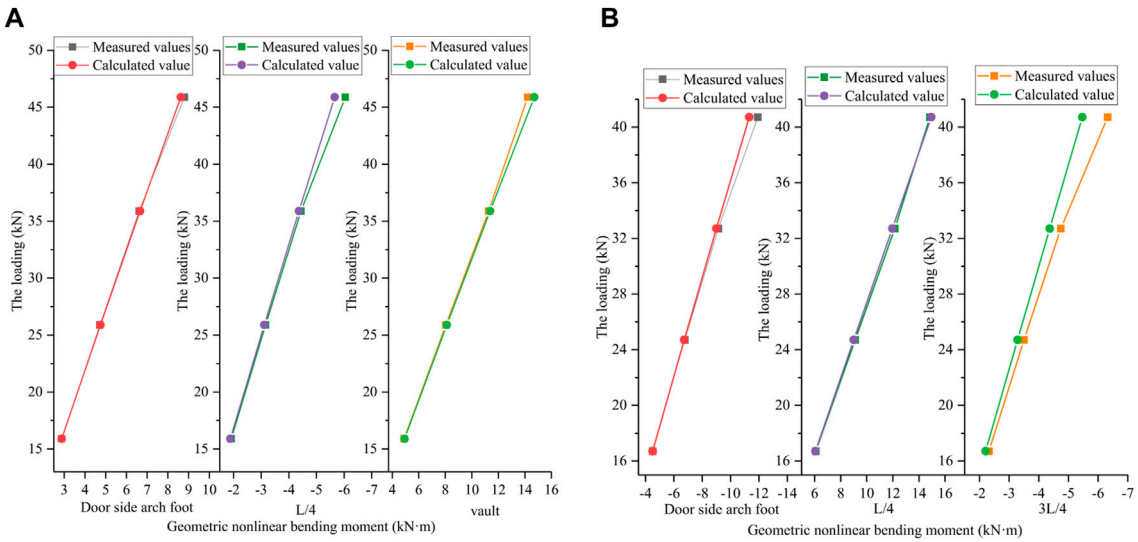

FIGURE 14
Comparison of geometric non-linear bending moment values between the "arch mode" and "rod mode": **(A)** A-1 arch;**(B)** A-2 arch.

5 Conclusion

The specific results of the analysis are as follows:

(1) The failure of the arch mainly comes from the linear bending moment generated by the internal force of the arch foot and the external load and the non-linear bending moment directly generated by the external load after deformation. In contrast, the eccentric compression column mainly comes from the linear bending moment generated by the eccentric force and the non-linear bending moment generated by the transverse deformation or transverse force. These two modes have different force structures, force transmission routes, and deformation sources, which lead to different bearing mechanisms.

(2) The deformation state of the arch in the whole process is divided into three stages: elastic deformation, elastic–plastic deformation, and plastic deformation. Similar to the eccentric compression column, its failure mode is also a hinge failure. However, the experimental phenomenon showed that due to different bearing mechanisms of the two modes, the final failure state of the arch exhibits 4-hinge failure and has strong plastic deformation ability. In contrast, the eccentric compression column exhibits single-hinge failure, which indicates that the deformation ability of the arch is inevitably reduced after the arch is equivalent to a column of considerable length.

(3) The initial geometric non-linear moments measured based on the "arch mode" are in good agreement with the calculated results of the "rod mode." However, the increase in load increased the proportion of geometric non-linear effects, and the geometric non-linear moments calculated by the eccentricity increase coefficient are conservative. In the complex force environment, there is a high possibility of local damage of other sections before the control section, which indicates that the calculation mode of the regulation considering the full arch affected by geometric non-linearity through the eccentricity increase coefficient is not good.

(4) This paper proposes a new calculation model for CFST arch bridges considering geometric non-linear internal forces, which can provide a new idea for the future large-span arch bridge bearing capacity and stability and other verification models. It can help optimize the arch axis and arch rib section form and structure and enhance the arch bridge span.

Data availability statement

The original contributions presented in the study are included in the article/Supplementary Material; further inquiries can be directed to the corresponding author.

Author contributions

SW mainly provided key ideas and insights. YL authored the paper. ZL and TC assisted with the paper.

Funding

This work was supported by Science and Technology Innovation Project of Chongqing Education Commission "Construction of Twin Cities Economic Circle in Chengdu-Chongqing Region" (KJCXZD2020032), Natural Science Foundation of Chongqing (cstc2021jcyj-msxm2491), Guangxi Key Research and Development Program (GuikeAB22036007-8), Chongqing Technology Innovation and Application Development Special Key Project (CSTB2022TIAD-KPX0205). This support is gratefully acknowledged.

Conflict of interest

The authors declare that the research was conducted in the absence of any commercial or financial relationships that could be construed as a potential conflict of interest.

Publisher's note

References

Bradford, M. A., and Pi, Y-L. (2014). Geometric nonlinearity and long-term behavior of crown-pinned CFST arches. *J. Struct. Eng.* 141 (8), 04014190. doi:10.1061/(asce)st.1943-541x.0001163

Chen, B. C. (2016). *Concrete filled steel tube Arch Bridge*. Beijing: People's Communications Publishing House, 276–277. [In Chinese].

Chen, B. C., Qin, Z. B., and Chen, Y. J. (2004). "Equivalent beam and column method for simplified calculation of ultimate bearing capacity of concrete-filled steel tubular arch," in Proceedings of the 16th National Bridge Conference 2, Changsha, China, 9–14. [In Chinese].

Guo, F., Li, P. F., and Mao, J. Y. (2022). Dong yanzhao. Calculation method for increasing coefficient of arch rib eccentricity of long-span arch bridge. *J. Jilin Univ. Eng. Technol. Ed.* 52 (06), 1404–1412. [In Chinese]. doi:10.13229/j.cnki.jdxbgxb20220147

Huo, X. J., and Han, L. Z. (2014). Analysis of geometric nonlinearity of special-shaped arch bridges. *J. Highw. Transp. Res. Dev. Engl. Ed.* 8 (3), 37–45. doi:10.1061/jhtrcq.0000395

Jiang, W., Wang, L., and Li, Y. J. (2018). Out-plane stability safety factors of CFST arches using inverse finite element reliability method. *IOP Conf. Ser. Mater. Sci. Eng.* 392 (2), 022035. doi:10.1088/1757-899X/392/2/022035

Li, J. (2012). *Study on the increase coefficient of bending moment of reinforced concrete arch bridge*. Sichuan, China: Southwest Jiaotong University. [In Chinese].

Li, L., and Lei, K. (2022). Research on influence factors of bearing capacity of concrete-filled steel tubular arch for traffic tunnel. *Symmetry* 14 (1), 167. doi:10.3390/SYM14010167

Lin, S. S., and Chen, B. C. (2016). Calculation of bearing capacity of reinforced concrete arch by equivalent beam-column method. *J. Fuzhou Univ. Nat. Sci. Ed.* 44 (01), 110–114. [In Chinese].

Liu, K. M., and Sun, X. Z. (2021). Bearing capacity of concrete filled steel tube circular arch under the six-point uniformly distributed loading and its engineering application. *Adv. Mater. Sci. Eng.* 2021, 2021–2113. doi:10.1155/2021/8288648

Liu, Y., Wang, D., and Zhu, Y. Z. (2011). Analysis of ultimate load-bearing capacity of long-span CFST arch bridges. *Appl. Mech. Mater.* 1446, 1149–1156. doi:10.4028/www.scientific.net/amm.90-93.1149

Ministry of Transport of the People's Republic of China (2015). *Code for design of concrete filled steel tube arch bridge for highway*. Beijing, China. (JTG/T D65-06-2015) [In Chinese].

Wang, J. Z., and Guo, J. F. (2020). Analysis of influence factors and stability of concrete-filled steel tube arch bridge. *IOP Conf. Ser. Mater. Sci. Eng.* 768 (3), 032053. doi:10.1088/1757-899X/768/3/032053

Wang, W. (2009). "Ultimate capacity analysis of concrete-filled steel tubular structure under eccentric compression," in International Conference on Transportation Engineering, Chengdu, China, 1481–1486.

Wei, J. G., Chen, B. C., and Wu, Q. X. (2010). Equivalent beam-column method for calculation of nonlinear critical Load of concrete-filled steel tube flexural arch. *Eng. Mech.* 27 (10), 104–109. [In Chinese].

Wei, J. G., Chen, B. C., and Wu, Q. X. (2009). Equivalent beam-column method for calculation of ultimate bearing capacity of bending steel pipe. *Chin. J. Comput. Mech.* 26 (01), 87–93. [In Chinese].

Wu, X. R., Liu, C. Y., Wang, W., and Wang, Y. Y. (2015). In-plane strength and design of fixed concrete-filled steel tubular parabolic arches. *J. Bridge Eng.* 20 (12). doi:10.1061/(ASCE)BE.1943-5592.0000766

Yang, L. F., Xie, W. W., Zhao, Y. F., and Zheng, J. (2020). Linear elastic iteration technique for ultimate bearing capacity of circular CFST arches. *J. Constr. Steel Res.* 172, 106135. doi:10.1016/j.jcsr.2020.106135

Ye, S. (2013). Parameter analysis on ultimate load-carrying capacity of CFST arch rib with new-type dumbbell-shaped section. *Adv. Mater. Res.* 2203, 634–638. doi:10.4028/www.scientific.net/AMR.634-638.3825

Yuan, C. C., Hu, Q., Wang, Y. Y., and Liu, C. (2020). Out-of-plane stability of fixed concrete-filled steel tubular arches under uniformly distributed loads. *Mag. Concr. Res.* 73 (18), 945–957. doi:10.1680/jmacr.19.00526

Zhang, Y. F., Guo, D. L., and Mei, B. R. (2022). Numerical analysis of eccentric compression performance of CFRP-confined concrete-filled steel tube (CFST) columns. *J. Institution Eng. (India) Ser. A* 103 (2), 543–555. doi:10.1007/S40030-022-00638-0

Zhang, Y. Y., and Yu, C. L. (2013). Nonlinear stability impact of concrete-filled steel tube arch bridge. *Adv. Mater. Res.* 2605, 1168–1171. doi:10.4028/www.scientific.net/amr.785-786.1168

Zhao, Y. F., Xie, W. W., and Yang, L. F. (2021). Elastic modulus reduction method for stable bearing capacity analysis of dumbbell-shaped CFST arches. *J. Phys. Conf. Ser.* 2044 (1), 012163. doi:10.1088/1742-6596/2044/1/012163

Zou, Y., Yu, K., Heng, J., Zhang, Z., Peng, H., Wu, C., et al. (2023). Feasibility study of new GFRP grid web - concrete composite beam. *Compos Struct.* 305, 116527. doi:10.1016/j.compstruct.2022.116527

Zou, Y., Zheng, K. D., Zhou, Z. X., Zhang, Z. Y., Guo, J. C., and Jiang, J. L. (2023). Experimental study on flexural behavior of hollow steel-UHPC composite bridge deck[J]. *Eng. Struct.* 274, 115087. doi:10.1016/j.engstruct.2022.115087

frontiers | Frontiers in Materials

TYPE Correction
PUBLISHED 16 February 2023
DOI 10.3389/fmats.2023.1158750

OPEN ACCESS

APPROVED BY
Frontiers Editorial Office,
Frontiers Media SA, Switzerland

*CORRESPONDENCE
Yingbin Li,
281650659@qq.com

SPECIALTY SECTION
This article was submitted to Structural Materials,
a section of the journal
Frontiers in Materials

RECEIVED 04 February 2023
ACCEPTED 06 February 2023
PUBLISHED 16 February 2023

CITATION
Wang S, Li Y, Liu Z and Cheng T (2023), Corrigendum: Calculation model of concrete-filled steel tube arch bridges based on the "arch effect".
Front. Mater. 10:1158750.
doi: 10.3389/fmats.2023.1158750

Corrigendum: Calculation model of concrete-filled steel tube arch bridges based on the "arch effect"

Shaorui Wang, Yingbin Li*, Zengwu Liu and Tianlei Cheng

School of Civil Engineering, Chongqing Jiaotong University, Chongqing, China

KEYWORDS

concrete-filled steel tube arch, arch mode, geometric non-linearity, coefficient of eccentricity increase, equivalent beam and column method, eccentric compression column

A Corrigendum on
Calculation model of concrete-filled steel tube arch bridges based on the "arch effect"

by Wang S, Li Y, Liu Z and Cheng T (2023). Front. Mater. 9:1084999. doi: 10.3389/fmats.2022.1084999

In the original article, the author names were incorrectly formatted. The correct names appear above.

In the original article, there was an error in the **Funding** statement. Information about the source of funds was not added to the article. The correct statement is as follows:

"This work was supported by Science and Technology Innovation Project of Chongqing Education Commission "Construction of Twin Cities Economic Circle in Chengdu-Chongqing Region" (KJCXZD2020032), Natural Science Foundation of Chongqing (cstc2021jcyj-msxm2491), Guangxi Key Research and Development Program (GuikeAB22036007-8), Chongqing Technology Innovation and Application Development Special Key Project (CSTB2022TIAD-KPX0205). This support is gratefully acknowledged."

The authors apologize for these errors and state that this does not change the scientific conclusions of the article in any way. The original article has been updated.

Publisher's note

All claims expressed in this article are solely those of the authors and do not necessarily represent those of their affiliated organizations, or those of the publisher, the editors and the reviewers. Any product that may be evaluated in this article, or claim that may be made by its manufacturer, is not guaranteed or endorsed by the publisher.

frontiers | Frontiers in Materials

TYPE Original Research
PUBLISHED 10 January 2023
DOI 10.3389/fmats.2022.1088554

OPEN ACCESS

EDITED BY
Zhigang Zhang,
Chongqing University, China

REVIEWED BY
M. Iqbal Khan,
King Saud University, Saudi Arabia
Yang Zou,
Chongqing Jiaotong University, China

*CORRESPONDENCE
A. Deifalla,
ahmed.deifalla@fue.edu.eg,
diffalaf@mcmaster.ca
Mahmood Ahmad,
ahmadm@uetpeshawar.edu.pk

SPECIALTY SECTION
This article was submitted to Structural Materials, a section of the journal Frontiers in Materials

RECEIVED 03 November 2022
ACCEPTED 21 December 2022
PUBLISHED 10 January 2023

CITATION
Awad A, Tawfik M, Deifalla A, Ahmad M, Sabri Sabri MM and El-said A (2023), Effect of hybrid-fiber- reinforcement on the shear behavior of high-strength-concrete beams.
Front. Mater. 9:1088554.
doi: 10.3389/fmats.2022.1088554

Effect of hybrid-fiber-reinforcement on the shear behavior of high-strength-concrete beams

Ahmed Awad[1], Maged Tawfik[2], A. Deifalla[3]*, Mahmood Ahmad[4]*, Mohanad Muayad Sabri Sabri[5] and Amr El-said[2]

[1]Faculty of Engineering, October University for Modern Sciences and Arts, Giza, Egypt, [2]Department of Civil Engineering, The Higher Institute of Engineering, El Shrouk, Cairo, Egypt, [3]Structural Engineering and Construction Management Department, Future University in Engineering, Cairo, Egypt, [4]Department of Civil Engineering, University of Engineering and Technology Peshawar (Bannu Campus), Bannu, Pakistan, [5]Peter the Great St. Petersburg Polytechnic University, St. Petersburg, Russia

The shear behavior of concrete beams is highly affected by the implementation of better performance concrete. Hybrid fibers addition to concrete mixture has proven to improve the performance compared to just using single type of fiber. Thus, in this current study, the shear behavior of hybrid-fiber-reinforced-high-strength-concrete beams was investigated experimentally. In addition, the effect of the span-to-depth ratio and the transverse reinforcement ratio were examined. Results showed that, when .45% of the cement weight is replaced with polypropylene fiber and 7% of the cement weight is replaced with steel fibers, the shear strength of the beam was enhanced by 18% in comparison to the control beam. The Formation and progression of cracks were also better controlled. The behavior of hybrid-polypropylene-steel-fibers-high-strength-concrete beams was observed to be comparable to that of conventional concrete ones as the shear strength increased with the decrease in span to depth ratio or the increase in transverse reinforcing ratio. A non-linear numerical model was developed and validated using the experimental results. The shear capacities of beams were calculated using ACI, which was compared to experimental and numerical results. The ACI's calculations were conservative when compared with the experimental or numerical results. The coefficient of variance between the ACI and experimental shear capacity results was 4.8%, while it was 9.2% between the ACI and numerical shear capacity results.

KEYWORDS

shear, fiber, steel, polyproplene, beams

1 Introduction

The reinforced concrete (RC) evolution have been an ongoing process with so many advancements (Ahmad et al., 2022; Ahmed et al., 2022; Ali et al., 2022; Ashraf et al., 2022; Ghareeb et al., 2022; Huang et al., 2022; Khan et al., 2022; Li et al., 2022; Mohammed et al., 2022; Shen et al., 2022; Zou et al., 2023a; Zou et al., 2023b). High-strength concrete (HSC), especially that with fiber-RC (FRC) is a versatile form of a concrete mixture with superior performance compared to that of normal RC without fiber reinforcement (Deifalla, 2021a; Deifalla et al., 2021). Higher cement demand during the production of HSC resulted in the consumption of resources and environmental issues (Juenger et al., 2019; Naqi and Jang, 2019). Researchers turned to add single or hybrid fibers to the concrete mixture as an alternative to cement to limit environmental destruction. Additionally for the significance of these fibers in enhancing

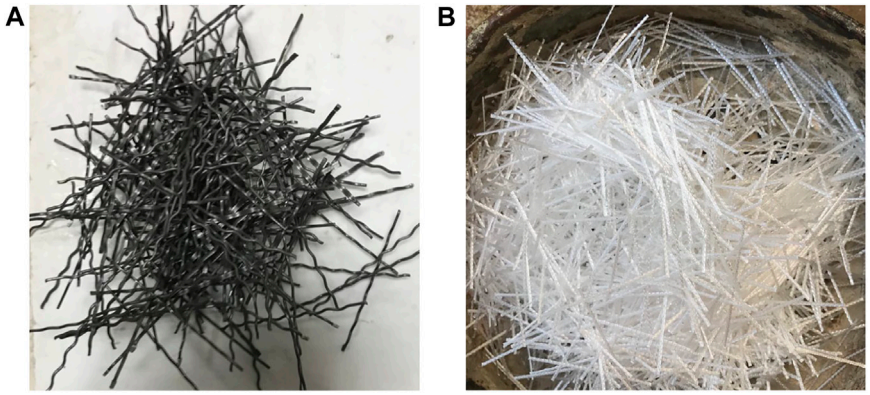

FIGURE 1
Shape of **(A)** steel fiber and **(B)** polypropylene fiber.

TABLE 1 Properties of steel fibers and polypropylene fibers.

Fiber type	Length (mm)	Cross-section	Modulus of elasticity (GPa)	Tensile strength (MPa)
Steel	35	1 mm × 4 mm	211	2,550
Polypropylene	20	Diameter of .04 mm	69	2,075

concrete's behavior in resisting tensile stresses and minimizing the formation and propagation of cracks. The findings of earlier studies demonstrated that utilizing hybrid fibers enhanced concrete strength and durability as well as minimized cracks compared to using a single type of fiber (Hoang and Fehling, 2017; Li et al., 2018; Zhang et al., 2018; Ali et al., 2020; Sivakumar et al., 2020; Zhong et al., 2020; Tawfik et al., 2022). Tawfik et al. (2022) observed that using hybrid fibers rather than only one kind of fiber increased the strength of the composite in terms of compressive, flexural, and tensile stresses by 50%, 46%, and 53%, respectively. This improvement in strength is caused by the incorporation of hybrid fibers with various characteristics, which stop the development of multiscale crack formation at various levels of stress. When incorporated into cementitious materials, fibers with such a greater young's modulus enhance the compressive behavior of concrete by suppressing the growth of macro-cracks at high-stress levels. Additionally, fibers with a minimal young's modulus massively increase concrete compressive behavior by restricting the forming of micro-cracks at small levels of stress.

Prior studies proved that the shear behavior of RC beams significantly enriched due to the steel fibers inclusion. Yavaş et al. (2019) concluded that the use of different volume content (1.5%, 1%, and .5%) of steel fibers, various lengths (6 mm, 13 mm, 30 mm, and 60 mm) of steel fibers, and several shapes (straight, double hooked, and hooked) of steel fibers. These additions enhanced the shear strength of ultrahigh strength FRC (UHSFRC) beams more than the control beam. Furthermore, using 1.5% straight steel fiber as a partial substitute for cement and with a length of 13 mm had the best impact on shear strength and cracking pattern for UHSFRC beams. Similar findings were produced by Lim and Hong (2017), who found that adding steel fiber with a volume content of 1.5% into UHSFRC beams resulted in a significant increase in shear strength. Shear reinforcement additionally improved the ductility of concrete beams. According to earlier research, steel fibers can be used instead of the transverse reinforcement in concrete beams while sustaining ductility and shear strength, or even perform a little bit better. Tahenni et al. (2016) explored that high-strength concrete beams without transverse reinforcing and having steel fibers with volume content up to 3% displayed slightly better shear behavior than high-strength concrete beams with transverse reinforcing and without steel fibers. The FRC beams showed improved shear strength and relatively minimal diagonal cracks, especially for steel fiber volume content from 1% to 3%. Also, Torres and Lantsoght (2019) revealed that the minimum transverse reinforcement required by ACI318 can be replaced by steel fibers in the amount of 1.2%, whereas the minimum transverse reinforcement required by Eurocode two can be replaced by steel fibers in the amount of .6%.

Even though the use of polypropylene fibers in concrete did not provide that resistance to shear stresses as steel fibers, it was demonstrated that it would be possible to slightly improve the behavior of the concrete beams in terms of cracking load, crack bridging, and shear capacity. Yang et al. (2021) showed that the inclusion of polypropylene fiber could further enhance the shear strength of concrete beams by up to 17% when compared to reinforced-concrete beams without fibers. Additionally, the presence of polypropylene fiber improved the initial crack shear load, prevented crack progression, maximized the number of cracks, and decreased crack width, thereby helping to increase beam ductility and improve strength properties. Ortiz Navas et al. (2018) demonstrated that the shear strength of FRC beams with or without stirrups increased noticeably when 10 kg/m^3 of polypropylene fibers were added, compared to the control specimens. The failure modes of fiber concrete beams with stirrups and those without stirrups were comparable.

TABLE 2 Mix properties.

Mix	Polypropylene fiber volume (%)	Steel fiber volume (%)	Silica fume (Kg/m3)	Cement (Kg/m3)	W/C ratio	Coarse Agg. (Kg/m3)	Fine Agg. (Kg/m3)	Super plasticizer (Lit./m3)
Control Mix	—	—	25	500	.40	1148	705	6.4
Hybrid fibers Mix	.45	7	25	463	.40	1148	705	6.4

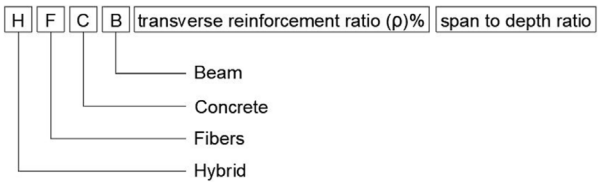

FIGURE 2
Designation for all concrete beams.

Few studies have focused on the impact of applying hybrid fibers rather than a single type on the shear behavior of concrete beams since, as was earlier mentioned, hybrid fibers provide improved mechanical properties and can control cracks at various stress levels. Shaaban et al. (2021) evaluated the effect of various shapes of silica fume, polyvinyl alcohol, polypropylene, or hybrid fibers on the shear behavior of reinforced concrete beams experimentally and numerically. When comparing the control beam which contains transverse reinforcement and no fibers, introducing hybrid fibers, increased shear strength and ductility. Hybrid fibers with .75% polyvinyl alcohol and .75% polypropylene and transverse reinforcement produced greater shear capacity and ductility when compared to beams without transverse reinforcement and containing hybrid fibers with 1.5% polyvinyl alcohol and .375% polypropylene. Depending upon these findings, it was suggested that hybrid fibers with .75% polyvinyl alcohol and .75% polypropylene, as well as stirrup reinforcement (7.5 Ø 6/m), be employed to accomplish high shear strength for hybrid FRC beams. The finite element predictions for the tested beams exhibited a strong agreement with the experimental observations regarding the shear capacity, maximum deflection, and failure pattern. Ismail and Hassan. (2021) explored the shear performance of FRC using various fiber kinds. Polyvinyl alcohol fiber lengths of 8 and 12 mm, polypropylene fibers length of 19 mm, and steel fibers length of 13 mm were the four different kinds of fiber employed. According to the findings, all FRC beams outperformed the control beam on basis of cracking behavior, shear strength, ductility, and energy absorption. The FRC beam containing polyvinyl alcohol fibers with 8 mm length showed higher shear strength and ductility than the FRC beam containing polyvinyl alcohol fibers with 12 mm length. Polypropylene FRC beams performed the least, whereas steel FRC beams performed the best in terms of first crack load, maximum strength, ductility, and ability to absorb energy. According to Alrefaei et al. (2018), inserting hybrid polypropylene-steel fibers up to a volume of 2% was significant in improving the shear capacity by approximately eight times compared to the concrete beams without fibers. Furthermore, the beams' ductility, multi-cracking behavior, and concrete strain capability were all significantly enhanced. It is demonstrated that, regardless of the hybridized ratio, a hybrid fiber volume content of 1% is a sufficient minimum transverse reinforcement for concrete beams having compression strength varying between 40 and 65 MPa.

The majority of previous work focused on the physical and mechanical characteristics of using single or hybrid fibers in cementitious materials (Tahenni et al., 2016; Lim and Hong, 2017; Alrefaei et al., 2018; Ortiz Navas et al., 2018; Zhang et al., 2018; Ayub et al., 2019; Koniki and Prasad, 2019; Torres and Lantsoght, 2019; Xu et al., 2019; Yavaş et al., 2019; Ali et al., 2020; Ismail and Hassan, 2021; Shaaban et al., 2021; Yang et al., 2021), and there have been fewer studies on the shear behavior of FRC elements that used a single type of fiber, whereas there is a lack of research into the effect of hybrid fibers on the shear behavior of high-strength concrete elements although the use of hybrid fibers had been shown to significantly improve the properties of concrete over the use of a single type of fiber (Alrefaei et al., 2018; Navas et al., 2018; Khan et al., 2020). Additionally, the previous studies that used hybrid fibers varied in terms of the type, proportion, characteristics, and shape of the fibers (Kumar et al., 2017; Fadil et al., 2018; Smarzewski, 2018; Wang et al., 2019; Zhang et al., 2019; Shi et al., 2020; Tran et al., 2020). As a result, prospective studies in this area are required to produce meaningful results. From this viewpoint, the current research was conducted to study experimentally and numerically the shear behavior of HFRHSC beams. The main parameters were concrete type, span to depth ratio, and transverse reinforcement ratio.

2 Experimental program

2.1 Materials and mix proportions

HSC was produced using cement, pure water, fine aggregate, coarse aggregate, silica fume, superplasticizer, and hybrid polypropylene-steel fibers. The cement used was ordinary Portland cement. The coarse aggregate was formed of crushed dolomite with a particle size of 10 mm and an apparent specific gravity of 2.6, while the fine aggregate was a siliceous natural with a fineness modulus of 3.35. Silica fume was added to the concrete mixture to fill the voids and thus improve the strength, while a superplasticizer was added to improve the workability of the concrete. The forms of the fibers are shown in Figure 1 and Table 1 displays the steel and polyethylene fiber characteristics as reported by the suppliers. The binder component was dry-mixed for about 3 min in a mechanical mixer before adding the full quantity of water and superplasticizer to the concrete mixture. Polypropylene and steel fibers were added to the mixture after the wet mixing process and mixed for around 5 min. The transverse reinforcement showed a tensile yield strength of 240 MPa and

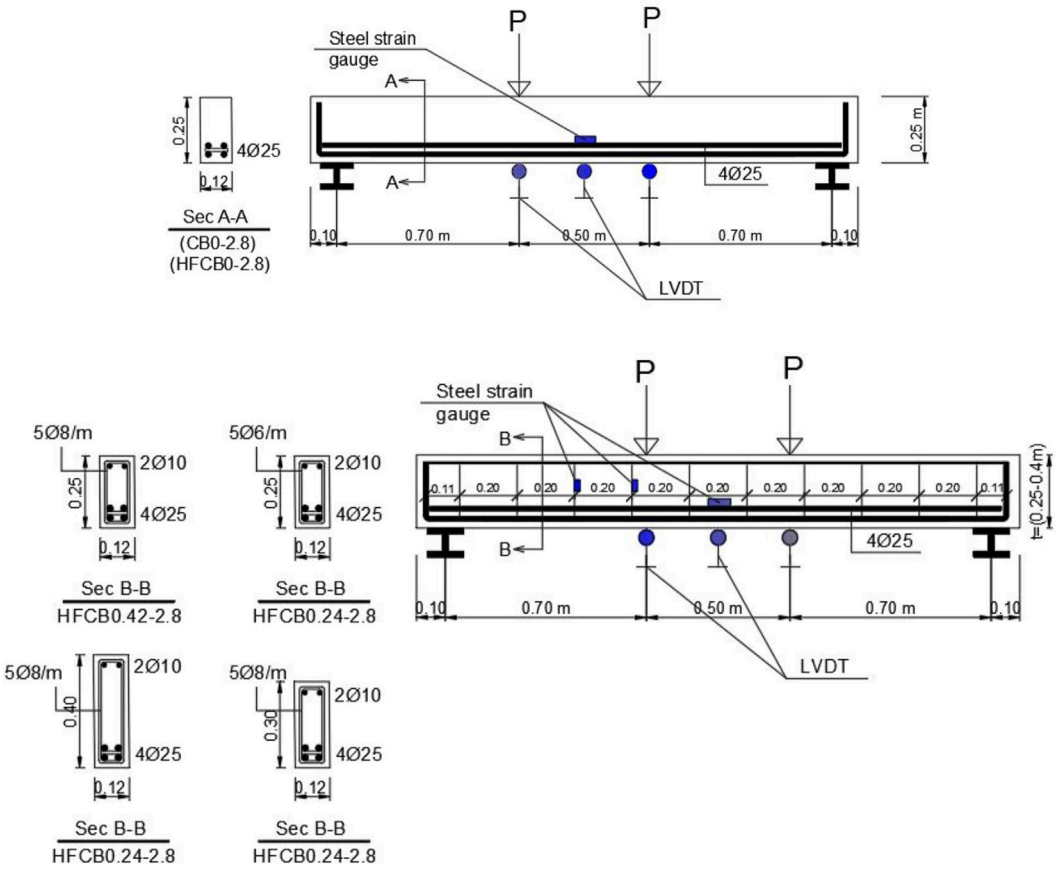

FIGURE 3
Typical dimensions, reinforcement, and instruments for all concrete beams.

TABLE 3 Details of all concrete beams.

Beam ID	Concrete type	Cross section cm^2	Stirrups	Transverse reinforcement ratio (ρ) %	Longitudinal reinforcement	Shear span cm	Span-to-depth ratio
CB0-2.8	Normal	12 × 25	—	0	4Ø25 Bottom 2Ø10 Upper	70	2.8
HFCB0-2.8	Hybrid	12 × 25	—	0		70	2.8
HFCB0.24-2.8	Hybrid	12 × 25	5Ø6/m	.24		70	2.8
HFCB0.42-2.8	Hybrid	12 × 25	5Ø8/m	.42		70	2.8
HFCB0.42-2.3	Hybrid	12 × 30	5Ø8/m	.42		70	2.8
HFCB0.42-1.75	Hybrid	12 × 40	5Ø8/m	.42		70	2.8

ultimate strength of 385 MPa, compared to the longitudinal reinforcement's tensile yield strength of 520 MPa and ultimate strength of 690 MPa. The mix quantities, which are based on Tawfik et al. (2022) are shown in Table 2. For the best mechanical characteristics in terms of compressive, tensile, flexural strength, and cracking control, the concrete mixture contains .45% of polypropylene fiber and 7% of steel fiber as a replacement ratio for the cement weight.

2.2 Description and preparation of beam specimens

Five hybrid-polypropylene-steel-fiber-reinforced-high-strength-concrete (HFRHSC) beams and one control high-strength reinforced concrete beam are included in the experimental program. The beams are labeled according to the shown in Figure 2. The control beam (CB0-2.8) was 120 mm and 250 mm in

FIGURE 4
Preparation of concrete beams.

FIGURE 5
Test setup for all concrete beams.

width and depth, respectively, while being 2,100 mm long, with no stirrups or fibers, and the flexure longitudinal reinforcement used was 4Ø25. All HFRHSC beams contain 7.45% hybrid fibers as a substitute for the weight of cement, which was divided into 7% steel fibers and .45% polypropylene fibers. The first hybrid FRC beam (HFCB0-2.8), was similar to the control beam in dimensions and proportion of longitudinal steel reinforcement, but the difference was the presence of a hybrid of polypropylene-steel fibers. The second hybrid FRC beam (HFCB0.24-2.8), was similar to the concrete beam (HFCB0-2.8) in dimensions, concrete type, and proportion of longitudinal steel reinforcement, except for the presence of 5Ø6/m transverse reinforcement. The transverse reinforcement ratio of the hybrid FRC beam (HFCB0.42-2.8) was higher than that of the concrete beam (HFCB0.24-2.8), while the dimensions, concrete type, and longitudinal reinforcement ratio were the same in both concrete beams. The hybrid FRC beams (HFCB0.42-2.3) and (HFCB0.42-1.75) differed from the concrete beam (HFCB0.42-2.8) in depth, which was 300 mm and 400 mm, respectively, however, they were similar in terms of width, length, concrete type, and proportion of longitudinal and transverse steel reinforcement. Figure 3 and Table 3 show the details for all concrete beams. To evaluate the mechanical characteristics, including compressive strength, tensile strength, and modulus of elasticity, six concrete cubes (150 × 150 × 150 mm) and 12 concrete cylinders (150 × 300 mm for diameter and height, respectively) were taken from that concrete mixture of each beam. The samples were prepared and examined as per the Egyptian code of concrete specifications.

The transverse reinforcement ratio (ρ) can be calculated using Eq. 1 as the area of transverse reinforcement (Av) multiplied by the spacing between stirrups (s) and the width of the beam (b).

$$\rho = \frac{Av}{b \times s}\% \quad (1)$$

The wooden forms of all concrete beams were prepared and thoroughly sprayed with water before the pouring process to maintain the water in the mixture and not being absorbed by the wood. Electrical strain gauges with a length of 10 mm and a resistance of 120.3 ± .5 Ω were attached to the longitudinal and transverse reinforcement bars in the location as seen in Figure 3, which is responsible for monitoring the strain in the reinforcements along the loading history. The reinforcement was then positioned in the forms as illustrated in Figure 4. The casting process then began, with a vibrator used during the casting to prevent separation between the concrete mortar and the coarse aggregate and to ensure regular fibers distribution. Following 24 h of casting, the forms were withdrawn, and the concrete beams were continually moistened with water for 28 days before being examined.

2.3 Test setup of beam specimens

Figure 5 illustrates the testing procedure used to examine the shear behavior of HFRHSC beams. The beams were supported by two

TABLE 4 Density, flexural, compressive strength, and modulus of elasticity results for control and hybrid FRC specimens.

Mix	Density (kg/m^3) at	Strength compressive (MPa)		Strength flexural (MPa)		Young's modulus (GPa)	
	28 days	7 days	28 days	7 days	28 days	7 days	28 days
Control mix	3,362 ± 90	30.2 ± 1.2	48 ± 1.8	3.2 ± 0.2	4.9 ± 0.2	21.5 ± 0.9	31 ± 1.2
Hybrid fibers mix	3,365 ± 75	49 ± 1	75 ± 1.5	4.1 ± 0.1	5.5 ± 0.3	28 ± 1	38 ± 1.4

TABLE 5 Experimental results for all concrete beams.

Beam ID	Shear load V (kN)		Mid-span deflection Δ (mm)		Strain at stirrups ε %		Strain at long. Reinforcement ε %		[a]Ductility ratio
	$V_{Failure}$	$V_{Cracking}$	$\Delta_{Failure}$	$\Delta_{Cracking}$	$\varepsilon_{Failure}$	$\varepsilon_{Cracking}$	$\varepsilon_{Failure}$	$\varepsilon_{Cracking}$	
CB0-2.8	45	12	2.84	1.56	—	—	.06	.017	1.82
HFCB0-2.8	53	20	3.19	1.10	—	—	.07	.018	2.90
HFCB0.24-2.8	71	31	3.89	1.21	.13	2.67E-03	.09	.034	3.21
HFCB0.42-2.8	80	37	4.11	1.09	.14	1.23E-03	.10	.045	3.76
HFCB0.42-2.3	111	52	4.80	1.80	.13	1.98E-03	.10	.047	2.66
HFCB0.42-1.75	137	60	4.04	1.74	.16	1.68E-03	.11	.054	2.32

[a]Ductility ratio = ($\Delta_{Failure}/\Delta_{Cracking}$).

supports (hinged and roller), with a distance of 2,000 mm between them. The load was applied using a hydraulic jack positioned in the middle of the beam. The hydraulic jack's load was transmitted through an I-steel beam so that it concentrated symmetrically in two points, provided that the distance between the concentrated load and the support was 700 mm on either side. Three LVDTs were installed in the critical sections as shown in Figure 5 to monitor the displacement values during loading. The deflection of concrete beams and reinforcement strain were measured every 10 kN of loading, as well as cracks, were marked. The load steadily increased until the concrete beam collapsed.

3 Results

3.1 Mechanical properties

Table 4 displays the mechanical properties of the concrete mix implemented for the casting of the specimens, which are represented in tensile and compressive strength as well as modulus of elasticity. The results were calculated as the average of three samples tested under the same conditions. For each mix, six cube specimens with a cross-section of 15 cm × 15 cm, and a height of 15 cm were implemented to measure the compressive strength. Three cube specimens were tested at 7-day, and three as well at 28-day. Furthermore, the elastic modulus was determined for each cementitious material by examining concrete cylinder specimens at 7-day as well as another three at 28-day. The cylinder specimens have a diameter of 15 cm and a height of 30 cm. Whereas the flexural strength of each cementitious material is evaluated by examining three concrete beam specimens at 7-day as well as three more at 28-day. The concrete beams have all been 70 cm long, 15 cm × 15 cm in cross-section.

3.2 Shear behavior of concrete beam specimens

This section displays the results of (shear load, mid-span deflection, and ductility) at the failure and cracking stages for every concrete beam specimen. Furthermore, relationships between load and various parameters such as mid-span deflection, stirrup strain, and longitudinal bar strain were studied. The strain in the stirrup was calculated by taking the average of the two strain gauges installed in the stirrup's vertical legs in the critical shear zone. While the longitudinal reinforcement strain was measured at the maximum flexure stress, which is at mid-span. Table 5 represents the experimental results for all concrete beams.

3.2.1 Load versus deflection for all concrete beams

The relationship between load and mid-span deflection for all concrete beams is illustrated in Figure 6. According to the findings, the mid-span deformation values at the first shear crack for concrete beams CB0-2.8, HFCB0-2.8, HFCB0.24-2.8, HFCB0.42-2.8, HFCB0.42-2.3, and HFCB0.42-1.75 were 1.56, 1.1, 1.21, 1.09, 1.8, and 1.74 mm, respectively. Additionally, the concrete beams CB0-2.8, HFCB0-2.8, HFCB0.24-2.8, HFCB0.42-2.8, HFCB0.42-2.3, and HFCB0.42-1.75 had maximum mid-span deformation values of 2.84, 3.19, 3.89, 4.11, 4.8, and 4.04 mm, respectively. It was noticeable that hybrid FRC beams with or without transverse steel reinforcement showed lower deformation values than the control beams CB0-2.8 at the same load, demonstrating the ability of fibers

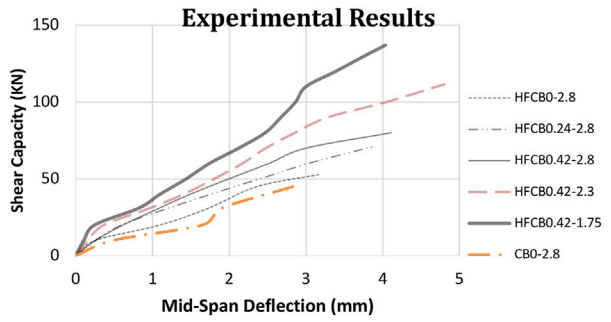

FIGURE 6
The relation between load and mid-span deflection for all concrete beams.

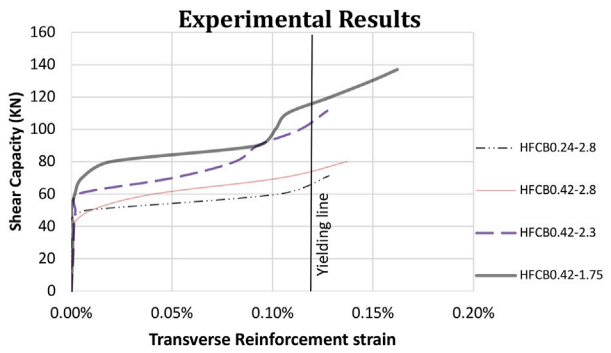

FIGURE 7
The relation between load and strain at transverse reinforcement for concrete beams HFCB0.24-2.8, HFCB0.42-2.8, HFCB0.42-2.3, and HFCB0.42-1.75.

and transverse steel reinforcement to delay the cracking process, improve stiffness and strength, and reduce deformation values at the same load. Adding hybrid fibers, increasing the transverse reinforcement ratio, as well as decreasing the span to depth ratio resulted in a decrease in the deflection values at the same load, due to the delay in the cracking process, which improved stiffness and strength and ultimately showed lower deformation values. However, the decrease in span to depth ratio reduced the ductility of the beam to the point where it could not be inelastically deformed without failure. The highest maximum deformation was reported in the hybrid FRC beam HFCB0.42-2.8, which contains transverse steel reinforcement and hybrid fibers. This demonstrates the significance of both hybrid fibers and transverse reinforcement in lowering the brittleness of concrete and enhancing its ability for plastic deformation without fracture (Khan et al., 2021a; Khan et al., 2021b; Abbas et al., 2022; Abbas and Khan, 2022).

3.2.2 Load versus strain of transverse reinforcement all concrete beams

The relationship between load and strain values in transverse steel reinforcement for hybrid FRC beams that contain transverse reinforcement is illustrated in Figure 7. The strain values in the transverse reinforcement at the crack load were .003%, .0012%, .002%, and .0017% For the concrete beams HFCB0.24-2.8, HFCB0.42-2.8, HFCB0.42-2.3, and HFCB0.42-1.75 respectively. While the strain values at failure load for the concrete beams HFCB0.24-2.8, HFCB0.42-2.8, HFCB0.42-2.3, and HFCB0.42-1.75 were .13%, .14%, .13%, and .16%, respectively. The findings demonstrate that the strain values in the transverse reinforcement were insignificant at the initial shear crack but significantly increased with increasing loading until they reached yield for all concrete beams that contain transverse reinforcement, explaining the occurrence of severe diagonal shear cracks at collapse.

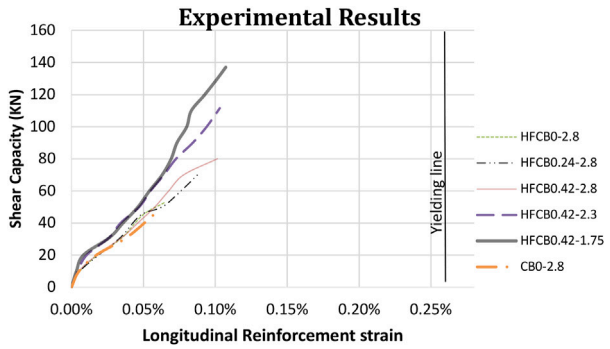

FIGURE 8
The relation between load and strain at longitudinal reinforcement for all concrete beams.

3.2.3 Load versus strain of longitudinal reinforcement all concrete beams

Figure 8 shows the relationship between load and strain values in longitudinal steel reinforcement for all concrete beams. For the concrete beams CB0-2.8, HFCB0-2.8, HFCB0.24-2.8, HFCB0.42-2.8, HFCB0.42-2.3, and HFCB0.42-1.75, the strain values in the longitudinal reinforcement at the crack load were .017%, .018%, .034%, .045%, .047%, and .054%, respectively. Whereas for the concrete beams CB0-2.8, HFCB0-2.8, HFCB0.24-2.8, HFCB0.42-2.8, HFCB0.42-2.3, and HFCB0.42-1.75, the longitudinal reinforcement strain values at failure load were .06%, .07%, .09%, .1%, .1%, and .11%, respectively. The results show that the longitudinal reinforcement strain did not reach yield for all concrete specimens, indicating that flexure stresses were insufficient to affect the failure mode, which was controlled by shear stresses.

4 Discussion

4.1 Cracking pattern and failure mode

Figure 9 shows the failure mode for all concrete beam specimens. Vertical cracks appeared in the flexure region for control beam CB0-2.8 which does not contain fibers, and then a single diagonal tension crack due to shear appeared in the shear region at the bottom and spread upwards with the increase in loading until it reached the location of the load's impact, and then a brittle collapse occurred as a result of a widening diagonal shear crack, recognizing that the beam collapsed shortly after the initiation of diagonal shear cracks, indicating low ductility. Also, just before failure, spalling was observed

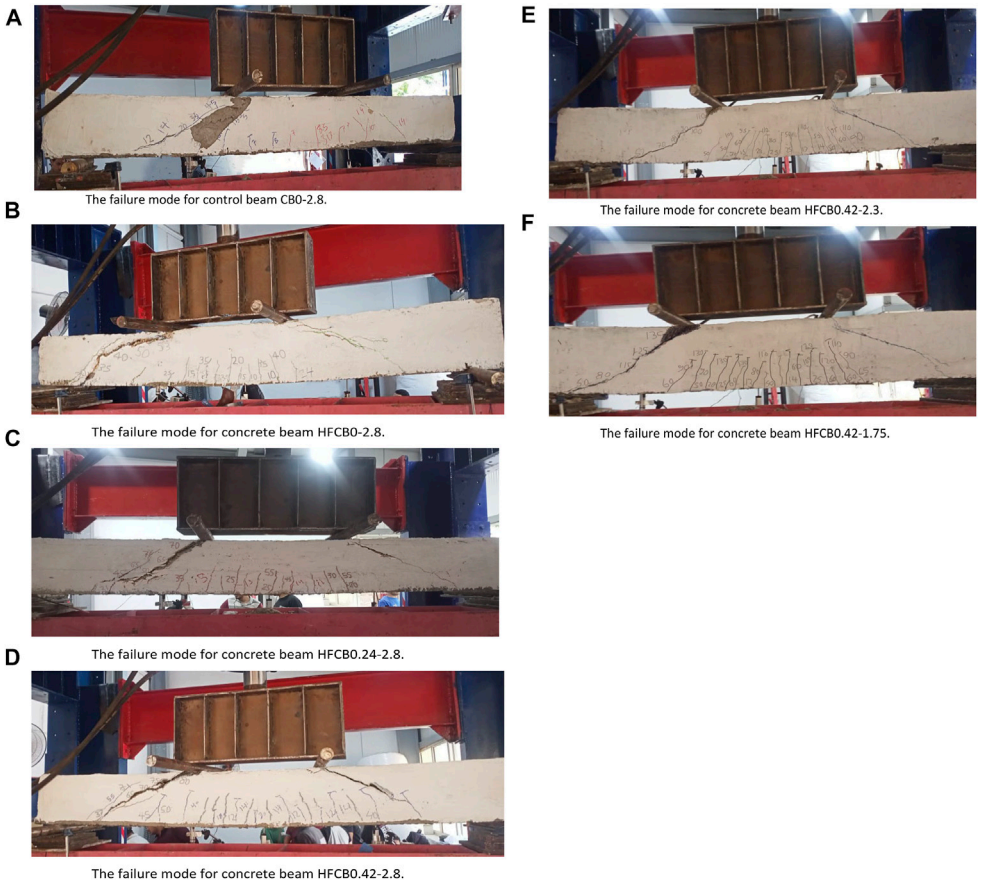

FIGURE 9
Failure modes for all concrete beams. **(A)** The failure mode for control beam CB0-2.8. **(B)** The failure mode for concrete beam HFCB0-2.8. **(C)** The failure mode for concrete beam HFCB0.24-2.8. **(D)** The failure mode for concrete beam HFCB0.42-2.8. **(E)** The failure mode for concrete beam HFCB0.42-2.3. **(F)** The failure mode for concrete beam HFCB0.42-1.75.

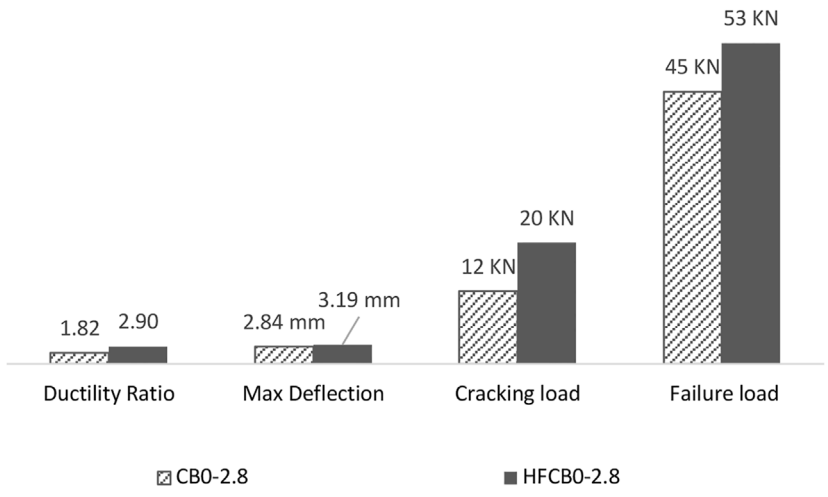

FIGURE 10
Effect of using hybrid polypropylene-steel fibers.

on the external surface of the concrete beam at the compression zone and extended along with the diagonal crack, indicating that the applied stresses exceeded the compressive strength of the concrete. The hybrid FRC beam HFCB0-2.8 failed due to the widening of a diagonal shear crack. The first diagonal shear crack for hybrid FRC beam HFCB0-2.8 appeared at a load of 20 kN

TABLE 6 Analysis of all concrete beams.

Beam ID	$\frac{V_{failure\ for\ HFCB}}{V_{failure\ for\ CB}}$	$\frac{V_{cracking\ for\ HFCB}}{V_{cracking\ for\ CB}}$	$\frac{\Delta_{max\ for\ HFCB}}{\Delta_{max\ for\ CB}}$	$\frac{Ductility\ for\ HFCB}{Ductility\ for\ CB}$
CB0-2.8	—	—	—	—
HFCB0-2.8	1.18	1.66	1.13	1.60
HFCB0.24-2.8	1.58	2.58	1.37	1.77
HFCB0.42-2.8	1.78	3.08	1.45	2.07
HFCB0.42-2.3	2.48	4.33	1.69	1.46
HFCB0.42-1.75	3.04	5.00	1.42	1.27

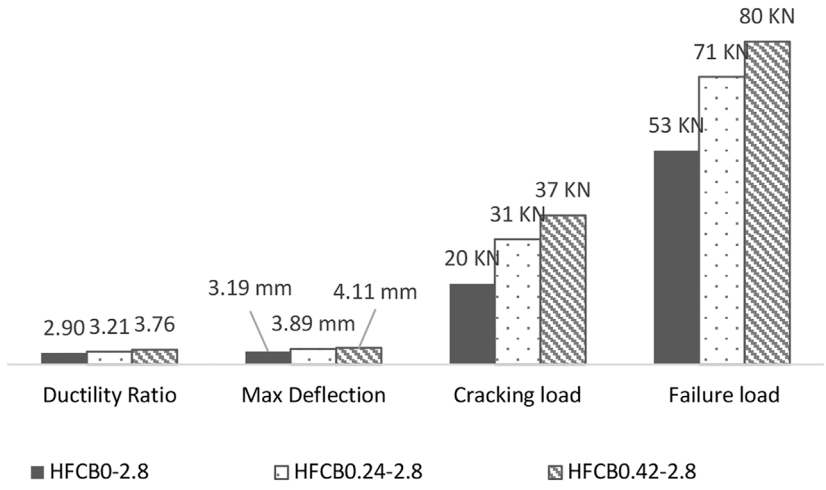

FIGURE 11
Effect of using transverse reinforcement.

while it appeared at a load of 12 kN for the control beam, demonstrating the significance of fibers in preventing crack initiation and propagation. More shear and flexure cracks appeared for the hybrid FRC beam HFCB0-2.8 than in the control beam due to the presence of fibers which prevents cracks from widening and spreading, causing high tensile stresses to be transmitted from the location of the existing cracks to the region between them. This leads to the development of new cracks, increasing the total number of cracks (Tahenni et al., 2016; Alrefaei et al., 2018; Shaaban et al., 2021). Hybrid FRC beam HFCB0-2.8 did not experience significant concrete spalling because the fibers improved the stiffness and strength. When transverse reinforcement was added to the prior hybrid FRC beam, the failure mechanism remained the same as the diagonal shear crack caused the collapse of the hybrid FRC beams HFCB0.24-2.8 and HFCB0.42-2.8. However, increasing the transverse reinforcement ratio resulted in higher shear strength, a slower rate of shear cracking, and more cracks, demonstrating the effectiveness of adding transverse reinforcement in delaying the cracking process and enhancing concrete's ductility, stiffness, and shear strength. The failure for both hybrid FRC beams HFCB0.42-2.3 and HFCB0.42-1.75 occurred due to diagonal shear cracks and was followed by crushing of concrete in the compression zone.

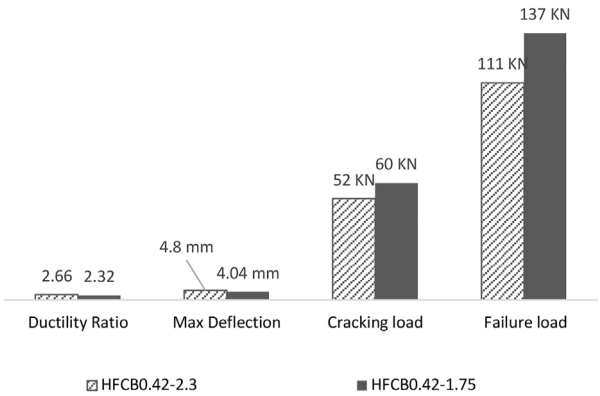

FIGURE 12
Effect of span to depth ratio.

However the shear crack width decreased, and the shear strength was noticeably improved for concrete beam HFCB0.42-1.75 more than the concrete beam HFCB0.42-2.3. This is due to a substantial proportion of the shear being immediately transferred to the support *via* an inclined strut. The direct load transfer's magnitude develops with a lowering span to depth ratio and

TABLE 7 Hybrid FRC properties.

Material model	Element type	Modulus of elasticity (GPa)	Poisson's ratio	Uniaxial crushing (MPa)	Uniaxial cracking (MPa)	Open shear coefficient	Close shear coefficient
1	Solid65	38	.2	60	5.5	.5	1

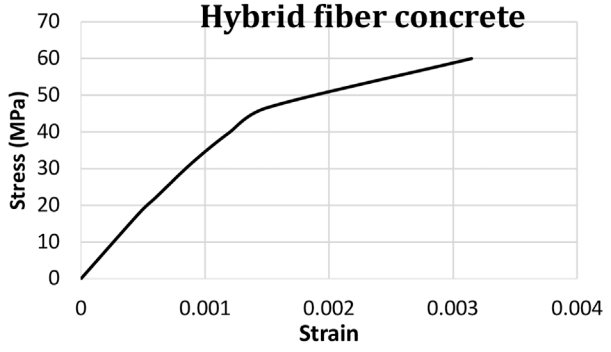

FIGURE 13
Stress-strain curve for hybrid fiber concrete.

has been known as the arch action mechanism (Ali et al., 2021; Ebid and Deifalla, 2021; Deifalla, 2021b; Li et al., 2021; Deifalla and Mukhtar, 2022a; Deifalla and Mukhtar, 2022b; Zhou and Wan, 2022). This mechanism inhibits cracks from growing larger and delays stirrup yielding. Additionally, it was observed that flexural cracks began growing larger and deeper as the span-to-depth ratio decreased. This refers to an increase in the tensile stresses caused by flexure in addition to the strain of the longitudinal reinforcement, however, the failure mode remained diagonal shear failure and did not transform for being combined shear-flexure or flexure failure since the longitudinal steel bars had not yet reached yielding.

4.2 Effect of using hybrid polypropylene-steel fibers

The use of hybrid polypropylene-steel fibers improved ultimate and cracking shear strength, as well as ductility, in concrete beams. As shown in Figure 10, the values of ultimate shear load, cracking shear load, maximum deformation, and ductility for hybrid FRC beam HFCB0-2.8 increased by 18%, 66%, 13%, and 60%, respectively, over the control beam CB0-2.8. Ductility is the ability of concrete to plastically deform without fracturing when subjected to tensile stress greater than its strength. It can be computed by dividing the ultimate deformation that occurs at the ultimate shear force by the cracking deformation that occurs at the cracking shear force (Pakravan et al., 2016; Yan et al., 2021). The fact that when the hybrid fibers were added, the cracking and ultimate shear strengths increased supports their ability to withstand macro and micro cracks at different stress levels, delaying the cracking process and improving stiffness and strength (Tahenni et al., 2016; Sivakumar et al., 2020; Ismail and Hassan, 2021; Shaaban et al., 2021; Yang et al., 2021; Tawfik et al., 2022). The increase in ultimate deformation and ductility values is a further indication of the efficacy of hybrid fibers in reducing concrete's brittleness and improving its capability for plastic deformation without fracture. Table 6 illustrates the analysis of shear failure load, shear cracking load, maximum deformation, and ductility results for all concrete beams.

4.3 Effect of using transverse reinforcement

Transverse reinforcement improved ultimate shear strength, cracking behavior, and ductility in concrete beams as shown in Figure 11. In comparison to the hybrid FRC beam HFCB0-2.8, the values of ultimate shear load, cracking shear load, maximum deformation, and ductility for hybrid FRC beam HFCB0.42-2.8 improved by 35%, 55%, 22%, and 11%, respectively. Additionally, the values of the ultimate shear load, cracking shear load, maximum deformation, and ductility increased by 12%, 19%, 6%, and 17%, respectively, as the transverse reinforcement ratio increased from .24% to .42%. Transverse steel reinforcement, which is similar to hybrid fibers, could postpone shear cracking while simultaneously enhancing shear strength and ductility (Alrefaei et al., 2018; Torres and Lantsoght, 2019; Yang et al., 2021).

4.4 Effect of span to depth ratio

As shown in Figure 12, the ultimate shear load and cracking shear load for hybrid FRC beam HFCB0.42-1.75, which has a span to depth ratio of 1.75 improved by 23% and 15%, respectively, more than for hybrid FRC beam HFCB0.42-2.3, which has a span to depth ratio of 2.3, and by 71% and 62%, respectively, more than for hybrid FRC beam HFCB0.42-2.8, which has a span to depth ratio of 2.8. These findings support the fact that lowering the span-to-depth ratio greatly improves shear strength because a considerable

TABLE 8 Transverse and longitudinal steel properties.

	Material model	Element type	Modulus of elasticity (GPa)	Poisson's ratio	Yield stress (MPa)
Longitudinal steel bars	2	Link180	200	.3	520
Transverse steel bars	3	Link180	200	.3	240

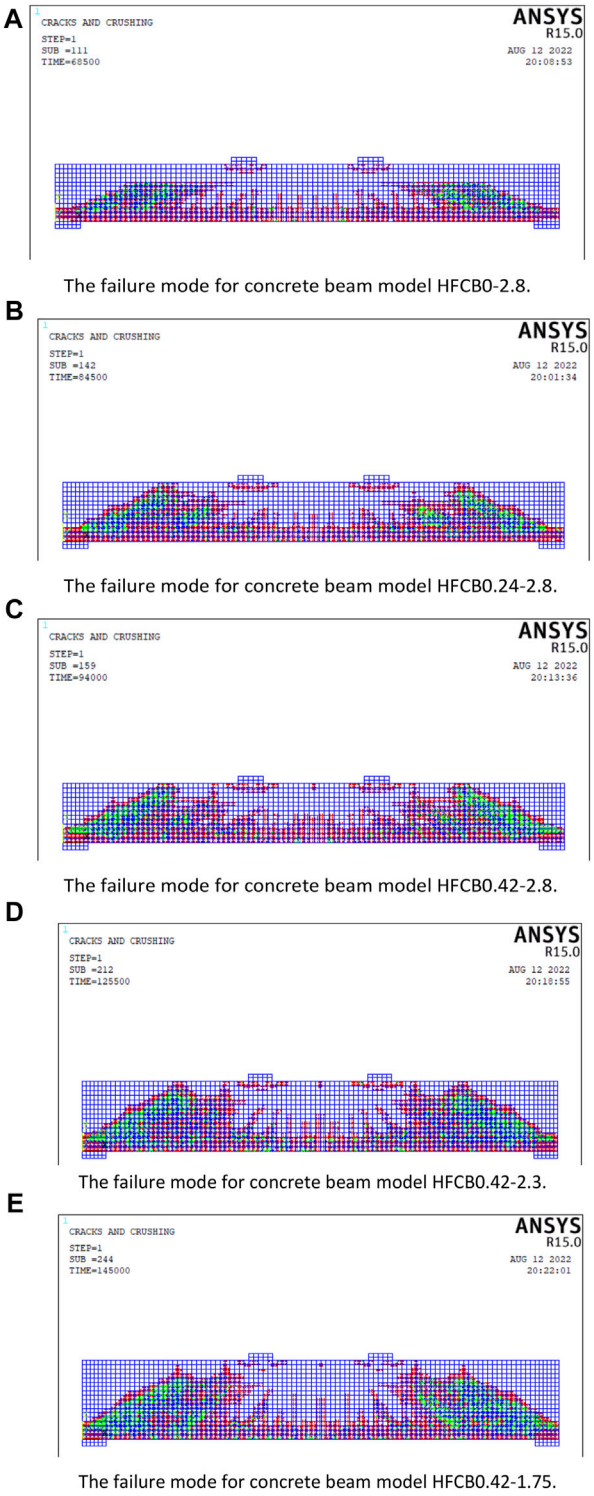

FIGURE 14
Failure modes for all hybrid FRC beam models. **(A)** The failure mode for concrete beam model HFCB0-2.8. **(B)** The failure mode for concrete beam model HFCB0.24-2.8. **(C)** The failure mode for concrete beam model HFCB0.42-2.8. **(D)** The failure mode for concrete beam model HFCB0.42-2.3. **(E)** The failure mode for concrete beam model HFCB0.42-1.75.

percentage of the shear force is transferred directly to the support by an inclined strut (arch action mechanism). This mechanism slows down the cracking process while enhancing stiffness and shear strength, which results in minor deformation occurring under the same load. In contrast, the hybrid FRC beam HFCB0.42-1.75, which has a span to depth ratio of 1.75, displayed the lowest deformation values at the same load and ductility, where they decreased by 16% and 13%, respectively,

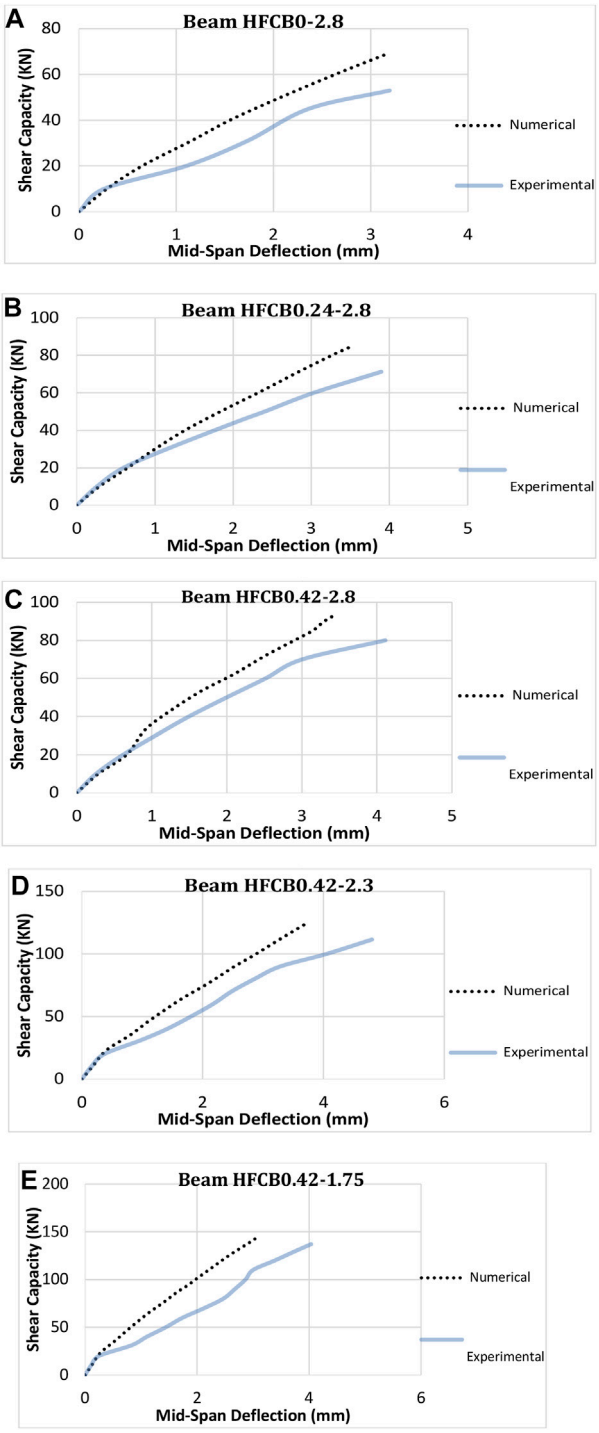

FIGURE 15
Experimental and numerical load-deflection curves for all hybrid FRC beams: **(A)** HFCB0-2.8, **(B)** HFCB0.24-2.8, **(C)** HFCB0.42-2.8, **(D)** HFCB0.42-2.3, and **(E)** HFCB0.42-1.75.

more than for the hybrid FRC beam HFCB0.42-2.3, which has a span to depth ratio of 2.3, and by 2% and 38%, respectively, more than for the hybrid FRC beam HFCB0.42-2.8, which has a span to depth ratio of 2.8. This indicates that although lowering the span to depth ratio increases the concrete's shear strength, it has a detrimental effect on the ductility because the concrete beam was unable to withstand inelastic deformation and collapsed suddenly once the first diagonal shear crack appeared.

5 Finite element model

ANSYS 15 software is used to produce a numerical model, which is then validated with experimental results. A total of five finite element models that accurately represent the experimental HPSFRC beams HFCB0-2.8, HFCB0.24-2.8, HFCB0.42-2.8, HFCB0.42-2.3, and HFCB0.42-1.75 were created.

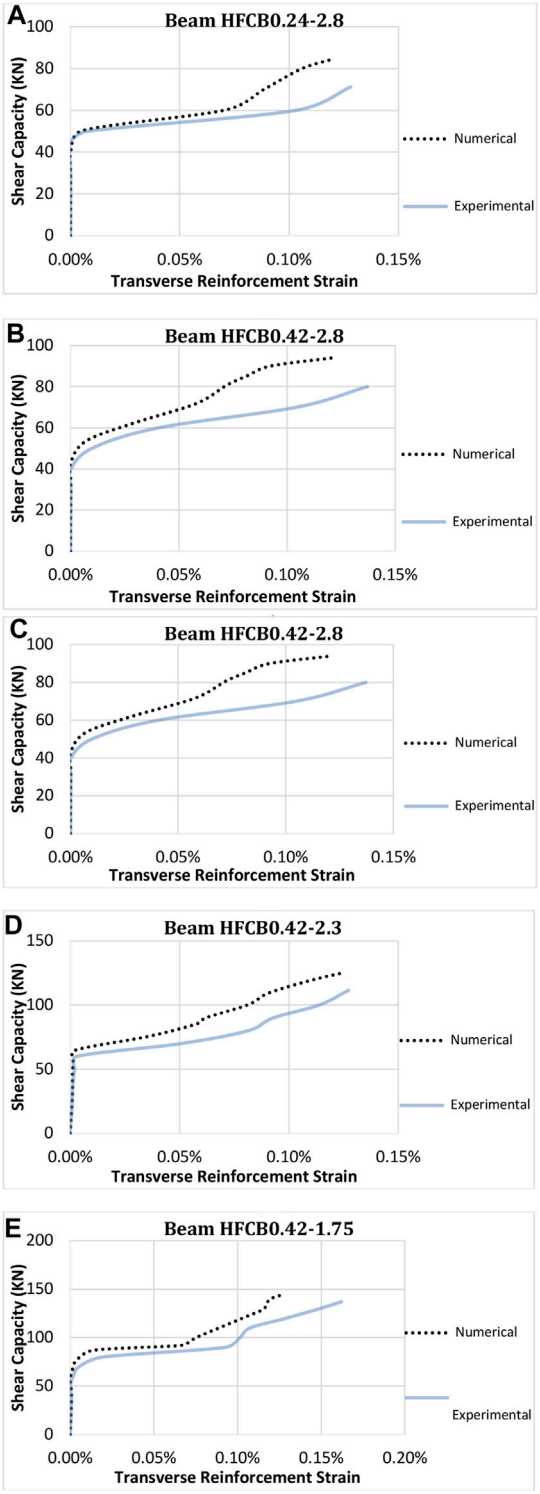

FIGURE 16
Experimental and numerical load-transverse reinforcement strain curves for all hybrid FRC beams: **(A)** HFCB0-2.8, **(B)** HFCB0.24-2.8, **(C)** HFCB0.42-2.8, **(D)** HFCB0.42-2.3, and **(E)** HFCB0.42-1.75.

5.1 Materials, loads, and boundary conditions modelling

The defined parameters of the concrete are shown in Table 7 and include the elastic modulus, Poisson's ratio, uniaxial crushing, uniaxial cracking, open shear, and close shear coefficient. The non-linear behavior of hybrid FRC beams was modeled using the stress-strain relationship shown in Figure 13, which was derived from the result of the uniaxial confined compressive strength test. Shear transfer coefficients are typically measured in the range of .0–1.0, with

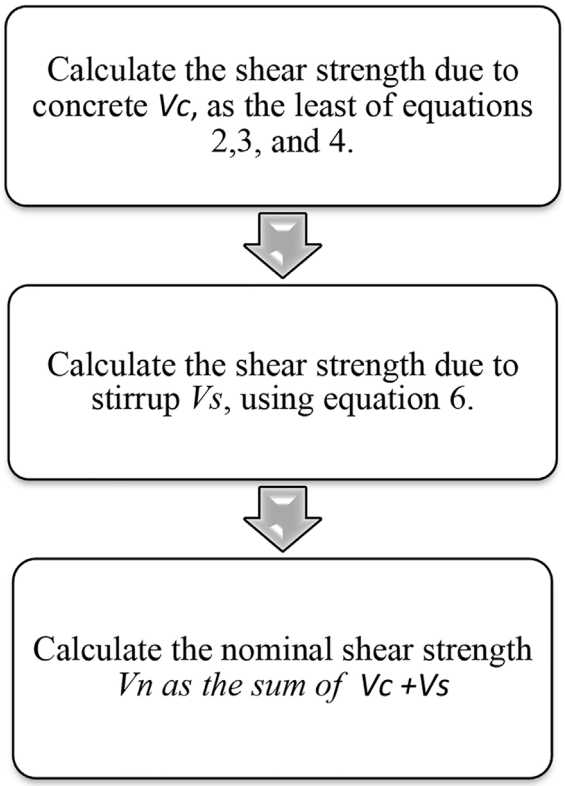

FIGURE 17
Flow chart for shear strength calculation using ACI.

.0 denoting a smooth crack (total loss of shear transfer) and 1.0 denoting a rough crack (no loss of shear transfer). According to (Tahenni et al., 2021), the shear transfer coefficient for open and closed fractures was estimated, and the results were reasonably close to the experimental results. The longitudinal and transverse reinforcements were modeled using the Link 180 element. Table 8 represents the inserted properties of the transverse and longitudinal reinforcements including modulus of elasticity, Poisson's ratio, and yield stress. The non-linear behaviors of transverse and longitudinal reinforcements were modeled based on the tensile test results. At a distance of 700 mm from the support on either side, double lines of nodes on the upper steel plates are where the force is acting. Two lines of nodes on the bottom end of the beam represent the hinged and roller supports. The roller support was restricted from moving in Y-direction, while the hinged support was restricted from moving in both X, Y, and Z-directions. The steel plates were represented by Link185 element.

5.2 Numerical analysis procedure

The software performs a linear solution for the numerical simulations, gradually increasing the load value, and analyzing convergence. When the requirements are not met, various solution is developed by modifying the stiffness matrix. Collapse can be recognized by cracking patterns, concrete compressive strain approaching maximum, steel reinforcing strain reaching yield, or non-convergence resulting from a total loss of load-bearing capacity. The convergence criteria throughout the current investigation were dependent on force and displacement.

5.3 Validation of the numerical models

The finite element and experimental outputs were compared to validate the experimental findings. This was accomplished to guarantee that the concrete beam's convergence conditions are suitable. Figure 14 illustrates the crack patterns and failure modes of hybrid FRC beams based on finite element models. All finite element models cracked similarly to all concrete beams in the experimental program. Where flexural cracks first appeared at the flexure region, followed by shear-flexure cracks, and finally diagonal shear cracks initiated and propagated upward at a 45-degree angle towards the applied load until the beams failed. The failure mode of the finite element model HFCB0-2.8 was similar to that of its experimental equivalent, where diagonal shear cracks occurred, followed by stirrup yielding, which caused the collapse. The finite element model differs in that the diagonal shear crack did not extend to the point where the load was impacting. This is likely because the stirrup reached yield stress before the diagonal shear crack was fully completed. This shows that the finite element model did not exhibit the same level of ductility as in the experimental beam sample to allow for the formation of a full diagonal crack before the collapse, but the failure mode is still the same for both as a diagonal shear crack followed by stirrup yielding. Regarding the finite element model HFCB0.24-2.8, the shown failure mode demonstrated that the addition of stirrups improved its ductility in such a way that it resulted in the formation

TABLE 9 Experimental, numerical, and ACI, results of shear failure load for all beams.

Mix ID	Shear failure load V(kN)			$\frac{V_{Exp}}{V_{Num}}$	$\frac{V_{Exp}}{V_{ACI}}$	$\frac{V_{Num}}{V_{ACI}}$
	V_{Exp}	V_{Num}	V_{ACI}			
HFCB0-2.8	53	68.5	40.6	.77	1.30	1.69
HFCB0.24-2.8	71	84.5	56.2	.84	1.27	1.50
HFCB0.42-2.8	80	94	68.3	.85	1.17	1.38
HFCB0.42-2.3	111	125.5	83.2	.89	1.34	1.51
HFCB0.42-1.75	137	145	112.9	.94	1.21	1.28
Average				.86	1.26	1.47
Standard deviation				.056	.061	.136
Coefficient of variance %				6.5	4.8	9.2

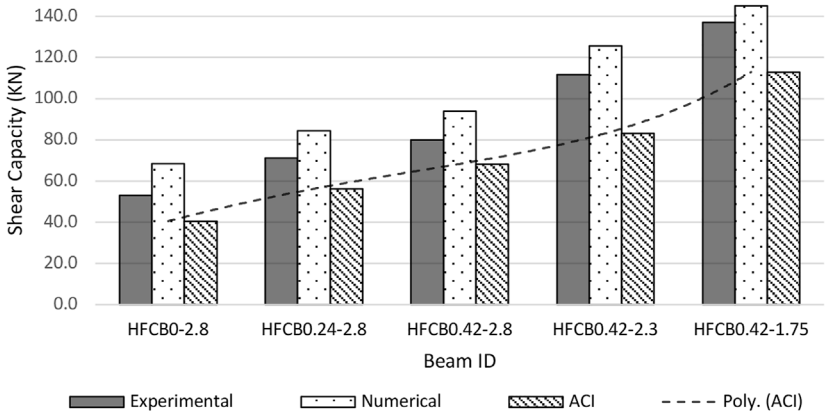

FIGURE 18
Comparison between the experimental, numerical, and ACI results of shear failure load for all concrete beams.

of a full diagonal shear crack from the support up to the upper edge, followed by the stirrup yielding, which was very similar failure behavior to that experimental equivalent. The failure mode for finite element model HFCB0.42-2.8 did not differ significantly from finite element model HFCB0.24-2.8, as the collapse occurred as a result of a full diagonal shear crack occurring and the stirrups reached yield except with clearer shear-flexure cracks, because the beam could bear higher loads and thus the flexure stresses increased, and consequently, the flexure cracks increased, however, this was ineffective in changing the failure mode. The failure mode and crack pattern for finite element model HFCB0.42-2.8 were very similar to the corresponding experimental sample. The failure mode of finite element model HFCB0.24-2.3 was very similar to that of finite element model HFCB0.24-2.8, but with more and clearer flexural cracks since the strength of the beam increased as the span to depth ratio decreased, and thus the flexure stresses and flexure cracks increased. This failure and crack pattern were quite similar to the equivalent experimental beam. The failure mode of finite element model HFCB0.42-1.75 was comparable to that of the corresponding experimental beam model, except that the diagonal shear crack did not reach the top edge. This confirms that decreasing the span to depth ratio reduced the ductility of the beam, and thus the stirrup reached yield before a complete diagonal shear crack occurred. Additionally, the experimental one had more concrete crushing at the compression zone although this had no effect on the collapse because it was governed by the diagonal shear crack followed by stirrup yielding. Figure 15 shows a comparison between the finite element and experimental load versus deflection curves for all concrete beams. The finite element failure load was higher than the experimental failure load by 29%, 19%, 18%, 13%, and 6% for hybrid reinforced concrete beams HFCB0-2.8, HFCB0.24-2.8, HFCB0.42-2.8, HFCB0.42-2.3, and HFCB0.42-1.75, respectively. The coefficient of variance between the finite element and the experimental results of failure load was 6.5%. The deflection values of all finite element and experimental samples appeared to be nearly equal as shown in the figure, and the relationship between load and deflection seemed to be linear until the crack occurs. Following the occurrence of the crack, the relationship became non-linear with an increase in the experimental sample's deflection values compared to the finite element model at the same load. The finite element maximum deflection was 2%, 10%, 16%, 22%, and 23% less than the experimental maximum deflection for hybrid reinforced concrete beams HFCB0-2.8, HFCB0.24-2.8, HFCB0.42-2.8, HFCB0.42-2.3, and HFCB0.42-1.75, respectively. The maximum deflection experimental results and the finite element results have a 9% coefficient of variation. Figure 16 compares the finite element

and experimental load-transverse strain curves for all concrete beams. The strain values in stirrups for all finite element and experimental samples were insignificant until the cracking load. Following that, the strain in the stirrups increased dramatically until it reached yield stress. The figure shows that the strain values for the experimental samples after the cracking load were greater than the strain values for the finite element models under the same load. For all experimental and finite element models, the strain in the stirrups reached yield. The finite element transverse reinforcement strain values at failure were 15%, 6%, 12%, 1%, and 2% lower for the hybrid reinforced concrete beams HFCB0-2.8, HFCB0.24-2.8, HFCB0.42-2.8, HFCB0.42-2.3, and HFCB0.42-1.75, respectively compared to the experimental transverse reinforcement strain values at failure. Transverse reinforcement strain experimental results and the results from the finite element had a 7.3% coefficient of variation. The comparison revealed that the experimental and finite element results were perfectly correlated.

6 Comparison with ACI

The shear strength for hybrid polypropylene-steel fibers reinforced concrete beams was calculated in this section using ACI provisions. The validation of the finite element and experimental results are demonstrated by comparing them to the ACI equations. As illustrated in Figure 17, the nominal shear strength *Vn* can be calculated as the summation of the nominal shear strength due to concrete *Vc*, and the nominal shear strength due to transverse reinforcement Vs. According to ACI318 (ACI 318-19, 2019), the nominal shear strength due to concrete can be calculated as the least of the followings:

$$V_c = 0.17\lambda \sqrt{f_c'}\, b_w d \tag{2}$$

$$V_c = 0.66\lambda\, \rho^{1/3} \sqrt{f_c'}\, b_w d \tag{3}$$

$$V_c = 0.42\lambda \sqrt{f_c'}\, b_w d \tag{4}$$

λ is the reduction factor equal to one for normal weight concrete as well as high strength concrete. f_c' is the cylindrical compressive strength of concrete.ρ is the ratio of the area of longitudinal reinforcement to the cross-section of the concrete area $b_w d$.

The correction factor for obtaining the equivalent compressive strength of the standard cube is given by ECP203 (ECP 203-18, 2018) as follows:

$$f_{cu} = 1.25\, f_c' \tag{5}$$

Where f_{cu} is the cubic ultimate compressive strength of concrete.

The nominal shear strength due to transverse reinforcement is calculated as the following:

$$V_s = \frac{A_v f_y}{s} d \tag{6}$$

A_v is the area of transverse reinforcement. f_y is the yield strength of transverse reinforcement.ρ is the spacing between the transverse reinforcement.

Table 9 shows a comparison between the numerical, experimental, and ACI predicted values of shear strength for hybrid polypropylene-steel fibers reinforced concrete beams. ACI results exhibited the lowest values of shear capacity for all hybrid FRC beams while the numerical exhibited the largest values. As shown in Figure 18, the ACI results for shear capacity were less than the experimental results by 23%, 21%, 15%, 25%, and 18% for concrete beams HFCB0-2.8, HFCB0.24-2.8, HFCB0.42-2.8, HFCB0.42-2.3, and HFCB0.42-1.75, respectively. On the other hand, the ACI results for shear capacity were less than the numerical results by 41%, 33%, 27%, 34%, and 22% for concrete beams HFCB0-2.8, HFCB0.24-2.8, HFCB0.42-2.8, HFCB0.42-2.3, and HFCB0.42-1.75, respectively. The coefficient of variance between the ACI and experimental shear capacity results was 4.8%, while it was 9.2% between the ACI and numerical shear capacity results. This indicates that the shear capacity of hybrid polypropylene-steel fibers reinforced concrete beams predicted by ACI is appropriate, However, the ACI underestimated shear strength. The ACI's calculations were conservative when compared with the experimental or numerical results, particularly for hybrid FRC beams with a lower transverse reinforcement ratio or a lower span-to-depth ratio (equal or less than 2.3).

7 Conclusion

The shear behavior of concrete elements is a dilemma. This study examined the shear behavior of high-strength concrete beams reinforced with hybrid polypropylene-steel fibers. Concrete type, transverse reinforcement ratio, and span to depth ratio were the investigated parameters that influenced the shear behavior. The following crucial findings were condensed from the theoretical and practical study:

1. Experimental HFRHSC beams with a span-to-depth ratio larger than 2.3 failed due to a significant diagonal shear crack, whereas concrete beams with a span-to-depth ratio equal to or less than 2.3 failed due to a diagonal shear crack followed by crushing of concrete. This is because decreasing the span-to-depth ratio changed the shear resistance behavior from truss to arch action, and thus the failure was controlled more by the compressive strength of inclined struts.
2. Adding hybrid polypropylene-steel fibers to high-strength concrete beams improved shear capacity, maximum deformation, and ductility, as well as delayed crack initiation by approximately 18%, 66%, 60%, and 13%, respectively. This is due to the capability of hybrid polypropylene-steel fibers to withstand macro and micro cracks at different stress levels, thus delaying the cracking process, improving stiffness and strength, reducing brittleness, and increasing plastic deformation without fracture.
3. Adding transverse reinforcement to high-strength concrete beams alongside hybrid polypropylene-steel fibers and longitudinal reinforcement at the compression zone improved the ability to prevent crack initiation and propagation, as well as increased the shear strength and ductility more than adding hybrid fibers alone, where the shear capacity, the cracking load, maximum deformation, and ductility for hybrid fiber reinforced high-strength concrete beams that had transverse reinforcement, were 35%, 55%, 22%, and 11% higher, respectively than those for hybrid fiber reinforced high-strength concrete beam without transverse reinforcement.
4. Reducing the span-to-depth ratio for HFRHSC beams from 2.8 to 1.75 increased shear capacity and cracking load by about 22% and 11%, respectively, however, decreased maximum deformation and ductility by about 2% and 38%, respectively. This is because the load was transmitted directly to the support with a decrease in the span-to-depth ratio, which delayed the occurrence of cracking and improved

shear strength while negatively affecting the ability to plastically deform and ductility, making concrete behave more brittle.
5. The numerical results for HFRHSC beams modeled with ANSYS 15 software showed a good correlation with the experimental results; however, the numerical solution overestimated the shear capacity. The average and coefficient of variance between the experimental and numerical results for shear capacity were .86% and 6.5%, respectively.
6. The ACI's calculations were conservative when compared with the experimental or numerical results, particularly for hybrid fiber-reinforced high-strength concrete beams with a lower transverse reinforcement ratio or a lower span-to-depth ratio. The coefficient of variance between the ACI and experimental shear capacity results was 4.8%, while it was 9.2% between the ACI and numerical shear capacity results.

8 Future studies

1. Studying the effect of different span-to-depth ratios (1, 1.5, 3, 4) on the shear behavior of HFRHSC beams.
2. Studying the effect of different proportions of hybrid polypropylene-steel fibers (10%, 15%, 20%, 25%) on the shear behavior of high-strength concrete beams.
3. Studying the effect of flange width for L-section and T-section on the shear behavior of HFRHSC beams.
4. Studying the flexural behavior of HFRHSC beams.
5. Studying the torsional behavior of HFRHSC beams.

Data availability statement

The original contributions presented in the study are included in the article/supplementary material, further inquiries can be directed to the corresponding authors.

Author contributions

Conceptualization, MS and AA; methodology, MT, MA, and MS; software and investigation, MT; validation, AD; formal analysis, AA and MA; resources and data curation, AE-s; writing—original draft preparation, AA and AD; writing—review and editing, MA and MS; visualization, AD; supervision, MS and AD; funding acquisition, MS. All authors have read and agreed to the published version of the manuscript.

Funding

The research is partially funded by the Ministry of Science and Higher Education of the Russian Federation under the strategic academic leadership program "Priority 2030" (Agreement 075-15-2021-1333, dated 30 September 2021).

Conflict of interest

The authors declare that the research was conducted in the absence of any commercial or financial relationships that could be construed as a potential conflict of interest.

Publisher's note

References

Abbas, W., and Khan, M. I. (2022). Experimental and numerical investigation of flexural behavior of hybrid fiber reinforced high strength incorporating binary and ternary blend of ultra fines. *Structures* 42, 53–64. doi:10.1016/j.istruc.2022.05.116

Abbas, Y. M., Hussain, L. A., and Khan, M. I. (2022). Constitutive compressive stress–strain behavior of hybrid steel-PVA high-performance fiber-reinforced concrete. *J. Mater. Civ. Eng.* 34. doi:10.1061/(ASCE)MT.1943-5533.0004041

ACI 318-19 (2019). *Building code requirements for structural concrete and commentary*. Farmington Hills, MI 48331, U.S.A.: American Concrete Institute. 2014.

Ahmad, J., Majdi, A., Al-Fakih, A., Deifalla, A. F., Althoey, F., El Ouni, M. H., et al. (2022). Mechanical and durability performance of coconut fiber reinforced concrete: A state-of-the-art review. *Materials* 15, 3601. doi:10.3390/ma15103601

Ahmed, A., Abbas, S., Abbass, W., Waheed, A., Razzaq, A., Ali, E., et al. (2022). Potential of waste marble sludge for repressing alkali-silica reaction in concrete with reactive aggregates. *Materials* 15, 3962. doi:10.3390/ma15113962

Ali, B., Kurda, R., Herki, B., Alyousef, R., Mustafa, R., Mohammed, A., et al. (2020). Effect of varying steel fiber content on strength and permeability characteristics of high strength concrete with micro silica. *Materials* 13, 5739. doi:10.3390/ma13245739

Ali, A., Hamady, M., Chalioris, C. E., and Deifalla, A. (2021). Evaluation of the shear design equations of FRP-reinforced concrete beams without shear reinforcement. *Eng. Struct.* 235, 112017. doi:10.1016/j.engstruct.2021.112017

Ali, B., Fahad, M., Ullah, S., Ahmed, H., Alyousef, R., and Deifalla, A. (2022). Development of ductile and durable high strength concrete (HSC) through interactive incorporation of coir waste and silica fume. *Materials* 15, 2616. doi:10.3390/ma15072616

Alrefaei, Y., Rahal, K., and Maalej, M. (2018). Shear strength of beams made using hybrid fiber-engineered cementitious composites. *J. Struct. Eng.* 144. doi:10.1061/(ASCE)ST.1943-541X.0001924

Ashraf, M. R., Akmal, U., Khurram, N., Aslam, F., and Deifalla, A. F. (2022). Impact resistance of styrene–butadiene rubber (SBR) latex-modified fiber-reinforced concrete: The role of aggregate size. *Materials* 15, 1283. doi:10.3390/ma15041283

Ayub, T., Khan, S. U., and Ayub, A. (2019). Analytical model for the compressive stress–strain behavior of PVA-FRC. *Constr. Build. Mater* 214, 581–593. doi:10.1016/j.conbuildmat.2019.04.126

Deifalla, A. F., Zapris, A. G., and Chalioris, C. E. (2021). Multivariable regression strength model for steel fiber-reinforced concrete beams under torsion. *Materials* 14, 3889. doi:10.3390/ma14143889

Deifalla, A. (2021a). Refining the torsion design of fibered concrete beams reinforced with FRP using multi-variable non-linear regression analysis for experimental results. *Eng. Struct.* 224, 111394. doi:10.1016/j.engstruct.2020.111394

Deifalla, A. (2021b). Assessment of one-way shear design of RC elements subjected to axial tension. *Case Stud. Constr. Mater.* 15, e00620. doi:10.1016/j.cscm.2021.e00620

Deifalla, A. F., and Mukhtar, F. M. (2022). Shear strength of lightweight and normal-weight concrete slender beams and slabs: An appraisal of design codes. *Adv. Struct. Eng.* 25, 2444–2466. doi:10.1177/13694332221098869

Deifalla, A., and Mukhtar, F. M. (2022). A mechanical and simplified model for RC elements subjected to combined shear and axial tension. *Sci. Rep.* 12, 7863. doi:10.1038/s41598-022-11577-y

Ebid, A., and Deifalla, A. (2021). Prediction of shear strength of FRP reinforced beams with and without stirrups using (GP) technique. *Ain Shams Eng. J.* 12 (3), 2493–2510. doi:10.1016/j.asej.2021.02.006

ECP 203-18 (2018). *Egyptian code for design and construction of concrete buildings"*. Cairo, Egypt: National Center for Research.

Fadil, D., Taysi, N., and Ahmed, A. (2018). *The investigation of basalt and glass Fibers on the behavior of reinforced concrete beams*. Available at: http://iraj.in (Accessed July 31, 2019).

Ghareeb, K. S., Ahmed, H. E., El-Affandy, T. H., Deifalla, A. F., and El-Sayed, T. A. (2022). The novelty of using glass powder and lime powder for producing UHPSCC. *Buildings* 12, 684. doi:10.3390/buildings12050684

Hoang, A. L., and Fehling, E. (2017). Influence of steel fiber content and aspect ratio on the uniaxial tensile and compressive behavior of ultra-high-performance concrete. *Constr. Build. Mat.* 153, 790–806. doi:10.1016/j.conbuildmat.2017.07.130

Huang, S., Wang, H., Ahmad, W., Ahmad, A., Ivanovich Vatin, N., Mohamed, A. M., et al. (2022). Plastic waste management strategies and their environmental aspects: A scientometric analysis and comprehensive review. *Int. J. Environ. Res. Public Health* 19, 4556. doi:10.3390/ijerph19084556

Ismail, M. K., and Hassan, A. A. (2021). Influence of fibre type on the shear behaviour of engineered cementitious composite beams. *Mag. Concr. Res.* 73 (9), 464–475. doi:10.1680/jmacr.19.00172

Juenger, M. C. G., Snellings, R., and Bernal, S. A. (2019). Supplementary cementitious materials: New sources, characterization, and performance insights. *Cem. Concr. Res.* 122, 257–273. doi:10.1016/j.cemconres.2019.05.008

Khan, M., Cao, M., and Ali, M. (2020). Cracking behaviour and constitutive modelling of hybrid fibre reinforced concrete. *J. Build. Eng.* 30, 101272. doi:10.1016/j.jobe.2020.101272

Khan, M. I., Fares, G., Abbas, Y. M., and Alqahtani, F. K. (2021). Behavior of non-shear-strengthened UHPC beams under flexural loading: Influence of reinforcement percentage. *Appl. Sci.* 11, 11346. doi:10.3390/app112311346

Khan, M. I., Fares, G., and Abbas, Y. M. (2021). Behavior of non-shear-strengthened UHPC beams under flexural loading: Influence of reinforcement depth. *Appl. Sci.* 11, 11168. doi:10.3390/app112311168

Khan, M. A., Aslam, F., Faisal Javed, M., Alabduljabbar, H., and Deifalla, A. F. (2022). New prediction models for the compressive strength and dry-thermal conductivity of bio-composites using novel machine learning algorithms. *J. Clean. Prod.* 350, 131364. ISSN 0959-6526. doi:10.1016/j.jclepro.2022.131364

Koniki, S., and Prasad, D. R. (2019). Influence of hybrid fibres on strength and stress-strain behaviour of concrete under uni-axial stresses. *Constr. Build. Mat.* 207, 238–248. doi:10.1016/j.conbuildmat.2019.02.113

Kumar, M. V., Niveditha, K., Anusha, B., and Sudhakar, B. (2017). Comparison study of basalt fiber and steel fiber as additives to concrete. *Int. J. Res. Appl. Sci. Eng. Technol.* 5, 2321–9653. www.ijraset.com6 (Accessed November 8, 2019).

Li, B., Chi, Y., Xu, L., Shi, Y., and Li, C. (2018). Experimental investigation on the flexural behavior of steel-polypropylene hybrid fiber reinforced concrete. *Constr. Build. Mat.* 191, 80–94. doi:10.1016/j.conbuildmat.2018.09.202

Li, C., Zhao, M., Geng, H., Fu, H., Zhang, X., and Li, X. (2021). Shear testing of steel fiber reinforced expanded-shale lightweight concrete beams with varying of shear-span to depth ratio and stirrups. *Case Stud. Constr. Mater.* 14, e00550. ISSN 2214 -5095. doi:10.1016/j.cscm.2021.e00550

Li, Y., Zhang, Q., KamiÑski, P., Deifalla, A., Sufian, M., Dyczko, A., et al. (2022). Compressive strength of steel fiber-reinforced concrete employing supervised machine learning techniques. *Materials* 15 (12), 4209. doi:10.3390/ma15124209

Lim, W. Y., and Hong, S. G. (2017). Shear tests for ultra-high performance fiber reinforced concrete (UHPFRC) beams with shear reinforcement. *Int. J. Concr. Struct. Material* 10 (2), 177–188. doi:10.1007/s40069-016-0145-8

Mohammed, H., Ahmed, H., Kurda, R., Alyousef, R., and Deifalla, A. F. (2022). Heat-induced spalling of concrete: A review of the influencing factors and their importance to the phenomenon. *Materials* 15, 1693. doi:10.3390/ma15051693

Naqi, A., and Jang, J. G. (2019). Recent progress in green cement technology utilizing low carbon emission fuels and raw materials: Review. *Sustainability* 11 (537), 1–18.

Navas, F. O., Navarro-Gregori, J., Herdocia, G. L., Serna, P., and Cuenca, E. (2018). An experimental study on the shear behaviour of reinforced concrete beams with macro-synthetic fibres. *Constr. Build. Mater* 169, 888–899. doi:10.1016/j.conbuildmat.2018.02.023

Ortiz Navas, F., Navarro-Gregori, J., Leiva Herdocia, G., Serna, P., and Cuenca, E. (2018). An experimental study on the shear behaviour of reinforced concrete beams with macro-synthetic fibres. *Constr. Build. Mater.* 169, 888–899. ISSN 0950-0618. doi:10.1016/j.conbuildmat.2018.02.023

Pakravan, H. R., Latifi, M., and Jamshidi, M. (2016). Ductility improvement of cementitious composites reinforced with polyvinyl alcohol-polypropylene hybrid fibers. *J. Ind. Text.* 45 (5), 637–651. doi:10.1177/1528083714534712

Shaaban, I., Said, M., Khan, S., Eissa, M., and Elrashidy, Kh. (2021). Experimental and theoretical behaviour of reinforced concrete beams containing hybrid fibres. *Structures* 32, 2143–2160. ISSN 2352-0124. doi:10.1016/j.istruc.2021.04.021

Shen, Z., Deifalla, A. F., Kamiński, P., and Dyczko, A. (2022). Compressive strength evaluation of ultra-high-strength concrete by machine learning. *Materials* 15, 3523. doi:10.3390/ma15103523

Shi, F., Pham, T. M., Hao, H., and Hao, Y. (2020). Post-cracking behaviour of basalt and macro polypropylene hybrid fibre reinforced concrete with different compressive strengths. *Constr. Build. Mater* 262, 120108. doi:10.1016/j.conbuildmat.2020.120108

Sivakumar, V., Karthik, K., Jachin, S. B., and Xavier, C. A. (2020). Experimental investigation on strength properties of hybrid fibre reinforced high strength concrete. *Mat. Today Proc.* doi:10.1016/j.matpr.2020.12.897

Smarzewski, P. (2018). Flexural toughness of high-performance concrete with basalt and polypropylene short fibres. *Adv. Civ. Eng.* 2018, 1–8. doi:10.1155/2018/5024353

Tahenni, T., Bouziadi, F., Boulekbache, B., and Amziane, S. (2021). Experimental and nonlinear finite element analysis of shear behaviour of reinforced concrete beams. *Structures* 29, 1582–1596. ISSN 2352-0124. doi:10.1016/j.istruc.2020.12.043

Tahenni, T., Chemrouk, M., and Lecompte, T. (2016). Effect of steel fibers on the shear behavior of high strength concrete beams. *Constr. Build. Mater.* 105, 14–28. ISSN 0950-0618. doi:10.1016/j.conbuildmat.2015.12.010

Tawfik, M., El-said, A., Deifalla, A., and Awad, A. (2022). Mechanical properties of hybrid steel-polypropylene fiber reinforced high strength concrete exposed to various temperatures. *Fibers* 10, 53. doi:10.3390/fib10060053

Torres, J. A., and Lantsoght, E. O. L. (2019). Influence of fiber content on shear capacity of steel fiber-reinforced concrete beams. *Fibers* 7, 102. doi:10.3390/fib7120102

Tran, T. T., Pham, T. M., and Hao, H. (2020). Effect of hybrid fibers on shear behaviour of geopolymer concrete beams reinforced by basalt fiber reinforced polymer (BFRP) bars without stirrups. *Compos Struct.* 243, 112236. doi:10.1016/j.compstruct.2020.112236

Wang, D., Ju, Y., Shen, H., and Xu, L. (2019). Mechanical properties of high performance concrete reinforced with basalt fiber and polypropylene fiber. *Constr. Build. Mater* 197, 464–473. doi:10.1016/j.conbuildmat.2018.11.181

Xu, L. H., Wu, F. H., Chi, Y., Cheng, P., Zeng, Y. Q., and Chen, Q. (2019). Effects of coarse aggregate and steel fibre contents on mechanical properties of high-performance concrete. *Constr. Build. Mat.* 206, 97–110. doi:10.1016/j.conbuildmat.2019.01.190

Yan, P., Chen, B., Afgan, S., Haque, M. A., Wu, M., and Han, J. (2021). Experimental research on ductility enhancement of ultra-high performance concrete incorporation with basalt fibre, polypropylene fibre and glass fibre. *Constr. Build. Mater* 279, 122489. doi:10.1016/j.conbuildmat.2021.122489

Yang, X., Liang, N., Hu, Y., and Feng, R. (2021). An experimental study of shear resistance for multisize polypropylene fiber concrete beams. *Int. J. Concr. Struct. Mater.* 15, 52–11. doi:10.1186/s40069-021-00492-7

Yavaş, A., Hasgul, U., Turker, K., and Birol, T. (2019). Effective fiber type investigation on the shear behavior of ultrahigh-performance fiber-reinforced concrete beams. *Adv. Struct. Eng.* 22 (7), 1591–1605. doi:10.1177/1369433218820788

Zhang, L. H., Liu, J. Z., Liu, J. P., Zhang, Q. Q., and Han, F. Y. (2018). Effect of steel fiber on flexural toughness and fracture mechanics behavior of ultra-high-performance concrete with coarse aggregate. *J. Mat. Civ. Eng.* 30, 4018323. doi:10.1061/(asce)mt.1943-5533.0002519

Zhang, Y., Wu, B., Wang, J., Liu, M., and Zhang, X. (2019). Reactive powder concrete mix ratio and steel fiber content optimization under different curing conditions. *Materials* 12, 3615. doi:10.3390/ma12213615

Zhong, C., Liu, M., Zhang, Y., Wang, J., Liang, D., and Chang, L. (2020). Study on mechanical properties of hybrid polypropylene-steel fiber RPC and computational method of fiber content. *Materials* 13, 2243. doi:10.3390/ma13102243

Zhou, L., and Wan, S. (2022). Shear behavior of UHPC beams with small shear span to depth ratios based on MSTM. *Case Stud. Constr. Mater.* 16 (2022), e01134. ISSN 2214-5095. doi:10.1016/j.cscm.2022.e01134

Zou, Y., Yu, K., Heng, J. L., Zhang, Z. Y., Peng, H. B., Wu, C. L., et al. (2023a). Feasibility study of new GFRP grid web - concrete composite beam. *Compos. Struct.* 305, 116527. doi:10.1016/j.compstruct.2022.116527

Zou, Y., Zheng, K., Zhou, Z., Zhang, Z., Guo, J., and Jiang, J. (2023b). Experimental study on flexural behavior of hollow steel-UHPC composite bridge deck. *Eng. Struct.* 274, 115087. doi:10.1016/j.engstruct.2022.115087

frontiers | Frontiers in Materials

TYPE Original Research
PUBLISHED 08 February 2023
DOI 10.3389/fmats.2023.1057637

OPEN ACCESS

EDITED BY
Dong Zhang,
Fuzhou University, China

REVIEWED BY
Mehmet Serkan KIRGIZ,
Istanbul Sabahattin Zaim University, Türkiye
Ali Shokrgozar,
Idaho State University, United States

*CORRESPONDENCE
Muhammad Abid,
abidkhg@gmail.com

SPECIALTY SECTION
This article was submitted to Structural Materials, a section of the journal Frontiers in Materials

RECEIVED 29 September 2022
ACCEPTED 19 January 2023
PUBLISHED 08 February 2023

CITATION
Khan MNA, Malik AH, Yaqub M, Umar M, Noman M, Abid M, Alabduljabbar H, Mohamed A and Zaidi SSA (2023), Development of high-temperature heavy density dolerite concrete for 4th generation nuclear power plants. *Front. Mater.* 10:1057637. doi: 10.3389/fmats.2023.1057637

Development of high-temperature heavy density dolerite concrete for 4th generation nuclear power plants

Muhammad Nasir Ayaz Khan[1], Azhar Hussain Malik[2], Muhammad Yaqub[1], Muhammad Umar[4], Muhammad Noman[3], Muhammad Abid[5]*, Hisham Alabduljabbar[6], Abdullah Mohamed[7] and Syed Salman Ahmad Zaidi[8]

[1]Civil Engineering Department, University of Engineering and Technology, Rawalpindi, Pakistan, [2]Department of Nuclear Engineering, Pakistan Institute of Engineering and Applied Sciences, Islamabad, Nilore, Pakistan, [3]Department of Civil Engineering, Faculty of Engineering and Technology, International Islamic University Islamabad, Islamabad, Pakistan, [4]Civil Engineering Department, Zhengzhou University in Zhengzhou, Harbin, China, [5]College of Aerospace and Civil Engineering, Harbin Engineering University, Harbin, China, [6]Department of Civil Engineering, College of Engineering in Al-Kharj, Prince Sattam bin Abdulaziz University, Al-Kharj, Saudi Arabia, [7]Research Centre, Future University in Egypt, New Cairo, Egypt, [8]Civil Engineering Department, Wah Engineering College, University of Wah, Wah Cantonment, Pakistan

This study examines the physical, mechanical, microstructural, and attenuation properties of high-density concrete exposed to temperatures ranging from 200°C to 1200°C. For this purpose, heavy-density concrete containing 25%, 50%, 75%, and 100% dolerite aggregates was developed and compared with three ordinary concrete mixes. Pre- and post-heated concrete specimens were evaluated for mass and density loss, compressive strength, rebound hammer, X-ray and gamma-ray attenuation, Half Value Layer (HVL), and Ten Value Layer (TVL) along with microstructural properties determined by scanning electron microscopy and Energy Dispersive X-ray. The results showed that the incorporation of 75% dolerite aggregate during pre- and post-heating yielded high compressive strength whereas low mass and density loss. The same mixture showed significant improvement in gamma ray shielding at all temperatures. The Half Value Layer and Ten Value Layer values showed a reduction in the thickness of concrete as a shield. It is recommended that dolerite heavy-density concrete is a potential radiation shield at high temperatures ranging from 200°C–1200°C in fourth-generation nuclear power plants.

KEYWORDS

compressive strength, heavy-density concrete, x-ray, gamma ray, nuclear power plants, half value layer (HVL), temperature, attenuation

1 Introduction

Due to the increasing application of gamma rays in studying the biologically harmful effects, several studies have already been performed on the shielding properties of various materials (Mollah et al., 1992; Gökçe et al., 2018; Moharram et al., 2020). Among all materials, concrete is widely accepted as a shield against gamma radiation due to its high strength, acceptable density, and inexpensive design flexibility (Tekin et al., 2018). However, the properties of concrete as a radiation shield, for instance, density, depend upon the composition of materials in concrete. Therefore, in the recent past, many studies have been devoted to developing concrete shields by

TABLE 1 Physical and chemical properties of cement.

Chemical composition	Values (%)	Physical properties	Value
CaO	57.35	Specific gravity (g Cm−3)	3.12
SiO2	20.30	Average particle size (μm)	18
Al2O3	9.24	Blaine fineness (Cm2 g-1)	3152
MgO	3.02	Initial setting time	1 h and 25 min
Fe2O3	3.61	Final setting time	3 h and 48 min
SO3	2.98	Consistency (%)	31
Na2O	0.25		

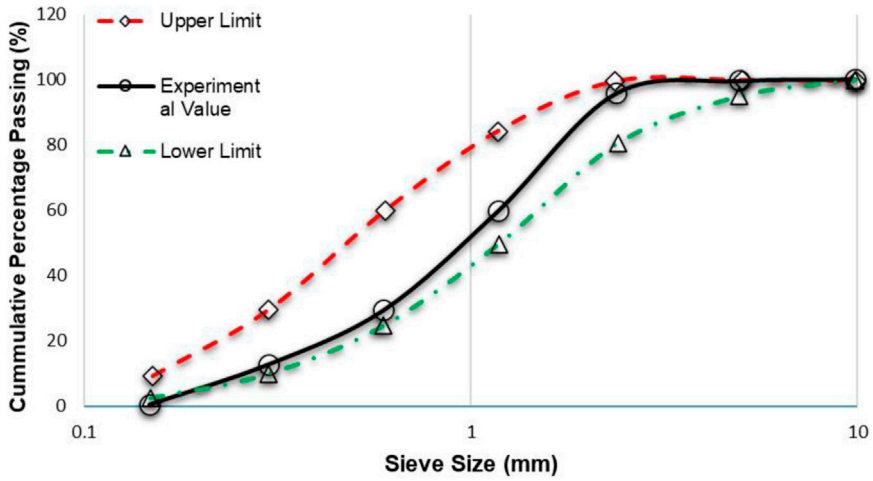

FIGURE 1
Gradation curves of fine aggregate.

introducing various types of special aggregates i e., natural such as magnetite (Thomas et al., 2019), barite (Almeida et al., 2017), serpentine (Kansouh 2012) as well synthetic aggregate like steel shots (Maslehuddin et al., 2013), steel furnace slag (Khalaf et al., 2019) Heavyweight concrete has a density greater than 2600 kg/m^3 (Lotfi-omran et al., 2019). The recent developments in heavyweight concrete have been explained in detail by (Malik et al., 2022).

Heavyweight aggregates are used to fabricate heavy-density concrete for the construction of radiation shielding (Horszczaruk, 2019). developed magnetite concrete as a radiation shield showed 11.7% higher attenuation of gamma rays than barite concrete and 44.8% than ordinary concrete (El-Samrah et al., 2018). fabricated barite-limonite concrete and concluded that the linear attenuation coefficient rises with increasing temperature up to 450°C. A prior study on barite concrete suggested that approximately 40% of wall thickness could be decreased compared to walls fabricated with ordinary concrete (Akkurt and El-Khayatt 2013). However, iron ores are expensive and difficult to work with (Gencel et al., 2012). Before utilization, these ores pass through many complex processes compared to traditional aggregates, such as mining, transportation from mines, screening, and cleaning. The other main problem is the diversity of aggregates in properties due to excavation location. Barite, for instance, may contain 90% $BaSO_4$ as well as 65% $BaSO_4$. Thus, concretes fabricated due to different properties in aggregates behave differently (Sikora et al., 2019). For these reasons, there is a clear need to develop heavy-density concrete utilizing other materials, preferably waste materials that are less expensive and serve as decent radiation shields with good mechanical properties (Gencel et al., 2012).

On the one hand, careful selection should be made while fabricating heavyweight concrete, as fabrication is a more critical process than conventional concrete. Each constituent, such as water, cement, and coarse aggregate, must be evaluated, whereas type and amount are the key consideration in the mixes (Khalaf et al., 2021). Water cement ratio is an important parameter in high-strength and high-density concrete preparation. However, the literature on improving concrete density by decreasing the water-cement ratio is scarce. Nevertheless, the water-cement ratios in heavyweight concrete range between 35% and 50% (Facure and Silva, 2007). A study concluded that the optimum water-cement ratio for barite concrete is 0.40 (Topçu, 2003). At the same time, the quality and type of cement also matter in the fabrication of heavyweight concrete because the cement content in heavyweight concrete is that it must be high enough to prevent any radiation seepage while low enough to affect shrinkage. For such reasons, 350 kg/m^3 is the recommended cement content for heavyweight concrete (Celik et al., 2015). However, barite and magnetite

TABLE 2 Physical and chemical properties of DHA.

Chemical analysis	Values (%)	Physical properties	Value
SiO2	46.12	Specific gravity (g Cm−3)	3.05
Al2O3	16.21	Bulk density (g Cm−3)	3.96
Fe2O3	16.45	Hardness (Moh's Scale)	9
CaO	7.8	Melting point °C	1430
MgO	5.3	Color	Grey
Na2O	3.4	Shape	Angular
Others	3.70	Water absorption (smooth)	0.9%
Total	98.98	Water absorption (porous)	2.3%

concrete required high cement content between 400 and 490 kg/m^3 to reach the desired strength (Ouda 2015; Yao et al., 2016). Moreover, heavyweight concrete can be developed using any Portland cement; however, cement produced from coarsely ground clinker should be avoided (Horszczaruk, 2019). Concretes fabricated with a cement content of 350–400 kg/m^3, the typical values of densities for some concretes are.

- steel scrap - 6–6.500 g/cm^3 (fc = 75 MPa, w/c = 0.29) (González-Ortega et al., 2014)
- barite + steel scrap—4.50–5.0 g/cm^3 (fc = 35–50 MPa, w/c = 0.3–0.4) (Kilincarslan et al., 2006)
- iron ore—4.0 g/cm^3 (fc = 75–80 MPa, w/c = 0.40) (Shirayama, 1963)
- magnetite - >3.50 g/cm^3 (fc = 75–80 MPa, w/c = 0.30) (Ouda 2015)
- limonite + steel shot - >3.50 g/cm^3 (fc = 60 MPa, w/c = 0.40) (lo Monte et al., 2014)
- barite or magnetite—3.50 g/cm^3 (fc = 35–45 MPa, w/c = 0.37–0.60) (lo Monte et al., 2014)
- copper slag aggregate—2.80–3.0 g/cm^3 (fc = 70–95 MPa, w/c = 0.33–0.45) (Behnood 2014)

Nuclear power plants (NPPs) are subjected to high temperatures during their entire operating life. High temperatures induce complex changes such as mass and strength loss in concrete due to loss of bound and unbound water from the hydrated products of cement. Exposure to high temperatures, calcination of calcareous aggregates, and volumetric instability of quartz aggregates are necessary changes that trigger mass and strength loss phenomena (Fillmore 2004). The more the loss in mass and strength, the more the density reduction, ultimately reducing the radiation shield's attenuation capability (Nikbin, 2020). Most NPPs operate at a temperature of 65°C; this situation could be worsened in case of any emergency or fire. The thermal properties of concrete get importance in the case of high-temperature reactors where temperature can reach 400°C in thick pre-stressed concrete shields in nuclear reactors (Sakr and El-Hakim 2005). Whereas the thermal properties of ordinary concrete have been the subject of investigation in the past, their parameters are well known. Increasing temperatures more than 100°C, the vapor pressure developed due to water inside the concrete increasing internal pressure, leading to cracking in concrete and sometimes spalling at high temperatures. Increasing temperature above 300°C leads to some severe changes inbound and unbound water to concrete. In contrast, considerable deterioration and degradation in strength have been reported in concrete exposed to a temperature above 600°C. The elastic modulus and compressive strength drop to half by increasing temperature beyond 700°C (Mehdipour et al., 2020). Likewise, in recent times, exposure of heavyweight concrete to high temperatures has been a subject of interest for many. For instance (Thomas et al., 2019), developed magnetite concrete and subjected it to high temperatures to measure its physical and mechanical properties. Up to 300°C, the temperature had no influence on concrete's physical and mechanical qualities, but at 500°C, 80% of its initial compressive strength was lost. The breakdown of portlandite $(CaOH)_2$ into carbon dioxide (CO_2) and calcium oxide caused a considerable loss of strength and structural deterioration between 500°C and 700°C (CaO). At 800°C, C-S-H gel decomposes while maintaining 50% of its initial strength. A recent study (Horszczaruk and Brzozowski 2019) found that magnetite concrete maintained its phase stability up to 570°C without losing strength. Magnetite concrete loses 20% of its strength at 800°C (Kodur and Agrawal 2016). There is still a knowledge gap in heavyweight concretes exposed to temperatures above 800°C (Demir, Gümüş, and Gökçe 2020; lo Monte et al., 2014).

Artificial aggregates, such as steel shots and iron pellets, do, in fact, increase the density of concrete more than natural aggregates. However, there are certain limitations to using artificial aggregates, such as the compaction of fresh concrete due to gap-graded aggregates, and iron and steel must be rusted before use in order to form strong bonds with other concrete ingredients (Lerman et al., 2020). Another factor is magnetic attraction, which interferes with the interlocking effect of steel or iron with other particles (Rohrig, 2016). As a result, natural aggregates can be utilized as heavy-density aggregates in concrete as gamma ray shields.

Based on the authors' knowledge, it can be concluded that waste or by-product aggregates with sufficient density could be used in gamma radiation shields to overcome the limitations explained in the literature. Utilization of waste and by-products is sustainable, environmentally friendly, and cost-effective approach. For this reason, Dolerite Heavyweight Aggregates (DHA) with a density of 3.12 g/cm^3 is utilized in concrete. The concrete is subjected to high temperatures from 200°C to 1200°C. The physio-mechanical properties (compressive strength, rebound hammer, mass, and density loss), as well as their ability to absorb harmful radiation (linear and mass attenuation coefficients, Half Value Layer (HVL), and 10th Value Layer (TVL)) for pre- and post-heated, concretes were analysed. Apart from that, to evaluate the chemical changes at a micro level, Scanning Electron Microscope (SEM) and X-ray

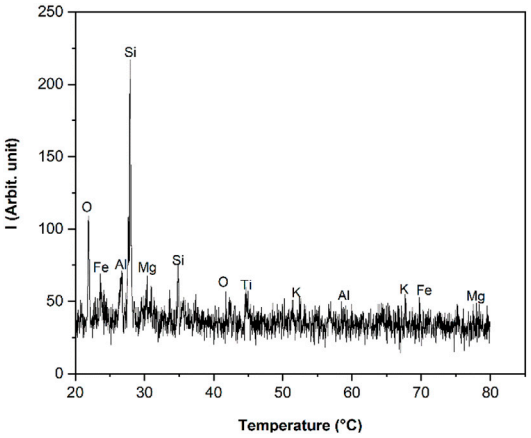

FIGURE 2
XRD analysis of DHA.

radiography for studying voids and cracks due to thermal changes are also part of this study. The evaluation of concrete shields at such high temperatures will help fulfill the current demand for the knowledge of fourth-generation nuclear power plants where temperatures can reach more than 1000°C (Thomas et al., 2019).

2 Materials and testing methodology

2.1 Materials

Ordinary Portland cement (OPC) ASTM Type 1, fouji brand, Pakistan, was used in the present study. The physical and chemical properties of the cement are given in Table 1, which shows the specific gravity value of 3.12 gm/cm^3.

Normal-weight limestone aggregate obtained from Margalla hills and fine aggregates from Lawarancepur, Pakistan were used in this research. The gradation curve of fine aggregates is shown in Figure 1. The gradation of fine aggregates is within the upper and lower limits defined by ASTM C33. Also, the fineness modulus calculated for fine aggregates is 2.7 which is also within limits.

To avoid harsh mixes and to achieve satisfactory consistency, Chemrite-SP 303 superplastisizer, Emporient Chemicals, was used.

Dolerite heavyweight aggregates (DHA) were obtained from two sources; one from the parent source (place of mining, located in Mansehra, KPK, Pakistan, situated (34° 25' 27″N, 72° 58' 05″E), while the other from a factory where these stones are cut and polished. So, there were two types of aggregates; one with a polished surface and the other with a coarse and rough surface. Trial mixes were prepared using both types of aggregates; however, concrete mixes prepared with polished surface aggregate tend to settle down in fresh mix due to no or very little inter-particles friction, resulting in mixes with no adhesion. Therefore, based on trials, a mixture of both types of aggregates was used to cast concrete. The density and other physical characteristics of DHA are shown in Table 2.

To study the phase identification of the crystalline nature of DHA, X-Ray diffraction (XRD) analysis was carried out in Centralized Resourced Laboratory (CRL), UoP, Pakistan, through JDX-3535 JOEL diffractometer. The peak positions of crystalline at 2-Alpha are plotted against the X-Ray counts (intensity) as shown in Figure 2. The figure shows that dolerite aggregates are rich in silica (Si) and Oxygen (O) contents. There are small traces of Magnesium (Mg), Aluminum (Al), Titanium (Ti), and Phosphorous (K). The element that contributes to the high density of dolerite aggregate is Iron (Fe) which could be found in abundance with various peaks.

2.2 Mixing details

In this study, seven mixes were considered to understand better the effect of high temperature on the mechanical properties of heavyweight concrete made with dolerite aggregates. The ratio of aggregates varied among the mixes. For instance, DC1 concrete indicates "dolerite concrete mix with 25% dolerite aggregate and 75% limestone aggregates. The other mixes designation is; DC2 (50% dolerite and 50% limestone), DC3 (75% dolerite and 25% limestone aggregate), and DC4 (100% replacement of limestone aggregates with dolerite aggregates). Control mix CM1 (5–9 mm limestone), CM2 (5–16 mm limestone), and CM3 (5–25 mm limestone) were also part of this study for comparison purposes.

The water-cement ratio w/c = 0.45 was kept constant for all mixes. The cement quantity (less than 400 kg/m^3) was the same for all the mixes. Chemrite SP-303 superplasticizer was introduced to get the acceptable consistency used for specimen preparation as per supplier recommendation (0.4%–1.5% by weight of cement). The mix design adopted in this study is shown in Table 3.

2.3 Specimen preparation

In this study, a total of 210 specimens were prepared for compressive testing for pre and post-heating in a furnace. The cylindrical specimens cast were 150 mm in diameter and 300 mm in length. Three specimens were poured for each mix and temperature, and the average value was taken at the end of each mix testing. Three specimens in each mix were exposed to 200°C, 400°C, 600°C, 800°C, 1000°C, and 1200°C.

For gamma-ray and X-ray attenuation, cubic specimens with dimensions 150 mm × 150 mm x 150 mm were poured. These specimens were then cut mechanically for 20 ± 2 mm thickness. This way, three specimens per mix per temperature with dimensions (150 mm × 150 mm x 20 ± 2 mm) were prepared. So, a total of 105 specimens were prepared for both gamma and X-ray attenuation. Specimens of each mix were exposed to 200°C, 400°C, 600°C, 800°C, 1000°C, and 1200°C temperatures. It may be noted that the same specimens were tested first for X-ray and then gamma rays attenuation. Before testing, all the specimens (315 No's) for mechanical and attenuation properties were cured in a water tank under controlled laboratory conditions.

2.4 Heating procedure for concrete specimens

The heating process was carried out in a trolley-operated electric furnace having dimensions of 500 mm × 600 mm × 1200 mm. Before heating, the specimens were oven-dried at 110°C for 24 h to remove any free water. This is to prevent the concrete specimens from

TABLE 3 Mix design of control and DC mixes.

Concrete type	Aggregate ratio	W/c	Water (kg/m3)	Cement (kg/m3)	Fine aggregate (kg/m3)	Coarse aggregate (kg/m3)	DHA (kg/m3)	Superplasticizer (kg/m3)	Total (g/cm3)
CM1	100% limestone aggregates (5–9 mm)	0.4	153	388	712	1273	-	0.65	2.53
CM2	100% limestone aggregates (5–16 mm)	0.4	153	388	712	1288	-	0.65	2.54
CM3	100% limestone aggregates (5–25 mm)	0.4	153	388	712	1310	-	0.75	2.56
DC1	25% DHA +75% limestone (5–25 mm)	0.4	153	369	765	1014	388	0.76	2.69
DC2	50% DHA +50% limestone (5–25 mm)	0.4	153	361	752	714	776	0.88	2.76
DC3	75% DHA +25% limestone (5–25 mm)	0.4	153	388	874	318	1164	0.91	2.90
DC4	100% DHA (5–25 mm)	0.4	153	388	875	-	1552	0.96	2.97

exploding during the heating process in the furnace. The furnace is installed with a ventilator to circulate air from the atmosphere into the furnace. The door and outside walls of the furnace were installed with water-cooling pipes that constantly circulate to keep the doors and outside walls cooled and exploded due to overheating. Before heating, specimens were assessed for mass and density at room temperature. This was done after heating specimens in an oven at 110°C for 24 h to obtain constant mass by eliminating any free water. The specimens were then loaded from the front on the machine-operated trolley, and the furnace doors were sealed. The specimens were heated to the desired temperature of 200°C, 400°C, 600°C, 800°C, 1000°C, and 1200°C with a 3°C–5°C/min loading temperature. Afterward, reaching the desired temperature, the furnace temperature was held constant for 120 min. After heating, the doors were shut to bring the temperature of the furnace to room temperature, and the specimens were then unloaded. The concrete mixes were measured again for mass and density loss after they were cooled to room temperature. The specimens were measured for weight loss and visual observation after removal from the furnace. Compressive strength test (ASTM C39/C39M − 17b), rebound hammer (ASTM, C 805–02), and mass and density loss were conducted immediately.

2.5 X-ray radiography and gamma-ray attenuation coefficient

X-ray computed radiography of concrete to measure the three-dimensional dispersal of pores, air voids, and air pockets in solid materials is a non-destructive technique that has proven to be effective in pore characterization of porous materials. For the same reason, this study presents the x-ray imaging of heavyweight concrete subjected to high temperatures. So, the concrete specimens with 150 mm × 150 mm × 20 mm of ambient and high temperatures have been shifted to Metallographic Testing Lab (MTL), Non-destructive Testing (NTD) in Heavy Mechanical Complex (HMC) Taxila, Pakistan. The specimens covered in D7 film were put on a lead table with minimum noise to get a better and more concise image. The exposure time of X-ray radiation for this setup was 1 min. The scheme of the experimental setup is shown in Figure 3.

Concrete specimens' gamma rays' characteristics were tested in the Nuclear Engineering and Radiation Measurement Laboratory (NERML), Pakistan Institute of Engineering and Applied Sciences (PIEAS), Islamabad, Pakistan. The schematic procedure of gamma irradiation through a ^{137}Cs source with 0.622 MeV energy enclosed in the lead shield is shown in Figure 4. To avoid stray radiation from reaching the detector and making good geometry, two lead collimators were introduced in front of the source and the other in front of the detector. Both collimators were aligned using laser points. Before un-shielding the source, concrete specimens were placed vertically with 20 ± 2 mm thickness in front of the source. The un-collided gamma rays were detected by NaI (Ti) detector. The detector counted the emitted rays from the source passing through the collimators and penetrating through the specimen. The weak detector signals are required to be amplified by an amplifier (PMT) prior to shaping. Before that, aluminum and copper samples with known parameters were tested before actual concrete testing for the calibration of the experimental setup. For the accuracy of results, the selection of window channel on Single Channel Analyzer (SCA) played a valuable role. So, a pulse of height representing full energy peak is selected on SCA, which is counted by the counter-timer. A similar experimental setup has been published previously by (Ouda and Abdel-Gawwad, 2017; Khan et al., 2022).

The variations in the radiation intensity are measured through Lamber-Beer law given in Equation 1. To measure the gamma rays shielding effectiveness of concrete, the half-value layer (HVL) and

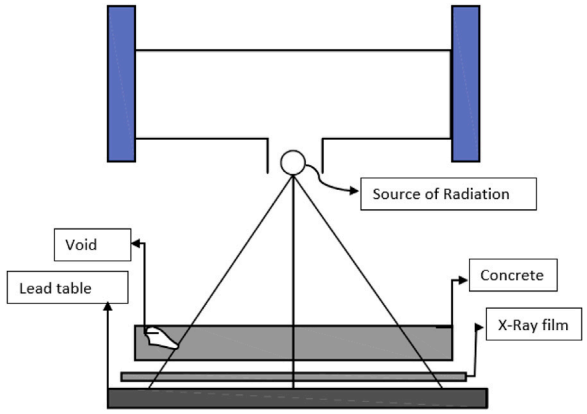

FIGURE 3
Schematic diagram of the X-ray test setup.

10th Value Layer (TVL) were measured through Eqs 2, 3 and respectively (Lamarsh et al., 2014; Singh and Singh, 2021)

$$I = I_0 e^{-\mu x} \quad (1)$$

$$HVL = \frac{\ln(2)}{\mu} \quad (2)$$

$$TVL = \frac{\ln(10)}{2} \quad (3)$$

Given that

I = intensity of radiation, I_0 = intensity of radiation without thickness, x = Thickness of shield, μ = Linear attenuation coefficient of the specimen.

3 Result and discussion

3.1 Physical observations

The pre and post-heated concrete specimens were physically observed for color changes, cracks, aggregate expansion, and voids. DC3 Specimen exposed to temperatures from 600°C to 1200°C is shown in Figure 5.

It was observed that up to 400°C, no physical changes were noticed except for slight color variations. No surface cracks could be observed in this temperature range as only free water tends to evaporate.

However, exposing specimens to a temperature of 600°C, few hair lines cracks were observed for control mixes as well as dolerite concrete. This is because chemically bound water tends to evaporate, which triggers chemical reactions and, in turn, leads to physical changes such as cracks (Koťátková et al., 2016). The control mixes suffered more than dolerite mixes against thermal stresses. The breakage in the cement matrix and decomposition of C-S-H and $CaCO_3$ to CO_2 and CaO occurs at 800°C and above (Naus, 2010). These breakages and chemical changes alter the specimen color to a large extent. Also, the cracks were more visible and could be measured with ordinary measuring tools. However, the width of the cracks were pronounced for control mixes compared to dolerite concrete. Complete decomposition of concrete specimens was noticed for control mixes when exposed to moisture, and their strength could not be assessed. In contrast, dolerite concrete showed some strength which was 12% of its original strength. At 1200°C, both control and dolerite mixes were completely decomposed. A large amount of aggregate expansion, internal core degradation, and cracks were observed in mixes.

Figure 6 shows the D3 mix having 75% dolerite aggregates before and after heating to a temperature of 1200°C. The cross-section of the mix shows that dolerite aggregates have made a good bonding with the cement matrix. They are firmly attached and adhered to the rest of the concrete constituents. The magnified part of the specimen shows a dolerite aggregate well embedded in a cement matrix, which provided extra resistance against external loads at ambient temperature. The same mix, when heated at a temperature of 1200°C, showed a different scenario: a complete degradation of cement matrix with large and wide cracks. The delamination of dolerite aggregates from the cement matrix could also be observed in the magnified part. However, the dolerite aggregates could be seen unharmed during heating up to 1200°C because the melting temperature of dolerite is above 1200°C (Ingham, 2013).

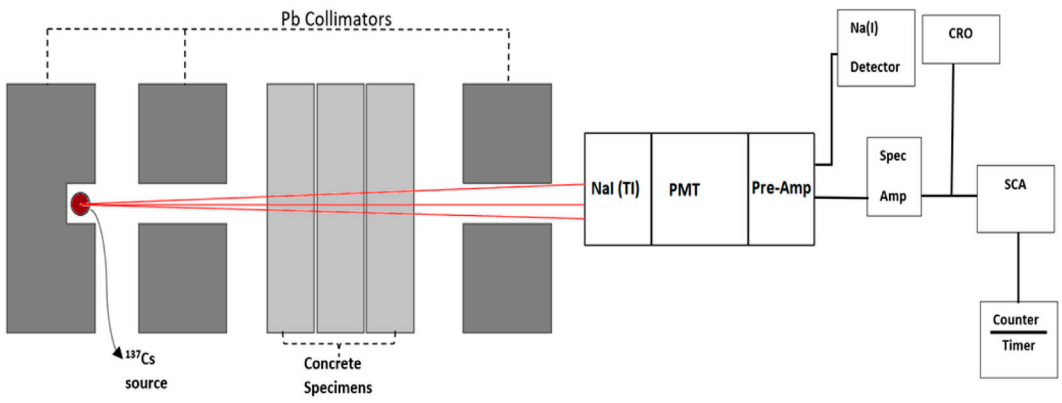

FIGURE 4
Systematic setup of gamma ray test.

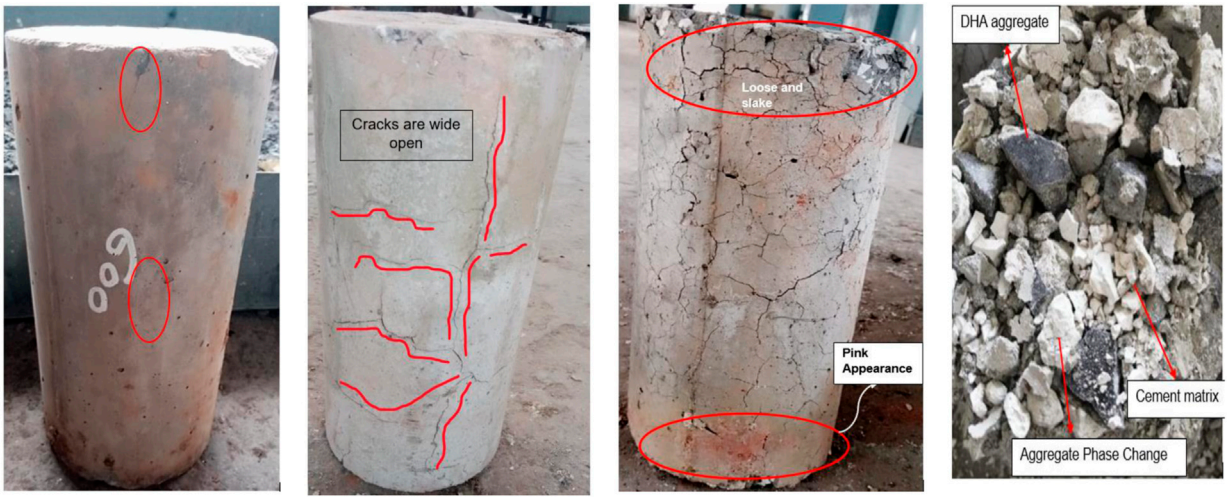

FIGURE 5
DC 3 mixes exposed to temperatures from 600°C to 1200°C.

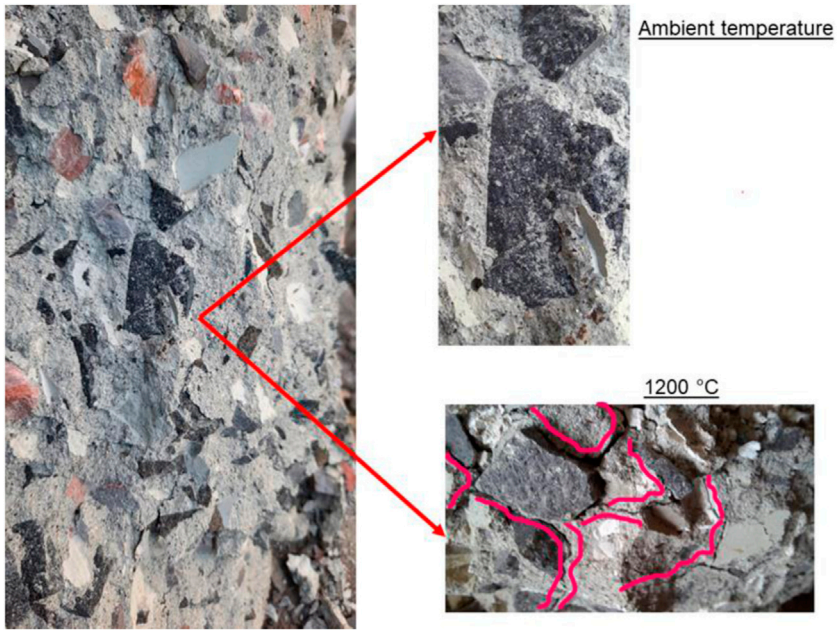

FIGURE 6
Delamination of DHA aggregates in Dolerite mix (D3) after exposed to 1200°C.

3.2 Mass and density loss

The mass and density loss of concretes were meaured before and after heating. The impacts of heating on mass and density loss of concrete were measured from 200°C to 1200°C is shown in Figures 7, 8, respectively. The mass and density loss followed a linear decrease with the variations in temperature. For instance, the density loss for CM1, CM2, and CM3 at 200°C showed a loss of −2%−1.5%, and−1.2%, respectively. No major loss in density has been observed at 400°C since only unbound or free water tends to evaporate from the mixes. Density loss has been increased to −12.4%−12.8% and−12.1% at 1000°C. Further heating of the specimens showed a major loss in density for CM1, CM2, and CM3 concrete, which was−16.6%−15.7%, and −14.9%. The high temperature has induced complex changes in concrete. The decomposition of C-S-H gel is one major reason for its loss of the chemically bound water, which decomposes the complex bonding of the cement matrix (Mohammed Haneefa et al., 2013).

On the other hand, due to the hard in nature and compact, dense structure of dolerite aggregates, the mixes sustain the elevated temperature as shown. For instance, compared to control mixes,

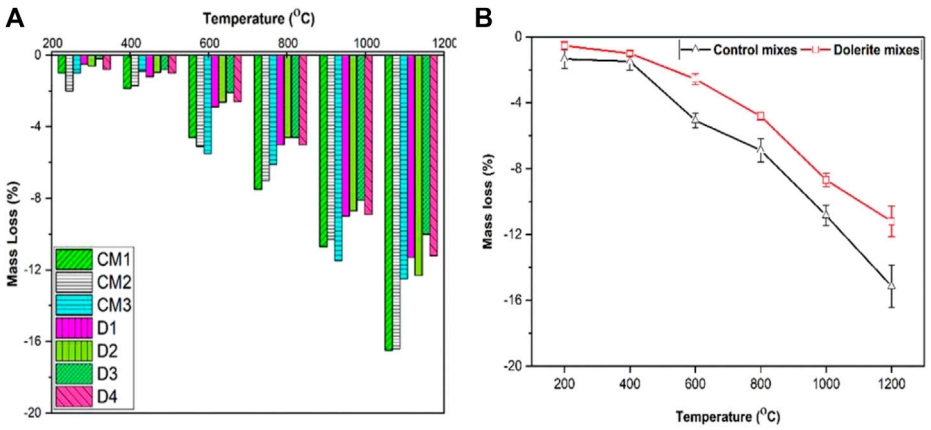

FIGURE 7
Mass loss of control and dolerite mixes as a function of temperature. **(A)** Mass loss **(B)** Mean and error as a function of temperature.

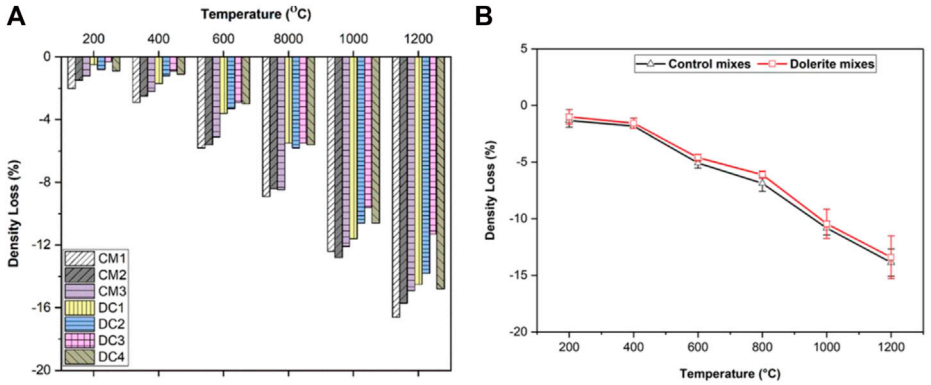

FIGURE 8
Density loss of control and dolerite mixes as function of temperature. **(A)** Density loss **(B)** mean and error bar as a function of temperature.

the D1, D2, D3, and D4 showed a density loss of −0.5%−0.8%−0.3%, and −0.9%, respectively. The density loss was not pronounced up to 600°C, maintaining its residual density up to 97%. Beyond 600°C, the D1, D2, D3 and D4 showed density losses of −11.6% −10.6% −9.6% and −10.6%, respectively. More severe changes have been observed at 1200°C, where the mixes retained 85.5%, 86.2%, 89.7%, and 86.8% of their initial density. It may be noted that the lowest density loss was observed for the D3 (having 75% dolerite aggregates) mix at low and high temperatures. The dolerite aggregates possess a rough and angular structure, providing extra resistance against thermal loads. Due to angular, they make a strong bond with the cement matrix and prevent the loss of hydrating water (Sloane, 1991).

3.3 Compressive strength

The compressive strength of control mixes and dolerite concrete as a function of temperature is shown in Figure 9 and mean values are depicted in Figure 10. At room temperature, dolerite concrete having 75% dolerite aggregates (D3) showed maximum strength among the specimens. The D3 mix showed a compressive strength of 57.6 MPa, more than the CM1, CM2, and CM3 mix by 31.9%, 29.3%, and 24.8%, respectively. The strength drops up to 400°C were not pronounced and showed a linear decrease in compressive strength. The strength values noted for D1, D2, D3, and D4 mixes were 40.94 MPa, 45.51 MPa, 52.704 MPa, and 48.42 MPa, respectively. Because, in this temperature range, the evaporation of free water, a rise in porosity, and dehydration of the C-S-H phase in the cement paste reduced the resistance (Shumuye et al., 2019) (Table 4).

Upon further heating, the mixes showed a rapid decrease in strength, which continued till 1200°C. The α-β-SiO_2- inversion occurs in the quartz crystals that make up the aggregate when the temperature reaches approximately 600°C. There is a 0.85%-point rise in the specific volume. The calcium hydroxide and other products of cement hydration start to dehydrate, which is one factor that contributes to the concrete structure's deterioration (Chang et al., 1994).

At 800°C, the strength loss for D1, D2, D3, and D4 concrete was found to be 53.0%, 50%, 55%, and 60% compared to ambient temperature strength. A 60% and 86% decrease was noted for D4 concrete at 800°C and 1000°C, respectively. As depicted in section 4.1, the delamination of dolerite aggregates occurs due to

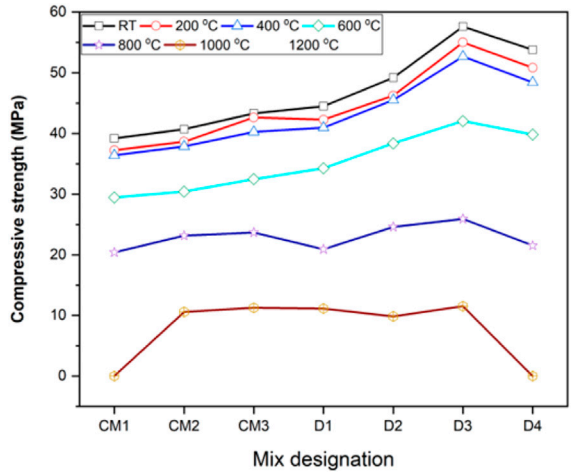

FIGURE 9
Compressive strength of control and dolerite mixes as function of temperature.

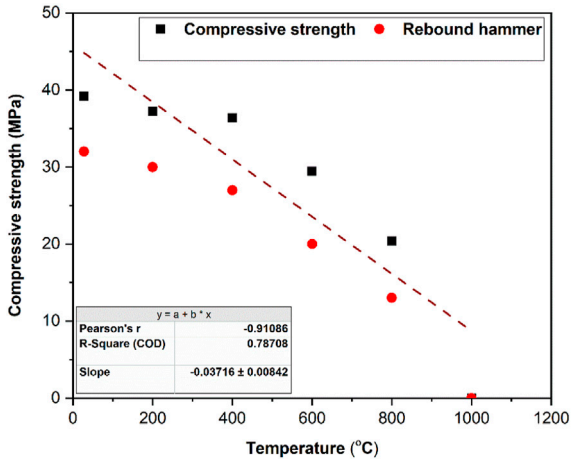

FIGURE 11
Correlation curve between compressive strength and rebound hammer for CM1 mix.

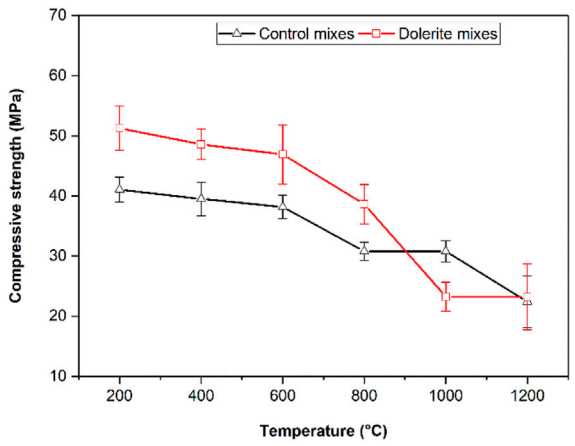

FIGURE 10
Mean and standard deviation of compressive strength against temperature.

extreme degradation in the cement core. Also, the calcium carbonate decomposes into CO_2, leading to further expansion of the specimen due to expansion in aggregates (Powe et al., 2020).

It may be shown that increasing the size of coarse aggregate tends to increase the compressive strength. For instance, CM1, CM2, and CM3 concrete showed a compressive strength of 39.2°MPa, 40.7°MPa, and 43.3 MPa at room temperature. The significant degradation in concrete was noted beyond the temperature at 400°C. Below 400°C, the residual strength of concrete specimens was found to be between 5%–7.1%. For instance, at 400°C, CM1, CM2, and CM3 concrete showed a loss in strength of 7.14%, 6.8%, and 6.9%, respectively of their initial values. However, at 600°C and beyond, the compressive strength decreased drastically, especially for CM1 mixes. At 600°C, 800°C, and 1000°C, the CM1 mixed showed a loss in compressive strength of 24.8%, 74.9%, and 100%, respectively. Where the highest compressive strength was noted for CM3 in this temperature range. At 600°C, 800°C, and 1000°C, a loss in compressive strength of 25%, 56%, and 73%, respectively, for CM3 mixes.

TABLE 4 Summary of test results with standard deviation.

Mix details	Compressive strength (MPa)		Mass loss (%)		Density loss (%)	
	Average	Standard deviation	Average	Standard deviation	Average	Standard deviation
CM1	46.90	4.23	−7.03	0.57	−8.10	0.59
CM2	44.70	3.11	−7.08	0.63	−7.75	0.77
CM3	43.16	5.94	−6.25	0.41	−7.33	1.27
DC1	35.26	4.87	−4.98	1.39	−6.23	1.61
DC2	22.88	2.03	−4.97	1.19	−5.92	1.16
DC3	10.29	1.36	−4.30	1.24	−5.08	1.67
DC4	2.79	2.68	−4.92	2.57	−6.00	1.15

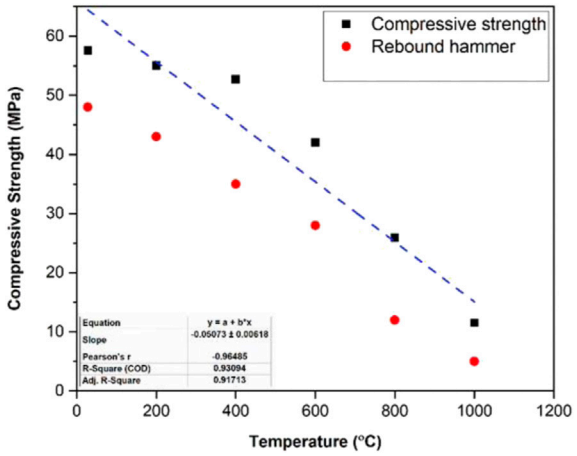

FIGURE 12
Correlation curve between compressive strength and rebound hammer for DC3 mix.

The strength could not be measured for the same mix at 1200°C due to complete decomposition of concrete. In addition, the gel has disintegrated, the structure of the cement paste has been damaged, as well as the structure is loose and slack in appearance (Hager 2013). At this temperature, the morphological behavior of the specimen is characterized by whitening of the specimen and appearance of fissures on the surface. At temperatures between 800°C and 1000°C, further disintegration and the formation of free and permeable material result in the creation of a significant number of long and wide fractures on the surface of the samples. With further exposure to moisture, the specimens are damaged and peeled off, a significant quantity of coarse aggregate is stripped off the cement paste, and the interfacial adhesion force is reduced or even gone (Burrow et al., 1979; Naus, 2010).

3.4 Rebound hammer

The results of rebound hammer in correlation with compressive strength for CM1 mix are shown in Figure 11. The rebound hammer for the CM1 mix was determined for temperatures between 28°C and 1000°C. The cumulative relation between compressive strength and rebound hammer yields an R-squared value of 0.787. The R-squared value is less than the DC3 mix, which is 0.93; this is because, beyond 600°C, a drastic decrease in compressive strength has been observed. The rebound values seem to follow the compressive trend. Increasing the temperature tends to decrease the rebound numbers. Up to 400°C, the values of the rebound hammer could be turned as a "good layer" beyond this temperature; all the values were termed as "fair," "poor," and "delaminated" at temperatures 600°C, 800°C, and 1000°C, respectively.

Figure 12 shows the variations of rebound hammer against temperatures for DC3 mix. Recalling the previous sections, this mix was qualified as the highest compressive strength mix with low mass and density loss. The rebound hammer and compressive strength R-squared were obtained as 0.930, which shows a good agreement between compressive and rebound values.

3.5 X-ray radiography

X-ray radiography is a conventional and highly effective non-destructive test (NDT) for measuring concrete defects such as air pockets, air voids, matrix, and bond cracks. Concrete underwent X-ray radiography to verify the qualities of the CM1 and DC3 mixes specified in sections 4.1, 4.3, and 4.4.

Figure 13A depicts a compact, dense construction with no gas pores and voids at a minimum. In the dark, the dolerite aggregates could be observed. No bonds or matrix cracks could be identified at this stage. Figure 13B displays a considerable number of cracks (shown in red), but no matrix cracks have yet emerged as a result of intense heating at 1000°C. The size of the gas pores (indicated in black) increases. At 1000°C, two types of cracks were seen in the CM1 mixture: matrix cracks and core cracks. The matrix cracks are marked in red. Due to intense heating, the border layer of concrete in the concrete disintegrated. In addition, many core fractures (marked in black) may be noticed in the concrete along with pores and voids (Hernandez-Murillo et al., 2020) as shown in Figure 13C.

3.6 Scanning electron microscopy (SEM)

The SEM analysis for the DC3 mix at ambient temperature is shown in Figure 14A. It could be shown that particles are induced into each other and make a strong bond against external resistance. It was discovered that the transition zone exhibited an entire matrix composed of ettringite, portlandite, and calcium silicate hydrate at ambient temperature. The white clouds are evidence of S-C-H gel formation in mixes. This concrete demonstrated the highest compressive strength at ambient temperature, which was 57.6 MPa. The EDX analysis was also taken of the same mix where traces of Fe, Si, Ca, Ti, and some minor traces of K and Al were found, as shown in Figure 15.

When the temperature reaches 1200°C, a significant proportion of water is evaporated, and many holes develop on the gelled layer in DC3 mix. In addition, the gel has disintegrated, the structure of the cement paste has been damaged, and the structure is loose and slack in appearance. In such temperatures, the macroscopic performance of the specimen exhibits whitening the specimen and the appearance of cracks on the surface of the specimen (Sivathanu Pillai et al., 2016), as shown in Figure 14D.

The CM1 mix at ambient temperature is shown in Figure 14B, where white clouds of C-S-H could be observed. Additionally, there are black holes identified in the mixes, which could be voids which depicts porous structure that results in low compressive strength compared to other mixes. The SEM analysis of the control mix (CM1) at 1200°C is shown in Figure 14C. At this stage, it is possible to identify the lack of cohesion and the friable, porous appearance of the C-S-H matrix and to identify some altered portions of the samples. As shown, there is no cohesion left between the particles, and complete degradation has been noticed.

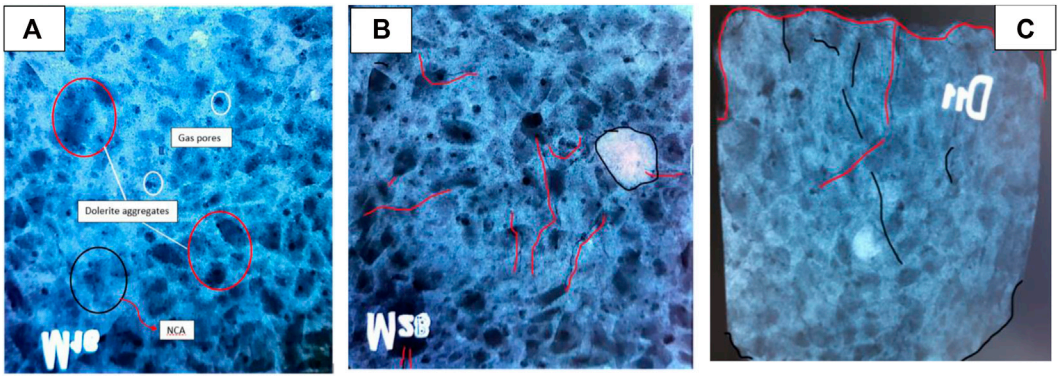

FIGURE 13
X-ray radiography **(A)** DC3 mix at ambient temperature, **(B)** Control mix at 1000°C and **(C)** DC3 mix at 1000°C.

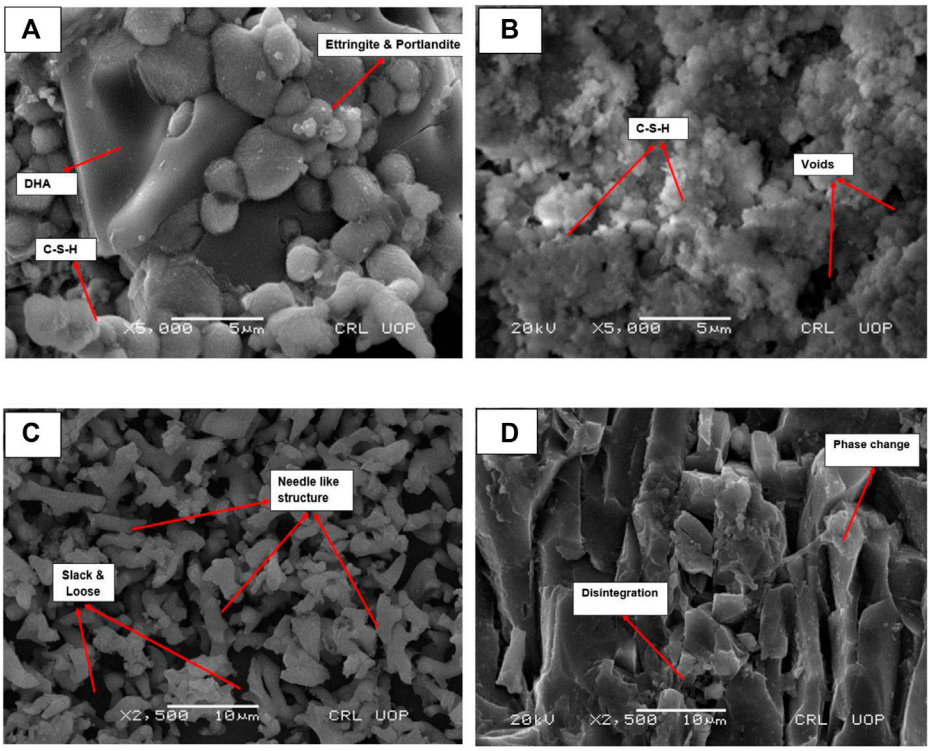

FIGURE 14
SEM analysis **(A)** DC3 mix at ambient temperature, **(B)** control mix at ambient temperature, **(C)** control mix at 1200°C, **(D)** DC3 mix at 1200°C.

High temperatures also affect the non-hydrated cement particles in the hydrated cement paste, causing them to expand more rapidly. Together with shrinkage in cement paste produced by variations in C-S-H and CH, this process promotes differential thermal expansion among the ingredients, resulting in microcracking and an increase in the porosity of the concrete mix (Diamond and Huang 2001). The cement mixture begins to melt at such high temperatures. Moreover, concrete specimens develop significant microstructure gaps and an interfacial transition zone between the aggregate and the cementitious matrix (Sadrmomtazi et al., 2012).

3.7 Gamma-ray attenuation

The gamma-ray attenuation was measured only for mixes that exhibited high and low compressive strength among all mixes at various temperatures. For this reason, DC3, DC4 and CM1concrete specimens were measured for gamma ray attenuation.

3.7.1 Linear attenuation coefficient (LAC)

The linear attenuation coefficient of CM1, DC3, and DC4 concrete is shown in Figure 16. The lowest linear

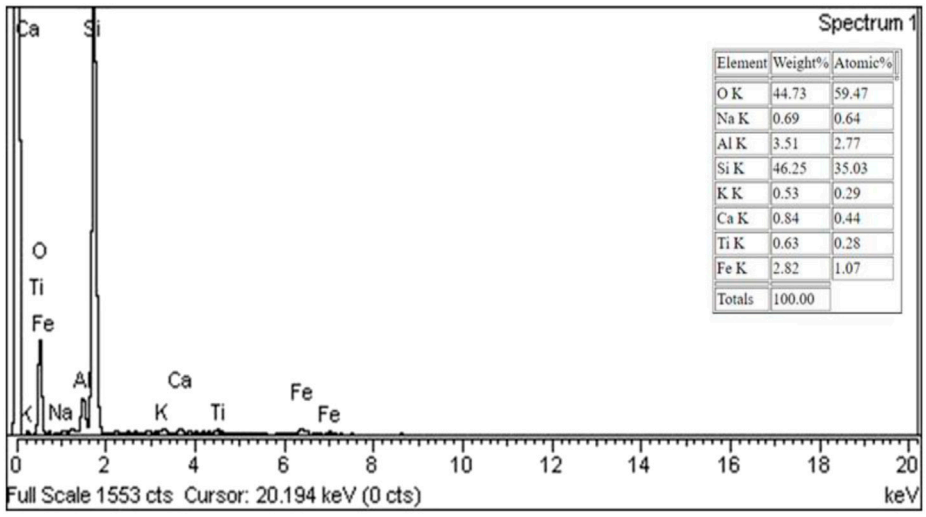

Element	Weight%	Atomic%
O K	44.73	59.47
Na K	0.69	0.64
Al K	3.51	2.77
Si K	46.25	35.03
K K	0.53	0.29
Ca K	0.84	0.44
Ti K	0.63	0.28
Fe K	2.82	1.07
Totals	100.00	

FIGURE 15
EDX analysis of DC3 mix at ambient temperature.

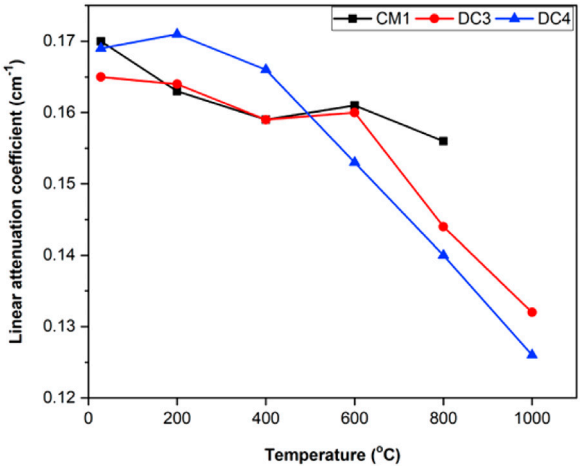

FIGURE 16
Linear Attenuation Coefficient (LAC) as function of temperature.

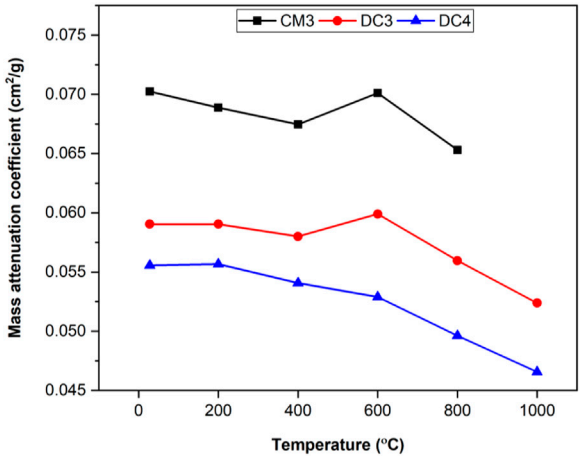

FIGURE 17
Mass Attenuation Coefficient as function of temperature.

attenuation is measured for DC3 concrete, whereas the highest was measured for DC4 concrete. Linear attenuation depends upon the density of the material. Since DC4 concrete exhibit more density among all mixes, therefore, linear attenuation was measured highest for this mix. It may also be noted that a sharp decrease in attenuation properties for all mixes was noted at 600°C since the compressive strength drastically decreased in mixes due to chemical and physical changes that occurred at this stage of heating. As shown in the figure, the control mix (CM1) decreases from room temperature to 400°C and then increases to 600°C. This is because gamma ray exhibits a shorter wavelength, less than 100 pm. It may be possible that the gamma-ray strike with heavy aggregate or cement particles at this temperature range tends to attenuate more compared to mixes at different temperatures (Khan et al., 2022). The attenuation of CM1 mix at 1000°C could not be measured due to complete disintegration and decomposition.

3.7.2 Mass attenuation coefficient (MAC)

Mass attenuation is the function of linear attenuation with respect to density of the material. The mass attenuation of CM3, DC3 and DC4 at various temperatures is shown in Figure 17. Since the DC4 exhibit the highest density among all the mixes, the mass attenuation was measured maximum for this mix. Additionally, DC4 concrete attenuation increased at 200°C, which may be evident of reverse hydration of un-hydrated cement. These values then tend to decrease at all temperatures. The DC3 mix showed more attenuation at room temperature than the CM3 mix. However, this value decreased at all temperatures later. There may be a few reasons that could explain this phenomenon such as bad mix where

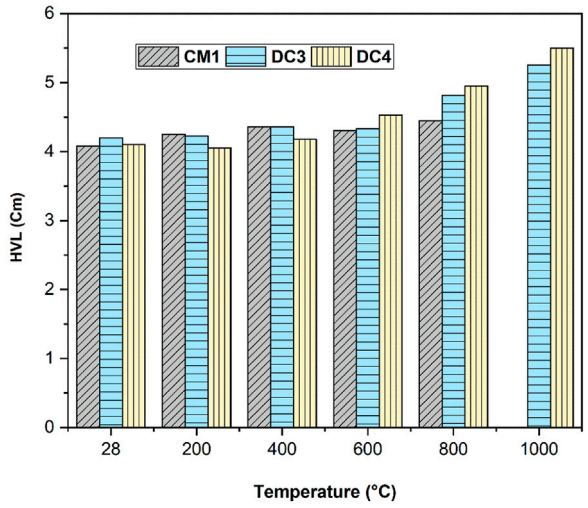

FIGURE 18
Half Value Layer (HVL) as function of temperature.

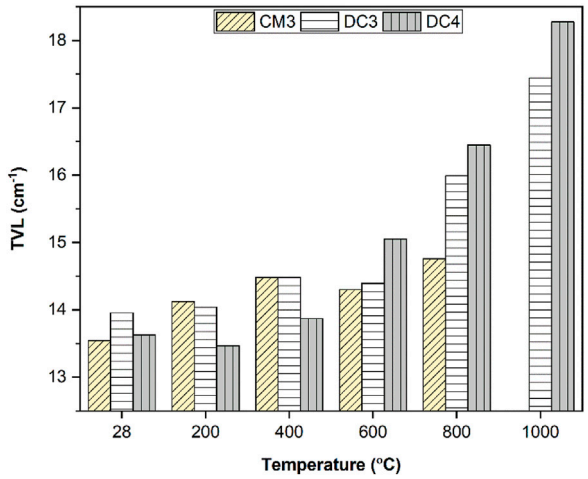

FIGURE 19
Tenth Value Layer (TVL) as a function of temperature.

the aggregates were clustered at once and not mixed thoroughly or due to the bad geometry of the gamma-ray setup (Lee et al., 2007; Kumar et al., 2021; Ouda, 2021).

3.7.3 Half Value Layer (HVL) and 10th Value Layer (TVL)

The HVL and TVL values of the control mix and dolerite mixes are shown in Figure 18 and Figure 19, respectively.

Both attenuation properties tend to rise by increasing the temperature. For instance, the HVL value of DC3 mix was found to be 4.1 Cm at ambient temperature where it was noted 4.8 cm at 800°C. Figure 18 also show that dolerite mixes (DC3 and DC4) exhibit lowest HVL values compared to control mix up to 600°C. However, beyond this temperature, the HVL values tends to increase by increasing temperature.

The same trend could be noted in TVL values. At ambient temperature, the TVL was found to be maximum for DC4 concrete and minimum for DC3 concrete. This trend was followed until the temperature reached 600°C, where the TVL increased linearly for DC4 mixes. The phenomena of increase and decrease have already been explained in sections 4.3, 4.4, and 4.6.1.

4 Conclusion

This paper investigates the physical, mechanical, and microstructural properties as well as X-ray and gamma rays attenuation measured for heavy-density dolerite concrete at temperatures of 200°C–1200°C. The study provides comprehensive experimental results which will be helpful in assessing the various properties of concrete as gamma ray shield at high temperatures. The following concluding remarks are drawn.

1) At all temperatures, the mass, and density loss were more pronounced in control mixes compared to dolerite mixes. The lowest density loss was observed for mixes with 75% dolerite aggregate.
2) Specimens with 75% dolerite aggregate mix showed a compressive strength of 57.6 MPa, more than the control mix1, control mix2, and control mix 3 by 31.9%, 29.3%, and 24.8%, respectively, at room temperature. The concrete with 75% dolerite aggregates showed a loss in compressive strength of 4.50%, 8.50%, 27.0%, 55.0%, 80.0%, and 65.0% at 200°C, 400°C, 600°C, 800°C, and 1000°C, respectively compared to room temperature.
3) The rebound hammer followed the same pattern of compressive strength for control and dolerite mixes at all temperatures. The X-ray radiography showed gas pores, bond, and matrix cracks as well as voids in post-heated specimens whereas showed a compact structure in pre-heated specimens.
4) Linear attenuation coefficient (LAC) values were found more for control mixes whereas less for mix incorporated with 100% dolerite aggregate. The linear attenuation coefficient is a function of thickness thus increasing the thickness tends to increase LAC.
5) Mass attenuation coefficient (MAC) is a function of the density of material therefore the specimen with 100% dolerite aggregates exhibited the lowest MAC because of the higher density among other mixes. The Half Value Layer (HVL) and Tenth Value Layer (TVL) followed the pattern of LAC and MAC at all temperatures. The specimen with 100% dolerite aggregates showed the highest attenuation of gamma rays to one-fifth and one-tenth levels.

Data availability statement

The original contributions presented in the study are included in the article/supplementary material, further inquiries can be directed to the corresponding author.

Author contributions

The author and contributions to the paper are as follows: MK and MY proposed the idea and designed the experimental program; AM

reviewed and formulated a design for gamma radiation, MU, MAb, and HA conducted the tests and analyzed the data; MN helped in arranging test data and writing the paper, AM and SA reviewed the paper. All authors contributed to the writing of the paper.

Acknowledgments

The authors are extremely grateful to Engr. Mir Qad MA (Head, foundry section, HMC, Taxila, Pakistan) for providing free heating and X-ray services. In addition, the authors would like to thank Noor Nawaz Khan for supplying free of cost dolerite aggregates from mines in Mansehra, Pakistan. The authors thank the NERML, PIEAS staff for their assistance in measuring the attenuation of concrete.

Conflict of interest

The authors declare that the research was conducted in the absence of any commercial or financial relationships that could be construed as a potential conflict of interest.

Publisher's note

References

Akkurt, I., and El-Khayatt, A. M. (2013). The effect of barite proportion on neutron and gamma-ray shielding. *Ann. Nucl. Energy* 51, 5–9. doi:10.1016/j.anucene.2012.08.026

Almeida, J., Airton, T., Nogueira, M. S., Vivolo, V., Potiens, M. P. A., and Campos, L. L. (2017). Mass attenuation coefficients of X-rays in different barite concrete used in radiation protection as shielding against ionizing radiation. *Radiat. Phys. Chem.* 140, 349–354. doi:10.1016/j.radphyschem.2017.02.054

AMERICAN SOCIETY FOR TESTING AND MATERIALS (ASTM) (2015). *'Astm C39'. Standard test method for compressive strength of cylindrical concrete Specimens1 i*, 1–7. doi:10.1520/C0039

Behnood, A. (2014). *High-strength concrete incorporating copper slag and ground pumice*. Sydney: Master Thesis March.

Burrow, R C., Griswold, G D., and Barry Oland, C. (1979). Properties of concrete at elevated temperatures. *Desalination*, 429–432.

Celik, K., Meral, C., Gursel, A. P., Kumar Mehta, P., Horvath, A., Paulo, J., et al. (2015). Mechanical properties, durability, and life-cycle assessment of self-consolidating concrete mixtures made with blended Portland cements containing fly ash and limestone powder. *Cem. Concr. Compos.* 56, 59–72. doi:10.1016/j.cemconcomp.2014.11.003

Chang, W T., ChenWang, T., Huang, C W., and Giang, Y-S. (1994). Concrete at temperatures above 1000°C. *Fire Saf. J.* 23 (3), 223–243. doi:10.1016/0379-7112(94)90030-2

Diamond, S., and Huang, J. (2001). The itz in concrete - a different view based on image analysis and SEM observations. *Cem. Concr. Compos.* 23 (2–3), 179–188. doi:10.1016/S0958-9465(00)00065-2

El-Samrah, G. M., Moamen, G., Abdel-Rahman, M A. E., and el Shazly, R. M. (2018). Effect of heating on physical, mechanical, and nuclear radiation shielding properties of modified concrete mixes. *Radiat. Phys. Chem.* 153, 104–110. doi:10.1016/j.radphyschem.2018.09.018

Facure, A., and Silva, A. X. (2007). The use of high-density concretes in radiotherapy treatment room design. *Appl. Radiat. Isotopes* 65 (9), 1023–1028. doi:10.1016/j.apradiso.2007.04.006

Fillmore, D. L. (2004). *Literature review of the effects of radiation and temperature on the aging of concrete*. Idaho: Idaho National Engineering and Environmental Laboratory. September: 1–26.

Gencel, O., Koksal, F., Ozel, C., and Brostow, W. (2012). Combined effects of fly ash and waste ferrochromium on properties of concrete. *Constr. Build. Mater.* 29, 633–640. doi:10.1016/j.conbuildmat.2011.11.026

Gökçe, H. S., Öztürk, B. C., Çam, N. F., and Andiç-Çakır, Ö. (2018). Gamma-ray attenuation coefficients and transmission thickness of high consistency heavyweight concrete containing mineral admixture. *Cem. Concr. Compos.* 92, 56–69. doi:10.1016/j.cemconcomp.2018.05.015

González-Ortega, M. A., Segura, I., Cavalaro, S. H. P., Toralles-Carbonari, B., Aguado, A., and Andrello, A. C. (2014). Radiological protection and mechanical properties of concretes with EAF steel slags. *Constr. Build. Mater.* 51, 432–438. doi:10.1016/j.conbuildmat.2013.10.067

Hager, I. (2013). Behaviour of cement concrete at high temperature. *Bull. Pol. Acad. Sci. Tech. Sci.* 61 (1), 145–154. doi:10.2478/bpasts-2013-0013

Hernandez-Murillo, G., Geovanni, C., Rafael Molina Contreras, J., Escalera-Velasco, L A., Leon-Martínez, H A d., Rodriguez-Rodriguez, J A., et al. (2020). X-ray and gamma ray shielding behavior of concrete blocks. *Nucl. Eng. Technol.* 52 (8), 1792–1797. doi:10.1016/j.net.2020.01.007

Horszczaruk, E., and Brzozowski, P. (2019). Investigation of gamma ray shielding efficiency and physicomechanical performances of heavyweight concrete subjected to high temperature. *Constr. Build. Mater.* 195, 574–582. doi:10.1016/j.conbuildmat.2018.09.113

Horszczaruk, E. (2019). Properties of cement-based composites modified with magnetite nanoparticles: A review. *Materials* 12 (2), 326. doi:10.3390/ma12020326

Ingham, J P. (2013). Building stone. *Geomaterials Under Microsc.* 21, 21–50. doi:10.1016/b978-0-12-407230-5.50010-8

Kansouh, W. A. (2012). Radiation distribution through serpentine concrete using local materials and its application as a reactor biological shield. *Ann. Nucl. Energy* 47, 258–263. doi:10.1016/j.anucene.2012.05.008

Khan, M. N. A., Yaqub, M., and Malik, Azhar H. (2022). High density concrete incorporating grit scale aggregates for 4th generation nuclear power plants. *Constr. Build. Mater.* 337, 127578. doi:10.1016/j.conbuildmat.2022.127578

Khalaf, M A., Ban, C. C., and Ramli, M. (2019). The constituents, properties and application of heavyweight concrete: A review. *Constr. Build. Mater.* 215, 73–89. doi:10.1016/j.conbuildmat.2019.04.146

Khalaf, M A., Cheah, C B., Ramli, M., Ahmed, N M., and Al-Shwaiter, A. (2021). Effect of nano zinc oxide and silica on mechanical, fluid transport and radiation attenuation properties of steel furnace slag heavyweight concrete. *Constr. Build. Mater.* 274, 121785. doi:10.1016/j.conbuildmat.2020.121785

Kilincarslan, S., Akkurt, I., and Basyigit, C. (2006). The effect of barite rate on some physical and mechanical properties of concrete. *Mater. Sci. Eng. A* 424 (1–2), 83–86. doi:10.1016/j.msea.2006.02.033

Koťátková, J., Jan, Z., Reiterman, P., Jan, P., Hlaváč, Z., and Brabec, P. (2016). The effect of elevated temperatures and nuclear radiation on the properties of biological shielding concrete. *Key Eng. Mater.* 677, 8–16. doi:10.4028/www.scientific.net/kem.677.8

Kumar, S., Mann, K S., Singh, T., and Singh, S. (2021). Investigations on the gamma-ray shielding performance of green concrete using theoretical, experimental and simulation techniques. *Prog. Nucl. Energy* 134, 103654. doi:10.1016/j.pnucene.2021.103654

Lamarsh, J R., Baratta, A J. B. n. d., Lamarsh, A. J., and John, R. (2014). *Introduction to nuclear engineering-pearson* `. Edinburgh: Pdf.

Lee, C-m, YoonLee, H, and Lee, K J (2007). Cracking effect on gamma-ray shielding performance in concrete structure. *Prog. Nucl. Energy* 49, 303–312. doi:10.1016/j.pnucene.2007.01.006

Lotfi-omran, O., Ali, S., and ImanNikbin, M. (2019). A comprehensive study on the effect of water to cement ratio on the mechanical and radiation shielding properties of heavyweight concrete. *Constr. Build. Mater.* 229, 116905. doi:10.1016/j.conbuildmat.2019.116905

Malik, A H., Ayaz, N., Khan, M., Yaqub, M., and Gul, A. (2022). *Recent developments in concrete as a gamma ray shielding material*. doi:10.31031/ACET.2022.05.000609

Maslehuddin, M., Naqvi, A. A., Ibrahim, M., and Kalakada, Z. (2013). Radiation shielding properties of concrete with electric arc furnace slag aggregates and steel shots. *Ann. Nucl. Energy* 53, 192–196. doi:10.1016/j.anucene.2012.09.006

Mehdipour, S., Nikbin, I M., Dezhampanah, S., Mohebbi, R., Moghadam, H H., Charkhtab, S., et al. (2020). Mechanical properties, durability and environmental evaluation of rubberized concrete incorporating steel fiber and metakaolin at elevated temperatures. *J. Clean. Prod.* 254, 120126. doi:10.1016/j.jclepro.2020.120126

Method, Standard Test (1998). *'Standard test method for rebound number of hardened concrete 1'*. Concrete *14*. nurol llc), 1–3. Available at:.

Mohammed Haneefa, K., Santhanam, Manu, and Parida, F. C. (2013). Review of concrete performance at elevated temperature and Hot sodium exposure applications in nuclear industry. *Nucl. Eng. Des.* 258, 76–88. doi:10.1016/j.nucengdes.2013.01.018

Moharram, B. M., Nagy, M. E., Shaat, M K., el Sayed, A. R., Fayiz, M., Dwidar, Samy A., et al. (2020). Performance of lead and iron oxides nanoparticle materials on shielding properties for γ-rays. *Radiat. Phys. Chem.* 173, 108880. doi:10.1016/j.radphyschem.2020.108880

Mollah, A. S., Ahmad, G. U., and Husain, S. R. (1992). Measurements of neutron shielding properties of heavy concretes using a Cf-252 source. *Nucl. Eng. Des.* 135 (3), 321–325. doi:10.1016/0029-5493(92)90199-6

Monte, F lo, and Pietro, G. G. (2014). Thermo-mechanical behavior of baritic concrete exposed to high temperature. *Cem. Concr. Compos.* 53, 305–315. doi:10.1016/j.cemconcomp.2014.07.009

Naus, D. 2010. 'A compilation of elevated temperature concrete material property data and information for use in assessments of nuclear power plant reinforced concrete structures', 328.

Nikbin, I M., Mehdipour, S., Dezhampanah, S., Mohammadi, R., Mohebbi, R., Moghadam, H., et al. (2020). Sadegh mehdipour, soudabeh dezhampanah, reza mohammadi, reza mohebbi, Hamid Habibi moghadam, and ali SadrmomtaziEffect of high temperature on mechanical and gamma ray shielding properties of concrete containing nano-TiO2. *Radiat. Phys. Chem.* 174, 108967. doi:10.1016/j.radphyschem.2020.108967

Ouda, A. S. (2021). A preliminary investigation on gamma-rayattenuation of alkali-activated concrete waste based-geopolymer modified with pozzocrete-fly ash. *Prog. Nucl. Energy* 134, 103681. doi:10.1016/j.pnucene.2021.103681

Ouda, A S. (2015). Development of high-performance heavy density concrete using different aggregates for gamma-ray shielding. *HBRC J.* 11 (3), 328–338. doi:10.1016/j.hbrcj.2014.06.010

Ouda, A S., and Abdel-Gawwad, H A. (2017). The effect of replacing sand by iron slag on physical, mechanical and radiological properties of cement mortar. *HBRC J.* 13 (3), 255–261. doi:10.1016/j.hbrcj.2015.06.005

Powe, A., Szulej, J., and Ogrodnik, P. (2020). Effect of high temperatures on the impact strength of concrete based on recycled aggregate made of Heat-resistant cullet. *Materials* 13 (2), 465–486. doi:10.3390/ma13020465

Sadrmomtazi, A., Sobhani, J., Mirgozar, M. A., and Najimi, M. (2012). Properties of multi-strength grade EPS concrete containing silica fume and rice Husk ash. *Constr. Build. Mater.* 35, 211–219. doi:10.1016/j.conbuildmat.2012.02.049

Sakr, K., and El-Hakim, E. (2005). Effect of high temperature or fire on heavy weight concrete properties. *Cem. Concr. Res.* 35 (3), 590–596. doi:10.1016/j.cemconres.2004.05.023

Shirayama, K. (1963). Properties of radiation shielding concrete'. *ACI J. Proc.* 60 (2). doi:10.14359/7855

Shumuye, E D., Zhao, J., and Wang, Z. (2019). Effect of fire exposure on physico-mechanical and microstructural properties of concrete containing high volume slag cement. *Constr. Build. Mater.* 213, 447–458. doi:10.1016/j.conbuildmat.2019.04.079

Sikora, P., Abd Elrahman, M., Horszczaruk, E., Brzozowski, P., and Stephan, D. (2019). Incorporation of magnetite powder as a cement additive for improving thermal resistance and gamma-ray shielding properties of cement-based composites. *Constr. Build. Mater.* 204, 113–121. doi:10.1016/j.conbuildmat.2019.01.161

Singh, S.l, and Singh, K. (2021). On the use of green concrete composite as a nuclear radiation shielding material. *Prog. Nucl. Energy* 136, 103730. doi:10.1016/j.pnucene.2021.103730

Sivathanu Pillai, C., Santhakumar, A. R., Poonguzhali, A., Pujar, M. G., Ashok Kumar, J., Preetha, R., et al. (2016). Evaluation of microstructural and microchemical aspects of high density concrete exposed to sustained elevated temperature. *Constr. Build. Mater.* 126, 453–465. doi:10.1016/j.conbuildmat.2016.09.053

Sloane, D. J. (1991). Some physical properties of dolerite. *Cercet. Agron. În Mold.* XLIII (1), 17–29. Available at:.

Tekin, H. O., Sayyed, M. I., and Issa, S A. M. (2018). Gamma radiation shielding properties of the Hematite-serpentine concrete blended with WO3 and Bi2O3 micro and nano particles using MCNPX code. *Radiat. Phys. Chem.* 150, 95–100. doi:10.1016/j.radphyschem.2018.05.002

Thomas, C., Rico, J., Tamayo, P., Ballester, F., Setién, J., and Polanco, J. A. (2019). Effect of elevated temperature on the mechanical properties and microstructure of heavy-weight magnetite concrete with steel fibers. *Cem. Concr. Compos.* 103, 80–88. doi:10.1016/j.cemconcomp.2019.04.029

Topçu, I B. (2003). Properties of heavyweight concrete produced with barite. *Cem. Concr. Res.* 33 (6), 815–822. doi:10.1016/S0008-8846(02)01063-3

Yao, Y., Zhang, X., Li, M., Yang, R., Jiang, T., and Lv, J. (2016). Investigation of gamma ray shielding efficiency and mechanical performances of concrete shields containing bismuth oxide as an environmentally friendly additive. *Radiat. Phys. Chem.* 127, 188–193. doi:10.1016/j.radphyschem.2016.06.028

frontiers | Frontiers in Materials

TYPE Original Research
PUBLISHED 20 February 2023
DOI 10.3389/fmats.2023.1110232

OPEN ACCESS

EDITED BY
Cong Zhang,
Jiangnan University, China

REVIEWED BY
Shao-Bo Kang,
Chongqing University, China
Wenbo Gao,
Hong Kong University of Science and Technology (Guangzhou), China
Xiaoqing Xu,
Tongji University, China
YL,
Tongji University, China in collaboration with reviewer XX

*CORRESPONDENCE
Zhichao Zheng,
zhichaozheng1@163.com

SPECIALTY SECTION
This article was submitted to Structural Materials, a section of the journal Frontiers in Materials

RECEIVED 28 November 2022
ACCEPTED 27 January 2023
PUBLISHED 20 February 2023

CITATION
Qin F, Huang Z, Zheng Z, Chou Y, Zou Y and Di J (2023), Analytical model for the load-slip relationship of bearing-shear connectors.
Front. Mater. 10:1110232.
doi: 10.3389/fmats.2023.1110232

Analytical model for the load-slip relationship of bearing-shear connectors

Fengjiang Qin[1], Zhipeng Huang[1], Zhichao Zheng[1]*, Yaling Chou[2], Yang Zou[3] and Jin Di[1]

[1]Key Laboratory of New Technology for Construction of Cities in Mountain Area, School of Civil Engineering, Chongqing University, Chongqing, China, [2]Key Laboratory of Disaster Prevention and Mitigation in Civil Engineering of Lanzhou University of Technology, Lanzhou, China, [3]State Key Laboratory of Mountain Bridge and Tunnel Engineering, Chongqing Jiaotong University, Chongqing, China

The shear behavior of shear connectors in steel-concrete composite structures mainly depends on its load-slip relationship. The load-slip relationship not only reflects the shear capacity and slip capacity of the shear connectors, but also the degradation of shear stiffness during loading. In this study, fifteen push-out tests were carried out to investigate the load-slip relationship of the novel bearing-shear (B-S) connectors, which consist of pressuring-bearing plates and shear plates. Based on push-out tests, the influence of the shape and height of the pressure-bearing plate, and the shear plate shape on the load-slip relationship of the B-S connectors was analyzed. Then, an effective finite element model, validated by push-out tests, was used to study the influence of the concrete strength, and the thickness and tensile strength of the shear plate on the load-slip relationship of B-S connectors. Finally, based on the push-out tests, numerical analysis and theoretical analysis, an analytical model expressing the load-slip relationship of the B-S connectors was proposed.

KEYWORDS

push-out test, numerical analysis, load-slip relationship, stiffness evolution, analytical model

1 Introduction

Prefabricated steel-concrete composite beams have been widely applied to the new construction of composite bridges and the replacement of deteriorated bridges decks due to their advantages of improving the construction quality, speeding up the construction and reducing the impact on the surrounding environment during construction (Shim et al., 2000; Shim et al., 2001). For prefabricated composite beams, shear connectors are usually installed in the shear pockets of the precast concrete decks. To ensure the integrity of the precast concrete decks and to avoid the intersection between the shear connectors and reinforcing bars in the shear pockets, the shear pockets should be as small as possible (Yu, 2020). For prefabricated composite beams with a large shear force at the steel beam-concrete slab interface, the grouped stud connectors need to be densely arranged in the shear pockets, resulting in the spacing between the studs is less than the specification requirements, which would reduce the shear capacity and shear stiffness per stud connector (Yu, 2020). In response to the above problems, Zou et al. (2021) proposed a novel bearing-shear (B-S) connectors to replace the grouped stud connectors in fabricated composite bridges. Figure 1

shows the structure of the B-S connectors and their application in prefabricated composite beams.

According to the theory of partial shear connection, the load of steel-concrete composite beams is redistributed among the concrete slabs, steel beams and shear connectors in the plastic stage (Ranzi et al., 2004; Xue et al., 2008). The composite action of the steel beam and concrete slab in composite structures is directly influenced by the mechanical properties of the shear connectors (Zou et al., 2023; Zou et al., 2023). The shear behavior of shear connectors in composite structures mainly depends on their load-slip relationship. To accurately analyze the ultimate flexural performance of the composite beams, it is necessary to derive the load-slip relationship of the B-S connectors.

Fifteen push-out tests were conducted to analyze the influence of the shape and height of the pressure-bearing plate, and the shear plate shape on the load-slip relationship of the B-S connectors. However, the data obtained from the push-out tests were limited. Thus, an effective 3D finite element (FE) model was established to analyze the influence of the concrete strength, and the thickness and tensile strength of the shear plate on the load-slip relationship of the B-S connectors (Guo et al., 2022; Hosseinpour et al., 2022; Lima et al., 2022; Wang et al., 2022). Then, based on the results of experiments and numerical analysis, the characteristics of the load-slip curves were analyzed mathematically. Finally, an analytical model was suggested to express the load-slip relationship of the B-S connectors.

2 Summary of the push-out tests

2.1 Test specimens

In this study, a total five groups of fifteen push-out specimens were performed to explore the shear behavior of the B-S connectors. These test specimens were manufactured based on the recommendations of Eurocode 4 (EN1992-1-4: Eurocode 4. Design of composite steel and concrete structures, 2004). The B-S connector is processed as follows: As shown in Figure 1A, the B-S connector had a simple structure and was composed of a pressure-bearing plate and a shear plate. The pressure-bearing plate and shear plate are fabricated from easily obtainable conventional steel plate and could be connected by fillet welding without special welding equipment in the factory. The weld leg length of fillet welding was 16 mm. Then, the B-S connectors are welded to the steel beams by full penetration welds.

Figures 2A, B shows the configuration and dimensions of the typical push-out test specimen BS-r20-r120, respectively. The naming rules of the push-out specimen as follows: "BS" represents the B-S connector, "r20" represents the radium of the shear plate as 20; "h120" represents the height of the pressure-bearing plate as 120. Each specimen consists of two precast concrete slabs, two B-S connectors and an H-steel beam. A 20 mm thick steel plate was welded to the top of the H-steel beam to distribute the load from the hydraulic jack. Each precast concrete slab has a shear pocket (120 × 140 mm) for the B-S connector. Such a small space ensures that the shear pocket has no reinforcing bars. After the steel beam and precast concrete slabs were positioned, high-strength non-shrinkage mortar was poured into the shear pocket to connect the precast concrete slabs and steel beam.

2.2 Materials properties

Table 1 presents the mechanical properties of steel and concrete in all push-out tests (Zou et al., 2021). Steel beams and bearing-pressure plates were made of Q345, and shear plates were made of Q420. HRB400 was used in the reinforcing bars. Figure 3A shows the mechanical properties tests of steel and concrete. Steel beams, B-S connectors and reinforcing bars were tested according to GB/T 228-2010 (Metallic materials Tensile testing-Part 1, 2010). Six concrete cube standard samples (150 × 150 × 150 mm) were prepared to test concrete mechanical properties after 28 days of air curing according to GB/T 50107-2010 (Standard for evaluation of concrete compressive strength, 2010).

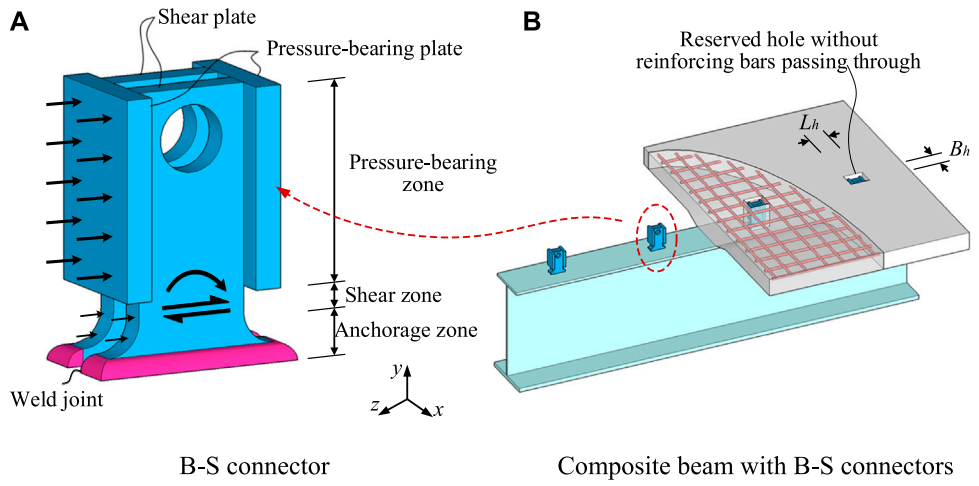

FIGURE 1
Steel-precast concrete slab composite beam structural system (Zou et al., 2021). **(A)** B-S connector. **(B)** Composite beam with B-S connectors.

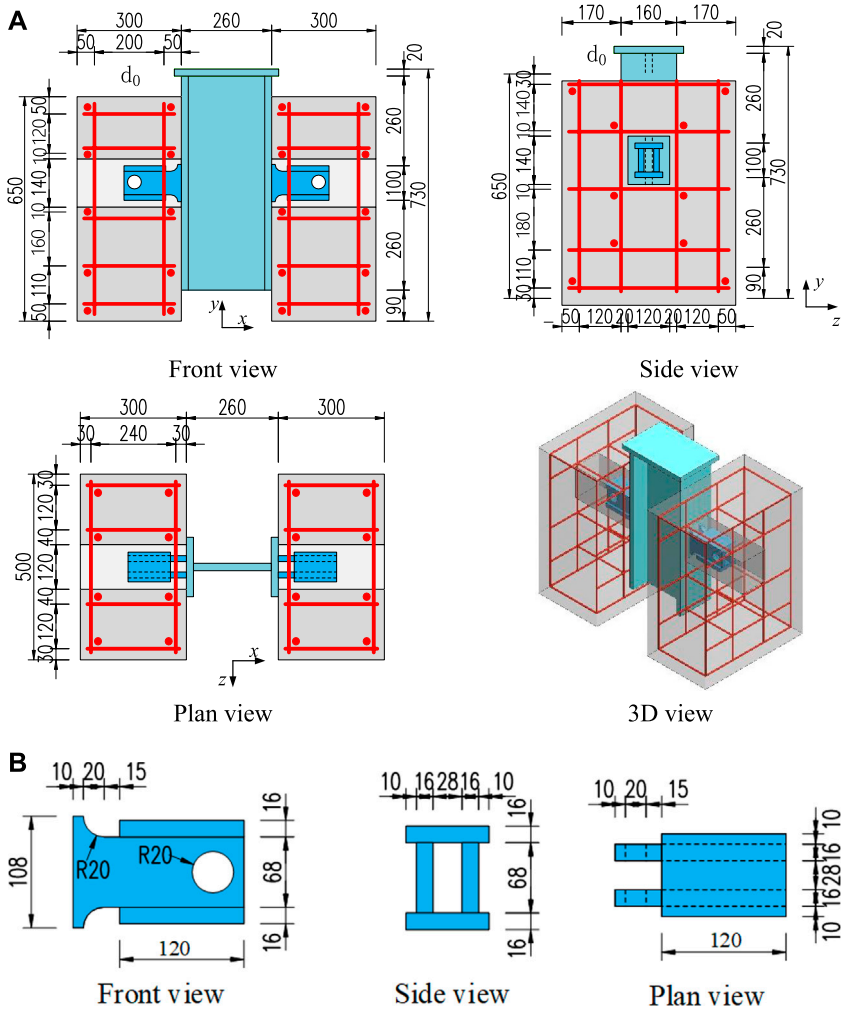

FIGURE 2
(A) Configuration and dimensions of the specimen BS-r20-h120 (mm) (Zou et al., 2021). **(B)** Configuration and dimensions of the connector BS-r20-h120 (mm) (Zou et al., 2021).

TABLE 1 Material properties of concrete and steel (Zou et al., 2021).

Materials	f_{cu} (MPa)	E_c (GPa)	f_y (MPa)	f_u (MPa)	E_s (GPa)
C50	54.4	35.1	—	—	—
Mortar	68.2	34.6	—	—	—
Q345		—	361.3	479.6	200.3
Q420		—	449.6	600.2	201.5
HRB400		—	439.3	577.1	203.7

Where: f_{cu} is the cubic compressive strength of concrete.

2.3 Test setup and instrumentation

As shown in Figure 3B, a total of four LVDTs (Linear Variable Displacement Transducer) were symmetrically arranged on the push-out test specimens and ensured that the four LVDTS and the center of the two B-S connectors were at the same height. Then, the average value of the four displacement meters was taken as the relative slip of at the steel beam-concrete slab interface. The load on the specimens can be recorded directly from the pressure sensor attached to the hydraulic jack.

To meet the requirements of quasi-static static load, in accordance with Eurocode 4 (EN 1992-1-4, Design of composite

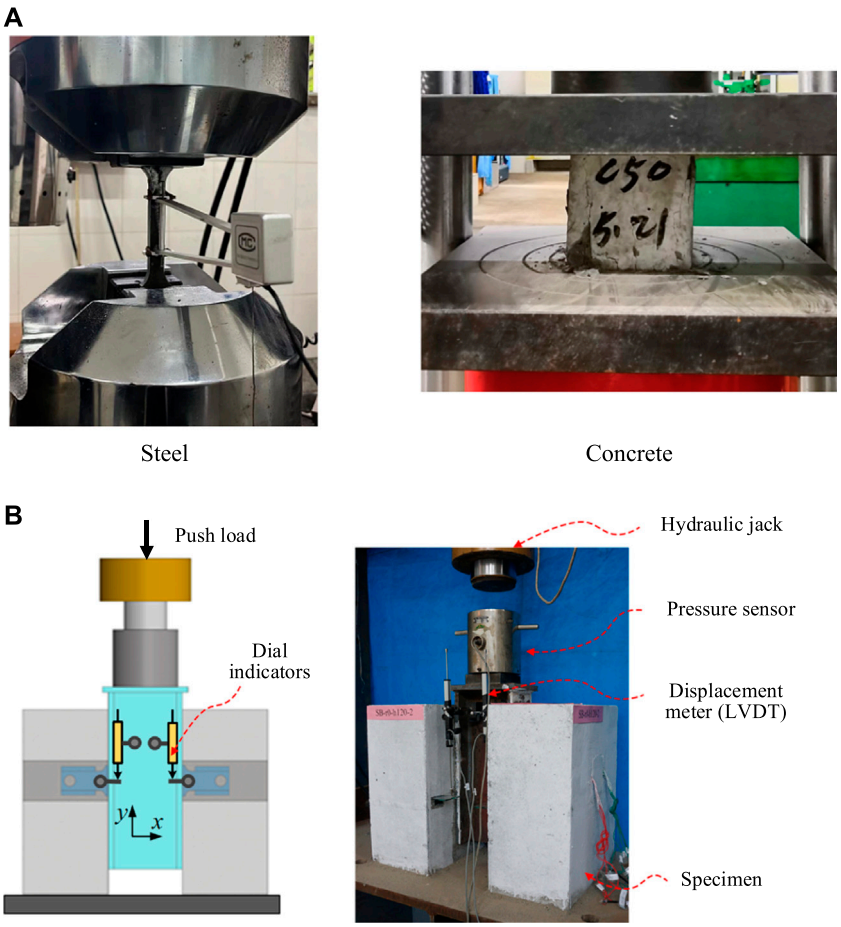

FIGURE 3
(A) Material properties tests. **(B)** Test setup and instrumentation (Zou et al., 2021).

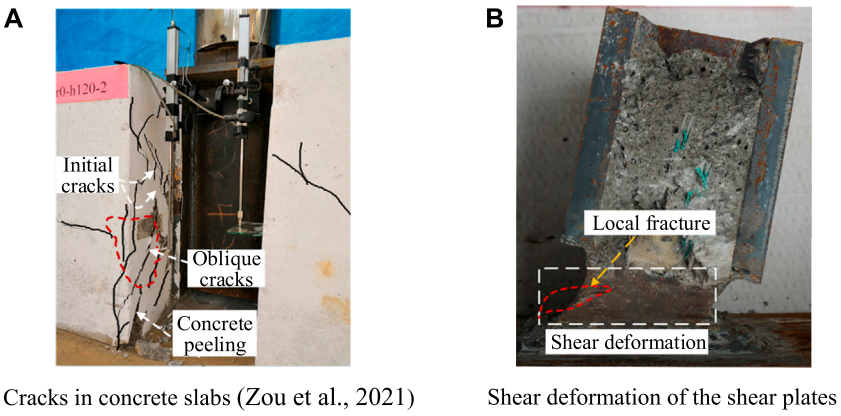

FIGURE 4
Failure modes of push-out test specimen (BS-r20-h120). **(A)** Cracks in concrete slabs (Zou et al., 2021) **(B)** Shear deformation of the shear plates.

steel and concrete structures, 2005), the loading time of each specimen was not less than 15 min. No. 1 specimens of each group were monotonously loaded, and No. 2 and No. 3 specimens of each group were cyclically loaded. The detailed loading protocol can be referred to the previous push-out tests (Zou et al., 2021).

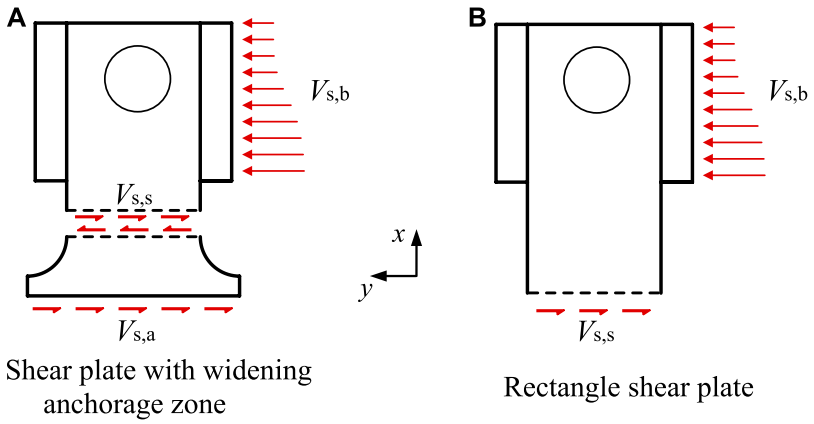

FIGURE 5
Shear mechanism (Zou et al., 2021). **(A)** Shear plate with widening anchorage zone **(B)** Rectangle shear plate.

3 Experiment results

3.1 Failure modes

As shown in Figure 4, the failure modes of the B-S connectors specimens were mainly characterized by the concrete slab splitting and shear failure of the shear plate. Figure 4A shows the cracks distribution of the concrete slabs after tests. The cracks in the concrete slabs first occurred near the B-S connectors and then gradually extended to the top and bottom of the concrete slab. As shown in Figure 4B, significant shear deformation and even a local fracture were observed in the shear plates, whereas no visible deformation was observed in the pressure-bearing plates.

3.2 Shear mechanism

Figure 5 shows the load transfer mechanism of the B-S connectors. When the composite beam is loaded, the pressure-bearing plates transfer the compressive force from the concrete slab to the shear plates, and finally the weld at the root of the shear plates transfers the load to the steel beam. By controlling that the shear zone strength is smaller than that of the anchorage zone and the pressure-bearing zone ($V_{s,s} = \min\{V_{s,b}, V_{z,a}\}$), the shear zone is the first to fail due to large shear deformation, which ensures that the B-S connectors presents an approximately elastic-plastic load-slip curve (Zhu et al., 2018; Zou et al., 2021).

3.3 Load-slip response

As shown in Figure 6, five groups of B-S connectors with different geometric shapes exhibited the similar load-slip curves. The typical load-slip curve of B-S connectors can be separated into three phases: a linear-elastic phase with little relative slip, followed by a non-linear phase with a decreasing slope and ended with a smooth declining phase. The main mechanical characteristics of the B-S connectors include the shear capacity (P_u), shear stiffness (K_s), peak slip (S_u) and ultimate slip ($S_{0.9}$), as presented in Table 2.

3.4 Stiffness evolution

The initial shear stiffness Ks reflects the ability of B-S connectors to resist shear slip deformation at the initial elastic phase, but it does not reflect the stiffness evolution process once the connectors are loaded and plastically deformed. The secant slope P/S of the load-slip curve reflects the continuous stiffness evolution of the B-S connectors. Taking the slip ratio S/S_u as the X-axis, and the stiffness ratio ($K_s/P/S$) as the Y-axis, the relationship between the stiffness ratio ($K_s/P/S$) and the slip ratio (S/S_u) of the B-S connectors was presented in Figure 7. It could be found that the stiffness evolution curves of the five groups of the B-S connectors with different geometric shapes were approximately parabolic in shape.

3.5 Phase identifications

As shown in Figure 8, based on the experimental results, the typical load-slip curve of the B-S connectors can be separated into three phases.

1) Elastic phase

When the relative slip did not exceed the initial slip Si, the load-slip curve followed the linear elastic relationship. Based on the experimental results, the initial slip (S_i) of was about 0.2 mm and the corresponding load was the yield capacity (P_y) (Zheng et al., 2016), which was approximately 30%–40% of the shear capacity (P_u). It indicated that the shear stiffness, determined by the secant modulus corresponding to the relative slip of 0.2 mm in this study, was close to that determined by the secant modulus corresponding to 1/3 Pu in (JCSE, 1996). Greater shear stiffness means that the shear load increases faster as the relative slip increases.

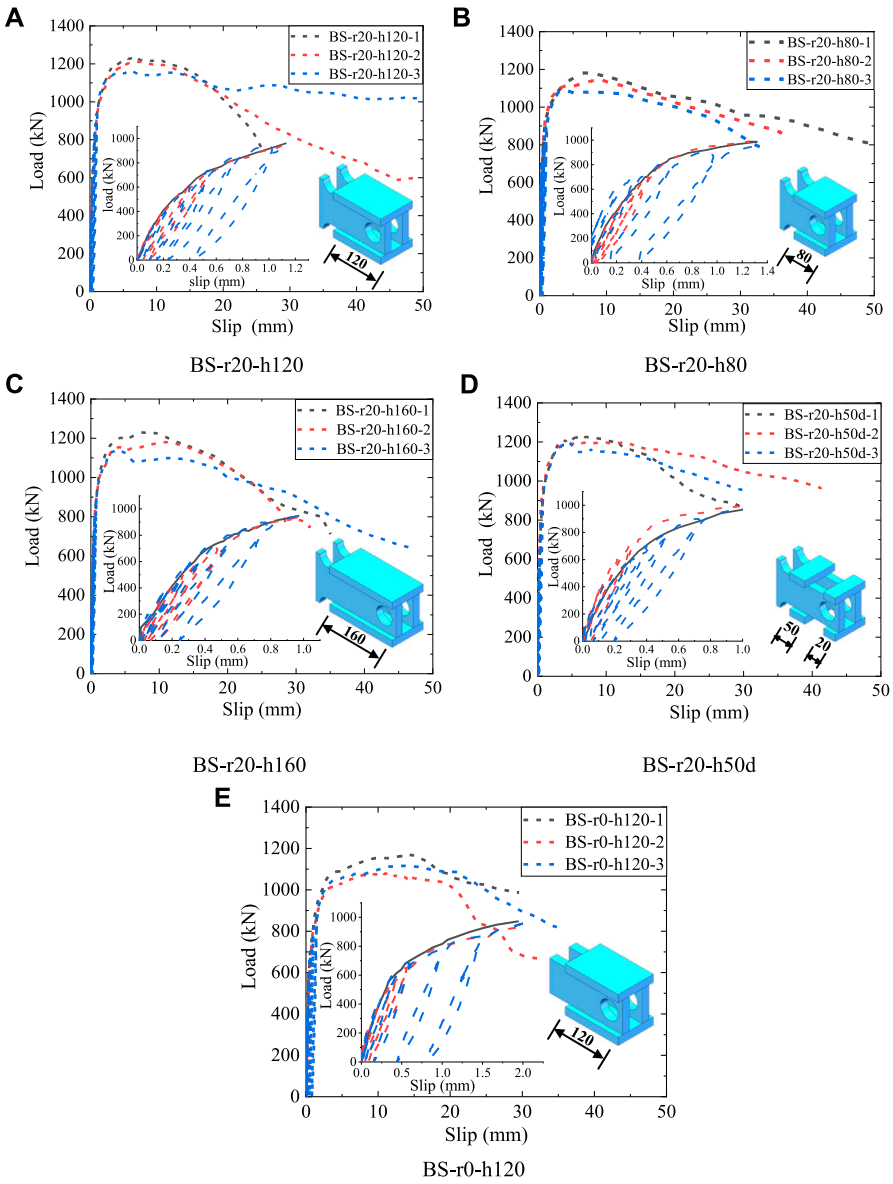

FIGURE 6
Load-slip curves of specimens. **(A)** BS-r20-h120 **(B)** BS-r20-h80 **(C)** BS-r20-h160 **(D)** BS-r20-h50d **(E)** BS-r0-h120.

2) Elastic-plastic phase

In the second non-linear elastic-plastic phase, the shear load continued to increase until the peak load (P_u). The scant modulus (P/S) decreased as the slip (S) increased. The non-linear phase (in the ascending phase) of the load slip-curves revealed plastic deformation in the concrete slabs and the B-S connectors. The unique peak load at this phase was determined as the shear capacity (P_u), and the corresponding slip was determined as the peak slip S_u.

3) Post-failure phase

In the final slowly descending phase, the shear load (P) gradually decreased as the relative slip S increased. As presented in Table 3, the ultimate slip ($S_{0.9}$) ranged from 17.2 mm to 35.0 mm, far exceeding the 6 mm requirements for ductile connections in Eurocode 4 (EN 1992-1-4, Design of composite steel and concrete structures, 2004).

4 Finite element analysis

4.1 Geometry, mesh, and boundary conditions

As shown in Figure 9, due to the biaxial symmetry of the push-out specimens, a quarter FE model was established to reduce the computation time. The FE model consisted of six components: precast concrete slab, post-poured mortar, steel beam, B-S connector, base plate and reinforcing bars. The symmetric boundary conditions “xsymm” and “zsymm” were applied to the

TABLE 2 Experiments results.

Specimens	$P_{u,\ i}$	$P_{u,\ avg}$	$K_{s,\ i}$	$K_{s,\ avg}$	$S_{u,\ i}$	$S_{u,\ avg}$	$S_{0.9,\ i}$	$S_{0.9,\ avg}$
	(kN)	(kN)	(kN/mm)	(kN/mm)	(mm)	(mm)	(mm)	(mm)
BS-r20-h120-1	1,230.0	1,217.4	2076.2	2073.7	6.3	6.5	17.4	23.2
BS-r20-h120-2	1,210.5		2013.7		7.5		17.2	
BS-r20-h120-3	1,162.2		1997.6		5.8		35.0	
BS-r20-h80-1	1,180.9	1,135.8	1987.3	2008.2	6.1	6.2	19.2	20.3
BS-r20-h80-2	1,146.2		2056.6		9.2		19.8	
BS-r20-h80-3	1,089.6		2051		3.3		21.8	
BS-r20-h160-1	1,231.5	1,219.0	2051.2	2060.7	6.9	7.4	18.3	18.9
BS-r20-h160-2	1,180.1		1984.7		11.1		19.1	
BS-r20-h160-3	1,140.9		1927.9		4.1		19.2	
BS-r20-h50d-1	1,228.1	1,216.7	2,142.3	2075.7	7.0	5.8	17.2	21.1
BS-r20-h50d-2	1,198.0		2,165.0		5.9		27.1	
BS-r20-h50d-3	1,197.6		2,125.1		4.5		19.0	
BS-r0-h120-1	1,168.8	1,149.2	1975.4	1940	14.3	13.0	21.2	22.4
BS-r0-h120-2	1,079.2		1928.7		11.1		21.3	
BS-r0-h120-3	1,116.1		1951.6		13.5		24.7	

Where: $S_{0.9}$ is the slip corresponding to a 10% load drop (descending phase).

symmetric Surface X and Surface Z, respectively. The reference point "Fixed point" for the base plate was fixed in all six directions of translation and rotation. An enforced downward displacement was applied to the reference point "Loading point" of the steel beam.

The solid element C3D8R was used to simulate concrete slab, H-steel beam, and post-poured mortar. The truss element T3D2 was used to mesh the reinforcing bars and the discrete rigid element R3D4 was used to mesh the base plate. The numerical model meshed with a global seeds size of 15 mm, and the local seeds size near the B-S connector was 5 mm.

4.2 Analysis method and interaction

The static general solver available in ABAQUS was used to simulate the shear behavior of B-S connectors in push-out tests (ABAQUS, 2014; ABAQUS, 2014). Surface-to-surface contacts were considered between the different components of the push-out tests, which included the concrete slab to the steel beam, the concrete slab to the B-S connector, and the concrete slab to the base plate. "Hard" contact pressure-over closure relationship was considered in the normal direction and "penalty" friction formulation was considered in the tangential direction. The friction coefficient between the concrete slab and steel beam was 0.6 (Guo et al., 2022), and the friction coefficient between the other components was 0.25 (Wang et al., 2022). The reinforcing bars were embedded into the concrete slab.

In addition to surface-to-surface contact, the cohesive contact, which includes the "cohesive behavior" and "damage", was applied to simulate the initial cohesive force between the steel beam flange and the concrete slab (Zou et al., 2023). According to the results of previous research (Nguyen, H. T., and Kim, S. E., 2009) and trial-and-error method, the parameters of "cohesive behavior" were determined as follows: K_{nn} was taken as 0.05 E_{cm}, K_{ss} and K_{tt} were taken as 0.05 G_{cm}, where E_{cm} and G_{cm} are the elastic modulus and shear modulus of concrete, respectively. The quadratic stress criterion was used as the damage initiation criterion of the surface-based cohesive behavior, and the parameters of "damage" were determined as follows: $t_n^0 = 0.05$,, $t_s^0 = t_t^0 = 0.3$, (Qin, 2007; Li et al., 2010), and $\delta_n^F = 0.8$ mm (Nguyen, H. T., and Kim, S. E., 2009).

4.3 Material modeling

4.3.1 Concrete

Concrete Damage Plastic model available in ABAQUS was considered to simulate concrete behavior (ABAQUS, 2014). Figures 10A, B shows the uniaxial behavior of concrete compression and tension, respectively.

The stress-strain curve of concrete compression is separated into three parts. The first part is assumed to be linear elastic where the compressive stress does not exceed 0.4 f_{cm} (Kwon et al., 2010; EN1992-1-2: Eurocode 2-Design of concrete structures, 2004, Design of concrete structures, 2004; Birtel and Mark, 2006; Alfarah et al., 2017):

$$\sigma_{c\ (1)} = E_{cm}\varepsilon_c, \backslash \left(0 \le \sigma_c \le 0.4 f_{cm}\right) \tag{1}$$

Where f_{cm} and E_{cm} are the concrete cylinder compressive strength and the concrete elastic modulus, respectively. $E_{cm} = E_{c0}\alpha_E\left(f_{cm}/10\right)^{1/3}$, $E_{c0} = 21.5$Gpa, $\alpha_E = 1.0$.

The second part of the compressive stress-strain curve is quadratic, where the compressive stress ranges from 0.4 f_{cm} to the peak stress fcm (CEB-FIP, 2010):

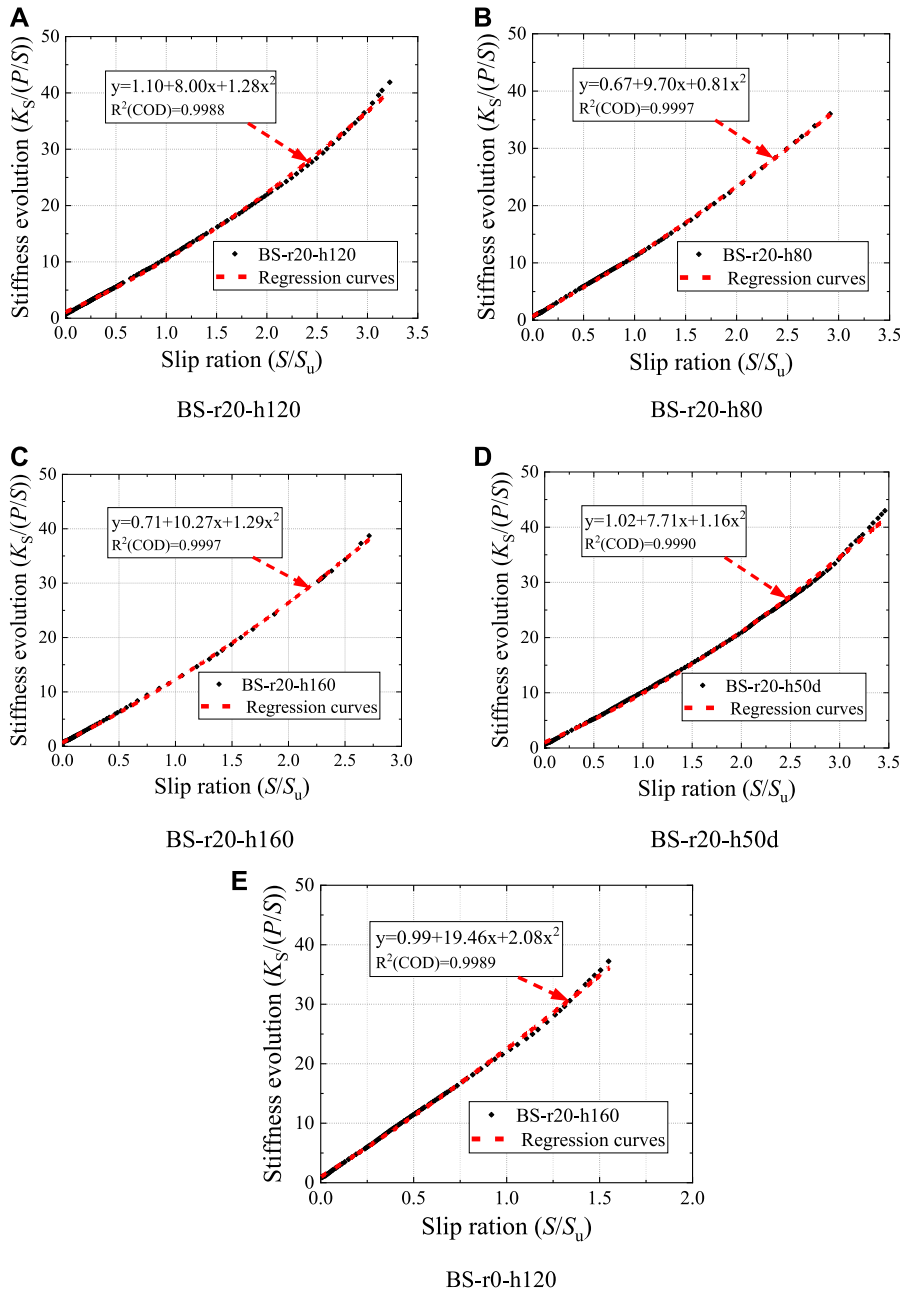

FIGURE 7
Stiffness evolution of specimens. **(A)** BS-r20-h120 **(B)** BS-r20-h80 **(C)** BS-r20-h160 **(D)** BS-r20-h50d **(E)** BS-r0-h120.

$$\sigma_{c\ (2)} = \left(\frac{k\eta - \eta^2}{1 + (k-2)\eta}\right) f_{cm},\ \ (0.4 f_{cm} < \sigma_c \le f_{cm}) \tag{2}$$

In Eq. 2, $k = E_{cm} \cdot \varepsilon_{cm}/f_{cm}; \eta = \varepsilon_c/\varepsilon_{cm} \cdot \varepsilon_{cm}(= 0.0025)$ is the peak strain corresponding to the peak stress f_{cm}.

The third part of the stress-strain curve is a slowly descending branch, which ensures the simulation results are almost independent of the element mesh by introducing a characteristic element length parameter lck (Birtel and Mark, 2006; Alfarah et al., 2017).

$$\sigma_{c\ (3)} = \left(\frac{2 + \gamma_c f_{cm} \varepsilon_{cm}}{2 f_{cm}} - \gamma_c \varepsilon_c + \frac{\varepsilon_c^2 \gamma_c}{2\varepsilon_{cm}}\right)^{-1} \tag{3}$$

$$\gamma_c = \frac{\pi^2 f_{cm} \varepsilon_{cm}}{2\left[\frac{G_{ch}}{l_{ck}} - 0.5 f_{cm}\left(\varepsilon_{cm}(1-b) + b\frac{f_{cm}}{E_0}\right)\right]^2} \tag{4}$$

In Eq. 4, Gch is the crushing energy per unit area, $G_{ch} = (f_{cm}/f_{tm})^2 G_F$; f_{tm} is the concrete tensile strength (Alfarah et al., 2017); G_F 1is the fracture energy per unit area, which is equates to $0.073 f_{cm}^{0.18}$ (N/mm) (CEB-FIP, 2010); l_{ck} is the characteristic element

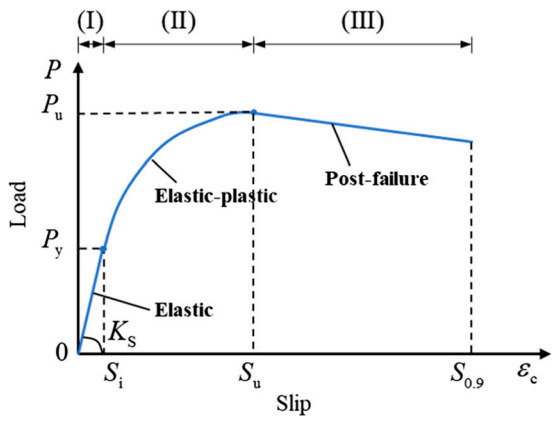

FIGURE 8
Phase identifications.

length, which depends on the element type and mesh size (ABAQUS, 2014); $b = \varepsilon_c^{p1}/\varepsilon_c^{in}$, a value of b is assumed to be 0.7 (Birtel and Mark, 2006).

As shown in Figure 10B, a non-linear stress-crack width relationship was adopted to explain the tensile behavior of concrete, which is given by Birtel and Mark (2006):

$$\frac{\sigma_t}{f_{tm}} = \left[1 + \left(c_1 \frac{w}{w_c}\right)^3\right] \exp\left(-c_2 \frac{w}{w_c}\right) - \frac{w}{w_c}\left(1 + c_1^3\right) \exp\left(-c_2\right) \quad (5)$$

In Eq. 5, w_c, which equates to $5.14G_f/f_{tm}$ (CEB-FIP, 2010), is the cracking width when the tensile stress is zero. The constants are $c_1 = 3$ and $c_2 = 6.93$ (Birtel and Mark, 2006; Alfarah et al., 2017).

Concrete damage coefficients d_c and d_t were expressed as follows (Birtel and Mark 2006):

$$d_c = 1 - \frac{1}{2 + \alpha_c}\left[2\left(1 + \alpha_c\right) \exp\left(-b_c \varepsilon_c^{ch}\right) - \alpha_c \exp\left(-2b_c \varepsilon_c^{ch}\right)\right] \quad (6)$$

$$d_t = 1 - \frac{1}{2 + \alpha_t}\left[2\left(1 + \alpha_t\right) \exp\left(-b_t \varepsilon_t^{ck}\right) - \alpha_t \exp\left(-2b_t \varepsilon_t^{ck}\right)\right] \quad (7)$$

4.3.2 Steel

As shown in Figure 11A, the ideal elastic-plastic model was used to simulate the stress-strain relationship of the steel beam, pressure-bearing plate and reinforcing bars (Ataei and Zeynalian, 2021; Lima et al., 2022). Figure 11B shows the stress-strain relationship of the shear plate (Ataei and Zeynalian, 2021; Guo et al., 2022). Experimental data in Table 1 can be used for the values of elastic modulus (E_s), yield strength (f_y) and ultimate tensile strength (f_u). Based on the material properties tensile tests, the ultimate strain ε_u and fracture strain ε_f of the shear plate were 0.13 and 0.135, respectively.

4.4 Verification of numerical model

The effectiveness of the FE model was verified by comparing the FE analysis results with the push-out tests from four aspects:

TABLE 3 Test results VS. FEM results.

Test specimens	$P_{u,\ test}$ (kN)	$P_{u,\ FEM}$ (kN)	$K_{0.2,\ test}$ (kN/mm)	$K_{0.2,\ FEM}$ (kN/mm)	$\frac{P_{u,test}}{P_{u,FEM}}$	$\frac{K_{0.2,test}}{K_{0.2,FEM}}$
BS-r20-h120-1	1,230.0	1,217.4	2076.2	2073.7	1.01	1.00
BS-r20-h120-2	1,210.5		2013.7		0.99	0.97
BS-r20-h120-3	1,162.2		1997.6		0.95	0.96
BS-r20-h80-1	1,180.9	1,135.8	1987.3	2008.2	1.04	0.99
BS-r20-h80-2	1,146.2		2056.6		1.01	1.02
BS-r20-h80-3	1,089.6		2051		0.96	1.02
BS-r20-h160-1	1,231.5	1,219.0	2051.2	2060.7	1.01	1.00
BS-r20-h160-2	1,180.1		1984.7		0.97	0.96
BS-r20-h160-3	1,140.9		1927.9		0.94	0.94
BS-r20-h50d-1	1,228.1	1,216.7	2,142.3	2075.7	1.02	1.03
BS-r20-h50d-2	1,198		2,165.0		0.94	1.04
BS-r20-h50d-3	1,197.6		2,125.1		0.97	1.02
BS-r0-h120-1	1,168.8	1,149.2	1975.4	1940	1.01	1.02
BS-r0-h120-2	1,079.2		1928.7		0.98	0.99
BS-r0-h120-3	1,116.1		1951.6		0.98	1.01
Mean					0.99	1.00
Standard deviation					0.03	0.03

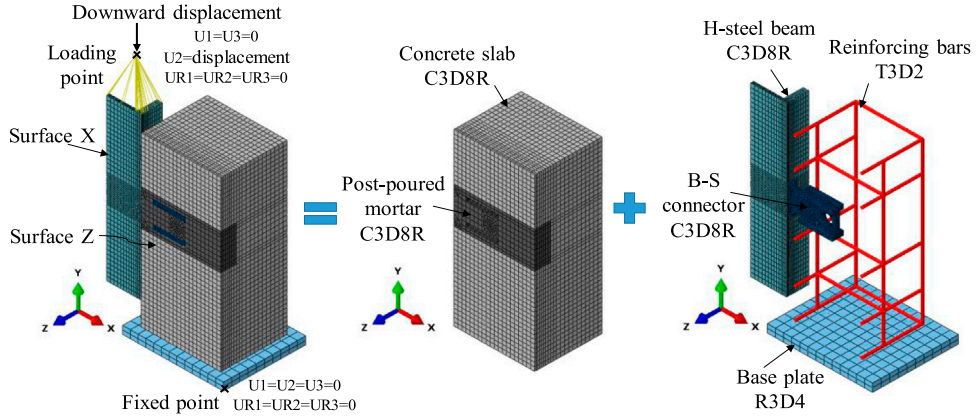

FIGURE 9
FE model and mesh.

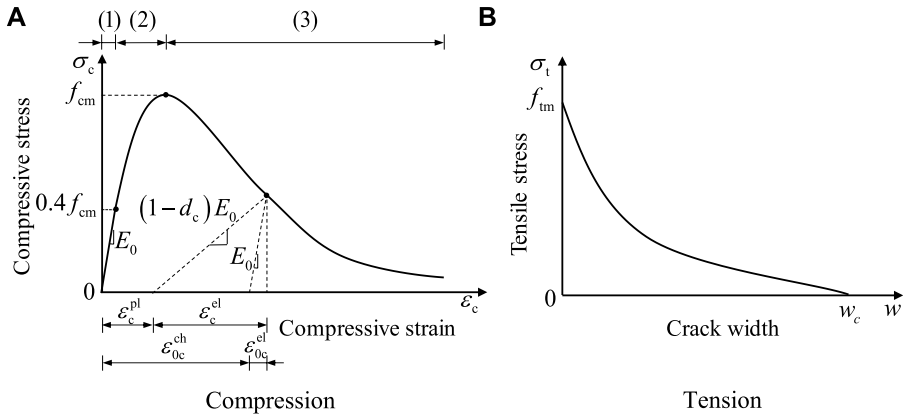

FIGURE 10
Concrete uniaxial behaviour. **(A)** Compression **(B)** Tension.

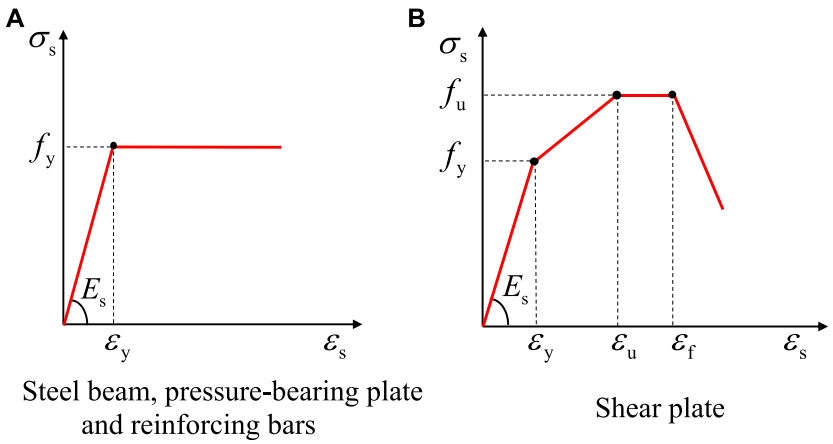

FIGURE 11
Stress-strain relationship of steel. **(A)** Steel beam, pressure-bearing plate and reinforcing bars **(B)** Shear plate.

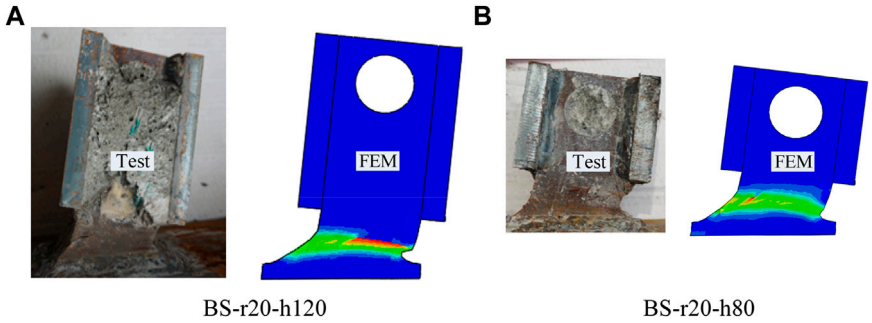

FIGURE 12
Shear deformation of the B-S connectors. **(A)** BS-r20-h120 **(B)** BS-r20-h80.

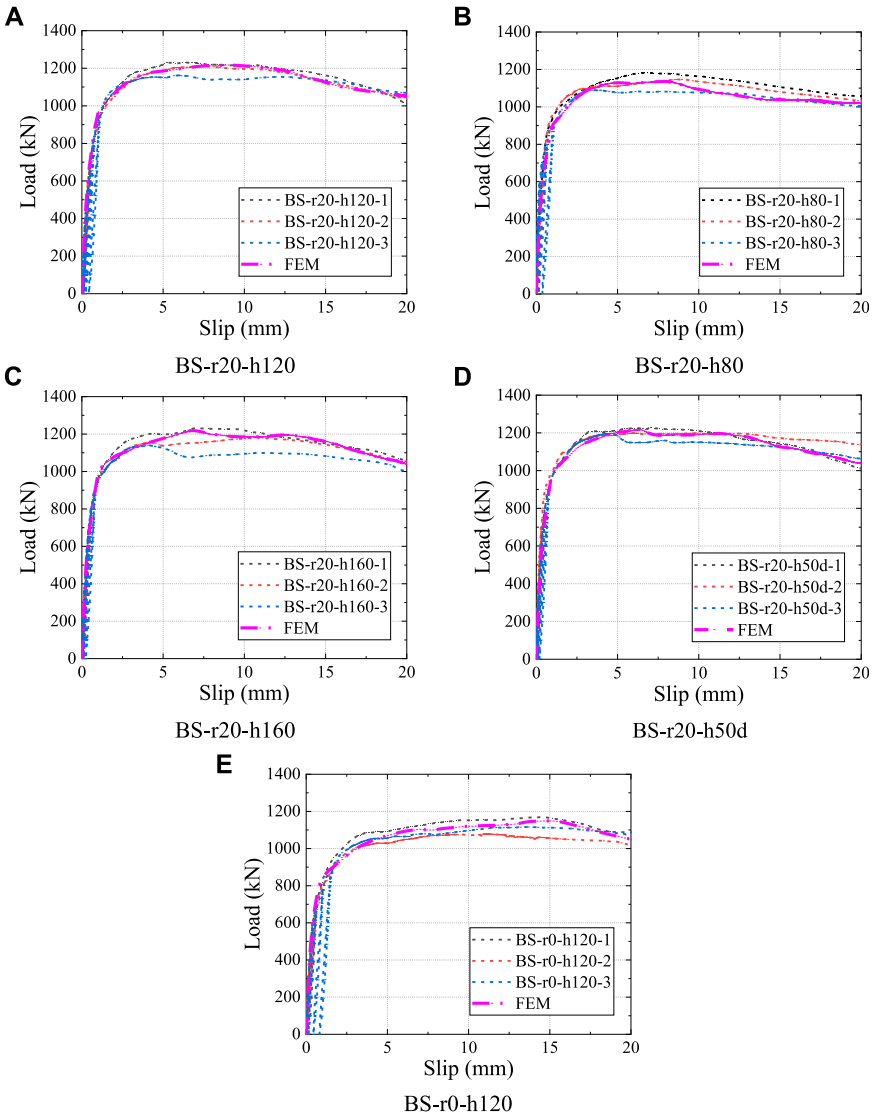

FIGURE 13
Comparison of the load-slip curves. **(A)** BS-r20-h120 **(B)** BS-r20-h80 **(C)** BS-r20-h160 **(D)** BS-r20-h50d **(E)** BS-r0-h120.

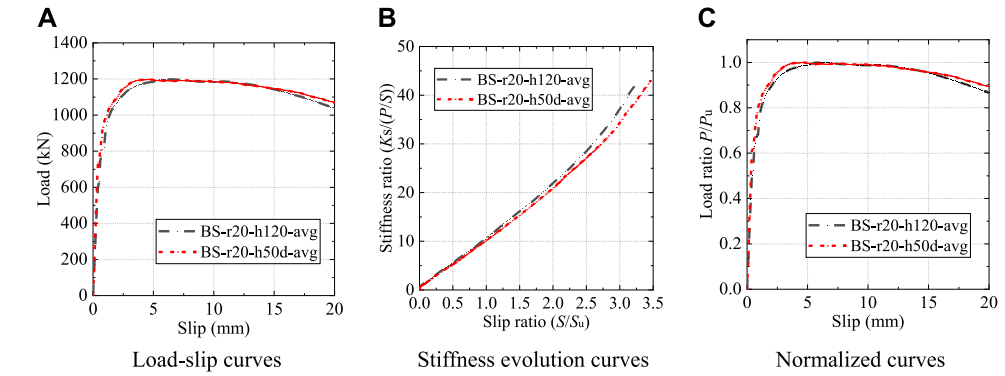

FIGURE 14
Influence of the pressure-bearing plate shape. **(A)** Load-slip curves **(B)** Stiffness evolution curves **(C)** Normalized curves.

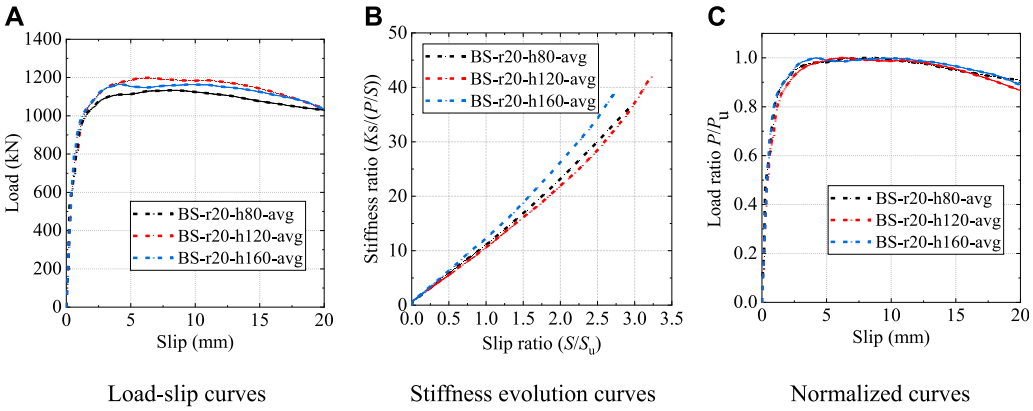

FIGURE 15
Influence of the pressure-baring plate height. **(A)** Load-slip curves **(B)** Stiffness evolution curves **(C)** Normalized curves.

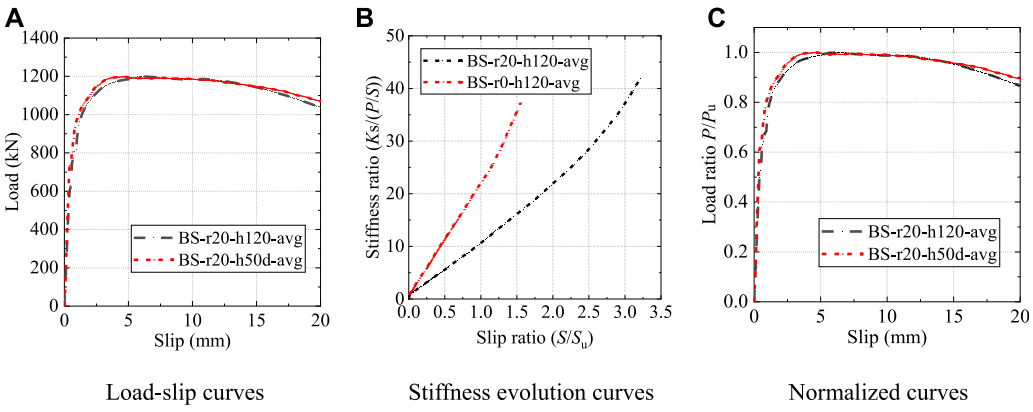

FIGURE 16
Influence of the shear plate shape. **(A)** Load-slip curves **(B)** Stiffness evolution curves **(C)** Normalized curves.

failure modes, load-slip curves, shear capacity and shear stiffness. Figure 12 shows the comparison of the deformation of the B-S connectors in the tests and FE analysis. Both in the push-out tests and FE analysis, the shear plates had a significant shear deformation, whereas the pressure-bearing plates had no obvious deformation. Figure 13 shows the comparison of the

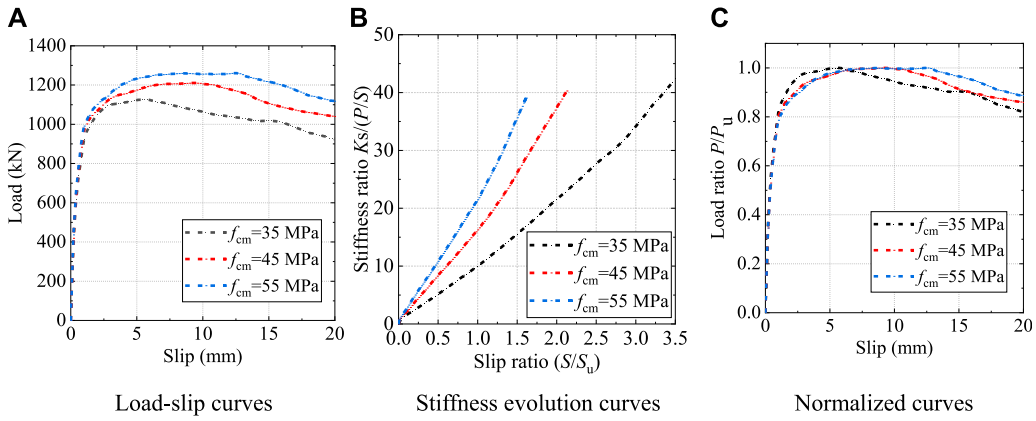

FIGURE 17
Influence of the concrete strength. **(A)** Load-slip curves **(B)** Stiffness evolution curves **(C)** Normalized curves.

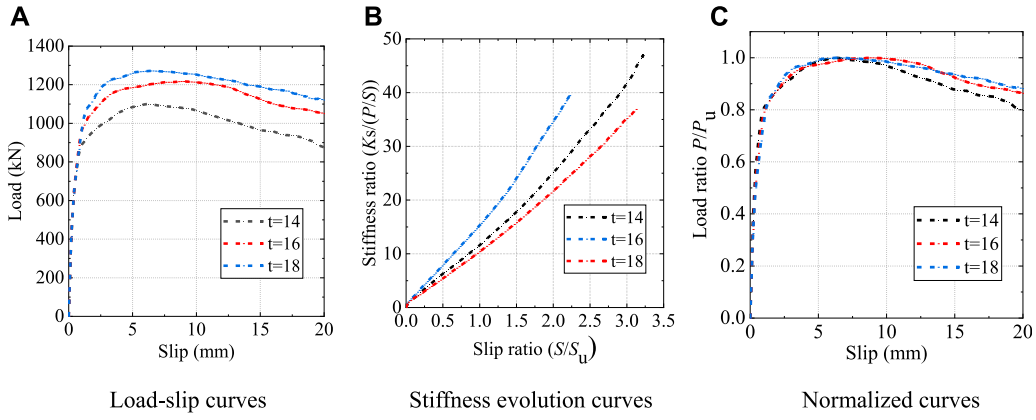

FIGURE 18
Influence of the shear plate thickness. **(A)** Load-slip curves **(B)** Stiffness evolution curves **(C)** Normalized curves.

TABLE 4 Steel properties of the shear plate.

Type of steel	Steel properties		
	E_s (GPa)	f_y (MPa)	f_u (MPa)
Q 390	210	390	490
Q 420	210	420	520
Q 460	210	460	550

load-slip curves obtained from tests and FE analysis. It could be found that the load-slip curves of the FE analysis were very similar to the curves tested.

In addition, Table 3 compares the shear capacity and shear stiffness between the tests and FE analysis. $P_{u,\ test}$ and $P_{u,\ FEM}$ are the shear capacity per B-S connector obtained from push-out tests and FE analysis, respectively. It could be found from Table 3 that the deviation between $P_{u,\ test}$ and $P_{u,\ FEM}$ ranges from −6% to 4%, and the mean value of the $P_{u,\ test}$ and $P_{u,\ FEM}$ is 0.99, with a standard deviation of 0.03. $K_{0.2,\ test}$ and $K_{0.2,\ FEM}$ are the shear stiffness per B-S connector obtained from the push-out tests and FE analysis, respectively. The mean value of the $K_{0.2,\ test}/K_{0.2,\ FEM}$ is 0.99, with a standard deviation of 0.03. From the previous analysis, it can be concluded that the shear behavior of the B-S connectors can be accurately simulated by using the FE model established in this study.

5 Parametric analysis

The load-slip curves of the shear connectors provide a detailed information on their shear behavior, including shear capacity, shear stiffness and slip capacity. To facilitate the comparison of the shear behavior between different shear connectors, the load-slip relationship can be presented in various ways, such as load-slip curves, stiffness evolution curves and normalized load-slip curves.

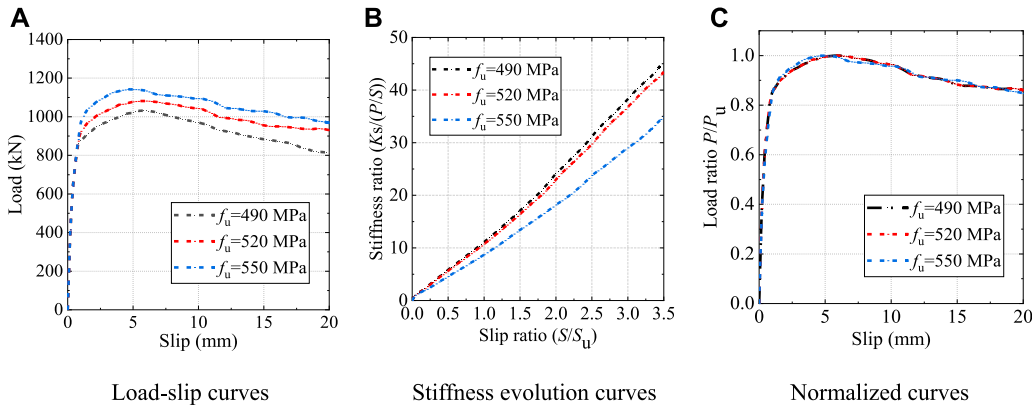

FIGURE 19
Influence of the shear plate tensile strength. **(A)** Load-slip curves **(B)** Stiffness evolution curves **(C)** Normalized curves.

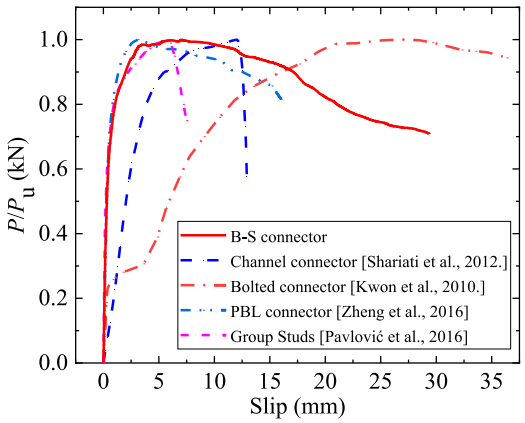

FIGURE 20
Normalized load-slip curves.

Based on the results of experiments and FE parametric analysis, six parameters that influence the load-slip relationship of the B-S connectors were studied in this section.

5.1 Parametric analysis based on the push-out tests

5.1.1 Influence of the pressure-bearing plate shape

Figure 14 shows the load-slip relationship of the B-S connectors with different pressure-bearing plate shapes. It could be found that the load-slip curves of specimen BS-r20-h120 and BS-r20-h50d almost coincided with each other, which indicates that the shape of the two pressure-bearing plates had little influence on the load-slip relationship of the B-S connectors.

5.1.2 Influence of the pressure-bearing plate height

Figure 15 shows the load-slip relationship of the B-S connectors with different pressure-bearing plate heights. When the pressure-bearing plate height changed from 80 mm to 120 mm and 160 mm, the shear capacity P_u increased by 5.4% and 4.0%, respectively. Despite the change in the height of pressure-bearing plate, the shear stiffness of B-S connectors gradually decreased with the increase of slip. It could be seen from Figure 15C that the height of the pressure-bearing plate had a negligible influence on the trends of the normalized load-slip curves.

5.1.3 Influence of the shear plate shape

As shown in Figure 16, the shear plate shape had a significant influence on the behavior of the B-S connectors. The root of the shear plate of specimen BS-r0-h120 was not locally widened, as shown in Figure 6E. Compared to the specimen BS-r20-h120, the shear capacity of the specimen BS-r0-h120 was reduced by 6.6%, and the shear stiffness was significantly reduced in the elastic-plastic phase. However, despite the varying shear plate shape, the stiffness of the B-S connectors gradually decreased with increasing slip. The normalized load-slip curves of the two B-S connectors with different shear plate shapes had the similar patterns.

5.2 Parametric analysis based on the numerical modeling

The numerical model, verified by the push-out tests, was used for the parametric study to analyze the influence of the cylinder compressive strength of concrete (35, 45, 55 MPa), and the thickness (14, 16, and 18 mm), the tensile strength (470, 490, 520 MPa) of shear plate on the shear behavior of the B-S connectors.

5.2.1 Influence of the concrete strength

As shown in Figure 17, the concrete strength had a significant influence on the shear behavior of the B-S connectors. When the concrete strength changed from 35 MPa to 45 MPa and 55 MPa, the shear capacity Pu increased by 1.6% and 3.1%, and the peak slip (S_u) increased 67.9% and 121.4%, respectively. Despite the varying of concrete strength, the stiffness of the B-S connectors

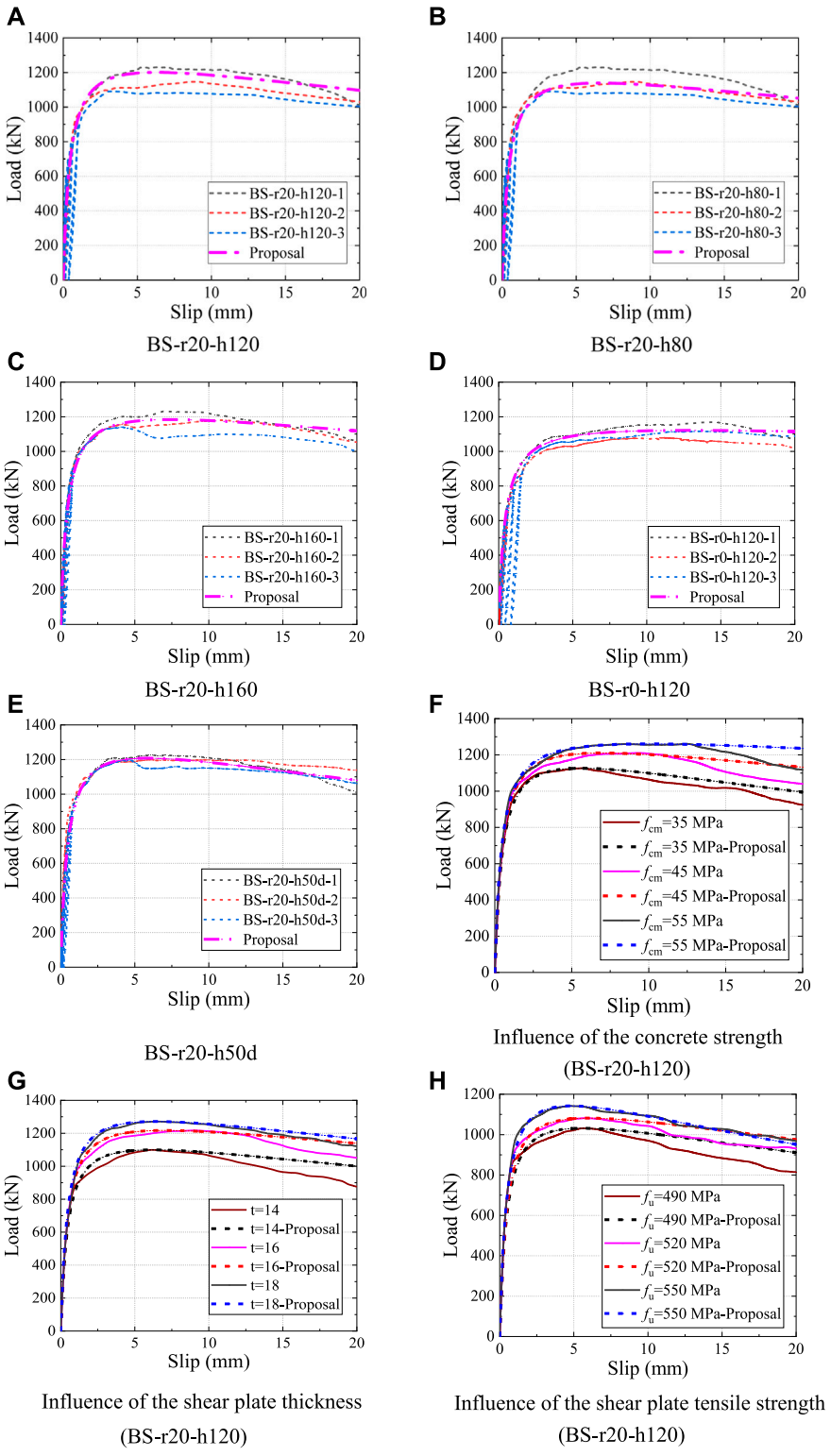

FIGURE 21
Predicted and tested load-slip curves. **(A)** BS-r20-h120 **(B)** BS-r20-h80 **(C)** BS-r20-h160 **(D)** BS-r0-h120 **(E)** BS-r20-h50d **(F)** Influence of the concrete strength (BS-r20-h120) **(G)** Influence of the shear plate thickness (BS-r20-h120) **(H)**Influence of the shear plate tensile strength (BS-r20-h120).

gradually decreased with the increase of the slip. The normalized load-slip curves with different concrete strengths exhibited the similar trends.

5.2.2 Influence of the shear plate thickness

As shown in Figure 18, the shear plate thickness had a significant influence on the shear behavior of the B-S

connectors. When the shear plate thickness changed from 14 mm to 16 mm and 18 mm, the shear capacity increased by 10.7% and 15.7%, and the peak slip S_u increased by 45.1% and 3.2%, respectively. Despite the variation of the shear plate thickness, the stiffness of the B-S connectors gradually decreased as the relative slip increased, and the normalized load-slip curves also exhibited the similar trends.

5.2.3 Influence of the shear plate tensile strength

As presented in Table 4, three types of structural steels were chosen for parametric study according to GB 50017-2017 (Standard for design of steel structures, 2017). Figure 19 shows the load-slip relationship of the B-S connectors with different shear plate tensile strength. It could be found that the shear plate tensile strength had a significant influence on the shear behavior of the B-S connectors. The shear capacity increased by 3.8% and 8.9%, and the peak slip S_u reduced by 9.6% and 3.2% when the shear plate tensile strength changed from 490 MPa to 520 MPa and 550 MPa, respectively. Regardless of the differences in the shear plate tensile strength, the stiffness of the B-S connectors gradually decreased as the slip increased, and the normalized load-slip curves also exhibited the similar trends.

6 Analytical model

The normalized load-slip curve is often used to compare the shear behavior of various shear connectors (Zou et al., 2021). Figure 20 shows the normalized load-slip curves of the common shear connectors. It could be found that the curves for the B-S connector and the PBL connector exhibit similar patterns, and both of them have three obvious phases: linear elastic phase, non-linear elastic-plastic phase and a slowly descending phase. Particularly in the descending phase, unlike other types of shear connectors, the load of the both types of connectors gradually decrease as the slip increases. Therefore, this study refers to the load-slip relationship of the PBL connector to establish the analytical model of the B-S connector (Zheng et al., 2018).

Based on the stiffness evolution curves of the B-S connectors discussed in Section 3.4, the stiffness ratio ($K_s/(P/S)$) increased as the slip ratio (S/S_u) increased. As illustrated in Figure 7, the fitting analysis of the stiffness evolution curves showed that the mean value of COD (Coefficient of determination) of the quadratic fitting was 0.998, which fully indicated that the relationship between stiffness ratio ($K_s/(P/S)$) and slip ratio (S/S_u) can be expressed by a quadratic expression 8).

$$K_s/(P/S) = C_1 + C_2(S/S_u) + C_3(S/S_u)^2 \tag{8}$$

In Eq. 8, C_1, C_2, and C_3 are the non-dimensional parameters which could be derived from the boundary conditions of the load-slip curves. The Eq. 8 expressing the load-slip relationship of the B-S connectors can be simplified into Eq. 9.

$$P = K_s \frac{S}{C_1 + C_2(S/S_u) + C_3(S/S_u)^2} \tag{9}$$

The first derivative of Eq. 9 represents the tangent slope of the load-slip curves:

$$\frac{dP}{dS} = K_s \frac{C_1 - C_3(S/S_u)^2}{\left[C_1 + C_2(S/S_u) + C_3(S/S_u)^2\right]^2} \tag{10}$$

According to the characteristics of the load-slip curves in push-out tests and numerical analysis, the load-slip relationship of the B-S connectors should satisfy the following two boundary conditions.

$$P\big|_{S=S_u} = P_u \tag{11}$$

$$\frac{dP_u}{dS}\Big|_{S=S_u} = 0 \tag{12}$$

Substituting Eq. 9 and Eq. 10, which represent the boundary conditions, into Eq. 11 and Eq. 12, the unknown parameters C_1, C_2 and C_3 should meet the following requirements.

$$C_1 = C_3 \tag{13}$$

$$C_2 = K_s S_u/P_u - 2C_1 \tag{14}$$

Substituting Eq. 13 and Eq. 14 into Eq. 9, the analytical expression of load-slip curves can be simplified to an equation with only one unknown parameter C1.

$$P = K_s \frac{S}{C_1(1 - S/S_u)^2 + K_s S/P_u} \tag{15}$$

According to Eq. 15, non-linear regression analysis was conducted on the results of the push-out tests and FE analysis, and the best fitting value of the unknown parameter C_1 was determined to be 0.8.

$$P = K_s \frac{S}{0.8(1 - S/S_u)^2 + K_s S/P_u} \tag{16}$$

The shear stiffness (K_s) in Eq. 16 is the secant slope corresponding to the relative slip of 0.2 mm in the load-slip curves. Based on the results of the push-out tests and FE analysis, the shear load corresponding to the relative slip of 0.2 mm was about 0.37 P_u. Therefore, the shear stiffness in Eq. 16 can be expressed as follows.

$$K_s = 0.37\ V_u/S_i \tag{17}$$

Finally, the Eq. 17 was substituted into Eq. 16, and the load-slip relationship of the B-S connectors can be expressed as Eq. 18.

$$P = \frac{P_u}{1 + (0.4/S)(1 - S/S_u)^2} \tag{18}$$

Figures 21A–H show the comparison of the predicted load-slip curves with the load-slip curves obtained from the push-out tests and numerical analysis, respectively. It could be found that the proposed analytical expression agrees well with the results of experiments and numerical analysis.

7 Conclusion

Push-out tests and numerical analysis were performed to investigate the shear behavior of the B-S connectors in prefabricated steel-concrete composite structures. Based on the

push-out tests, FE analysis and theoretical analysis, the following conclusion can be drawn.

1) The failure modes of the B-S connectors specimens were mainly characterized by the concrete slabs splitting and shear failure of the shear plates.
2) The shape, thickness and tensile strength of the shear plate and the concrete strength significantly influenced the shear behavior of the B-S connectors, but the normalized load-slip curves with these different parameters exhibited the similar trends.
3) The typical load-slip curve of the B-S connectors can be obviously separated into three phases: starting with a linear elastic phase with little slip, followed by an elastic-plastic phase with a decreasing slope, and ending with a slow descending phase.
4) The typical load-slip curve of the B-S connectors contains five key characteristic parameters, including shear stiffness (K_s), initial slip (S_i), peak slip (S_u), peak load (P_u), and ultimate slip ($S_{0.9}$). These five characteristic parameters with specific physical meaning are used to establish the analytical model of the load-slip relationship of the B-S connectors.
5) According to the push-out tests, FE analysis and theoretical analysis, an analytical model was suggested to express the load-slip relationship of the B-S connectors. The analytical model agrees well with the results of push-out tests and FE analysis, indicating that this expression can accurately predict the non-linear behavior of the B-S connectors.

Data availability statement

The raw data supporting the conclusions of this article will be made available by the authors, without undue reservation.

Author contributions

FQ: Software, Validation, Writing. Supervision. ZH: Writing-review and editing. ZZ: Investigation, Review. YC: Supervision, Review. YZ: Supervision, Review. JD: Investigation.

Funding

The authors express their sincere gratitude for the financial support provided by the National Natural Science Foundation of China (No. 52078081), Chongqing Technology Innovation and Application Development Project (No. cstc2020jscx-msxmX0079, CSTB2022TIAD-KPX0103), the Natural Science Foundation of Chongqing (No. cstc2021jcyj-msxmX0937), and the Fundamental Research Funds for the Central Universities (No. 2022CDJKYJH006).

Conflict of interest

The authors declare that the research was conducted in the absence of any commercial or financial relationships that could be construed as a potential conflict of interest.

Publisher's note

All claims expressed in this article are solely those of the authors and do not necessarily represent those of their affiliated organizations, or those of the publisher, the editors and the reviewers. Any product that may be evaluated in this article, or claim that may be made by its manufacturer, is not guaranteed or endorsed by the publisher.

References

Abaqus, Software (2014). *Software version 6.14-5*. Providence, RI, USA: Dassault Systemes Simulia Corp.

ABAQUS (2014). *Theory manual, version 6.14-5*. Providence, RI, USA: Dassault Systemes Simulia Corp.

Alfarah, B., López-Almansa, F., and Oller, S. (2017). New methodology for calculating damage variables evolution in Plastic Damage Model for RC structures. *Eng. Struct.* 132, 70–86. doi:10.1016/j.engstruct.2016.11.022

Ataei, A., and Zeynalian, M. (2021). A study on structural performance of deconstructable bolted shear connectors in composite beams. *Structures* 29, 519–533. doi:10.1016/j.istruc.2020.11.065

Birtel, V., and Mark, P. (2006). Parameterised finite element modelling of RC beam shear failure. ABAQUS users' conference (Bochum, Germany: Universitätsstr).

Ceb-Fip (2010). *Model code 2010*. London: Thomas Telford.

EN1992-1-2: Eurocode 2-Design of concrete structures (2004). *EN1992-1-2: Eurocode 2-Design of concrete structures. Part 1-1: General rules and rules for buildings*. Brussels, Belgium: European Committee for Standardization CEN.

EN1992-1-4: Eurocode 4. Design of composite steel and concrete structures (2004). *EN1992-1-4: Eurocode 4. Design of composite steel and concrete structures. Part 1.1: General rules and rules for buildings*. Brussels, Belgium: European Committee for Standardization CEN.

GB 50017- (2017). *Standard for design of steel structures*. Beijing, China: China Architecture and Building press.

GB/T 228-2010 (2010). *Metallic materials Tensile testing-Part 1: Method of test at room temperature*. Beijing: Standardization Administration of the P.R.C. (In Chinese).

GB/T 50107-2010 (2010). *Standard for evaluation of concrete compressive strength*. Beijing: Ministry of Housing and Urban-Rural Development of the People's Republic of China. (In Chinese).

Guo, J., Zhou, Z., Zou, Y., Zhang, Z., Jiang, J., and Wang, X. (2022). Static behavior of novel shear connectors with post-poured UHPC for prefabricated composite bridge. *Structures* 43, 1114–1133. doi:10.1016/j.istruc.2022.06.061

Hosseinpour, M., Zeynalian, M., Daei, M., and Ataei, A. (2022). Numerical study on behavior of bolted shear connector used in composite cold-formed steel beams. *Thin-Walled Struct.* 177, 109377. doi:10.1016/j.tws.2022.109377

JSCE (Japan Society of Civil Engineers) (1996). *Standard on push-out test for headed stud*. Tokyo: JSCE.

Kwon, G., Engelhardt, M. D., and Klingner, R. E. (2010). Behavior of post-installed shear connectors under static and fatigue loading. *J. Constr. Steel Res.* 66 (4), 532–541. doi:10.1016/j.jcsr.2009.09.012

Li, H., Liu, B., Wu, B., and Ma, H. (2010). Failure mechanism study on the bond-slip between T section steel and concrete in SRC structures. *Sichuan Build. Sci.* (5), 45–48. (In Chinese).

Lima, J. M., Bezerra, L. M., Bonilla, J., and Barbosa, W. C. (2022). Study of the behavior and resistance of right-angle truss shear connector for composite steel concrete beams. *Eng. Struct.* 253, 113778. doi:10.1016/j.engstruct.2021.113778

Nguyen, H. T., and Kim, S. E. (2009). Finite element modeling of push-out tests for large stud shear connectors. *J. Constr. Steel Res.* 65 (10-11), 1909–1920. doi:10.1016/j.jcsr.2009.06.010

Pavlović, M., Spremić, M., Marković, Z., and Veljković, M. (2016). Headed shear studs versus high-strength bolts in prefabricated composite decks. *Compos. Constr. Steel Concr.* 7, 687–702. doi:10.1061/9780784479735.052

Qin, Y. (2007). *Analysis bond-slip of the steel reinforce concrete structure by nonlinear finite element*. China: Xi'an University of Technology.

Ranzi, G., Bradford, M. A., and Uy, B. (2004). A direct stiffness analysis of a composite beam with partial interaction. *Int. J. Numer. Methods Eng.* 61 (5), 657–672. doi:10.1002/nme.1091

Shariati, M., Sulong, N. R., and Khanouki, M. A. (2012). Experimental assessment of channel shear connectors under monotonic and fully reversed cyclic loading in high strength concrete. *Mater. Des.* 34, 325–331. doi:10.1016/j.matdes.2011.08.008

Shim, C. S., Kim, J., Chang, S. P., and Chung, C. H. (2000). The behaviour of shear connections in a composite beam with a full-depth precast slab. *Proc. Institution Civ. Engineers-Structures Build.* 140 (1), 101–110. doi:10.1680/stbu.2000.140.1.101

Shim, C. S., Lee, P. G., and Chang, S. P. (2001). Design of shear connection in composite steel and concrete bridges with precast decks. *J. Constr. Steel Res.* 57 (3), 203–219. doi:10.1016/S0143-974X(00)00018-3

Wang, S., Fang, Z., Ma, Y., Jiang, H., and Zhao, G. (2022). Parametric investigations on shear behavior of perforated transverse angle connectors in steel–concrete composite bridges. *Structures* 38, 416–434. doi:10.1016/j.istruc.2022.01.015

Xue, W., Ding, M., Wang, H., and Luo, Z. (2008). Static behavior and theoretical model of stud shear connectors. *J. bridge Eng.* 13 (6), 623–634. doi:10.1061/(asce)1084-0702(2008)13:6(623)

Yu, J. (2020). *Study on mechanical behavior of assembled steel concrete composite beams with group stud and steel block connections*. Chongqing, China: Chongqing University.

Zheng, S., Liu, Y., Yoda, T., and Lin, W. (2016). Parametric study on shear capacity of circular-hole and long-hole perfobond shear connector. *J. Constr. Steel Res.* 117, 64–80. doi:10.1016/j.jcsr.2015.09.012

Zheng, S., Zhao, C., and Liu, Y. (2018). Analytical model for load–slip relationship of perfobond shear connector based on push-out test. *Materials* 12 (1), 29. doi:10.3390/ma12010029

Zhu, B., Wang, T., and Zhang, L. (2018). Quasi-static test of assembled steel shear panel dampers with optimized shapes. *Eng. Struct.* 172, 346–357. doi:10.1016/j.engstruct.2018.06.004

Zou, Y., Jiang, J. L., Yang, J., Zhang, Z. Y., and Guo, J. C. (2023). Enhancing the toughness of bonding interface in steel-UHPC composite structure through fiber bridging. *Cem. Concr. Compos.* 137, 104947. doi:10.1016/j.cemconcomp.2023.104947

Zou, Y., Qin, F., Zhou, J., Zheng, Z., Huang, Z., and Zhang, Z. (2021). Shear behavior of a novel bearing-shear connector for prefabricated concrete decks. *Constr. Build. Mater.* 268, 121090. doi:10.1016/j.conbuildmat.2020.121090

Zou, Y., Qin, F., Zhou, J., Zhang, Z., Huang, Z., and Zhang, Z. (2021). Shear behavior of a novel bearing-shear connector for prefabricated concrete decks. *Constr. Build Mater* 268, 121090. doi:10.1016/j.conbuildmat.2020.121090

Zou, Y., Zheng, K., Zhou, Z., Zhang, Z., Guo, J., and Jiang, J. (2023). Experimental study on flexural behavior of hollow steel-UHPC composite bridge deck. *Eng. Struct.* 274, 115087. doi:10.1016/j.engstruct.2022.115087

frontiers | Frontiers in Materials

TYPE Original Research
PUBLISHED 03 April 2023
DOI 10.3389/fmats.2023.1153421

OPEN ACCESS

EDITED BY
Zhigang Zhang,
Chongqing University, China

REVIEWED BY
Shaker Qaidi,
University of Duhok, Iraq
Hadee Mohammed Najm,
Aligarh Muslim University, India

*CORRESPONDENCE
Ahmed Deifalla,
Ahmed.deifalla@fue.edu.eg
Taha Elsayed,
taha.ibrahim@feng.bu.edu.eg

SPECIALTY SECTION
This article was submitted to Structural Materials, a section of the journal Frontiers in Materials

RECEIVED 29 January 2023
ACCEPTED 06 March 2023
PUBLISHED 03 April 2023

CITATION
Gasser M, Mahmoud O, Elsayed T and Deifalla A (2023), Reliable machine learning for the shear strength of beams strengthened using externally bonded FRP jackets.
Front. Mater. 10:1153421.
doi: 10.3389/fmats.2023.1153421

Reliable machine learning for the shear strength of beams strengthened using externally bonded FRP jackets

Moamen Gasser[1], Omar Mahmoud[2], Taha Elsayed[3]* and Ahmed Deifalla[2]*

[1]Harold Vance Department of Petroleum Engineering, Texas A&M University, Texas, TX, United States, [2]Faculty of Engineering and Technology, Future University in Egypt, New Cairo, Egypt, [3]Department of Structural Engineering, Shoubra Faculty of Engineering, Benha University, Cairo, Egypt

All over the world, shear strengthening of reinforced concrete elements using external fiber-reinforced polymer jackets could be used to improve building sustainability. However, reports issued by the American Concrete Institute called for heavy scrutiny before actual field implementation. The very limited number of proposed shear equations lacks reliability and accuracy. Thus, further investigation in this area is needed. In addition, machine-learning techniques are being implemented successfully to develop strength models for complex problems including shear, flexure, and torsion. This study aims to provide a reliable machine-learning model for reinforced concrete beams strengthened in shear using externally reinforced fiber polymer sheets. The proposed model was developed and validated against the experimental database and the very limited models in existing literature. The model showed better agreement with the experimentally measured strength compared to the previous models, which accounted for the effect of various parameters including but not limited to: the element geometry, strengthening details, and configurations. The model could guide the further developments of design codes and mechanical models.

KEYWORDS

shear strength, FRP, anchorage devices, effective FRP strain., reliable machine learning

1 Introduction

The significant shear acts upon reinforced concrete (RC) elements in many buildings. Various shear failures of RC buildings have been reported in previous research papers (Whittle, 2013). The shear failure of RC beams is brittle (Chalioris and Karayiannis, 2009; Karayannis et al., 2018; Deifalla et al., 2020a; Deifalla et al., 2020b), and the elevated cost of replacing infrastructure has driven research into strengthening techniques. Shear strength is vital in many projects (Gosbell and Meggs, 2002; FIB. FRP Reinforcement in RC Structures, 2007; Oller et al., 2021). The fiber-reinforced polymer (FRP) sheets have various benefits over steel plates. Thus, research has been conducted to investigate the behavior of FRP externally and internally in RC beams (De Lorenzis and Nanni, 2001; Deifalla, 2020a; Kotynia et al., 2021). FRP has been used effectively in the automotive and aerospace industries for a few decades. It has been used for new structural elements in recent years, particularly in aggressive environments including but not limited to chemical

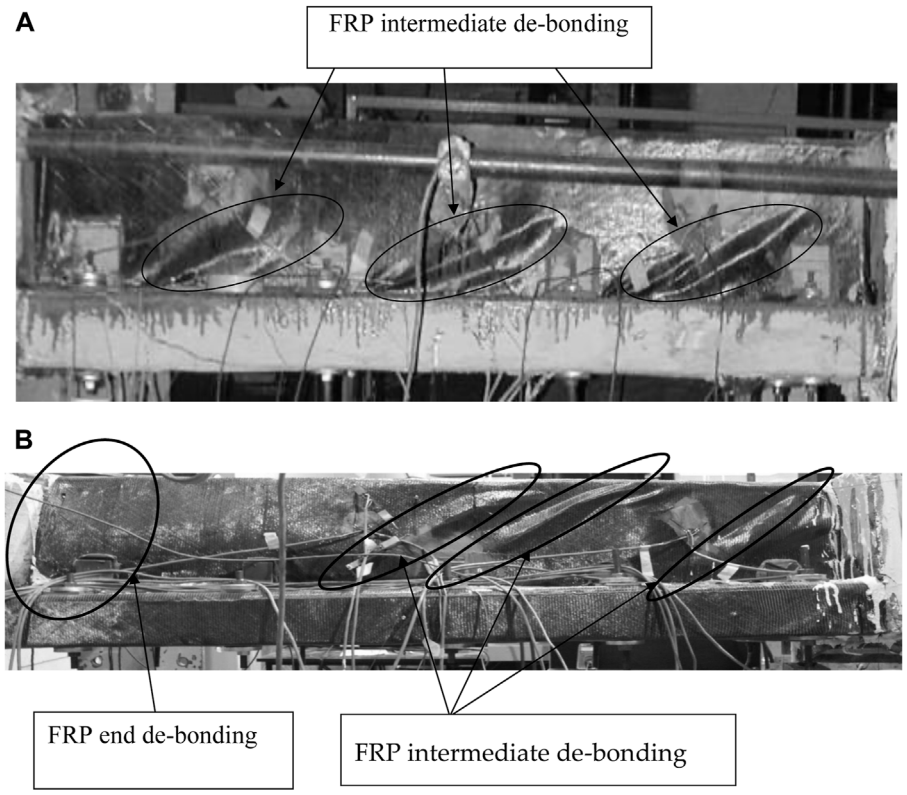

FIGURE 1
FRP end and intermediate debonding.

plants because it is corrosion free (Deifalla, 2015; Deifalla, 2020b; Deifalla et al., 2021). In addition, FRP can be used in situations where the use of steel would be impossible or impractical (Hassan and Deifalla, 2016; Salem and Deifalla, 2022). For instance, it can be formed on-site to fit any irregular shape. FRP fabrics can be wrapped around curves (i.e., beams' sides, columns' corners, or beams' soffits). It is lighter in weight than steel but has the same strength, (Deifalla et al., 2013), and it is easy to handle and cut to the required length.

Worldwide, there is a lack of consensus on the shear strength contribution of externally bonded (EB)-FRP jackets. Several design guidelines and codes exist worldwide (fib Task group 5.1, 2019; ACI Committee 440, 2017; Construction C–AC on TR for. CNR-DT 200 R1/2013, 2013; TR-55 CSTR, 2012; JSCE Japanese Society of Civil Engineers, 2000; Abuodeh et al., 2020; Ly et al., 2020; Chalioris et al., 2020; Benzeguir and Chaallal, 2021; Kim, 2021; Isleem et al., 2021). The lack of consensus is due to the following reasons:

- The shear strength and mechanism are complex.
- The premature debonding failure is difficult to predict for several EB-FRP strengthening schemes.
- The EB-FRP is linear to the brittle failure, while no yield is observed.
- The interaction between the concrete, internal steel reinforcements, and the EB-FRP reinforcement.
- The shear strengthening using EB-FRP can be executed in different patterns:

1) Fully wrapping the sheets around the cross-section (full jacket).
2) Bonding L-shaped EB-FRP sheets to the bottom or the sides of the cross-section (U-jacket).
3) Bonding EB-FRP sheets to the sides of the cross-section (side jacket).

The sheets can be adhesively bonded in a continuous or discrete configuration. However, both U-jacket and side-jacket schemes are vulnerable to premature debonding failure, which occurs once a critical shear crack opens and widens. In this case, the EB-FRP bonded length is not adequate to provide anchorage for the transfer of the tensile force between the FRP and the concrete; thus, the EB-FRP fails by debonding prematurely, which can be prevented using appropriate anchorage devices. The shear strength of EB-FRP beams can be calculated as the summation of the shear resistance of the transverse steel (if any), the concrete, and the EB-FRP. In addition, several guidelines add the resistance of the EB-FRP to the shear capacity of the un-strengthened element (fib Task group 5.1, 2019; ACI Committee 440, 2017; Construction C–AC on TR for. CNR-DT 200 R1/2013, 2013; TR-55 CSTR, 2012; JSCE Japanese Society of Civil Engineers, 2000). However, previous studies have shown that EB-FRP jackets will affect the effective stress level of internal steel. Thus, this superposition approach could lead to non-conservative results (Pellegrino and Modena, 2002; Bousselham and Chaallal, 2006; Bousselham and Chaallal, 2008; Chen et al., 2010; Pellegrino and Vasic, 2013). The lack of conservative results could be because of

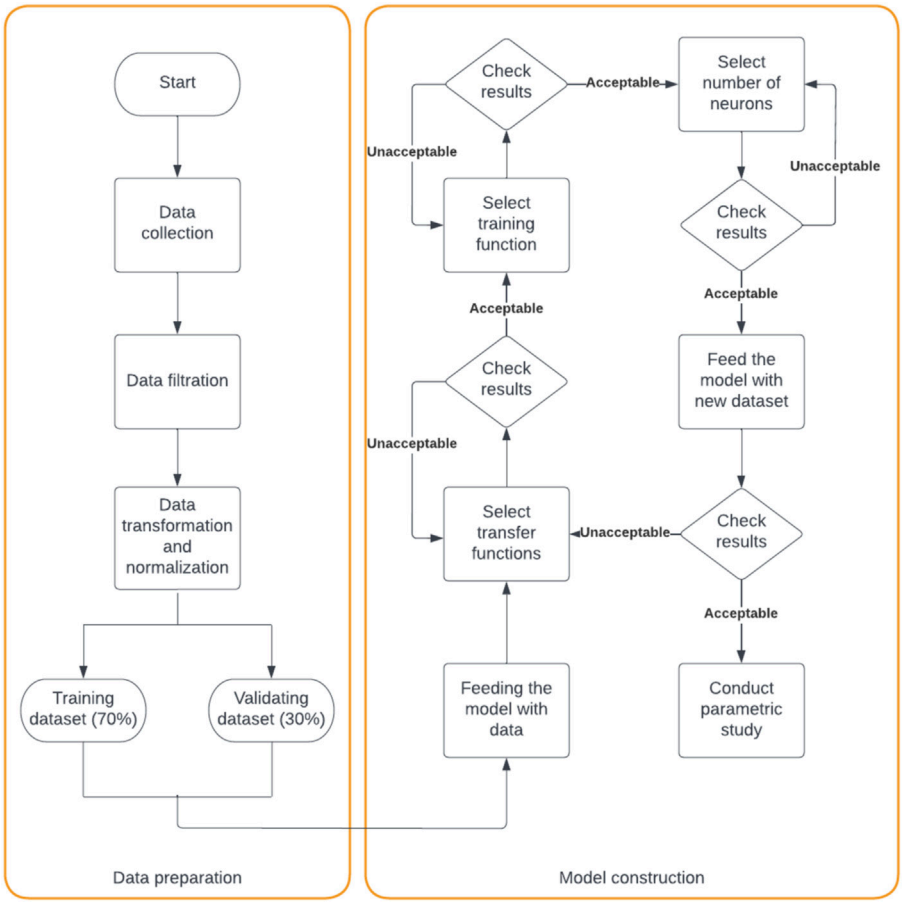

FIGURE 2
Work scheme.

changes in concrete diagonal cracking, diagonal strut orientation, or transverse reinforcement stress.

The engineering community is increasingly using EB-FRP systems to improve the strength of existing RC beams. Recent studies have led to a worldwide execution of this technique. However, debonding of EB-FRP sheets has been the main issue for EB-FRP RC beams in shear and torsion. For EB-FRP RC beams, premature failure by EB-FRP debonding is generally a sudden type of failure; therefore, for EB-FRP RC beams, debonding is an unwanted failure mode. Two types of EB-FRP debonding were observed by Deifalla (Deifalla et al., 2013), namely end or intermediate debonding, as shown in Figure 1, which are caused by either cover spalling or concrete cracking. Although beams are rarely subjected to pure shear and shear is often accompanied by flexure, beams are usually heavily reinforced in order to avoid the effect of flexure.

The anchorage systems of EB-FRP jackets have no rational and reliable design rules. Thus, FRP design codes and guidelines specify that physical experimental testing should be conducted as a supplement for the implementation of these machine-learning techniques(fib Task group 5.1, 2019; ACI Committee 440, 2017; Construction C–AC on TR for. CNR-DT 200 R1/2013, 2013; TR-55 CSTR, 2012; JSCE Japanese Society of Civil Engineers, 2000). However, the procedure for experimental testing is not specified by existing guidelines and design codes (Pellegrino and Modena, 2002; Sas et al., 2009a; Pellegrino and Vasic, 2013). In addition, because of the time and budget constraints of projects, it is rarely possible to perform such testing. Thus, the potential benefits of FRP anchorages are usually substituted by using an additional increase in the EB-FRP, which is not economical. The experimental studies conducted in this area are limited by case dependency and usually use a small-scale model; thus, it has a small impact in understanding the behavior of the FRP.

The contribution of EB-FRP to the resistance of RC beams is affected by EB-FRP type, direction, arrangement, and allocation. The efficacy of EB-FRP is boosted by attaching the EB-FRP in a direction parallel to the maximum tensile stress. Therefore, EB-FRP arrangements change the shear capacity of strengthened RC beams. A comprehensive investigation into the shear strength of EB-FRP RC beams is rare, and many queries regarding the mechanisms involved are not yet resolved. With the following exception, many researchers have proposed idealized models similar to that used for the internal steel stirrups, which is

TABLE 1 Statistical measures for all parameters.

	Minimum	Maximum	Average	Stdev
X1	70	600	189	84
X2	102	720	336	119
X3	85	660	291	107
X4	600	6400	2205	1012
X5	1.3	6.9	2.85	0.74
X6	4	63.4	27.37	11.16
X7	0.75	7.54	2.89	1.41
X8	0.02	0.84	0.10	0.14
X10	89	720	319	121
X11	1	300	47	75
X12	0.044	4000	223	575
X13	1	500	99	134
X14	0.0029	0.0895	0.0042	0.0084
X15	20	90	80	19
X16	112	4840	3112	1108
X17	5	392	202	85
X18	6.6	47.4	16.6	6.3
X19	3	494	69	64

only valid if the shear contribution of EB-FRP comes from the tensile fiber capacity at a strain close to the ultimate tensile strain of the EB-FRP.

If full FRP wrapping is not feasible, to achieve the full design capacity, anchorage systems can be used for EB-FRP-strengthened beams using FRP (Mofidi and Chaallal, 2011a; Mofidi and Chaallal, 2014). The European fib (fib Task group 5.1, 2019) code suggests that anchorage systems should be at the compressive zone of the EB-FRP RC beams; however, no further details were provided. On the other hand, the ACI (TR-55 CSTR, 2012) indicated that anchorage systems at the termination points of EB-FRP will produce larger tensile stress transfer. However, the efficiency of these anchorage systems and the developed level of tensile stress before failure should be validated using experimental testing of a scaled model before execution (TR-55 CSTR, 2012). A study by Mofidi (Mofidi and Chaallal, 2011a; Mofidi and Chaallal, 2011b; Mofidi and Chaallal, 2014) concluded that experimental testing is needed to validate the proposed anchorage factors for the end-anchorage systems. Kalfat (Kalfat et al., 2013) demonstrated the validity of upgrading the shear strength with anchoring systems for EB-FRP materials. However, there remains a lack of sufficient research in this area. A more recent review by Godat (Godat et al., 2020) has shown that further research is essential to enhance the reliability of the shear strength predictions of EB-FRP RC beams. The interaction between the FRP shear strength, strain, and parameters is required for robust design equations.

Machine learning is being implemented in various applications because it can capture the actual behavior for complex problems involving many parameters (Deifalla, Salem). This research investigation aims at developing a reliable and accurate strength model based on advanced machine-learning techniques. An extensive database was collected and used to train and validate the model, as shown in Figure 2. A machine learning model was developed and compared with available models from the existing literature. Concluding remarks were outlined.

2 Research significance

The reliability of the existing strength models for concrete elements under shear is being questioned by many researchers, where investigations have shown a significant discrepancy and large scattering between the measured and predicted strength of

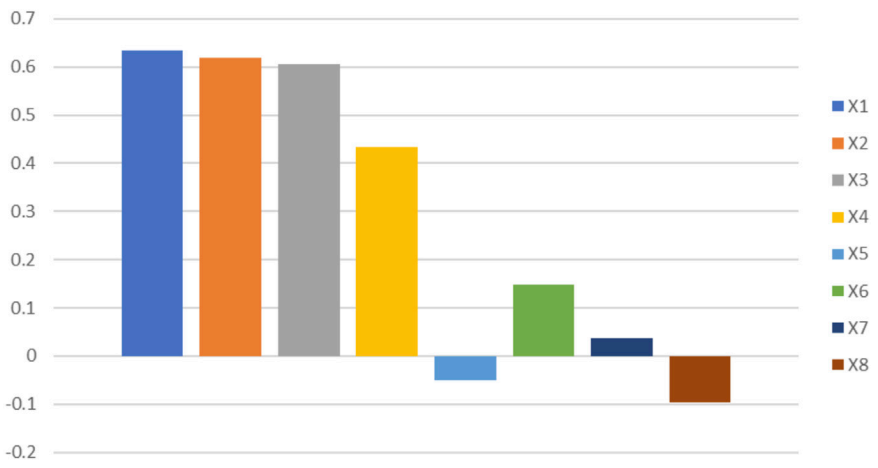

FIGURE 3
Results of Pearson variables study on FRP shear strength.

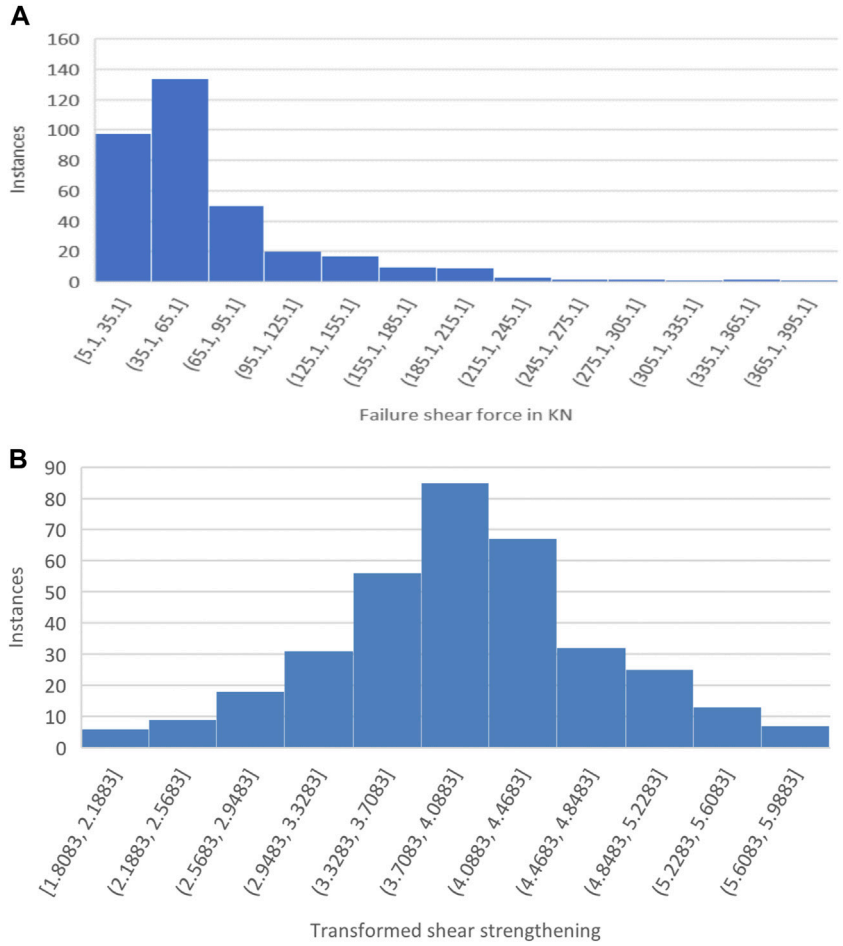

FIGURE 4
Distribution of the shear force failure **(A)** before and **(B)** after transformation.

the existing models, especially those used in current design guidelines (Colotti and Swamy, 2011; Lima and Barros, 2011; Isleem et al., 2022; Qaidi et al., 2022; SuhadAbd et al., 2022; Isleem et al., 2023). Thus, existing models are deemed to be inadequate and need further improvement. That shortcoming has motivated comprehensive investigations in all aspects related to shear. This current study investigates the implementation of artificial intelligence in the shear of strengthened concrete elements, which could guide further developments of design codes and mechanical models.

3 Previous studies

Relatively limited detailed studies have investigated the shear strength of RC beams; in addition, many questions regarding the strength mechanism, especially the usage of anchorage devices, are yet to be resolved. Many studies have idealized the EB-FRP jacket in a manner similar to that of steel shear reinforcements with the assumption that the contribution of the EB-FRP to shear capacity arises from the capacity of the EB-FRP to resist tensile stresses at a strain, which is less than or equal to the FRP ultimate tensile strain (Salem and Deifalla, 2022; Deifalla et al., 2013; fib Task group 5.1, 2019). Numerous experimental tests have been conducted in this field of research, and existing design codes and guidelines were available for designing EB-FRP elements (fib Task group 5.1, 2019; ACI Committee 440, 2017; Construction C–AC on TR for. CNR-DT 200 R1/2013, 2013; TR-55 CSTR, 2012; JSCE Japanese Society of Civil Engineers, 2000). Both the empirical evidence and code suggested that performance enhancement can be attained by using the EB-FRP; however, more detailed work is required to quantify its contribution to the strength of the beams under shear (fib Task group 5.1, 2019; ACI Committee 440, 2017; Construction C–AC on TR for. CNR-DT 200 R1/2013, 2013; TR-55 CSTR, 2012; JSCE Japanese Society of Civil Engineers, 2000). Many parameters influence the effective FRP strain for shear-strengthened RC beams, including but not limited to: 1) The type of fibers in terms of Young's Modulus; 2) The fiber orientation in terms of the inclination angle to the beam longitudinal axis; 3) The fiber distributions in terms of the number of plies and thickness of the FRP fabrics; 4) The FRP

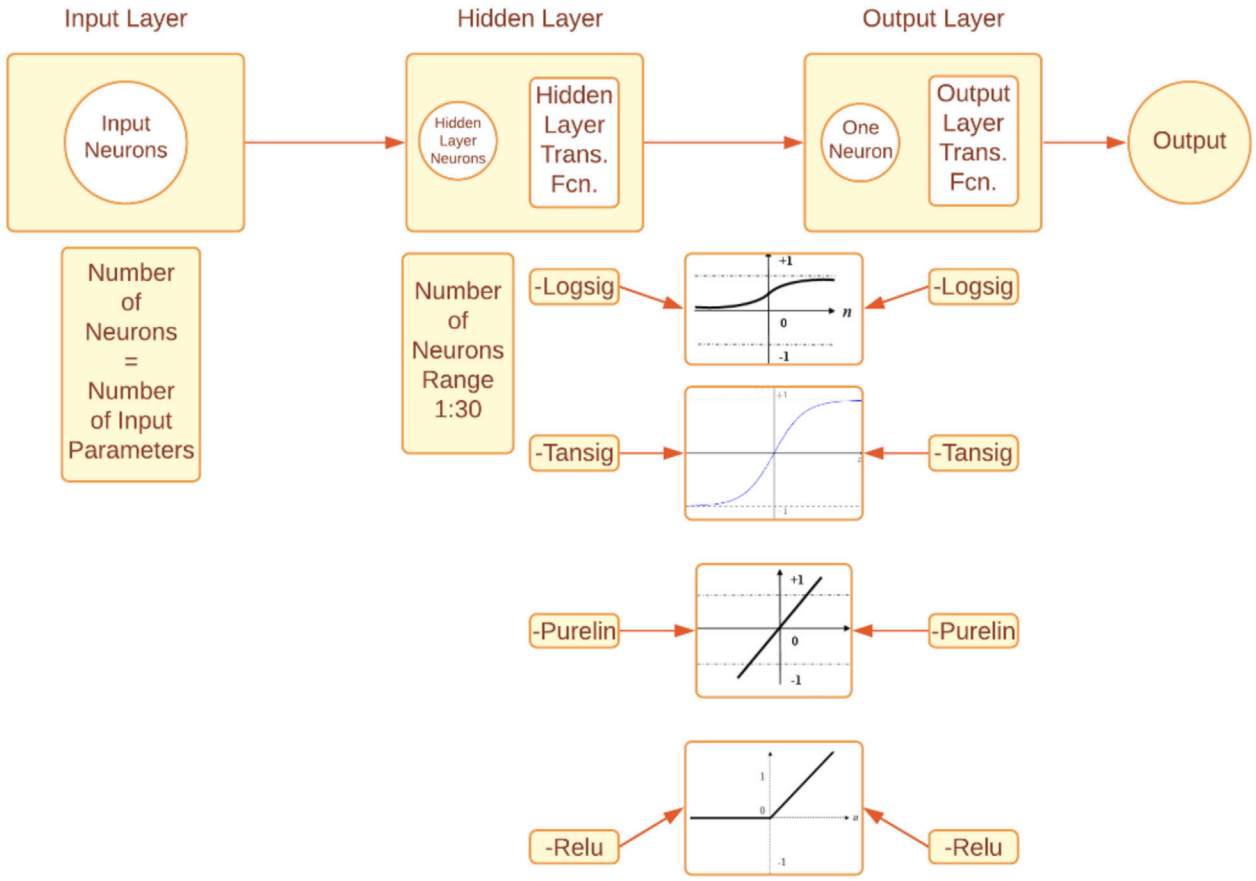

FIGURE 5
Combination of different model parameters.

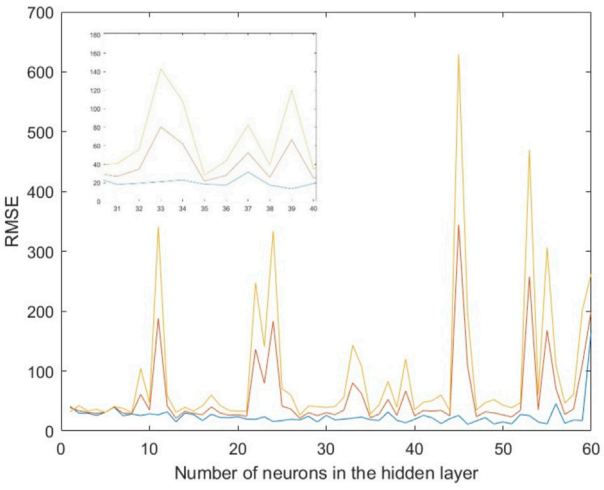

FIGURE 6
Number of neurons in the hidden layer *versus* RMSE.

bond schemes in terms of the sides the FRP is bonded to (i.e., side bonding U-jacket, and full wrapping); 5) The concrete compressive strength; 6) The usage of anchorage devices.

4 Experimental database

An extensive database of 200 beams collected from existing literature was strengthened using an EB-FRP jacket under shear. The database contains results from more than 80 experimental studies. In addition, this database includes EB-FRP beams available in existing literature (Pellegrino and Vasic, 2013; Colotti and Swamy, 2011; Sas et al., 2009b; Kotynia, Oller, Mari, Kaszubska). Although the data is available in existing databases, all data was validated using the original study.

Collected parameters were related to the beam and the FRP jacket as follows: Width of beam cross-section (X1), beam height (X2), the effective depth of beam cross-section (X3), beam span (X4), shear span to depth ratio (X5), concrete compressive strength (X6), steel flexure reinforcement ratio (X7), steel shear reinforcement ratio (X8), strength technique (X9), FRP jacket height (X10), the width of FRP jacket (X11), the thickness of FRP jacket (X12), spacing between FRP strips (X13), FRP reinforcement ratio (X14), angle of fiber orientation (X15), ultimate stress of FRP in GPa (X16), FRP young's modulus in GPa (X17), FRP rupture strain (X18), and shear strength in kN (X19). Table 1 shows the statistical measures for all parameters.

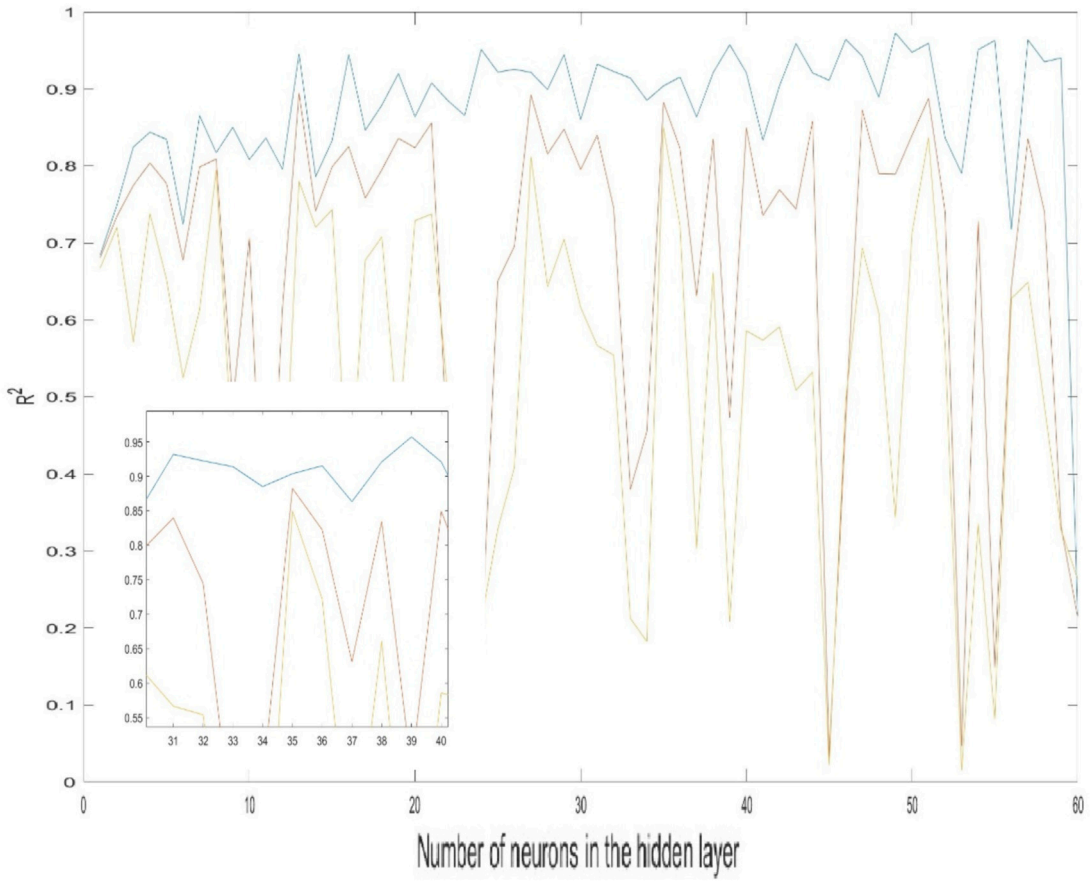

FIGURE 7
Number of neurons in the hidden layer *versus* R^2.

5 Parameters selection

Pearson parametric method was used to determine the influence of beam details on the FRP shear strength, as shown in Figure 3. The selected parameters included X1, X2, and X3, while parameters X4, X5, X6, X7, and X8 were not chosen as they had a lower Pearson coefficient. For a more efficient and faster training and validating process, the input parameters have been normalized to be between zero and one, according to Equation 1, while FRP's shear strength (model's output) has been transformed according to Equation 2 for better output distribution, as shown in Figure 4.

$$X_{i,norm} = \frac{X_i - X_{min}}{X_{max} - X_{min}} \quad (1)$$

where i is the number index for each input parameter, $X_{i,norm}$ is the normalized value for the input parameter; X_i is the value of the input parameter before normalization; X_{max} and X_{min} are the values of the maximum and minimum values of the input parameter X_i.

$$S^T = ln(S + 1) \quad (2)$$

S is the value of the added shear strength by FRP in kN while S^T is its transformed value; the input parameter for the proposed model data has been filtered and transformed to follow a normal distribution curve for a better training process to build the model, as shown in Figure 4.

6 Model development

A script has been developed to generate more than 6750 different artificial neural network (ANN) models to compare and boost the developed model performance using MATLAB. In addition, different combinations of various parameters have been tested, as shown in Figure 5.

During the model construction, the transfer function of the hidden and output layers were the first parameters to be determined. Then, the training function and the number of neurons in the hidden layer were optimized by plotting the number of neurons *versus* the correlation coefficient (R^2) and root mean square error (RMSE), as shown in Figures 6, 7.

The number of neurons was optimized to be 35 neurons in the hidden layer, while the transfer functions were TANSIG and

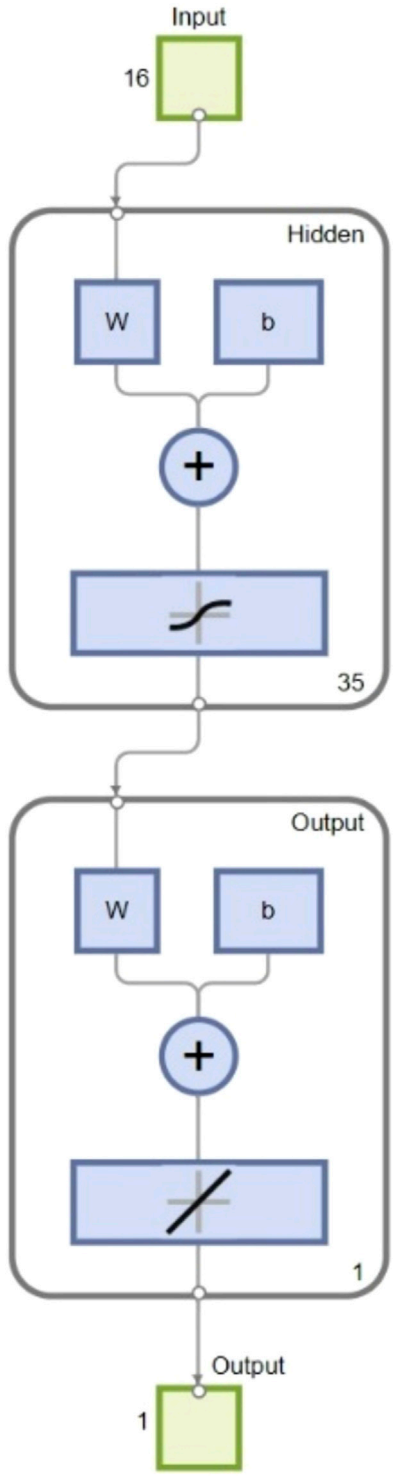

FIGURE 8
The proposed ANN model architecture.

PURELIN for the hidden and output layers, respectively (Figure 8). Based on the constricted model, a mathematical equation has been developed to predict the shear strength added by the FRP (Equation 3).

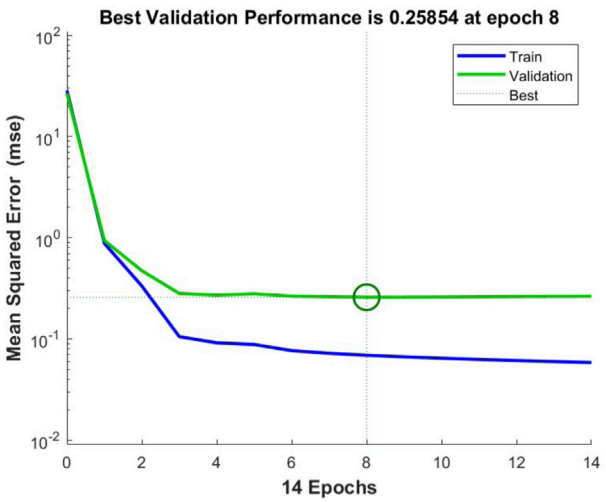

FIGURE 9
Epochs *versus* Mean square error.

$$S = Exp\left[PURELIN\left[\sum_{i=1}^{N} W_{2i}TANSIG\left(\sum_{j=1}^{J} W_{1j} \times \frac{X_j - X_{avg}}{X_{max} - X_{min}} + b_{1i}\right)\right] + b_2\right] - 1 \quad (3)$$

where Exp is the exponential function, N is the number of neurons in the hidden layer, which has been optimized to be 35 neurons; W2i is the weight of the output layer; J is the number of input variables; W1 is the weight of the hidden layer; Xj is the value of the input variable (strength configuration, X1, X2, X3, X9, X10, X11, X12, X13, X14, X15, X16, X17, and X18); b1 is the bias of the hidden layer; b2 is the bias of the output layer.

The values of the input parameters go through the input layer to be multiplied by the weights that connect the input layer with the hidden layer. The bias of the first layer is added to the multiplication results before they transform through the activation function of the hidden layer (TANSIG). The outcome of the transfer function is then multiplied by the weights of the output layer and added to the bias of the hidden layer. Finally, the product goes through the output layer's transfer function (PURELIN) to give the predicted value of the shear strength in kN.

Later, the performance of the ANN model was boosted by 1000 epochs; the best model outcome was found to be at the 8th epoch; then, the validation check stopped the training process at the 14th epoch, as shown in Figure 9.

7 Model validation

After the model construction, the model was used to predict the shear strength for FRP in kN; then, the predicted value *versus* the actual values was plotted, as shown in Figure 10. In addition, statistical tests have been conducted to test the accuracy of the newly developed model. Training, validating, and overall datasets have been evaluated using average relative error (ARE), average

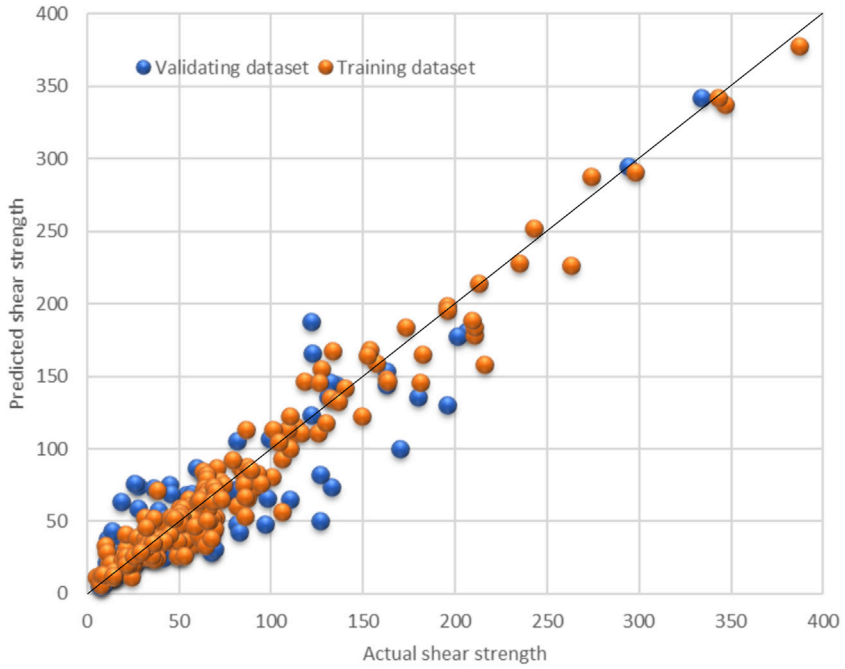

FIGURE 10
Actual *versus* predicted shear strength value in kN.

absolute relative error (AARE), relative deviation (RD), standard deviation (SD), RMSE, and R2 according to equations three to eight. Also, a comparison between the actual and predicted values is presented in Figure 11 Figure 12. Moreover, the ratio between the predicted and actual values has been calculated according to Equation 9 for both the training and validating datasets and is presented in Figure 13.

$$ARE = \left(\frac{1}{N} \times \sum_{i=1}^{N} \frac{S^{Predicted} - S^{Actual}}{S^{Actual}}\right) \times 100 \quad (4)$$

$$AARE = \left(\frac{1}{N} \times \sum_{i=1}^{N} \left|\frac{S^{Predicted} - S_i^{Actual}}{S_i^{Actual}}\right|\right) \times 100 \quad (5)$$

$$RD = \frac{S^{Predicted} - S^{Actual}}{S^{Actual}} \times 100 \quad (6)$$

$$SD = \left\{\frac{1}{N-1} \times \sum_{i=1}^{N} \left(\frac{S^{Predicted} - S^{Actual}}{S^{Actual}}\right)^2\right\}^{0.5} \quad (7)$$

$$RMSE = \left\{\frac{1}{N} \times \sum_{i=1}^{N} \left(S^{Predicted} - S^{Actual}\right)^2\right\}^{0.5} \quad (8)$$

$$R^2 = 1 - \frac{\sum_{i=1}^{N} \left(S^{Predicted} - S^{Actual}\right)^2}{\left(S_{Actual}^{Mean} - S^{Actual}\right)^2} \quad (9)$$

$$Ratio = \frac{F^{Predicted}}{F^{Actual}} \quad (10)$$

where N is the number of tested data points, $S^{Predicted}$ is the predicted shear strength value in kN; S^{Actual} is the corresponding actual shear strength value in kN; S_{Actual}^{Mean} is the average of the actual shear strength value in kN.

The model showed excellent performance as it has R^2 and RMSE of 0.91 and 17.45 for the overall dataset, respectively. The R^2, RMSE, ARE, AARE, and SD statistical tests are summarized and listed in Figures 13–17, respectively. In addition, the results of the different datasets were compared to check the fitting of the proposed model, while RD *versus* the actual shear strength was plotted and is presented in Figure 18.

After validating the model and demonstrating its credibility in predicting the shear strength value added by the FRP, the model was then used to conduct a parametric study to study the impact of each parameter individually. When investigating a certain parameter, the rest of the variables were set to a constant at their average value while changing the value of the tested parameter. X10, X14, X15, and X17 were investigated, and their values *versus* the model outcome were plotted, as shown in Figures 19–22.

8 Comparisons between the proposed model and existing machine models

In 2020, machine learning was used to predict the FRP shear strength capacity with a certain accuracy [50]. In this work, the proposed model performance has been evaluated and compared to the models from the existing literature. R^2 is one of the

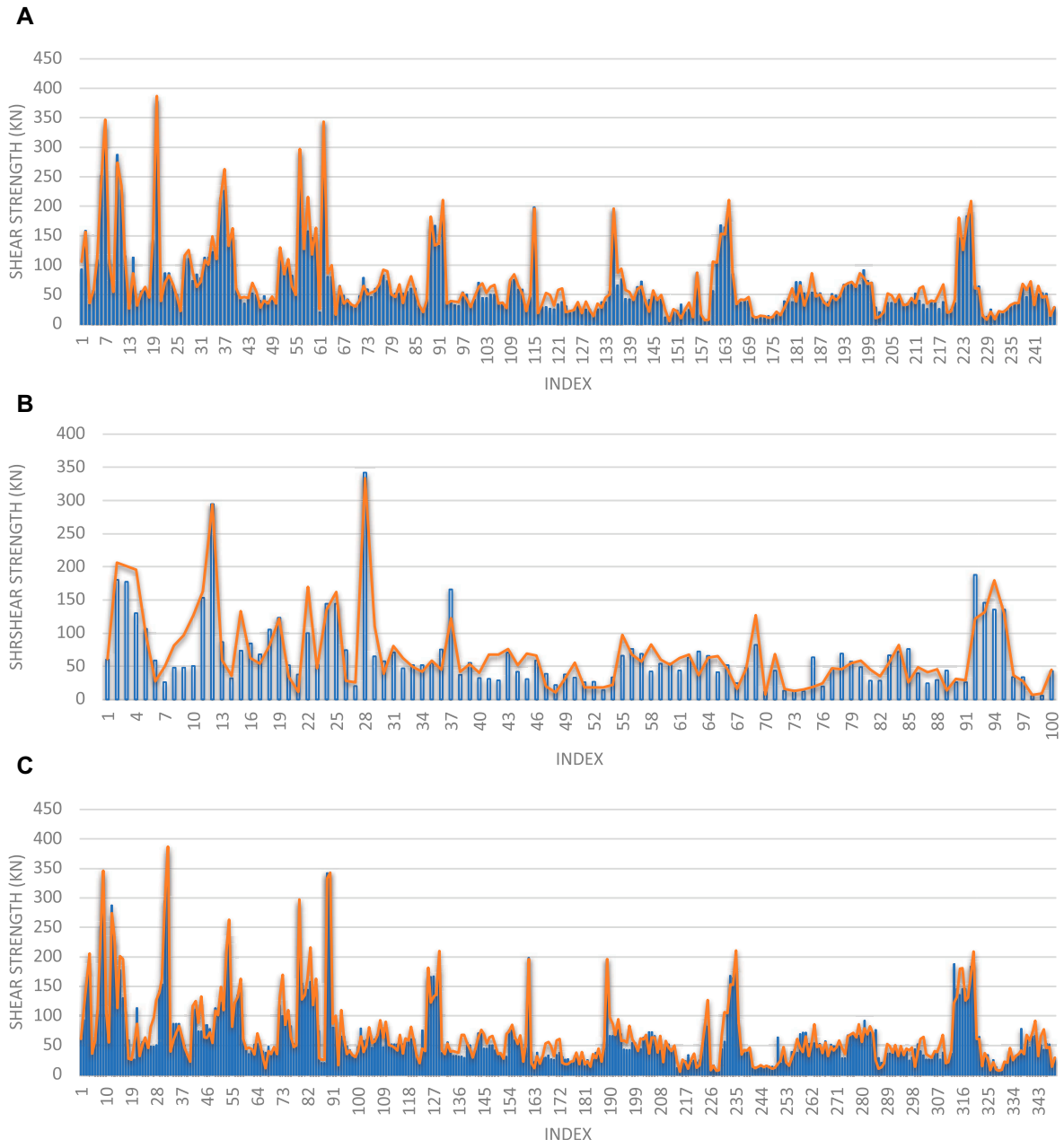

FIGURE 11
Comparing the actual and predicted shear strength values in kN for the **(A)** training dataset, **(B)** validating dataset, and **(C)** overall dataset.

essential statistical parameters that can determine the accuracy of any model regardless of the values of the used data. R^2 for the overall datasets and the number of data used in developing the new model have been compared with their corresponding values from the previous model, as shown in Figure 23. The model from this work was constructed using a larger number of dataset points, giving the model a wide range of applicability. In addition, R^2 shows better performance and more accurate results than the models from the existing literature for all datasets.

9 Comparison between the existing design codes and guidelines and the proposed model

Table 2 shows the statistical measures for various selected models' safety ratios, namely average and coefficient of variation. The safety ratio was defined as the ratio between the measured and the calculated FRP contribution. At the same time, selected models include the proposed model, the Fib 90 (fib Task group 5.1, 2019), the ACI (ACI Committee 440, 2017), the CNR (Construction C–AC

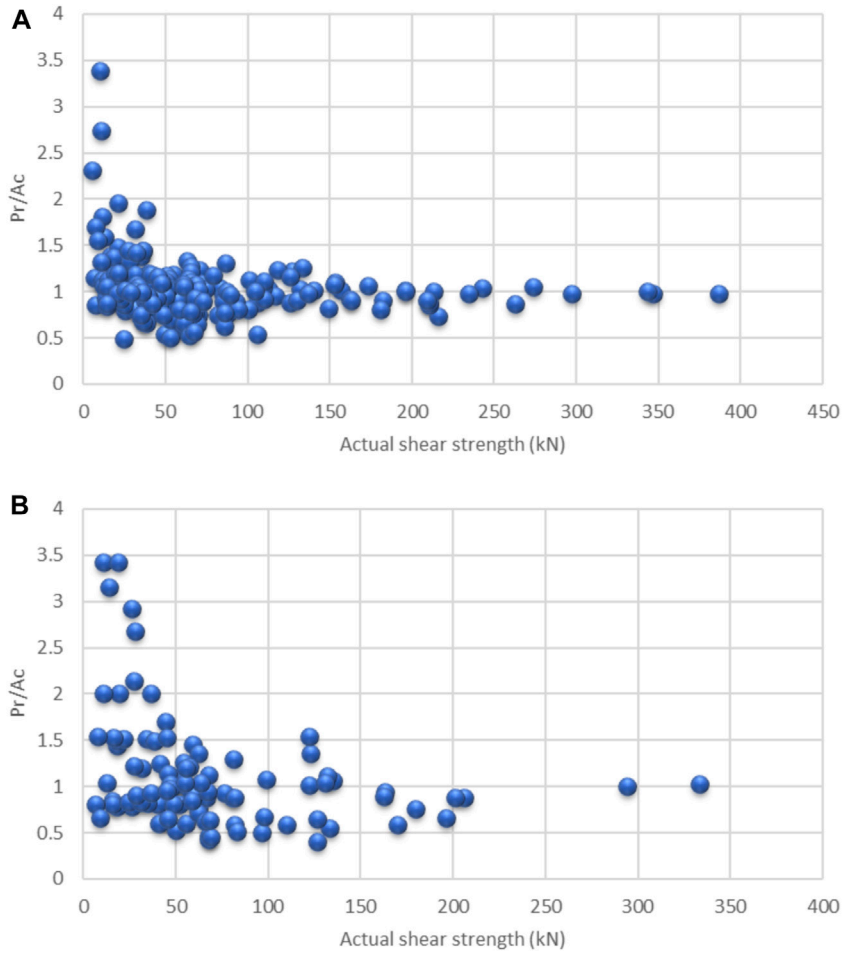

FIGURE 12
The ratio between predicted to actual shear strength *versus* the actual shear strength value in kN for the **(A)** training dataset and **(B)** validating dataset.

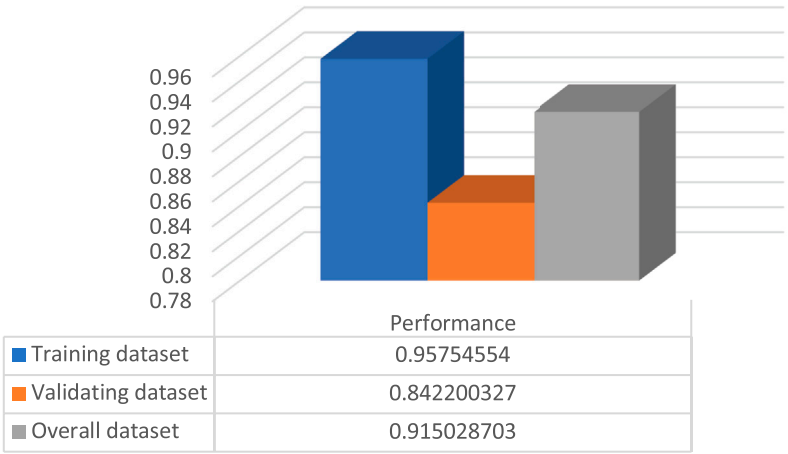

FIGURE 13
R^2 for training, validating, and overall datasets.

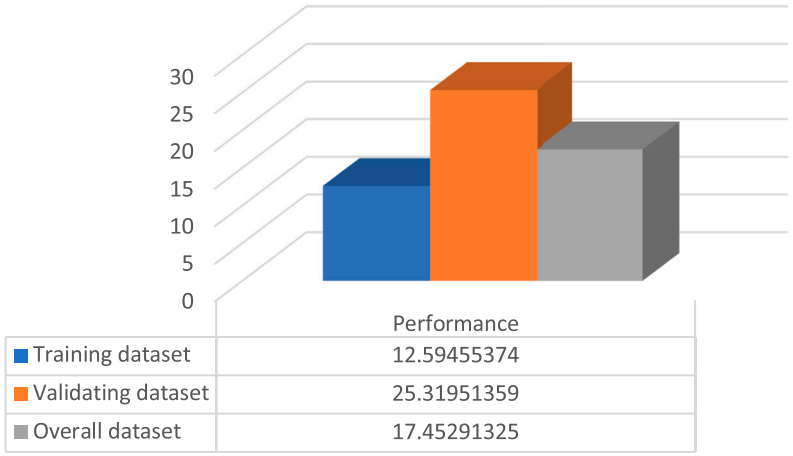

FIGURE 14
RMSE for training, validating, and overall datasets.

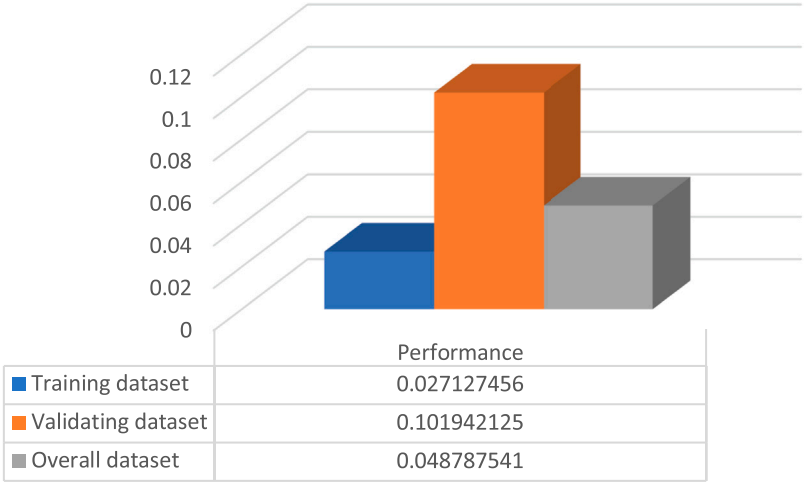

FIGURE 15
ARE for training, validating, and overall datasets.

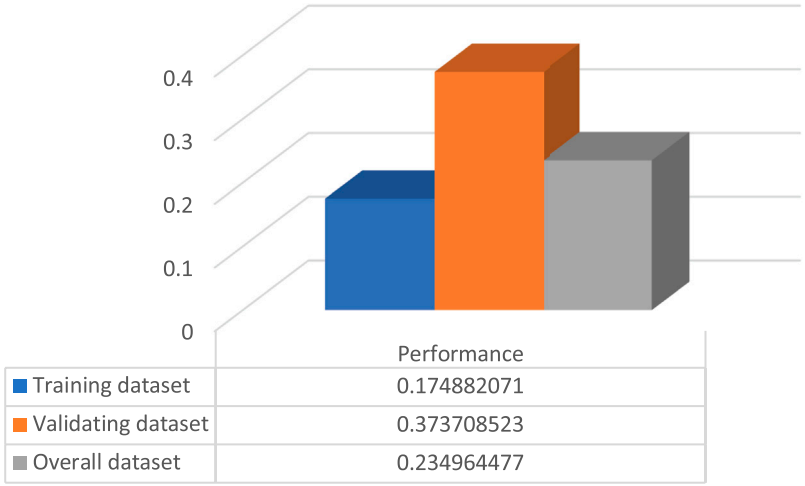

FIGURE 16
AARE for training, validating, and overall datasets.

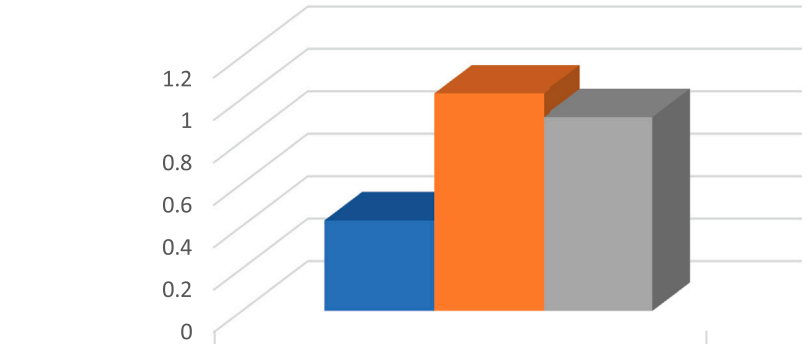

	Performance
Training dataset	0.426344956
Validating dataset	1.024556902
Overall dataset	0.912735053

FIGURE 17
SD for training, validating, and overall datasets.

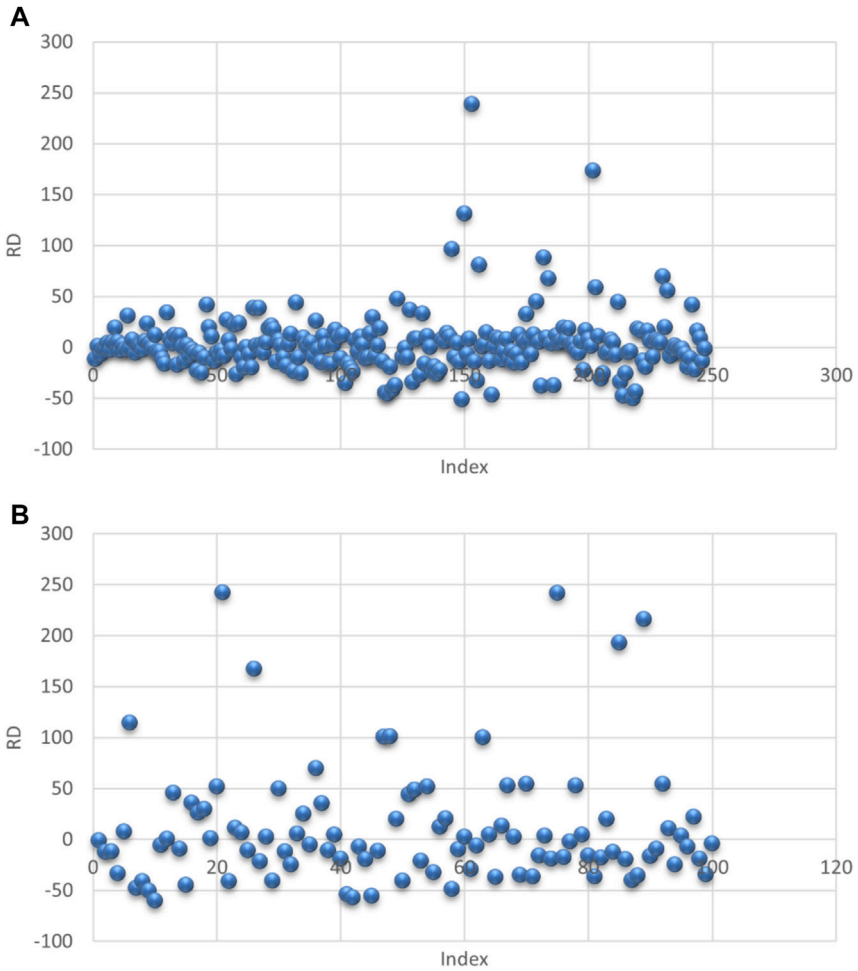

FIGURE 18
RD *versus* the testing point index for **(A)** training and **(B)** validating datasets.

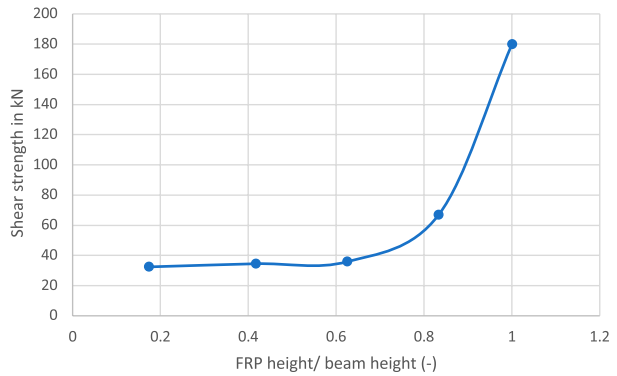

FIGURE 19
The effect of X10 on shear strength value.

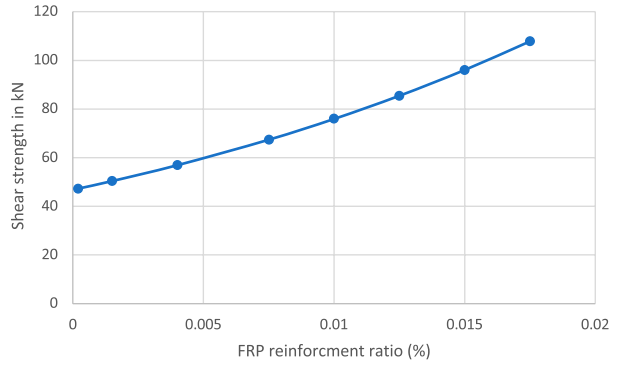

FIGURE 20
The effect of X14 on the shear strength.

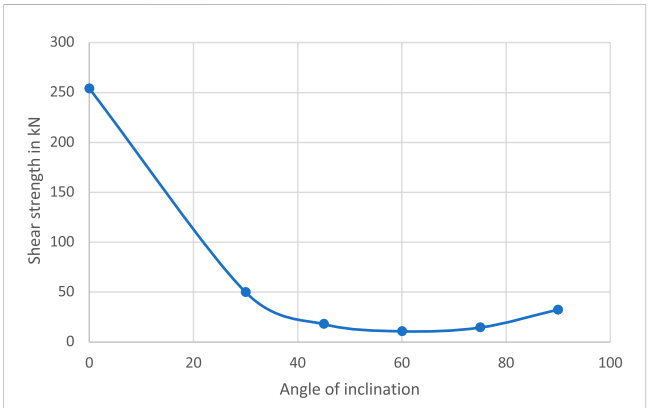

FIGURE 21
The effect of X15 on shear strength value.

on TR for. CNR-DT 200 R1/2013, 2013), the TR-55 (TR-55 CSTR, 2012), and the JSCE (JSCE Japanese Society of Civil Engineers, 2000). The proposed model captured the behavior of FRP-strengthened beams and precited the FRP contribution accurately and consistently. The range of the average was from 0.98 to 1.14, and the range of the coefficient of variation was from 24% to 36%. The range of the selected models' average was from 0.48 to 4.46, and the range of the coefficient of variation was from 35% to 95%.

10 Recommendations

Based on the findings from this current study, the following is recommended:

- The use of artificial intelligence methods to predict the true strength as it provides more accurate strength compared to other methods.
- The implementation of an FRP Jacket with a height of at least 80% of the element height.

11 Future studies

Based on the findings from this current study, the following are recommended for the strength modeling of shear-strengthened beams:

- Using anchorage strengthening schemes.
- Using near-surface mounted techniques.
- Using advanced materials.
- Using design equations and the relationship between parameters.

12 Conclusion

An artificial intelligence model for the shear strength of FRP-strengthened elements was proposed, which accounts for the following parameters: the width of the beam cross-section, beam height, the effective depth of beam cross-section, strength technique, FRP jacket height, the width of FRP jacket, the thickness of FRP jacket, spacing between FRP strips, angle of fiber orientation, ultimate stress of FRP, FRP young's modulus, and FRP rupture strain. The model's accuracy compared to the existing model is superior, where statistical tests R^2, RMSE, ARE, AARE, and SD were found to be 0.91, 17.45, 0.048, 0.23, and 0.91, respectively, for the overall dataset. A parametric study was conducted to study the influence of the FRP jacket height, the width of the FRP jacket, the thickness of the FRP jacket, spacing between FRP strips, angle of fiber orientation, ultimate stress of FRP, FRP young's modulus, and FRP rupture strain.

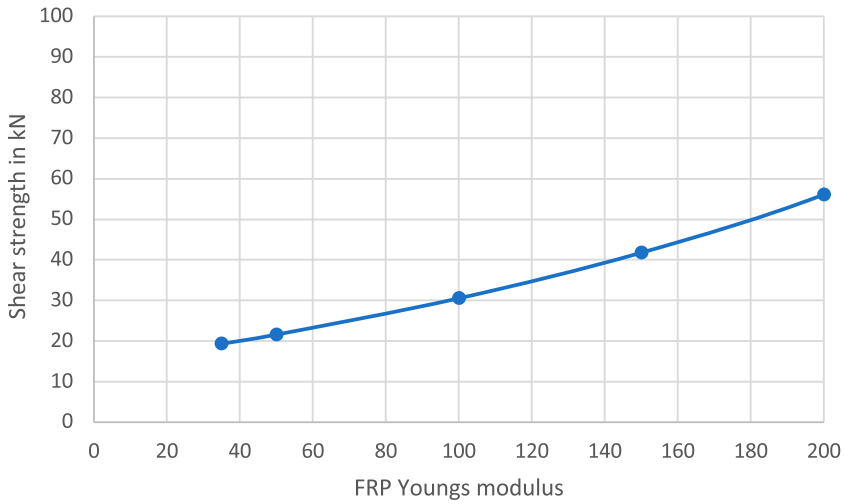

FIGURE 22
The effect of X17 on shear strength value.

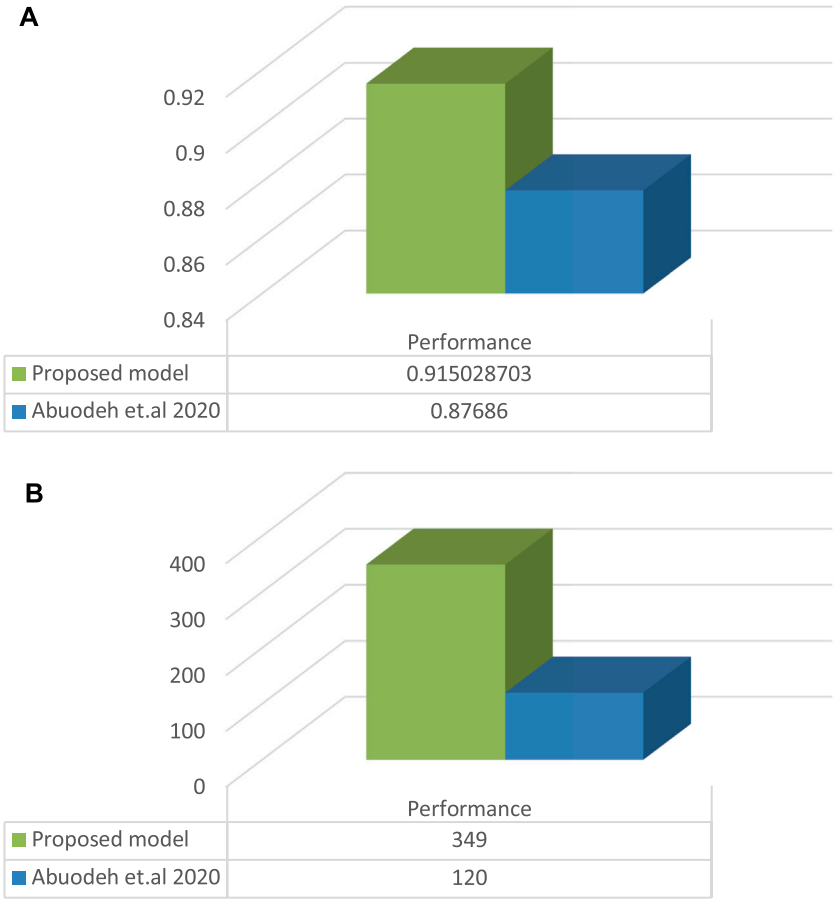

FIGURE 23
Comparison between the existing models from previous literature and the proposed model based on **(A)** R^2 and **(B)** the number of data points used.

TABLE 2 Statistical measures for proposed and selected model's a/d ≥ 2.5.

Scheme	Steel stirrups	Continuity	Proposed model		Fib 90		ACI		CNR		TR-55		JSCE	
			SR	C.O.V.	SR	C.O.V.	SR	C.O.V.	SR	C.O.V.	SR	C.O.V.	SR	C.O.V.
Wrapped	Without	Strips	0.98	24%	2.91	49%	3.85	58%	3.00	54%	3.85	58%	1.14	47%
		Continuous	1.14	33%	2.07	38%	-	-	2.15	38%	4.46	59%	0.93	37%
	With	Strips	0.98	24%	1.77	37%	2.32	49%	2.52	42%	2.49	44%	0.88	43%
		Continuous	1.14	33%	0.83	39%	-	-	1.03	43%	1.27	58%	0.43	33%
U-jacket	Without	Strips	1.08	31%	1.50	51%	1.64	64%	1.72	53%	1.58	49%	0.62	46%
		Continuous	1.07	36%	1.12	35%	-	-	1.05	43%	1.07	36%	0.45	36%
	With	Strips	1.08	31%	0.85	87%	1.23	62%	1.20	81%	1.10	68%	0.38	95%
		Continuous	1.07	36%	0.53	45%	-	-	0.51	43%	0.52	46%	0.19	44%
One side	Without	Strips	1.00	29%	-	-	1.34	73%	-	-	1.05	72%	0.74	51%
		Continuous	1.08	30%	-	-	-	-	-	-	0.91	49%	0.84	40%
	With	Strips	1.00	29%	-	-	1.15	72%	-	-	0.71	37%	0.61	47%
		Continuous	1.08	30%	-	-	-	-	-	-	0.41	41%	0.48	52%

Data availability statement

The datasets presented in this study can be found in online repositories. The names of the repository/repositories and accession number(s) can be found in the article/Supplementary Material.

Author contributions

Conceptualization, MG, OM, AD, and TE; methodology, MG, OM, AD, and TE; software, MG, OM, AD, and TE; validation, AD; formal analysis, MG, OM, AD, and TE; investigation, MG, OM, AD, and TE; resources, MG, OM, AD, and TE; data curation, MG, OM, AD, and TE; writing—original draft preparation, MG, OM, AD, and TE; writing—review and editing, MG, OM, AD, and TE; visualization, AD; supervision, TE and AD; funding acquisition, TE. All authors have read and agreed to the published version of the manuscript.

Conflict of interest

The authors declare that the research was conducted in the absence of any commercial or financial relationships that could be construed as a potential conflict of interest.

Publisher's note

All claims expressed in this article are solely those of the authors and do not necessarily represent those of their affiliated organizations, or those of the publisher, the editors and the reviewers. Any product that may be evaluated in this article, or claim that may be made by its manufacturer, is not guaranteed or endorsed by the publisher.

References

Construction C– AC on TR for. CNR-DT 200 R1/2013 (2013). *Guide for the design and construction of externally bonded FRP systems for strengthening existing structures*. Rome, Italy.

Abuodeh, O. R., Abdalla, J. A., and Hawileh, R. A. (2020). Prediction of shear strength and behavior of RC beams strengthened with externally bonded FRP sheets using machine learning techniques. *Compos. Struct.* 234, 111698. doi:10.1016/j.compstruct.2019.111698

ACI Committee 440 (2017). *ACI 440.2r-17, guide for the design and construction of externally bonded FRP systems for strengthening concrete structures*. Michigan, USA: Farmington Hills.

Benzeguir, Z. E. A., and Chaallal, O. (2021). Size effect in FRP shear-strengthened RC beams: Design models versus experimental data. *CivilEng* 2, 874–894. doi:10.3390/civileng2040047

Bousselham, A., and Chaallal, O. (2006). Behavior of reinforced concrete t-beams strengthened in shear with carbon fiber-reinforced polymer-an experimental study. *ACI Struct. J.* 103, 339–347.

Bousselham, A., and Chaallal, O. (2008). Mechanisms of shear resistance of concrete beams strengthened in shear with externally bonded FRP. *J. Compos Constr.* 12: 499–512. doi:10.1061/(asce)1090-0268(2008)12:5(499)

Chalioris, C. E., and Karayiannis, C. (2009). Effectiveness of the use of steel fibres on the torsional behaviour of flanged concrete beams. *Cem. Concr. Compos.* 31, 331–341. doi:10.1016/j.cemconcomp.2009.02.007

Chalioris, C. E., Zapris, A. G., and Karayannis, C. G. (2020). U-jacketing applications of fiber-reinforced polymers in reinforced concrete T-beams against shear—tests and design. *Fibers* 8, 13. doi:10.3390/fib8020013

Chen, G. M., Teng, J. G., Chen, J. F., and Rosenboom, O. A. (2010). Interaction between steel stirrups and shear strengthening FRP strips in RC beams. *J. Compos Constr.* 14, 498–509. doi:10.1061/(ASCE)CC.1943-5614.0000120

Colotti, V., and Swamy, R. N. (2011). Unified analytical approach for determining shear capacity of RC beams strengthened with FRP. *Eng. Struct.* 33, 827–842. doi:10.1016/j.engstruct.2010.12.005

De Lorenzis, L., and Nanni, A. (2001). Characterization of FRP rods as near-surface mounted reinforcement. *J. Comp. Constr.* 5 (2), 114–121. doi:10.1061/(asce)1090-0268(2001)5:2(114)

Deifalla, A. (2020). Refining the torsion design of fibered concrete beams reinforced with FRP using multi-variable non-linear regression analysis for experimental results. *Eng. Struct.* 224, 111394. doi:10.1016/j.engstruct.2020.111394

Deifalla, A., Awad, A., and El-Garhy, M. (2013). Effectiveness of externally bonded CFRP strips for strengthening flanged beams under torsion: An experimental study. *Eng. Struct.* 56, 2065–2075. doi:10.1016/j.engstruct.2013.08.027

Deifalla, A., Awad, A., Seleem, H., and AbdElrahman, A. (2020). Experimental and numerical investigation of the behavior of LWFC L-girders under combined torsion. *Structures* 26, 362–377. doi:10.1016/j.istruc.2020.03.070

Deifalla, A., Awad, A., Seleem, H., and AbdElrahman, A. (2020). Investigating the behavior of lightweight foamed concrete T-beams under torsion, shear, and flexure. *Eng. Struct.* 219, 110741. doi:10.1016/j.engstruct.2020.110741

Deifalla, A. F., Zapris, A. G., and Chalioris, C. E. (2021). Multivariable regression strength model for steel fiber-reinforced concrete beams under torsion. *Materials* 14, 3889. doi:10.3390/ma14143889

Deifalla, A., and Salem, N. M. (2022). A machine learning model for torsion strength of externally bonded FRP-reinforced concrete beams. *Polymers* 14, 1824. doi:10.3390/polym14091824

Deifalla, A. (2020). Torsion design of lightweight concrete beams without or with fibers: A comparative study and a refined cracking torque formula. *Structures* 28, 786–802. doi:10.1016/j.istruc.2020.09.004

Deifalla, A. (2015). Torsional behavior of rectangular and flanged concrete beams with FRP reinforcements. *J. Struct. Eng.* 141, 04015068. doi:10.1061/(asce)st.1943-541x.0001322

fib Task group 5.1 (2019). *FIB Bulletin 90, Externally applied FRP reinforcement for concrete structures*. Lausanne, Switzerland.

FIB. FRP Reinforcement in RC Structures (2007). *Technical report prepared by a working party of Task group 9.3; FIB bulletin 40*. Lausanne, Switzerland: International Federation for Structural Concrete, 151.

Godat, A., Hammad, F., and Chaallal, O. (2020). State-of-the-art review of anchored FRP shear-strengthened RC beams: A study of influencing factors. *Compos. Struct.* 254 112767, doi:10.1016/j.compstruct.2020.112767

Gosbell, T., and Meggs, R. (2002). in *Proceedings of the IABSE symposium* (Melbourne, Australia.*West gate bridge approach spans FRP strengthening Melbourne*

Hassan, M. M., and Deifalla, A. (2016). Evaluating the new CAN/CSA-S806-12 torsion provisions for concrete beams with FRP reinforcements. *Mat. Struct.* 49, 2715–2729. doi:10.1617/s11527-015-0680-9

Isleem, H. F., Augustino, D. S., Mohammed, A. S., Najemalden, A. M., Jagadesh, P., Qaidi, S., et al. (2023). Finite element, analytical, artificial neural network models for carbon fibre reinforced polymer confined concrete filled steel columns with elliptical cross sections. *Front. Mat.* 9, 1115394. doi:10.3389/fmats.2022.1115394

Isleem, H. F., Jagadesh, P., Qaidi, S., Althoey, F., Rahmawati, C., Najm, H. M., et al. (2022). Finite element and theoretical investigations on PVC–CFRP confined concrete columns under axial compression. *Front. Mater* 9, 1055397. doi:10.3389/fmats.2022.1055397

Isleem, H. F., Abid, M., Alaloul, W. S., Shah, M. K., Zeb, S., Musarat, M. A., et al. (2021). Axial compressive strength models of eccentrically-loaded rectangular reinforced concrete columns confined with FRP. *Materials* 14, 3498. doi:10.3390/ma14133498

JSCE Japanese Society of Civil Engineers (2000). *Recommendations for upgrading of concrete structures with use of continuous fiber sheets*.

Kalfat, R., Al-Mahaidi, R., and Smith, S. (2013). Anchorage devices used to improve the performance of reinforced concrete beams retrofitted with FRP composites: State-of-the-art review. *J. Compos. Constr.* 17 (1), 14–33. doi:10.1061/(asce)cc.1943-5614.0000276

Karayannis, G., Kosmidou, K., and Chalioris, E. (2018). Reinforced concrete beams with carbon-fiber-reinforced polymer bars—experimental study. *Fibers* 6, 99. doi:10.3390/fib6040099

Kim, S.-W. (2021). Prediction of shear strength of reinforced high-strength concrete beams using compatibility-aided truss model. *Appl. Sci.* 11, 10585. doi:10.3390/app112210585

Kotynia, R., Oller, E., Mari, A. R., and Kaszubska, M. Efficiency of shear strengthening of RC beams with externally bonded FRP materials – state-of-the-art in the experimental tests *Compos Part B Eng.*

Kotynia, R., Oller, E., Marí, A., and Kaszubska, M. (2021). Efficiency of shear strengthening of RC beams with externally bonded FRP materials – state-of-the-art in the experimental tests. *Compos. Struct.* 267, 113891. doi:10.1016/j.compstruct.2021.113891

Lima, J. L., and Barros, J. A. (2011). Reliability analysis of shear strengthening externally bonded FRP models. *Proc. Inst. Civ. Eng. Struct. Build.* 164 (SB1), 43–56. doi:10.1680/stbu.9.00042

Ly, H.-B., Le, T.-T., Vu, H.-L., Tran, V. Q., Le, L. M., and Pham, B. T. (2020). Computational hybrid machine learning based prediction of shear capacity for steel fiber reinforced concrete beams. *Sustainability* 12, 2709. doi:10.3390/su12072709

Mofidi, A., and Chaallal, O. (2011). Shear strengthening of RC beams with EB FRP: Influencing factors and conceptual debonding model. *J. Compos Constr.* 15, 62–74. doi:10.1061/(ASCE)CC.1943-5614.0000153

Mofidi, A., and Chaallal, O. (2011). Shear strengthening of RC beams with externally bonded FRP composites: Effect of strip-width-to-strip-spacing ratio. *J. Compos Constr.* 15, 732–742. doi:10.1061/(ASCE)CC.1943-5614.0000219

Mofidi, A., and Chaallal, O. (2014). Tests and design provisions for reinforced-concrete beams strengthened in shear using FRP sheets and strips. *Int. J. Concr. Struct. Mater* 8, 117–128. doi:10.1007/s40069-013-0060-1

Oller, E., Kotynia, R., and Antonio Marí, A. (2021). Assessment of the existing models to evaluate the shear strength contribution of externally bonded frp shear reinforcements. *Compos. Struct.* 264, 113641. doi:10.1016/j.compstruct.2021.113641

Pellegrino, C., and Modena, C. (2002). Fiber reinforced polymer shear strengthening of reinforced concrete beams with transverse steel reinforcement. *J. Compos Constr.* 6: 104–111. doi:10.1061/(asce)1090-0268(2002)6:2(104)

Pellegrino, C., and Vasic, M. (2013). Assessment of design procedures for the use of externally bonded FRP composites in shear strengthening of reinforced concrete beams. *Compos Part B Eng.* 45, 727–741. doi:10.1016/j.compositesb.2012.07.039

Qaidi, S., Al-Kamaki, S., Al-Mahaidi, R., Mohammed, A. S., Ahmed, H. U., Zaid, O., et al. (2022). Investigation of the effectiveness of CFRP strengthening of concrete made with recycled waste PET fine plastic aggregate. *PLOS ONE* 17 (7), e0269664. doi:10.1371/journal.pone.0269664

Salem, N. M., and Deifalla, A. (2022). Evaluation of the strength of slab–column connections with FRPs using machine learning algorithms. *Polymers* 14, 1517. doi:10.3390/polym14081517

Sas, G., Täljsten, B., Barros, J., Lima, J., and Carolin, A. (2009). Are available models reliable for predicting the FRP contribution to the shear resistance of RC beams? *J. Compos Constr.* 13, 514–534. doi:10.1061/(ASCE)CC.1943-5614.0000045

Sas, G., Täljsten, B., Barros, J., Lima, J., and Carolin, A. (2009). Are available models reliable for predicting the FRP contribution to the shear resistance of RC beams. *J. Compos. Constr.* 13, 514–534. doi:10.1061/(ASCE)CC.1943-5614.0000045

SuhadAbd, M., Mhaimeed, I. S., Tayeh, B. A., Mohammed Najm, H., and Qaidi, S. (2022). Flamingo technique as an innovative method to improve the shear capacity of reinforced concrete beam. *Case Stud. Constr. Mater.* 17 (2022), e01618. ISSN 2214-5095. doi:10.1016/j.cscm.2022.e01618

TR-55 CSTR (2012). *Design guidance for strengthening concrete structures using fiber composite materials*. London, Great Britain.

Whittle, R. *Failures in concrete structures—case studies in reinforced and prestressed concrete; FL 33487-2742*; CRC Press: Boca Raton, FLorida, USA; Taylor and Francis Group, Abingdon, UK, 2013; 140 pp.

Frontiers in Materials

Investigates the discovery and design of materials for future application

A multidisciplinary journal that explores the breadth of materials science, engineering and mechanics - from carbon-based materials to smart materials.

Discover the latest Research Topics

See more →

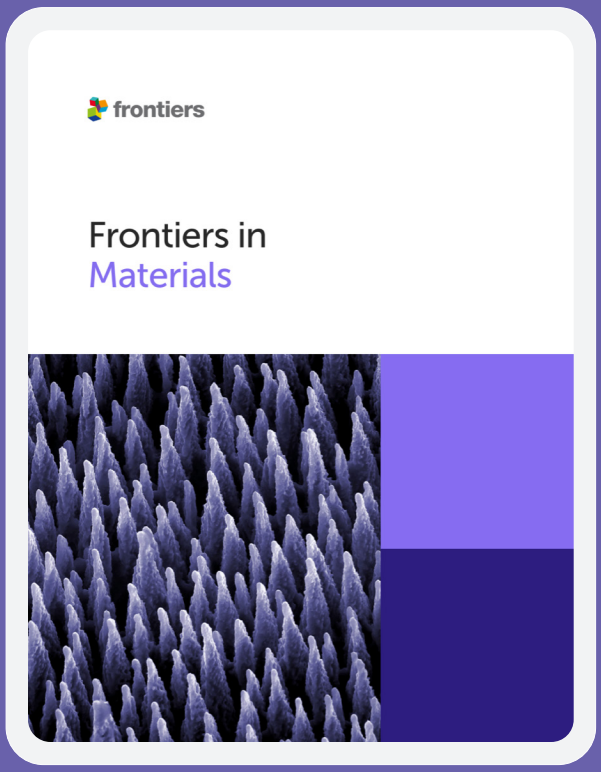

Frontiers

Avenue du Tribunal-Fédéral 34
1005 Lausanne, Switzerland
frontiersin.org

Contact us

+41 (0)21 510 17 00
frontiersin.org/about/contact